東北医科薬科大学

TOHOKU MEDICAL AND PHARMACEUTICAL UNIVERSITY

東北医科薬科大学　分子生体膜研究所年報

二〇二四年度【令和６年度】

# 東北医科薬科大学
# 分子生体膜研究所年報

## 2024年度研究成果報告書

2024 Annual Report of
Institute of Molecular Biomembrane and Glycobiology

目次

■ 巻頭言 …… 1

■ 箱守仙一郎賞 ……..… 3
「箱守仙一郎賞規約」
「第 8 回箱守仙一郎賞（2024 年度） 優秀論文賞」

■ 研究報告 …… 9

＜細胞制御学部門＞
「がんや免疫・炎症反応における糖鎖発現とその意義」
顧 建国、福田 友彦、伊左治 知弥

＜分子認識部門＞
「レクチンの抗腫瘍メカニズムの解明と糖脂質のかかわり 2024」
細野 雅祐、菅原 栄紀、立田 岳生

＜糖鎖構造生物学部門＞
「糖鎖の立体構造・ダイナミクスと相互作用に着目した糖鎖機能の解明」
山口 芳樹、真鍋 法義、大野 詩歩

＜機能病態分子部門＞
「糖脂質生合成に関わる糖転移酵素の新規バリアントの機能的評価」
稲森 啓一郎

＜免疫学部門＞
「中枢神経系自己免疫疾患モデルにおける免疫制御受容体の解析」
中村 晃、海部 知則、武田 和也

＜内科学第二(消化器内科) 部門＞

「消化器疾患の病態解明を目指して」

佐藤　賢一、廣田　衛久、小暮　高之、遠藤　克哉、上野　正道、高須　充子、支倉さやか、福士　大介、小岩井　昭信、佐々木　義輝、佐藤　麻里、吉野　祐貴、永井千菜津、金　諒、片山　智文、伊藤　豪仁、宮下　優輝

＜脳神経内科学部門＞

「神経免疫疾患の病態解析」

中島　一郎、藤盛　寿一、中村　正史、小林　理子、宮澤　康一、石垣　あや、市川　大、東野　将志、八木橋　崇仁、萩野　琢郎

＜耳鼻咽喉科学部門＞

「耳鼻咽喉科領域疾患におけるペリオスチンの発現」

太田　伸男、鈴木　貴博、佐藤　輝幸、舘田　豊

＜臨床検査医学部門＞

「造血器腫瘍の病態解明とより良い臨床検査を目指した研究」

髙橋　伸一郎、遠藤　康弘、鈴木　歩

＜神経科学部門＞

「機械学習による大規模ニューロンデータの解析」

松坂　義哉、坂本　一寛、西村　嘉晃

# 巻 頭 言

分子生体膜研究所長　顧　建国

近年の糖鎖生物学の進展により、生体膜に発現する複合糖質とレクチン、または糖鎖認識受容体の生理的・病態的意義の重要性が認識されるようになりました。さらに特定の糖鎖自身が特別な機能をもつことも知られるようになってきています。このように、「第三の生命鎖」といわれる糖鎖の構造や機能の解明は、様々な疾患の診断あるいは治療方法を確立するために非常に重要であり、ポストゲノム時代における糖鎖生物学の重要性がますます高まっています。

このような動向を踏まえ、本学では、1959年に開設された「癌研究所」を、時代の要請に応えるべく進化させ、 2006年4月に「分子生体膜研究所」として誕生させました。2024年3月まで分子生体膜研究所では、がんや生活習慣病を含む様々な疾患における糖鎖機能の解明と糖鎖構造を基盤とした診断・治療薬の開発を目指してきました。そして、2016年日本で37年ぶりとなる医学部が新設されたことを契機に、医薬連携を強化して、病態の解明や新薬の開発、様々な疾患の診断や治療法の確立を目指すため、2024年4月に既存の薬学部4部門に新たに医学部6部門を加え、計10部門で構成される新しい分子生体膜研究所が誕生しました。

4月20日には、本学小松島キャンパスにおいて、「新・分子生体膜キックオフセミナー」を開催しました。セミナー当日は「炎症と糖鎖」、「神経と糖鎖」、「がんと糖鎖」の3つのセッションで、各部部門の講演と、活発な質疑・意見交換が行われました。今後の研究における貴重な情報交換の場となった本セミナーは休日の開催にもかかわらず学長や両学部長をはじめとする多くの方々にご参加いただき、盛

**新・分子生体膜研究所キックオフセミナー**

**医・薬・生命科学の連携により糖鎖研究の実用化に向けて**

日　時　　令和６年４月20日（土）
場　所　　小松島キャンパス中央棟２階　２A

プログラム
13:00-13:05 開会の辞　顧 建国（分子生体膜研究所長）
13:05-13:20 ご挨拶　大野 勲 学長
小澤 浩司 医学部長
吉村 祐一 薬学部長

発表時間は講演20分、討論５分です。

セッション１：(13:20~15:00)　炎症と糖鎖　座長：稲森 啓一郎
顧 建国
太田 伸男
中村 晃
稲森 啓一郎

~休憩10分~
セッション２：(15:10~16:25)　神経と糖鎖　座長：山口 芳樹
藤盛 寿一
松坂 義哉
山口 芳樹

セッション３：(16:25~17:40)　がんと糖鎖　座長：細野 雅祐
佐藤 賢一
細野 雅祐
高橋 伸一郎

17:40～　閉会の辞　高橋　伸一郎（研究推進委員会委員長）

況に終わりました。特に、学生の姿多くが見られ、今後が期待されます。

さらに、二年に一度の開催となる第 3 回東北医科薬科大学と台湾アカデミアシニカ（AS）合同シンポジウムが 2025 年 2 月に AS の生物化学研究所で開催されました。本学からは大野学長をはじめ、両学部から 10 名の教員が参加しました。今後も交流を深め、糖鎖科学の研究を中心とした共同研究が進展することが期待されます。

本研究所は本学における医薬の垣根を超えて研究をより一層盛り上げていきたいと考えています。2024 年度においても国内外の研究者と積極的に共同研究を行い、素晴らしい成果を上げています。例えば、第18回東北糖鎖研究会みちのく糖鎖ポスター賞（吴天贵と王丹, D3）や第 8 回箱守優秀論文賞（徐興と孫钰涵, D3）などを受賞しました。また、機能病態分子学教室の稲森啓一郎准教授が教授に昇格され、今後のご活躍が期待されます。さらに、研究所から薬科学博士前期課程1名および後期課程4名が無事卒業しました。それぞれの新天地でご活躍されることを心よりお祈り申し上げます。

今後も研究所の皆様と共に一丸となって、さらなる飛躍を果たしていけることを願っています。

# 東北医科薬科大学分子生体膜研究所
# 「箱守仙一郎賞」（Sen-itiroh Hakomori Glycoscience Award）規約

令和 6 年 5 月 16 日
東北医科薬科大学分子生体膜研究所
顧　建国

名称　　箱守仙一郎賞

授与機関　　東北医科薬科大学分子生体膜研究所

目的　　生物系化学系を問わず広く糖鎖科学を専攻し、日夜努力を続けている東北エリアの研究者を顕彰することにより、日本の糖鎖科学研究の増進を図る。

賞の種別　　奨励賞　　1~２名　顕彰楯および副賞
優秀論文賞　若干名　顕彰楯および副賞

対象　　（１）奨励賞：東北 6 県、新潟県、群馬県および茨城県で研究に従事する応募時 45 歳までの研究者
（２）優秀論文賞：同地域で研究に従事し，申請時点で大学院生もしくは博士研究員である者
＊ いずれも指定された期間内に発表（accepted でも可）された学術論文に対して審査・授与する。
**第 8 回箱守賞の応募対象論文は、2023 年 4 月 1 日から 2024 年 3 月 31 日までに発表または受理された原著論文です。**

選考方法　　自薦および他薦によるものとし、東北糖鎖研究会世話人が審査する。
評価を点数化（次項参照）して決する。

授賞方法　　東北糖鎖研究会開催時に授賞および受賞講演を行う。

運用方法　　顕彰楯および副賞の購入費は、東北医科薬科大学の箱守賞基金を原資とし、分子生体膜研究所がこれを支弁する。

その他　　事務局は分子生体膜研究所内に置く。

審査

（1）応募資格および応募方法

東北 6 県、新潟県、群馬県および茨城県（東北糖鎖研究会エリア）で研究を行っている 45 歳以下の糖鎖科学研究者（大学院生、博士研究員は自動的に優秀論文賞へのノミネートとなる)。対象論文は、その年度内に Impact factor が付与されている英文学術雑誌（査読有）に出版、または掲載が決定されている原著論文（accepted でも可）とし、応募者が筆頭著者となっているものとする。要旨和訳と論文 PDF を添えて既定のエントリーフォームに記入してメールにて応募する。化学系・生物系は問わない。自薦および他薦どちらでも受け付ける。応募期間等についてはその都度決定し、周知する。

書類送付先：東北医科薬科大学 分子生体膜研究所　所長 顧　建国
メールアドレス：jgu@tohoku-mpu.ac.jp；　応募締め切り：6 月 10 日

（2）エントリーフォーム（別添）

（3）審査委員および審査方法

1）分子生体膜研究所所長が審査員長を務める。
2）東北糖鎖研究会世話人が審査員となる。ただし、世話人が推薦者または自薦者の所属責任者あるいは論文の共著者である場合は審査に参加しない。
3）期限内に提出された論文について事務局が一次審査（下記基礎点と推薦者の評価点の合計による）を行い、奨励賞および優秀論文賞それぞれ上位 4 報を選定する。
4）上位 4 報について審査員が下記評価項目を採点し、全員（その都度人数は異なる）の評価平均点＋基礎点＋推薦者の評価点から最上位者を受賞者として決定する。
5）最高点が複数出た場合は審査員長の判断に委ねる。

基礎点

Impact factor (IF)：　IF×　5　点

推薦者（自薦または他薦）の評価点（推薦書に記入、最高点 10 点）

共同研究者の貢献を考慮し、以下の項目を参考して該当研究に対する応募者の貢献度を客観的にみて公正に評価する。

1）　研究の考案（最高点 2 点）
2）　実験の実行（最高点 5 点）
3）　論文作成（最高点 3 点）

評価最高点

| | |
|---|---|
| 独創性 | 10 点 |
| インパクト（重要性） | 10 点 |
| 論文構成 | 10 点 |
| 将来性 | 10 点 |

## 第 8 回箱守仙一郎賞（2024 年度）

### 優秀論文賞

**１）Brain-specific glycosylation enzyme GnT-IX maintains levels of protein tyrosine phosphatase receptor PTPRZ, thereby mediating glioma growth**

Nagai K., Muto Y., Miura S., Takahashi K., Naruse Y., Hiruta R., Hashimoto Y., Uzuki M., Haga Y., Fujii R., Ueda K., Kawaguchi Y., Fujii M., and Kitazume S.

***J Biol Chem.,*** 299, 9, 105128, https://doi.org/10.1016/j.jbc.2023.105128

長井健一郎 (福島県立医科大学 脳神経外科学講座)

論文要旨

神経膠腫は中枢神経系で最も頻度の高い原発性脳腫瘍です。画像診断技術、脳神経外科手術および放射線治療の進歩にもかかわらず、悪性神経膠腫を根治させる治療法はいまだ見つかっていません。以前から、プロテインチロシンホスファターゼレセプターZ(PTPRZ)が神経膠腫で高発現しており、PTPRZ を標的とする実験で腫瘍増殖が抑制されることが報告されていました。PTPRZ は、脳に特異的な HNK-1 エピトープを付加した O-結合型マンノースコア M2 糖鎖(NHK-1-O-Man)を含む多様な糖鎖で修飾されています。しかし、これらの特徴的な糖鎖の制御や機能は不明のままでした。

まず我々は CRISPR ゲノム編集技術を用いて、ヒト神経膠腫細胞 LN-229 において PTPRZ 遺伝子を欠損させると、異種移植片マウスにおいて腫瘍増殖が著しく抑制されることを証明し、神経膠腫の治療標的としての PTPRZ の可能性を確認しました。さらに、複数の糖鎖解析から、神経膠腫患者由来の PTPRZ および異種移植片神経膠腫由来の PTPRZ は、外因性シグナルを介して NHK-1-O-Man 糖鎖を豊富に発現していることを明らかにしました。

最後に、この NHK-1-O-Man 糖鎖合成に関わる糖転移酵素である N-アセチルグルコサミン転移酵素 IX (GnT-IX)の欠損が PTPRZ タンパク質レベルを低下させることが報告されているため、LN-229 細胞で GnT-IX 遺伝子を欠損させたところ、in vitro および異種移植片マウスの両方で神経膠腫の増殖が有意に低下しました。これらの結果から、PTPRZ および PTPRZ の糖鎖修飾酵素 GnT-IX が共に神経膠腫の有望な治療標的となる可能性が期待されます。

## 2）TMEM2 suppresses TLR3-mediated IFN-β/ISG56/CXCL10 expression in BEAS-2B bronchial epithelial cells

Kobori Y., Tachizaki M., Imaizumi T., Tanaka Y., Seya K., Miki Y., Kawaguchi S., Matsumiya T., Tobisawa Y., Ohyama C., and Tasaka S.

***Molecular Biology Reports,*** 2024;51(1):417. DOI: 10.1007/s11033-024-09346-3.

小堀　由璃 (弘前大学 大学院医学研究科呼吸器内科学講座)

論文要旨

背景：気管支上皮細胞はウイルス感染の最前線にある。Toll 様受容体 3（TLR3）は、インターフェロン（IFN）- β および IFN 刺激遺伝子（ISG）の発現を誘導し、抗ウイルス応答を引き起こす。膜貫通タンパク質（TMEM）ファミリーは様々な細胞で発現している。TMEM2 は、ヒアルロン酸代謝に関わる分子として、注目されている。様々な癌における TMEM2 の予後との相関は報告されているが、感染症との関連は不明である。本研究では、TMEM2 が気管支上皮細胞（BEAS-2B）の抗ウイルス免疫に及ぼす影響を検討した。

方法と結果：TMEM2 タンパク質は、正常ヒト気管支上皮細胞の細胞質で認められ、免疫組織化学的に臓器間で異なっていた。BEAS-2B 細胞を培養し、TMEM2 siRNA でトランスフェクトした後、TLR3 のリガンドであるポリイノシン酸-ポリシチジル酸（poly IC）または組換えヒト（r(h)）IFN-β を投与した。TMEM2、IFN-β、ISG56、C-X-C モチーフケモカインリガンド 10（CXCL10）およびヒアルロン酸の発現は、ウェスタンブロット法や定量的逆転写ポリメラーゼ連鎖反応、酵素結合免疫吸着測定法（ELISA）を用いて評価した。TMEM2 の発現は poly IC 刺激によって変化しなかった。TMEM2 のノックダウンは、poly IC 刺激時には IFN-β、CXCL10 および ISG56 の発現を増加させたが、IFN-β 刺激では ISG56 および CXCL10 の発現を変化させなかった。培地中のヒアルロン酸濃度は TMEM2 ノックダウンまたは poly IC のいずれかによって減少したが、相加的または相乗的な効果は観察されなかった。

結論：TMEM2 のノックダウンは、BEAS-2B 細胞において TLR3 を介した IFN-β、CXCL10、ISG56 の発現を増強した。このことから、TMEM2 は抗ウイルス免疫応答を抑制し、気管支上皮細胞の組織傷害を予防することが示唆される。

## 3）Focal adhesion kinase regulates sialylation of N-glycans via the PI4KIIα-PI4P pathway

Sun Y., Isaji T., Oyama Y., Xu X., Liu J., Hanamatsu H., Yokota I., Miura N., Furukawa J., Fukuda T., and Gu J.

***J Biol Chem.***, 299, 9, 2023, https://doi.org/10.1016/j.jbc.2023.105051

孫 钰涵（東北医科薬科大学・分子生体膜研究所）

論文要旨

シアリル化は、細胞接着や免疫応答などの重要な生物学的イベントを制御する糖タンパク質の末端糖鎖修飾の一つです。以前の研究では、インテグリン α3β1 が N 型糖鎖のシアリル化の制御に重要な役割を果たしていることを示しましたが、詳細な分子メカニズムは不明のままです。

本研究では、インテグリン β1 の重要な下流シグナル分子であるフォーカルアドヒージョンキナーゼ（FAK）がシアリル化にどのように影響するかを調べました。HeLa 細胞で CRISPR / Cas9 システムを使用して、安定した FAK ノックアウト（KO）細胞株を確立しました。レクチンブロット、フローサイトメトリー分析、質量分析（MS）から得られた結果から、KO 細胞では野生型（WT）細胞と比較してシアリル化レベルが著しく低下していることが示されました。さらに、ホスファチジルイノシトール 4-リン酸 (PI4P) の発現レベルも、ホスファチジルイノシトール 4-キナーゼ IIα (PI4KIIα) の安定性の低下により、KO 細胞で低下しました。特に、シアリル化、PI4P のレベル低下、および N 型糖鎖の修飾のための主要なシアリルトランスフェラーゼである GOLPH3 と ST3GAL4 または ST6GAL1 との複合体形成は、FAK の再発現によって大幅に回復しました。さらに、FAK 欠損によって引き起こされたシアリル化とリン酸化 Akt の減少、および細胞移動は PI4KIIα の過剰発現によってすべて回復しました。これは、PI4KIIα が FAK の下流分子の一つであることを示唆しています。

これらの発見は、FAK が PI4P 合成経路を介してシアリル化を制御していることを示し、インテグリン-FAK-PI4KIIα-GOLPH3-シアリルトランスフェラーゼという軸を介して N 型糖鎖のシアリル化の調節に関する新規な分子メカニズムが示唆されています。

## 4）Exogenous L-fucose attenuates neuroinflammation induced by lipopolysaccharide

Xu X., Fukuda T., Takai J., Morii S., Sun Y., Liu J., Ohno S., Isaji T., Yamaguchi Y., Nakano M., Moriguchi T., and Gu J.

***J Biol Chem.***, 300, 1, 2024, https://doi.org/10.1016/j.jbc.2023.105513

徐　興（東北医科薬科大学・分子生体膜研究所）

論文要旨

α1,6-フコシルトランスフェラーゼ（Fut8）は、N 型糖鎖の最も内側の N-アセチルグルコサミン残基へのフコースの転移を触媒し、コアフコシル化を形成する。
私たちの以前の研究では、リポ多糖（LPS）処理は、野生型（$Fut8^{+/+}$）マウスと比較して、Fut8 ホモ接合ノックアウト（$Fut8^{-/-}$）またはヘテロ接合ノックアウト（$Fut8^{+/-}$）マウスで神経炎症を強く誘発することを示した。その詳細な分子メカニズムを理解するために、ルシフェラーゼ（Luc）レポーターカセットで改変されたヒトインターロイキン-6（hIL-6）人工染色体（BAC）トランスジェニックを含む高感度の炎症モニタリングマウスシステムを使用しました。このシステムを利用することで、中枢神経系における LPS 誘発性神経炎症（IL-6 の発現）を検出することに成功しました。
次に、$Fut8^{+/-}$マウスの神経炎症に対する外因性 L-フコースの効果を調べました。レクチンブロットおよび質量分析の結果、L-フコースの投与により $Fut8^{+/-}$マウスのコアフコシル化レベルが上昇することが示されました。特に、外因性 L-フコースは、LPS によって誘発された脳組織における IL-6 mRNA および Luc mRNA の発現を減弱させ、それが Luc 生物発光イメージングシステム（IVIS）を用いて確認されました。LPS 刺激により神経炎症反応を誘発するミクログリア細胞の活性化は、L-フコースの投与によって阻害されました。その外因性 L-フコースは、JAK2、AKT、および STAT3 のリン酸化レベルなど、IL-6 の下流細胞内シグナル伝達も抑制しました。L-フコース投与により、Fut8+/−マウスの gp130 コアフコシル化レベルが上昇したが、gp130 と IL-6 受容体との複合体形成が減少しました。そのコアフコシル化による複合体形成を負に制御するのは、Fut8 欠損 BV-2 細胞でも確認されました。
これらの結果は、L-フコースの投与が $Fut8^{+/-}$マウスにおける LPS 誘発性神経炎症を軽減することや、コアフコシル化が抗炎症において重要な役割を果たしていることを示し、さらに、L-フコースが神経炎症に対する潜在的な予防化合物であることを示唆しています。

<細胞制御学>

教授　顧 建国
准教授　福田 友彦
准教授　伊左治 知弥

## がんや免疫・炎症反応における糖鎖発現とその意義

糖鎖修飾は最も一般的な翻訳後修飾であり、その複雑で多様な構造はさまざまな受容体の機能を精密に調節していることが知られている。糖タンパク質には、O 結合型、N 結合型糖鎖が付加している。私たちは、主に N 型糖鎖の生合成経路(下図)に関わる糖転移酵素 N-acetylglucosaminyltransferase(GnT)、Sialyltransferase (ST)、およびFucosyltransferase (FUT) に注目し、生体反応に与える影響とその作用機序、発現機構について研究している。本年度は慢性骨髄性白血病細胞の赤血球分化における GnT-III の機能、コアフコシル化糖鎖による血清 IgG の安定化および抗神経炎症活性、FUT4 による多剤耐性化について検討した。さらに、O 結合型 β-N-アセチルグルコサミン (O-GlcNAc) による Focal Adhesion Kinase (FAK)の機能制御についても検討した。

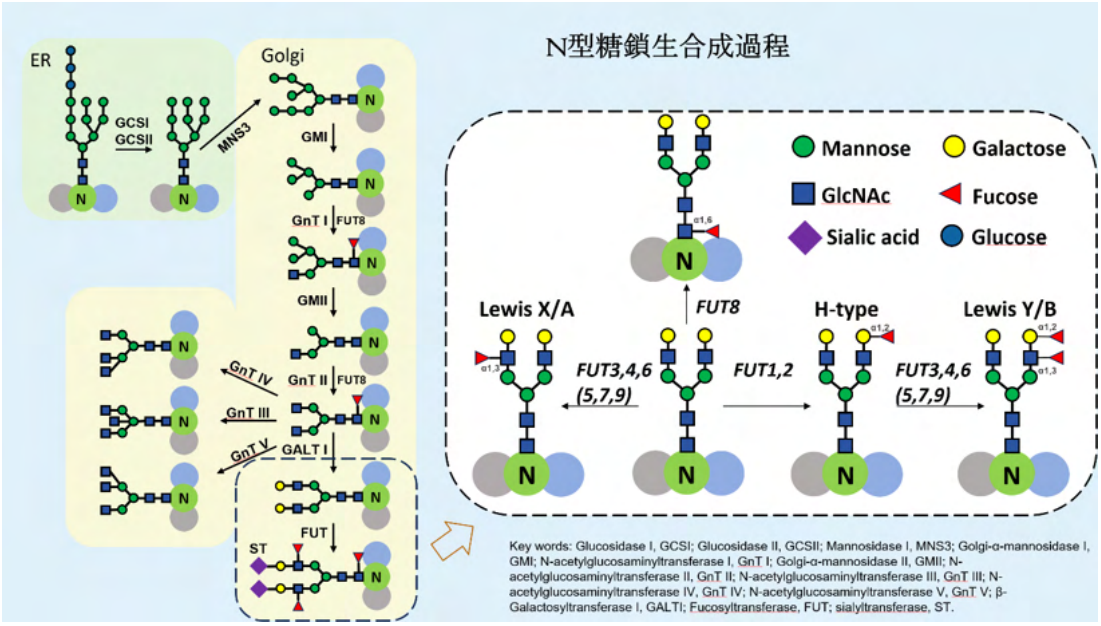


### I　糖転移酵素 GnT-IIIによる、ERK/MAPK シグナル伝達を介した赤血球分化制御

慢性骨髄性白血病(CML)は、フィラデルフィア染色体(BCR-ABL1 融合遺伝子)によりつくられるチロシンキナーゼの活性化を特徴とする骨髄増殖性腫瘍である。現在、ABL1 チロシンキナーゼに対する分子標的薬により、患者の平均余命が著しく改善されているが、薬剤耐性が生じるため、白血病細胞の未熟細胞または悪性細胞の成熟と分化を促進し、正常細胞と同様の特性を獲得させる分

化誘導療法が寛解を達成する方法として注目されている。CML 細胞株である K562 細胞に酪酸ナトリウム(NaBu)を用いて赤血球分化を誘導し、糖鎖構造の変化を検討したところ、GnT-III とその産物であるバイセクト糖鎖の発現が顕著に増加し、逆に GnT-III を欠損させた K562 細胞は赤血球マーカーの減少と分化が抑制された。また、赤血球分化に重要な ERK/MAPK 経路を阻害すると GnT-III の発現が著しく抑制された。さらに、GnT-III は、赤血球分化誘導に密接に関連する膜受容体 c-Kit や CD71 などの発現を誘導し、下流の ERK/MAPK の活性化を促進した(右図)。

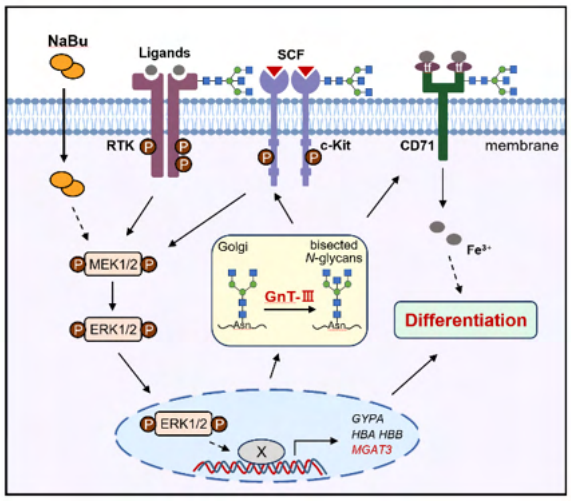


GnT-IIIによる ERK/MAPK シグナル伝達を介した赤血球分化制御の解明は、GnT-IIIが慢性骨髄性白血病に対する分化療法における潜在的な標的であり、糖鎖を介した新しい治療法につながることが期待される。

## II L-フコース投与による血中 IgG 濃度の向上とその分子機構

免疫グロブリン G (IgG)は、免疫応答の主要分子で、IgG 上の糖鎖構造の違いは、IgG の機能(質)に大きな影響を与える。N 型糖鎖は、IgG の最も一般的な修飾で、その多くがコアフコシル化されている。α1,6-フコシルトランスフェラーゼ(Fut8)によって触媒されるコアフコシル化は Fc 受容体(FcγR)の N 型糖鎖と IgG の N 型糖鎖の相互作用を妨げ、FcγRIIIa(マウスの FcγRIVの相当)に対する結合親和性を大きく低下させる。一方、コアフコシル化されていない IgG は、ADCC 活性が著しく上昇するなど IgG のコアフコシル化は、抗体治療・ワクチン・免疫療法の有効性などに重要な意味を持つ。しかし、抗体(薬)の効果は機能だけでなく、(発現)量や半減期の長さ(安定性)も重要である。

Fut8 欠損マウスや Fut8 ヘテロ欠損マウスは野生型マウスと比較して IgG 量が低下していることを見いだした。コアフコシル化が血清 IgG の量を変化させるメカニズムを検討するため、先天性糖鎖形成異常症に対する糖鎖補充療法を参考に、L-フコースを Fut8 ヘテロ欠損マウスに経口投与し、コアフコシル化を促進させると、IgG 量が回復した。しかし、コアフコシル化 IgG と総 IgG の比率には有意差が見られず、mRNA の発現量にも変化が無かった。そこで、合成量ではなく分解・クリアランスの差異が血中濃度に影響を与えている可能性が考えられ IgG の安定性に注目したところ、Fut8 ヘテロ欠損マウスで FcγRIVの発現が有意に高いが、L-フコース投与でその発現が低下した。L-フコースの投与は、IgG の保護作用を有する胎児性 Fc 受容体(FcRn)の発現に影響を与えなかったことから、血中 IgG 濃度が主

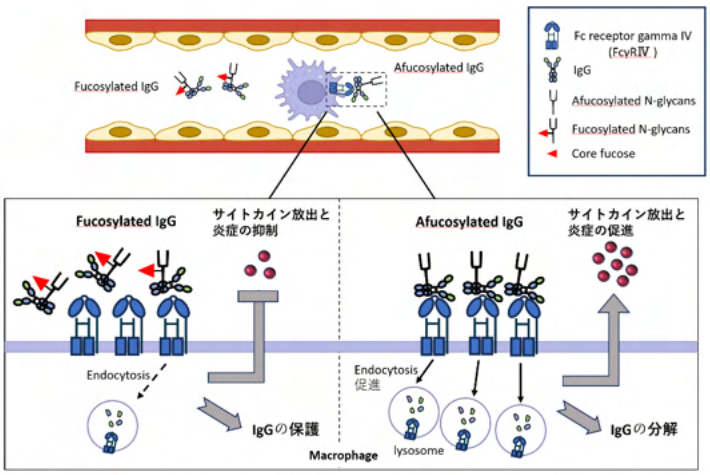


コアフコースをもつIgGと持たないIgGの免疫センチネル細胞での挙動

に IgG のコアフコシル化のレベルによる Fc-FcγRIV 分解経路（上図）を介して調節されていることが示唆された。

これらの知見は、コアフコシル化が IgG 安定性を調節するという新しい概念を提案するもので、L-フコース投与という副作用の少ない方法での、IgG の血中滞留性の向上は抗体医薬品の治療戦略に貢献することが期待される。

## III　コアフコシル化糖鎖によるうつ病発症リスクの低下

神経炎症は、精神疾患に共通して見られる病態基盤と考えられており、神経炎症仮説が提唱されている。Fut8 欠損マウスの解析を通じて、Fut8 の産物であるコアフコシル化糖鎖の減少がミクログリアの過剰な活性化を引き起こすことや、Fut8 ヘテロ欠損マウスは野生型マウスとホモ欠損マウスの中間の表現型を示すことから、コアフコース糖鎖の減少が炎症反応に対する脆弱性をもたらす。

最近ストレスによるうつ症状の誘導には脳内炎症が重要であることが提唱されているので、コアフコシル化糖鎖が減少した Fut8 ヘテロ欠損マウスに比較的軽微なストレスをランダムに長期的に負荷する慢性予測不可能なストレス(CUS)モデルを適用し、人間のうつ病をよく再現するモデルマウスを作成したところ、うつ様行動が誘導されるまでの期間が野生型マウスと比較して有意に短縮され、神経炎症反応を増加させた(下図)。L-フコースの経口投与により、Fut8 の糖供与体である GDP-フコースの生合成経路を活性化させると、うつ様行動が誘導されるまでの期間が改善し、炎症性サイトカインの発現が大幅に減少した。L-フコースは陽性対照の抗うつ薬フルオキセチン(FLX)と同様に JAK2/STAT3 経路を阻害することで抗炎症効果を示した。さらに、正常な高次脳機能にとって、樹状突起スパインが一定の密度で維持されることが重要であることが知られているので、コアフコシル化糖鎖の減少が引き起こすミクログリアの活性化が、スパイン形成にどのような影響を及ぼすかを検討したところ、ヘテロ欠損マウスは野生型と比較してスパインの数が減少していた。ストレス負荷でスパインの数がさらに減少したが、L-フコースを投与すると改善した。興味深いことに、人為的に Fut8 の発現を抑制した Fut8 ヘテロ欠損マウスだけでなく、CUS に曝露された野生型マウスでも Fut8 の発現が抑制され、この抑制も L-フコース投与によって

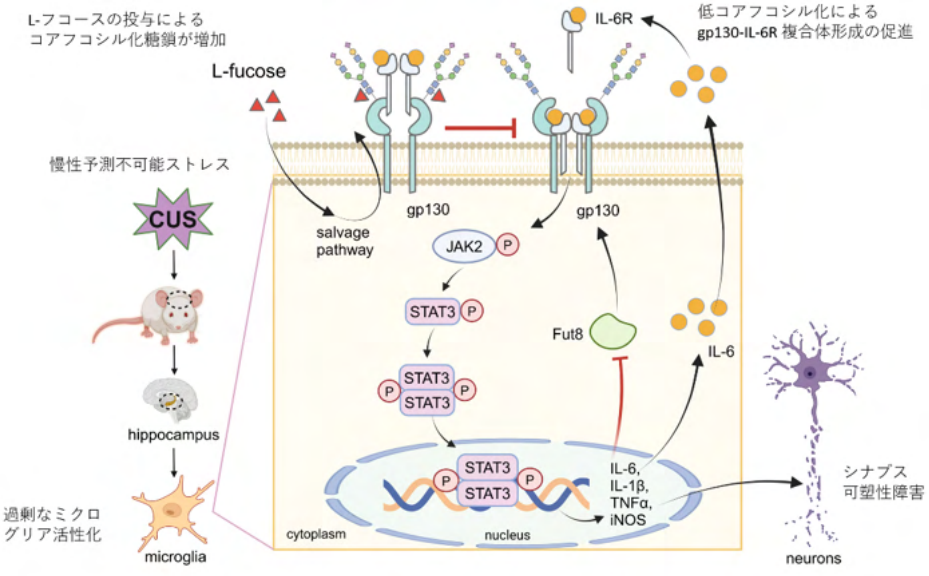


**L-フコースの投与でCUS負荷により誘導した神経炎症やうつ様変化の抑制効果とその機序**

L-フコースの投与によるコアフコシル化糖鎖の増加は、炎症性サイトカイン 複合体の受容体形成を阻害し、さらに炎症サイトカインの発現を抑制することによって、神経細胞可塑性を保護する。逆に、長期炎症はFut8の発現を抑制する。

部分的に回復した。

これらの結果は、うつ病の病態にコアフコシル化糖鎖の減少によるミクログリアの活性化が重要な役割を果たしていることを示している。また、L-フコース投与がうつ病(様行動)の緩和に寄与するだけでなく、脳内炎症仮説に基づく特定の疾病にターゲットを限定しない、疾病横断的な中枢神経系疾患の予防・治療薬としての可能性を示唆している。

**IV フコース転移酵素 FUT4 による NF-κB シグナル伝達経路を介した化学療法抵抗性獲得**

多剤耐性（MDR）は、化学療法開発における大きな障害となっている。ヒト慢性骨髄性白血病由来 K562 細胞を用いたアドリアマイシン耐性（ADR）モデルを用いた先行研究において、GnT-III の発現が化学療法耐性を負に制御することを報告している。ADR 細胞はフコシル化レベルも上昇していることから、多剤耐性とフコシル化に注目したて解析したところ、ADR 細胞のフコシル化レベルの上昇が、FUT4 およびその産物である LewisX 抗原に起因していた。FUT4 の発現を消失させると P 糖タンパク質(P-gp)の発現レベルを低下させ、化学療法薬に対する感受性を高めた。逆に FUT4 の発現を回復させると、P-gp 発現、薬剤排出、化学療法抵抗性が効果的に逆転した。また、FUT4 は、NF-κB シグナル伝達経路を介して、化学療法抵抗性に関連する P-gp 発現を特異的に促進することが明らかとなった。

これらの結果は、FUT4 が MDR 獲得阻害の有望なターゲットであることを示唆している。

**V β-N-アセチルグルコサミン (O-GlcNAc) による Focal Adhesion Kinase (FAK)の機能制御**

がん細胞の浸潤転移に関わる細胞接着分子として最重要視されるインインテグリンの機能が O-GlcNAc 化により制御されている。腫瘍形成および進行における O-GlcNAc 化の役割明らかにするため、インテグリンの刺激によって活性化される非受容体型チロシンキナーゼ FAK に着目した。LC-MS/MS 解析により、FAK の Ser708、Thr739、および Ser886 の O-GlcNAc 化を同定した。Ser708、Thr739、および Ser886 が Ala に置換された FAK 変異体は、Tyr397 および AKT のリン酸化レベルが低下した。また、細胞増殖および遊走も、変異体細胞で有意に抑制された。さらに、変異体細胞では、FAK の細胞接着斑に存在するタリンやパキシリンとの相互作用の強化および異常な細胞接着が観察された。

これらの結果は、O-GlcNAc 化が腫瘍形成および進行に必須であり、FAK の O-GlcNAc 化を標的とすることが癌治療の有望な治療戦略となる可能性を支持している。

＜論文発表＞

**Fucosylation inhibitor 6-alkynylfucose enhances the ATRA-induced differentiation effect on acute promyelocytic leukemia cells.** Suzuki S, Liu J, Sato Y, Miyake R, Suzuki S, Okitsu Y, Fukuda T, Isaji T, Gu J, Takahashi S. ***Biochem Biophys Res Commun.*** 710:149541. doi: 10.1016/j.bbrc.2024.149541. 2024

**An emerging role of N-glycosylation in cancer chemoresistance.** Sun Y, Wu T, Gu J. ***Carbohydr Res.*** 539:109107. doi: 10.1016/j.carres.2024.109107, 2024

**Importance of PTM of FLT3 in acute myeloid leukemia.** Liu J, Gu J. ***Acta Biochim Biophys Sin (Shanghai)***. 56:1199-1207. doi: 10.3724/abbs.2024112. 2024

**The K346T mutant of GnT-III bearing weak in vitro and potent intracellular activity.** Hashimoto Y, Kawade H, Bao W, Morii S, Nakano M, Nagae M, Murakami R, Tokoro Y, Nakashima M, Cai Z, Isaji T, Gu J, Nakajima K, Kizuka Y. ***Biochim Biophys Acta Gen Subj.*** 1868:130663. doi: 10.1016/j.bbagen.2024.130663. 2024

**The acetylglucosaminyltransferase GnT-III regulates erythroid differentiation through ERK/MAPK signaling.** Wu T, Sun Y, Wang D, Isaji T, Fukuda T, Suzuki C, Hanamatsu H, Nishikaze T, Tsumoto H, Miura Y, Furukawa JI, Gu J. ***J Biol Chem.*** 300:108010. doi: 10.1016/j.jbc.2024.108010. 2024

**Fucosyltransferase 4 upregulates P-gp expression for chemoresistance via NF-κB signaling pathway.** Cai Z, Isaji T, Liang C, Fukuda T, Zhang D, Gu J. ***Biochim Biophys Acta Gen Subj.*** 1869:130753. doi: 10.1016/j.bbagen.2024.130753. 2025

**O-GlcNAcylation of Focal Adhesion Kinase Regulates Cell Adhesion, Migration, and Proliferation via the FAK/AKT Pathway.** Zhang Z, Isaji T, Oyama Y, Liu J, Xu Z, Sun Y, Fukuda T, Lu H, Gu J. ***Biomolecules.*** 14:1577. doi: 10.3390/biom14121577. 2024

**Exogenous L-fucose attenuates depression induced by chronic unpredictable stress: Implicating core fucosylation has an antidepressant potential.** Wang D, Fukuda T, Wu T, Xu X, Isaji T, Gu J. ***J Biol Chem.*** 301:108230. doi: 10.1016/j.jbc.2025.108230. 2025

＜学会発表と講演＞

ミクログリア活性化に関わるコアフコースの役割

福田 友彦, 徐 興, 王 丹, 伊左治 知弥, 顧 建国

第 90 回日本生化学会東北支部例会・シンポジウム, 秋田, 2024 年 6 月, 演題番号 O-19

**Exogenous L-fucose attenuates depression induced by chronic unpredictable stress: implicating core fucosylation has an antidepressant potential**

王 丹, 徐 興, 福田 友彦, 伊左治 知弥, 顧 建国

第 90 回日本生化学会東北支部例会・シンポジウム, 秋田, 2024 年 6 月, 演題番号 P-5

**GnT-III contributes to sodium butyrate-induced REK/MAPK signaling pathway**

吴 天貴, 孫 鈺涵, 伊左治 知弥, 福田 友彦, 顧 建国

第 90 回日本生化学会東北支部例会・シンポジウム, 秋田, 2024 年 6 月, 演題番号 P-4

**脳・神経炎症における α1,6 フコース転移酵素**

福田 友彦, 王 丹, 徐 興, 伊左治 知弥, 顧 建国

第 43 回糖質学会年会, 横浜, 2024 年 9 月, 演題番号1A-01A

**K562 細胞の赤血球分化誘導における糖転移酵素 GnT-III の役割**

呉 天貴, 孫 鈺涵, 王 丹, 伊左治 知弥, 福田 友彦, 鈴木 千春 [a], 花松 久寿 [a], 西風 隆司 [b], 古川 潤一 [a], 顧建国 ([a]名大糖鎖生命コア, [b]島津製作所)

第 18 回東北糖鎖研究会, 仙台, 2024 年 10 月, 演題番号 P-12

**慢性的な予測不可能なストレスによって引き起こされるうつ病モデルマウスにおけるコアフコシル化の役割**

王 丹, 福田 友彦, 呉 天貴, 徐 興, 伊左治 知弥, 顧 建国

第 18 回東北糖鎖研究会, 仙台, 2024 年 10 月, 演題番号 P-14

**神経炎症の調節におけるコアのフコシル化の重要性**

**Importance of core fucosylation in regulating neuroinflammation**

徐 興

第 18 回東北糖鎖研究会, 仙台, 2024 年 10 月, 演題番号 H-1

**FAK による N-グリカンのシアリル化の制御メカニズム**

Regulatory mechanism of Focal-adhesion kinase on sialylation of N-glycans

孫 鈺涵

第 18 回東北糖鎖研究会, 仙台, 2024 年 10 月, 演題番号 H-3

**ST3GAL3 による LDL 受容体の α2,3-シアル化は VSV-G 偽型レンチウイルスの受容体である**

伊左治 知弥, 祁 峰, 大山 嘉順, 福田 友彦, 顧 建国

第 97 回生化学会年会, 横浜, 2024 年 11 月, 演題番号 2T09-01

**神経炎症とうつ病の予防効果に関わるコアフコースの役割**

福田友彦, 王丹, 徐興, 伊左治知弥, 顧建国

第 97 回生化学会年会, 横浜, 2024 年 11 月, 演題番号 2T09-05

**脳炎症の抑制や血清 IgG の安定性に寄与する L-fucose の機能とその分子機序:コアフコシル化の重要性**

顧　建国

第 21 回糖鎖科学コンソーシアムシンポジウム（JCGG）,福島, 2024 年 11 月

**Function of L-fucose on neuroinflammation and serum IgG stability: Importance of core fucosylation**

GU Jianguo

第十届中国糖科学与糖工程学術会議兼産業フォーラム, 広東省湛江市, 2024 年 11 月

**Effects of exogenous L-fucose on depression induced by chronic unpredictable stress: importance of core fucosylation**

GU Jianguo

The 3rd Academia Sinica-Tohoku Medical and Pharmaceutical University Bilateral Meeting, 台北, 2025 年 2 月

JBC RESEARCH ARTICLE

# The acetylglucosaminyltransferase GnT-III regulates erythroid differentiation through ERK/MAPK signaling

Received for publication, July 17, 2024, and in revised form, November 5, 2024 Published, Papers in Press, November 19, 2024,
https://doi.org/10.1016/j.jbc.2024.108010

**Tiangui Wu[1], Yuhan Sun[1], Dan Wang[1], Tomoya Isaji[1], Tomohiko Fukuda[1], Chiharu Suzuki[2], Hisatoshi Hanamatsu[2], Takashi Nishikaze[3], Hiroki Tsumoto[4], Yuri Miura[4], Jun-ichi Furukawa[2,5], and Jianguo Gu[1,*]**

*From the [1]Division of Regulatory Glycobiology, Institute of Molecular Biomembrane and Glycobiology, Tohoku Medical and Pharmaceutical University, Sendai, Miyagi; [2]Division of Glyco-Systems Biology, Institute for Glyco-Core Research, Tokai National Higher Education and Research System, Nagoya; [3]Solutions COE, Analytical & Measuring Instruments Division, Shimadzu Corporation, Kyoto; [4]Research Team for Mechanism of Aging, Tokyo Metropolitan Institute for Geriatrics and Gerontology, Tokyo; [5]Department of Orthopedic Surgery, Hokkaido University Graduate School of Medicine, Sapporo, Japan*

Reviewed by members of the JBC Editorial Board. Edited by Robert Haltiwanger

**Differentiation therapy is an alternative strategy used in treating chronic myelogenous leukemia to induce the differentiation of immature or cancerous cells toward mature cells and inhibit tumor cell proliferation. We aimed to explore *N*-glycans' roles in erythroid differentiation using the sodium butyrate (NaBu)-induced model of K562 cells (WT/NaBu cells). Here, using lectin blot, flow cytometry, real-time PCR, and mass spectrometry analyses, we demonstrated that the mRNA levels of *N*-acetylglucosaminyltransferase III ((encoded by the *MGAT3* gene) and its product (bisected *N*-glycans) were significantly increased during erythroid differentiation. To address the importance of GnT*N*-acetylglucosaminyltransferase-III in this progress, we established a stable *MGAT3* KO K562 cell line using the CRISPR/Cas9 technology. Compared to WT/NaBu cells, *MGAT3* KO significantly impeded the progression of erythroid differentiation, as shown in decreased cell color and levels of erythroid markers, glycophorin A (CD235a), and β-globin. Consistently, *MGAT3* KO mitigated the inhibitory impact of NaBu on cell proliferation. During induction, *MGAT3* KO suppressed the cellular phosphorylated tyrosine and phospho-extracellular signal–regulated kinase (ERK)1/2 levels. Inhibition of the ERK/mitogen-activated protein kinase signaling pathway using U0126 blocked erythroid differentiation while concurrently suppressing the expression levels of *MGAT3* and bisected *N*-glycans. Furthermore, the lack of bisecting GlcNAc modification on c-Kit and transferrin receptor 1 (CD71) suppressed cellular signaling and accelerated the degradation of the CD71 protein, respectively. Our study highlights the critical role of *MGAT3* in regulating erythroid differentiation associated with the ERK/mitogen-activated protein kinase signaling pathway, which may shed light on identifying new differentiation therapy in chronic myelogenous leukemia.**

Chronic myelogenous leukemia (CML) is a clonal myeloproliferative neoplasm originating from a transformed hematopoietic stem cell. This abnormality leads to the emergence of a significant population of clones that proliferate extensively but are unable to undergo complete self-renewal or differentiation (1). This disease is characterized by a reciprocal chromosomal translocation referred to as t (2, 3), resulting in the formation of the Philadelphia chromosome harboring the BCR-ABL gene (4). Currently, molecular target therapies that focus on the ABL1 tyrosine kinase, particularly the application of tyrosine kinase inhibitors, have significantly enhanced the life expectancy of patients with CML and markedly improved their quality of life (5, 6). Unfortunately, the long-term use of tyrosine kinase inhibitors can lead to adverse effects in some patients, and also impose a substantial financial burden (7, 8). In recent years, there has been a growing interest in the potential of inducing differentiation in leukemia cells as a method for achieving disease remission, with differentiation therapy emerging as a promising complementary or alternative approach (9). This therapeutic strategy seeks to promote the maturation and specialization of immature or malignant cells, thereby enabling them to acquire characteristics akin to those of normal cells (10). A notable example of this approach is the differentiation therapy used in acute promyelocytic leukemia (APL), which employs retinoic acid and arsenic trioxide (2).

K562, a CML cell line, is a typical model for investigating erythroid differentiation using sodium butyrate (NaBu) to explore the mechanism of differentiation therapy (11). The induction of erythroid differentiation is a complex and highly orchestrated process. Erythrocytes originate from hematopoietic stem cells *via* a well-defined, sequential differentiation pathway (12). The induction of specific proteins, such as hemoglobin and transferrin receptor 1, also called CD71 (encoded by *TFRC* gene), and activation of signaling pathways are critical in this progression. Consequently, CD71 plays a vital role in erythropoiesis by assisting in regulating iron homeostasis and promoting the development and proper functioning of red blood cells (13). Activation of multiple pathways, particularly the extracellular signal–regulated kinase/mitogen-activated protein kinase (ERK/MAPK) pathway, is crucial in erythroid differentiation. Studies on primary human erythroid

* For correspondence: Jianguo Gu, jgu@tohoku-mpu.ac.jp.



© 2024 THE AUTHORS. Published by Elsevier Inc on behalf of American Society for Biochemistry and Molecular Biology. This is an open access article under the CC BY license (http://creativecommons.org/licenses/by/4.0/).

progenitor cells have shown that activation of the RAS/ERK pathway is necessary for effective erythropoietin–dependent erythroblast formation (14). Notably, many erythroid markers are glycosylated proteins, and *N*-glycosylation plays a crucial role in regulating pathways (15–17).

*N*-glycosylation is a prevalent posttranslational modification in mammalian cells (18, 19). Alterations in glycosylation play a critical role in tumor progression and are considered a hallmark of cancer (20). *N*-acetylglucosaminyltransferase III (GnT-III), encoded by the *MGAT3* gene, is a crucial glycosyltransferase known for synthesizing a bisecting *N*-acetylglucosamine residue and has gained attention for its role in physiology (21) and tumor biology (3, 22). For instance, *MGAT3* overexpression suppresses TGF-β–induced epithelial-mesenchymal transition (EMT) by prolonging E-cadherin turnover and inhibiting the formation of the β-catenin/p-Smad complex (23). Additionally, GnT-III negatively regulates chemoresistance by suppressing P-glycoprotein expression *via* the TNFR2-NF/κB signaling pathway (3). These findings underscore GnT-III's significant role in modulating cancer progression and resistance mechanisms. In addition, some studies show that *N*-glycosylation is associated with cell differentiation. For instance, overexpression of α-1,6-fucosyltransferase suppresses hemoglobin production in both murine and human erythroleukemia (HEL) cells, while its downregulation promotes erythroid differentiation and hemoglobin production (24). These studies highlight the intricate roles of *N*-glycosylation in tumor initiation, progression, and differentiation. However, mechanisms linking *N*-glycosylation to differentiation remain understudied, warranting further investigation.

In this study, we utilized a conventional differentiation model employing NaBu treatment (WT/NaBu cells) and observed a notable increase in the expression levels of *MGAT3* and its product, bisected *N*-glycans, during the differentiation process. KO of *MGAT3* inhibited this differentiation progression, correlating with reduced levels of erythroid markers such as glycophorin A (CD235a, encoded by *GYPA* gene) and β-globin. Importantly, treatment with U0126, a specific MEK inhibitor, significantly suppressed the differentiation and *MGAT3* expression. These findings uncover a novel mechanism underlying cell differentiation, demonstrating that GnT-III plays a crucial role in promoting erythroid differentiation. The induction of GnT-III or ERK suggests potential strategies to enhance the efficacy of differentiation therapy, potentially offering new avenues for therapeutic intervention in conditions like CML where differentiation defects are implicated.

## Results

### *NaBu-induced differentiation toward the erythroid lineage in K562 cells*

In this study, we induced differentiation of HEL K562 cells towards the erythroid lineage using NaBu, a well-established inducer (25). This differentiation process is characterized by changes in cell color, increased production of hemoglobin (specifically α-globin and β-globin), and the acquisition of erythrocyte surface markers such as CD235a and CD71 (26). Here, we cultured K562 cells with different concentrations of NaBu for 96 h to assess its efficacy in inducing erythroid differentiation. Visual observation of cell color changes indicated that NaBu at 1 mM was the most effective concentration for inducing differentiation in WT/NaBu cells (Fig. 1*A*). Quantitative PCR (qPCR) analysis revealed significant increases in the mRNA levels of α-globin and β-globin following NaBu treatment, particularly at 1 mM (Fig. 1*B*). Similarly, flow cytometry (Fig. 1*C*) and Western blotting analysis (Fig. 1*D*) confirmed significant upregulation of CD235a and CD71 protein expression upon treatment with NaBu 1 mM. These findings strongly indicate that NaBu at a concentration of 1 mM effectively induces erythroid differentiation in K562 cells, as evidenced by changes in cell morphology, hemoglobin production, and expression of erythrocyte surface markers.

### *Bisected* N*-glycans were increased in WT/NaBu cells*

In our comparative analysis of *N*-glycans expression patterns between WT and WT/NaBu cells, we employed six distinct lectins: *Phaseolus vulgaris* erythroagglutinin (E4-PHA), *Datura stramonium* agglutinin (DSA), *Phaseolus vulgaris* leucoagglutinin (L4-PHA), *Lens culinaris* agglutinin (LCA), *M. amurensis* (MAA), and *S. nigra agglutinin* (SNA). Each lectin preferentially recognizes specific glycan structures: E4-PHA recognizes bisected *N*-glycans, DSA binds to β1,4-GlcNAc-branched *N*-glycans, L4-PHA recognizes β1,6-GlcNAc-branched *N*-glycans, LCA detects α1,6-linked fucose, and MAA and SNA recognize α2,3 sialylation and α2,6 sialylation, respectively (27). Lectin blot analysis revealed a significant increase in reactivity with E4-PHA in WT/NaBu cells compared to WT cells, particularly evident at NaBu concentration of 1 mM, which corresponds with the observed erythroid differentiation (Fig. 2*A*). Conversely, no significant changes were observed in the other lectin blots)—such as DSA (Fig. 2*B*), L4-PHA (Fig. 2*C*), LCA (Fig. 2*D*), MAA (Fig. 2*E*), and SNA (Fig. 2*F*)—between WT and WT/NaBu cells. These bands, mobility at approximately 70 kDa and 130 kDa, were still observed in all types of lectins after removal *N*-glycans using peptide-*N*-glycosidase F (PNGase F), including the ABC kit without a lectin (Fig. S1), suggesting they represent nonspecific staining. The increased reactivity with E4-PHA in WT/NaBu cells was further confirmed by flow cytometry (Fig. 2*G*). Additionally, qPCR analysis showed a significant increase in the mRNA level of *MGAT3* in WT/NaBu cells compared to WT cells, corroborating the lectin blot results (Fig. 2*H*).

Given that NaBu acts as a histone deacetylase inhibitor, we employed another histone deacetylase inhibitor, suberanilohydroxamic acid (SAHA), to investigate the relationship between histone acetylation and *MGAT3* expression. As shown in Fig. S2, SAHA did not induce erythroid differentiation in K562 cells (as indicated by the lack of reddish color). In addition, results from lectin blot and flow cytometry analysis using E4-PHA, along with qPCR, demonstrated that the levels of bisected *N*-glycans and *MGAT3* expression remained unchanged with SAHA treatment. Conversely, Frank CL *et al.*

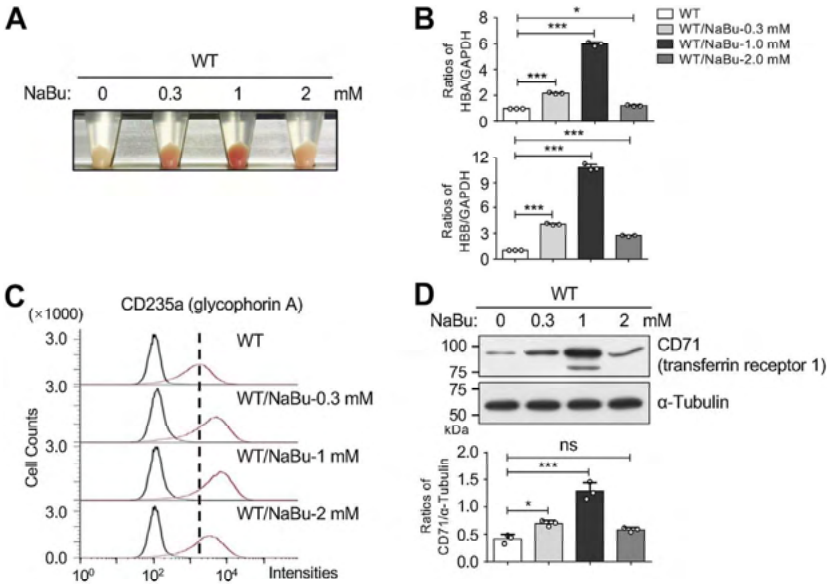


**Figure 1. NaBu induced differentiation of K562 cells toward the erythroid lineage**. *A*, K562 cells were cultured with varying concentrations of NaBu (0, 0.3, 1, 2 mM) for 96 h, and cells treated with 1 mM NaBu appeared significantly *reddish*. *B*, mRNA levels of the *HBA* and *HBB* were detected by qPCR, with GAPDH used as an internal control. The intensity ratio of WT was set as 1.0. Data are presented as mean ± SD from three independent experiments. *p* values were calculated using one-way ANOVA. $*p < 0.05$ and $***p < 0.001$. *C*, protein levels of CD235a on the cell surface after treatment with varying concentrations of NaBu were analyzed by flow cytometry using an anti-CD235a antibody. *D*, equal amounts of cell lysates were subjected to Western blotting using an anti-CD71 antibody to assess CD71 expression, with α-Tubulin serving as a loading control. Data were quantified using Image J software (https://imagej.net/ij/) and obtained from three independent experiments. All values reflect one-way ANOVA with Tukey's *post hoc* analysis as the mean ± SD. $*p < 0.05$; $***p < 0.001$; and ns, no significance. NaBu, sodium butyrate.

reported that NaBu and SAHA exhibited similar effects on chromatin accessibility in K562 cells (28). These findings suggest that NaBu upregulates GnT-III independently of histone acetylation.

To further investigate whether the phenomenon is consistent during NaBu induction, we employed another widely recognized erythroid differentiation inducer, hemin, to establish a hemin-induced erythroid differentiation model in K562 cells. Consistently, levels of bisected *N*-glycans and *MGAT3* expression were significantly increased during this induction (Fig. S3). Furthermore, we selected another cell line, HEL cells, to test this phenomenon. The results indicated that hemin could also induce erythroid differentiation in HEL cells, with significant upregulation of bisected *N*-glycans and *MGAT3* during the process (Fig. S3). These results suggest GnT-III can be upregulated in erythroid differentiation.

To validate the changes in the *N*-glycan structures as described above, we conducted matrix-assisted laser desorption/ionization time-of-flight mass spectrometry (MALDI-TOF MS) analysis, which revealed 108 distinct *N*-glycans in WT and WT/NaBu cells (Table S1). The spectra of major *N*-glycans are shown in Fig. 3*A*. While the relative amounts of *N*-glycan types (paucimannose-, hybrid-, and complex-type) did not show significant differences (Fig. 3*B*), two signals of *N*-77 and *N*-88 were notably increased in WT/NaBu cells (Fig. 3*C*). Furthermore, we confirmed that bisecting GlcNAc was included in both *N*-glycans (*N*-77 and *N*-88) by LC-tandem mass spectrometry (MS/MS) analysis as shown in Fig. S4. In addition, putative bisected *N*-glycans from glycan compositions were summarized in Table S2. The expression of most bisected *N*-glycans was increased in WT/NaBu cells. This finding aligns with the lectin blot results and provides robust evidence that NaBu-induced erythroid differentiation is associated with upregulated expression of GnT-III and its product, bisected *N*-glycans.

### MGAT3 *KO inhibited the erythroid differentiation induced by NaBu in K562 cells*

To investigate the role of GnT-III in this process, we generated an *MGAT3* KO (*MGAT3* KO) K562 cell line using CRISPR/Cas9 technology. Subsequently, we randomly selected two KO single-cell lines confirmed by genomic sequence analysis (Fig. S5). As anticipated, both WT and WT/NaBu *MGAT3* KO cells exhibited nearly abolished reactivity with E4-PHA lectin (Fig. 4*A*). In comparison to WT cells, *MGAT3* KO cells showed significant impairment in cellular differentiation induced by NaBu (Fig. 4*B*). We further investigated changes in markers associated with erythroid differentiation. qPCR analysis revealed that NaBu induction significantly upregulated α-globin and β-globin mRNA levels in both WT and *MGAT3* KO cells (Fig. 4*C*). However, *MGAT3* KO specifically suppressed the induction of β-globin mRNA levels, while α-globin mRNA levels remained unaffected in *MGAT3* KO cells compared to WT/NaBu cells (Fig. 4*C*). The expression levels of CD235a protein on the cell surface (Fig. 4*D*) and CD71 protein in cell lysates (Fig. 4*E*) were downregulated in *MGAT3* KO cells compared the corresponding WT cells.

Since both KO cells showed similar phenotypes as described above, we selected KO-1 for the following studies. Similar to

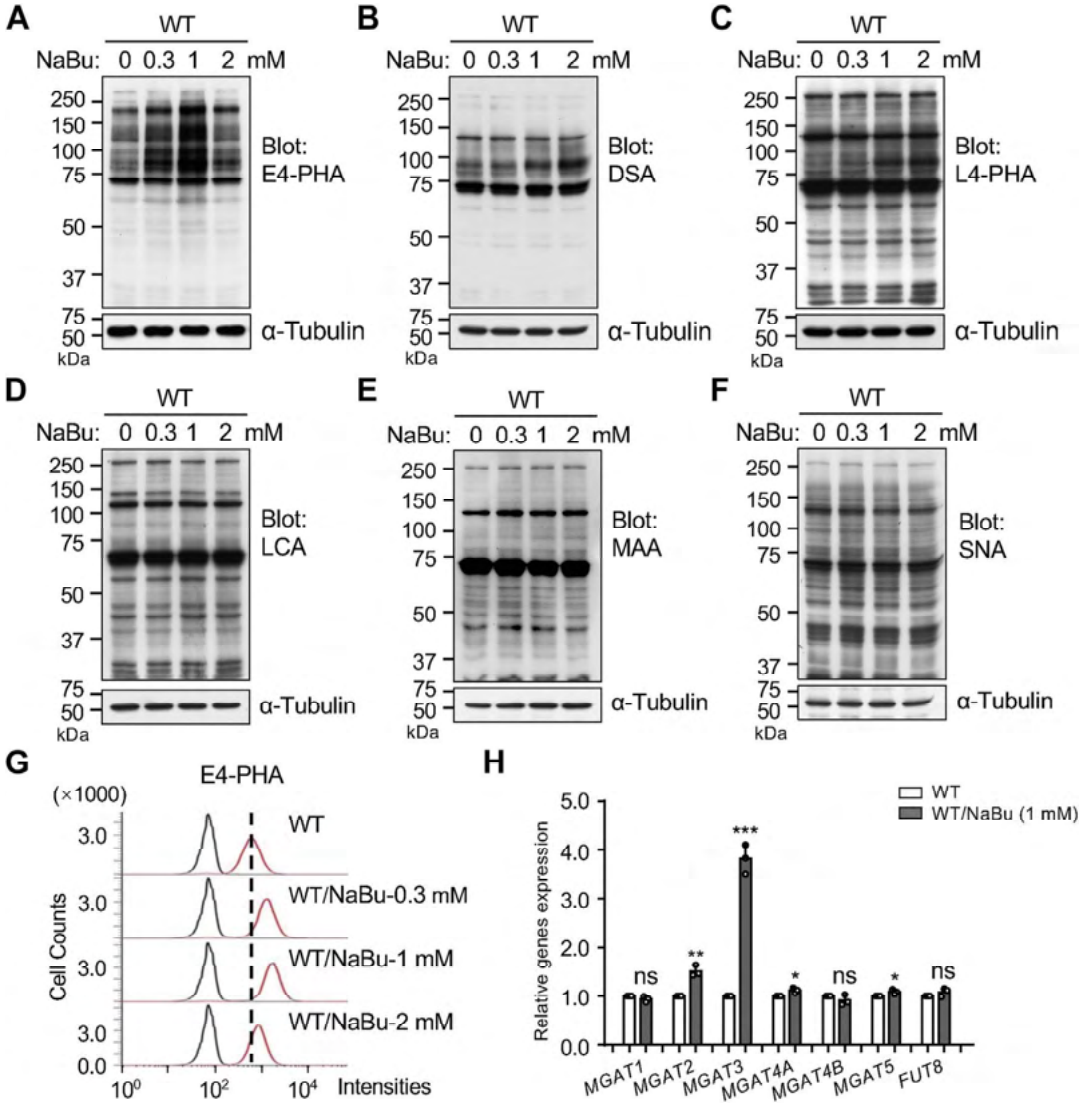


**Figure 2. Comparison of the expression levels of *N*-glycans and related glycosyltransferases between WT and WT/NaBu cells**. The same amounts of cell lysates from WT and NaBu-induced K562 cells were subjected to 7.5% SDS-PAGE gel and stained with various lectins to assess glycosylation changes, such as E4-PHA (*A*), DSA (*B*), L4-PHA (*C*), LCA (*D*), MAA (*E*), and SNA (*F*) lectins, which preferentially recognizes the bisecting GlcNAc, GlcNAcβ1,4 mannosyl-, GlcNAcβ1,6 mannosyl-, α1,6 fucose, α2,3 sialylated, and α2,6 sialylated *N*-glycans, respectively. α-Tubulin was used as a loading control. *G*, expression levels of bisected *N*-glycans on the cell surface were detected by flow cytometry using E4-PHA lectin. *H*, mRNA levels of several *N*-acetylglucosaminyltransferases involved in the synthesis of GlcNAc branched *N*-glycans were determined using qPCR. GAPDH was used as an internal control, and values were normalized to WT cells without NaBu (set as 1.0). Statistical significance was assessed using the unpaired Student's *t* test, with *p* values indicated as $*p < 0.05$; $**p < 0.01$; $***p < 0.001$, or denoted as no significance (ns). DSA, *Datura stramonium* agglutinin; E4-PHA, *Phaseolus vulgaris* erythroagglutinin, LCA, *Lens culinaris* agglutinin; MAA, *M. amurensis*; NaBu, sodium butyrate; qPCR, quantitative PCR; SNA, *S. nigra* agglutinin.

*HBB* mRNA expression, as shown in Fig. 4*C*, *MGAT3* KO also suppressed the induction of *GYPA* mRNA (Fig. 4*F*). Surprisingly, although NaBu induction significantly increased both *TFRC* mRNA (Fig. 4*G*) and CD71 protein levels (Fig. 4*E*) in both WT and *MGAT3* KO cells, *MGAT3* KO specifically suppressed the induction for CD71 protein levels, but not CD71 mRNA levels, in *MGAT3* KO cells compared to the WT/NaBu cells (Fig. 4, *E* and *G*). CD71 is known to be a heavily *N*-glycosylated membrane protein (16, 29). As shown in Fig. 4*H*, the pulldown assay using E4-PHA indicated that CD71 protein underwent bisecting GlcNAc modification upon NaBu induction. The ratio of bisected *N*-glycosylated CD71 to total CD71 was also increased during the induction. To elucidate the underlying molecular mechanism for the decreased CD71 protein levels in *MGAT3* KO cells, we employed cycloheximide, a protein synthesis inhibitor, to assess CD71 protein stability. The decay rates of CD71 protein in *MGAT3* KO cells were significantly accelerated compared to WT cells (Fig. 4*I*). Subsequently, the intracellular localization of the CD71 protein was observed using immunofluorescence. As shown in Fig. 4*J*, the staining of CD71 on the cell surface was lower in *MGAT3* KO cells than in WT cells. These results suggest that *MGAT3* KO suppresses CD71 expression on the cell surface.

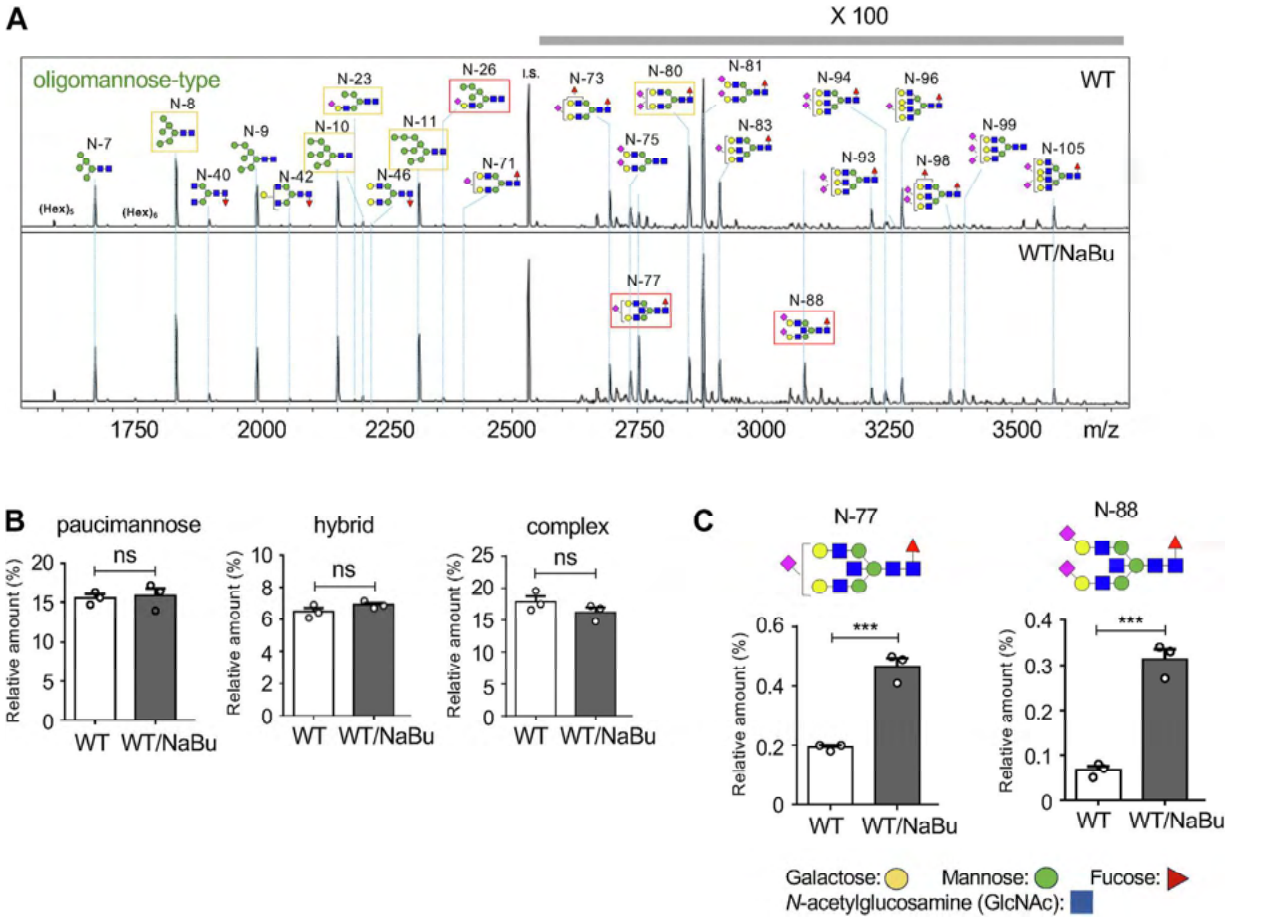


**Figure 3. MALDI-TOF MS analysis of *N*-glycans in K562 and K562/NaBu cells**. *A*, MALDI-TOF MS spectra of *N*-glycans from K562 and K562/NaBu cells were shown. To highlight differences in expression levels, the region from *m/z* over 2600 to 3750 was magnified 100-fold. *B*, the relative expression levels of three types of *N*-glycans (paucimannose, hybrid, and complex) were compared. The total expression level of oligomannose-type in each cell was set as 100% for comparison. *C*, the relative expression levels of bisected *N*-glycans were compared between K562 and K562/NaBu cells. Data was acquired from three independent experiments using the unpaired Student's *t* test as mean ± SD. ***$p < 0.001$; ns, no significance. MALDI-TOF MS, matrix-assisted laser desorption/ionization time-of-flight mass spectrometry; NaBu, sodium butyrate.

### MGAT3 *KO efficiently increased cell proliferation during NaBu-induced differentiation*

It is widely recognized that there exists a notable inverse relationship between cell proliferation and differentiation (30). Given that *MGAT3* KO markedly suppressed NaBu-induced differentiation, as previously described, we further investigated its impact on cell proliferation. While *MGAT3* KO did not exhibit a significant effect on basal cell proliferation, it hindered the suppression of cell proliferation, as validated by cell counts (Fig. 5*A*) and the Cell Counting Kit-8 (CCK-8) assay (Fig. 5*B*) during NaBu-induced differentiation, further supporting that GnT-III does play a crucial role in the differentiation.

### MGAT3 *KO suppressed the activation of the ERK1/2/MAPK signaling pathway in the induction by NaBu*

To investigate the underlying molecular mechanisms by which GnT-III regulates NaBu-induced erythroid differentiation, we examined cellular signaling. Previous studies have shown that the receptor tyrosine kinases (RTKs)/MAPK pathway is one of the most crucial pathways associated with differentiation (31–33). Here, we first examined the phospho-tyrosine levels to evaluate RTK activation. As shown in Fig. 6*A*, the phospho-tyrosine levels were induced by NaBu in WT cells in a dose-dependent manner, but this induction was greatly inhibited by *MGAT3* KO, regardless of NaBu treatment, compared to the WT cells. Subsequently, downstream signals were further examined. Western blot analysis showed increased phosphorylation levels of ERK1/2, p38, and JNK in both WT and *MGAT3* KO cells (Fig. 6*B*). However, interestingly, *MGAT3* KO suppressed the induction of phospho-ERK1/2 by NaBu in *MGAT3* KO cells compared to the WT cells, while phospho-p38 and phospho-JNK levels remained unaffected. Based on these results, we speculated that the ERK1/2 signal pathway is involved in regulating NaBu-induced differentiation by GnT-III.

The c-Kit protein, a crucial member of the RTKs family that mediates ERK1/2 activation (34, 35), plays a significant role in erythropoiesis. The interaction between c-Kit and ligand stem cell factor is essential for this process. Interestingly, the modification by bisecting GlcNAc on c-Kit was significantly upregulated in a dose-dependent manner (Fig. 6*C*), suggesting

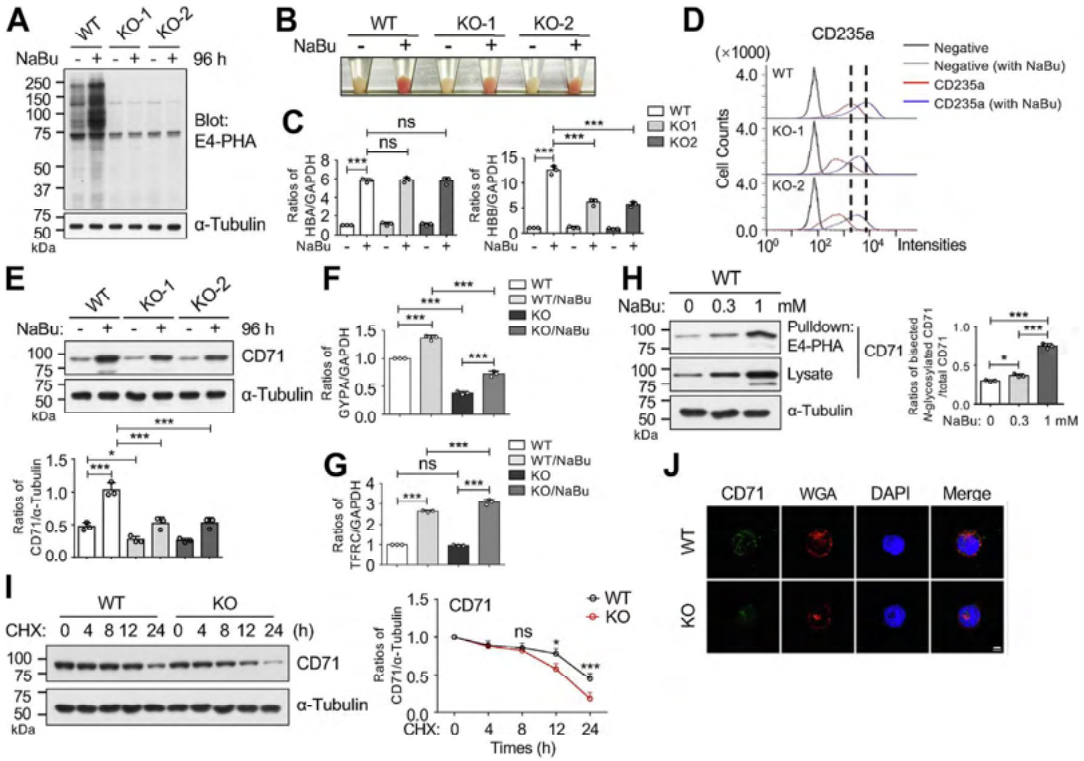


**Figure 4. Effects of GnT-III on NaBu-induced erythroid differentiation**. *A*, *MGAT3* KO K562 cell line was established by using CRISPR/Cas9 technology. Equal amounts of proteins from WT and two *MGAT3* KO cell lines, with or without NaBu treatment, were subjected to lectin blotting using E4-PHA. α-Tubulin was used as a loading control. *B*, coloration was compared between WT and *MGAT3* KO cells after treatment with 1 mM NaBu for 96 h. *C*, mRNA expression levels of *HBA* and *HBB* in WT and two *MGAT3* KO cell lines, with or without NaBu treatment, were compared using qPCR. GAPDH served as the internal control. All values were normalized to the GAPDH levels, with the ratio of WT without NaBu set as 1.0. Data are presented as the mean ± SD from three independent experiments. $^{***}p < 0.001$; ns, no significance. *D*, expression levels of CD235a protein on the cell surface were analyzed by flow cytometry. *E*, expression levels of CD71 were analyzed by Western blotting. α-Tubulin was used as a loading control. The results are presented as the mean ± SD from three independent experiments. $^{*}p < 0.05$ and $^{***}p < 0.001$. mRNA expression levels of *GYPA* (*F*) and *TFRC* (*G*) in WT and *MGAT3* KO-1 cells, with or without NaBu treatment, were compared using qPCR. GAPDH served as the internal control. All values were normalized to the GAPDH levels, with the ratio of WT without NaBu set as 1.0. Data are presented as mean ± SD from three independent experiments using one-way ANOVA with Tukey's *post hoc* analysis. $^{***}p < 0.001$; ns, no significance. *H*, equal amounts of proteins were pulled down with E4-PHA-agarose, and the samples or cell lysates were subjected to Western blotting with an anti-CD71 antibody. α-Tubulin was used as a loading control. The relative ratios of CD71 containing bisecting GlcNAc were normalized to the total CD71 levels at each point. Data were quantified using ImageJ software and derived from three independent experiments. All values reflect one-way ANOVA with Tukey's *post hoc* analysis as the mean ± SD. $^{*}p < 0.05$ and $^{***}p < 0.001$. *I*, WT and *MGAT3* KO cells were cultured with or without 50 mM cycloheximide (CHX), a protein synthesis inhibitor, for indicated times (0, 4, 8, 12, and 24 h). Equal amounts of proteins were subjected to Western blotting with anti-CD71 antibodies. α-Tubulin was used as a loading control. Relative ratios were calculated based on the density of CD71 relative to α-Tubulin at each indicated time point, with the ratio at 0 h (without CHX) set as 1.0. Values represent mean ± SD from three independent experiments. $^{*}p < 0.05$; $^{***}p < 0.001$; and ns, no significance. *J*, CD71 protein expression in WT and *MGAT3* KO cells was detected using anti-CD71 antibody (*green*). The plasma membrane was stained using WGA lectin (*red*). Detection was accomplished using a ZEISS LSM 900 confocal microscope a ZEISS LSM 900 confocal microscope cells. Scale bars represent 10 μm. E4-PHA, *Phaseolus vulgaris* erythroagglutinin; NaBu, sodium butyrate; qPCR, quantitative PCR; WGA, Wheat germ agglutinin.

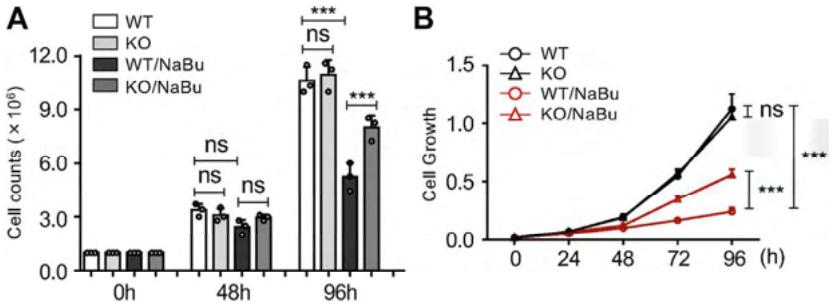


**Figure 5. *MGAT3* KO resulted in increased cell proliferation during NaBu-induced differentiation**. *A*, WT and *MGAT3* KO cells were cultured with or without NaBu treatment for indicated times, and then cell numbers were evaluated using a cell counter (ERMA). The results are presented as the mean ± SD from three independent experiments using one-way ANOVA with Tukey's *post hoc* analysis. $^{***}p < 0.001$; ns, no significance. *B*, WT and *MGAT3* KO cells were seeded in 96-well plates and cultured with 1 mM NaBu for indicated times. Cell proliferation was measured *via* Cell Counting Kit-8 assay as described in "Experimental procedures." Data are present as the mean ± SD (n = 3), two-way ANOVA. $^{***}p < 0.001$; ns, no significance. NaBu, sodium butyrate.

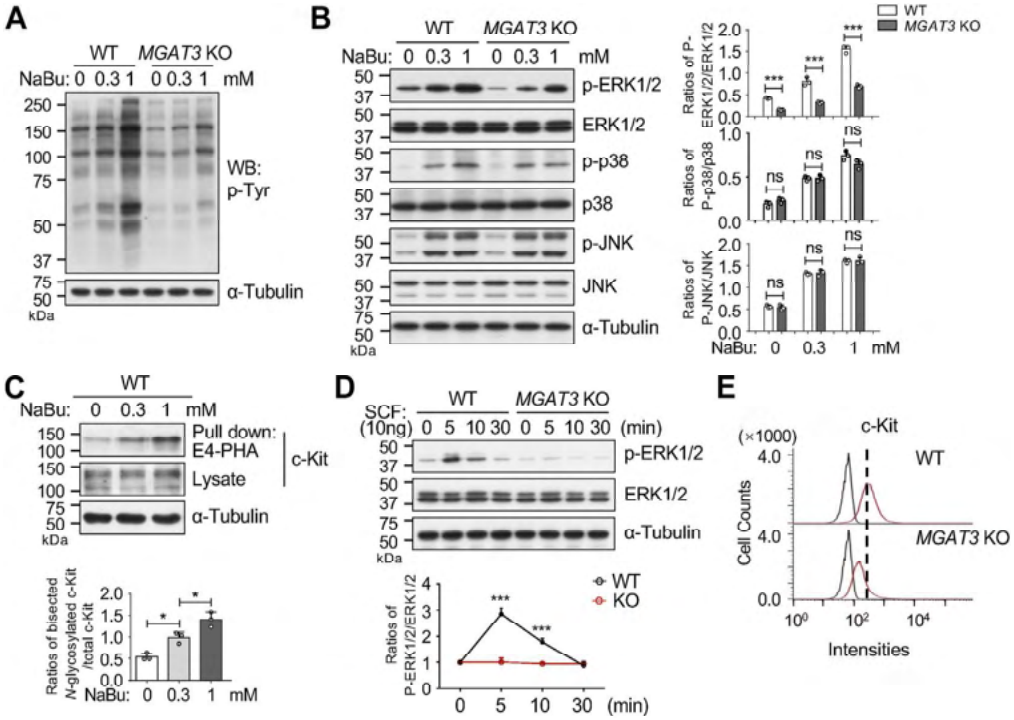


**Figure 6. Effects of *MGAT3* KO on cellular signaling**. WT and *MGAT3* KO cells were cultured with or without NaBu at indicated concentrations for 96 h. *A*, equal amounts of proteins from these cells were subjected to Western blotting using an anti-p-Tyr antibody. α-Tubulin was used as a loading control. *B*, equal amounts of proteins were loaded into a 15% SDS-PAGE gel to compare the expression levels and phosphorylation states of ERK1/2, p38, and JNK in the indicated cells. α-Tubulin was used as a loading control. Relative ratios were calculated based on the density of each phosphorylated form relative to the total form at each indicated time point. Data were quantified using Image J software and obtained from three independent experiments. *p* values were calculated using two-way ANOVA as the mean ± SD. ***$p < 0.001$; ns, no significance. *C*, equal amounts of proteins were incubated with E4-PHA-agarose, and the samples were subjected to Western blotting with an anti-c-Kit antibody. α-Tubulin was used as a loading control. The experiments were independently repeated three times. Relative ratios were calculated based on the intensity of c-Kit containing bisecting GlcNAc relative to total c-Kit at each point. All values represent one-way ANOVA with Tukey's *post hoc* analysis as mean ± SD. *$p < 0.05$. *D*, effects of SCF stimulation on the ERK1/2 signaling were compared between WT and *MGAT3* KO cells. Equal amounts of proteins were subjected to Western blotting with indicated antibodies. α-Tubulin was used as a loading control. Relative ratios were calculated based on the band intensity of each phosphorylated ERK1/2 relative to the total ERK1/2 at each time point, and the ratio at 0 min for each group was set as 1.0. The experiments were independently repeated three times. *p* values were calculated using two-way ANOVA. ***$p < 0.001$. *E*, comparison of c-Kit expression levels on the cell surface in WT and *MGAT3* KO cells using flow cytometry. ERK, extracellular signal–regulated kinase.

that c-Kit is one of the target proteins for GnT-III during NaBu-induced differentiation. The total c-Kit expression levels in cell lysates were similar among the cells treated with or without NaBu (Fig. 6*C*). Moreover, stimulation with stem cell factor resulted in a significant increase in the ERK pathway activation, which was significantly inhibited in the *MGAT3* KO cells (Fig. 6*D*). Interestingly, the result of the flow cytometry analysis showed the absence of *MGAT3* significantly reduced the expression of c-Kit on the cell surface, compared to WT cell (Fig. 6*E*). Therefore, it can be interpreted that that GnT-III–mediated modification of RTKs such as c-Kit may upregulate their expression levels on the cell surface, as well as may enhance ligand–receptor interactions, thereby upregulating ERK activation. The detailed mechanism remains further study.

### *U0126, a MEK inhibitor, inhibited NaBu-induced erythroid differentiation in K562 cells*

To demonstrate the importance of the MEK/ERK1/2 pathway in NaBu-induced erythroid differentiation, K562 cells were treated with or without U0126. After incubating K562 cells with U0126 for the indicated times, the phosphorylation levels of ERK1/2 induced by NaBu were effectively suppressed by U0126 as early as 1 h, with a gradual rebound at 8, 12, or 24 h (Fig. 7*A*), suggesting the inhibitory effect of U0126 last for 8 h. Consequently, we replaced the cell culture medium containing fresh U0126 every 8 h during the induction period, as depicted in Fig. 7*B*. As expected, U0126 significantly suppressed the phospho-ERK1/2 levels in both WT cells and WT/NaBu cells (Fig. 7*C*). Concurrently, visual inspection of cell differentiation supported a pronounced inhibition by U0126 of NaBu-induced erythroid differentiation (Fig. 7*D*).

Furthermore, mRNA levels of α-globin and β-globin were significantly decreased after U0126 treatment, as validated by qPCR assay (Fig. 7*E*). Additionally, expression levels of CD235a protein were examined by flow cytometry (Fig. 7*F*), and CD71 protein levels were assessed by Western blotting (Fig. 7*G*). The results showed that U0126 inhibited the expression levels of CD235a protein induced by NaBu (Fig. 7*F*) and suppressed CD71 protein expression in both WT and

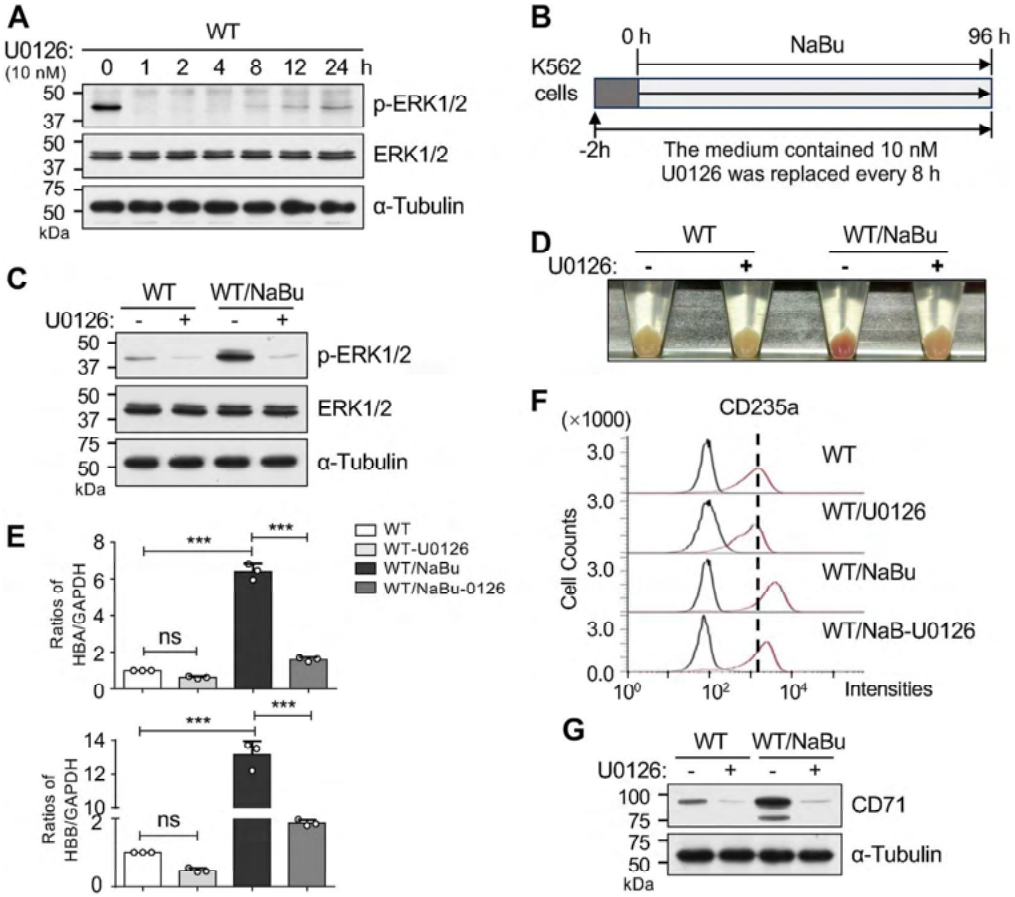


**Figure 7. Inhibition of ERK1/2 signaling suppressed NaBu-induced erythroid differentiation**. *A*, WT K562 cells were cultured with or without 10 nM U0126, a highly selective inhibitor of MEK1/2, for the indicated times (0, 1, 2, 4, 8, 12, and 24 h). Equal amounts of proteins from these cells were subjected to Western blotting using the indicated antibodies. α-Tubulin was used as a loading control. *B*, a schedule depicts inhibition of the ERK1/2 pathway using U0126 during the NaBu-induced erythroid differentiation. *C*, based on the treatment as described in (*B*), equal amounts of cell lysates were subjected to Western blotting using indicated antibodies. α-Tubulin was used as a loading control. *D*, effects of U0126 on coloration in WT cells with or without NaBu treatment. *E*, mRNA expression levels of *HBA* and *HBB* were compared using qPCR in WT and WT/NaBu cells treated with or without U0126. GAPDH served as the internal control. All values were normalized to the GAPDH levels, with the ratio of WT without U0126 set as 1.0. Data are presented as mean ± SD from three independent experiments using one-way ANOVA with Tukey's *post hoc* analysis. ***$p < 0.001$; ns, no significance. *F*, expression levels of CD235a on the cell surface were analyzed by flow cytometry using CD235a antibody. *G*, expression levels of CD71 were analyzed by Western blotting. α-Tubulin was used as a loading control. The experiments were independently repeated three times. ERK, extracellular signal–regulated kinase; NaBu, sodium butyrate; qPCR, quantitative PCR.

WT/NaBu cells (Fig. 7*G*). These findings further confirm the critical role of the ERK1/2 signaling pathway in NaBu-induced erythroid differentiation.

### *Inhibition of the ERK1/2 signaling downregulated the expression levels of GnT-III and bisected* N*-glycans*

To elucidate the relationship between the ERK1/2 signaling and GnT-III, we investigated the impact of inhibiting the ERK1/2 pathway with U0126 on the expression of bisected *N*-glycans. Lectin blot analysis using E4-PHA demonstrated that the levels of bisected *N*-glycans were significantly suppressed as early as 1 h after U0126 treatment, reaching the lowest expression at 2, 4, and 8 h, followed by a rebound observed from 12 h onward (Fig. 8*A*), which paralleled the phospho-ERK1/2 dynamics shown in Fig. 7*A*. This suppression was corroborated by qPCR analysis of *MGAT3* levels (Fig. 8*B*), where U0126 markedly inhibited *MGAT3* expression in both WT cells and WT/NaBu cells. Furthermore, lectin blotting (Fig. 8*C*) and flow cytometry using E4-PHA (Fig. 8*D*) revealed that U0126 downregulated the expression levels of bisected *N*-glycans induced by NaBu. These findings collectively support the idea that the ERK1/2 signaling is crucial for the expression of GnT-III and its product, bisected *N*-glycans, in K562 cells.

## Discussion

In the present study, we established an erythroid differentiation model using K562 cells induced by NaBu and identified four results: (1) the expression levels of MGAT3 and bisected N-glycans were greatly increased in the erythroid differentiation cells; (2) MGAT3 KO suppressed the induction of differentiation as validated by cell coloration, β-globin, CD235a expression, and the activation of the RTKs/ERK1/2 pathway; (3) inhibition of the ERK1/2 signaling impaired the NaBu-induced erythroid differentiation, accompanied by the

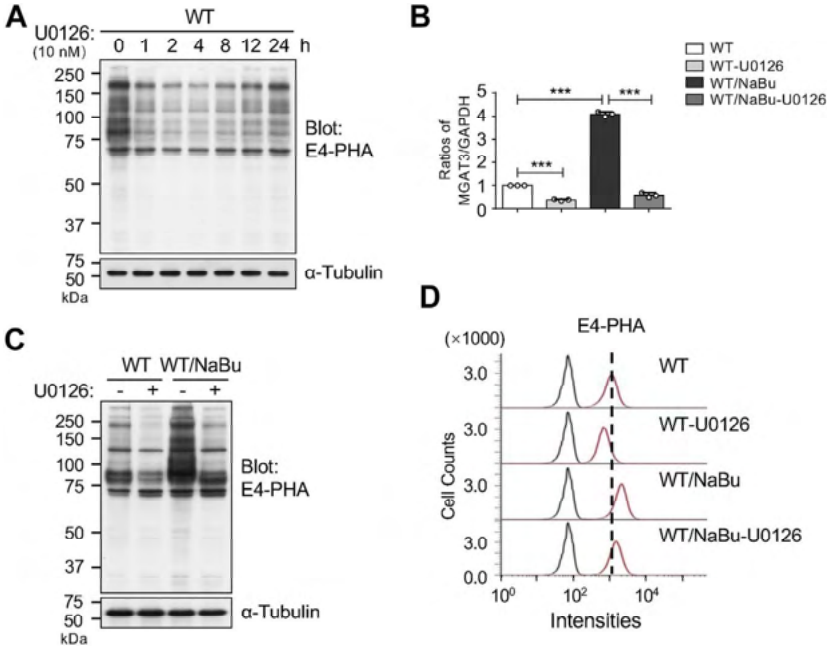


**Figure 8. Expression levels of bisected *N*-glycans and *MGAT3* were significantly decreased after treatment with U0126.** *A*, equal amounts of proteins from K562 WT cells treated with or without U0126 for the indicated times were subjected to lectin blotting using E4-PHA. α-Tubulin was used as a loading control. *B*, mRNA levels of *MGAT3* were measured using qPCR in WT and WT/NaBu cells treated with or without U0126. GAPDH served as the internal control. All values were normalized to the GAPDH levels, with the ratio of WT without U0126 set as 1.0. Data are presented as mean ± SD from three independent experiments. *p* values were calculated using one-way ANOVA with Tukey's *post hoc* analysis. ***$p < 0.001$. *C*, effects of U0126 on expression levels of bisected *N*-glycans in cell lysates using E4-PHA lectin blotting in WT and WT/NaBu cells. α-Tubulin was used as a loading control. *D*, effects of U0126 on expression levels of bisected *N*-glycans on the cell surface were analyzed using flow cytometry in WT and WT/NaBu cells. NaBu, sodium butyrate; qPCR, quantitative PCR.

decreased the expression levels of MGAT3 and bisected N-glycans; and (4) membrane proteins, such as c-Kit and CD71, which are closely related to erythroid differentiation, were modified by GnT-III to regulate their biological functions. Therefore, we conclude that GnT-III plays a pivotal role in erythroid differentiation *via* the ERK1/2 signaling pathway (Fig. 9). This study elucidates a novel mechanism underlying the involvement of GnT-III in erythroid differentiation, providing new insights into the role of *N*-glycosylation in regulating cancer differentiation.

On the other hand, previous studies have shown that *Mgat3*-KO mice are viable and reproduced normally, without significant alterations in circulating leukocytes and erythrocytes compared to WT mice (36), which seems to contradict to the results observed in the present study. The different phenotypes could be speculated to arise from 1) the complexity of erythrocyte differentiation *in vivo*, which involves the coordination of a network of transcription factors and epigenetic regulators from surrounding cells; 2) the possibility that other pathways *in vivo* may compensate for *Mgat3*-KO–mediated deficiencies; and 3) the role of BCR-ABL, formed by a reciprocal chromosomal translocation to create an aberrant BCR-ABL gene on chromosome 22, which is critical to the pathogenesis of CML due to its effects on aberrant cell signaling. Coincidently, the human *MGAT3 is mapped* on chromosome 22, suggesting that the translocation of BCR-ABL may alter the functions of GnT-III, as observed in this study. The precise mechanisms require further investigation.

Aberrant glycosylation of membrane or secreted proteins, associated with neoplastic transformation, is a prominent characteristic of cancer (37, 38). GnT-III has been reported to be profoundly involved in cell adhesion, growth, invasion, differentiation, and cancer metastasis (22, 39, 40). For instance, EMT is crucial in cancer initiation and metastasis (41). TGF-β1–induced EMT downregulates GnT-III expression, whereas overexpression of GnT-III inversely suppresses EMT by prolonging E-cadherin turnover on the cell surface (23). GnT-III negatively regulates cell adhesion and migration by modulating integrin family proteins such as α3β1 and α5β1 (42, 43). The molecular mechanism has been speculated that the modification by the bisecting GlcNAc on integrin may change its conformation and interrupt ligand binding (44). In fact, the crystal structure of integrin α5β1 has revealed that the interface between fibronectin and α5β1 is surrounded by some *N*-glycans, which may participate in the regulation of their interaction (45). Furthermore, GnT-III specifically modifies site-4 from among 14 other potential *N*-glycosylation sites on integrin α5 (46). GnT-III also selectively modifies specific target glycoproteins; for example, it modifies potential *N*-glycosylation sites on TNFR2 but not TNFR1, influencing downstream signaling pathways (3). Loss of bisecting GlcNAc on TNFR2 promotes auto-trimerization and up-regulates P-glycoprotein, promoting chemoresistance, which can be suppressed by GnT-III overexpression. Here, we demonstrate that GnT-III modifies c-Kit and CD71 membrane proteins, critical in erythroid differentiation. c-Kit–mediated cellular

## *Importance of bisected* N*-glycans in differentiation*

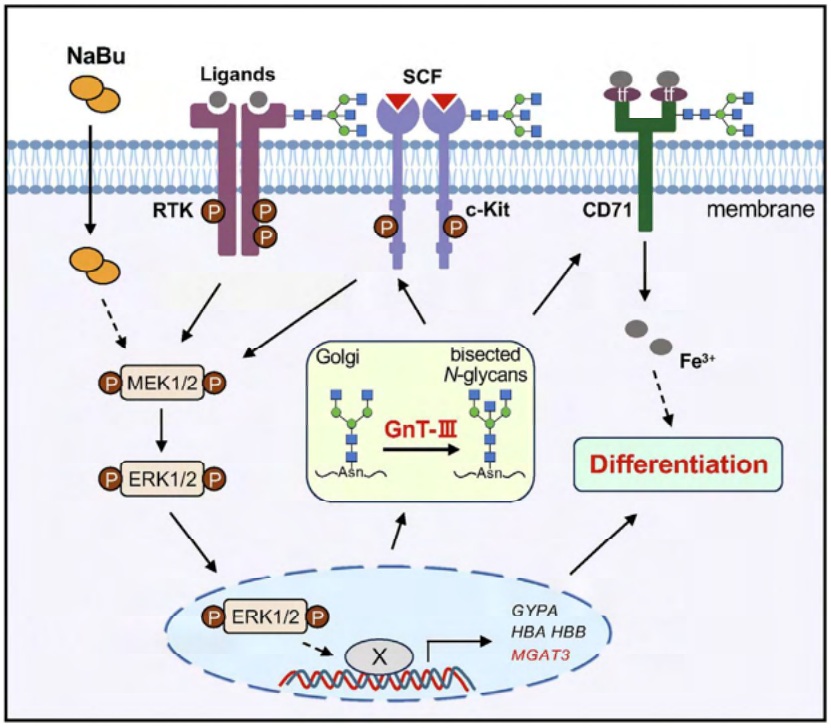


**Figure 9. Proposed molecular mechanism for the regulation of NaBu-induced erythroid differentiation by GnT-III**. This study demonstrates that GnT-III expression can regulate NaBu-induce erythroid differentiation through the RTKs/ERK1/2 pathway. GnT-III modifies membrane glycoproteins such as c-Kit and CD71, which are critical for erythroid differentiation, enhancing their biological functions including protein stability and signal transduction. c-Kit, a potent receptor tyrosine kinase (RTK), is pivotal in erythroid differentiation (68), while CD71 facilitates the cellular internalization of iron ions from transferrin (69). Conversely, GnT-III expression and bisected *N*-glycans are augmented *via* ERK1/2 activation during NaBu-induced erythroid differentiation. Inhibition of ERK1/2 activation suppresses GnT-III expression and erythroid differentiation, suggesting a positive feedback loop between GnT-III and ERK1/2 activation. Whether NaBu can directly activate MEK1/2 or P-ERK1/2 enters the nucleus to act directly as transcription factors or form a complex with others (X) for transcriptional regulation remains to be studied further. The *dotted line* (- - -) indicates unclear and/or indirect effects. Given the essential role of ERK1/2 signaling in NaBu-induced erythroid differentiation of K562 cells, manipulating GnT-III could represent a novel approach for differentiation therapy. ERK, extracellular signal–regulated kinase; GnT, *N*-acetylglucosaminyltransferase; NaBu, sodium butyrate.

signaling and CD71 stability were significantly suppressed in *MGAT3* KO cells compared to WT cells, suggesting that GnT-III expression profoundly impacts tumor biology, including malignancy and differentiation. Therefore, although the amount of bisected *N*-glycans is only minor among *N*-glycans (Fig. 3 and Table S2), they may specifically modify *N*-glycosylation sites on specific proteins, such as c-Kit, contributing significantly to cell differentiation.

GnT-III expression is regulated by cell–cell adhesion, significantly up-regulated in epithelial cells expressing E-cadherin but not in E-cadherin–deficient cells (47, 48). *N*-glycosylation at Asn-633 of E-cadherin is essential for its expression, folding, and trafficking (49, 50). GnT-III overexpression enhances E-cadherin retention at the cell border, enhancing E-cadherin–mediated homotypic adhesion, suggesting a positive feedback loop with E-cadherin expression (40). However, this does not apply to K562 cells, which do not express E-cadherin. β-catenin, a downstream factor of E-cadherin and a central player in the canonical Wnt signaling pathway, suppresses GnT-III expression by binding to lymphoid enhancer factor-1/T-cell factor, thereby inhibiting *MGAT3* expression (23). Wnt signaling promotes tumor progression, potentially promoting cell proliferation and invasion rather than differentiation. Here, we demonstrate an alternative GnT-III induction pathway *via* NaBu-induced ERK/MAPK signaling, enhancing GnT-III expression and erythroid differentiation. Conversely, ERK/MAPK signaling inhibition suppresses differentiation and *MGAT3* expression (Fig. 8). *MGAT3* KO significantly inhibited NaBu-induced erythroid differentiation while enhancing cell proliferation (Fig. 5), indicating a positive feedback loop between cell differentiation and GnT-III expression (Fig. 9). In addition, we cannot exclude the influences from an interplay between glycan and redox (51). Glycan synthesis occurs in the endoplasmic reticulum and Golgi, so it is reasonable to assume that redox changes in these compartments affect glycosylation reactions, especially in erythroid differentiation, warranting further study.

CML is characterized by abnormal hematopoietic cell proliferation in the bone marrow. Unfortunately, many patients develop drug resistance or experience severe side effects from the targeted therapy, tyrosine kinase inhibitor (8). Differentiation therapy offers a less toxic approach, using drugs to induce cancer cell differentiation, reducing proliferative capacity, and promoting terminal differentiation or apoptosis (52). For example, all-trans retinoic acid treats APL by inducing leukemia cell differentiation, improving patient outcomes (53). We found that inhibiting fucosylation enhances all-trans retinoic acid–induced differentiation in APL cells

(54). Together, these findings, including ours, further suggest glycosylation's role in cell functions and differentiation.

A deeper understanding of differentiation mechanisms may lead to new therapeutic targets. The ERK/MAPK pathway, crucial in cell proliferation, apoptosis, and differentiation (55), is often hyperactive in various cancers (56). GnT-III overexpression enhances ERK activation in several cancer cell lines, modifying RTK receptors such as EGFR and c-Met to enhance downstream signaling (57, 58). However, GnT-III can also downregulate RTK receptors like TrKA and EGFR-mediated signals in PC12 cells (59, 60) and other cells (61). Thus far, these discrepancies remain unclear, but we can speculate that it is due to different target proteins and/or cell lines. Here, we show that GnT-III modifies c-Kit, a potential RTK receptor in erythroid differentiation, suppressing its mediated ERK activation in *MGAT3* KO cells (Fig. 6), suggesting that GnT-III expression upregulates the ERK activation. Inhibiting ERK activation effectively blocks NaBu-induced erythroid differentiation. Recently, Feng J. *et al.* reported lower GnT-III levels and bisecting GlcNAc on bone marrow stroma in myelodysplastic syndrome and acute myeloid leukemia patients compared to healthy donors (62), further suggesting GnT-III as a potential target associated with the ERK pathway in differentiation therapy.

## Experimental procedures

### *Antibodies and reagents*

The experiments were performed using the following antibodies and reagents: Antibodies against CD71 (13113), c-Kit (3074), p44/42 MAPK (ERK1/2; 9102), phospho-p44/42 MAPK (Thr202/Tyr204) (p-ERK1/2; 4370), SAPK/JNK (9252), phospho-SAPK/JNK (Thr183/Tyr185) (4668), p38 MAPK (9212), phospho-p38 MAPK (Thr180/Tyr182) (4511), the peroxidase-conjugated secondary antibody against rabbit (7074S), and U0126 (9903) were purchased from Cell Signaling Technology; biotinylated E4-PHA (B-1385), DSA (B-1185), biotinylated L4-PHA (B-1115–2), biotinylated SNA (B-1305), biotinylated Wheat germ agglutinin (B-1025-5), and ABC kit (PK-4000) were from Vector Laboratories; biotinylated LCA (J207) and E4-PHA agarose (J311) were obtained from J-Oil Mills; biotinylated MAM lectin (#BA-s7801-2) was purchased from EY Laboratories; The anti-α-Tubulin (T6199) antibody and peroxidase-conjugated secondary agents against mouse (AP124P), NaBu (303410), SAHA (HY-10221), and hemin (HY-19424) were acquired from Sigma; The antibody against CD235a (JC159) was from Thermo Fisher Scientific; The goat anti-mouse IgG Alexa Fluor 568, goat anti-rabbit IgG Alexa Fluor 488 and streptavidin conjugate Alexa Fluor 647 antibody were from Invitrogen; phosphotyrosine (p-Tyr) antibody (sc-7020) was from Santa Cruz; PNGase F was from Roche. The cycloheximide (037-20991) was from Wako; CCK-8 was obtained from DOJINDO (341-07761).

### *Cell culture and induction of erythroid differentiation*

The human leukemia cell line K562 was obtained from the Cell Resource Center for Biomedical Research, Tohoku University. The HEL cells were purchased from RIKEN Cell Bank. The cells were cultured in RPMI 1640 medium supplemented with 10% fetal bovine serum (endotoxin level 10 EU/ml/ml) and 1% antibiotic/antimycotic agent (Gibco) in a 5% $CO_2$, 37 °C humidified atmosphere. During erythroid differentiation, K562 cells at a density of $1 \times 10^5$ cells/ml were treated with NaBu at different concentrations over a period of 4 days. In addition, the K562 cells and HEL cells were treated with 10 μM hemin for 6 days. These cells were confirmed to be free from *mycoplasma* using the e-Myco *Mycoplasma* PCR Detection kit (iNtRON Biotechnology, Republic of Korea).

### *Pull-down assay, Western blot, and lectin blot*

Cells were washed three times with ice-cold PBS and subsequently lysed in cell lysis buffer (comprising 20 mM Tris–HCl, pH 7.4, 150 mM NaCl, 1% Triton X-100) containing protease and phosphatase inhibitors (Nacalai Tesque) on ice for 30 min. The lysates were then centrifugated at 15,000 *g* and 4 °C for 10 min. The supernatant was immediately transferred to a fresh centrifuge tube, and the pellet was discarded. Protein concentration in the supernatant was quantified using a bicinchoninic acid protein assay kit (Pierce).

For the pull-down assay, equal quantities of proteins from each cell lysate were incubated with PHA-E4-Agarose at 4 °C overnight with rotation. Subsequently, the precipitates were washed twice with tris-buffered saline and detected by Western blotting using specific antibodies as indicated.

Western blot and lectin blot were performed as follows: equal amounts of protein (10 ug) were separated on 7.5% or 15% SDS/PAGE gels at 100 V and transferred to polyvinylidene difluoride membranes (Millipore Sigma) at 10 V for 1 h. These membranes were blocked with freshly prepared 5% bovine serum albumin (BSA) for lectin blotting or 5% nonfat dried milk for Western blotting, supplemented with 0.05% Tween-20, at room temperature for 90 min. Subsequently, the membranes were incubated with specific primary antibodies or biotinylated lectins at 4 °C overnight. After washing three times for 5 min each, the membranes were incubated with appropriate secondary antibodies. Immunoreactive bands were detected using an immobilon Western Chemiluminescent horseradish peroxidase Substrate (Millipore) according to the manufacturer's instructions.

### *Establishment of* MGAT3*-KO cells*

The pSpCas9(BB)-2A-GFP (PX458) plasmid was obtained from Addgene (PX458: Addgene #48138). *MGAT3* KO cells were generated using guide RNA (5′- CATGCG-CAAGTCGCTCTACG -3′) targeted to human GnT-III genes, which are adjacent to Cas9 in the pSpCas9(BB)-2A-GFP vector. GFP-expressing cells were sorted to select for successful transfection. The stable K562-*MGAT3* KO cell line was established by electroporating cells following the manufacturer's recommendations (Amaxa cell line Nucleofector kit; Lonza). After 24 h, cells showing positive fluorescence were sorted using FACSAria II (BD Bioscience), diluted, and seeded on 96-well plates to obtain single clones. These single clones

were expanded over a 4-week period. Genomic DNA was extracted from these clones, and the CRISPR target region was validated by PCR amplification using the following primers: Forward primer, 5′- TTCCTCACCCAGGACGGC -3′; Reverse primer, 5′- CGAGCTTGAAGTAGATGCCCT-3′. Sequencing was performed using the reverse primer to confirm the desired genomic modifications.

### *Real-time PCR qPCR*

RNAs were extracted using TRI Reagent (Molecular Research Center, Lnc), and then 1 μg of total RNAs was reverse transcribed into complementary DNA using a PrimeScript RT reagent with a genomic DNA Eraser (Takara, Japan) according to the manufacturer's instructions. The specific primer sequences are listed in Table 1. PCR products were diluted to 50 ng/μl and analyzed using StepOnePlus (Applied Biosystem). Real-time PCR analyses were performed using TB Green Premix Ex Taq II (Tli RNaseH Plus) (Takara) under the following conditions: initial denaturation at 95 °C for 30 s, followed by 40 cycles of denaturation at 95 °C for 5 s, and annealing and extension at 60 °C for 30 s.

### *Flow cytometry*

Cells ($1 \times 10^6$) were harvested and washed with ice-cold PBS. Equal amounts of cells were then incubated with biotinylated lectins (E4-PHA) or antibodies against CD235a in magnetic-activated cell sorting buffer (0.1% BSA in PBS) for 30 min on ice. After incubation, the cells were further incubated with streptavidin conjugate Alexa Fluor 647 (1:3000) or goat anti-mouse IgG Alexa Fluor 568 (1:500) for 30 min at room temperature in the dark. Subsequently, the cells were washed and resuspended in 800 μl of magnetic-activated cell sorting buffer. Fluorescence intensities were detected using the Attune flow cytometer (BD Biosciences) following flow cytometry experiment standard (63) and analyzed using FlowJo software (https://www.flowjo.com).

### *Immunofluorescence staining*

Cells ($1 \times 10^6$) were collected into 1.5 ml tubes. After washing twice with PBS, the cells were fixed with 4% paraformaldehyde for 30 min. Subsequently, the cells were treated with 0.1% Triton X-100 in PBS for 10 min, followed by incubation with 5% BSA in PBS at room temperature for 2 h to block nonspecific staining. The cells were then stained with an antibody against CD71 (green) at a dilution of 1:100 at 4 °C overnight. Meanwhile, the plasma membrane was stained using Wheat germ agglutinin lectin (red) at a dilution of 1:300. After washing with PBS, the cells were incubated with secondary antibodies (goat anti-rabbit IgG Alexa Fluor 488 and streptavidin conjugate Alexa Fluor 647) for 2 h. Additionally, the cells were stained with 4′,6-diamidino-2-phenylindole at room temperature for 8 min in the dark. Detection was accomplished using a ZEISS LSM 900 confocal microscope.

### N*-glycan analysis of cell membrane proteins* via *MALDI-TOF MS analysis*

For *N*-glycan analyses, cell pellets were prepared by homogenate and separated by ethanol precipitation, following previously described methods (64). *N*-glycans were extracted from protein pellets through a series of steps, including reduction, alkylation, trypsin digestion, and deglycosylation using PNGase F (65). The released *N*-glycans were subjected to a glycoblotting procedure in combination with the aminolysis-sialic acid linkage specific alkylamidation method, as outlined in previous studies (66, 67). Subsequently, purified and labeled *N*-glycans were analyzed by MALDI-TOF MS analysis, following established protocols (66).

### *LC-ESI-MS/MS analysis of bisected* N*-glycans*

Hydrophilic interaction chromatography-purified *N*-glycans from WT/NaBu cells were dissolved in 2% acetonitrile (MeCN) containing 0.1% formic acid (FA) at a concentration of 0.5 μg proteins/μl and subjected to LC-ESI-MS/MS analysis. The analysis of bisected *N*-glycans was performed on an UltiMate 3000 RSLCnano system (Thermo Fisher Scientific) coupled to a Q Exactive mass spectrometer (Thermo Fisher Scientific) equipped with a nano ESI source. The LC system had a trap column (C18 PepMap 100, 0.3 × 5 mm, 5 μm, Thermo Fisher Scientific) and an analytical column (NTCC-360/75–3-125, Nikkyo Technos). After loading the sample onto a trap column, the valve was switched to allow the separation of *N*-glycans using the analytical column. Separation was carried out with a 30-min gradient of water containing

**Table 1**
**Primer sequences for real-time PCR**

| Target genes | Primer sequences (5′-3′) | |
|---|---|---|
| | Forward sequences | Reverse sequences |
| HBA | CCAAGACCTACTTCCCGCAC | CGTTGGGCATGTCGTCCA |
| HBB | TCCTGATGCTGTTATGGGCA | CTCACTCAGTGTGGCAAAGGT |
| GYPA | TGATACGCACAAACGGGACA | ACCAGCCATCACCCCAAAAA |
| TFRC | TCGGAGAAACTGGACAGCAC | ATCACGCCAGACTTTGCTGA |
| MGAT1 | TGACCAGCACCTCAAGTTTATC | CGGAACTGGAAGGTGACAATAC |
| MGAT2 | AGAGTGCCCTGAATGTGATG | CACAGTCTCCAGCATGAAAGA |
| MGAT3 | GCCGCGTCATCAACGCCATCAA | CAGGTAGTCGTCGGCGATCCA |
| MGAT4A | GGCTATCACACCGATAGCTGGAG | TCCACCATTCCTTCTGCAACACC |
| MGAT4B | ACAACCCTCAGTCAGACAAGGAGG | GGTACCCTCAGAAGCCCGCAGCTT |
| MGAT5 | GACCTGCAGTTCCTTCTTCG | CCATGGCAGAAGTCCTGTTT |
| FUT8 | GACAGAACTGGTTCAGCGGAGA | GCAGTAGACCACATGATGGAGC |
| GAPDH | ACTCCACTCACGGCAAATTC | CCCTGTTGCTGTAGCCGTAT |

0.1% FA (mobile phase A) and MeCN containing 0.1% FA (mobile phase B) at a flow rate of 300 nl/min. The gradient was performed as follows: 0 to 3 min, 2% B; 3 to 33 min, 2% to 40% B; 33 to 35 min, 40% to 95% B; 35 to 45 min, 95% B; 45 to 47 min, 95%–2% B; and 47 to 60 min, 2% B. MS/MS spectra were obtained using targeted selected ion monitoring/data-dependent–MS/MS acquisition mode. Parameters for selected ion monitoring are as follows: polarity, positive; resolution, 70,000; automatic gain control (AGC) target, 5e4; maximum ion trap, 100 msec; and isolation window, 4.0 *m/z*. Parameters for data-dependent–MS/MS are as follows: resolution, 35,000; AGC target, 2e5; maximum ion trap, 100 msec; isolation window, 1.6 *m/z*; normalized collision energy, 15; minimum AGC target, 8e3; intensity threshold, 8e4; and dynamic exclusion, 0.2 s.

### *Cell proliferation assay*

Equal amounts of cells ($2 \times 10^3$ cells/100 μl/well) were plated into a 96-well plate and cultured in normal media with or without NaBu at 1 mM. The cells were then incubated for various durations (0, 24, 48, 72, and 96 h). After the respective incubation periods, 10 μl of CCK-8 solution was added to each well and further incubated for another 1 h at 37 °C. Subsequently, cell viability was assessed by measuring the absorbance at 450 nm using a microplate reader (SYNERGY multimode reader; BioTek).

### *Statistical analysis*

All data are presented as the mean ± SD obtained from at least three independent experiments. Statistics analyses were performed using a one-way ANOVA with Tukey's *post hoc* test, two-way ANOVA with Tukey's multiple comparisons test or an unpaired Student *t* test using GraphPad Prism 6.0 software (GraphPad Software, Inc). A probability value of $p$ was considered as follows: ns (no significance) for $p > 0.05$; $^{*}p < 0.05$; $^{**}p < 0.01$; and $^{***}p < 0.001$.

## Data availability

All data presented in the figures, tables, and supplementary information of this paper are available. The Glycoproteomic raw MS data and the identification result file for analysis of glycan structures on peptides have been deposited at the GlycoPOST (announced ID: GPST000415; https://glycopost.glycosmos.org/preview/1024471763666be582292fb; PIN CO DE:1143).

*Supporting information*—This article contains supporting information.

*Acknowledgments*—The authors would like to acknowledge Dr Shin Yomogida from the Division of Clinical rmacotherapeutics, Tohoku Medical and Pharmaceutical University, Japan, for the valuable discussions on K562 cell culture and differentiation.

*Author contributions*—T. W. and J. G. writing–review and editing; T. W. and Y. S. writing–original draft; T. W., Y. S., D. W., T. I., T. F., C. S., H. H., T. N., and J.-i. F. visualization; T. W., Y. S., D. W., T. I., T. F., C. S., H. H., T. N., and J.-i. F. validation; T. W., Y. S., D. W., T. I., T. F., C. S., H. H., T. N., H. T., Y. M., and J.-i. F. methodology; T. W., Y. S., D. W., C. S., H. H., T. N., H. T., Y. M., and J.-i. F. investigation; T. W., Y. S., D. W., T. I., C. S., H. H., T. N., H. T., Y. M., and J.-i. F. formal analysis; T. W., Y. S., D. W., T. I., T. F., C. S., H. H., T. N., H. T., Y. M., and J.i. F. data curation; T. W., Y. S., T. I., T. F., and J. G. conceptualization; T. I., T. F., and J. G. resources; T. I., T. F., and J. G. funding acquisition; J.-i. F. and J. supervision; J. G. project administration.

*Funding and additional information*—This work was partly supported by a Grant-in-Aid for Scientific Research (23K27133 to J. G., 22K06615 to T. I. and 21K06547 to T. F.), and by a Grant-in-Aid for Challenging Exploratory Research (22K19443 to J. G.) from the Japan Society for the Promotion of Science. This work was also conducted under the Collaborative Open Research Program to promote the Human Glycome Atlas Project (HGA) as strategic interdisciplinary research in the J-GlycoNet cooperative network, which is accredited by the Minister of Education, Culture, Sports, Science and Technology, MEXT, Japan, as a Joint Usage/Research Center.

*Conflicts of interest*—The authors declare that they have no conflicts of interest with the contents of this article.

*Abbreviations*—The abbreviations used are: AGC, automatic gain control; APL, acute promyelocytic leukemia; BSA, bovine serum albumin; CCK-8, Cell Counting Kit-8; CML, chronic myelogenous leukemia; DSA, *Datura stramonium* agglutinin; E4-PHA, *Phaseolus vulgaris* erythroagglutinin; EMT, epithelial-mesenchymal transition; ERK, extracellular signal–regulated kinase; FA, formic acid; GnT, *N*-acetylglucosaminyltransferase; HEL, human erythroleukemia; L4-PHA, *Phaseolus vulgaris* leucoagglutinin; LCA, *Lens culinaris* agglutinin; MAA, *M. amurensis*; MALDI-TOF MS, matrix-assisted laser desorption/ionization time-of-flight mass spectrometry; MAPK, mitogen-activated protein kinase; MS/MS, tandem mass spectrometry; NaBu, sodium butyrate; PNGase F, peptide-*N*-glycosidase F; qPCR, quantitative PCR; RTK, receptor tyrosine kinase; SAHA, suberanilohydroxamic acid; SNA, *S. nigra* agglutinin.

## References

1. Höpner, S. S., Raykova, A., Radpour, R., Amrein, M. A., Koller, D., Baerlocher, G. M., *et al.* (2021) LIGHT/LTβR signaling regulates self-renewal and differentiation of hematopoietic and leukemia stem cells. *Nat. Commun.* **12**, 1065
2. de Thé, H., and Chen, Z. (2010) Acute promyelocytic leukaemia: novel insights into the mechanisms of cure. *Nat. Rev. Cancer* **10**, 775–783
3. Song, W., Liang, C., Sun, Y., Morii, S., Yomogida, S., Isaji, T., *et al.* (2023) Expression of GnT-III decreases chemoresistance via negatively regulating P-glycoprotein expression: involvement of the TNFR2-NF-κB signaling pathway. *J. Biol. Chem.* **299**, 103051
4. Kurzrock, R., Kantarjian, H. M., Druker, B. J., and Talpaz, M. (2003) Philadelphia chromosome-positive leukemias: from basic mechanisms to molecular therapeutics. *Ann. Intern. Med.* **138**, 819–830
5. Druker, B. J., Tamura, S., Buchdunger, E., Ohno, S., Segal, G. M., Fanning, S., *et al.* (1996) Effects of a selective inhibitor of the Abl tyrosine kinase on the growth of Bcr-Abl positive cells. *Nat. Med.* **2**, 561–566
6. Braun, T. P., Eide, C. A., and Druker, B. J. (2020) Response and resistance to BCR-ABL1-targeted therapies. *Cancer Cell.* **37**, 530–542
7. Breccia, M., Chiodi, F., Nardozza, A. P., Valsecchi, D., Perrone, V., Sangiorgi, D., *et al.* (2023) The economic burden of chronic myeloid leukemia

in patients with later lines: findings from a real-world analysis in Italy. *Adv. Ther.* **40**, 961–974
8. Shyam Sunder, S., Sharma, U. C., and Pokharel, S. (2023) Adverse effects of tyrosine kinase inhibitors in cancer therapy: pathophysiology, mechanisms and clinical management. *Signal. Transduct. Target. Ther.* **8**, 262
9. Fu, Y. H., Ou, D. L., Yang, Y. R., Su, K. W., Chen, C. Y., Tien, H. F., *et al.* (2022) Cabozantinib promotes erythroid differentiation in K562 erythroleukemia cells through global changes in gene expression and JNK activation. *Cancer Gene Ther.* **29**, 784–792
10. de Thé, H. (2018) Differentiation therapy revisited. *Nat. Rev. Cancer* **18**, 117–127
11. Wang, F., Yu, J., Yang, G. H., Wang, X. S., and Zhang, J. W. (2011) Regulation of erythroid differentiation by miR-376a and its targets. *Cell Res.* **21**, 1196–1209
12. Grover, A., Mancini, E., Moore, S., Mead, A. J., Atkinson, D., Rasmussen, K. D., *et al.* (2014) Erythropoietin guides multipotent hematopoietic progenitor cells toward an erythroid fate. *J. Exp. Med.* **211**, 181–188
13. Kerenyi, M. A., Grebien, F., Gehart, H., Schifrer, M., Artaker, M., Kovacic, B., *et al.* (2008) Stat5 regulates cellular iron uptake of erythroid cells via IRP-2 and TfR-1. *Blood* **112**, 3878–3888
14. Arcasoy, M. O., and Jiang, X. (2005) Co-operative signalling mechanisms required for erythroid precursor expansion in response to erythropoietin and stem cell factor. *Br. J. Haematol.* **130**, 121–129
15. Jaskiewicz, E., Jodłowska, M., Kaczmarek, R., and Zerka, A. (2019) Erythrocyte glycophorins as receptors for Plasmodium merozoites. *Parasit. Vectors* **12**, 317
16. Hayes, G. R., Williams, A., Costello, C. E., Enns, C. A., and Lucas, J. J. (1995) The critical glycosylation site of human transferrin receptor contains a high-mannose oligosaccharide. *Glycobiology* **5**, 227–232
17. Bua, R. O., Messina, A., Sturiale, L., Barone, R., Garozzo, D., and Palmigiano, A. (2021) N-glycomics of human erythrocytes. *Int. J. Mol. Sci.* **22**, 8063
18. Varki, A. (2017) Biological roles of glycans. *Glycobiology* **27**, 3–49
19. Lee, J. M., Hammarén, H. M., Savitski, M. M., and Baek, S. H. (2023) Control of protein stability by post-translational modifications. *Nat. Commun.* **14**, 201
20. Stowell, S. R., Ju, T., and Cummings, R. D. (2015) Protein glycosylation in cancer. *Annu. Rev. Pathol.* **10**, 473–510
21. Kizuka, Y. (2024) Regulation of intracellular activity of N-glycan branching enzymes in mammals. *J. Biol. Chem.* **300**, 107471
22. Taniguchi, N., Ohkawa, Y., Maeda, K., Harada, Y., Nagae, M., Kizuka, Y., *et al.* (2021) True significance of N-acetylglucosaminyltransferases GnT-III, V and α1,6 fucosyltransferase in epithelial-mesenchymal transition and cancer. *Mol. Aspects Med.* **79**, 100905
23. Xu, Q., Isaji, T., Lu, Y., Gu, W., Kondo, M., Fukuda, T., *et al.* (2012) Roles of N-acetylglucosaminyltransferase III in epithelial-to-mesenchymal transition induced by transforming growth factor β1 (TGF-β1) in epithelial cell lines. *J. Biol. Chem.* **287**, 16563–16574
24. Sasaki, H., Toda, T., Furukawa, T., Mawatari, Y., Takaesu, R., Shimizu, M., *et al.* (2013) α-1,6-Fucosyltransferase (FUT8) inhibits hemoglobin production during differentiation of murine and K562 human erythroleukemia cells. *J. Biol. Chem.* **288**, 16839–16847
25. Koeffler, H. P., and Golde, D. W. (1980) Human myeloid leukemia cell lines: a review. *Blood* **56**, 344–350
26. Peschle, C. (1980) Erythropoiesis. *Annu. Rev. Med.* **31**, 303–314
27. Cummings, R. D., and Etzler, M. E. (2009) Antibodies and lectins in glycan analysis. In: Varki, A., Cummings, R. D., Esko, J. D., Freeze, H. H., Stanley, P., Bertozzi, C. R., *et al.* eds. *Essentials of Glycobiology*, Cold Spring Harbor Laboratory Press Copyright © 2009, The Consortium of Glycobiology Editors, La Jolla, California., Cold Spring Harbor (NY)
28. Frank, C. L., Manandhar, D., Gordân, R., and Crawford, G. E. (2016) HDAC inhibitors cause site-specific chromatin remodeling at PU.1-bound enhancers in K562 cells. *Epigenetics. Chromatin.* **9**, 15
29. Mehlert, A., Wormald, M. R., and Ferguson, M. A. (2012) Modeling of the N-glycosylated transferrin receptor suggests how transferrin binding can occur within the surface coat of Trypanosoma brucei. *Plos. Pathog.* **8**, e1002618
30. Ruijtenberg, S., and van den Heuvel, S. (2016) Coordinating cell proliferation and differentiation: Antagonism between cell cycle regulators and cell type-specific gene expression. *Cell. Cycle.* **15**, 196–212
31. Wagner, E. F., and Nebreda, A. R. (2009) Signal integration by JNK and p38 MAPK pathways in cancer development. *Nat. Rev. Cancer.* **9**, 537–549
32. Lavoie, H., Gagnon, J., and Therrien, M. (2020) ERK signalling: a master regulator of cell behaviour, life and fate. *Nat. Rev. Mol. Cell. Biol.* **21**, 607–632
33. Du, Z., and Lovly, C. M. (2018) Mechanisms of receptor tyrosine kinase activation in cancer. *Mol. Cancer* **17**, 58
34. Jeong, H., Kim, R. I., Koo, H., Choi, Y. H., Kim, M., Roh, H., *et al.* (2024) Stem cell factor and cKIT modulate endothelial glycolysis in hypoxia. *Cardiovasc. Res.* **120**, 745–755
35. Demetri, G. D., von Mehren, M., Blanke, C. D., Van den Abbeele, A. D., Eisenberg, B., Roberts, P. J., *et al.* (2002) Efficacy and safety of imatinib mesylate in advanced gastrointestinal stromal tumors. *N. Engl. J. Med.* **347**, 472–480
36. Priatel, J. J., Sarkar, M., Schachter, H., and Marth, J. D. (1997) Isolation, characterization and inactivation of the mouse Mgat3 gene: the bisecting N-acetylglucosamine in asparagine-linked oligosaccharides appears dispensable for viability and reproduction. *Glycobiology* **7**, 45–56
37. Taniguchi, N., and Kizuka, Y. (2015) Glycans and cancer: role of N-glycans in cancer biomarker, progression and metastasis, and therapeutics. *Adv. Cancer. Res.* **126**, 11–51
38. Lin, Y., and Lubman, D. M. (2024) The role of N-glycosylation in cancer. *Acta. Pharm. Sin. B.* **14**, 1098–1110
39. Lu, J., Isaji, T., Im, S., Fukuda, T., Kameyama, A., and Gu, J. (2016) Expression of N-acetylglucosaminyltransferase III suppresses α2,3-sialylation, and its distinctive functions in cell migration are attributed to α2,6-sialylation levels. *J. Biol. Chem.* **291**, 5708–5720
40. Gu, J., Sato, Y., Kariya, Y., Isaji, T., Taniguchi, N., and Fukuda, T. (2009) A mutual regulation between cell-cell adhesion and N-glycosylation: implication of the bisecting GlcNAc for biological functions. *J. Proteome. Res.* **8**, 431–435
41. Lamouille, S., Xu, J., and Derynck, R. (2014) Molecular mechanisms of epithelial-mesenchymal transition. *Nat. Rev. Mol. Cell Biol.* **15**, 178–196
42. Zhao, Y., Nakagawa, T., Itoh, S., Inamori, K., Isaji, T., Kariya, Y., *et al.* (2006) N-acetylglucosaminyltransferase III antagonizes the effect of N-acetylglucosaminyltransferase V on alpha3beta1 integrin-mediated cell migration. *J. Biol. Chem.* **281**, 32122–32130
43. Isaji, T., Gu, J., Nishiuchi, R., Zhao, Y., Takahashi, M., Miyoshi, E., *et al.* (2004) Introduction of bisecting GlcNAc into integrin alpha5beta1 reduces ligand binding and down-regulates cell adhesion and cell migration. *J. Biol. Chem.* **279**, 19747–19754
44. Isaji, T., Sato, Y., Zhao, Y., Miyoshi, E., Wada, Y., Taniguchi, N., *et al.* (2006) N-glycosylation of the beta-propeller domain of the integrin alpha5 subunit is essential for alpha5beta1 heterodimerization, expression on the cell surface, and its biological function. *J. Biol. Chem.* **281**, 33258–33267
45. Nagae, M., Re, S., Mihara, E., Nogi, T., Sugita, Y., and Takagi, J. (2012) Crystal structure of α5β1 integrin ectodomain: atomic details of the fibronectin receptor. *J. Cell Biol.* **197**, 131–140
46. Isaji, T., Sato, Y., Fukuda, T., and Gu, J. (2009) N-glycosylation of the I-like domain of β1 integrin is essential for β1 integrin expression and biological function: identification of the minimal N-glycosylation requirement for α5β1. *J. Biol. Chem.* **284**, 12207–12216
47. Akama, R., Sato, Y., Kariya, Y., Isaji, T., Fukuda, T., Lu, L., *et al.* (2008) N-acetylglucosaminyltransferase III expression is regulated by cell-cell adhesion via the E-cadherin-catenin-actin complex. *Proteomics* **8**, 3221–3228
48. Iijima, J., Zhao, Y., Isaji, T., Kameyama, A., Nakaya, S., Wang, X., *et al.* (2006) Cell-cell interaction-dependent regulation of N-acetylglucosaminyltransferase III and the bisected N-glycans in GE11 epithelial cells. Involvement of E-cadherin-mediated cell adhesion. *J. Biol. Chem.* **281**, 13038–13046

49. Zhou, F., Su, J., Fu, L., Yang, Y., Zhang, L., Wang, L., *et al.* (2008) Unglycosylation at Asn-633 made extracellular domain of E-cadherin folded incorrectly and arrested in endoplasmic reticulum, then sequentially degraded by ERAD. *Glycoconj. J.* **25**, 727–740
50. Liwosz, A., Lei, T., and Kukuruzinska, M. A. (2006) N-glycosylation affects the molecular organization and stability of E-cadherin junctions. *J. Biol. Chem.* **281**, 23138–23149
51. Khoder-Agha, F., and Kietzmann, T. (2021) The glyco-redox interplay: Principles and consequences on the role of reactive oxygen species during protein glycosylation. *Redox. Biol.* **42**, 101888
52. Leszczyniecka, M., Roberts, T., Dent, P., Grant, S., and Fisher, P. B. (2001) Differentiation therapy of human cancer: basic science and clinical applications. *Pharmacol. Ther.* **90**, 105–156
53. Ni, X., Hu, G., and Cai, X. (2019) The success and the challenge of all-trans retinoic acid in the treatment of cancer. *Crit. Rev. Food Sci. Nutr.* **59**, S71–s80
54. Suzuki, S., Liu, J., Sato, Y., Miyake, R., Suzuki, S., Okitsu, Y., *et al.* (2024) Fucosylation inhibitor 6-alkynylfucose enhances the ATRA-induced differentiation effect on acute promyelocytic leukemia cells. *Biochem. Biophys. Res. Commun.* **710**, 149541
55. Mendoza, M. C., Er, E. E., and Blenis, J. (2011) The Ras-ERK and PI3K-mTOR pathways: cross-talk and compensation. *Trends Biochem. Sci.* **36**, 320–328
56. Bahar, M. E., Kim, H. J., and Kim, D. R. (2023) Targeting the RAS/RAF/MAPK pathway for cancer therapy: from mechanism to clinical studies. *Signal Transduct. Target. Ther.* **8**, 455
57. Sato, Y., Takahashi, M., Shibukawa, Y., Jain, S. K., Hamaoka, R., Miyagawa, J., *et al.* (2001) Overexpression of N-acetylglucosaminyltransferase III enhances the epidermal growth factor-induced phosphorylation of ERK in HeLaS3 cells by up-regulation of the internalization rate of the receptors. *J. Biol. Chem.* **276**, 11956–11962
58. Hyuga, M., Hyuga, S., Kawasaki, N., Ohta, M., Itoh, S., Niimi, S., *et al.* (2004) Enhancement of hepatocyte growth factor-induced cell scattering in N-acetylglucosaminyltransferase III-transfected HepG2 cells. *Biol. Pharm. Bull.* **27**, 781–785
59. Ihara, Y., Sakamoto, Y., Mihara, M., Shimizu, K., and Taniguchi, N. (1997) Overexpression of N-acetylglucosaminyltransferase III disrupts the tyrosine phosphorylation of Trk with resultant signaling dysfunction in PC12 cells treated with nerve growth factor. *J. Biol. Chem.* **272**, 9629–9634
60. Gu, J., Zhao, Y., Isaji, T., Shibukawa, Y., Ihara, H., Takahashi, M., *et al.* (2004) Beta1,4-N-Acetylglucosaminyltransferase III down-regulates neurite outgrowth induced by costimulation of epidermal growth factor and integrins through the Ras/ERK signaling pathway in PC12 cells. *Glycobiology* **14**, 177–186
61. Cheng, L., Cao, L., Wu, Y., Xie, W., Li, J., Guan, F., *et al.* (2020) Bisecting N-acetylglucosamine on EGFR inhibits malignant phenotype of Breast cancer via down-regulation of EGFR/Erk signaling. *Front. Oncol.* **10**, 929
62. Feng, J., Wang, Y., Li, B., Yu, X., Lei, L., Wu, J., *et al.* (2023) Loss of bisecting GlcNAcylation on MCAM of bone marrow stoma determined pro-tumoral niche in MDS/AML. *Leukemia* **37**, 113–121
63. Lee, J. A., Spidlen, J., Boyce, K., Cai, J., Crosbie, N., Dalphin, M., *et al.* (2008) MIFlowCyt: the minimum information about a flow cytometry experiment. *Cytometry. A.* **73**, 926–930
64. Hanamatsu, H., and Furukawa, J. I. (2022) Comprehensive cellular glycan profiling of glycoproteins and glycosphingolipids by glycoblotting and BEP methods. *Methods. Mol. Biol.* **2556**, 1–18
65. Kita, Y., Miura, Y., Furukawa, J., Nakano, M., Shinohara, Y., Ohno, M., *et al.* (2007) Quantitative glycomics of human whole serum glycoproteins based on the standardized protocol for liberating N-glycans. *Mol. Cell. Proteomics.* **6**, 1437–1445
66. Hanamatsu, H., Nishikaze, T., Miura, N., Piao, J., Okada, K., Sekiya, S., *et al.* (2018) Sialic acid linkage specific derivatization of glycosphingolipid glycans by ring-opening aminolysis of lactones. *Anal. Chem.* **90**, 13193–13199
67. Furukawa, J., Shinohara, Y., Kuramoto, H., Miura, Y., Shimaoka, H., Kurogochi, M., *et al.* (2008) Comprehensive approach to structural and functional glycomics based on chemoselective glycoblotting and sequential tag conversion. *Anal. Chem.* **80**, 1094–1101
68. Lacombe, J., Krosl, G., Tremblay, M., Gerby, B., Martin, R., Aplan, P. D., *et al.* (2013) Genetic interaction between kit and scl. *Blood* **122**, 1150–1161
69. Kawabata, H. (2019) Transferrin and transferrin receptors update. *Free Radic. Biol. Med.* **133**, 46–54

# Exogenous L-fucose attenuates depression induced by chronic unpredictable stress: Implicating core fucosylation has an antidepressant potential

Received for publication, December 17, 2024, and in revised form, January 14, 2025 Published, Papers in Press, January 27, 2025,
https://doi.org/10.1016/j.jbc.2025.108230

**Dan Wang**[1], **Tomohiko Fukuda**[1,2,*], **Tiangui Wu**[1], **Xing Xu**[1], **Tomoya Isaji**[1,2], **and Jianguo Gu**[1,2,*]

*From the* [1]*Division of Regulatory Glycobiology, Graduate School of Pharmaceutical Sciences, Tohoku Medical and Pharmaceutical University, Sendai, Miyagi, Japan;* [2]*Institute of Molecular Biomembrane and Glycobiology, Tohoku Medical and Pharmaceutical University, Sendai, Miyagi, Japan*

Reviewed by members of the JBC Editorial Board. Edited by Robert Haltiwanger

**Core fucosylation is one of the most essential modifications of the *N*-glycans, catalyzed by α1,6-fucosyltransferase (Fut8), which transfers fucose from guanosine 5′-diphosphate (GDP)-fucose to the innermost *N*-acetylglucosamine residue of *N*-glycans in an α1-6 linkage. Our previous studies demonstrated that lipopolysaccharide (LPS) can induce a more robust neuroinflammatory response in *Fut8* homozygous knockout (KO) (*Fut8*$^{-/-}$) and heterozygous KO (*Fut8*$^{+/-}$) mice contrasted to the wild-type (*Fut8*$^{+/+}$) mice. Exogenous administration of L-fucose suppressed LPS-induced neuroinflammation. Numerous studies indicate that neuroinflammation plays a vital role in the development of depression. Here, we investigated whether core fucosylation regulates depression induced by chronic unpredictable stress (CUS), a well-established model for depression. Our results showed that *Fut8*$^{+/-}$ mice exhibited depressive-like behaviors and increased neuroinflammation earlier than *Fut8*$^{+/+}$ mice. Administration of L-fucose significantly reduced CUS-induced depressive-like behaviors and pro-inflammatory cytokine levels in *Fut8*$^{+/-}$ mice. The L-fucose treatment produced antidepressant effects by attenuating the complex formation between gp130 and the interleukin-6 (IL-6) receptor and the JAK2/STAT3 signaling pathway. Notably, L-fucose treatment increased dendritic spine density and postsynaptic density protein 95 (PSD-95) expression, which were suppressed in CUS-induced depression. Furthermore, the effects of L-fucose on the CUS-induced depression were also observed in *Fut8*$^{+/+}$ mice. Our results clearly demonstrate that L-fucose ameliorates neuroinflammation and synaptic defects in CUS-induced depression, implicating that core fucosylation has significant anti-neuroinflammatory activity and an antidepressant potential.**

Major depressive disorder (MDD) is a common mental disorder characterized by persistent symptoms of depressed mood and anhedonia (1, 2). MDD heavily impacts patients' sleep quality, appetite, cognitive flexibility, and mobility (3–5). In severe cases, individuals with depression may exhibit suicidal tendencies (6). Approximately 300 million people worldwide suffer from MDD, and its prevalence continues to rise (7). The World Health Organization listed MDD as the third largest disease burden globally in 2018, with projections indicating it will rank first by 2030 (8).

Numerous studies have shown that MDD is closely related to elevated levels of neuroinflammatory biomarkers, such as interleukin (IL)-6 (9–11), IL-1β (12, 13), and tumor necrosis factor-alpha (TNF-α) (14–16). Inflammation has even been proposed as a biomarker in the treatment of depression (17). Rodent models of chronic stress also exhibit increased levels of pro-inflammatory cytokines (18–20). Depression is increasingly recognized as a microglial disease (21). As immune effector cells in the central nervous system (CNS), microglia play a crucial role in neuroprotection. In depression and its animal models, microglia become overactivated, accelerating the neuroinflammatory response by secreting large amounts of pro-inflammatory (22–24) cytokines. Excessive inflammation can lead to neuronal apoptosis and cell death (25, 26).

L-fucose is a dietary deoxyhexose sugar that is taken up and processed in cells, converted into guanosine 5′-diphosphate (GDP)-fucose, which is utilized in the endoplasmic reticulum or Golgi by 13 fucosyltransferases to synthesize fucosylated glycans (27–29). GDP-fucose can be synthesized in two ways: the *de novo* pathway and the salvage pathway, and the *de novo* pathway is dominant (30, 31). Dietary intake or lysosomal breakdown of glycoproteins can provide L-fucose in the salvage pathway. When the *de novo* pathway is compromised, the salvage pathway supplements GDP-fucose to maintain normal physiological functions (32). L-fucose has shown anti-tumor and anti-inflammatory effects in various diseases. For example, in melanoma models, dietary L-fucose enhanced immunotherapy response; it has also been shown to reduce gut inflammation and mitigate high-salt diet-induced inflammation (33–35). Ample evidence suggests that L-fucose, the predominant bioactive component of fucoidan, possesses neuroprotective and neurogenic effects in the CNS (36–38). However, the underlying molecular mechanisms for these effects remain unclear.

* For correspondence: Tomohiko Fukuda, tfukuda@tohoku-mpu.ac.jp; Jianguo Gu, jgu@tohoku-mpu.ac.jp.



© 2025 THE AUTHORS. Published by Elsevier Inc on behalf of American Society for Biochemistry and Molecular Biology. This is an open access article under the CC BY license (http://creativecommons.org/licenses/by/4.0/).

### *Fut8 negatively regulates neuroinflammation*

Core fucosylation is a process catalyzed by α1,6-fucosyltransferase (Fut8), which transfers a fucose residue from GDP-fucose to the innermost *N*-acetylglucosamine residue of *N*-linked glycans in complex and hybrid glycoproteins (39, 40). Patients with FUT8-congenital disorders of glycosylation, characterized by impaired core fucosylation, often present with epilepsy, short stature, microcephaly, and intellectual disabilities (41). Our previous studies demonstrated that *Fut8* homozygous knockout (KO) ($Fut8^{-/-}$) mice exhibit memory impairments and abnormal behaviors consistent with schizophrenia-like phenotypes (42), along with decreased hippocampal long-term potentiation (LTP) compared to the wild-type ($Fut8^{+/+}$) mice (43). Additionally, Fut8 deficiency *via* shRNA has been shown to impair memory, learning, and neurogenesis in adult mice (44). These findings suggest that a lack of core fucosylation may contribute to developing CNS disorders. Both $Fut8^{-/-}$ mice and $Fut8^{+/-}$ mice display heightened microglial activation and a more severe inflammatory response to lipopolysaccharide (LPS) stimulation than $Fut8^{+/+}$ mice (45, 46), indicating that neuroinflammation may be negatively regulated by core fucosylation. Lack of the *Fut8* gene significantly enhances the complex formation between the IL-6 receptor (IL-6R) and glycoprotein 130 (gp130), resulting in stronger neuroinflammation. Conversely, L-fucose administration increases core fucosylation of gp130, thereby reducing the complex formation and exerting anti-neuroinflammation effects (45). Given the close relationship between neuroinflammation and CNS disorders, we hypothesize that core fucosylation may also influence the onset and progression of depression. In this study, we investigated the effects of core fucosylation on depression induced by chronic unpredictable stress (CUS), one of the most established models for depression (47). Our findings indicate that $Fut8^{+/-}$ mice develop depressive-like behaviors earlier than $Fut8^{+/+}$ mice, which can be rescued by L-fucose administration. Furthermore, L-fucose ameliorated neuroinflammation and synaptic defects in CUS-induced depression mice. Therefore, L-fucose may hold potential as a therapeutic agent for CNS diseases.

## Results

### Fut8$^{+/-}$ *mice exhibited depression-like behavior earlier than* Fut8$^{+/+}$ *mice*

Our previous studies revealed that core fucosylation negatively regulates the neuroinflammation induced by LPS; specifically, lower core fucosylation can induce severe neuroinflammation (45, 46). Given the established link between neuroinflammation and depression (12, 15), we explored whether core fucosylation affects the onset and progression of depression. Stress is a significant risk factor for several psychiatric illnesses, including MDD, and is often a trigger for depressive episodes (48–50). The CUS model of depression is a valid, reliable, and widely used model (47), and the method for simulating the stress variations is quite similar to what humans are exposed to in their daily lives (51, 52). Following 7, 14, 21, 28, and 35 days of exposure to the CUS model, we tested the depressive behavior of $Fut8^{+/+}$ and $Fut8^{+/-}$ mice. At 35 days, compared to each control mice without CUS, both $Fut8^{+/+}$ and $Fut8^{+/-}$ CUS mice exhibited increased immobility times in the tail suspension test (TST) (Fig. 1*A*) and forced swimming test (FST) (Fig. 1*B*), as well as decreased sucrose intake in the sucrose preference test (SPT) (Fig. 1*C*), indicating the success of the CUS model. Notably, in the CUS-28-days group, $Fut8^{+/-}$ mice showed significantly higher immobility time in the TST (Fig. 1*D*) and FST (Fig. 1*E*) than controls without CUS. In addition, $Fut8^{+/-}$ mice exhibited significant attenuation in sucrose preference at 28 days of CUS compared to controls in the SPT (Fig. 1*F*). However, these differences were not observed in $Fut8^{+/+}$ mice at 28 days. All mice did not display depressive-like behaviors after 7, 14, and 21 days of CUS (Fig. S1, *A*–*I*). These findings demonstrate that the mice with lower core fucosylation are more susceptible to exhibiting depressive-like behaviors.

### *L-fucose administration abolished increased depressive-like behaviors induced by CUS in* Fut8$^{+/-}$ *mice*

Previous studies found that L-fucose has an inhibitory effect on LPS-induced neuroinflammation (45). Thus, we investigated whether exogenous L-fucose could affect the depressive-like behavior of $Fut8^{+/-}$ mice subjected to CUS. The role of serotonin in CNS immunity is still unclear, but serotonin is indeed linked to inflammation (53, 54). The treatment of MDD patients with selective serotonin reuptake inhibitors (SSRIs) reduces IL-6 and TNF-α levels, and their antidepressant therapeutic effects may be partly attributed to their anti-inflammatory properties (55). The classic antidepressant FLX is an SSRI medication and is known to exert significant anti-neuroinflammatory effects (56), which is achieved by inhibiting microglia activation and reducing the release of inflammatory factors (57–59). FLX is often served as a positive control in studies of depression models (60, 61). Here, we also used FLX as a positive control to evaluate the degree of antidepressant effect of L-fucose since FLX is one of the most widely used drugs in clinical practice and has significant anti-inflammatory effects. As depicted in the schematic (Fig. 2*A*), L-fucose was administered intragastrically at a dose of 36 mg/day throughout the CUS model (45), while FLX was administered intraperitoneally at 20 mg/kg (62) during the last 10 days. Behavioral tests revealed that L-fucose eliminated the depressive-like behaviors in $Fut8^{+/-}$ mice following CUS, exhibiting similar effects to FLX (Fig. 2). Exogenous L-fucose significantly decreased the immobility time in TST (Fig. 2*B*) and FST (Fig. 2*C*) and increased sucrose intake in the SPT (Fig. 2*D*). These results suggest that L-fucose may possess antidepressant effects similar to FLX.

### *L-fucose suppression increased neuroinflammation induced by CUS in* Fut8$^{+/-}$ *mice*

Neuroinflammation is implicated in MDD through various neurobiological mechanisms (7). Evidence indicates that CUS stress induces the release of pro-inflammatory cytokines, such as IL-6, IL-1β, TNF-α, and inducible NO synthase (iNOS) (18–20). The structure and function of the hippocampus have

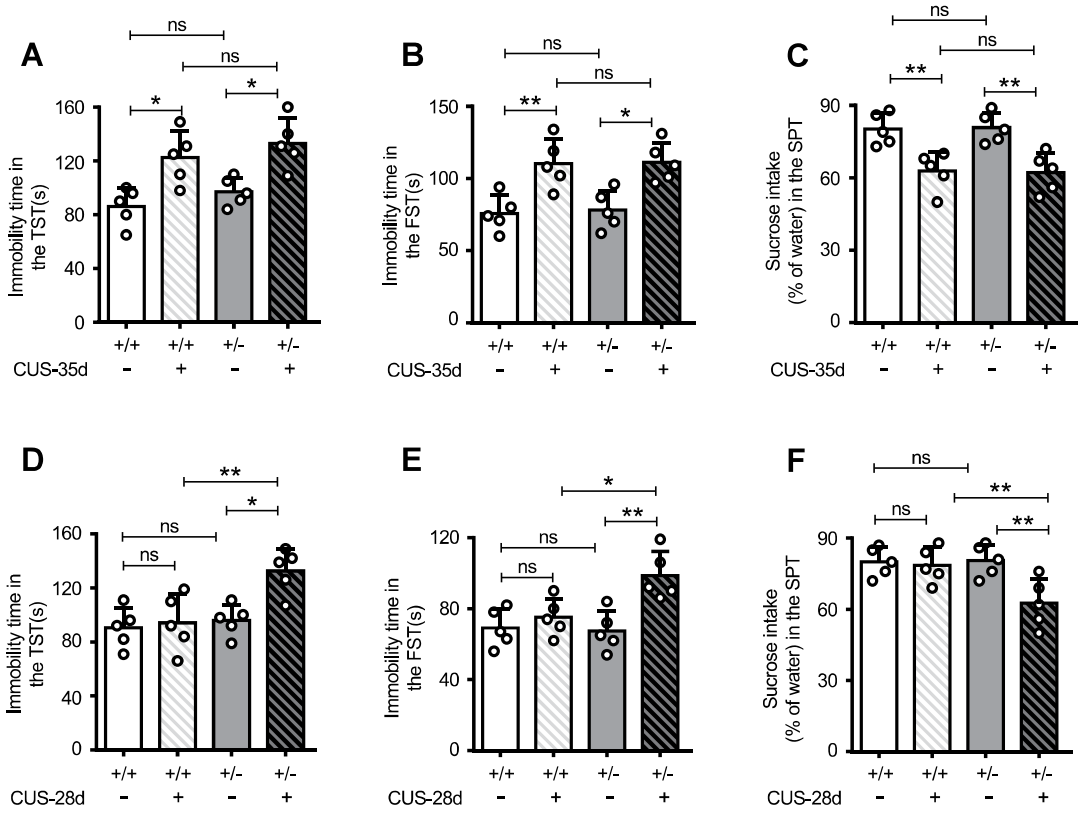


**Figure 1. Comparison of depression-like behaviors upon CUS treatment between *Fut8*$^{+/-}$ and *Fut8*$^{+/+}$ mice, Chronic unpredictable stress (CUS) models were established in *Fut8*$^{+/+}$ and *Fut8*$^{+/-}$ mice, grouped at 7, 14, 21, 28, and 35 days post-CUS.** Behavioral assessments were conducted using the tail suspension test (TST) (*A*), forced swimming test (FST) (*B*), and sucrose preference test (SPT) (*C*) after 35 days of CUS. Data for TST (*D*), FST (*E*), and SPT (*F*) at 28 days of CUS are also presented. Data were analyzed by one-way ANOVA with Tukey's multiple comparison tests and shown as mean ± SD. n = 5 mice per group. n.s. $p > 0.05$; *$p < 0.05$; **$p < 0.01$.

been linked to the pathophysiology and progression of MDD (63–65). Thus, we focused on the hippocampus to evaluate the effect of L-fucose on CUS-induced neuroinflammation. After 28 days of CUS, real-time PCR analysis revealed that the mRNA levels of the *Il6* (Fig. 3*A*), *Il1b* (Fig. 3*B*), *TNF-α* (Fig. 3*C*), and *iNOS* (Fig. 3*D*) were increased significantly in *Fut8*$^{+/-}$ mice, but not in *Fut8*$^{+/+}$ mice. Moreover, *Fut8*$^{+/-}$ mice showed higher levels of *Il1b* mRNA than *Fut8*$^{+/+}$ mice in the absence of CUS exposure. Treatment with exogenous L-fucose and FLX both obviously reversed the increased neuroinflammation in *Fut8*$^{+/-}$ mice after CUS exposure. These findings suggest that L-fucose may reduce depressive-like behavior by mitigating neuroinflammation.

### *L-fucose inhibited CUS-induced microglial activation in* Fut8$^{+/-}$ *mice*

Microglia are innate immune cells of the CNS, and the alterations of number and function in microglia are closely related to the onset of depression (66, 67). It is widely known that chronic stress can induce the activation of microglia in specific brain regions and alter their phenotypic and functional properties (68). We performed immunofluorescence staining to detect the level of ionized calcium-binding adaptor molecule 1 (Iba1), a microglial activation marker in the dentate gyrus (DG) of the hippocampus (63, 69–71). After 28 days of CUS, the number of microglia in *Fut8*$^{+/-}$ mice was significantly increased, which was suppressed after treatment with L-fucose and FLX (Fig. 4, *A* and *B*). Real-time PCR analysis also showed that the mRNA level of *Iba1* was significantly elevated in *Fut8*$^{+/-}$ mice exposed to CUS, but not in *Fut8*$^{+/+}$ mice. In addition, L-fucose or FLX exerted an effective suppression on this increase (Fig. 4*C*). Without CUS exposure, *Fut8*$^{+/-}$ mice had more Iba1-positive cells in immunofluorescence results than *Fut8*$^{+/+}$ mice (Fig. 4*B*); although there was no significant difference in the mRNA levels of *Iba1* between the two mice (Fig. 4*C*). These results further support the notion that core fucosylation negatively regulates microglia activation and consequently suppresses neuroinflammation.

### *L-fucose attenuated the JAK2/STAT3 signaling pathway*

The dysregulation of the JAK/STAT (Janus kinase-signal transducer and activator of transcription) signaling pathway plays a significant role in neuroinflammatory diseases (72–74). STAT3, a downstream effector of IL-6, is involved in the pro-inflammatory activation of microglia and astrocytes in various neuroinflammatory contexts (75–77). The inhibition of the JAK2/STAT3 pathway has been shown to have anti-neuroinflammatory and neuroprotective effects (78, 79).

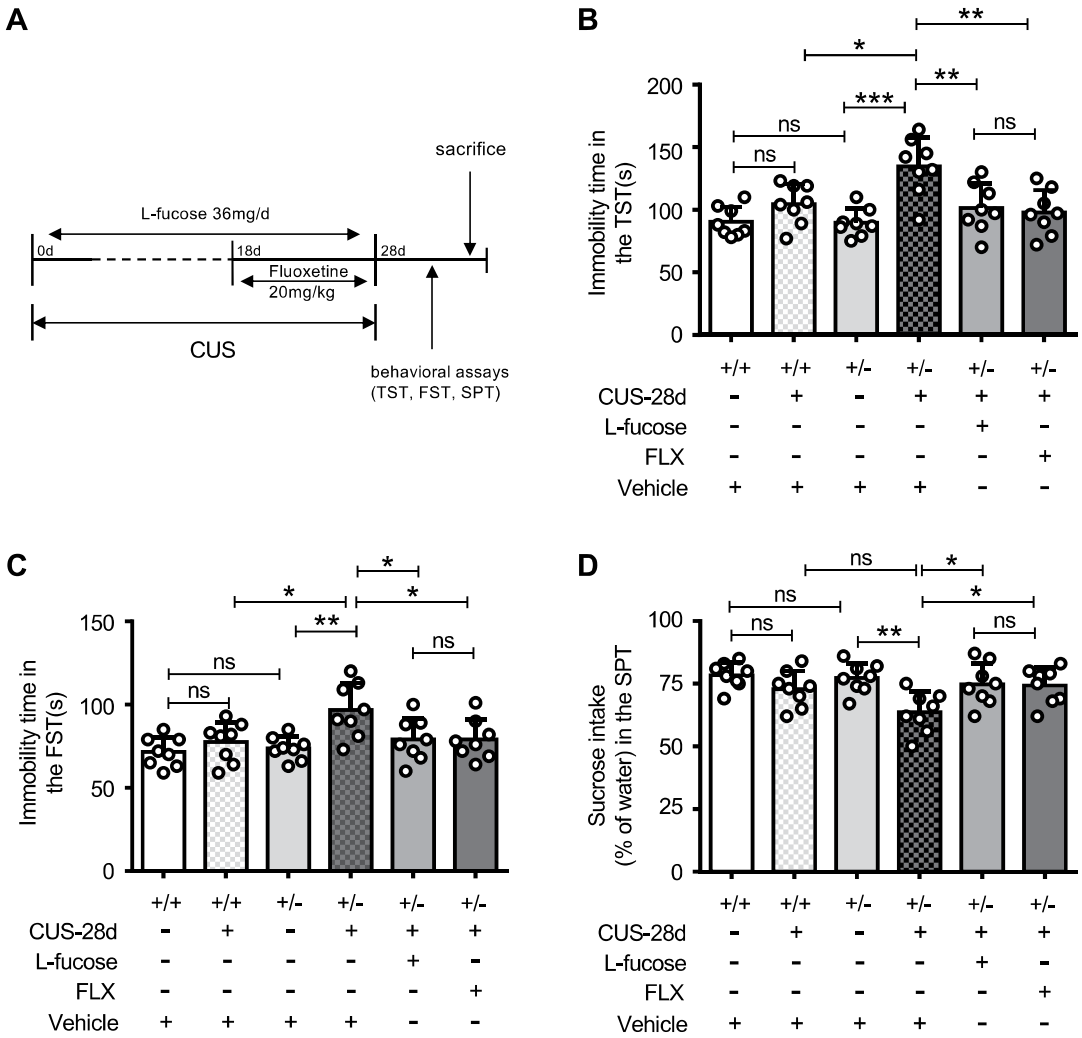


**Figure 2. L-fucose administration abolished depressive-like behaviors induced by CUS in *Fut8*$^{+/-}$ mice.** *A*, schedule of CUS modeling, with *Fut8*$^{+/-}$ mice administered 36 mg/day of L-fucose or 20 mg/kg of fluoxetine (FLX) during the last 10 days. Behavioral tests were performed, and brain tissues were extracted afterward. *B*, the immobility time of mice in the TST. *C*, the immobility time of mice in the FST. *D*, the sucrose consumption of mice in the SPT. Data was analyzed by one-way ANOVA with Tukey's multiple comparison tests and shown as mean ± SD. n = 8 mice per group. n.s. $p > 0.05$; *$p < 0.05$; **$p < 0.01$; ***$p < 0.001$.

Meanwhile, FLX attenuated the neuroinflammation by suppressing the activation of JAK/STAT3 signaling (80). Western blotting has been used to assess the phosphorylation levels of JAK2 and STAT3. Quantitative analysis revealed that the phosphorylation levels of JAK2 and STAT3 were significantly increased in *Fut8*$^{+/-}$ mice after 28 days of CUS, but not in *Fut8*$^{+/+}$ mice. L-fucose could inhibit the elevated phosphorylation levels of JAK2 and STAT3 in *Fut8*$^{+/-}$ mice subjected to CUS. FLX also displayed a similar inhibitory trend regarding the phosphorylation levels of JAK2 and STAT3, although no significant differences were observed for p-JAK2 (Fig. 5*A*). IL-6 signaling includes the gp130 receptor and the JAK/STAT pathway (81). We used co-immunoprecipitation to explore the molecular mechanisms for the effect of exogenous L-fucose administration in the CUS model. According to immunoprecipitation results, the interaction between gp130 and IL-6R was increased upon exposure to CUS in *Fut8*$^{+/-}$ mice, compared to without CUS. Concomitantly, gp130 in *Fut8*$^{+/-}$ mice exposed to CUS contained less core fucosylation than in *Fut8*$^{+/+}$ mice or *Fut8*$^{+/-}$ mice treated with L-fucose (Fig. 5*B*). Moreover, exogenous L-fucose administration inhibited the association between gp130 and IL-6R (Fig. 5*B*), which is similar to the observation in LPS-induced neuroinflammation (45). We further investigated the effects of WP1066, a JAK2/STAT3 inhibitor (82), on neuroinflammation and depression-like behaviors induced by CUS. After the first injection on the fourth day of the CUS model, the intraperitoneal injection was carried out once every 3 days at 30 mg/kg for nine injections, based on dose usage in the previous study (83). The effects of WP1066 on the behavioral experiments of depression were quite similar to those of L-fucose (Fig. S2, *A*–*C*). The combined treatment of WP1066 and L-fucose did not observe additive effects. Furthermore, the impact of WP1066 on the expression of inflammatory factors and *Fut8* in CUS-induced depression also showed a similar tendency with L-fucose (Fig. S3, *A*–*E*). However, WP1066 did not significantly

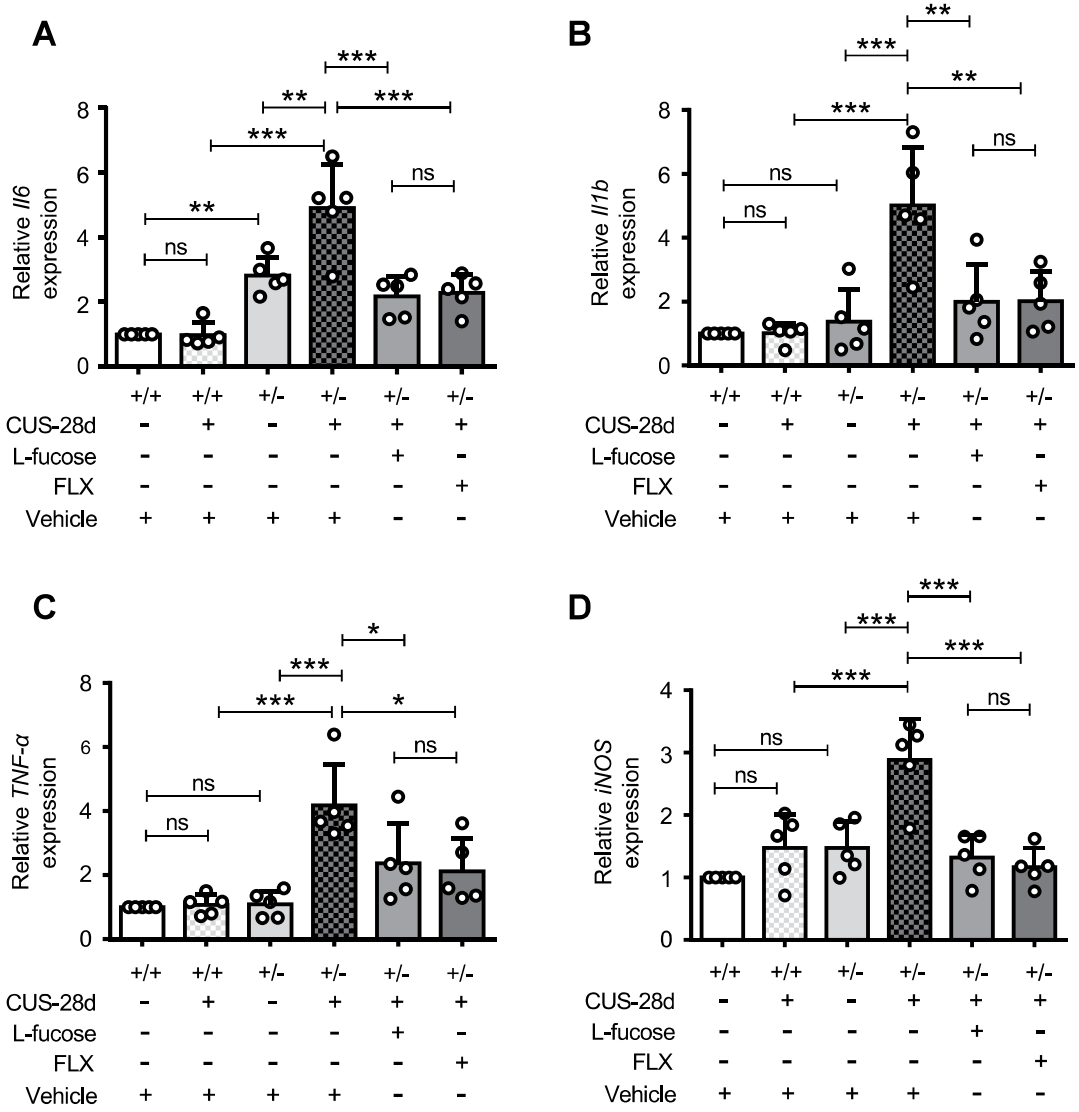


**Figure 3. L-fucose suppressed neuroinflammation induced by CUS in *Fut8*$^{+/-}$ mice.** The mRNA levels of neuroinflammatory factors were analyzed by real-time PCR, including interleukin-6 (*Il6*) (*A*), interleukin 1 beta (*Il1b*) (*B*), tumor necrosis factor-alpha (*TNF-α*) (*C*), and inducible nitric oxide synthase (*iNOS*) (*D*) in the hippocampus. Glyceraldehyde-3-phosphate dehydrogenase (*Gapdh*) was used as an internal control. Values were normalized to that of the *Gapdh*. The value for *Fut8*$^{+/+}$ mice with vehicle treatment was set as 1.0. The one-way ANOVA test with Tukey's multiple comparison test was used to calculate the quantitative data, which were displayed as the mean ± SD of five independent experiments. n = 5 mice per group. n.s. $p > 0.05$; *$p < 0.05$; **$p < 0.01$; ***$p < 0.001$.

suppress *Il1b* and *iNOS* expression. The combined treatment of WP1066 and L-fucose did not observe additive effects, except for the phosphorylated JAK2 levels (Fig. S3*F*). These results further suggest the suppression of CUS-induced depression by exogenous L-fucose *via* neutralizing neuroinflammation. These results indicate that L-fucose exerts its anti-inflammatory effects by inhibiting the JAK2/STAT3 pathway, thereby playing an antidepressant role.

### *Exogenous L-fucose reversed CUS-induced damage in synaptic plasticity*

Through the activation of microglia, inflammatory cytokine overproduction causes synaptic dysfunction and neuronal damage in the hippocampus, which in turn induces depressive behaviors (24). Spines possess highly dynamic, and the alterations in their density and morphology are the basis of structural synaptic plasticity (84). Neuroinflammation following depression may lead to impaired synaptic plasticity, decreased dendritic spine density, and synaptic plasticity-related proteins, such as postsynaptic density protein 95 (PSD-95) (47, 85). FLX has the effect of improving synaptic plasticity (86, 87). Given the observed behavioral alterations and cytokine levels in *Fut8*$^{+/-}$ mice, we hypothesized that neuroinflammation triggered from excessive microglia activation may affect neuronal plasticity. To explore the role of L-fucose in synaptic plasticity, we need to detect the spine density through Golgi staining. Decreased dendritic spine

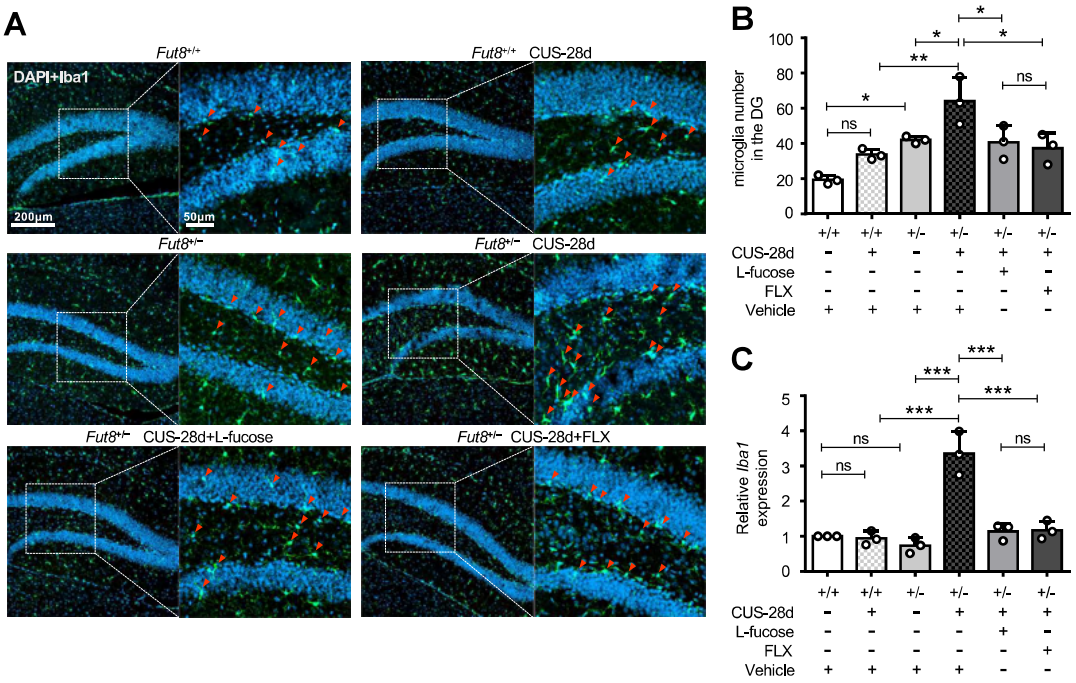


**Figure 4. L-fucose inhibited CUS-induced microglial activation.** *A*, representative immunofluorescence staining images of the dentate gyrus (DG) in hippocampal coronal sections, showing Iba1 as a microglia marker. DAPI was used for nuclear staining. *Green* fluorescent cells co-localized with DAPI (*blue*) are identified as Iba1-positive microglia. Arrows indicate Iba1-positive cells. *B*, quantification of Iba1-positive microglia in the DG region using ImageJ software. The one-way ANOVA test with Tukey's multiple comparison test was used to calculate the quantitative data. Data from three independent experiments are presented as mean ± SD. n = 3 mice per group. n.s. $p > 0.05$; *$p < 0.05$; **$p < 0.01$. *C*, real-time PCR analysis of *Iba1* mRNA expression, normalized to *Gapdh* (internal control), and *Fut8*$^{+/+}$ mice with vehicle treatment were set as 1.0. All data were analyzed by one-way ANOVA test with Tukey's multiple comparison test and displayed as the mean ± SD from three independent experiments. n = 3 mice per group. n.s. $p > 0.05$; ***$p < 0.001$.

density in the CA1 hippocampus region is associated with depressive-like behavior following CUS (88). Therefore, we examined the synaptic density in the CA1 region of the mouse hippocampus. The results demonstrated that synaptic density in the hippocampus of *Fut8*$^{+/-}$ mice was lower than that in *Fut8*$^{+/+}$ mice. There was no significant change in synaptic density in *Fut8*$^{+/+}$ mice after 28 days of CUS (Fig. 6*A*). After 28 days of CUS, synaptic densities in *Fut8*$^{+/-}$ mice were significantly decreased, whereas L-fucose and FLX significantly alleviated this impairment (Fig. 6*A*). Additionally, the level of synaptic plasticity-related proteins was detected by western blotting. We found the expression level of PSD-95 was significantly suppressed in the hippocampus of *Fut8*$^{+/-}$ mice exposed to the CUS, compared to the control without CUS (Fig. 6*B*). Importantly, L-fucose or FLX partially rescued the decreased PSD-95 expression in *Fut8*$^{+/-}$ CUS mice (Fig. 6*B*). These data suggest that L-fucose may exert antidepressant effects by restoring synaptic plasticity.

### *L-fucose recovered the CUS-induced down-regulation of Fut8 expression*

To investigate the alteration in core fucosylation after CUS exposure, we checked the level of core fucosylation *via* lectin blotting using the Lens Culinaris Agglutinin (LCA). LCA can specifically recognize core fucosylation (89). After 28 days of CUS, *Fut8*$^{+/-}$ mice exhibited a significant reduction in core fucosylation levels, which was reversed by exogenous L-fucose (Fig. 7*A*). Since L-fucose administration may also affect other fucosylation (90), and studies have found that mice lacking α1,3-fucosyltransferase IX exhibit increased anxiety-like behaviors (91), we also examined the expression levels of Lewis X by western blotting with anti-Lewis X antibody. After CUS exposure, curiously, both *Fut8*$^{+/+}$ and *Fut8*$^{+/-}$ mice exhibited decreased Lewis X expression levels, which could not be rescued by L-fucose treatment (Fig. S4, *A* and *B*), suggesting the effect of L-fucose on CUS is not dependent on expression levels of Lewis antigen. Given the notable increase in inflammatory factors in *Fut8*$^{+/-}$ CUS mice, we hypothesized that inflammation might downregulate *Fut8* gene expression. Real-time PCR analysis of *Fut8* mRNA levels showed a significant decrease in *Fut8* expression due to CUS-induced inflammation in *Fut8*$^{+/-}$ mice. However, this downregulation was reversed in *Fut8*$^{+/-}$ CUS mice treated with L-fucose or FLX (Fig. 7*B*). These findings suggest that neuroinflammation may downregulate *Fut8* expression. To investigate if the suppression of inflammation or cell autonomy is responsible for the upregulation of *Fut8* mRNA following L-fucose treatment, we established the neuroinflammation model by treating BV2 cells cultured *in vitro* with LPS (1 μg/ml) (92). The results of LCA lectin blotting demonstrated that the core fucosylation levels were increased by L-fucose. The dose of 5 μM L-fucose was adequate for the increasing effect (Fig. 7*C*). After LPS treatment, *Il6* mRNA levels increased significantly (Fig. 7*D*), and

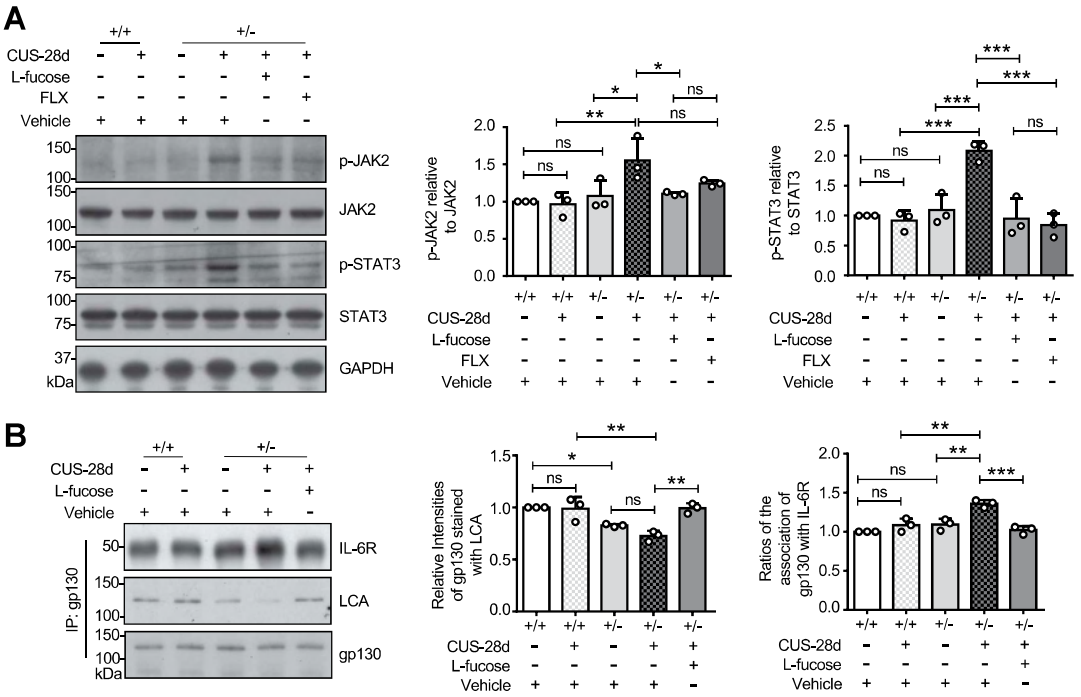


**Figure 5. L-fucose attenuated the JAK2/STAT3 signaling pathway.** *A*, Western blot analysis of hippocampal tissues after 28 days of CUS, using antibodies against JAK2, phosphor-JAK2 (p-JAK2), STAT3, and phosphor-STAT3 (p-STAT3). GAPDH was used as a loading control. Data was quantified by ImageJ software. The ratio of p-JAK2 to JAK2 for *Fut8*$^{+/+}$ mice treated with vehicle was set as 1.0. The ratio of p-STAT3 to STAT3 for *Fut8*$^{+/+}$ mice treated with vehicle was set as 1.0. All data were analyzed by one-way ANOVA test with Tukey's multiple comparison test and displayed as the mean ± SD from three independent experiments. n = 3 mice per group. n.s. $p > 0.05$; *$p < 0.05$; **$p < 0.01$, ***$p < 0.001$. *B*, equal amounts of hippocampus lysates were immunoprecipitated using an anti-gp130 antibody following a 28-days exposure to CUS. The immunoprecipitates were analyzed by western blotting with anti-IL-6R and anti-gp130 antibodies or lectin blotting with LCA lectin. ImageJ software was used to quantify the data. The ratio of LCA or IL-6R *versus* gp130 of *Fut8*$^{+/+}$ mice treated with the vehicle was 1.0. All Data were shown as the mean ± SD from three independent experiments. n = 3 mice per group. n.s. $p > 0.05$; *$p < 0.05$; **$p < 0.01$, ***$p < 0.001$. (One-way ANOVA test with Tukey's multiple comparison test).

*Fut8* mRNA levels increased after 12 h and 24 h of LPS treatment. Interestingly, as the LPS treatment time was postponed, *Fut8* mRNA levels decreased (Fig. 7*E*), suggesting biphase responses in the induction. BV2 cells were pretreated with L-fucose for 4 h and then stimulated with LPS for 48 h. The real-time PCR analysis showed decreased *Fut8* expression while increasing *Il6* expression, significantly rescued by L-fucose (Fig. 7, *F* and *G*). Curiously, L-fucose alone did not change *Fut8* expression (Fig. 7*F*).

### *Effects of L-fucose on* Fut8$^{+/+}$ *mice exposed to CUS*

We examined the effects of L-fucose on *Fut8*$^{+/+}$ mice after CUS exposure to further explore the role of L-fucose in *Fut8*$^{+/+}$ mice. Following 35 days of CUS, *Fut8*$^{+/+}$ mice displayed increased immobility time in TST (Fig. S5*A*) and FST (Fig. S5*B*), alongside reduced sucrose preference in the SPT (Fig. S5*C*) compared to the controls without CUS. Importantly, these alterations were ameliorated by L-fucose treatment. Additionally, the real-time PCR analysis showed that the elevated mRNA levels of *Il6* (Fig. 8*A*), *Il1b* (Fig. 8*B*), *TNF-α* (Fig. 8*C*), and *iNOS* (Fig. 8*D*) in *Fut8*$^{+/+}$ mice following CUS were significantly suppressed by exogenous L-fucose. The levels of phospho-JAK2 (Fig. 8*E*) and phospho-STAT3 (Fig. 8*F*) were also significantly increased in *Fut8*$^{+/+}$ mice after CUS, which were inhibited by L-fucose treatment. Measurements of core fucosylation using LCA revealed that CUS exposure resulted in a significant decrease in LCA reactivity, which was partially rescued by L-fucose (Fig. 8*G*). Notably, *Fut8* mRNA expression levels were downregulated in *Fut8*$^{+/+}$ mice after CUS (Fig. 8*H*), and this downregulation could also be partially reversed by L-fucose treatment. These results strongly indicate that core fucosylation is crucial for CNS maintenance, and L-fucose treatment can mitigate depressive-like behaviors in *Fut8*$^{+/+}$ mice.

## Discussion

Our current study demonstrated that excessive microglia activation caused *Fut8*$^{+/-}$ mice to exhibit depressive-like behaviors and increased neuroinflammatory factors earlier than *Fut8*$^{+/+}$ mice following exposure to CUS. However, increased core fucosylation through exogenous L-fucose inhibited the overactivation of hippocampal microglia *via* the JAK2/STAT3 pathway, suppressed subsequent hippocampal neuroinflammation, reversed CUS-induced impairments in synaptic plasticity, and ultimately abolished the depressive-like behavior in *Fut8*$^{+/-}$ mice (Fig. 9).

Changes in microglia activity are associated with the onset of depression (21, 22). Multiple studies have reported an increase in microglia numbers in the hippocampus of animal models of depression exposed to chronic stress (93–96). It has

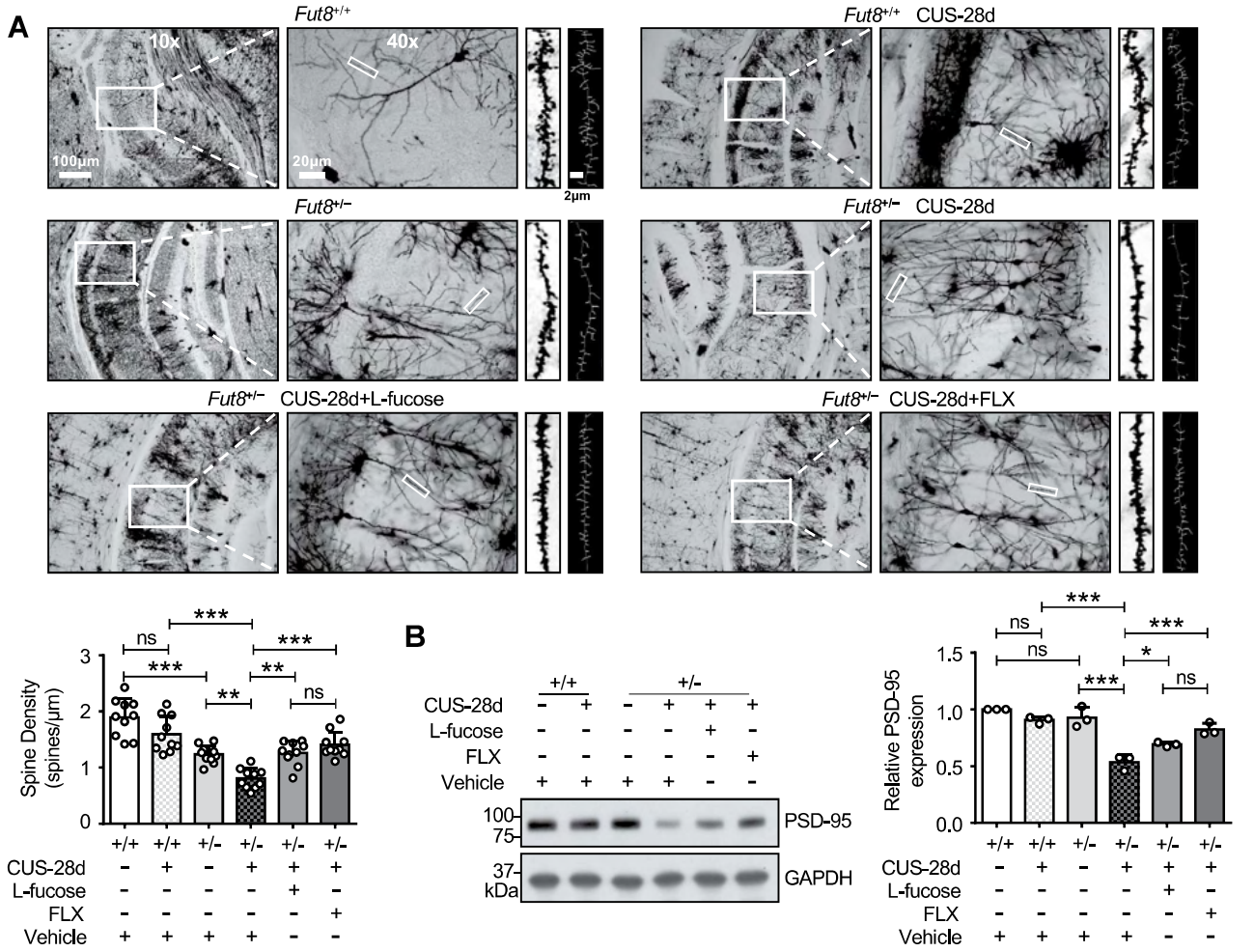


**Figure 6. Exogenous L-fucose reversed CUS-induced damage in synaptic plasticity.** *A*, representative images of the dendritic spine in Golgi staining. Images of the hippocampal region under 10x and 40x magnifications, as well as representative synaptic spine images and ImageJ-processed images, are shown from *left* to *right*. Spine density is the number of spines divided by the dendritic shaft length. ImageJ software measured the number of branches and total dendritic length. Data from 10 dendritic segments across three mice is mean ± SD. n.s. $p > 0.05$; $^{**}p < 0.01$; $^{***}p < 0.001$ (one-way ANOVA test with Tukey's multiple comparison test). *B*, Western blotting analysis of PSD-95 levels in hippocampal tissues after 28 days of CUS, quantified using ImageJ. GAPDH was used as a loading control, and the ratio of PSD-95 to GAPDH for *Fut8*$^{+/+}$ mice treated with vehicle was set as 1.0. All data were analyzed by one-way ANOVA test with Tukey's multiple comparison test and displayed as the mean ± SD from three independent experiments. n = 3 mice per group. n.s. $p > 0.05$; $^{*}p < 0.05$; $^{***}p < 0.001$.

also been shown that the density of glial cells in the dentate gyrus of the hippocampus is significantly increased in MDD (97). Our results indicate that the total number of Iba1-positive microglia in the hippocampus DG area of *Fut8*$^{+/-}$ mice after 28 days of CUS was significantly higher than that in control mice, suggesting that CUS exposure increases microglia numbers, which is suppressed by L-fucose administration. Numerous studies highlight the central role of neuroinflammation in the development of MDD (14, 15). Stress can cause homeostasis dysregulation, resulting in excessive microglia activation, and cause the production of proinflammatory cytokines. This neuroinflammation impairs neurons subsequently and contributes to depressive symptoms (25, 26). This study focused only on microglia. That does not mean that other cells, such as astrocytes and neurons, are not involved in neuroinflammation because core fucosylation is highly expressed in brain tissue (42). Depression is also known to be associated with astrocyte-mediated neuroinflammation (98). This study mainly focused on the relationship between IL-6/gp130-mediated signaling, a key inflammatory response pathway, and core fucosylation, while the IL-6R is present in microglia but not in astrocytes (99). In addition to the neuroinflammation hypothesis, there are other hypotheses about depression, such as the monoamine hypothesis, hypothalamic-pituitary-adrenal axis dysfunction hypothesis, *etc.* (7). In subsequent studies, we will use new technologies to explore whether other cells or other mechanisms are involved in the relationship between core fucosylation and depression.

Several studies have reported that the levels of multiple inflammatory markers were increased in patients with MDD (15, 16). Notably, alterations in IL-6 serum levels are among the most reproducible abnormalities in depression patients (16). Children with high circulating IL-6 levels have a 10% higher risk of developing MDD in adulthood compared to the

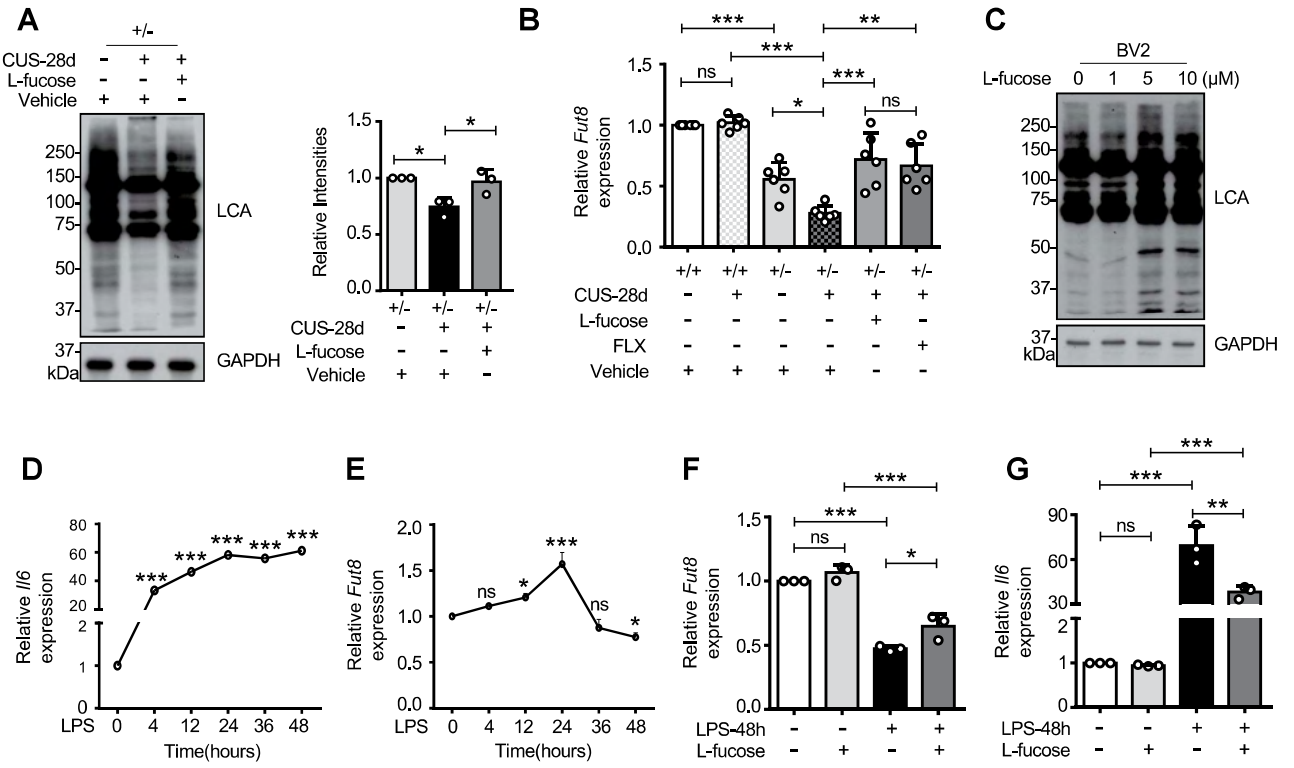


**Figure 7. L-fucose rescued the CUS-induced down-regulation of Fut8 expression.** *A*, Lectin blot analysis of hippocampal tissues after 28 days of CUS, using Lens Culinaris Agglutinin (LCA), specifically recognizing Core fucosylation. GAPDH was used as a loading control. The ratio of LCA *versus* GAPDH of $Fut8^{+/-}$ mice with the vehicle was set as 1.0. All data were analyzed by one-way ANOVA test with Tukey's multiple comparison test and displayed as the mean ± SD from three independent experiments. $^{*}p < 0.05$. *B*, real-time PCR analysis of *Fut8* mRNA expression. *Gapdh* was used as an internal control. Each value was normalized to that of the *Gapdh*. The values of *Fut8 versus Gapdh* in $Fut8^{+/+}$ mice treated with vehicle were set to 1.0. All data were analyzed by one-way ANOVA test with Tukey's multiple comparison test and displayed as the mean ± SD from six independent experiments. n = 6 mice per group. n.s. $p > 0.05$; $^{*}p < 0.05$; $^{**}p < 0.01$; $^{***}p < 0.001$. *C*, BV2 cells were treated with L-fucose at the indicated concentrations and cultured for 48 h. The same amounts of cell lysates were lectin blotted with LCA. GAPDH served as a loading control. *D* and *E*, BV2 cells were treated with LPS at 1 μg/ml for the indicated times. Real-time PCR was used to analyze the mRNA levels of *Il6* and *Fut8*. *Gapdh* was used as an internal control. Each value was normalized to that of the *Gapdh*. *Il6* or *Fut8 versus Gapdh* values in BV2 cells without LPS treatment were set to 1.0. All data were analyzed by one-way ANOVA with Tukey's multiple comparison test and shown as the mean ± SD from three independent experiments. n.s. $p > 0.05$; $^{*}p < 0.05$; $^{***}p < 0.001$. *F* and *G*, after pre-treatment with or without L-fucose at 5 μM for 4 h, the cells were stimulated with LPS for 48 h. Real-time PCR was used to analyze the mRNA levels of *Il6* and *Fut8*. *Gapdh* was used as an internal control. Each value was normalized to that of the *Gapdh*. *Il6* or *Fut8 versus Gapdh* values in BV2 cells without LPS and L-fucose treatment were set to 1.0. All data were analyzed by one-way ANOVA with Tukey's multiple comparison test and displayed as the mean ± SD from three independent experiments. n.s. $p > 0.05$; $^{*}p < 0.05$; $^{**}p < 0.01$; $^{***}p < 0.001$.

general population or children with low IL-6 levels (100). Furthermore, it has been reported that two-thirds of mice exhibit depressive-like behaviors after exposure to social defeat stress (101). In our study, we found that $Fut8^{+/-}$ mice had higher *Il6* levels than the $Fut8^{+/+}$ group (Fig. 3*A*), indicating that diminished core fucosylation predisposes mice to depression (Fig. 2). Additionally, other studies also suggest a link between core fucosylation and neuroinflammation in the central nervous system (CNS). For instance, core-fucosylated *N*-glycans were significantly decreased in mouse brain tissues treated with LPS (102). FUT8 expression was also significantly reduced in schizophrenia patients compared to controls (103). Patients with Multiple sclerosis exhibited lower levels of core-fucosylated *N*-glycans compared to matched controls (104), a similar finding also observed in Alzheimer's disease (105). Interestingly, it has been reported that female patients with MDD show decreased core fucosylation and increased IL-6 levels in serum (106). Consistent with these studies, we observed decreased core fucosylation levels in the hippocampus of mice exposed to the CUS model (Figs. 7*A*, 8*G*), which was supported by the observation in the BV2 cell model treated with LPS (Fig. 7*F*). L-fucose treatment of BV2 cells alone did not cause changes in *Fut8* mRNA levels. However, L-fucose could reduce the LPS-induced inflammation level in BV2 cells, thereby affecting the *Fut8* mRNA level, indicating that inflammation is the cause of alterations in *Fut8* mRNA levels (Fig. 7, *F* and *G*). It is notable to mention that there are bi-phase responses in LPS induction. The mRNA levels of *Fut8* were significantly increased during the shorter time treatment, such as 12 and 24 h, but decreased during the longer time treatment (Fig. 7*E*). Thus, the phenomenon could be explained by the possibility that *Fut8* mRNA levels are upregulated in response to acute inflammatory stimulation and downregulated in response to chronic inflammatory stimulation. This is consistent with the findings that our chronic depression model CUS stimulation mice exhibit reduced *Fut8* mRNA levels (Figs. 7*B*; 8*H*). The underlying mechanism for L-fucose-upregulating *Fut8* has yet to

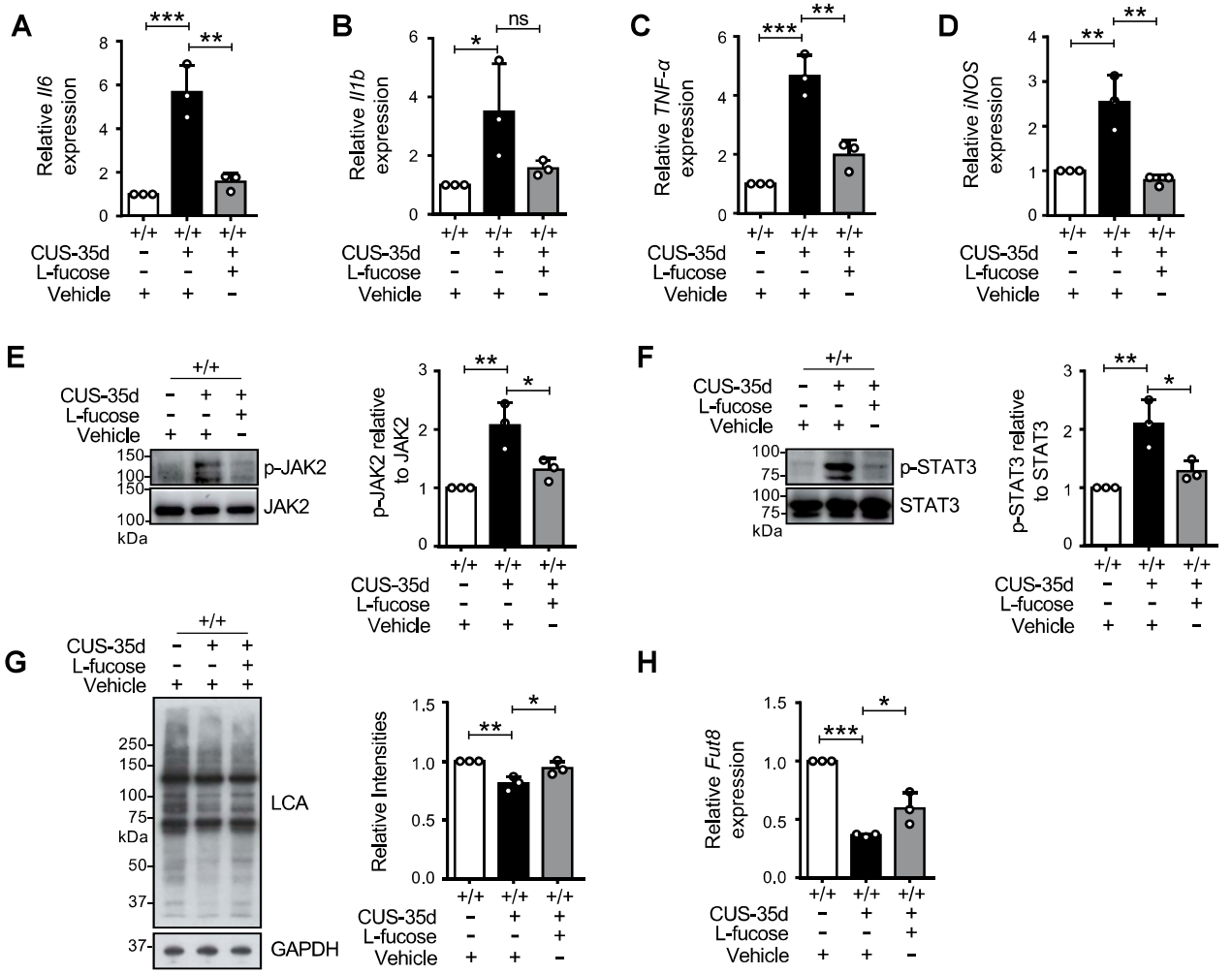


**Figure 8. Effects of L-fucose on *Fut8*$^{+/+}$ mice exposed to CUS at 35 days.** *Fut8*$^{+/+}$ mice were subjected to the CUS for 35 days and treated with L-fucose. *A–D*, the mRNA levels of cytokines were analyzed by real-time PCR, including *Il6* (*A*), *Il1b* (*B*), *TNF-α* (*C*), and *iNOS* (*D*) in the hippocampus. The *Gapdh* was used to normalize each value. The value of *Il6*, *Il1b*, *TNF-α* or *iNOS versus Gapdh* in *Fut8*$^{+/+}$ mice treated with the vehicle was set as 1.0. All data were analyzed by one-way ANOVA test with Tukey's multiple comparison test and displayed as the mean ± SD from three independent experiments. n = 3 mice per group. n.s. $p > 0.05$; *$p < 0.05$; **$p < 0.01$; ***$p < 0.001$. *E* and *F*, Western blotting analyses for p-JAK2 (*E*) and p-STAT3 (*F*) were conducted on hippocampal tissues, with data quantified using ImageJ software. The ratios of p-JAK2 to JAK2 and p-STAT3 to STAT3 for *Fut8*$^{+/+}$ vehicle-treated mice were set as 1.0. GAPDH was used as a loading control. All data were analyzed by one-way ANOVA test with Tukey's multiple comparison test and displayed as the mean ± SD from three independent experiments. n = 3 mice per group. *$p < 0.05$; **$p < 0.01$. *G*, lectin blot analysis with LCA, normalized to GAPDH, with the *Fut8*$^{+/+}$ vehicle-treated mice set as 1.0. Data were shown as mean ± SD from three independent experiments. n = 3 mice per group. *$p < 0.05$; **$p < 0.01$. (One-way ANOVA test with Tukey's multiple comparison test). *H*, real-time PCR analysis of *Fut8* mRNA level. *Gapdh* was used as a loading control. The *Gapdh* was used to normalize each value. The value of *Fut8 versus Gapdh* in *Fut8*$^{+/+}$ vehicle-treated mice set as 1.0. Data are shown as mean ± SD from three independent experiments. n = 3 mice per group. *$p < 0.05$; ***$p < 0.001$. (One-way ANOVA test with Tukey's multiple comparison test).

be entirely understood. However, based on the observations in (Fig. 7, *D–F*), we speculate that chronic inflammation may suppress *Fut8* expression, while L-fucose can reduce chronic inflammation, which results in upregulation of *Fut8*. On the other hand, acute inflammation induces the mRNA level of *Fut8* (Fig. 7*E*). The underlying mechanism for the different responses to acute and chronic inflammation remains to be studied further. These above results further suggest that core fucosylation is important for CNS maintenance and negatively regulates neuroinflammation.

The reduction or loss of core fucosylation may upregulate the pro-inflammatory reaction. Previous research indicated that a lack of core fucosylation leads to emphysema-like changes in *Fut8*$^{-/-}$ mice (107). Moreover, in a cigarette smoke-induced emphysema model, *Fut8*$^{+/-}$ mice were more sensitive than *Fut8*$^{+/+}$ mice (108). After LPS treatment, IL-6 expression levels in the lung and brain tissues of *Fut8*$^{+/-}$ mice were significantly higher than in *Fut8*$^{+/+}$ mice, and L-fucose treatment could reduce the IL-6 levels in *Fut8*$^{+/-}$ mice (45, 108). The GDP-fucose level in *Fut8*$^{+/-}$ mice was lower than that in *Fut8*$^{+/+}$ mice, and exogenous administration of L-fucose could significantly increase the GDP-fucose level in *Fut8*$^{+/-}$ mice (45). Therefore, exogenous L-fucose administration can increase core fucosylation in *Fut8*$^{+/-}$ mice. Mechanistic studies

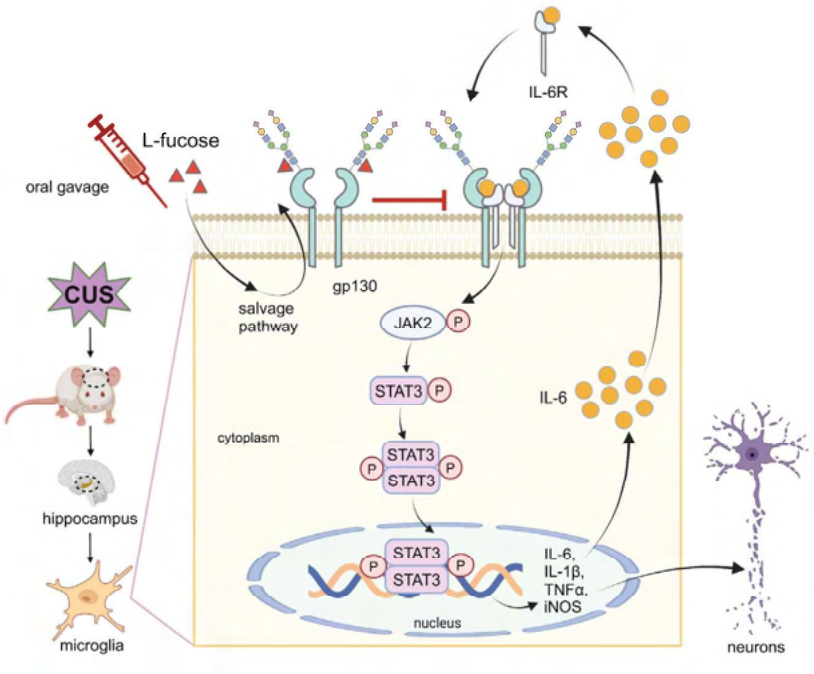


**Figure 9. L-fucose inhibits neuroinflammation and acts as an antidepressant.** *Fut8*$^{+/-}$ mice exhibited depressive-like behaviors earlier than *Fut8*$^{+/+}$ mice following CUS and displayed excessive microglia activation along with elevated cytokine expression levels. These changes may impair neuronal synaptic plasticity. Administration of exogenous L-fucose enhanced core fucosylation of gp130 through the salvage pathway for GDP-fucose synthesis, subsequently preventing the complex formation between gp130 and IL-6R, then inhibiting hippocampal microglia activation and subsequent neuroinflammation *via* the JAK2/STAT3 pathway. This intervention may reverse the synaptic plasticity disorder induced by CUS and ultimately alleviate depressive-like behaviors. Our previous research showed that the suppressive effect of L-fucose on IL-6 induction by LPS was observed only in the *Fut8*$^{+/+}$ cells, not in the *Fut8*$^{-/-}$ microglia (45), highlighting the significance of core fucosylation in neuroinflammation. Additionally, complex formation between gp130 and IL-6R was significantly increased in the *Fut8*$^{-/-}$ cells compared to *Fut8*$^{+/+}$ cells. Thus, we conclude that L-fucose inhibits neuroinflammation and acts as an antidepressant, at least partly through the upregulation of core fucosylation, which negatively regulates specific cytokine receptors, including the interaction between gp130 and IL-6R. This figure is created with BioRender.com.

suggested that core fucosylation negatively regulates the formation of IL-6R and gp130 complex by increasing core fucosylation of gp130 in *Fut8*$^{+/-}$ mice, this complex can mediate the JAK2/STAT3 pathway (Fig. 5). Similarly, we found that after CUS stress exposure, neuroinflammatory factors, including IL-6, were significantly higher in *Fut8*$^{+/-}$ mice compared to *Fut8*$^{+/+}$ mice, while exogenous L-fucose significantly inhibited their expression. It is noteworthy that GDP-fucose from exogenous L-fucose is preferentially utilized by Fut8 (109). This may explain why the expression levels of Lewis X were not increased in mice exposed to CUS with L-fucose treatment (Fig. S4, *A* and *B*). Although core fucosylation and other fucosylation, such as α1,3-fucosylation, were reduced after CUS, core fucosylation, not α1,3-fucosylation on Lewis X, could partially be rescued by L-fucose (Figs. 7*A*; 8*G*). Our previous study also showed that administration of exogenous L-fucose rescued the reduced IgG amount in *Fut8*$^{+/-}$ mice (110). We believe that the effects of L-fucose on CUS-induced depression are Fut8-dependent, as a previous study indicated that supplementation of L-fucose suppressed the enhanced IL-6 expression level in *Fut8*$^{+/+}$ cells, but not in *Fut8*$^{-/-}$ cells (45). We do not exclude other potential functions of L-fucose, which warrant further investigation. It has been reported that serotonin release is reduced in patients with depression (111). Lower levels of serotonin release in key parts of the brain may lead to stronger suicidal thoughts and higher mortality rates in people with depression (112). In our previous study, we observed the levels of serotonin metabolites were reduced in the *Fut8*$^{-/-}$ mice compared with *Fut8*$^{+/+}$ mice (42), suggesting that core fucosylation may be associated with serotonin metabolism. Furthermore, in this experiment, we found that the effect of L-fucose was similar to that of FLX. Perhaps L-fucose administration can increase the level of serotonin in the brain and thus alleviate the depressive-like behavior caused by CUS. We will conduct further exploration on this aspect in the future. Taken together, these data suggest that core fucosylation negatively regulates inflammation induced by CUS exposure.

One of the key contributors to refractory depression is the dysregulation of the JAK2/STAT3 signaling pathway (74). In the nervous system, the JAK-STAT pathway plays a crucial role in neurons, astrocytes, and oligodendrocytes (113–115). This pathway is also critical in the complex relationship between depression and systemic manifestations of chronic inflammation (116, 117). Inhibition of STAT3 can block IL-6 effects *in vitro* and regulate depressive-like behaviors *in vivo* (118). Microglial STAT3 inhibition may improve depressive behavior through neuron-microglia interaction (119). These findings suggest that targeting this pathway could enhance existing

depression treatments. In our study, we found that L-fucose administration inhibited the JAK2/STAT3 signaling pathway and reduced neuroinflammation in microglia induced by CUS exposure, indicating that L-fucose can target the JAK2/STAT3 pathway to exert its antidepressant effect. It is notable that although there was no significant difference between L-fucose and WP1066, JAK2/STAT3 inhibitor, in their antidepressant effects (Fig. S2, *A*–*C*), the combined administration of L-fucose and WP1066 had a better inhibitory effect on p-JAK2 than L-fucose alone (Fig. S3*F*). This may indicate that L-fucose exerts anti-inflammatory and antidepressant effects through not only the JAK2/STAT3 pathway but also other signal pathways. And this point needs further exploration.

Higher depression severity has been linked to lower synaptic density in the hippocampus, dorsolateral prefrontal cortex, and anterior cingulate cortex in imaging synaptic density in depressed patients (120). Strong inflammatory activation disrupts the normal microglia structure and function, contributing to depression and neuroplasticity impairment (24). Chronic stress, such as CUS, inhibits the expression of synaptic proteins, including PSD-95, synaptophysin, and decreases dendritic spine density (47, 121, 122). Our study found that the synaptic density in *Fut8*$^{+/-}$ mice exposed to CUS was significantly reduced in the hippocampus, and the protein expression of PSD-95 was also diminished, likely due to the release of inflammatory factors by microglia, which disrupts synaptic plasticity (Fig. 6, *A* and *B*). We also found that synaptic density in *Fut8*$^{+/-}$ mice was lower than that in *Fut8*$^{+/+}$ mice (Fig. 6*A*); this suggests that decreased core fucosylation may affect synaptic density in mice. JAK2 and STAT3 are highly expressed in the brain and are involved in synaptic plasticity (123). Inhibition of neuroinflammation caused by spinal cord injury through the JAK2/STAT3 signaling pathway can prevent neuronal apoptosis (124). IL-6 inhibits LTP, and blocking endogenous IL-6 can enhance LTP duration and long-term memory while reducing neuronal damage (125, 126). The absence of the *Fut8* gene significantly suppressed LTP in *Fut8*$^{-/-}$ mice (43). Interestingly, 30 years ago, Matthies *et al.* reported that L-fucose and fucosyllactose could enhance hippocampal LTP *in vitro* (127), although the underlying mechanism was unclear. This study provides a molecular mechanism by which exogenous L-fucose increases core fucosylation of gp130, negatively regulating the JAK2/STAT3 signaling pathway to ameliorate neuroinflammation of CUS maintenance (Figs. 5*B*; 9).

In summary, L-fucose negatively regulates CUS-induced neuroinflammation and improves synaptic plasticity impairment through the JAK2/STAT3 pathway, ultimately exerting an antidepressant effect, indicating that L-fucose possesses significant anti-neuroinflammatory activity and antidepressant potential.

## Experimental procedures

### Antibodies and reagents

Biotinylated LCA (J207) was obtained from J-oil Mills. The anti-GAPDH antibody (G9545) and anti-Mouse IgG antibody (AP124P) were obtained from Sigma. Anti-JAK2 (catalog no.: 3230), anti-Phospho-JAK2 (catalog no.: 3771), anti-STAT3 (catalog no.: 9139), anti-Phospho-STAT3 (catalog no.: 9145) antibodies and anti-rabbit IgG, HRP-linked antibody (catalog no.: 7074) were acquired from Cell Signaling Technology. The Iba1 antibody (catalog no. 019–19741) was purchased from FUJIFILM Wako Pure Chemical Corporation, and the anti-PSD-95 antibody (catalog no.:04–1066) was obtained from Millipore Corporation. The ABC kit (catalog no.: PK-4000) was from Vector Laboratories, and the goat anti-rabbit antibody Alexa Fluor 488 (catalog no.: A-11008) was obtained from Invitrogen. L-fucose (F0065) and Anti-Lewis X (A2578) were acquired from TCI, while fluoxetine (56,296–78–7) was sourced from Merck. WP1066 (HY-15312) was acquired from MCE. LPS was obtained from Sigma and purified from *Escherichia coli* O111:B4 (L2630). Ab-Capcher MAG2 was from ProteNova. The anti-IL-6R (#MA5-29721) and anti-gp130 (#A304–929A) antibodies were purchased from Thermo Fisher Scientific.

### Animal

*Fut8*$^{+/-}$ heterozygous mice with the ICR genetic background were intercrossed to generate *Fut8*$^{+/+}$ littermates and *Fut8*$^{+/-}$ mice (42). To investigate the underlying mechanism, we used a sensitive inflammation-monitoring mouse system containing the human interleukin-6 (*hIL6*) bacterial artificial chromosome (BAC) transgene modified with luciferase (*Luc*) reporter cassette (128). The *Fut8*$^{+/-}$ mice were mated with *hIL6*-BAC-*Luc* reporter transgenic mice to produce *Fut8*$^{+/+}$::*hIL6-Luc* and *Fut8*$^{+/-}$::*hIL6-Luc* compound transgenic mice for LPS-induced inflammation as described (45). All experiments were conducted using 5- to 6-week-old male mice weighing approximately 25 to 30 g. Mice were housed in groups under standard vivarium conditions, with free access to food and water, a 12-h light-dark cycle (lights on from 7:00–19:00), an ambient temperature of 22 ± 2 °C, and relative humidity of 55 ± 5%. Mice received oral L-fucose twice daily *via* gavage at a dose of 36 mg/day. All animal experiments adhered to protocols approved by the Animal Care and Use Committee of the Graduate School of Pharmaceutical Sciences, Tohoku Medical and Pharmaceutical University.

### Cell culture

BV2 (mouse microglia cell line) was generously gifted by Professor Elisabetta Blasi (University of Modena and Reggio Emilia, Modena). At 37 °C and 5% CO2, BV2 cells were cultured in Dulbecco's modified Eagle's medium supplemented with 10% fetal bovine serum in a humidified environment. The cells were confirmed free from *mycoplasma* using the e-Myco *Mycoplasma* PCR Detection kit (iNtRON Biotechnology, Republic of Korea).

### Chronic unpredictable stress (CUS)

Following established procedures (62), we constructed the CUS model by randomly exposing mice to two stressors daily for 28 days (*Fut8*$^{+/-}$ mice) or 35 days (*Fut8*$^{+/+}$ mice), as detailed in Table 1. Stressors included 1 h of cage shaking, 12 h

**Table 1**
**Construction of the CUS model, in which mice were randomly exposed to two stressors daily**

| Times | Monday | Tuesday | Wednesday | Thursday | Friday | Saturday | Sunday |
|---|---|---|---|---|---|---|---|
| Week 1 | lights-off | shaking | no water | restraint | light restraint | lights-off | shaking |
| | cage tilt | lights-on | no food | lights-on | wet cage | lights-on | cage tilt |
| Week 2 | restraint | light restraint | lights-off | restraint | lights-off | shaking | light restraint |
| | no water | no food | lights-on | shaking | cage tilt | wet cage | no water |
| Week 3 | lights-off | light restraint | restraint | shaking | no water | lights-off | light restraint |
| | cage tilt | lights-on | no food | cage tilt | wet cage | no food | lights-on |
| Week 4 | restraint | lights-off | shaking | light restraint | restraint | shaking | lights-off |
| | no water | cage tilt | wet cage | lights-on | no food | wet cage | cage tilt |
| Week 5 | shaking | lights-off | restraint | shaking | light restraint | lights-off | shaking |
| | no food | lights-on | cage tilt | no water | wet cage | no food | cage tilt |

of lights-on during the night, 3 h of lights-off during the day, 2 h of light restraint (housing in small cages), 1 h of restraint (placing mice in a 50 ml plastic tube with breathing holes), 14 h of 45°cage tilt, 14 h of wet cage, and 12 h of food or water deprivation during the dark period.

### *Tail suspension test (TST)*

The TST was performed as previously described (62). Mice were suspended 50 cm above the ground with tape attached to their tails (1 cm from the tip) for 6 min. A blinded researcher recorded the duration of immobility during the last 4 min. Mice were considered immobile only when they were passively suspended and completely motionless. Any mice that climbed up the tail were excluded from the analysis.

### *Forced swimming test (FST)*

The FST was conducted as previously outlined (62). Mice were placed individually in a transparent glass cylinder (height: 25 cm, diameter: 10 cm) filled with 10 cm of water at 25 ± 1 °C for 6 min. An investigator unaware of the study recorded the immobility time during the last 4 min, defined as the duration the mouse floated in the water without struggling, only making movements necessary to keep its head above water.

### *Sucrose preference test (SPT)*

This experiment followed established protocols (62). Mice were given access to two bottles in their cages: one containing 1% sucrose solution and the other containing water. All mice were acclimated to the two-bottle choice condition for 2 days, with bottle positions changed every 6 h to prevent positional preference. After a 24-h period of food and water deprivation, mice had free access to both bottles for 12 h, after which the positions were swapped. The volumes of water and sucrose solution consumed were recorded, and sucrose preference was calculated as the percentage of sucrose solution consumed relative to total fluid intake.

### *Western blotting and lectin blotting*

Equal amounts of proteins were separated by sodium dodecyl sulfate-polyacrylamide gel electrophoresis (SDS-PAGE) and transferred to polyvinylidene difluoride membranes (Millipore Sigma) at 10 V for 1 h. For Western blotting, membranes were blocked with 5% nonfat dry milk for 1.5 h at room temperature, incubated with specific primary antibodies overnight at 4° C, and then with appropriate HRP-conjugated secondary antibodies. For lectin blotting, membranes were blocked in 5% BSA for 1.5 h at room temperature, followed by incubation with biotinylated LCA lectin overnight at 4° C. The Vectastain ABC kit (Vector Laboratories) was then used to probe the immunoreactive bands. Specific proteins were visualized using ECL select reagent (Amersham).

### *Immunoprecipitation*

The MT-360 Micro Tube Mixer was used to combine 1.5 μl anti-gp130 antibody with 15 μl Ab-Capcher MAG2 at 4 °C for 2 hours. After three times of washes with PBS, 500 μg of proteins from each tissue were added and incubated overnight at 4 °C. After two PBS washes, these immunoprecipitates were identified using western blotting and lectin blotting.

### *Real-time PCR*

RNA was extracted using TRIzol reagent (Invitrogen) and reverse-transcribed (1 μg total RNA) into cDNA using PrimeScript RT reagent with gDNA Eraser (Takara). Primer sequences for real-time PCR are shown in Table 2. Real-time PCR was performed using TB Green Premix Ex Taq II (Tli

**Table 2**
**Primer sequences for real-time PCR**

| Target genes | Primer sequences (5′-3′) | |
|---|---|---|
| | Forward sequences | Reverse sequences |
| *Il6* | CTGCAAGAGACTTCCATCCAG | AGTGGTATAGACAGGTCTGTTGG |
| *TNF-α* | AAGTCAACCTCCTCTCTGCC | CCGGACTCCGCAAAGTCTAA |
| *Il1b* | TGTCTGAAGCAGCTATGGC | TGTTGATGTGCTGCTGCG |
| *iNOS* | ATGACTCCCAGCACAAAGGG | AACAGCACTCTCTTGCGGACC |
| *Iba1* | TCTGAGGAGCTATGAGCC | TCCATGTACTTCGTCTTGAAGGC |
| *Gapdh* | GTCGTGGAGTCTACTGGTGTCTT | GAGATGATGACCCTTTTGGC |
| *Fut8* | AACAGAAGCAGCCTTCCACC | TACCGATTGTGTAGTCCAGC |

RNaseH Plus) (Takara) under the following conditions: initial denaturation at 95 °C for 30 s, followed by 40 cycles of denaturation at 95 °C for 5 s and annealing at 60 °C for 30 s.

### *Immunofluorescence*

Mice were deeply anesthetized with sodium pentobarbital and perfused intracardially with 4% paraformaldehyde in 0.01 M phosphate buffer. After perfusion, brains were removed and fixed in 4% paraformaldehyde for 24 h, followed by dehydration in 30% sucrose solution. Brains were frozen and sectioned at 25 μm using a cryostat. Sections were collected in 24-well plates, washed three times with PBS, permeabilized with 0.3% Triton X-100 for 30 min, and blocked with 4% BSA in PBS for 30 min at room temperature. They were then incubated overnight at 4 °C with 1% BSA, 0.3% Triton X-100, and anti-Iba1 antibody (1:500) in PBS. After three washes with PBS, sections were incubated with the goat anti-rabbit antibody Alexa Fluor 488 for 2 h at room temperature. Following three additional washes in PBS, sections were incubated with 4′,6-diamidino-2-phenylindole (DAPI) for 10 min to label cell nuclei. Sections were then transferred to slides, sealed with fluorescence mounting medium, and examined using a ZEISS LSM 900 confocal microscope. The number of Iba1-labeled microglia was quantified using ImageJ software (https://imagej.net/ij/).

### *Golgi staining*

Golgi staining was performed using FD Rapid GolgiStain Kit (PK401). Following deep anesthesia, the mouse brain was removed and washed with double-distilled water. Brain tissue was treated according to the manufacturer's protocol. Tissue was sectioned into 100 μm slices, transferred to gelatin-coated microscope slides (catalog no. PO101), and air-dried at room temperature. Sections were rinsed with double-distilled water, stained in the staining solution for 10 min, and then rinsed again. Stained sections were dehydrated in a series of ethanol concentrations (50%, 75%, 95% ethanol, and anhydrous ethanol) and finally cleared with xylene. Mounting with Permount Mounting Medium (E17986–01). Three or four neurons were selected per mice in the CA1 region of the hippocampus, and three mice were used per group. Images were captured using an Olympus IX71 microscope at 10X and 40X magnification. Spine density is defined as the number of protrusions divided by the dendritic shaft length. Total dendritic length and number of branches were measured using ImageJ software.

### *Statistical analysis*

All data are presented as mean ± SD from at least three independent experiments. Statistical analysis was conducted using a one-way analysis of variance (ANOVA) with Tukey's *post hoc* test *via* GraphPad Prism 5.0 software (GraphPad Software, Inc). A probability value of $p$ was considered as follows: n.s. (no significance), $p > 0.05$; $^{*}p < 0.05$; $^{**}p < 0.01$; $^{***}p < 0.001$.

## Data availability

All data presented in the figures and tables, and supplementary information of this paper are available.

*Supporting information*—This article contains supporting Information.

*Author contributions*—T. I., J. G., X. X., D. W., and T. F. writing–review & editing; T. I., X. X., D. W., and T. F. visualization; T. I. supervision; T. I., J. G., T. W., X. X., D. W., and T. F. methodology; T. I., J. G., T. W., X. X., D. W., and T. F.data curation; T. I., J. G., D. W., and T. F. conceptualization. J. G. and T. F. supervision; J. G. project administration; J. G. and T. F. funding acquisition; T. W., X. X., and D. W. validation; T. W., X. X., and D. W. investigation.

*Funding and additional information*—This work was partially supported by a Grant-in-Aid for Scientific Research (23K27133 to J.G. and 24K09817 to T.F.) and by a Grant-in-Aid for Challenging Exploratory Research (22K19443 to J.G.) from the Japan Society for the Promotion of Science. Additionally, this research was conducted under the Collaborative Open Research Program to promote the Human Glycome Atlas Project (HGA) as strategic interdisciplinary research in the J-GlycoNet cooperative network, accredited by the Minister of Education, Culture, Sports, Science and Technology, MEXT, Japan, as a Joint Usage/Research Center.

*Conflicts of interest*—The authors declare that they have no conflicts of interest with the contents of this article.

*Abbreviations*—The abbreviations used are: AAL, *Aleuria aurantia* lectin; CNS, central nervous system; CUS, chronic unpredictable stress; DG, dentate gyrus; FLX, Fluoxetine; FST, Forced swimming test; Fut8, α1,6-fucosyltransferase; GAPDH, Glyceraldehyde-3-phosphate dehydrogenase; GDP, guanosine 5′-diphosphate; gp130, glycoprotein 130; Iba1, ionized calcium-binding adaptor molecule-1; IL-1β, interleukin-1β; Il1b, interleukin 1 beta; IL-6, interleukin-6; IL-6R, IL-6 receptor; JAK2, Janus kinase 2; LPS, lipopolysaccharide; LTP, long term potentiation; MDD, major depressive disorder; PSD-95, postsynaptic density protein 95; SPT, sucrose preference test; SSRI, selective serotonin reuptake inhibitors; STAT3, signal transducer and activator of transcription 3; TNF-α, tumor necrosis factor-alpha; TST, Tail suspension test.

## References

1. Zhu, Y. J., Huang, J., Chen, R., Zhang, Y., He, X., Duan, W. X., *et al.* (2024) Autophagy dysfunction contributes to NLRP1 inflammasome-linked depressive-like behaviors in mice. *J. Neuroinflammation* **21**, 6
2. Kong, S., Chen, Y., Huang, H., Yang, W., Lyu, D., Wang, F., *et al.* (2024) Efficacy of transcranial direct current stimulation for treating anhedonia in patients with depression: a randomized, double-blind, sham-controlled clinical trial. *J. Affect. Disord.* **350**, 264–273
3. Zu, X., Xin, J., Xie, H., Xu, X., Shen, Y., Wang, J., *et al.* (2024) Characteristics of gut microbiota and metabolic phenotype in patients with major depressive disorder based on multi-omics analysis. *J. Affect. Disord.* **344**, 563–576
4. Ren, F. F., Hillman, C. H., Wang, W. G., Li, R. H., Zhou, W. S., Liang, W. M., *et al.* (2024) Effects of aerobic exercise on cognitive function in adults with major depressive disorder: a systematic review and meta-analysis. *Int. J. Clin. Health Psychol.* **24**, 100447

5. Zhang, Y., Lai, S., Zhang, J., Wang, Y., Zhao, H., He, J., *et al.* (2024) The effectiveness of vortioxetine on neurobiochemical metabolites and cognitive of major depressive disorders patients: a 8-week follow-up study. *J. Affect. Disord.* **351**, 799–807
6. Yu, X., Wang, S., Wu, W., Chang, H., Shan, P., Yang, L., *et al.* (2023) Exploring new mechanism of depression from the effects of virus on nerve cells. *Cells* **12**, 1767
7. Cui, L., Li, S., Wang, S., Wu, X., Liu, Y., Yu, W., *et al.* (2024) Major depressive disorder: hypothesis, mechanism, prevention and treatment. *Signal Transduct. Target. Ther.* **9**, 30
8. Malhi, G. S., and Mann, J. J. (2018) Depression. *Lancet.* **392**, 2299–2312
9. Sukoff Rizzo, S. J., Neal, S. J., Hughes, Z. A., Beyna, M., Rosenzweig-Lipson, S., Moss, S. J., *et al.* (2012) Evidence for sustained elevation of IL-6 in the CNS as a key contributor of depressive-like phenotypes. *Transl. Psychiatry* **2**, e199
10. Wiener, C. D., Moreira, F. P., Portela, L. V., Strogulski, N. R., Lara, D. R., da Silva, R. A., *et al.* (2019) Interleukin-6 and Interleukin-10 in mood disorders: a population-based study. *Psychiatry Res.* **273**, 685–689
11. Ting, E. Y., Yang, A. C., and Tsai, S. J. (2020) Role of interleukin-6 in depressive disorder. *Int. J. Mol. Sci.* **21**, 2194
12. Ellul, P., Boyer, L., Groc, L., Leboyer, M., and Fond, G. (2016) Interleukin-1 beta-targeted treatment strategies in inflammatory depression: toward personalized care. *Acta Psychiatr. Scand.* **134**, 469–484
13. Lu, J., Jin, K., Jiao, J., Liu, R., Mou, T., Chen, B., *et al.* (2023) YY1 (Yin-Yang 1), a transcription factor regulating systemic inflammation, is involved in cognitive impairment of depression. *Psychiatry Clin. Neurosci.* **77**, 149–159
14. Yang, Y., Gu, K., Meng, C., Li, J., Lu, Q., Zhou, X., *et al.* (2023) Relationship between sleep and serum inflammatory factors in patients with major depressive disorder. *Psychiatry Res.* **329**, 115528
15. Enache, D., Pariante, C. M., and Mondelli, V. (2019) Markers of central inflammation in major depressive disorder: a systematic review and meta-analysis of studies examining cerebrospinal fluid, positron emission tomography and post-mortem brain tissue. *Brain Behav. Immun.* **81**, 24–40
16. Dowlati, Y., Herrmann, N., Swardfager, W., Liu, H., Sham, L., Reim, E. K., *et al.* (2010) A meta-analysis of cytokines in major depression. *Biol. Psychiatry* **67**, 446–457
17. Kopschina Feltes, P., Doorduin, J., Klein, H. C., Juarez-Orozco, L. E., Dierckx, R. A., Moriguchi-Jeckel, C. M., *et al.* (2017) Anti-inflammatory treatment for major depressive disorder: implications for patients with an elevated immune profile and non-responders to standard antidepressant therapy. *J. Psychopharmacol.* **31**, 1149–1165
18. Elizabeth, A., Adegbuyi, A., Olusegun, A., Benneth, B. A., Anthony, E., Abayomi, A., *et al.* (2020) Morin hydrate attenuates chronic stress-induced memory impairment and degeneration of hippocampal subfields in mice: the role of oxidative, nitrergic and neuroinflammatory pathways. *Metab. Brain Dis.* **35**, 1145–1156
19. Liu, L., Tang, J., Liang, X., Li, Y., Zhu, P., Zhou, M., *et al.* (2024) Running exercise alleviates hippocampal neuroinflammation and shifts the balance of microglial M1/M2 polarization through adiponectin/AdipoR1 pathway activation in mice exposed to chronic unpredictable stress. *Mol. Psychiatry* **29**, 2031–2042
20. Wang, H., Yang, Y., Yang, S., Ren, S., Feng, J., Liu, Y., *et al.* (2021) Ginsenoside Rg1 ameliorates neuroinflammation via suppression of Connexin43 ubiquitination to attenuate depression. *Front. Pharmacol.* **12**, 709019
21. Yirmiya, R., Rimmerman, N., and Reshef, R. (2015) Depression as a microglial disease. *Trends Neurosci.* **38**, 637–658
22. Wang, H., He, Y., Sun, Z., Ren, S., Liu, M., Wang, G., *et al.* (2022) Microglia in depression: an overview of microglia in the pathogenesis and treatment of depression. *J. Neuroinflammation* **19**, 132
23. Li, B., Yang, W., Ge, T., Wang, Y., and Cui, R. (2022) Stress induced microglial activation contributes to depression. *Pharmacol. Res.* **179**, 106145
24. Li, W., Ali, T., He, K., Liu, Z., Shah, F. A., Ren, Q., *et al.* (2021) Ibrutinib alleviates LPS-induced neuroinflammation and synaptic defects in a mouse model of depression. *Brain Behav. Immun.* **92**, 10–24
25. Wei, H., Yu, C., Zhang, C., Ren, Y., Guo, L., Wang, T., *et al.* (2023) Butyrate ameliorates chronic alcoholic central nervous damage by suppressing microglia-mediated neuroinflammation and modulating the microbiome-gut-brain axis. *Biomed. Pharmacother.* **160**, 114308
26. Kokkosis, A. G., Madeira, M. M., Hage, Z., Valais, K., Koliatsis, D., Resutov, E., *et al.* (2024) Chronic psychosocial stress triggers microglial-/macrophage-induced inflammatory responses leading to neuronal dysfunction and depressive-related behavior. *Glia* **72**, 111–132
27. Villar-Portela, S., Muinelo-Romay, L., Cuevas, E., Gil-Martin, E., and Fernandez-Briera, A. (2013) FX enzyme and GDP-L-Fuc transporter expression in colorectal cancer. *Histopathology.* **63**, 174–186
28. Bonin, C. P., Freshour, G., Hahn, M. G., Vanzin, G. F., and Reiter, W. D. (2003) The GMD1 and GMD2 genes of Arabidopsis encode isoforms of GDP-D-mannose 4,6-dehydratase with cell type-specific expression patterns. *Plant Physiol.* **132**, 883–892
29. Yamaguchi, Y., Ikeda, Y., Takahashi, T., Ihara, H., Tanaka, T., Sasho, C., *et al.* (2000) Genomic structure and promoter analysis of the human alpha1, 6-fucosyltransferase gene (FUT8). *Glycobiology* **10**, 637–643
30. Ayukawa, T., Matsumoto, K., Ishikawa, H. O., Ishio, A., Yamakawa, T., Aoyama, N., *et al.* (2012) Rescue of Notch signaling in cells incapable of GDP-L-fucose synthesis by gap junction transfer of GDP-L-fucose in Drosophila. *Proc. Natl. Acad. Sci. U. S. A.* **109**, 15318–15323
31. Becker, D. J., and Lowe, J. B. (2003) Fucose: biosynthesis and biological function in mammals. *Glycobiology* **13**, 41R–53R
32. Adhikari, E., Liu, Q., Burton, C., Mockabee-Macias, A., Lester, D. K., and Lau, E. (2022) L-fucose, a sugary regulator of antitumor immunity and immunotherapies. *Mol. Carcinog.* **61**, 439–453
33. Lester, D. K., Burton, C., Gardner, A., Innamarato, P., Kodumudi, K., Liu, Q., *et al.* (2023) Fucosylation of HLA-DRB1 regulates CD4(+) T cell-mediated anti-melanoma immunity and enhances immunotherapy efficacy. *Nat. Cancer* **4**, 222–239
34. Feofanova, N. A., Bets, V. D., Borisova, M. A., and Litvinova, E. A. (2022) L-fucose reduces gut inflammation due to T-regulatory response in Muc2 null mice. *PLoS One* **17**, e0278714
35. Li, W., Wu, P., Jin, T., Jia, J., Chen, B., Liu, T., *et al.* (2024) L-fucose and fucoidan alleviate high-salt diet-promoted acute inflammation. *Front. Immunol.* **15**, 1333848
36. Yao, H., Shi, H., Jiang, C., Fan, M., Zhang, Y., Qian, W., *et al.* (2023) L-Fucose promotes enteric nervous system regeneration in type 1 diabetic mice by inhibiting SMAD2 signaling pathway in enteric neural precursor cells. *Cell Commun. Signal.* **21**, 273
37. Hayes, A. J., and Melrose, J. (2018) Glycans and glycosaminoglycans in neurobiology: key regulators of neuronal cell function and fate. *Biochem. J.* **475**, 2511–2545
38. Alghazwi, M., Smid, S., Karpiniec, S., and Zhang, W. (2019) Comparative study on neuroprotective activities of fucoidans from Fucus vesiculosus and Undaria pinnatifida. *Int. J. Biol. Macromol.* **122**, 255–264
39. Takahashi, M., Kizuka, Y., Ohtsubo, K., Gu, J., and Taniguchi, N. (2016) Disease-associated glycans on cell surface proteins. *Mol. Aspects Med.* **51**, 56–70
40. Wang, X., Gu, J., Miyoshi, E., Honke, K., and Taniguchi, N. (2006) Phenotype changes of Fut8 knockout mouse: core fucosylation is crucial for the function of growth factor receptor(s). *Methods Enzymol.* **417**, 11–22
41. Hullen, A., Falkenstein, K., Weigel, C., Huidekoper, H., Naumann-Bartsch, N., Spenger, J., *et al.* (2021) Congenital disorders of glycosylation with defective fucosylation. *J. Inherit. Metab. Dis.* **44**, 1441–1452
42. Fukuda, T., Hashimoto, H., Okayasu, N., Kameyama, A., Onogi, H., Nakagawasai, O., *et al.* (2011) Alpha1,6-fucosyltransferase-deficient mice exhibit multiple behavioral abnormalities associated with a schizophrenia-like phenotype: importance of the balance between the dopamine and serotonin systems. *J. Biol. Chem.* **286**, 18434–18443
43. Gu, W., Fukuda, T., Isaji, T., Hang, Q., Lee, H. H., Sakai, S., *et al.* (2015) Loss of alpha1,6-fucosyltransferase decreases hippocampal long term potentiation: implications for core fucosylation in the regulation of ampa receptor heteromerization and cellular signaling. *J. Biol. Chem.* **290**, 17566–17575

44. Guo, H., Sun, Q., Huang, X., Wang, X., Zhang, F., Qu, W., *et al.* (2024) Fucosyltransferase 8 regulates adult neurogenesis and cognition of mice by modulating the Itga6-PI3K/Akt signaling pathway. *Sci. China. Life Sci.* **67**, 1427–1440
45. Xu, X., Fukuda, T., Takai, J., Morii, S., Sun, Y., Liu, J., *et al.* (2024) Exogenous l-fucose attenuates neuroinflammation induced by lipopolysaccharide. *J. Biol. Chem.* **300**, 105513
46. Lu, X., Zhang, D., Shoji, H., Duan, C., Zhang, G., Isaji, T., *et al.* (2019) Deficiency of alpha1,6-fucosyltransferase promotes neuroinflammation by increasing the sensitivity of glial cells to inflammatory mediators. *Biochim. Biophys. Acta Gen. Subj.* **1863**, 598–608
47. Duman, R. S., and Aghajanian, G. K. (2012) Synaptic dysfunction in depression: potential therapeutic targets. *Science* **338**, 68–72
48. Allen, L., and Dwivedi, Y. (2020) MicroRNA mediators of early life stress vulnerability to depression and suicidal behavior. *Mol. Psychiatry* **25**, 308–320
49. Kendler, K. S., Karkowski, L. M., and Prescott, C. A. (1999) Causal relationship between stressful life events and the onset of major depression. *Am. J. Psychiatry* **156**, 837–841
50. Walton, N. L., Antonoudiou, P., Barros, L., Dargan, T., DiLeo, A., Evans-Strong, A., *et al.* (2023) Impaired endogenous neurosteroid signaling contributes to behavioral deficits associated with chronic stress. *Biol. Psychiatry* **94**, 249–261
51. Malta, M. B., Martins, J., Novaes, L. S., Dos Santos, N. B., Sita, L., Camarini, R., *et al.* (2021) Norepinephrine and glucocorticoids modulate chronic unpredictable stress-induced increase in the type 2 CRF and glucocorticoid receptors in brain structures related to the HPA Axis activation. *Mol. Neurobiol.* **58**, 4871–4885
52. Shin, H. S., Lee, S. H., Moon, H. J., So, Y. H., Jang, H. J., Lee, K. H., *et al.* (2024) Prolonged stress response induced by chronic stress and corticosterone exposure causes adult neurogenesis inhibition and astrocyte loss in mouse hippocampus. *Brain Res. Bull.* **208**, 110903
53. Wu, H., Denna, T. H., Storkersen, J. N., and Gerriets, V. A. (2019) Beyond a neurotransmitter: the role of serotonin in inflammation and immunity. *Pharmacol. Res.* **140**, 100–114
54. Li, W., Ali, T., Zheng, C., Liu, Z., He, K., Shah, F. A., *et al.* (2021) Fluoxetine regulates eEF2 activity (phosphorylation) via HDAC1 inhibitory mechanism in an LPS-induced mouse model of depression. *J. Neuroinflammation* **18**, 38
55. Wang, L., Wang, R., Liu, L., Qiao, D., Baldwin, D. S., and Hou, R. (2019) Effects of SSRIs on peripheral inflammatory markers in patients with major depressive disorder: a systematic review and meta-analysis. *Brain Behav. Immun.* **79**, 24–38
56. Garcia-Garcia, M. L., Tovilla-Zarate, C. A., Villar-Soto, M., Juarez-Rojop, I. E., Gonzalez-Castro, T. B., Genis-Mendoza, A. D., *et al.* (2022) Fluoxetine modulates the pro-inflammatory process of IL-6, IL-1beta and TNF-alpha levels in individuals with depression: a systematic review and meta-analysis. *Psychiatry Res.* **307**, 114317
57. Zhang, F., Zhou, H., Wilson, B. C., Shi, J. S., Hong, J. S., and Gao, H. M. (2012) Fluoxetine protects neurons against microglial activation-mediated neurotoxicity. *Parkinsonism Relat. Disord.* **18**(Suppl 1), S213–S217
58. Liu, Q. R., Shi, C. N., Wang, F., and Tong, J. H. (2023) Neuroinflammation-induced parvalbumin interneuron and oscillation deficits might contribute to neurobehavioral abnormities in a two-hit model of depression. *Heliyon* **9**, e18468
59. Liu, D., Wang, Z., Liu, S., Wang, F., Zhao, S., and Hao, A. (2011) Anti-inflammatory effects of fluoxetine in lipopolysaccharide(LPS)-stimulated microglial cells. *Neuropharmacology* **61**, 592–599
60. Wakasugi, D., Kondo, S., Ferdousi, F., Mizuno, S., Yada, A., Tominaga, K., *et al.* (2024) A rare olive compound oleacein functions as a TrkB agonist and mitigates neuroinflammation both in vitro and in vivo. *Cell Commun. Signal.* **22**, 309
61. Albrakati, A., Alsharif, K. F., Al Omairi, N. E., Alsanie, W. F., Almalki, A. S. A., Abd Elmageed, Z. Y., *et al.* (2021) Neuroprotective efficiency of prodigiosins conjugated with selenium nanoparticles in rats exposed to chronic unpredictable mild stress is mediated through antioxidative, anti-inflammatory, anti-apoptotic, and neuromodulatory activities. *Int. J. Nanomedicine.* **16**, 8447–8464
62. Wang, D., Xu, X., Wu, Y., Lin, Y., Gao, M., Hu, P., *et al.* (2019) SMIP004: a compound with antidepressant-like activities in mouse models. *Eur. J. Pharmacol.* **843**, 260–267
63. Wu, A., and Zhang, J. (2023) Neuroinflammation, memory, and depression: new approaches to hippocampal neurogenesis. *J. Neuroinflammation* **20**, 283
64. Tartt, A. N., Mariani, M. B., Hen, R., Mann, J. J., and Boldrini, M. (2022) Dysregulation of adult hippocampal neuroplasticity in major depression: pathogenesis and therapeutic implications. *Mol. Psychiatry* **27**, 2689–2699
65. Fuchs, E., Czeh, B., Kole, M. H., Michaelis, T., and Lucassen, P. J. (2004) Alterations of neuroplasticity in depression: the hippocampus and beyond. *Eur. Neuropsychopharmacol.* **14**(Suppl 5), S481–S490
66. Singhal, G., and Baune, B. T. (2017) Microglia: an interface between the loss of neuroplasticity and depression. *Front. Cell. Neurosci.* **11**, 270
67. Xiao, K., Luo, Y., Liang, X., Tang, J., Wang, J., Xiao, Q., *et al.* (2021) Beneficial effects of running exercise on hippocampal microglia and neuroinflammation in chronic unpredictable stress-induced depression model rats. *Transl. Psychiatry* **11**, 461
68. Schramm, E., and Waisman, A. (2022) Microglia as central protagonists in the chronic stress response. *Neurol. Neuroimmunol. Neuroinflamm.* **9**, e200023
69. Imai, Y., and Kohsaka, S. (2002) Intracellular signaling in M-CSF-induced microglia activation: role of Iba1. *Glia* **40**, 164–174
70. Yu, L., Huang, L., Zhao, Y., Liu, S., Zhou, R., Yue, Y., *et al.* (2024) Atorvastatin promotes pro/anti-inflammatory phenotypic transformation of microglia via wnt/beta-catenin pathway in hypoxic-ischemic neonatal rats. *Mol. Neurobiol.* **61**, 3559–3577
71. Bennett, M. L., Bennett, F. C., Liddelow, S. A., Ajami, B., Zamanian, J. L., Fernhoff, N. B., *et al.* (2016) New tools for studying microglia in the mouse and human CNS. *Proc. Natl. Acad. Sci. U. S. A.* **113**, E1738–E1746
72. Liang, Y., Aditi, Onyoni, F., Wang, H., Gonzales, C., Sunyakumthorn, P., *et al.* (2023) Brain transcriptomics reveal the activation of neuroinflammation pathways during acute Orientia tsutsugamushi infection in mice. *Front. Immunol.* **14**, 1194881
73. Hamsalakshmi, Alex, A. M., Arehally Marappa, M., Joghee, S., and Chidambaram, S. B. (2022) Therapeutic benefits of flavonoids against neuroinflammation: a systematic review. *Inflammopharmacology* **30**, 111–136
74. Almutabagani, L. F., Almanqour, R. A., Alsabhan, J. F., Alhossan, A. M., Alamin, M. A., Alrajeh, H. M., *et al.* (2023) Inflammation and treatment-resistant depression from clinical to animal study: a possible link? *Neurol. Int.* **15**, 100–120
75. Hu, Y., Zhang, X., Zhang, J., Xia, X., Li, H., Qiu, C., *et al.* (2021) Activated STAT3 signaling pathway by ligature-induced periodontitis could contribute to neuroinflammation and cognitive impairment in rats. *J. Neuroinflammation* **18**, 80
76. Millot, P., San, C., Bennana, E., Porte, B., Vignal, N., Hugon, J., *et al.* (2020) STAT3 inhibition protects against neuroinflammation and BACE1 upregulation induced by systemic inflammation. *Immunol. Lett.* **228**, 129–134
77. Zheng, Z. V., Chen, J., Lyu, H., Lam, S. Y. E., Lu, G., Chan, W. Y., *et al.* (2022) Novel role of STAT3 in microglia-dependent neuroinflammation after experimental subarachnoid haemorrhage. *Stroke Vasc. Neurol.* **7**, 62–70
78. Zhou, K., Chen, J., Wu, J., Wu, Q., Jia, C., Xu, Y. X. Z., *et al.* (2019) Atractylenolide III ameliorates cerebral ischemic injury and neuroinflammation associated with inhibiting JAK2/STAT3/Drp1-dependent mitochondrial fission in microglia. *Phytomedicine* **59**, 152922
79. Tian, Y. S., Zhong, D., Liu, Q. Q., Zhao, X. L., Sun, H. X., Jin, J., *et al.* (2018) Upregulation of miR-216a exerts neuroprotective effects against ischemic injury through negatively regulating JAK2/STAT3-involved apoptosis and inflammatory pathways. *J. Neurosurg.* **130**, 977–988
80. Mojiri-Forushani, H., Khajehali, E., Adelipour, M., and Mohammadi, A. (2023) Inhibitory effects of fluoxetine on the secretion of inflammatory

mediators and JAK/STAT3 and JNK/TLR4 gene expression. *Mol. Biol. Rep.* **50**, 2231–2241
81. Zanders, L., Kny, M., Hahn, A., Schmidt, S., Wundersitz, S., Todiras, M., *et al.* (2022) Sepsis induces interleukin 6, gp130/JAK2/STAT3, and muscle wasting. *J. Cachexia Sarcopenia Muscle* **13**, 713–727
82. Hussain, S. F., Kong, L. Y., Jordan, J., Conrad, C., Madden, T., Fokt, I., *et al.* (2007) A novel small molecule inhibitor of signal transducers and activators of transcription 3 reverses immune tolerance in malignant glioma patients. *Cancer Res.* **67**, 9630–9636
83. Hatiboglu, M. A., Kong, L. Y., Wei, J., Wang, Y., McEnery, K. A., Fuller, G. N., *et al.* (2012) The tumor microenvironment expression of p-STAT3 influences the efficacy of cyclophosphamide with WP1066 in murine melanoma models. *Int. J. Cancer* **131**, 8–17
84. Zaccard, C. R., Gippo, I., Song, A., Geula, C., and Penzes, P. (2023) Dendritic spinule-mediated structural synaptic plasticity: implications for development, aging, and psychiatric disease. *Front. Mol. Neurosci.* **16**, 1059730
85. Bai, Z., Gao, T., Zhang, R., Lu, Y., Tian, J., Wang, T., *et al.* (2023) Inhibition of IL-6 methylation by Saikosaponin C regulates neuroinflammation to alleviate depression. *Int. Immunopharmacol.* **118**, 110043
86. Popova, D., Castren, E., and Taira, T. (2017) Chronic fluoxetine administration enhances synaptic plasticity and increases functional dynamics in hippocampal CA3-CA1 synapses. *Neuropharmacology* **126**, 250–256
87. Djordjevic, A., Djordjevic, J., Elakovic, I., Adzic, M., Matic, G., and Radojcic, M. B. (2012) Fluoxetine affects hippocampal plasticity, apoptosis and depressive-like behavior of chronically isolated rats. *Prog. Neuropsychopharmacol. Biol. Psychiatry* **36**, 92–100
88. Bijata, M., Baczynska, E., Muller, F. E., Bijata, K., Masternak, J., Krzystyniak, A., *et al.* (2022) Activation of the 5-HT7 receptor and MMP-9 signaling module in the hippocampal CA1 region is necessary for the development of depressive-like behavior. *Cell Rep.* **38**, 110532
89. Egashira, Y., Suganuma, M., Kataoka, Y., Higa, Y., Ide, N., Morishita, K., *et al.* (2019) Establishment and characterization of a fucosylated alpha-fetoprotein-specific monoclonal antibody: a potential application for clinical research. *Sci. Rep.* **9**, 12359
90. Feichtinger, R. G., Hullen, A., Koller, A., Kotzot, D., Grote, V., Rapp, E., *et al.* (2021) A spoonful of L-fucose-an efficient therapy for GFUS-CDG, a new glycosylation disorder. *EMBO Mol. Med.* **13**, e14332
91. Kudo, T., Fujii, T., Ikegami, S., Inokuchi, K., Takayama, Y., Ikehara, Y., *et al.* (2007) Mice lacking alpha1,3-fucosyltransferase IX demonstrate disappearance of Lewis x structure in brain and increased anxiety-like behaviors. *Glycobiology* **17**, 1–9
92. Guo, L. T., Wang, S. Q., Su, J., Xu, L. X., Ji, Z. Y., Zhang, R. Y., *et al.* (2019) Baicalin ameliorates neuroinflammation-induced depressive-like behavior through inhibition of toll-like receptor 4 expression via the PI3K/AKT/FoxO1 pathway. *J. Neuroinflammation* **16**, 95
93. Dong, S. Q., Zhang, Q. P., Zhu, J. X., Chen, M., Li, C. F., Liu, Q., *et al.* (2018) Gypenosides reverses depressive behavior via inhibiting hippocampal neuroinflammation. *Biomed. Pharmacother.* **106**, 1153–1160
94. Zhao, Q., Wu, X., Yan, S., Xie, X., Fan, Y., Zhang, J., *et al.* (2016) The antidepressant-like effects of pioglitazone in a chronic mild stress mouse model are associated with PPARgamma-mediated alteration of microglial activation phenotypes. *J. Neuroinflammation* **13**, 259
95. Tynan, R. J., Naicker, S., Hinwood, M., Nalivaiko, E., Buller, K. M., Pow, D. V., *et al.* (2010) Chronic stress alters the density and morphology of microglia in a subset of stress-responsive brain regions. *Brain Behav. Immun.* **24**, 1058–1068
96. Bian, Y., Pan, Z., Hou, Z., Huang, C., Li, W., and Zhao, B. (2012) Learning, memory, and glial cell changes following recovery from chronic unpredictable stress. *Brain Res. Bull.* **88**, 471–476
97. Stockmeier, C. A., Mahajan, G. J., Konick, L. C., Overholser, J. C., Jurjus, G. J., Meltzer, H. Y., *et al.* (2004) Cellular changes in the postmortem hippocampus in major depression. *Biol. Psychiatry* **56**, 640–650
98. Du Preez, A., Onorato, D., Eiben, I., Musaelyan, K., Egeland, M., Zunszain, P. A., *et al.* (2021) Chronic stress followed by social isolation promotes depressive-like behaviour, alters microglial and astrocyte biology and reduces hippocampal neurogenesis in male mice. *Brain Behav. Immun.* **91**, 24–47
99. Hsu, M. P., Frausto, R., Rose-John, S., and Campbell, I. L. (2015) Analysis of IL-6/gp130 family receptor expression reveals that in contrast to astroglia, microglia lack the oncostatin M receptor and functional responses to oncostatin M. *Glia* **63**, 132–141
100. Khandaker, G. M., Pearson, R. M., Zammit, S., Lewis, G., and Jones, P. B. (2014) Association of serum interleukin 6 and C-reactive protein in childhood with depression and psychosis in young adult life: a population-based longitudinal study. *JAMA Psychiatry* **71**, 1121–1128
101. Hodes, G. E., Pfau, M. L., Leboeuf, M., Golden, S. A., Christoffel, D. J., Bregman, D., *et al.* (2014) Individual differences in the peripheral immune system promote resilience versus susceptibility to social stress. *Proc. Natl. Acad. Sci. U. S. A.* **111**, 16136–16141
102. Rebelo, A. L., Gubinelli, F., Roost, P., Jan, C., Brouillet, E., Van Camp, N., *et al.* (2021) Complete spatial characterisation of N-glycosylation upon striatal neuroinflammation in the rodent brain. *J. Neuroinflammation* **18**, 116
103. Mueller, T. M., Yates, S. D., Haroutunian, V., and Meador-Woodruff, J. H. (2017) Altered fucosyltransferase expression in the superior temporal gyrus of elderly patients with schizophrenia. *Schizophr. Res.* **182**, 66–73
104. Cvetko, A., Kifer, D., Gornik, O., Klaric, L., Visser, E., Lauc, G., *et al.* (2020) Glycosylation alterations in multiple sclerosis show increased proinflammatory potential. *Biomedicines* **8**, 410
105. Chen, C. C., Engelborghs, S., Dewaele, S., Le Bastard, N., Martin, J. J., Vanhooren, V., *et al.* (2010) Altered serum glycomics in Alzheimer disease: a potential blood biomarker? *Rejuvenation Res.* **13**, 439–444
106. Boeck, C., Pfister, S., Burkle, A., Vanhooren, V., Libert, C., Salinas-Manrique, J., *et al.* (2018) Alterations of the serum N-glycan profile in female patients with major depressive disorder. *J. Affect. Disord.* **234**, 139–147
107. Wang, X., Inoue, S., Gu, J., Miyoshi, E., Noda, K., Li, W., *et al.* (2005) Dysregulation of TGF-beta1 receptor activation leads to abnormal lung development and emphysema-like phenotype in core fucose-deficient mice. *Proc. Natl. Acad. Sci. U. S. A.* **102**, 15791–15796
108. Gao, C., Maeno, T., Ota, F., Ueno, M., Korekane, H., Takamatsu, S., *et al.* (2012) Sensitivity of heterozygous alpha1,6-fucosyltransferase knock-out mice to cigarette smoke-induced emphysema: implication of aberrant transforming growth factor-beta signaling and matrix metalloproteinase gene expression. *J. Biol. Chem.* **287**, 16699–16708
109. Sosicka, P., Ng, B. G., Pepi, L. E., Shajahan, A., Wong, M., Scott, D. A., *et al.* (2022) Origin of cytoplasmic GDP-fucose determines its contribution to glycosylation reactions. *J. Cell Biol.* **221**, e202205038
110. Sun, Y., Xu, X., Wu, T., Fukuda, T., Isaji, T., Morii, S., *et al.* (2024) Core fucosylation within the Fc-FcgammaR degradation pathway promotes enhanced IgG levels via exogenous L-fucose. *J. Biol. Chem.* **300**, 107558
111. Erritzoe, D., Godlewska, B. R., Rizzo, G., Searle, G. E., Agnorelli, C., Lewis, Y., *et al.* (2023) Brain serotonin release is reduced in patients with depression: a [(11)C]Cimbi-36 positron emission tomography study with a d-amphetamine challenge. *Biol. Psychiatry* **93**, 1089–1098
112. Sullivan, G. M., Oquendo, M. A., Milak, M., Miller, J. M., Burke, A., Ogden, R. T., *et al.* (2015) Positron emission tomography quantification of serotonin(1A) receptor binding in suicide attempters with major depressive disorder. *JAMA Psychiatry* **72**, 169–178
113. You, Y. H., Qin, Z. Q., Zhang, H. L., Yuan, Z. H., and Yu, X. (2019) MicroRNA-153 promotes brain-derived neurotrophic factor and hippocampal neuron proliferation to alleviate autism symptoms through inhibition of JAK-STAT pathway by LEPR. *Biosci. Rep.* **39**, BSR20181904
114. Henrik Heiland, D., Ravi, V. M., Behringer, S. P., Frenking, J. H., Wurm, J., Joseph, K., *et al.* (2019) Tumor-associated reactive astrocytes aid the evolution of immunosuppressive environment in glioblastoma. *Nat. Commun.* **10**, 2541
115. Wang, L., Zhao, D., Wang, H., Wang, L., Liu, X., and Zhang, H. (2021) FPS-ZM1 inhibits LPS-induced microglial inflammation by suppressing JAK/STAT signaling pathway. *Int. Immunopharmacol.* **100**, 108117

116. Ji, Y., Li, M., Chang, M., Liu, R., Qiu, J., Wang, K., *et al.* (2022) Inflammation: roles in skeletal muscle atrophy. *Antioxidants (Basel)* **11**, 1686
117. Milaneschi, Y., Simmons, W. K., van Rossum, E. F. C., and Penninx, B. W. (2019) Depression and obesity: evidence of shared biological mechanisms. *Mol. Psychiatry* **24**, 18–33
118. Kong, E., Sucic, S., Monje, F. J., Savalli, G., Diao, W., Khan, D., *et al.* (2015) STAT3 controls IL6-dependent regulation of serotonin transporter function and depression-like behavior. *Sci. Rep.* **5**, 9009
119. Kwon, S. H., Han, J. K., Choi, M., Kwon, Y. J., Kim, S. J., Yi, E. H., *et al.* (2017) Dysfunction of microglial STAT3 alleviates depressive behavior via neuron-microglia interactions. *Neuropsychopharmacology* **42**, 2072–2086
120. Holmes, S. E., Abdallah, C., and Esterlis, I. (2023) Imaging synaptic density in depression. *Neuropsychopharmacology* **48**, 186–190
121. Shang, C., Yao, R. M., Guo, Y., Ding, Z. C., Sun, L. J., Ran, Y. H., *et al.* (2020) Translocator protein-mediated fast-onset antidepressant-like and memory-enhancing effects in chronically stressed mice. *J. Psychopharmacol.* **34**, 441–451
122. Li, N., Liu, R. J., Dwyer, J. M., Banasr, M., Lee, B., Son, H., *et al.* (2011) Glutamate N-methyl-D-aspartate receptor antagonists rapidly reverse behavioral and synaptic deficits caused by chronic stress exposure. *Biol. Psychiatry* **69**, 754–761
123. Nicolas, C. S., Peineau, S., Amici, M., Csaba, Z., Fafouri, A., Javalet, C., *et al.* (2012) The Jak/STAT pathway is involved in synaptic plasticity. *Neuron* **73**, 374–390
124. Xiao, S., Zhang, Y., Liu, Z., Li, A., Tong, W., Xiong, X., *et al.* (2023) Alpinetin inhibits neuroinflammation and neuronal apoptosis via targeting the JAK2/STAT3 signaling pathway in spinal cord injury. *CNS Neurosci. Ther.* **29**, 1094–1108
125. Balschun, D., Wetzel, W., Del Rey, A., Pitossi, F., Schneider, H., Zuschratter, W., *et al.* (2004) Interleukin-6: a cytokine to forget. *FASEB J.* **18**, 1788–1790
126. Sparrow, N. A., Anwar, F., Covarrubias, A. E., Rajput, P. S., Rashid, M. H., Nisson, P. L., *et al.* (2021) IL-6 inhibition reduces neuronal injury in a murine model of ventilator-induced lung injury. *Am. J. Respir. Cell Mol. Biol.* **65**, 403–412
127. Matthies, H., Staak, S., and Krug, M. (1996) Fucose and fucosyllactose enhance in-vitro hippocampal long-term potentiation. *Brain Res.* **725**, 276–280
128. Hayashi, M., Takai, J., Yu, L., Motohashi, H., Moriguchi, T., and Yamamoto, M. (2015) Whole-body in vivo monitoring of inflammatory diseases exploiting human interleukin 6-luciferase transgenic mice. *Mol. Cell. Biol.* **35**, 3590–3601

＜分子認識学＞
教授　細野雅祐
准教授　菅原栄紀
講師　立田岳生

## レクチンの抗腫瘍メカニズムの解明と糖脂質のかかわり 2024

### 1）微小管重合阻害剤 MMAE 修飾ナマズ卵レクチンは Gb3 発現がん細胞選択的に細胞死を誘導する

ナマズ卵レクチン（SAL）は，バーキットリンパ腫細胞株 Raji および子宮頸部がん由来細胞株 HeLa の細胞膜に発現している Gb3 に結合した後，エンドサイトーシスにより細胞内に取り込まれるが，Gb3 を発現していない慢性骨髄性白血病細胞株 K562 には取り込まれないことを明らかにしている．この現象は，SAL が Gb3 発現がん細胞の細胞内へ効果的に化合物を運ぶキャリアーになる可能性を示している．本年度は，SAL に微小管重合阻害剤 Monomethyl auristatin E（MMAE）を 30 および 50% 付加した SM30 および SM50 を受託合成し，Raji および K562 に対する効果を検討した．まず初めに，ウサギ赤血球凝集反応を用いて SM30 および 50 の活性を調べた．その結果，SAL の最低凝集濃度は，0.195 μg/mL であったのに対して，SM30 は 0.78 μg/mL，SM50 は 1.56 μg/mL となり MMAE を修飾することにより SAL のレクチン活性が低下することが分かった．しかし，SAL-MMAE のレクチン活性が残存していたことから，がん細胞に対する SAL-MMAE の効果を検討した．トリパンブルー色素排除試験により細胞生存率を測定した結果，Raji を SAL（10 μg/mL）で 72 時間処理しても生存率に大きな変化は認められなかったが，SM30 および SM50 処理により処理濃度依存的に Raji の生存率が低下し，SM50（10 μg/mL）処理により Raji では約 39% まで低下した．一方，Gb3 を発現していない K562 あるいは□1, 4-ガラクトース転移酵素遺伝子を欠損させることにより Gb3 の発現を失った Raji（Gb3-KO Raji）を SAL-MMAE で処理しても細胞生存率に有意な低下は認められなかった（図1，2）．さらに，同一ウェル内に K562 および GFP を発現する Gb3-K562 細胞を播種した場合でも Gb3 発現細胞選択的に SAL-MMAE が細胞死を引き起こすか否かを検討したところ，K562 細胞は SAL-MMAE で処理しても AnnexinV 陽生細胞の割合に変化が見られなかったが，Gb3-K562 細胞においては SAL-MMAE 処理により AnnexinV 陽生細胞の割合が増加した（図3）．これらの結果から，SAL-MMAE は，Gb3 発現細胞に対して選択的に抗腫瘍効果を発揮する可能性が示された．

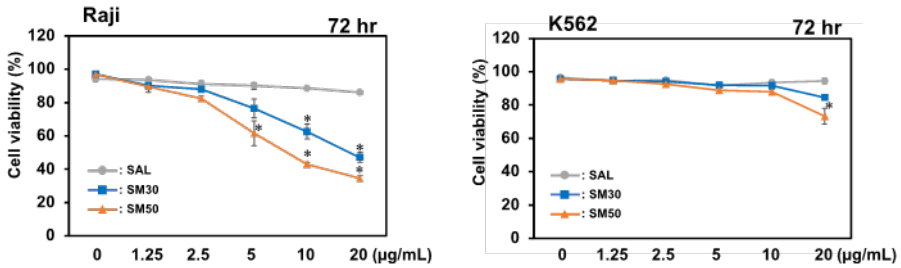


図1 Raji および K562 に対する SM30 および SM50 の影響

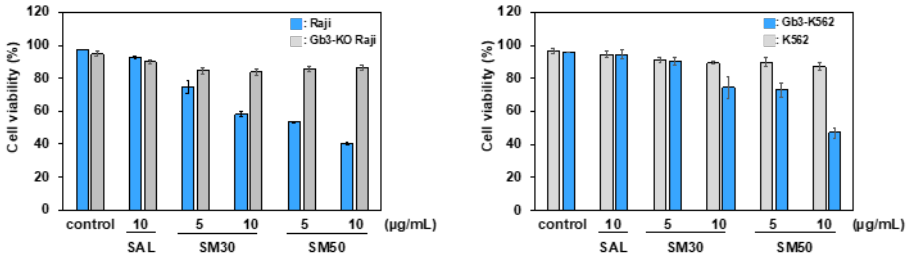


図2 Gb3-KO Raji および Gb3-K562 に対する SM30 および SM50 の影響

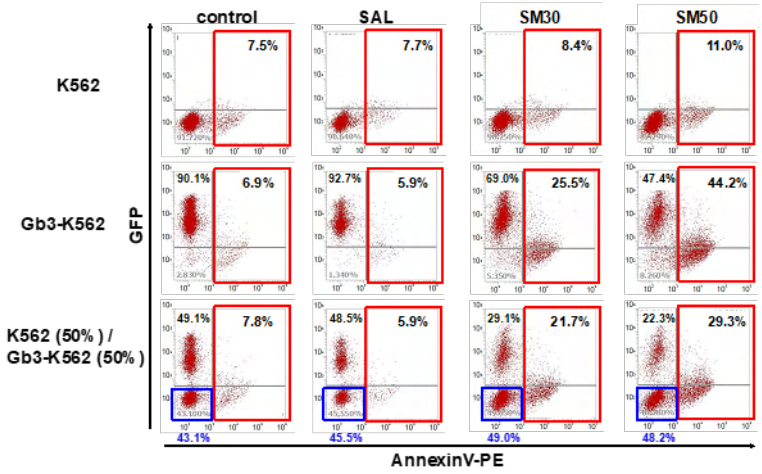


図3 同一ウエルに K562 および Gb3-K562 を播種した状況における SM30 および SM50 の影響

**2) cSBL の RNA 分解作用と cSBL 耐性細胞の性質**

ウシガエル卵から単離されたシアル酸結合性レクチン (cSBL) は、RNA 分解を機序として、がん細胞選択的なアポトーシスを誘導することから新規抗がん剤として期待されている。

これまでの研究で cSBL が細胞内に取り込まれ, RNA の分解を引き起こし,主にミトコンドリア経路によるアポトーシスを誘導することが明らかになっている一方で、その作用機序には不明

な点が多くある。そこで今回、RNA 分解作用の詳細を解析することを目的に研究を行った。また、本研究室では、cSBL 耐性悪性中皮種細胞(cSR 細胞)を樹立しており、この cSR 細胞では一部の抗がん剤の効果が増強されるという興味深い知見を得ているので、今回、cSR 細胞の性質を併せて解析した。

キャピラリー電気泳動装置を用い定量的に RNA 分解を解析したところ、cSBL 処理 H28 細胞において、濃度依存的な RNA 分解が観察され、24 時間処理における RNA 分解は、cSBL 0.5 μM から認められた。H28 細胞と cSR 細胞である B1 細胞における cSBL の RNA 分解作用を比較した結果、B1 細胞は 1.0 μM から分解が認められ、H28 細胞より B1 細胞の方が cSBL による RNA 分解作用をうけにくいことが示唆された(Fig. 1)。B1 細胞のこの性質が cSBL への耐性機序に関係すると考えられ、B1 細胞では、細胞への結合・取り込みやそれに続く RNase としての機能の部分で何らかの耐性を獲得しているのではないかと考えられた。また、cSR 細胞でも高濃度では cSBL による細胞死誘導効果が観察されるが、これは、cSBL を長期間暴露してもその耐性の程度は低い可能性などが考えられた。さらに、本研究ではこれまでに cSR 細胞において悪性中皮腫治療薬のペメトレキセド作用が増強することを見出しており、今回、ペメトレキセドによるアポトーシス誘導効果に着目し、カスパーゼの活性化を解析した。その結果、B1 細胞ではペメトレキセド処理時にカスパーゼが活性化しやすくなっており、それによってペメトレキセドの効果が増強されていることが示唆された。これらのことから、cSBL は耐性を付与しにくい性質や、他薬剤の効果を高める性質をもつことが明らかになり、そのことから、cSBL が抗がん剤として好ましい性質があり、cSBL の抗がん剤としての利用はこれまでにない治療戦略になる可能性があると考えられた。

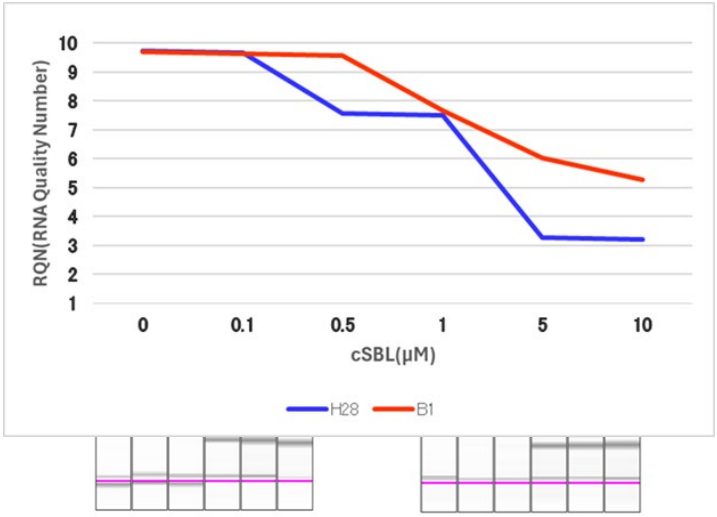

＜論文発表＞

＜学会発表と講演＞

**シアリダーゼ NEU3 は膀胱がんの浸潤性に寄与する**

立田 岳生、伊藤 淳、山本 晃司、菅原 栄紀、細野 雅祐、宮城 妙子

日本薬学会第 144 年会, 横浜, 2024 年 3 月, 29P-am190

**微小管重合阻害剤 MMAE 修飾ナマズ卵レクチンの Raji 細胞に対する効果**

菅原栄紀, 菊地洸太朗, 立田岳生, 細野雅祐

第 43 回日本糖質学会年会, 横浜, 2024 年 9 月, p.196

**Raji 細胞における STAT5 シグナル経路は p21 の発現を負に制御する**

菊地洸太朗, 菅原 栄紀, 齊藤美紅, 立田 岳生, 細野 雅祐

第 18 回東北糖鎖研究会, 仙台, 2024 年 10 月, p.18

**微小管重合阻害剤 MMAE 修飾ナマズ卵レクチンの Raji 細胞に対する効果**

宍戸蒔歩, 菅原栄紀, 半澤実空, 菊地洸太朗, 立田岳生, 細野雅祐

第 63 回日本薬学会東北支部大会, 青森, 2024 年 10 月, OB-13

**cSBL は JNK を活性化する**

立田 岳生, 菅原 栄紀, 細野 雅祐

第 97 回日本生化学会大会, 横浜, 2024 年 11 月, 3P-188

**微小管重合阻害剤 MMAE 修飾ナマズ卵レクチンは Gb3 発現がん細胞選択的に細胞死を誘導する**

菅原栄紀, 菊地洸太朗, 立田岳生, 細野雅祐

第 47 回日本分子生物学会年会, 福岡, 2024 年 11 月, 2P-879

＜糖鎖構造生物学＞
教授　山口 芳樹
講師　真鍋 法義
助手　大野 詩歩

## 糖鎖の立体構造・ダイナミクスと相互作用に着目した糖鎖機能の解明

糖鎖の生理機能を明らかにするためには，糖鎖の立体構造・ダイナミクスの特徴を理解し，タンパク質との相互作用様式を解明することが重要であるとの立場から研究を進めている．特に核磁気共鳴（NMR）法は，生体分子のダイナミクスを原子レベルで調べるための理想的な方法であり，分子動力学（MD）計算と合わせて相補的な解析を進めている。また，立体構造データの多変量解析や機械学習に取り組んでおり，データ解析からの仮説形成と実証を目指している。本年度は，重篤なミスセンス変異を判別するための方法論の開発，*N*-結合型糖鎖を獲得するミスセンスバリアントの構造解析，および C 型レクチン様受容体ヒト Dectin-1 の構造解析を指向した大量発現系の構築を主に行った。

### I. 重篤なミスセンス変異を判別するための VarMeter2 の開発

ミスセンス変異の重篤度を予測する手法としては，進化的保存性やヒト集団における変異データを用いる方法が一般的である。我々は創価大学，国立成育医療研究センター，名古屋大学，大阪大学との共同研究により，AlphaFold の 3D モデルを活用し，2つの物理化学的パラメータ（規格化溶媒露出表面積（nSASA）および変異エネルギー（ΔG））を用いて，パラメータの基準値に基づくミスセンス変異の重篤度を予測する方法 VarMeter を開発していた（Aoki*, Manabe*, Ohno* et al., *Mol. Genet. Metab. Rep.,* **37**, 2023）。本研究で新たに開発した VarMeter2 は，同様に AlphaFold の 3D モデルを活用しつつ，新たに物理化学的パラメータを追加し，パラメータの基準値に依存することなく予測を行う点に特徴がある。

VarMeter2 を構築するにあたり，ClinVar データベースから 296 の Pathogenic 変異と 240 の Benign 変異を収集し，各変異の構造的特徴（nSASA，ΔG，および pLDDT 値）を解析した。その結果，Pathogenic 変異と Benign 変異の間に明確な構造的特徴の違いがあることが示された。これらの特徴を基に，マハラノビス距離を用いた分類モデルを構築し開発した。ClinVar データセットを用いた評価では，VarMeter2 の予測精度は 82%に達し，従来の VarMeter の予測精度（74%）を上回った。また，サンフィリッポ症候群 A に関連する *N*-sulphoglucosamine sulphohydrolase（SGSH）のミスセンス変異に VarMeter2 の予測を適用したところ，予測精度は 84%に達し，疾患関連変異の同定にも有効であることが示された。さらに，SGSH 変異体の一つである Q365P を重篤な変異として特定し，実験的にその機能喪失を確認した。この変異体

の組み換えタンパク質は，野生型と比較して酵素活性を持たず，小胞体に留まりゴルジ体に輸送されないことが判明した。これは，タンパク質のミスフォールディングによるものと考えられる。さらに，安定性試験においても，この変異体は野生型に比べて低い安定性を示した。

以上の結果から，VarMeter2 はミスセンス変異の重篤度の評価において高い予測精度を持つことが実証された。特に，SGSH 変異体の評価において，臨床データとの整合性が確認され，新たな重篤な変異の同定にも寄与することが示された。この手法は，従来の進化的手法に依存せず，物理化学的パラメータを基にした独自のアプローチを提供する点で優れており，未解明の疾患関連変異の特定に貢献する。

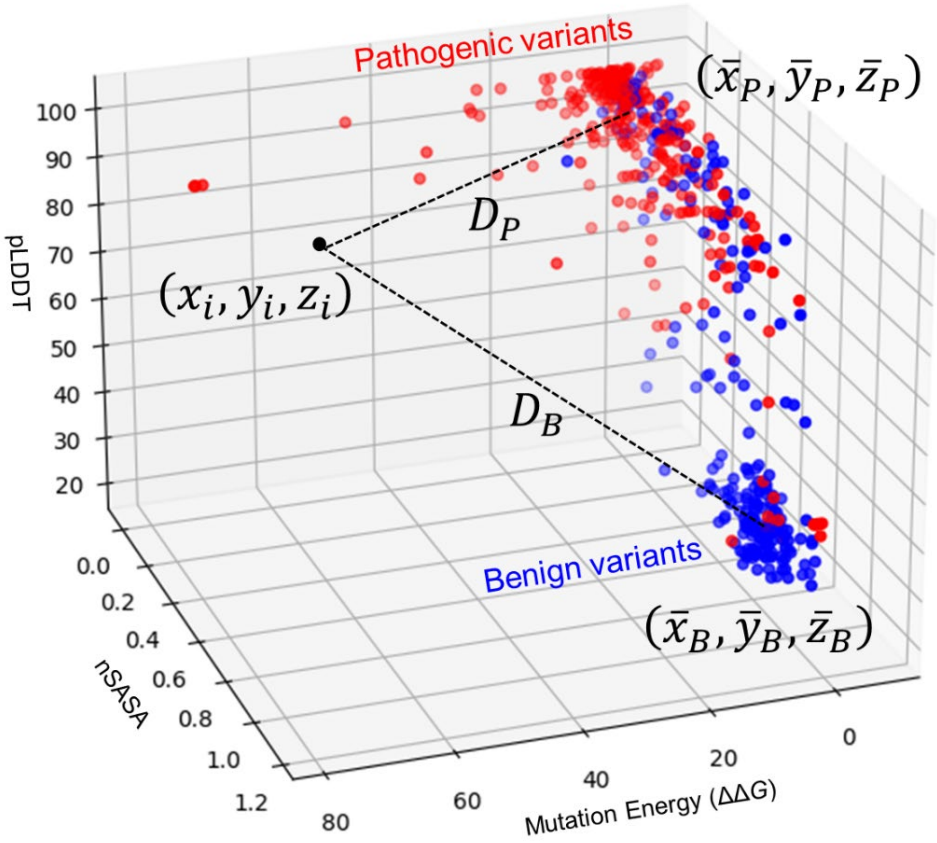


図 1. ClinVar データセットの variant の nSASA，ΔG，pLDDT の散布図
（青: Benign $n$ = 240，赤: Pathogenic $n$ =296）

**II. *N*-結合型糖鎖を獲得するミスセンスバリアントの構造解析**

*N*-型糖鎖修飾は最も一般的な翻訳後修飾の一つであり，タンパク質のフォールディング，細胞内局在化，分解など，生物学的機能に深く影響を与えることが知られている。特に遺伝子多型によって Asn-X-Ser/Thr コンセンサス配列が出現あるいは喪失し，*N*-型糖鎖修飾が新たに付加されたり喪失したりする現象が注目されている。我々はこのような遺伝子変異による *N*-型

糖鎖修飾の獲得に着目し，ゴーシェ病のバイオマーカーである Chitotriosidase-1（CHIT1）をモデルとして研究を行った。CHIT1 の一般的な変異型である G102S 変異により新たな *N*-型糖鎖付加部位（Asn100）が形成され，酵素活性が低下することが報告されていたが，その分子メカニズムの詳細は不明であった。

野生型，G102S 変異型，N100Q+G102S 二重変異型の CHIT1 を組み換えタンパク質として発現・精製し，グリコシダーゼ処理やレクチンブロットにより糖鎖修飾を解析した。また，$^{13}C$ 安定同位体標識利用 NMR（Pan et al., *Biochim. Biophys. Acta Gen. Subj.* **1868**, 2024 他）および LC-MS/MS を用いて糖鎖構造を詳細に解析した結果，Asn100 には 50%の修飾率で糖鎖が付加していること，また主な糖鎖の構造は複合型であった。さらに，CHIT1 の触媒ドメインとキチン結合ドメインを結ぶヒンジ領域に *O*-型糖鎖が修飾されていることを見出した。

G102S 変異や糖鎖修飾が CHIT1 の活性に影響をおよぼす分子メカニズムを解明するため，野生型，G102S 変異型，および糖鎖修飾型 G102S 変異型の酵素活性を調べた。その結果，G102S 変異により活性が低下する一方で，Asn100 への糖鎖付加がその活性を部分的に回復させることが分かった。分子動力学シミュレーションによる構造解析では，G102S 変異が 102 番近傍の主鎖コンフォメーションを変化しさせ，揺らぎを増大させること，また Asn100 への糖鎖修飾がその揺らぎを抑制し，酵素活性の部分的回復を説明する分子基盤となることが示唆された。以上より，一般的に解明が困難とされる部分的な酵素活性低下のメカニズムをダイナミクスの観点から明らかにした。

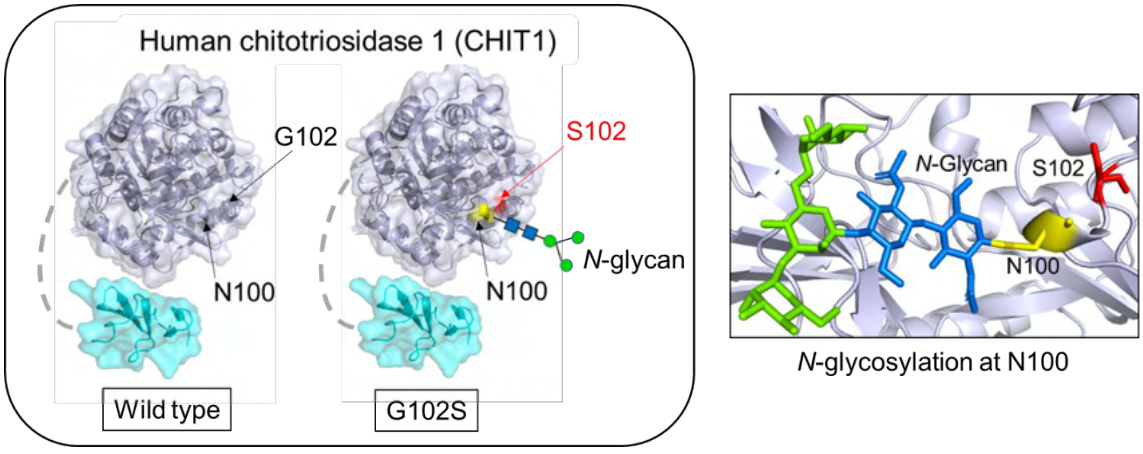


図 2. ヒトキトトリオシダーゼ 1（CHIT1）の G102S バリアントへの *N*-型糖鎖修飾

**Ⅲ. 構造解析を指向したヒト Dectin-1 レクチンドメインの大量発現系構築**

外因性の病原体を非自己と認識して発動する免疫システムの多くは，哺乳類のパターン認識受容体が，病原体の表面に存在する種特異的なβグルカンなどの多糖（糖鎖）を認識することで開始される。糖鎖の構造は多種多様であるにも関わらず，限られた数のレクチン受容体が各糖鎖リガンドへの親和性を獲得している機構は学術的に興味深く，原子レベルで解明す

べき事柄である。我々は，パターン認識受容体の中で哺乳類レクチン受容体の病原体認識機構を分類し，βグルカン受容体による認識について報告してきた (Manabe et al., *Front. Mol. Biosci.*, **8**, 2021，Manabe et al., *Int. J. Mol. Sci.*, **22**, 2021)。このβグルカン受容体による多様なリガンド受容のメカニズムや高親和性の発揮機構は，ほとんど解明されておらず解決すべき課題も多く残っている。

本研究では，多様なβグルカンを受容しつつも高い親和性を発揮するレクチン受容体の巧妙な受容メカニズムを，構造生物学的に明らかにすることを目的とした。それにより，標的糖鎖の分岐構造・立体構造や受容体の協同性の視点から外来糖鎖認識メカニズムを解明し，免疫システムにおける多糖認識機構の礎を築くことを目指した。対象とするレクチン受容体には，Dectin-1 のレクチン様ドメインを選定した。これまでの大腸菌を宿主とした組み換え Dectin-1 発現では，マウス由来の Dectin-1 を利用していた。一方，ヒトにおける Dectin-1 の遺伝性変異による機能不全は，真菌症と関連することが報告されている。そのため，ヒト Dectin-1 の構造生物学解析を進めるために，ヒト Dectin-1 大量発現法の確立を行った。また，確立した発現方法を用いて均一 $^{15}$N 標識を施したヒト Dectin-1 レクチンドメインを対象とした NMR 解析を行った。得られた $^{15}$N 標識ヒト Dectin-1 について，2D $^{1}$H-$^{15}$N HSQC スペクトルを測定して，ヒト Dectin-1 とリガンド糖鎖との結合を調べた。

その結果，リガンド糖鎖を加えることにより，高次の複合体が形成され，ほとんどのNMRシグナルのブロードニングが観察された。さらに，$^{15}$N 標識ヒト Dectin-1 に EDTA を添加したところ，Dectin-1 由来の特定の NMR シグナルにおいて化学シフト変化が観察された。このことより，ヒト Dectin-1 は $Ca^{2+}$と直接的に相互作用していることが判明した（図 3）。

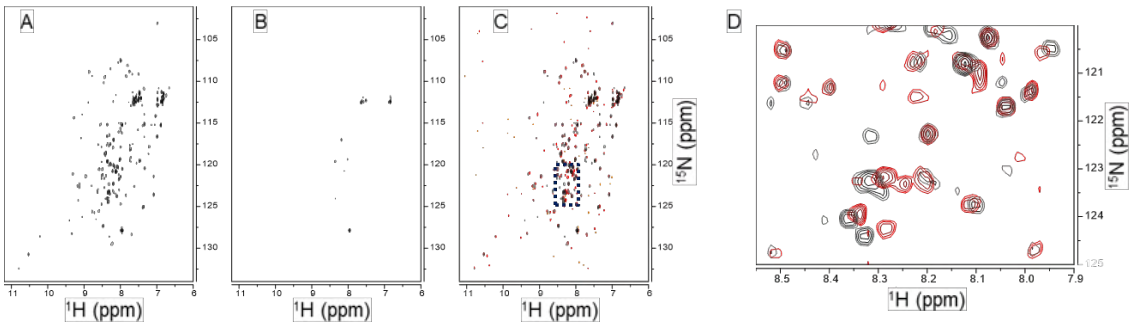


図 3. $^{15}$N 標識ヒト Dectin-1 レクチンドメインの NMR 測定

(A)均一 $^{15}$N 標識ヒト Dectin-1 レクチンドメイン 2D $^{1}$H-$^{15}$N HSQC スペクトル (B) 50 当量のラミナリンを加えた $^{15}$N 均一標識ヒト Dectin-1 レクチンドメイン 2D $^{1}$H-$^{15}$N HSQC スペクトル (C) 1 mM EDTA の有（赤），無（黒）のスペクトル重ね合わせ像. (D) (C)の選択範囲の拡大図

＜論文発表＞

**NMR characterization of uniformly $^{13}C$- and/or $^{15}N$-labeled, unsulfated chondroitins with high molecular weights.** Ichikawa M, Otsuka Y, Minamisawa T, Manabe N, Yamaguchi Y. ***Magn. Reson. Chem.*** 62(6):439-451. doi: 10.1002/mrc.5426. 2024

**Functional evaluation of novel variants of B4GALNT1 in a patient with hereditary spastic paraplegia and the general population.** Inamori K, Nakamura K, Shishido F, Hsu J, Nagafuku M, Nitta T, Ikeda J, Yoshimura H, Kodaira M, Tsuchida N, Matsumoto N, Uemura S, Ohno S, Manabe N, Yamaguchi Y, Togayachi A, Aoki-Kinoshita K, Nishihara S, Furukawa J, Kaname T, Nakamura M, Shimohata T, Tadaka S, Shirota M, Kinoshita K, Nakamura Y, Ohno I, Sekijima Y, Inokuchi J. ***Front. Neurosci.*** 18. doi: 10.3389/fnins.2024.1437668. 2024

**Imaging α-synuclein pathologies in animal models and patients with Parkinson's and related diseases.** Endo H, Ono M, Takado Y, Matsuoka K, Takahashi M, Tagai K, Kataoka Y, Hirata K, Takahata K, Seki C, Kokubo N, Fujinaga M, Mori W, Nagai Y, Mimura K, Kumata K, Kikuchi T, Shimozawa A, Mishra S, Yamaguchi Y, Shimizu H, Kakita A, Takuwa H, Shinotoh H, Shimada H, Kimura Y, Ichise M, Suhara T, Minamimoto T, Sahara N, Kawamura K, Zhang M, Hasegawa M, Higuchi M. ***Neuron***. 112(15):2540-2557.e8. doi: 10.1016/j.neuron.2024.05.006. 2024

**Theoretical framework for novel catalytic biomolecules composed of multiple peptides.** Ambo A, Ohno S, Yamaguchi Y, Seki M. ***Chem. Pharm. Bull.*** 72(9):804-809. doi: 10.1248/cpb.c24-00155. 2024

**Systematic preparation of a 66-IgG library with symmetric and asymmetric homogeneous glycans and their functional evaluation.** Manabe S, Iwamoto S, Nagatoishi S, Hoshinoo A, Mitani A, Sumiyoshi W, Kinoshita T, Yamaguchi Y, Tsumoto K. ***J. Am. Chem. Soc.*** 146(33):23426-23436. doi: 10.1021/jacs.4c06558. 2024

**3D structural insights into the effect of *N*-glycosylation in human chitotriosidase variant G102S.** Xu X, Manabe N, Ohno S, Komatsu S, Fujimura T, Yamaguchi Y. ***Biochim. Biophys. Acta Gen. Subj.*** 1869 :130730-130730. doi: 10.1016/j.bbagen.2024.130730. 2025

**Chemical extension and glycodendrimer formation of the matriglycan decasaccharide, -**

**(3Xylα1-3GlcAβ1)$_5$- and its affinity for laminin.** Kotera K, Miyamoto R, Mochizuki G, Tamura T, Manabe N, Yamaguchi Y, Tamura J. ***Carbohydr. Res.*** 547:109328. doi: 10.1016/j.carres.2024.109328. 2024

**G-quadruplex-forming small RNA inhibits coronavirus and influenza A virus replication.** Sekine R, Takeda K, Suenaga T, Tsuno S, Kaiya T, Kiso M, Yamayoshi S, Takaku Y, Ohno S, Yamaguchi Y, Nishizawa S, Sumitomo K, Ikuta K, Kanda T, Kawaoka Y, Nishimura H, Kuge S. ***Commun. Biol.*** 8:27. doi: 10.1038/s42003-024-07351-7. 2025

**Bacterial expression, purification and characterization of the human Dectin-1 lectin domain for structural and functional studies.** Chiba H, Manabe N, Naito J, Nishida N, Ohno N, Yamaguchi Y. ***Protein Expr. Purif.*** 229:106668. doi: 10.1016/j.pep.2025.106668. 2025

**VarMeter2: An enhanced structure-based method for predicting pathogenic missense variants through Mahalanobis distance.** Ohno S, Ogura C, Yabuki A, Itoh K, Manabe N, Angata K, Togayachi A, Aoki-Kinoshita K, Furukawa J, Inamori K, Inokuchi J, Kaname T, Nishihara S, Yamaguchi Y. ***Comput. Struct. Biotechnol. J.*** 27:1034-1047. doi: 10.1016/j.csbj.2025.02.008. 2025

＜学会発表と講演＞

筋ジストロフィー症に関係する *O*-マンノース型糖鎖の構造と機能に関する研究

山口 芳樹

新分子生体膜研究所キックオフセミナー, 仙台, 2024 年 4 月, 演題番号 7

ヒト IgA および J 鎖を修飾する *N*-結合型糖鎖の構造と機能

潘 順麗, 真鍋 法義, 大野 詩歩, 小松 祥子, 藤村 務, 山口 芳樹

第 90 回日本生化学会東北支部例会, 秋田, 2024 年 5 月, P-3

分子動力学計算を用いた新規未分化 iPS 細胞抗体デザイン

大野 詩歩, 田岡 千拓, 大内 陽翔, 齋藤 祐希, 真鍋 法義, 湯浅 徳行 [a], 松崎 祐二 [a], 築地 信 [b], 川嵜 敏祐 [c], 山口 芳樹

([a] 東京化成工業, [b] 星薬大, [c] 立命館大)

JHPCN: 学際大規模情報基盤共同利用・共同研究拠点 第 16 回 シンポジウム, 東京, 2024 年 7 月 11 日, EX24201

**外因性病原体が有する多様なβグルカン構造を認識する Dectin-1 受容体の分子メカニズムの解明**

真鍋 法義

令和 6 年度東北医科薬科大学研究・症例セミナー, 仙台, 2024 年 8 月, 3

**筋ジストロフィーを制御する *O*-マンノース型糖鎖の構造生物学的研究**

大野 詩歩

令和 6 年度東北医科薬科大学研究・症例セミナー, 仙台, 2024 年 8 月, 4

**新規機能性食品素材パラミロンの加熱加工に対する安定性**

内藤 淳子 [a], 千葉 花子, 真鍋 法義, 西田 典永 [a], 大野 尚仁 [b], 山口 芳樹

([a](株)神鋼環境ソリューション, [b] 東京薬大・薬)

第 71 回日本食品科学工学会, 名古屋, 2024 年 8 月, 3Fp-08

**部位特異的コアフコシル化のメカニズム解明を目指した分子動力学計算**

後藤 優輝, 大野 詩歩, 真鍋 法義, 山口 芳樹

第 43 回日本糖質学会年会, 横浜, 2024 年 9 月, 3A-01A

**マトリグリカン複合糖質の合成とラミニン結合親和性評価**

小寺 康太 [a], 宮本 廉, 田村 敬裕 [b], 望月 楽斗 [c], 真鍋 法義, 山口 芳樹, 田村 純一 [a,b,c]

([a] 鳥取大院・持社創生農, [b] 鳥取大院・連大農, [c] 鳥取大・農・生命環境農)

第 43 回日本糖質学会年会, 横浜, 2024 年 9 月, 1B-02B

**ガングリオシド生合成酵素の新規バリアントの機能解析**

稲森 啓一郎, 宍戸 史, 山口 芳樹, 木下 賢吾 [a], 西原 祥子 [b], 井ノ口 仁一 [c]

([a] 東北大・ToMMo, [b] 創価大・GaLSIC, [c] 大阪大・院理・FRC)

第 43 回日本糖質学会年会, 横浜, 2024 年 9 月, 3C-08A

**NMR 法による均一 $^{13}C/^{15}N$ 標識コンドロイチンの構造解析**

市川 めぐみ [a], 大塚 祐也 [a], 南澤 俊和 [a], 真鍋 法義, 山口 芳樹

([a] 生化学工業 (株)・中央研究所)

第 43 回日本糖質学会年会, 横浜, 2024 年 9 月, P-028

**マンノースリン酸イソメラーゼによる中心代謝の制御機構の解明に向けて**

原田 陽一郎 [a], 平山 明由 [b,c], 池田 五月 [b], 真鍋 法義, 栗原 大輝 [a], 藤田 晶大 [d], 長江 雅倫 [e,f], 木下 聖子 [d,g,h], 山口 芳樹, 東山 繁樹 [a,i], 谷口 直之 [a]

([a] OICI・研究所, [b] 慶大・先端生命研, [c] 慶大・政策・メディア研究科, [d] 名大・iGCORE, 阪大・[e] 微研, [f] IFReC, [g] 創価大・GalSIC, [h] 京大・化研, [i] 愛媛大院・医)

第 43 回日本糖質学会年会, 横浜, 2024 年 9 月, P-039

**糖鎖の可視化技術の現状と展望**

山口 芳樹

第 6 回糖鎖技術研究セミナー, オンライン, 2024 年 10 月, 1

**日本人における SIGLEC ファミリー遺伝子多型と発症リスク**

井ノ口 仁一 [a], 稲森 啓一郎, 山口 芳樹, 田高 周 [b], 木下 賢吾 [b], 山本 雅之 [b], 西原 祥子 [c], 木下 聖子 [c], 栂谷内 晶 [c], 安形 清彦 [c], 佐藤 ちひろ [d], 羽根 正弥 [d], 古川 潤一 [d], 石田 秀治 [e], 矢木 宏和 [f]

([a] 大阪大・理学研究科・FRC, [b] 東北メディカルメガバンク(ToMMo) , [c] 創価大・GaLSIC, [d] 名古屋大・iGCORE, [e] 岐阜大・iGCORE, [f] 自然科学研究機構・ExCELLS ）第 18 回東北糖鎖研究会, 仙台, 2024 年 10 月, O-1

**ガングリオシド生合成に関わる糖転移酵素の新規ミスセンスバリアントの機能的評価**

稲森 啓一郎, 宍戸 史, 山口 芳樹, 木下 賢吾 [a], 西原 祥子 [b], 井ノ口 仁一 [c]

([a] 東北大・ToMMo, [b] 創価大・GaLSIC, [c] 大阪大・院理・FRC)

第 18 回東北糖鎖研究会, 仙台, 2024 年 10 月, O-2

**糖鎖均一抗体トラスツズマブの作製と ADCC, 熱安定性測定**

眞鍋 史乃 [a,b], 岩本 将吾 [c], 長門石 曉 [d], 星野尾 麻子 [c], 三谷 藍 [c], 住吉 渉 [c], 木下 崇司 [d], 山口 芳樹, 津本 浩平 [d]

([a] 星薬科大・薬・機能分子創成化学, [b] 東北大・薬・医薬品開発研究センター, [c] 伏見製薬所, [d] 東大・工・バイオエンジニアリン)

第 18 回東北糖鎖研究会, 仙台, 2024 年 10 月, O-4

**分子動力学計算と NMR 法による lacto-*N*-fucopenaose I と抗体の複合体モデル構築**

大野 詩歩, 田岡 千拓, 大内 陽翔, 齋藤 祐希, 真鍋 法義, 湯浅 徳行 [a], 松崎 祐二 [a], 築地 信 [b], 川嵜 敏祐 [c], 山口 芳樹

([a] 東京化成工業, [b] 星薬大, [c] 立命館大)
第 18 回東北糖鎖研究会, 仙台, 2024 年 10 月, O-5

**Dectin-1 のリガンド結合指向性とオリゴマー形成過程の解析**
真鍋 法義, 大崎 暁斗, 兒玉 篤治 [a], 山口 祐希 [b], 内山 進 [a,b], 内橋 貴之 [a,c], 加藤 晃一 [a,d], 山口 芳樹
([a] ExCELLS, [b] 阪大院, [c] 名大院, [d] 名市大院)
第 18 回東北糖鎖研究会, 仙台, 2024 年 10 月, O-6

**ヒトキトトリオシダーゼバリアント G102S における *N*-グリコシル化の立体構造的影響**
徐 瀟, 真鍋 法義, 大野 詩歩, 小松 祥子, 藤村 務, 山口 芳樹
第 18 回東北糖鎖研究会, 仙台, 2024 年 10 月, P-6

**IgE-Fc の糖鎖修飾とその構造的役割**
野村 桜子, 澤田石 遥香, 加茂 希萌, 岩渕 立郎, 真鍋 法義, 上松 亮平 [a], 坂本 泉 [a], 廣瀬 賢治 [b,c], 權 垠相 [b], 山口 芳樹
([a] 糖鎖工学研究所, [b] 東北大, [c] 日本ウォーターズ)
第 18 回東北糖鎖研究会, 仙台, 2024 年 10 月, P-13

**BLI 法によるマトリグリカンとラミニンの相互作用の親和性評価**
宮本 廉, 湊谷 敬太, 伊藤 良汰, 真鍋 法義, 小寺 康太 [a], 田村 敬裕 [b], 望月 楽斗 [c], 田村 純一 [a,b,c], 山口 芳樹
([a] 鳥取大院・持社創生農, [b] 鳥取大院・連大農, [c] 鳥取大農・生命環境農)
第 18 回東北糖鎖研究会, 仙台, 2024 年 10 月, P-15

**VarMeter2:タンパク質の立体構造データに基づくミスセンスバリアントの重篤度予測**
山口 芳樹, 矢吹 茜 [a], 大野 詩歩, 真鍋 法義, 古川 潤一 [b], 栂谷内 晶 [a], 木下 聖子 [a], 安形 清彦 [a], 井ノ口 仁一 [c], 要 匡 [d], 西原 祥子 [a]
([a] 東北大・ToMMo, [b] 名古屋大学 糖鎖生命コア研究所, [c] 大阪大・院理・FRC, [d] 国立成育医療研究センター)
第 97 回日本生化学会大会, 横浜, 2024 年 11 月, 2S11e-4

**細胞質 Peptide:*N*-glycanase が持つ非触媒ドメインの機能についての再検証**
平山 弘人 [a], 立田 由里子 [b], 藤田 盛久 [c], 真鍋 法義, 山口 芳樹, 鈴木 匡 [b]

([a] 理研・鈴木糖鎖代謝生化学研究室 /T-CiRA NGLY1 プロジェクト, [b] 群馬大院・理工, [c] 岐阜大学糖鎖生命コア研究所)
第 97 回日本生化学会大会, 横浜, 2024 年 11 月, 2S09e-01

**出芽酵母におけるカルシウム依存性の複合型スフィンゴ脂質クラスター形成**
紀平 怜, 上村 聡志, 大野 詩歩, 山口 芳樹, 森口 尚
第 97 回日本生化学会大会, 横浜, 2024 年 11 月, 1P-007

**ヒトポリシアル酸転移酵素における新規疾患関連モチーフの発見**
畑中 理菜 [a,b], 羽根 正弥 [a,b,c], 早川 開都 [a,b], 森下 沙世 [a,b], 大野 詩歩, 山口 芳樹, 呉 迪 [a,b,c], 北島 健 [a,b,c], 佐藤 ちひろ [a,b,c]
([a] 名大・生物機能セ, [b] 名大院・生命農, [c] 名大・iGMED and iGCORE)
第 97 回日本生化学会大会, 横浜, 2024 年 11 月, 3P-017

**「糖鎖構造生物学」による糖鎖構造多様性の生物学的意義の探求**
山口 芳樹
第 1 回 GlyCosmos シンポジウム, つくば, 2024 年 12 月, 3

**抗体の糖鎖修飾とその構造・機能的役割**
山口 芳樹
第 3 回日本抗体学会, 仙台, 2024 年 12 月, LS5

**組換え Dectin-1 の哺乳細胞による発現と修飾糖鎖および β グルカン結合能の解析**
真鍋 法義, 中野 総星, 佐藤 健太, 山田 有紗, 山口 芳樹
第 8 回東北医真菌研究会東北支部会, 仙台, 2024 年 12 月, 2

**抗体の基本構造と糖鎖修飾を利用した均一 ADC の合成**
山口 芳樹
サイエンス&テクノロジーセミナー, オンライン, 2024 年 12 月

**Mechanisms of site-specific *N*-glycosylation: experimental and computational approaches**
Yoshiki Yamaguchi
Academia Sinica – TMPU Bilateral Meeting, Taipei, 2025 年 2 月, 5

**マトリグリカン複合糖質の合成とラミニン結合親和性評価**

小寺 康太[a], 宮本 廉, 望月 楽斗[b], 田村 敬裕[c], 真鍋 法義, 山口 芳樹, 田村 純一[a, b, c]

（鳥取大院 持続性社会創生科学[a], 鳥取大農 生命環境農[b], 鳥取大院 連合農[c]）

日本農芸化学会 2025 年大会, 札幌, 2025 年 3 月, 3H014

**Fmoc-Asn G1M9 を対象とした $^{1}H$ 及び $^{13}C$ NMR シグナルの完全帰属**

上松 亮平[a], 橋本 奈央子[a], 坂本 泉[a], 吉田 慎一朗[b], 真鍋 法義, 金谷 章生[a], 權 垠相[b], 山口 芳樹 ([a] 糖鎖工学研究所, [b] 東北大院理巨大分子解析研セ)

第 145 回日本薬学会年会, 福岡, 2025 年 3 月, 27-17-am07

**レクチン様受容体 Dectin-1 の不溶性 β グルカン結合アッセイを用いた各種パラミロンの機能性評価**

千葉 花子, 真鍋 法義, 内藤 淳子[a], 西田 典永[a], 大野 尚仁[b], 山口 芳樹

([a] 神鋼環境ソリューション, [b] 東京薬大薬)

第 145 回日本薬学会年会, 福岡, 2025 年 3 月, 27P-am361S

**哺乳細胞による組換え Dectin-1 の発現とその修飾糖鎖ならびに β グルカン結合能の解析**

真鍋 法義, 中野 総星, 山田 有紗, 佐藤 健太, 山口 芳樹

第 145 回日本薬学会年会, 福岡, 2025 年 3 月, 28-10-am11

Computational and Structural Biotechnology Journal 27 (2025) 1034–1047

Contents lists available at ScienceDirect

Computational and Structural Biotechnology Journal

journal homepage: www.elsevier.com/locate/csbj

Research article

# VarMeter2: An enhanced structure-based method for predicting pathogenic missense variants through Mahalanobis distance

Shiho Ohno [a], Chika Ogura [b], Akane Yabuki [c], Kazuyoshi Itoh [d], Noriyoshi Manabe [a], Kiyohiko Angata [d], Akira Togayachi [d], Kiyoko Aoki-Kinoshita [c,d,e], Jun-ichi Furukawa [e], Kei-ichiro Inamori [f], Jin-Ichi Inokuchi [g], Tadashi Kaname [h,*], Shoko Nishihara [c,d,**], Yoshiki Yamaguchi [a,***]

[a] Division of Structural Glycobiology, Institute of Molecular Biomembrane and Glycobiology, Tohoku Medical and Pharmaceutical University, Sendai, Miyagi 981-8558, Japan
[b] Department of Science and Engineering for Sustainable Innovation, Faculty of Science and Engineering, Soka University, Japan
[c] Department of Biosciences, Graduate School of Science and Engineering, Soka University, Japan
[d] Glycan and Life Systems Integration Center (GaLSIC), Soka University, Hachioji 192-8577, Japan
[e] Institute for Glyco-Core Research (iGCORE), Nagoya University, Nagoya 466-8601, Japan
[f] Division of Glycopathology, Institute of Molecular Biomembrane and Glycobiology, Tohoku Medical and Pharmaceutical University, Sendai, Miyagi 981-8558, Japan
[g] Forefront Research Center, Graduate School of Science, Osaka University, Toyonaka, Osaka 560-0043, Japan
[h] Department of Genome Medicine, National Center for Child Health and Development, Tokyo 157-0074, Japan

ARTICLE INFO

*Keywords:*
Missense variant
Pathogenicity
*N*-sulphoglucosamine sulphohydrolase
Solvent accessible surface area
Mutation energy
pLDDT

ABSTRACT

Various computational methods have been developed to predict the pathogenicity of missense variants, which is crucial for diagnosing rare diseases. Recently, we introduced VarMeter, a diagnostic tool for predicting variant pathogenicity based on normalized solvent-accessible surface area (nSASA) and mutation energy calculated from AlphaFold 3D models, and validated it on arylsulfatase L. To evaluate the broader applicability of VarMeter and enhance its predictive accuracy, here we analyzed 296 pathogenic and 240 benign variants extracted from the ClinVar database. By comparing structural features including nSASA, mutation energy, and predicted local distance difference test (pLDDT) score, we identified distinct characteristics between pathogenic and benign variants. These features were used to develop VarMeter2, which classifies variants based on Mahalanobis distance. VarMeter2 achieved a prediction accuracy of 82 % for the ClinVar dataset, a marked improvement over the original VarMeter (74 %), and 84 % for published missense variants of *N*-sulphoglucosamine sulphohydrolase (SGSH), an enzyme associated with Sanfillippo syndrome A. Application of VarMeter 2 to SGSH variants in our clinical database identified a novel SGSH variant, Q365P, as pathogenic. The recombinant Q365P protein lacked enzymatic activity as compared with wild-type SGSH. Furthermore, it was largely retained in the endoplasmic reticulum and failed to reach the Golgi, probably due to misfolding. Protein stability assays confirmed reduced stability of the variant, further explaining its loss of function. Consistently, the patient homozygous for this variant was diagnosed with Sanfilippo syndrome A. These results underscore the predictive power and versatility of VarMeter2 in assessing the pathogenicity of missense variants.

## 1. Introduction

Advancements in genome sequencing technologies have led to the accumulation of vast data on human genetic variants. Due to the challenges in distinguishing pathogenic variants from benign ones, however, many rare genetic diseases remain without identified causative variants. One approach to addressing this issue has been the development of algorithms that assess missense variants based on 3D

* Correspondence to: Department of Genome Medicine, National Center for Child Health and Development, 2-10-1 Okura, Setagaya-ku, Tokyo 157-0074, Japan.
** Correspondence to: Glycan and Life Systems Integration Center (GaLSIC), Soka University, 1-236 Tangi-machi, Hachioji 192-8577, Japan.
*** Correspondence to: Division of Structural Biology, Institute of Molecular Biomembrane and Glycobiology, Tohoku Medical and Pharmaceutical University, 4-4-1 Komatsushima, Aoba-ku, Sendai, Miyagi 981-8558, Japan.
*E-mail addresses:* kaname-t@ncchd.go.jp (T. Kaname), shoko@soka.ac.jp (S. Nishihara), yyoshiki@tohoku-mpu.ac.jp (Y. Yamaguchi).

https://doi.org/10.1016/j.csbj.2025.02.008
Received 31 October 2024; Received in revised form 14 February 2025; Accepted 14 February 2025
Available online 1 March 2025
2001-0370/© 2025 The Author(s). Published by Elsevier B.V. on behalf of Research Network of Computational and Structural Biotechnology. This is an open access article under the CC BY-NC-ND license (http://creativecommons.org/licenses/by-nc-nd/4.0/).

protein structures [1,2].

In this context, we recently developed a novel prediction method called VarMeter (VARiant impact predicting MEthod combining muTation Energy and solvent-accessible surface aRea) [3]. Unlike many other pathogenicity prediction tools, which frequently incorporate sequence conservation and human variation data, VarMeter focuses solely on physical parameters derived from AlphaFold2 structural models [4,5]. The two key parameters are (i) normalized solvent-accessible surface area (nSASA) of the amino acid residue in the wild-type protein; and (ii) mutation energy, which reflects the difference in Gibbs free energy ($\Delta\Delta G$) of protein folding between wild-type and variant proteins. This unique approach enables VarMeter to make predictions independent of evolutionary data, facilitating its application to proteins with limited sequence conservation or functional annotations. The initial version of VarMeter was developed using 70 pathogenic and 16 benign missense variants from three proteins: arylsulfatase L (ARSL), chitobiosyldiphosphodolichol β-mannosyltransferase (ALG1), and mannose-6-phosphate isomerase (MPI). This method was successfully applied to predict the pathogenicity of a newly identified ARSL variant in a patient with undiagnosed disease [3].

A crucial factor in improving the accuracy of missense variant predictions is determining the optimal thresholds for nSASA and mutation energy to discriminate between pathogenic and benign variants. This can be achieved by increasing the number of variants analyzed across a wider variety of proteins. Additionally, the confidence level of AlphaFold2 models, reflected in the predicted local distance difference test (pLDDT) score, is important as it directly affects prediction reliability. Because VarMeter relies on AlphaFold2 models, careful consideration of residue-level confidence is essential for accurate predictions.

To improve the precision and generalizability of VarMeter, here we analyzed key structural parameters — nSASA, mutation energy, and pLDDT scores — using missense variants from the ClinVar database [6], a widely used resource for training and validating pathogenicity prediction models [7,8]. By incorporating Mahalanobis distance into the analysis of these three parameters, we developed an enhanced version of our tool, termed VarMeter2. To evaluate its effectiveness, we applied VarMeter2 to *N*-sulphoglucosamine sulphohydrolase (SGSH), a protein associated with numerous missense variants linked to Sanfilippo syndrome A (mucopolysaccharidosis type III) [9]. We compared our results with those from VarMeter [3], AlphaMissense [10], and CADD [11]. Furthermore, the pathogenicity of an SGSH variant (Q365P), newly identified by VarMeter2 was experimentally confirmed through enzymatic activity, immunostaining, and protein stability assays.

## 2. Materials and methods

### 2.1. Missense variants from the ClinVar database and related parameters

To update VarMeter, missense variants were extracted from the ClinVar database as of July 6, 2023. The dataset includes 296 pathogenic missense variants of 24 proteins and 240 benign variants of 23 proteins, with a review status of "Expert panel" (three stars). The amino acid sequences of each protein were retrieved from the UniProt database [12]. Allele frequencies of the missense variants were extracted from the Genome Aggregation Database (gnomAD) v4.1 (December 3, 2024) [13], and data were obtained from the TogoVar ftp site [14]. AlphaMissense scores were obtained from Zendo (https://zenodo.org/records/8208688; June 2024), and CADD v1.7 scores were downloaded from the CADD homepage (https://cadd.bihealth.org/; December 19, 2024) [15]. The ClinVar dataset analyzed in this study is included in Supplemental Table S1.

### 2.2. Preparation of 3D models of variants

The 3D models of the reference (wild-type) proteins were obtained from the AlphaFold2 Protein Structure Database [4]. The 3D models of each missense variant were generated using the "Calculate Mutation Energy/Stability" module in Discovery Studio 2021 (BIOVIA, Dassault Systèmes, San Diego, CA, USA).

### 2.3. Calculation of mutation energy and normalized solvent-accessible surface area

Mutation energy ($\Delta\Delta G$), reflecting the impact of the mutation on protein stability in kcal/mol, was calculated using the "Calculate Mutation Energy/Stability" module in Discovery Studio 2021, as described previously [3]. The solvent-accessible surface area (SASA) of each residue was calculated based on the AlphaFold2 model of the wild-type protein using Discovery Studio 2021. Each SASA was normalized (nSASA) by using reference SASA values [16].

### 2.4. Calculation of Mahalanobis distance from mutation energy, nSASA and pLDDT

The squared Mahalanobis distance ($D_i^2$) was calculated for the 296 pathogenic variants and 240 benign variants in the ClinVar dataset using mutation energy ($x_i$), nSASA ($y_i$) and pLDDT ($z_i$). The following equation, which incorporates the inverse covariance matrix (3 × 3), was used:

$$D_i^2 = \begin{pmatrix} x_i - \overline{x} & y_i - \overline{y} & z_i - \overline{z} \end{pmatrix} \begin{pmatrix} s_x^2 & s_{xy} & s_{xz} \\ s_{xy} & s_y^2 & s_{yz} \\ s_{xz} & s_{yz} & s_z^2 \end{pmatrix}^{-1} \begin{pmatrix} x_i - \overline{x} \\ y_i - \overline{y} \\ z_i - \overline{z} \end{pmatrix}$$

where $\overline{x}$, $\overline{y}$ and $\overline{z}$ represent the mean values of mutation energy, nSASA and pLDDT, respectively; $s_x^2$, $s_y^2$ and $s_z^2$ are the variances of mutation energy, nSASA and pLDDT, respectively; and $s_{xy}$, $s_{xz}$ and $s_{yz}$ are the covariances between mutation energy and nSASA, mutation energy and pLDDT, and nSASA and pLDDT, respectively. The squared Mahalanobis distances ($D_P^2$ for pathogenic and $D_B^2$ for benign variants) were calculated and used to predict the pathogenicity of the variants.

### 2.5. Missense variants of SGSH

Missense variants of SGSH were collected from published studies using the Human Gene Mutation Database (HGMD). Pathogenic variants of SGSH were identified from patients clinically diagnosed with Sanfilippo syndrome A and were experimentally validated to have reduced enzymatic activity. In-house whole-exome sequencing data from patients with rare or undiagnosed disease were screened for the presence of SGSH gene variants. The studies for in-house database were approved by the ethical committee of the National Center for Child Health and Development (Approval No. 2020-326). SGSH variants with a ClinVar clinical significance of "benign" and a homozygote count of 2 or more were extracted from the gnomAD database (v2.1.1) (https://gnomad.broadinstitute.org/) as benign variants. The amino acid sequence of SGSH was obtained from the UniProt database (UniProt ID: P51688). Allele frequencies and prediction scores (AlphaMissense and CADD) were obtained using the same approach applied to the ClinVar dataset, as described in Section 2.1.

### 2.6. Plasmid construction

All expression vectors were generated using the Gateway cloning system (Thermo Fisher Scientific, Waltham, MA, USA). In brief, the gene encoding *SGSH* (NCBI reference sequence NM_000199) was amplified from cDNA prepared from HEK293 cells (Human Embryonic Kidney cells 293) using attB adaptor primers, and recombined into pDONR201 (Thermo Fisher Scientific, Waltham, MA, USA) to generate an entry clone. Nucleotide substitutions (A1094 to C: corresponding to amino

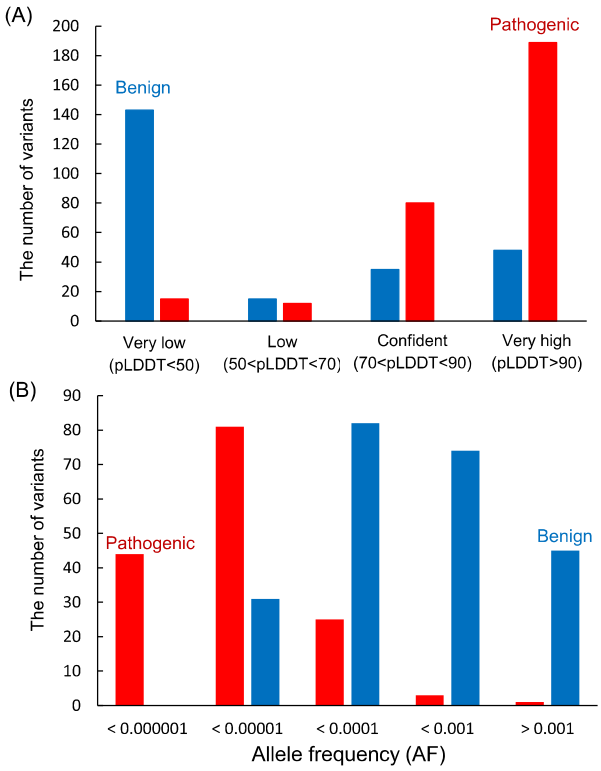


**Fig. 1.** Distribution of benign and pathogenic variants by pLDDT score and by allele frequency. (A) Benign and pathogenic variants were grouped into four confidence levels: very low (pLDDT<50), low (50 <pLDDT<70), confident (70 <pLDDT<90), and very high (pLDDT>90). (B) Benign and pathogenic variants were grouped into five levels of allele frequency (AF): AF< 0.000001, 0.000001 <AF< 0.00001, 0.00001 <AF< 0.0001, 0.0001 <AF< 0.001, and AF> 0.001. In (A) and (B), red bars indicate pathogenic variants; blue bars indicate benign variants.

**Table 1**
Statistical parameters of mutation energy, nSASA and pLDDT for the pathogenic and benign variants from the ClinVar dataset.

| | Pathogenic ($n$ = 296) | | | Benign ($n$ = 240) | | |
|---|---|---|---|---|---|---|
| | Mutation energy (kcal/mol) | nSASA | pLDDT | Mutation energy (kcal/mol) | nSASA | pLDDT |
| Mean ± SD | 3.9 ± 9.6 | 0.21 ± 0.28 | 88.2 ± 14.2 | 0.1 ± 2.0 | 0.64 ± 0.29 | 53.1 ± 27.9 |
| Variance | 91.3 | 0.076 | 202.0 | 3.9 | 0.086 | 775.5 |
| Covariance | –0.4 (mutation energy–nSASA)<br>18.0 (mutation energy–pLDDT)<br>–2.7 (nSASA–pLDDT) | | | –0.1 (mutation energy–nSASA)<br>9.8 (mutation energy–pLDDT)<br>–6.1 (nSASA–pLDDT) | | |

Abbreviations: nSASA, normalized surface-accessible area; pLDDT, predicted local distance difference test.

acid substitution Q365 to P) were introduced by site-directed mutagenesis using a KOD-Plus-Mutagenesis Kit (TOYOBO, Osaka, Japan). The entry clone encoding wild-type or variant *SGSH* genes without signal peptide (M1 to A20) was recombined via LR reaction into plasmid pFLAG-CMV-3-DEST-IRES-puro (a kind gift of Dr. Takashi Sato) [17], which contains the secretory signal peptide of Preprotrypsin, a FLAG tag at the N-terminus with a linker (LAAANSSIDLISTSLYKK), and the IRES-puro fragment from pIRESpuro3 (Takara Bio USA, Inc., Mountain View, CA, USA).

### 2.7. HEK293 cell transfection and selection of stable transformants

HEK293 cells were maintained in DMEM (Thermo Fisher Scientific, Waltham, MA, USA) supplemented with 10 % FBS (BioWest, Nuaillé, France) and 1 × Penicillin-Streptomycin Solution (FUJIFILM Wako Pure Chemical Corporation, Osaka, Japan) at 37℃ and 5 % $CO_2$. Cells were seeded in a 10-cm dish at 6 × $10^6$ cells and incubated for 24 h. Cultured cells were transfected with 30 μg of expression vector (wild-type or Q365P SGSH-FLAG fusion protein) using 30 μL of Lipofectamine 2000 (Thermo Fisher Scientific, Waltham, MA, USA). Cells were grown for an additional 48 h, and then one-tenth of the cells were transferred to medium containing 2 μg/mL of puromycin (Merck, Darmstadt, Germany) to select transformants: HEK293-WT cells and HEK293-Q365P cells, stably expressing wild-type and Q365P SGSH-FLAG fusion proteins, respectively. The transformants were harvested, detached by treatment with 0.02 % EDTA (Kanto Chemical Co., Inc. Tokyo, Japan), washed three times with PBS, and stored at −80°C until use.

### 2.8. Protein expression and purification

The stored cell pellet was thawed on ice, resuspended in 50 mM Tris-HCl (pH 7.5), 150 mM NaCl, 1 % Triton X-100, and 1 × Protease inhibitor cocktail (Nacalai Tesque, Kyoto, Japan), and incubated on ice with occasional mixing for 10 min. The supernatant containing solubilized protein was obtained by centrifugation at 20,600 ×*g* for 5 min at 4℃, diluted five times with 50 mM Tris-HCl (pH 7.5) and 150 mM NaCl, and incubated with anti-FLAG magnetic beads (Anti-DYKDDDDK tag Antibody Magnetic Beads; FUJIFILM Wako Pure Chemical Corporation, Osaka, Japan), overnight at 4℃. After removing the supernatant, the beads were washed with 5 mM Tris-HCl (pH 7.5), 13.8 mM NaCl and 0.27 mM KCl. The beads with purified wild-type or Q365P SGSH-FLAG fusion protein were used for SGSH activity assay.

### 2.9. Western blot analysis

Samples were solubilized with 62.5 mM Tris-HCl (pH 6.8) containing

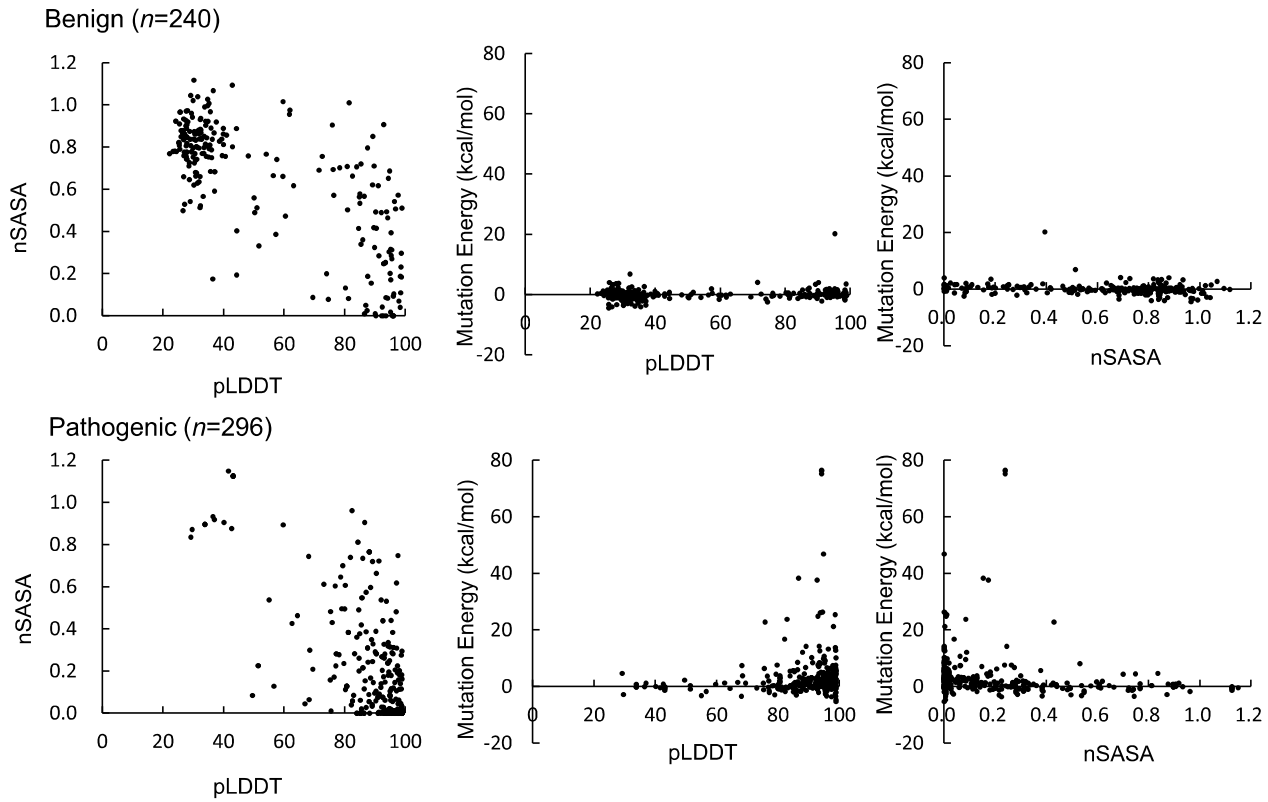


**Fig. 2.** Scatter plots of nSASA, mutation energy, and pLDDT for variants from the ClinVar dataset. Upper panels, benign variants ($n = 240$); lower panels, pathogenic variants ($n = 296$). Each plot illustrates the relationships between these three parameters, highlighting differences between benign and pathogenic variant behavior.

**Table 2**
Square of Mahalanobis distance ($D_P^2$ and $D_B^2$) for the pathogenic and benign variants.

| | Pathogenic ($n = 296$) | Benign ($n = 240$) |
|---|---|---|
| $D_P^2$ (mean ± SD) | 3.0 ± 6.8 | 11.6 ± 7.5 |
| $D_B^2$ (mean ± SD) | 30.5 ± 157.9 | 3.0 ± 7.0 |

10 % glycerol, 2 % SDS, 1 % 2-mercaptoethanol and 0.01 % bromophenol blue, denatured at 99℃, separated on an SDS–PAGE, and transferred to a PVDF membrane (Millipore, Burlington, MA, USA). Membranes were blocked with 1 % BSA and incubated with HRP-conjugated anti-FLAG mouse monoclonal antibody (Sigma, St. Louis, MO, USA) at 4 °C overnight. Detection was performed with ECL Prime (Cytiva, Tokyo, Japan).

### *2.10. Immunostaining of HEK293 stable transformants expressing wild-type or Q365P SGSH protein*

Cells were fixed with 4 % paraformaldehyde in PBS at room temperature for 10 min and then washed three times with PBS. Fixed cells were blocked with 1 % BSA/0.1 % Triton X-100 in PBS. For primary labeling, cells were incubated with anti-FLAG mouse monoclonal antibody (Sigma-Aldrich, St. Louis, MO, USA) and anti-calnexin (CANX) rabbit polyclonal antibody (GeneTex, Irvine, CA, USA) or anti-GOLPH2 rabbit polyclonal antibody (GeneTex, Irvine, CA, USA) at 4℃ overnight. After three washes with PBS, the cells were stained with Alexa Fluor 647-conjugated anti-mouse IgG1 (Thermo Fisher Scientific, Waltham, MA, USA) and Alexa Fluor 555-conjugated anti-rabbit IgG (Thermo Fisher Scientific, Waltham, MA, USA). Hoechst 33258 (FUJIFILM Wako Pure Chemical Corporation, Osaka, Japan) was used as a nuclear counterstain. Images were obtained using an LSM 700 confocal laser microscope (Carl Zeiss, Oberkochen, Baden-Württemberg, Germany). Three-dimensional images were constructed by IMARIS software

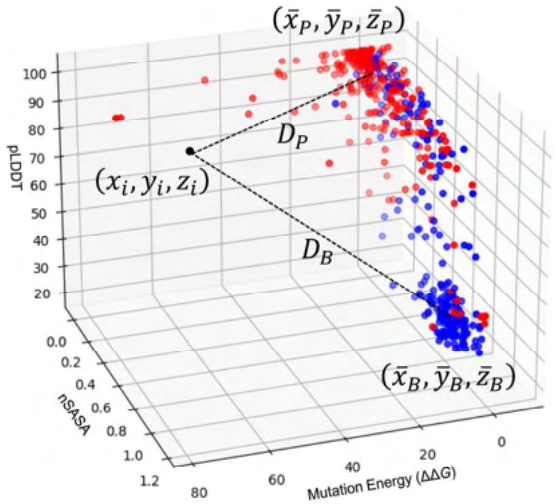


**Fig. 3.** Conceptual diagram of variant classification using Mahalanobis distance. The means of three variables (mutation energy, nSASA and pLDDT) are calculated for the pathogenic (red) and benign (blue) groups, denoted as $(\bar{x}_P, \bar{y}_P, \bar{z}_P)$ and $(\bar{x}_B, \bar{y}_B, \bar{z}_B)$, respectively. The Mahalanobis distances ($D_P$ and $D_B$) are calculated for each data point $(x_i, y_i, z_i)$ using the inverse covariance matrix (see Materials and Methods). A variant is classified as pathogenic if $D_P < D_B$ and as benign if $D_P > D_B$.

**Table 3**
Prediction accuracy of VarMeter, VarMeter2, AlphaMissense and CADD for the ClinVar dataset.

| Prediction tool | Pathogenic (%) | Benign (%) | Overall accuracy (%) |
|---|---|---|---|
| VarMeter | 72 | 75 | 74 |
| VarMeter2 | 85 | 78 | 82 |
| AlphaMissense[a] | 91 | 92 | 91 |
| CADD[a] | 96 | 85 | 91 |

[a] Ambiguous variants were not included in the calculation of prediction accuracy.

(Bitplane, Belfast, United Kingdom). Colocalization analysis was performed by ImarisColoc software (Bitplane AG, Zurich, Switzerland).

### 2.11. Quantitative analysis of SGSH colocalization in confocal microscopy images

Quantitative analysis of SGSH colocalization with the Golgi marker GOLPH2 or the ER marker calnexin (CANX) was evaluated in two-dimensional images using ZEN 2012 software (Black Edition, Carl Zeiss). Quantitative results were calculated as the ratio of the total intensity of SGSH colocalizing with GOLPH2 or CANX to the total intensity of SGSH (Figs. 6F and 6G), or the ratio of the total number of pixels representing GOLPH2 or CANX colocalizing with SGSH to the total number of pixels representing GOLPH2 or CANX (Supplemental Fig. S2A and S2B). At least 12 cells were analyzed for each colocalization measurement.

### 2.12. Real-time PCR

Total RNA was isolated from cells using TRI Reagent (Molecular Research Center, Cincinnati, OH, USA) and reverse transcribed using Oligo dT primer (Thermo Fisher Scientific, Waltham, MA, USA) and Super Script II Reverse Transcriptase (Thermo Fisher Scientific, Waltham, MA, USA). Real-time PCR of *SGSH* mRNA in each HEK293 transformant was performed by Quant Studio 12 K Flex (Applied Biosystems, Waltham, MA, USA) using primers for *SGSH* (forward, 5'-GCATCAGAATGGGATGTACGG-3'; reverse, 5'-GAAGAAAGGCCGGTCATCC-3') and *glyceraldehyde-3-phosphate dehydrogenase* (*GAPDH*; forward, 5'-CAAAGTTGTCATGGATGACC-3'; reverse, 5'- CCATGGAGAAGGCTGGGG-3'). The amount of each *SGSH* mRNA was normalized to that of *GAPDH* mRNA in the same sample.

### 2.13. Enzymatic assay of SGSH variant

The activity of the purified wild-type and Q365P SGSH proteins was measured by a fluorometric two-step enzyme assay using 4-methylumbelliferyl 2-deoxy-2-sulfamino-α-D-glucopyranoside (4-MU-GlcNS) (Biosynth, Zurich, Switzerland) as substrate, as described previously [18,19] with a slight modification. In this assay, 4MU-GlcNS is hydrolyzed by SGSH to 4-methylumbelliferyl 2-deoxy-2-amino-α-D-glucopyranoside (4-MU-GlcNH$_2$), which is then hydrolyzed to the fluorescent product, 4-methylumbelliferone (4-MU), by yeast α-glucosidase (Sigma-Aldrich, St. Louis, MO, USA). The purified protein on beads was incubated in 30 μL of McIlvaine's buffer containing 3.3 mM substrate for 16 h at 37°C; 30 μL of McIlvaine's buffer containing 0.1 units of α-glucosidase was then added, followed by incubation for 24 h at 37°C.

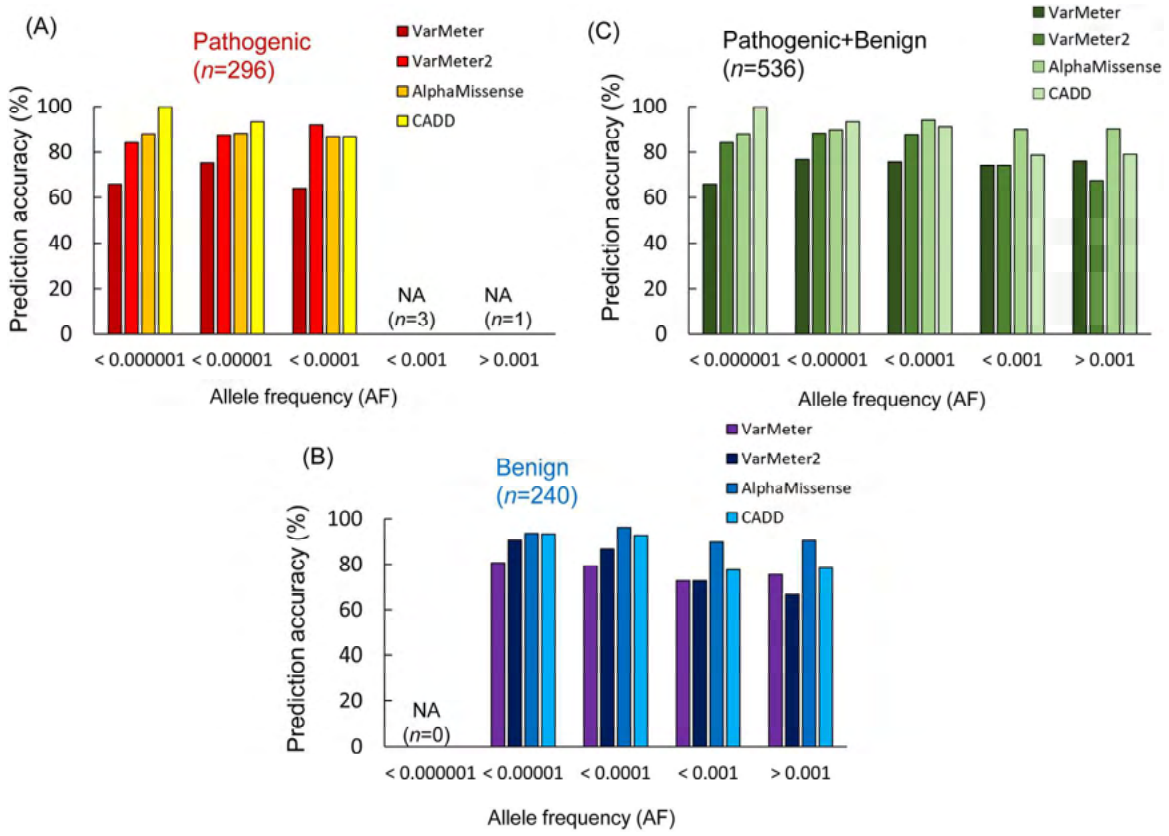


**Fig. 4.** Prediction accuracy of VarMeter, VarMeter2, AlphaMissense, and CADD methods for the ClinVar dataset based on allele frequency. (A) Prediction accuracy for pathogenic variants ($n = 296$). (B) Prediction accuracy for benign variants ($n = 240$). (C) overall prediction accuracy for all variants (pathogenic and benign, $n = 536$).

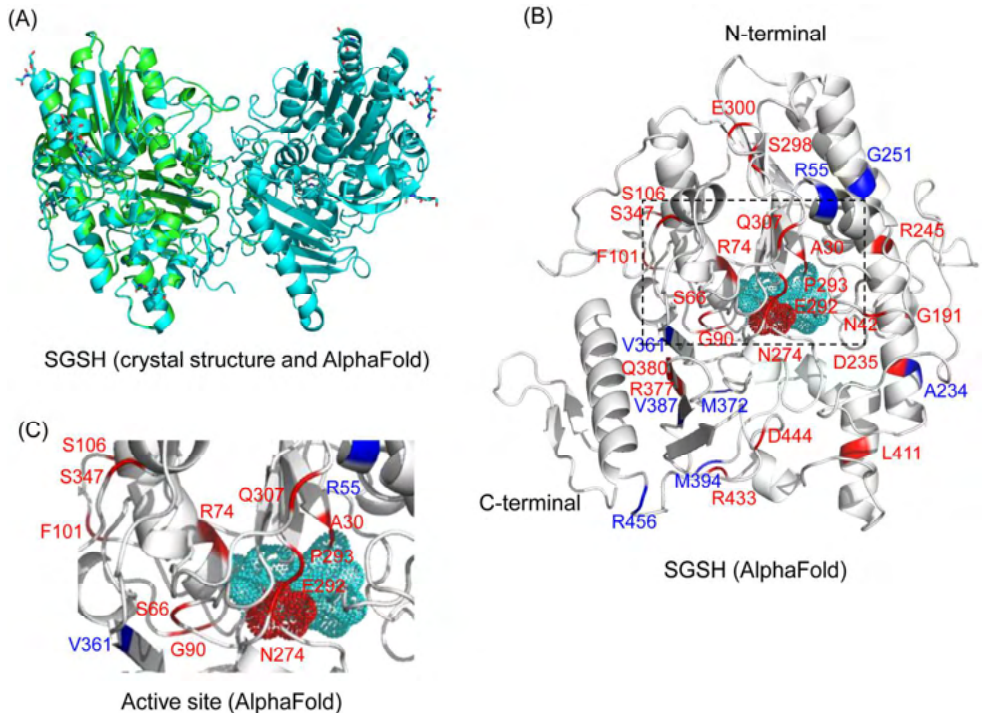


**Fig. 5.** Structural comparison and variant mapping of human SGSH. (A) Crystal structure of human SGSH dimer resolved at 2 Å resolution (PDB ID: 4MHX, cyan) and the 3D AlphaFold model of monomeric human SGSH (green). The AlphaFold model is superimposed on the A chain of the crystal structure for comparison. (B) AlphaFold model of monomeric wild-type SGSH with missense variants mapped onto the structure. The positions of pathogenic and benign variants are highlighted in red and blue, respectively. The active site residues of SGSH (D31, D32, C70 and D273) are shown as blue mesh, while N274 is shown as red mesh. (C) Detailed view of the SGSH active site from the AlphaFold model, corresponding to the dotted box in (B). The structure is depicted in cartoon representation; the figure was generated using PyMOL software.

The reaction was terminated by the addition of 200 μL stop buffer (0.5 M $Na_2CO_3$, pH 10.7, 0.025 % Triton X-100), and 50 μL was transferred to a 384-well plate. Fluorescence of 4-MU was measured by a Varioskan LUX instrument (Thermo Fisher Scientific, Waltham, MA, USA) at room temperature with excitation at 360 nm (bandwidth 12 nm), emission at 445 nm, and a measurement time of 100 ms.

### 2.14. Cycloheximide chase assay

To assess protein stability, a cycloheximide chase assay was performed on HEK293-WT and HEK293-Q365P cells. Cells were collected at 2, 4, and 8 hours after the addition of 100 μg/mL of cycloheximide (CHX) to the cell culture. Western blot analysis was subsequently conducted using 10 μg of cell lysate proteins, probed with an HRP-conjugated anti-FLAG mouse monoclonal antibody.

### 2.15. Trypsin sensitivity assay

Wild-type and variant SGSH proteins, whose concentrations were quantified using DYKDDDDK-BAP (FUJIFILM Wako Pure Chemical Corporation, Osaka, Japan) as a standard, were diluted to 3 μg/μL in TBS (pH 7.5) (25 mM Tris-HCl, 2.7 mM KCl, 137 mM NaCl), and mixed with 10 ng/μL of sequencing-grade modified trypsin (Promega, Madison, WI, USA) in an 8:1 ratio. Control samples were prepared using the same buffer without trypsin. The reaction was incubated at 37°C for 1 h and stopped by adding 10 mM PMSF to a final concentration of 1 mM. After SDS–PAGE, the gels were stained using Lumitein Protein Gel Stain (Biotium, Fremont, CA, USA), and the bands were quantified using ImageJ.

### 2.16. Statistical analysis

Statistical evaluation of differences between the groups was carried out by Student's *t*-test or Tukey-Kramer test, implemented in Microsoft Excel. Differences were considered to be significant at a *p*-value of less than 0.05.

## 3. Results and discussion

### 3.1. Comparison of pathogenic and benign variants from the ClinVar dataset

Our previous prediction tool was based on the mutation energy and nSASA of 70 pathogenic and 16 benign missense variants of ARSL, ALG1 and MPI [3]. To improve the accuracy of the prediction, we expanded the dataset to 536 missense variants extracted from the ClinVar database, comprising 296 pathogenic and 240 benign variants (Supplemental Table S1), all of which had a review status classified as "Expert panel" (three stars). We chose this dataset to ensure both the reliability and feasibility of our analyses. It should be noted that the trained dataset predominantly includes variants of BRCA1 and MLH1 (Supplemental Fig. S1), which together comprise nearly half of the dataset, limiting overall gene representation. Further studies will be needed to expand and diversify the dataset for future development and variation.

We first investigated the correlation between pathogenicity and the predicted local distance difference test (pLDDT) score, which reflects the per-residue structural accuracy provided by the AlphaFold structure database [4]. The pLDDT scores of the 296 pathogenic and 240 benign variants were categorized into four confidence levels: very low (pLDDT<50), low (50 <pLDDT<70), confident (70 <pLDDT<90), and

**Table 4**
Prediction outcomes for published SGSH variants using VarMeter, VarMeter2, AlphaMissense and CADD [a].

| SGSH variants (AA change) | Var Meter | Var Meter2 | Alpha Missense | CADD | Reference |
|---|---|---|---|---|---|
| Pathogenic ($n = 24$) | | | | | |
| A30P | P | P | P | P | [38] |
| N42K | P | P | P | B | [39] |
| S66W | PD | P | P | P | [40] |
| R74C | P | P | P | P | [41] |
| G90R | PD | P | P | P | [42] |
| F101S[b] | PD | P | P | P | [43] |
| S106R | P | P | P | B | [44] |
| G191R | P | P | P | P | [44] |
| D235N | PD | P | P | P | [45] |
| R245H | P | P | P | P | [40] |
| N274D | P | P | P | A | [46] |
| E292K | PD | P | P | P | [47] |
| P293S | P | P | P | A | [39] |
| S298P | PD | P | P | P | [42] |
| E300V | B | B | B | B | [48] |
| Q307P | PD | P | A | P | [48] |
| S347F | PD | P | P | P | [49] |
| R377H | P | P | P | P | [41] |
| R377L | P | P | P | P | [38] |
| R377C | P | P | P | P | [50] |
| Q380R | PD | P | B | B | [41] |
| L411R | P | P | P | P | [51] |
| R433W | PD | P | P | P | [45] |
| D444G | PD | P | P | P | [49] |
| Benign ($n = 8$) | | | | | |
| R55C | PD | B | B | A | |
| A234G | PD | B | B | B | [41] |
| G251A | PD | P | A | P | [52] |
| V361I | P | P | B | B | |
| M372I | P | P | P | P | |
| V387M | PD | P | A | B | [53] |
| M394I[b] | B | B | A | A | |
| R456H | B | B | B | B | |

[a] The classifications are denoted as follows: P (pathogenic), PD (possibly damaging), B (benign), and A (ambiguous). 3D structural parameters, allele frequencies, and prediction scores are shown in Supplemental Table S2.
[b] Located at dimer interface.

**Table 5**
Comparison of prediction accuracy (%) for SGSH variants by VarMeter, VarMeter2, AlphaMissense and CADD [a].

| | Pathogenic (P + PD) | Benign (B) | Total |
|---|---|---|---|
| VarMeter | 96 | 25 | 78 |
| VarMeter2 | 96 | 50 | 84 |
| AlphaMissense[b] | 91 | 80 | 89 |
| CADD[b] | 82 | 67 | 79 |

[a] Abbreviations: P, pathogenic (damaging); PD, possibly damaging; B, benign.
[b] Ambiguous variants were not included in the calculation of prediction accuracy.

very high (pLDDT>90). Whereas the majority of pathogenic variants had high pLDDT values (pLDDT>70), a significant proportion of benign variants had lower pLDDT values (pLDDT<50) and only a small proportion had high pLDDT values (pLDDT>70) (Fig. 1A).

Intrinsically disordered regions are frequently associated with low pLDDT scores [20–22], which suggests that the mutations in pathogenic variants are predominantly located in well-structured (folded) regions of proteins. By contrast, those in benign variants tend to occur in unstructured regions, and are present to a lesser extent in folded regions. This trend highlights the importance of considering protein folding status when evaluating the potential pathogenicity of missense variants.

We then analyzed the correlation between pathogenicity and allele frequency for the 296 pathogenic and 240 benign variants. The resulting histogram revealed that most pathogenic variants tend to have lower allele frequencies compared with benign variants (Fig. 1B), consistent with previous findings that lower allele frequencies are strongly associated with pathogenicity [23,24]; however, there is an overlap in allele frequencies between pathogenic and benign variants within the range of 0.000001–0.0001. While allele frequency can be a valuable parameter for distinguishing pathogenic variants from benign ones, this overlap highlights the need for careful interpretation.

Next, we calculated mutation energy and nSASA for the 240 benign and 296 pathogenic variants. The mean ± SD pLDDT for benign variants was 53.1 ± 27.9, while that for pathogenic variants was significantly higher at 88.2 ± 14.2 (Table 1). The mean nSASA for benign variants was 0.64 ± 0.29 as compared with 0.21 ± 0.28 for pathogenic variants. A negative correlation was observed between pLDDT and nSASA for both benign and pathogenic variants (Fig. 2). Variants with low pLDDT scores (20−40) tended to have high nSASA values (0.6–1.0), indicating that the mutated residues are generally solvent-exposed, while those with high pLDDT scores (80−100) tended to have low nSASA values (0–0.4), reflecting the location of the mutations in more structured, buried region. This result is consistent with previous studies reporting that pathogenic variants are more buried than benign variants [25,26].

The correlation between mutation energy and pLDDT was analyzed for both benign and pathogenic variants (Fig. 2, upper and lower middle panels). On average, benign variants exhibited a mutation energy of 0.1 ± 2.0 kcal/mol, while pathogenic variants displayed a significantly higher average of 3.9 ± 9.6 kcal/mol (Table 1). This trend confirmed that pathogenic variants generally show greater destabilization of protein structure, reflected by higher mutation energy, and is consistent with the findings of previous studies that used using Gibbs free energy ($\Delta\Delta G$) to distinguish between benign and pathogenic variants [27–30].

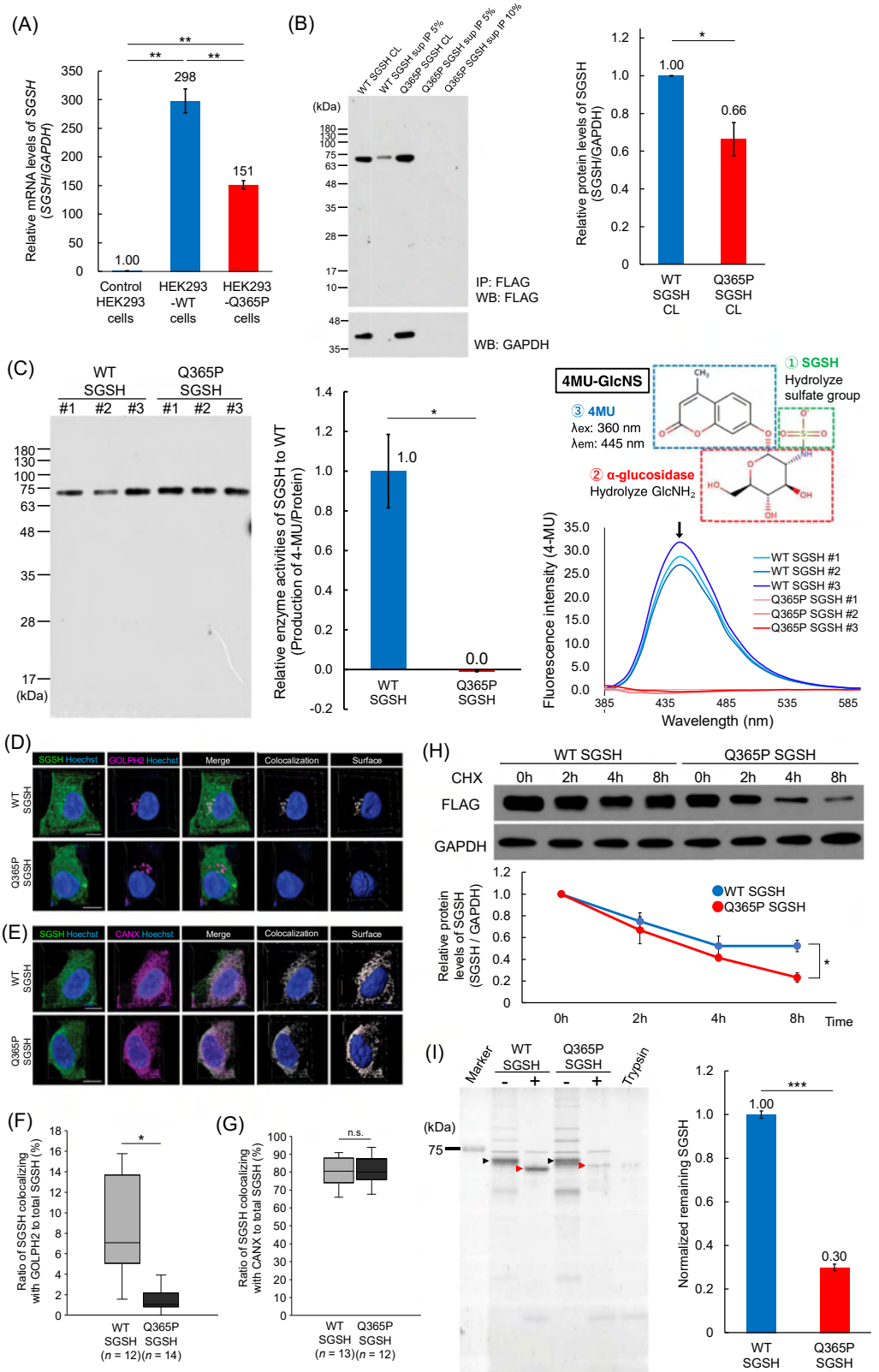


*(caption on next page)*

**Fig. 6.** Enzymatic activity of the wild-type and Q365P SGSH proteins. (A) *SGSH* mRNA levels in HEK293-WT and HEK293-Q365P cells stably expressing the respective wild-type and Q365P SGSH-FLAG fusion proteins, were analyzed by real-time PCR and normalized to *GAPDH* mRNA in the same sample. Expression levels are shown relative to those of control HEK293 cells (1.0) in which an empty vector was transfected. $^{**}p < 0.001$ by one-way ANOVA followed by Tukey-Kramer test ($n = 3$). (B) Western blot analysis of wild-type (WT) and Q365P SGSH FLAG fusion proteins in the culture supernatant (sup) and cell lysate (CL) from HEK293-WT cells and HEK293-Q365P cells using anti-FLAG. For cell lysates, 10 μg of total protein was applied; for supernatants, 5 % of WT SGSH-FLAG or 5 % or 10 % of immuno-precipitated Q365P SGSH-FLAG was applied. (left) Representative Western blots. (right) Quantification of the protein bands in each cell lysate. Protein levels are shown relative to those of HEK293-WT cells (1.0). $^{*}p < 0.05$ by Student's *t*-test ($n = 3$). (C) Activity of the Q365P SGSH protein. (left) Western blot analysis using anti-FLAG of purified wild-type (WT) and Q365P SGSH FLAG fusion proteins used in the activity assay ($n = 3$). (middle) 4-MU production by Q365P SGSH is normalized by the protein amount used and shown relative to that of WT SGSH. Ratios are given as mean ± S.E. of three independent experiments. $^{*}p < 0.05$ by Student's *t*-test. (right top) Scheme of activity assay. Production of 4-MU after SGSH enzymatic reaction (16 h) using 4MU-GlcNS as a substrate, followed by α-glucosidase reaction (24 h). (right bottom) The fluorescence spectra of each sample are shown. The amount of 4-MU was determined from the fluorescence intensity at 445 nm. (D and E) Three-dimensional confocal images of the intracellular localization of wild-type (WT) and Q365P SGSH-FLAG fusion proteins in HEK293-WT cells and HEK293-Q365P cells, respectively. SGSH (green) and nucleus (blue) are labeled with anti-FLAG and Hoechst 33258, respectively. Cis-Golgi body (magenta in D) and endoplasmic reticulum (ER; magenta in E) are labeled with anti-GOLPH2 and anti-CANX, respectively. Colocalization of SGSH/GOLPH2 (D) or SGSH/CANX (E) is indicated in white in the second panels from the right. Surface rendering models of the colocalization image are shown in the rightmost panels. Scale bar: 10 μm. (F and G) Quantitative analysis of SGSH colocalization with Golgi and ER markers. The ratio of SGSH colocalizing with GOLPH2 (F) or CANX (G) to total SGSH in HEK293-WT cells and HEK293-Q365P cells is shown. $^{**}p < 0.001$, n.s.: not significant by Student's *t*-test. (H) CHX chase assay performed in HEK293-WT and HEK293-Q365P cells. Cells were incubated for 0 hours (untreated), 2, 4, and 8 hours (h) with 100 μg/mL of CHX. (Upper) Representative Western blot images of wild-type (WT) and Q365P SGSH-FLAG fusion proteins detected using anti-FLAG antibody. (Lower) Quantification of protein bands normalized to GAPDH and expressed relative to the 0-hour sample. $^{*}p < 0.05$ by Student's *t*-test ($n = 3$). (I) Stability of the wild-type (WT) and Q365P SGSH proteins. (left) SDS–PAGE analysis of SGSH proteins treated with trypsin. Black arrowhead indicates full-length SGSH; red arrowhead indicates the trypsin-resistant fragment. (right) Proportion of trypsin-resistant fragment remaining after trypsin digestion, calculated as the intensity of the trypsin digestion-resistant band relative to that of full-length SGSH in untreated samples. The values shown have been normalized to WT SGSH. $^{***}p < 0.0001$ by Student's *t*-test ($n = 3$).

However, a subset of pathogenic variants showed low mutation energy (Fig. 2, lower middle). One possible explanation is that the mutations in these variants occur at functionally critical sites, such as residues involved in ligand or protein binding, where even minor structural changes might impair function. Assessing this phenomenon in future studies will be important for further refining pathogenicity prediction models.

As observed in our previous study [3], there was a negative correlation between nSASA and mutation energy (Fig. 2, right panels). In benign variants, high nSASA values were typically associated with low mutation energy (Fig. 2, upper right); in pathogenic variants, conversely, low nSASA values tended to be connected with relatively higher mutation energy (Fig. 2, lower right). This suggests that pathogenic mutations are more likely to occur in buried, structurally important regions, where even small changes may have a significant destabilizing effect.

### 3.2. Classification of missense variants based on Mahalanobis distance

To classify pathogenic and benign variants using mutation energy, nSASA and pLDDT, we applied Mahalanobis distance [31], a statistical method used in various applications to determine members of groups. First, the mean, variance and covariance of the three variables were calculated for the pathogenic and benign variants (Table 1). These parameters were then used to calculate Mahalanobis distance for both pathogenic and benign variants (Supplemental Table S1 and Table 2). These Mahalanobis distances ($D_P$ and $D_B$) were used to update the VarMeter prediction method as VarMeter2, integrating mutation energy, nSASA, and pLDDT scores into a unified framework (Fig. 3). To evaluate the performance of VarMeter2, defined by Condition (ii) below, we applied it to the ClinVar dataset alongside the original VarMeter [3], AlphaMissense [10], and CADD [11] methods, defined by Conditions (i), (iii) and (iv), respectively.

Condition (i), original VarMeter [3]:

Requirement #1: nSASA $\leq 0.11$

Requirement #2: mutation energy $\geq 0.88$ kcal/mol

- Damaging (pathogenic) variant (D): satisfying both requirements #1 and #2
- Possibly damaging (pathogenic) (PD): satisfying either requirement #1 or #2
- Benign variant (B): satisfying neither requirement #1 or #2

Condition (ii), VarMeter2 (this study):

- Pathogenic variant (P): $D_P^2 < D_B^2$
- Benign variant (B): $D_P^2 > D_B^2$

Condition (iii), AlphaMissense [10]:

- Pathogenic variant (P): 0.564 < AM score < 1
- Ambiguous variant (A): 0.340 < AM score < 0.564
- Benign variant (B): 0 < AM score < 0.340

Condition (iv), CADD [11,32]:

- Pathogenic variant (P): CADD score ≥ 25.3
- Ambiguous variant (A): 22.7 < CADD score < 25.3
- Benign variant (B): CADD score ≤ 22.7

The prediction accuracies are summarized in Table 3. VarMeter2 showed 85 % prediction accuracy for pathogenic variants and 78 % accuracy for benign variants, yielding an overall accuracy of 82 %. This represents a significant improvement over the prediction accuracy of the original VarMeter (74 %). However, AlphaMissense [10], a deep learning approach adapted from AlphaFold [4], outperformed VarMeter2 with an overall accuracy of 91 % for the ClinVar dataset. CADD showed a similar accuracy of 91 %.

To evaluate whether prediction accuracy depends on allele frequency, we plotted accuracy against allele frequency (Fig. 4). The results indicated that the prediction accuracy of VarMeter2 is not significantly influenced by the allele frequency, probably because VarMeter2 relies solely on 3D structural parameters and does not incorporate allele frequency into calculations. In contrast, CADD demonstrated higher prediction accuracy for variants with lower allele frequencies, probably because it incorporates annotations reflecting population-level metrics as part of its scoring framework [33]. Despite these advances, challenges remain in 3D structure-based prediction, including the refinement of variant protein models, more precise mutation energy calculations ($\Delta\Delta G$) and optimizing structural parameters for greater predictive power. Further developments in these areas will be essential for improving pathogenicity predictions.

### 3.3. Evaluation of VarMeter2 using SGSH variant data

To validate VarMeter2 further, we applied it to published data on

variants of SGSH, an enzyme responsible for catalyzing the conversion of *N*-sulfo-D-glucosamine into D-glucosamine during the degradation of heparan sulfate. This enzyme was selected due to the large number of reported pathogenic variants linked to Sanfilippo syndrome A. The crystal structure of glycosylated SGSH has been reported at 2 Å resolution (Fig. 5A) [34]; the root mean square deviation (RMSD) of Cα atoms between the crystal structure and the corresponding AlphaFold model is 0.2 Å, indicating that the AlphaFold model of SGSH is sufficiently accurate for calculating mutation energy and solvent-accessible surface area. We therefore mapped the positions of the pathogenic variants onto the 3D structural model of SGSH (Figs. 5B, 5C).

First, we calculated the mutation energy, nSASA and pLDDT for the pathogenic ($n = 24$) and benign ($n = 8$) SGSH variants (Table 4). VarMeter2 was then used to classify the SGSH variants as pathogenic or benign. For comparison, we also carried out predictions using the original VarMeter, AlphaMissense and CADD methods (Table 4). The overall accuracy of VarMeter2 (84 %) to predict variants of SGSH was higher than either the original VarMeter (78 %) or CADD (79 %), and lower than AlphaMissense (89 %) (Table 5). In addition, the accuracy of VarMeter2 to predict pathogenic variants was 96 %. This evaluation demonstrates VarMeter2's potential to accurately classify SGSH variants, offering an improved approach over previous prediction methods.

### 3.4. Characterization of a novel SGSH variant

To test the ability of VarMeter2 to identify novel pathogenic variants, we applied it to the prediction of SGSH variants identified in our in-house database of 900 individuals with rare or undiagnosed diseases. Among the missense variants in the database, the Q365P variant was newly identified and predicted to be pathogenic by VarMeter2 with the following parameters: $D_P^2$, 0.7; $D_B^2$, 14.8; nSASA, 0.03; mutation energy, 7.2 kcal/mol; and pLDDT, 98.89. Additionally, the AlphaMissense score for this variant was 0.90, similarly predicting it as pathogenic. Based on the clinical symptoms observed in the patient, we suspected that this variant might be pathogenic. Therefore, to determine whether this newly identified Q365P mutation directly contributes to the observed symptoms and to support diagnosis, we assessed the activity and expression of the Q365P SGSH protein through detailed experimental studies.

The wild-type and Q365P SGSH proteins were expressed, purified, and subjected to an enzymatic assay using the artificial substrate 4-MU-GlcNS (Fig. 6). First, HEK293-WT cells and HEK293-Q365P cells, stably expressing the respective wild-type and Q365P SGSH-FLAG fusion proteins, were established. The exogenous expression of *SGSH* mRNA was approximately 300 times higher in HEK293-WT cells, and about 150 times higher in HEK293-Q365P cells, as compared with the expression of endogenous *SGSH* mRNA in control HEK293 cells (Fig. 6A). The amount of the Q365P protein in HEK293-Q365P cells was 66 % of that of the wild-type protein in HEK293-WT cells (Fig. 6B). In contrast, the Q365P SGSH-FLAG fusion protein was not detected in the culture medium, whereas the wild-type SGSH-FLAG fusion protein was secreted.

To test the enzymatic activity of the Q365P variant, we purified the wild-type and Q365P SGSH proteins from their respective cell lysates using anti-FLAG magnetic beads. The SGSH enzymatic activity using 4MU-αGlcNS, showed that the Q365P protein had no activity, whereas the wild-type protein had high activity (Fig. 6C).

Next, we compared the intracellular localization of the Q365P and wild-type SGSH proteins by immunostaining of the respective HEK293 stable transformants. Whereas wild-type SGSH colocalized with the cis-Golgi marker GOLPH2, the Q365P SGSH protein showed minimal colocalization with this marker (Fig. 6D and Supplemental Movies 1–4), consistent with our above observation that the Q365P SGSH-FLAG fusion protein was not secreted. However, both wild-type and Q365P SGSH proteins colocalized with the endoplasmic reticulum (ER) marker calnexin (CANX) (Fig. 6E and Suppmenental Movies 5–8). Quantitative analysis showed that the ratio of SGSH colocalizing with the Golgi marker GOLPH2 to total SGSH was significantly decreased in HEK293-Q365P cells as compared with HEK293-WT cells (Fig. 6F); similarly, the ratio of GOLPH2 colocalizing with SGSH to total GOLPH2 was significantly lower in HEK293-Q365P cells than in HEK293-WT cells (Supplemental Fig. S2A). In contrast, both the ratio of SGSH colocalizing with the ER marker CANX to total SGSH and that of CANX colocalizing with SGSH to total CANX were comparable between HEK293-WT and HEK293-Q365P cells (Fig. 6G and Supplemental Fig. S2B). Thus, almost all of the Q365P SGSH protein was localized in the ER rather than in the Golgi.

Collectively, these results suggest that the Q365P variant SGSH protein fails to fold into a stable 3D structure, cannot be transferred to the Golgi, and is retained in the ER, which is likely to be the cause of its loss of activity. Moreover, a cycloheximide chase assay showed that the stability of Q365P SGSH protein was decreased as compared with wild-type SGSH (Fig. 6H and Supplemental Fig. S3). Incompletely folded proteins, such as destabilized proteins, are much more sensitive to protease digestion than native proteins [35]. Therefore, we compared the protease resistance of the two purified SGSH proteins. After treatment with trypsin, the intensity of the trypsin-resistant band was significantly reduced for the Q365P protein as compared with wild-type SGSH (Fig. 6I), further confirming that the loss of activity of Q365P SGSH is due to a decrease in protein stability, as predicted by VarMeter2.

Mutations such as Q365P SGSH, identified here as causing protein destabilization, not only may reduce enzymatic activity and serve as a primary cause of disease but also, as reported in conditions like Congenital Insensitivity to Pain with Anhidrosis (CIPA) [36], may lead to the accumulation of destabilized proteins in the ER, inducing ER stress and further exacerbating disease pathology.

### 3.5. Clinical manifestation of the patient with SGSH variant Q365P

The patient with the Q365P variant of SGSH was diagnosed with Sanfilippo syndrome or mucopolysaccharidosis type III, a rare autosomal recessive lysosomal storage disease caused by impaired degradation of heparan sulfate. This diagnosis aligns with the prediction by V[illegible]t

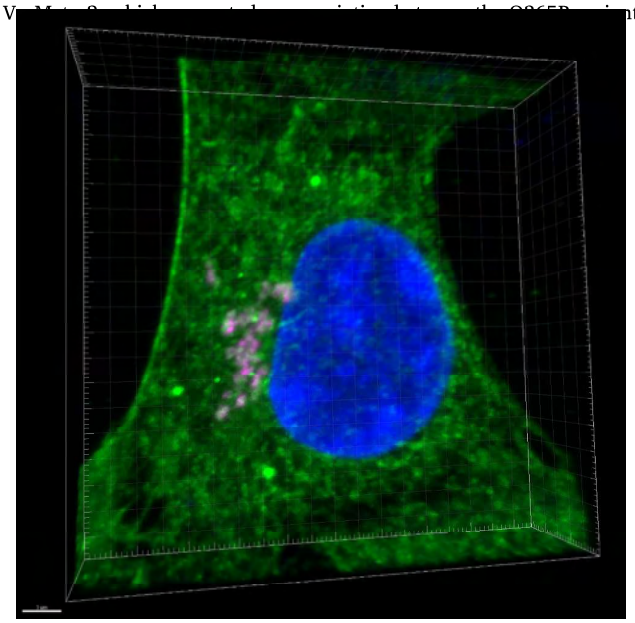

**Supplemental Movie S1. Three-dimensional confocal image of a wild-type SGSH-expressing cell with visualization of the cis-Golgi body. SGSH protein, cis-Golgi body, and the nucleus are indicated in green, magenta, and blue, respectively. Movie corresponds to the image in Fig. 6D..** A video clip is available online. Supplementary material related to this article can be found online at doi:10.1016/j.csbj.2025.02.008.

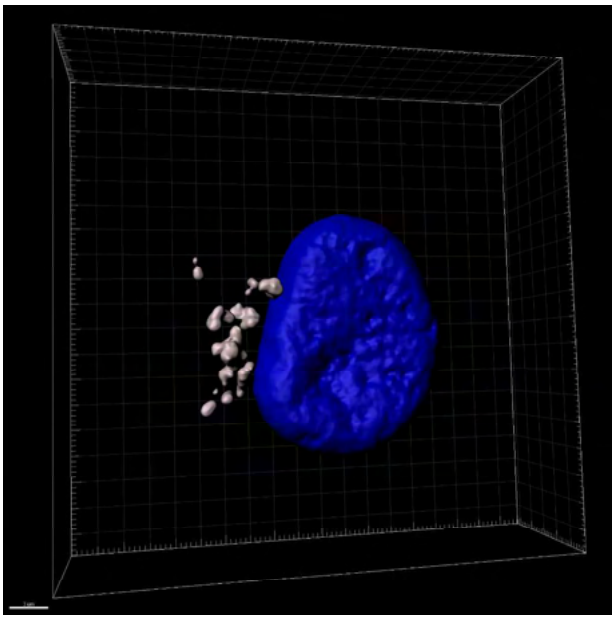

**Supplemental Movie S2. Surface rendering model of a wild-type SGSH-expressing cell in which SGSH protein and GOLPH2 are colocalized. Colocalization is indicated in white; the nucleus is indicated in blue. Movie corresponds to the image in Fig. 6D..** A video clip is available online. Supplementary material related to this article can be found online at doi:10.1016/j.csbj.2025.02.008.

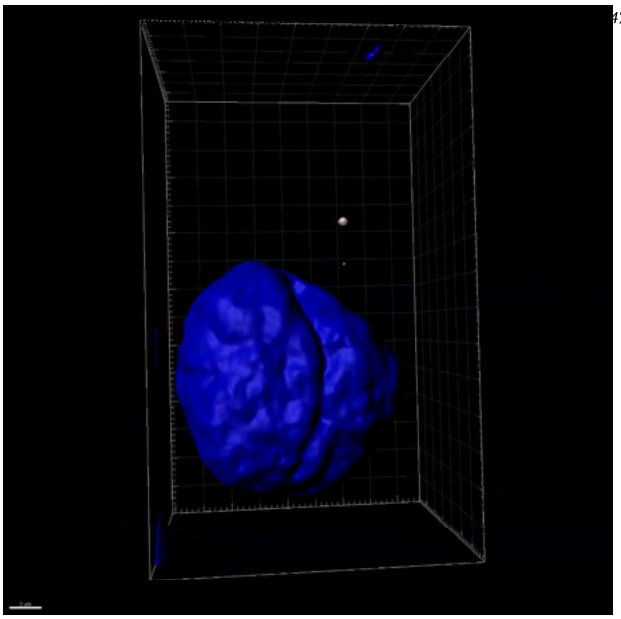

**Supplemental Movie S4. Surface rendering model of a Q365P SGSH-expressing cell in which SGSH protein and GOLPH2 are colocalized scarcely. Colocalization is indicated in white; the nucleus is indicated in blue. Movie corresponds to the image in Fig. 6D..** A video clip is available online. Supplementary material related to this article can be found online at doi:10.1016/j.csbj.2025.02.008.

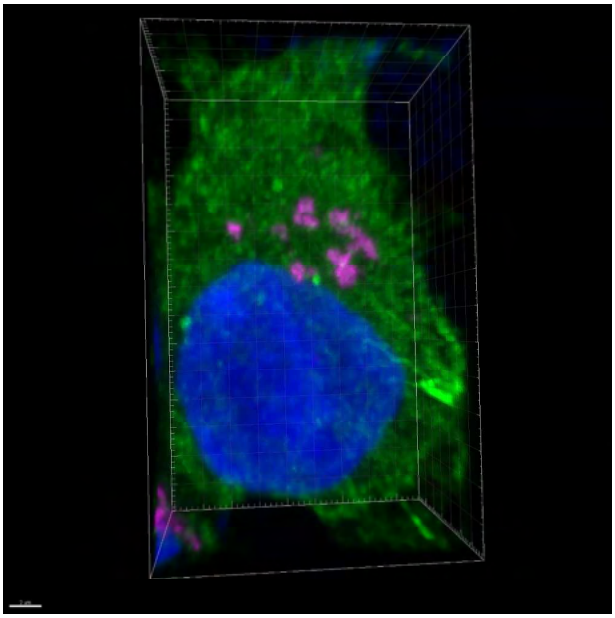

**Supplemental Movie S3. Three-dimensional confocal image of a Q365P SGSH-expressing cell with visualization of the cis-Golgi body. SGSH protein, cis-Golgi body, and the nucleus are indicated in green, magenta, and blue, respectively. Movie corresponds to the image in Fig. 6D..** A video clip is available online. Supplementary material related to this article can be found online at doi:10.1016/j.csbj.2025.02.008.

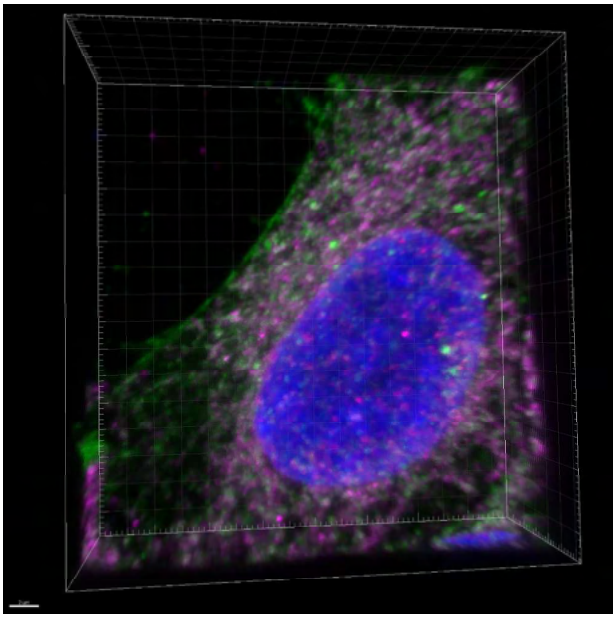

**Supplemental Movie S5. Three-dimensional confocal image of a wild-type SGSH-expressing cell with visualization of the ER. SGSH protein, ER, and the nucleus are indicated in green, magenta, and blue, respectively. Movie corresponds to the image in Fig. 6E..** A video clip is available online. Supplementary material related to this article can be found online at doi:10.1016/j.csbj.2025.02.008.

and reduced protein stability, contributing to the disease manifestation. Sanfilippo syndrome is characterized by severe degeneration of the central nervous system.

The patient was a 16-year-old female. She was born at 28 weeks of gestation with a birth weight of 1338 g. At the age of 2 years and 1 month, she underwent surgery for a right inguinal hernia, and 5 months later she underwent surgery for a ventral wall scarring hernia. She was noted to have hearing loss, hepatomegaly, hypertrichosis and developmental delay. She also had adenoids, which were removed. At the age of 5 years and 3 months, an increase in urinary mucopolysaccharides and a decrease in heparan *N*-sulfatase activity in the blood were detected. At the age of 11, the homozygous pathogenic variant (p.Q365P) in the

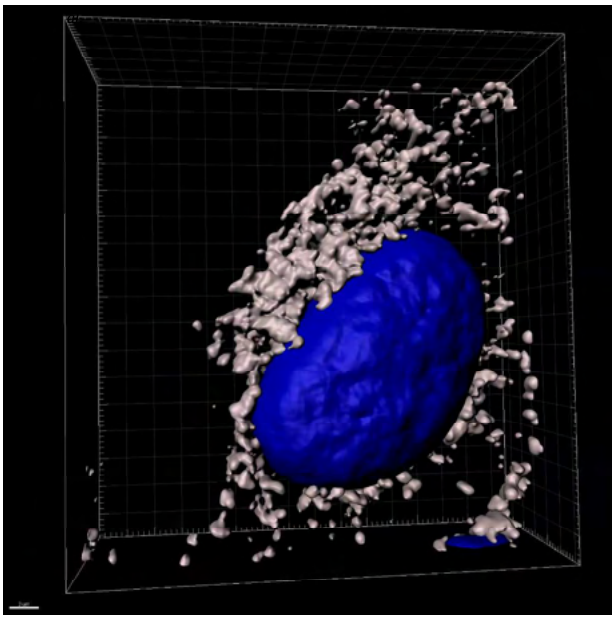

**Supplemental Movie S6. Surface rendering model of a wild-type SGSH-expressing cell in which SGSH protein and CANX are colocalized. Colocalization is indicated in white; the nucleus is indicated in blue. Movie corresponds to the image in Fig. 6E..** A video clip is available online. Supplementary material related to this article can be found online at doi:10.1016/j.csbj.2025.02.008.

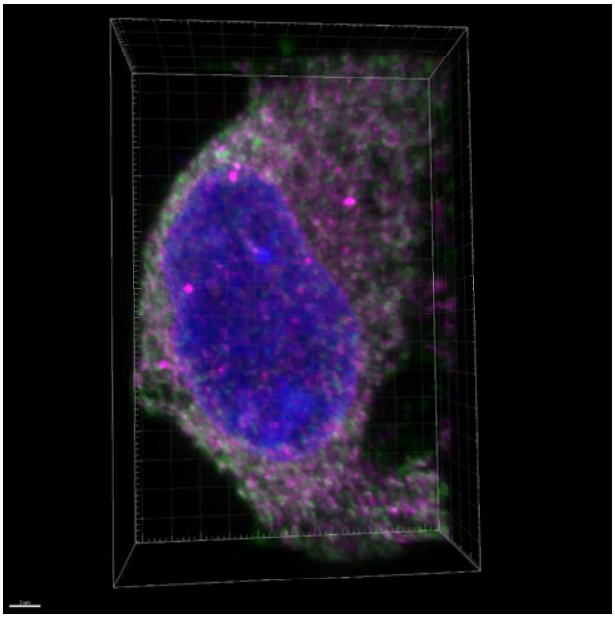

**Supplemental Movie S7. Three-dimensional confocal image of a Q365P SGSH-expressing cell with visualization of the ER. SGSH protein, ER, and the nucleus are indicated in green, magenta, and blue, respectively. Movie corresponds to the image in Fig. 6E..** A video clip is available online. Supplementary material related to this article can be found online at doi:10.1016/j.csbj.2025.02.008.

*SGSH* gene was identified in the patient by trio-whole-exome sequencing analysis. This diagnosis was further supported by VarMeter2, which predicted that the Q365P variant is associated with reduced protein stability, contributing to disease manifestation. She gradually showed regression, and her digital quotient score was less than 10 at the age of 16 years.



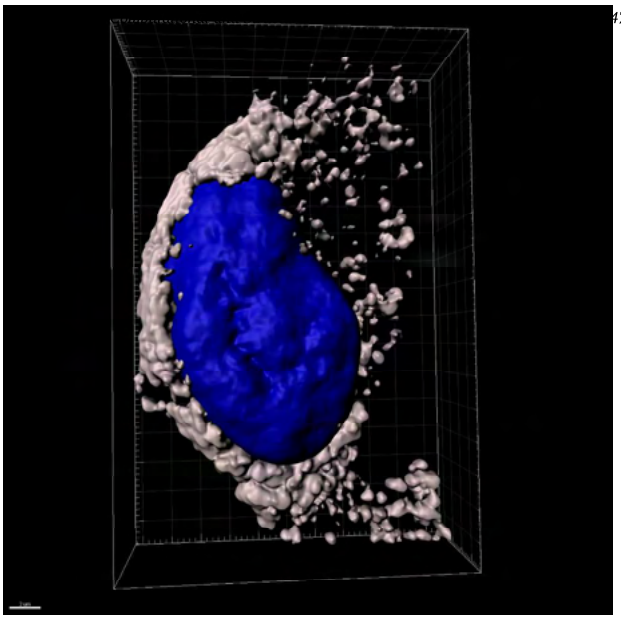

**Supplemental Movie S8. Surface rendering model of a Q365P SGSH-expressing cell in which SGSH protein and CANX are colocalized. Colocalization is indicated in white; the nucleus is indicated in blue color. Movie corresponds to the image in Fig. 6E..** A video clip is available online. Supplementary material related to this article can be found online at Movie 8doi:10.1016/j.csbj.2025.02.008.

In summary, we have developed VarMeter2, an improved tool for predicting the pathogenicity of missense variants. Utilizing nSASA, mutation energy and pLDDT values, VarMeter2 applies Mahalanobis distance calculations to distinguish pathogenic from benign variants with 82 % accuracy based on the ClinVar dataset. We validated the method with both reported and novel SGSH variants, demonstrating its practical application and confirming its effectiveness. Unlike many other prediction tools, VarMeter2 relies solely on physical parameters derived from 3D structural models, setting it apart from conservation-based tools but also complementing them by focusing on physicochemical changes that may be directly associated with the mechanism of pathogenicity [37]. As a result, VarMeter2 may serve as a complementarily approach, especially for variants that are challenging for conservation-based methods. However, this reliance on structural data also introduces limitations. First, the performance of VarMeter2 is contingent on the accuracy of AlphaFold models, which may be less reliable for disordered regions or proteins with low-confidence structural predictions. Second, the absence of sequence conservation analysis might limit its predictive power for variants in highly conserved regions where evolutionary information is critical. Ongoing efforts are underway to refine the tool further to address these limitations and to enhance its power to identify pathogenic missense variants. VarMeter analyses for missense variants can be conducted collaboratively upon request, and in future we will develop an online tool to further facilitate accessibility.

## Funding

This work was supported by AMED (Japan Agency for Medical Research and Development) under Grant Number JP22ek0109446.

## CRediT authorship contribution statement

**Togayachi Akira:** Writing – review & editing, Validation, Supervision. **Aoki-Kinoshita Kiyoko:** Writing – review & editing, Validation, Supervision. **Manabe Noriyoshi:** Writing – review & editing, Writing – original draft, Visualization, Validation, Investigation. **Angata**

**Kiyohiko:** Writing – review & editing, Validation, Supervision. **Inokuchi Jin-Ichi:** Writing – review & editing, Validation, Supervision. **Kaname Tadashi:** Writing – review & editing, Writing – original draft, Validation, Supervision, Project administration, Investigation. **Ohno Shiho:** Writing – review & editing, Writing – original draft, Visualization, Validation, Methodology, Investigation. **Furukawa Jun-ichi:** Writing – review & editing, Validation, Supervision. **Inamori Kei-ichiro:** Writing – review & editing, Validation, Supervision. **Itoh Kazuyoshi:** Writing – review & editing, Writing – original draft, Visualization, Validation, Investigation. **Nishihara Shoko:** Writing – review & editing, Writing – original draft, Visualization, Validation, Supervision, Project administration, Investigation, Funding acquisition, Conceptualization. **Yabuki Akane:** Writing – review & editing, Writing – original draft, Visualization, Validation, Investigation. **Yamaguchi Yoshiki:** Writing – review & editing, Writing – original draft, Visualization, Validation, Supervision, Project administration, Methodology, Investigation, Conceptualization. **Ogura Chika:** Writing – review & editing, Writing – original draft, Visualization, Validation, Investigation.

## Declaration of Competing Interest

The authors declare that they have no known competing financial interests or personal relationships that could have appeared to influence the work reported in this paper.

## Acknowledgements

The authors thank Eiji Akama (Tohoku Medical and Pharmaceutical University) for his initial analysis of SGSH variants. The authors also thank Dr. Takashi Sato (National Institute of Advanced Industrial Science and Technology (AIST)) for providing the pFLAG-CMV-3-DEST-IRES-puro plasmid. Shoko Nishihara, Kazuyoshi Itoh, Kiyohiko Angata, Akira Togayachi, Kiyoko Aoki-Kinoshita, and Jun-ichi Furukawa are supported by the "Human Glycome Atlas Project" as one of the "Large-Scale Academic Frontier Promotion Projects" of the Ministry of Education, Culture, Sports, Science and Technology (MEXT). GaLSIC and iGCORE are also supported by J-GlycoNet, one of the official Joint Usage/Research Centers of Japan by MEXT.

## Appendix A. Supporting information

Supplementary data associated with this article can be found in the online version at doi:10.1016/j.csbj.2025.02.008.

## References

[1] Keskin Karakoyun H, Yuksel SK, Amanoglu I, Naserikhojasteh L, Yesilyurt A, et al. Evaluation of AlphaFold structure-based protein stability prediction on missense variations in cancer. Front Genet 2023;14:1052383.
[2] David A, Sternberg MJE. Protein structure-based evaluation of missense variants: resources, challenges and future directions. Curr Opin Struct Biol 2023;80:102600.
[3] Aoki E, Manabe N, Ohno S, Aoki T, Furukawa J, et al. Predicting the pathogenicity of missense variants based on protein instability to support diagnosis of patients with novel variants of ARSL. Mol Genet Metab Rep 2023;37:101016.
[4] Jumper J, Evans R, Pritzel A, Green T, Figurnov M, et al. Highly accurate protein structure prediction with AlphaFold. Nature 2021;596:583–9.
[5] Varadi M, Anyango S, Deshpande M, Nair S, Natassia C, et al. AlphaFold protein structure database: massively expanding the structural coverage of protein-sequence space with high-accuracy models. Nucleic Acids Res 2022;50:D439–44.
[6] Landrum MJ, Chitipiralla S, Brown GR, Chen C, Gu B, et al. ClinVar: improvements to accessing data. Nucleic Acids Res 2020;48:D835–44.
[7] Alirezaie N, Kernohan KD, Hartley T, Majewski J, Hocking TD. ClinPred: prediction tool to identify disease-relevant nonsynonymous single-nucleotide variants. Am J Hum Genet 2018;103:474–83.
[8] Ioannidis NM, Rothstein JH, Pejaver V, Middha S, McDonnell SK, et al. REVEL: an ensemble method for predicting the pathogenicity of rare missense variants. Am J Hum Genet 2016;99:877–85.
[9] Andrade F, Aldamiz-Echevarria L, Llarena M, Couce ML. Sanfilippo syndrome: overall review. Pedia Int 2015;57:331–8.
[10] Cheng J, Novati G, Pan J, Bycroft C, Zemgulyte A, et al. Accurate proteome-wide missense variant effect prediction with AlphaMissense. Science 2023;381:eadg7492.
[11] Rentzsch P, Witten D, Cooper GM, Shendure J, Kircher M. CADD: predicting the deleteriousness of variants throughout the human genome. Nucleic Acids Res 2019;47:D886–94.
[12] UniProt Consortium. UniProt: the universal protein knowledgebase in 2023. Nucleic Acids Res 2023;51:D523–31.
[13] Chen S, Francioli LC, Goodrich JK, Collins RL, Kanai M, et al. A genomic mutational constraint map using variation in 76,156 human genomes. Nature 2024;625:92–100.
[14] Mitsuhashi N, Toyo-oka L, Katayama T, Kawashima M, Kawashima S, et al. TogoVar: a comprehensive Japanese genetic variation database. Hum Genome Var 2022;9:44.
[15] Schubach M, Maass T, Nazaretyan L, Röner S, Kircher M. CADD v1.7: using protein language models, regulatory CNNs and other nucleotide-level scores to improve genome-wide variant predictions. Nucleic Acids Res 2024;52:D1143–54.
[16] Miller S, Janin J, Lesk AM, Chothia C. Interior and surface of monomeric proteins. J Mol Biol 1987;196:641–56.
[17] Sato T, Sato M, Kiyohara K, Sogabe M, Shikanai T, et al. Molecular cloning and characterization of a novel human β1,3-glucosyltransferase, which is localized at the endoplasmic reticulum and glucosylates *O*-linked fucosylglycan on thrombospondin type 1 repeat domain. Glycobiology 2006;16:1194–206.
[18] Boado RJ, Lu JZ, Hui EK, Pardridge WM. Reduction in brain heparan sulfate with systemic administration of an IgG Trojan Horse-sulfamidase fusion protein in the mucopolysaccharidosis type IIIA mouse. Mol Pharm 2018;15:602–8.
[19] Karpova EA, Voznyi YaV, Keulemans JL, Hoogeveen AT, Winchester B, et al. A fluorimetric enzyme assay for the diagnosis of Sanfilippo disease type A (MPS IIIA). J Inherit Metab Dis 1996;19:278–85.
[20] Wilson CJ, Choy WY, Karttunen M. AlphaFold2: a role for disordered protein/region prediction? Int J Mol Sci 2022;23:4591.
[21] Guo HB, Perminov A, Bekele S, Kedziora G, Farajollahi S, et al. AlphaFold2 models indicate that protein sequence determines both structure and dynamics. Sci Rep 2022;12:10696.
[22] Akdel M, Pires DEV, Pardo EP, Janes J, Zalevsky AO, et al. A structural biology community assessment of AlphaFold2 applications. Nat Struct Mol Biol 2022;29:1056–67.
[23] Bomba L, Walter K, Soranzo N. The impact of rare and low-frequency genetic variants in common disease. Genome Biol 2017;18:77.
[24] Duzkale H, Shen J, McLaughlin H, Alfares A, Kelly MA, et al. A systematic approach to assessing the clinical significance of genetic variants. Clin Genet 2013;84:453–63.
[25] de Beer TA, Laskowski RA, Parks SL, Sipos B, Goldman N, et al. Amino acid changes in disease-associated variants differ radically from variants observed in the 1000 genomes project dataset. PLoS Comput Biol 2013;9:e1003382.
[26] Iqbal S, Pérez-Palma E, Jespersen JB, May P, Hoksza D, et al. Comprehensive characterization of amino acid positions in protein structures reveals molecular effect of missense variants. Proc Natl Acad Sci USA 2020;117:28201–11.
[27] Scheller R, Stein A, Nielsen SV, Marin FI, Gerdes AM, et al. Toward mechanistic models for genotype-phenotype correlations in phenylketonuria using protein stability calculations. Hum Mutat 2019;40:444–57.
[28] Abildgaard AB, Stein A, Nielsen SV, Schultz-Knudsen K, Papaleo E, et al. Computational and cellular studies reveal structural destabilization and degradation of MLH1 variants in Lynch syndrome. eLife 2019;8:e49138.
[29] Nielsen SV, Stein A, Dinitzen AB, Papaleo E, Tatham MH, et al. Predicting the impact of Lynch syndrome-causing missense mutations from structural calculations. PLoS Genet 2017;13:e1006739.
[30] Buonfiglio PI, Bruque CD, Lotersztein V, Luce L, Giliberto F, et al. Predicting pathogenicity for novel hearing loss mutations based on genetic and protein structure approaches. Sci Rep 2022;12:301.
[31] Mahalanobis PC. On the generalized distance in statistics. Proc Natl Inst Sci India 1936;2:49–55.
[32] Pejaver V, Byrne AB, Feng BJ, Pagel KA, Mooney SD, et al. Calibration of computational tools for missense variant pathogenicity classification and ClinGen recommendations for PP3/BP4 criteria. Am J Hum Genet 2022;109:2163–77.
[33] Kircher M, Witten DM, Jain P, O'Roak BJ, Cooper GM, et al. A general framework for estimating the relative pathogenicity of human genetic variants. Nat Genet 2014;46:310–5.
[34] Sidhu NS, Schreiber K, Propper K, Becker S, Uson I, et al. Structure of sulfamidase provides insight into the molecular pathology of mucopolysaccharidosis IIIA. Acta Crystallogr D Biol Crystallogr 2014;70:1321–35.
[35] Vestweber D, Schatz G. Point mutations destabilizing a precursor protein enhance its post-translational import into mitochondria. EMBO J 1988;7:1147–51.
[36] Franco ML, Melero C, Sarasola E, Acebo P, Luque A, et al. Mutations in TrkA causing congenital insensitivity to pain with Anhidrosis (CIPA) induce misfolding, aggregation, and mutation-dependent neurodegeneration by dysfunction of the autophagic flux. J Biol Chem 2016;291:21363–74.
[37] Caswell RC, Gunning AC, Owens MM, Ellard S, Wright CF. Assessing the clinical utility of protein structural analysis in genomic variant classification: experiences from a diagnostic laboratory. Genome Med 2022;14:77.
[38] Pollard LM, Jones JR, Wood TC. Molecular characterization of 355 mucopolysaccharidosis patients reveals 104 novel mutations. J Inherit Metab Dis 2013;36:179–87.
[39] Lee-Chen GJ, Lin SP, Ko MH, Chuang CK, Chen CP, et al. Identification and characterization of mutations underlying Sanfilippo syndrome type A (mucopolysaccharidosis type IIIA). Clin Genet 2002;61:192–7.
[40] Blanch L, Weber B, Guo XH, Scott HS, Hopwood JJ. Molecular defects in Sanfilippo syndrome type A. Hum Mol Genet 1997;6:787–91.

[41] Weber B, Guo XH, Wraith JE, Cooper A, Kleijer WJ, et al. Novel mutations in Sanfilippo A syndrome: implications for enzyme function. Hum Mol Genet 1997;6:1573–9.
[42] Bunge S, Ince H, Steglich C, Kleijer WJ, Beck M, et al. Identification of 16 sulfamidase gene mutations including the common R74C in patients with mucopolysaccharidosis type IIIA (Sanfilippo A). Hum Mutat 1997;10:479–85.
[43] Wen Z, Cheng TL, Yin DZ, Sun SB, Wang Z, et al. Identification of the genetic cause for childhood disintegrative disorder by whole-exome sequencing. Neurosci Bull 2017;33:251–4.
[44] Muschol N, Storch S, Ballhausen D, Beesley C, Westermann JC, et al. Transport, enzymatic activity, and stability of mutant sulfamidase (SGSH) identified in patients with mucopolysaccharidosis type III A. Hum Mutat 2004;23:559–66.
[45] Beesley CE, Young EP, Vellodi A, Winchester BG. Mutational analysis of Sanfilippo syndrome type A (MPS IIIA): identification of 13 novel mutations. J Med Genet 2000;37:704–7.
[46] Knottnerus SJG, Nijmeijer SCM, L IJ, Te Brinke H, van Vlies N, et al. Prediction of phenotypic severity in mucopolysaccharidosis type IIIA. Ann Neurol 2017;82:686–96.
[47] Piotrowska E, Jakóbkiewicz-Banecka J, Tylki-Szymańska A, Czartoryska B, Węgrzyn A, et al. Correlation between severity of mucopolysaccharidoses and combination of the residual enzyme activity and efficiency of glycosaminoglycan synthesis. Acta Paediatr 2009;98:743–9.
[48] Bekri S, Armana G, De Ricaud D, Osenda M, Maire I, et al. Early diagnosis of mucopolysaccharidosis III A with a nonsense mutation and two *de novo* missense mutations in *SGSH* gene. J Inherit Metab Dis 2005;28:601–2.
[49] Miyazaki T, Masuda N, Waragai M, Motoyoshi Y, Kurokawa K, et al. An adult Japanese Sanfilippo A patient with novel compound heterozygous S347F and D444G mutations in the sulphamidase gene. J Neurol Neurosurg Psychiatry 2002;73:777–8.
[50] Di Natale P, Balzano N, Esposito S, Villani GR. Identification of molecular defects in Italian Sanfilippo A patients including 13 novel mutations. Hum Mutat 1998;11:313–20.
[51] Valstar MJ, Neijs S, Bruggenwirth HT, Olmer R, Ruijter GJ, et al. Mucopolysaccharidosis type IIIA: clinical spectrum and genotype-phenotype correlations. Ann Neurol 2010;68:876–87.
[52] Meyer A, Kossow K, Gal A, Steglich C, Mühlhausen C, et al. The mutation p.Ser298Pro in the sulphamidase gene (*SGSH*) is associated with a slowly progressive clinical phenotype in mucopolysaccharidosis type IIIA (Sanfilippo A syndrome). Hum Mutat 2008;29:770.
[53] Di Natale P, Pontarelli G, Villani GR, Di Domenico C. Gene symbol: SGSH. Disease: Sanfilippo type A syndrome, mucopolysaccharidosis IIIA. Hum Genet 2006;119:679.

BBA - General Subjects 1869 (2025) 130730

Contents lists available at ScienceDirect

BBA - General Subjects

journal homepage: www.elsevier.com/locate/bbagen

# 3D structural insights into the effect of *N*-glycosylation in human chitotriosidase variant G102S

Xiao Xu [a], Noriyoshi Manabe [a], Shiho Ohno [a], Sachiko Komatsu [b], Tsutomu Fujimura [b], Yoshiki Yamaguchi [a,*]

[a] *Division of Structural Glycobiology, Institute of Molecular Biomembrane and Glycobiology, Tohoku Medical and Pharmaceutical University, 4-4-1 Komatsushima, Aoba-ku, Sendai 981-8558, Miyagi, Japan*
[b] *Division of Bioanalytical Chemistry, Tohoku Medical and Pharmaceutical University, 4-4-1 Komatsushima, Aoba-ku, Sendai 981-8558, Miyagi, Japan*

ARTICLE INFO

*Keywords:*
Chitotriosidase-1 (CHIT1)
*N*-glycosylation
G102S variant
Enzymatic activity
Structural analysis
Molecular dynamics simulations

ABSTRACT

*Background:* *N*-glycosylation is a key post-translational modification critical for protein function and stability. Chitotriosidase-1 (CHIT1), belonging to glycoside hydrolase family 18, is clinically utilized as a biomarker of Gaucher disease. A G102S variant is common in some populations, but the implications of this missense mutation on CHIT1 function and in disease pathology are unknown. We have investigated the effects of the G102S mutation on the *N*-glycosylation, structure, and activity of CHIT1.
*Methods:* Three recombinant CHIT1 proteins, wild-type (WT), G102S, and N100Q+G102S double mutants, were expressed, purified, and analyzed for glycosylation using SDS-PAGE, MALDI-MS, PNGase F treatment, and lectin blotting. NMR and LC-MS/MS were employed to characterize glycan structures. Enzymatic assays and molecular dynamics simulations were used to assess the effects of mutations on CHIT1 function and dynamics.
*Results:* The G102S mutation introduced a new *N*-glycosylation site at N100, confirmed by SDS-PAGE and MALDI-MS, and the composition of the *N*-glycan structures was verified by lectin blotting, NMR, and MS. Both G102S and N100Q+G102S proteins exhibited reduced catalytic efficiency compared to WT. Molecular dynamics simulations suggested that G102S mutation induces significant structural changes and reduces stability, particularly without *N*-glycan, likely impairing substrate binding and enzymatic activity.
*Conclusion:* Our findings indicate that the common G102S mutation affects the structure and function of CHIT1, partially by introducing a new *N*-glycosylation site. They provide a foundation for further research on the impact of *N*-glycosylation on its hydrolase activity and structural dynamics, with potential implications for understanding the role of CHIT1 in Gaucher disease.

## 1. Introduction

*N*-glycosylation is one of the most common post-translational modifications of proteins, profoundly influencing their biological functions, including protein folding, cellular localization, and turnover [1–7]. In particular, the gain or loss of *N*-glycosylation sites due to the respective presence or absence of the Asn-X-Ser/Thr sequon has attracted much attention [5,8], because changes in *N*-glycosylation may affect protein function, localization, and stability, and are closely correlated with the development of diseases [9–11].

Previous studies have substantiated the notion that glycosylation exerts a considerable influence on the catalytic activity of certain proteases. Glycans have been demonstrated to alter substrate recognition, specificity, binding affinity, and turnover rates [12–14]. However, glycosylation has been observed to both enhance and inhibit enzyme activity [15–17], with no discernible pattern in the underlying mechanisms. For instance, Nelboeck et al. observed that single mutations of the glycosylated Asn632 and Asn651 in the metalloprotease endothelin-converting enzyme had no effect, whereas the double mutation resulted in complete inactivation [18]. Further exploration is required to elucidate the mechanisms by which glycosylation affects enzyme activity.

Chitotriosidase-1 (CHIT1) is a 50-kDa protein belonging to glycosyl hydrolase family 18. It comprises a chitin-binding domain, a hinge region, and a 39-kDa catalytic domain responsible for the hydrolysis of chitin [19,20]. The enzyme is secreted into the bloodstream as a 50-kDa

* Corresponding author.
*E-mail address:* yyoshiki@tohoku-mpu.ac.jp (Y. Yamaguchi).

https://doi.org/10.1016/j.bbagen.2024.130730
Received 9 September 2024; Received in revised form 1 November 2024; Accepted 1 November 2024
Available online 8 November 2024
0304-4165/© 2024 Elsevier B.V. All rights are reserved, including those for text and data mining, AI training, and similar technologies.

protein [21], and elevated plasma chitotriosidase activity has been observed in several lysosomal and non-lysosomal diseases [22–24]. Together with the crystal structure, binding experiments of CHIT1 have revealed that its active site can accommodate long-chain chitin polymers, thereby demonstrating characteristics of an endochitinase [25]. Notably, a common polymorphism has been identified in the *CHIT1* gene, namely the G102S variant in which a glycine residue at position 102 is replaced by serine. Data from the gnomAD database and ToMMo jMorp indicate that the allele frequency of this variant is approximately 30 % [26,27]. The widespread nature of the G102S variant across different populations suggests that it may possess biological significance.

Gaucher disease (MIM 230800) is a recessive genetic disorder caused by the accumulation of glucosylceramide in the lysosomes of macrophages due to a deficiency of lysosomal glucocerebrosidase (MIM 606463, EC 3.2.1.45) [28]. In clinical practice, the activity of CHIT1 in plasma is commonly utilized to indicate the presence of lipid-laden macrophages in patients with Gaucher disease, because CHIT1 is secreted by activated macrophages. The enzyme activity of CHIT1 is typically measured using fluorescent substrates such as 4-methylumbelliferyl-chitobiose (4MU-chitobiose) or 4MU-chitotriose. Notably, CHIT1 activity is increased by an average of 600-fold in the plasma of symptomatic patients as compared with healthy individuals [29]. As a result, plasma CHIT1 activity has proven invaluable for monitoring the severity of Gaucher disease and the efficacy of therapeutic treatment [30–33]. Interestingly, studies have shown that, relative to wild-type CHIT1, the G102S variant exhibits reduced catalytic efficiency towards 4MU-chitotriose [34]. Thus, the structure–function relationship of CHIT1 is a crucial aspect in both fundamental scientific inquiry and the development of disease biomarkers.

While many studies have explored the impact of *N*-glycosylation on protein function, knowledge on the effects of gain and loss of *N*-glycosylation in missense variants remains limited. In this study, we have examined the impact of the G102S missense mutation of CHIT1 on the enzyme's structure and activity. In addition, we have explored the glycosylation patterns present in the wild type (WT) and G102S variants by NMR and LC–MS/MS and used molecular dynamics (MD) simulations to determine how substrate binding is altered by the G102S mutation.

## 2. Materials and methods

### 2.1. Construction of plasmids

The amino acid sequence of human chitotriosidase-1 (CHIT1) was obtained from the UniProt database (Q13231). The insert DNAs were codon-optimized for mammalian expression and chemically synthesized by Thermo Fisher Scientific Inc. Genes encoding human CHIT1 (22–466) containing an N-terminal IL-2 signal sequence (1−21) and a C-terminal 8 × His tag, were cloned into a pcDNA3.4 mammalian expression vector (Thermo Fisher Scientific).

### 2.2. Protein expression and purification

Expi293F cells were cultured in Expi293 Expression Medium (Gibco) in an incubator set at 37 °C and 8 % $CO_2$ with shaking. Plasmids encoding CHIT1 were transiently transfected into Expi293F or Expi293F-GnT-I (−) cells using ExpiFectamine 293 Transfection Reagent and Enhancer (Gibco). For $^{13}$C-labeling of the glycans, the cells were cultured in medium containing [$^{13}C_6$] D-glucose (CIL). Transfection was performed using the Gxpress 293 Transfection & Medium Kit (Gmep, Japan) in accordance with the manufacturer's instructions. Seven days after transfection, the supernatant was collected by centrifugation at 2000 ×*g* for 30 min and applied to an Ni Sepharose™ 6 Fast Flow column (Cytiva Inc.). The column was washed with phosphate-buffered saline (PBS), and the bound proteins were eluted with PBS containing imidazole (400 mM). To remove imidazole, the eluted proteins were repeatedly concentrated using a 30-kDa molecular weight cut-off Amicon centrifugal filter (Millipore, Ireland) at 4 °C and re-diluted with PBS. The protein was checked by SDS-PAGE using a 10 % polyacrylamide gel. Prior to electrophoresis, the protein samples were mixed with a reducing loading buffer (10 mM dithiothreitol) and heated in a metal bath for 5 min. The gels were stained with Coomassie Brilliant Blue (CBB) for 1 h and washed with milli-Q water.

### 2.3. MALDI-TOF MS

The CHIT1 proteins were dialyzed against 20 mM ammonium bicarbonate buffer (pH 7.6) and freeze-dried. Subsequently, each protein was dissolved in ultrapure water to a concentration of approximately 20 pmol/μL. A 0.5-μL sample was spotted on the MALDI plate and mixed with 0.5 μL of matrix solution (ferulic acid). The dried spot was analyzed with a MALDI-TOF mass spectrometer (AXIMA-Performance, Shimadzu Corporation) operated in positive-ion mode using a nitrogen laser (λ = 337 nm). Masses were calibrated using bovine serum albumin (BSA; $[M+H]^+$ and $[M+2H]^{2+}$) as an external reference.

### 2.4. Deglycosylation with PNGase F

Non-denatured and denatured proteins were subjected to digestion with PNGase F (New England Biolabs) in accordance with the manufacturer's protocol. For denaturation, 10 μg of protein was mixed with 1 μL of glycoprotein denaturing buffer (10×) (0.5 % SDS, 40 mM DTT) and milliQ water to a total volume of 10 μL. The samples were boiled at 100 °C for 10 min and then cooled on ice for 10 s. A set of non-denatured proteins dissolved in PBS was also prepared. Subsequently, 2 μL of GlycoBuffer 2 (10×) (50 mM sodium phosphate, pH 7.5), 2 μL of 10 % NP-40, and 6 μL of $H_2O$ were added to each protein sample, followed by 1 μL of PNGase F. The samples were mixed gently, and then incubated at 37 °C for either 1 h (denatured samples) 8 h (non-denatured samples). SDS–PAGE was carried out, followed by CBB staining and western blotting.

### 2.5. Lectin blotting

Equal amounts of purified proteins were applied to SDS-PAGE. After electrophoresis, the proteins were transferred to a PVDF membrane (Millipore, USA) and blocked with 5 % BSA for 1 h. The membranes were then incubated overnight at 4 °C with a 1:10,000 dilution of the following biotinylated lectins (J-CHEMICAL, Inc): concanavalin A (ConA), *Phaseolus vulgaris* erythroagglutinin (PHA-E4), *Aleuria aurantia* lectin (AAL), *Sambucus sieboldiana* (SSA), *Maackia amurensis* (MAM), and Wheat germ agglutinin (WGA). A Vectastain ABC kit (Vector Laboratories, Burlingame, USA) was used to facilitate the binding of avidin to biotinylated horseradish peroxidase (HRP). The immunoreactive bands were also detected by using Immobilon® Forte Western HRP Substrate (Merck) in accordance with the manufacturer's instructions.

### 2.6. Removal of sialic acid with sialidase

CHIT1 protein samples were digested with *Arthrobacter ureafaciens* neuraminidase (sialidase) (Nacalai Tesque, Kyoto, Japan) to remove sialic acid. In brief, the reaction mixture was incubated at 37 °C for 24 h in the presence of 1 unit/mL of sialidase. Asialo-CHIT1 protein was purified by an Ni affinity column as described in Section 2.2.

### 2.7. NMR spectroscopy

All nuclear magnetic resonance (NMR) experiments were conducted on an 800-MHz spectrometer equipped with a cryogenic triple resonance probe (Bruker). The probe temperature was set to 308 K. The CHIT1 samples were dissolved in 20 mM sodium phosphate (pH 7.4) containing 100 mM NaCl in $D_2O$ (D: 99.96 %). Two-dimensional

$^{1}H$—$^{13}C$ heteronuclear multiple quantum coherence (HMQC) spectra were recorded with 128 scans. $^{1}H$ and $^{13}C$ chemical shifts were expressed in ppm and calibrated at 0 ppm using an internal reference, 4,4-dimethyl-4-silapentane-1-sulfonic acid. Spectral display, data processing, and spectral measurements were performed using TopSpin Version 4 (Bruker).

### 2.8. Trypsin digestion and reverse-phase HPLC separation

The CHIT1 samples were dissolved at a concentration of 0.5 mg/mL in 500 mM Tris-HCl (pH 8.0) containing 8 M urea and incubated with 5 mg/mL DTT for 90 min at 37 °C. Subsequently, alkylation was performed with 40 mg/mL of iodoacetamide for 30 min. The solution was then dialyzed against 20 mM ammonium bicarbonate (pH 7.6). The samples were digested with Mono-Spin Trypsin (GL Sciences) in accordance with the manufacturer's protocol.

After digestion, the reaction mixture was lyophilized and dissolved in 0.1 % (*v*/v) TFA. The solution was loaded onto a C18 reverse-phase column (COSMOSIL $5C_{18}$-AR, 4.6 × 250 mm, Nacalai Tesque, Japan) connected to an HPLC system (SCL-10Avp, Shimadzu, Japan) with mobile phases A [0.1 % (v/v) trifluoroacetic acid (TFA)/water] and B [0.1 % (v/v) TFA/water (containing 90 % (v/v) acetonitrile]. Elution followed a linear gradient of 0 %–90 % acetonitrile in 0.1 % TFA for 45 min. Absorbance was measured at 230 nm and 280 nm using a UV-VIS detector (SPD-10Avp, Shimadzu, Japan). Fractions were collected at 1-min intervals, lyophilized and subsequently subjected to LC-MS and LC-MS/MS analysis.

### 2.9. LC-MS and LC-MS/MS analysis

The peptide fractions were subject to LC-MS/MS analysis on an EASY-nLC 1200 HPLC, connected to a Q Exactive mass spectrometer equipped with a nanoelectrospray ion source (Thermo Fisher Scientific). The peptides were separated on a 75-μm inner diameter × 125 mm C18 reverse-phase column (Nikkyo Technos NTCC-360) using a linear gradient of 0 %–35 % acetonitrile with 0.1 % formic acid over 0–30 min, followed by a linear gradient of 35 %–95 % acetonitrile over 30–35 min. Lastly, 95 % acetonitrile was applied over 35–45 min. The mass spectrometer was operated in data-dependent acquisition mode, utilizing a top 10 MS/MS method. MS1 spectra were acquired at a resolution of 70,000, with an Automatic Gain Control (AGC) target of $3e^6$ and a mass range spanning 380–4000 *m/z*. Higher-energy C-trap dissociation [35] MS/MS spectra were acquired with a resolution of 17,500, an AGC target of $5e^5$, an isolation window of 1.6 *m/z*, a maximum injection time of 150 ms, and a normalized collision energy of 27. A 15-s dynamic exclusion period was implemented. In addition, LC-MS (full MS) analysis was conducted under the same conditions to measure the intensity of each ion peak.

The raw LC-MS/MS data obtained from the Q Exactive mass spectrometer were analyzed using Proteome Discoverer version 3.0 SP1 software (Thermo Fisher Scientific). The software identified and quantified the peptides in the raw data by searching the UniProt-SwissProt database (release 2024_03) using only entries for *Homo sapiens*. The following search parameters were employed: the enzyme was set as trypsin, with allowance for up to two missed cleavages; the precursor mass tolerance was 6 ppm and the fragment mass tolerance was 20 ppm; lastly, carbamidomethylation of cysteine was designated as a fixed modification, and methionine oxidation and serine/threonine phosphorylation as variable modifications.

Glycopeptides were identified and quantified using Byonic™ (Protein Metrics) [36]. The Byonic™ stand-alone software was used without employing the Proteome Discoverer mode. Peptides were filtered on the basis of a false discovery rate of 1 %, thereby ensuring that the probability of a peptide being a false positive identification was less than 1 %. The Byonic Glycopeptide Search was then applied to the MS/MS data to identify glycopeptides in reference to the internal table of *N*-linked and *O*-linked glycans. Byonic scores exceeding 500 and 300 were considered for the *N*-linked and *O*-linked glycopeptides, respectively. The Symbol Nomenclature for Glycans was used to display glycans [37].

### 2.10. Enzyme assay

Proteins were treated with the fluorogenic substrates 4-methylumbelliferyl (4MU) *N*,*N*′,*N*′′-triacetyl-β-D-chitotrioside (Carbosynth, USA) and 4MU-chitobioside (Sigma, USA). To individual wells of a black 96-microwell plate (Thermo Fisher Scientific, USA), 10 μL of 1 mM substrate, 5 μL of protein solution (diluted appropriately), and 85 μL of 10 mM sodium phosphate buffer as a diluent (pH 5.2) were added. After a reaction time of 0, 10, 20, 30, or 60 min, 100 μL of 100 mM glycine-NaOH (pH 10) was applied as a stop solution. Fluorescence spectra were recorded at an excitation wavelength of 365 nm, and emission wavelength of 445 nm using a SpectraMax iD5 multi-mode microplate reader (Molecular Devices, USA). The mean values of three independent experiments were calculated.

### 2.11. Molecular dynamics simulations

The 3D structural model of human CHIT1 was obtained from AlphaFold database (AF-Q13231-F1) [38,39] and the N-terminal region (residues 1–21) was removed using Discovery Studio 2021 software to obtain CHIT1 (residues 22–388). The 3D models of the mutant proteins were constructed using the "Solution Builder" protocol of CHARMM-GUI [40]. $Man_3GlcNAc_2$ glycan was added to the N100 side chain of CHIT1 according to the CHARMM force field [41]. Hydrogens and explicit water molecules were generated. The 3D protein structure was then visualized using PyMOL software (Schrödinger, LLC). CHARMM-GUI was also used to build a 3D model of the free $Man_3GlcNAc_2$ glycan attached to N100.

The MD simulations were performed using GENESIS 1.7.0 [42,43] with a simulation time of 100 ns. The root mean square deviation (RMSD) of all atoms in the protein and the radius of gyration (RG) were calculated using GENESIS software. Hydrogen bonds were defined on the basis of the following criteria: (1) the donor and acceptor oxygens were within 3.4 Å; (2) the angle (donor hydrogen–donor oxygen–acceptor oxygen) was within 30°; and (3) the angle (donor oxygen–donor hydrogen–acceptor oxygen) was greater than 120°. For the Ramachandran plots, φ was defined by the torsion angle formed by C(i-1)-N(i)-Cα(i)-C(i), and ψ as that formed by N(i)-Cα(i)-C(i)-N(i + 1). For the N100 side chain dihedral angle, $\chi_1$ was defined as the torsion angle formed by N(i)-Cα(i)-Cβ(i)-Cγ(i), and $\chi_2$ as that formed by Cα(i)-Cβ(i)-Cγ(i)-Nδ2(i). For the *N*-glycan dihedral angle, φ was defined as the torsion angle formed by O5(i)-C1(i)-O4(i-1)-C4(i-1) for the β1–4 linkage, ψ as that formed by C1(i)-O4(i-1)-C4(i-1)-C3(i-1) for the β1–4 linkage, and ω as that formed by O6(i-1)-C6(i-1)-C5(i-1)-O5(i-1) for the α1–6 linkage.

### 2.12. Molecular docking simulations

According to the crystal structure of CHIT1 bound to chitobiose containing two GlcNAc units (PDB ID: 4WKF) [44], chitotriose was built by using CHARMM-GUI to add a β(1–4)GlcNAc to the non-reducing end of chitobiose, and to add an *N*-glycan ($Man_3GlcNAc_2$) to the G102S variant protein. The docking structure was visualized in PyMOL.

## 3. Results and discussion

### 3.1. The CHIT1 G102S variant contains a new N-glycosylation site

To probe the structure–function of the CHIT1 variant, we first prepared three plasmids encoding the wild-type enzyme (WT), the G102S variant, and an artificial N100Q+G102S double mutant designed to remove the *N*-glycosylation site in the G102S variant (Fig. 1A). We considered that the N-to-Q mutation would be suitable for evaluating

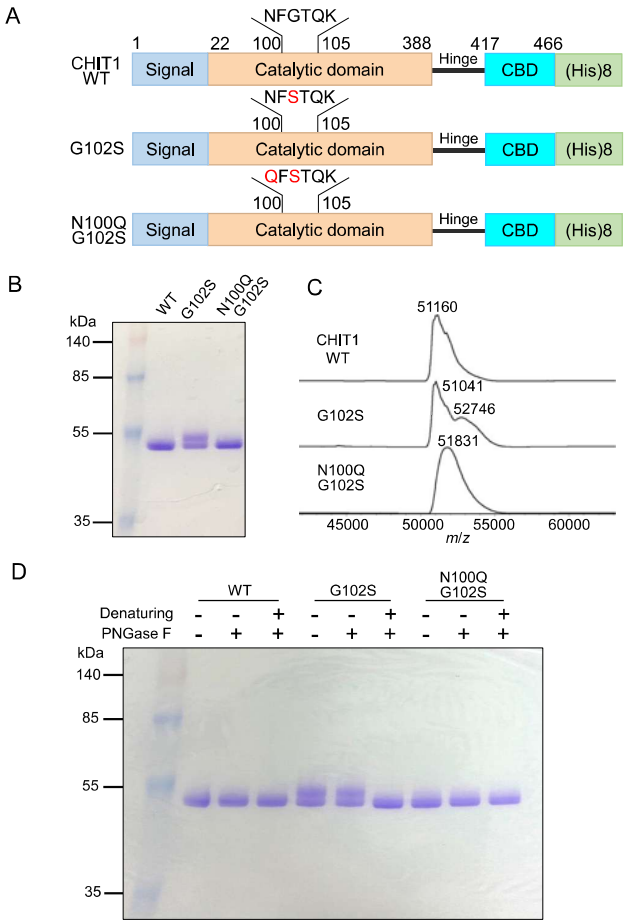


**Fig. 1.** Recombinant expression of CHIT1 in Expi293F cells and validation. (A) Constructs of the three CHIT1 proteins (WT, G102S and N100Q+G102S). Signal, secretion signal sequence from IL-2; CBD, carbohydrate (chitin) binding domain; (His)8, octa-histidine tag. (B) SDS-PAGE analysis of WT, G102S and N100Q+G102S purified from Expi293F cells. (C) MALDI-MS spectra of WT, G102S and N100Q+G102S. (D) SDS-PAGE analysis of WT, G102S and N100Q+G102S after PNGase F treatment under denaturing and non-denaturing conditions. In (B,D), protein bands were stained with CBB.

the role of *N*-glycan in a site-specific manner, but acknowledge that the substitution itself, although conservative, might have an effect.

Initial characterization of the three proteins by SDS-PAGE under denaturing conditions showed that the WT and N100Q+G102S proteins exhibited a single band at 50–55 kDa, whereas the G102S protein displayed two bands (Fig. 1B). The higher molecular weight band of G102S is likely to be the *N*-glycosylated protein, whereas the lower band is likely to be a non-glycosylated or partially glycosylated protein. Similarly, two peaks were observed for the G102S protein in MALDI-TOF, whereas WT and N100Q+G102S exhibited a single peak (Fig. 1C). The mass difference between the two peaks of G102S was 1705 Da, which may correspond to the mass of one *N*-glycan; however, the mass is likely to be an average because the *N*-glycan structure attached to G102S may not be homogeneous.

We further probed the *N*-glycans on the three proteins by treatment with PNGase F, followed by SDS-PAGE analysis. Under denaturing conditions, treatment with PNGase F led to disappearance of the higher molecular weight band of G102S, resulting in a single band (Fig. 1D). We concluded that the higher molecular weight band of G102S contains an *N*-glycan, while WT, N100Q+G102S, and the lower molecular weight band of G102S lack *N*-glycans.

Next, we analyzed the structure of the *N*-glycan in G102S by lectin blotting (Fig. 2). The higher molecular weight band of G102S showed signals with ConA, PHA-E4, AAL, SSA, WGA and MAM, indicating the presence of high-mannose and complex-type *N*-glycans, possibly modified with bisecting GlcNAc, fucose and sialic acid. By contrast, WT, N100Q+G102S, and the lower molecular weight band of G102S showed signals with only WGA and MAM. Notably, signals were detected with WGA and MAM, even after PNGase F treatment. This observation suggested that *O*-glycosylation is present in all three proteins; therefore, we examined *O*-glycosylation, in addition to *N*-glycosylation, in the following experiments.

### 3.2. NMR and mass spectrometry analysis of recombinant CHIT1

To gain further insight into the structure of *N*- and *O*-glycans attached to WT and G102S CHIT1, the recombinant proteins were expressed in medium containing [$^{13}C_6$]D-glucose, allowing for incorporation of $^{13}C$ into the *N*-glycans. The $^{13}C$-labeled proteins were then subjected to NMR analysis and 2D $^{1}H$-$^{13}C$ HMQC measurements (Fig. 3). The observation of characteristic signals in the carbohydrate region ($^{13}C$ anomeric signals at 95–110 ppm and non-anomeric signals at 50–80 ppm) verified that $^{13}C$ was enriched in the *N*-glycans and *O*-glycans attached to the proteins. In the case of WT, which lacks *N*-glycosylation sites, weak but discernible signals were observed in the 95–110 ppm region characteristic of glycans (Fig. 3A), corroborating the lectin blotting results indicating that WT contains *O*-glycans.

In the case of the G102S, several anomeric and non-anomeric signals were observed with high intensity (Fig. 3B), suggesting that *N*-glycans

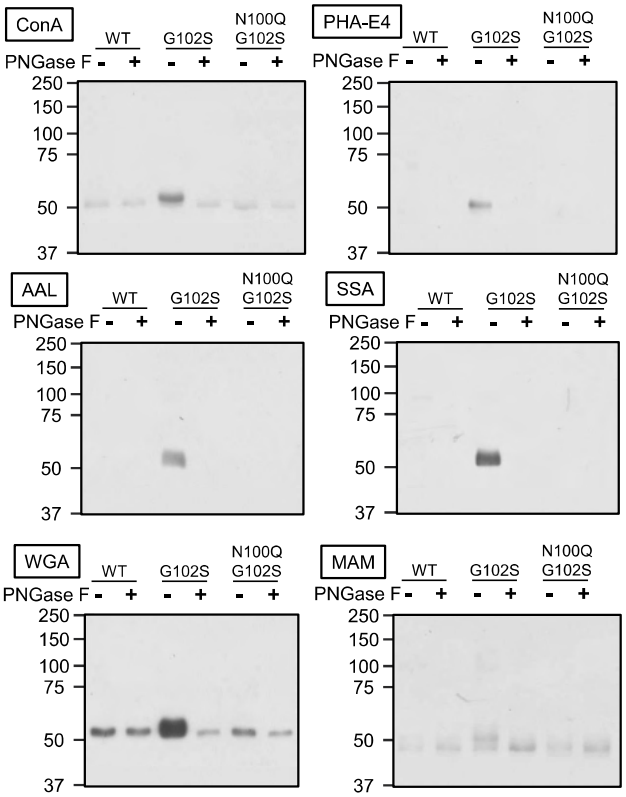


**Fig. 2.** Lectin blotting of CHIT1 proteins.
Shown are the lectin blotting results of WT, G102S and N100Q+G102S without and with PNGase F treatment under denaturing conditions. Glycans were detected by ConA (high mannose), PHA-E4 (bisecting GlcNAc), AAL (fucose), SSA (α2–6 sialic acid), WGA (GlcNAc and sialic acid) and MAM (for α2–3 sialic acid).

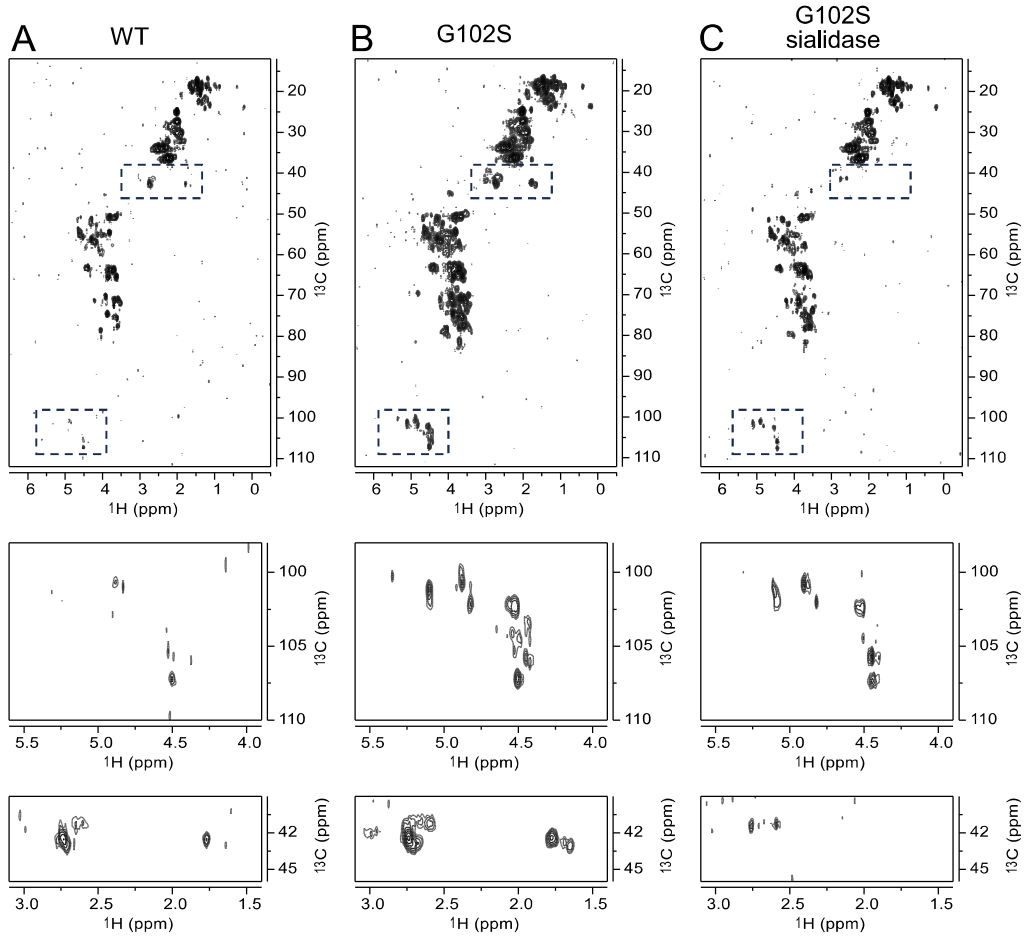


**Fig. 3.** NMR analysis of $^{13}$C-labeled CHIT1 proteins.
(Top panel) 2D $^{1}$H–$^{13}$C HMQC spectra of $^{13}$C-labeled WT (A), G102S (B) and G102S after sialidase treatment (C) at the $^{1}$H observation frequency of 800 MHz. (Middle panel) Anomeric signals ($^{13}$C signals at 95–110 ppm and $^{1}$H signals at 3.9–5.6 ppm), corresponding to the fingerprint region of attached glycans, extracted from $^{1}$H-$^{13}$C HMQC spectra. (Bottom panel) C3-H3 signals ($^{13}$C signals, 39–45 ppm; $^{1}$H signals, 1.4–3.1 ppm), which are characteristic methylene signals of Neu5Ac, extracted from $^{1}$H-$^{13}$C HMQC spectra.

with significant heterogeneity were present. In addition, *N*-acetylneuraminic acid (Neu5Ac) C3-H3(axial) and C3-H3(equatorial) methylene signals ($^{13}$C at 39–45 ppm, $^{1}$H at 1.4–3.1 ppm) were observed, indicating the presence of Neu5Ac in the G102S sample. Low-intensity Neu5Ac C3-H3 signals were also observed in WT. These observations indicated that Neu5Ac is present in the *N*-glycan of G102S and in the *O*-glycan of G102S and WT. To confirm that the signals in the Neu5Ac C3-H3 region were indeed originating from sialic acid residues, we treated the $^{13}$C-labeled G102S protein with *Arthrobacter ureafaciens* sialidase. As a result, the signals in the Neu5Ac C3-H3 region disappeared (Fig. 3C), confirming the presence of sialic acid in G102S.

To probe the *N*-glycan structure on G102S further, we expressed WT and G102S proteins with homogeneous $Man_5GlcNAc_2$ glycans using the Expi293F GnT-I (−) cell line, which lacks *N*-acetylglucosaminyltransferase I (GnT-I) activity (Supplementary Fig. 1). As expected, the 95–110 ppm region of the spectrum of GnT-I (−)-WT (Supplementary Fig. 1A) was similar to that of WT (Fig. 3A), because both proteins lack *N*-glycans and thus would be unaffected by the loss of GnT-I activity. In contrast, we postulated that the *N*-glycan structure of the G102S from the GnT-I(−) cells would predominantly comprise $Man_5GlcNAc_2$ glycans. As anticipated, the anomeric signals of G102S from GnT-I(−) cells were simplified relative to those of the G102S protein from Expi293 cells, which displayed a more intricate *N*-glycan structure with low intensity peaks of $Man_5GlcNAc_2$. Thus, there is a low abundance of the $Man_5GlcNAc_2$ glycan structure in the G102S expressed from Expi293 cells.

To determine the *N*-glycan structures introduced onto the G102S variant of CHIT1, we treated the protein with trypsin and analyzed the resulting peptides by LC–MS/MS. In reverse-phase HPLC, the peak eluting at 23–24 min was identified as glycopeptide [T92–K105] containing N100 (Fig. 4A), whereas the unglycosylated peptide [T92–K105] mainly eluted at 25–26 min (Fig. 4B). Using Byonic software with ion peak intensities read from LC-MS (full MS), we determined the different *N*-glycan structures present and their corresponding intensities (Supplementary Table S1). Analysis of the fragment ions derived from the glycopeptide TLLAIGGWNFGTQK revealed several characteristic ion peaks indicative of glycan modification. The y-series fragment ions indicated an additional modification (+203) commencing from y6, suggesting the presence of a HexNAc at the sixth position from the C-terminus (Asn100). A diagnostic HexNAc3Hex ion was also detected, indicating the presence of bisecting GlcNAc, consistent with the results of PHA-E4 lectin blotting (Fig. 2). The mass of the most abundant ion HexNAc5Hex3Fuc was 1667 Da, which was roughly consistent with the mass difference (1705 Da) between the two major peaks in the MALDI-MS data of the G102S protein.

While glycan structures cannot be definitely determined from the MS data alone, the composition data allowed us to consider the types of *N*-glycan present. Those at N100 were predominantly bi-tri antennary

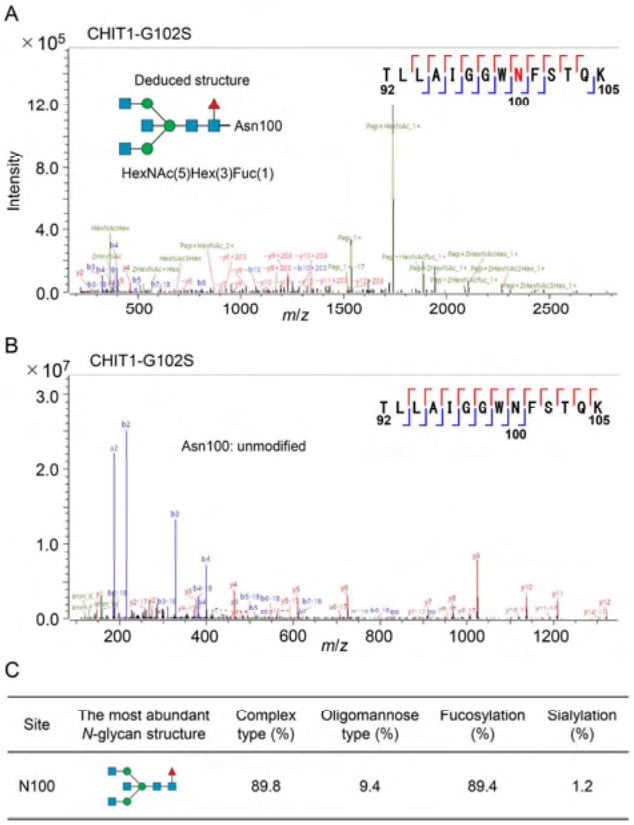


**Fig. 4.** LC–MS/MS analysis of recombinant CHIT1 G102S.
(A) LC-MS/MS spectrum of the glycopeptide [T92–K105] containing N100 with the assignment of fragment ions. (B) LC-MS/MS spectrum of the non-glycosylated peptide [T92–K105] containing N100. In (A,B), b and y ions are shown in blue and red, respectively; other fragment ions are shown in green. (C) Summary of the type of *N*-glycans attached to N100 of G102S. The *N*-glycans detected are listed in Supplementary Table S1. (For interpretation of the references to colour in this figure legend, the reader is referred to the web version of this article.)

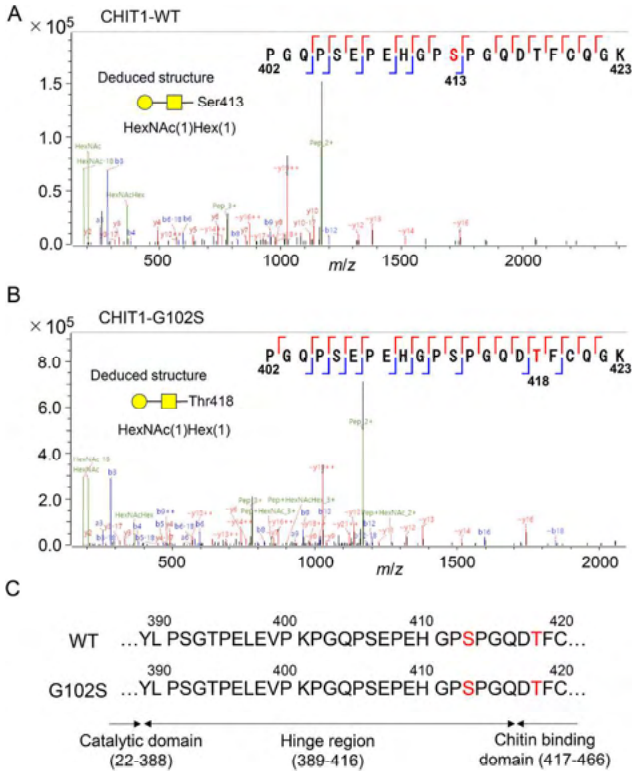


**Fig. 5.** LC-MS/MS analyses of *O*-glycopeptides derived from WT and G102S CHIT1.
LC-MS/MS spectra of the glycopeptide [P402–K423] of WT containing Ser413 (A) and the glycopeptide [P402–K423] of G102S containing Thr418 (B) are shown with assignment of fragment ions. (C) Amino acid sequences showing the main location of *O*-glycosylation sites in red. (For interpretation of the references to colour in this figure legend, the reader is referred to the web version of this article.)

complex types and mostly fucosylated (Fig. 4C), largely consistent with our lectin blotting data. Regarding sialylated glycans, however, there was a discrepancy between the NMR and LC-MS/MS data. In LC-MS/MS analysis, the amount of sialylated glycans was very low. By contrast, the significant differences between the NMR spectra of sialidase-treated and untreated G102S suggested the presence of substantial sialylated glycans. This discrepancy might be due to the low ionization efficiency and/or the frequent loss of sialic acid residues during post-ionization in conventional MS analysis of sialylated glycans and glycopeptides.

Previous studies have reported that CHIT1 protein may contain *O*-glycan [45]. In our study, both lectin blotting and NMR analyses indicated the possible presence of *O*-glycans in CHIT1. Next, therefore, we used LC–MS/MS to identify the main *O*-glycan structures and modification sites in the WT and G102S proteins (Fig. 5). In reverse-phase HPLC of WT, the peak eluting at 28–29 min contained the peptide sequence PGQPSEPEHGPSPGQDTFCQGK [P402–K423] with HexNAcHex *O*-glycosylation at S413, providing strong evidence of *O*-glycosylation in the WT CHIT1 protein. For the G102S variant, *O*-glycosylation primarily occurred at T418 within the same peptide segment, with the main *O*-glycan structure predicted to be HexNAcHex. Notably, the major *O*-glycosylation site was not identical in the two CHIT1 variants, indicating that the introduction of mutations may change the primary sites of *O*-glycosylation.

The immunoglobulin A (IgA) is also known to be *O*-glycosylated [46,47], and the extent of *O*-glycosylation seems to be associated with protein function and disease [48]. The *O*-glycosylation sites are primarily concentrated in the hinge region, which might be associated with the high structural flexibility of this region. In addition, several studies indicate that the *O*-glycan structure within the hinge region is not fixed [49–51]. Given the potential link between *O*-glycosylation of IgA and disease [48], the potential impact of *O*-glycans on CHIT1 protein stability warrants further investigation.

### 3.3. Mutation of CHIT1 affects enzyme activity

As mentioned above, the activity of CHIT1 in plasma is used to identify the presence of lipid-laden macrophages in patients with Gaucher disease. To determine whether the activity of the common variant G102 differs from that of WT, we measured the enzyme activity of the three CHIT1 proteins (WT, G102S, N100Q+G102S) using the fluorescent substrates 4MU-chitobiose and 4MU-chitotriose (Fig. 6). With both substrates, WT exhibited the highest enzymatic activity, followed by the G102S and then N100Q+G102S variants. Of note, the activity of G102S was considerably higher than that of the N100Q+G102S double mutant. It is possible that partial *N*-glycosylation in G102S may allow some activity based on intramolecular *N*-glycan–polypeptide interactions, although we need to consider the potential effect of the N-to-Q substitution on the catalytic site. Further investigation into the effects of these mutations is crucial for understanding the function of CHIT1 protein and its role in disease,

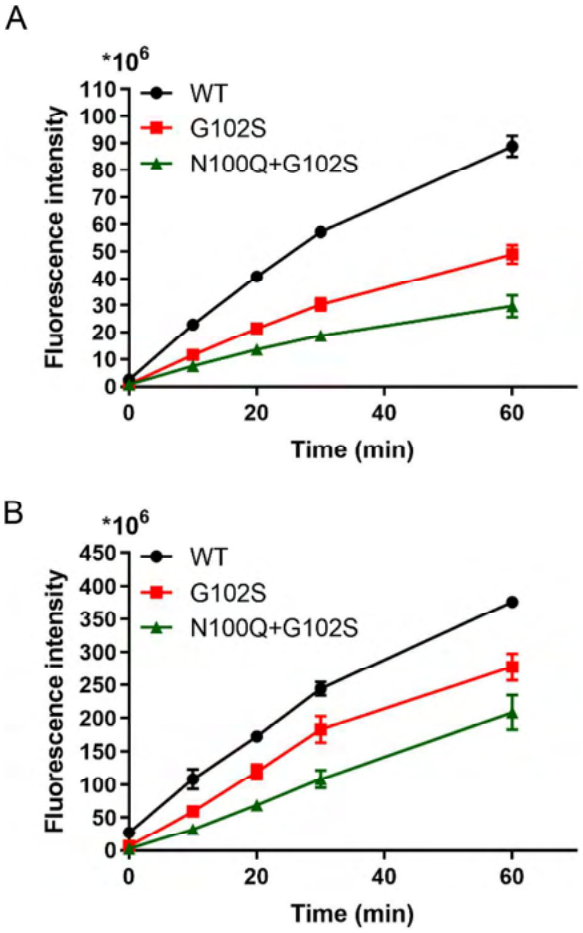


**Fig. 6.** The G102S mutation affects CHIT1 enzyme activity.
(A) Enzyme activity assay using 4MU-chitobiose as the substrate. (B) Enzyme activity assay using 4MU-chitotriose as the substrate. The excitation and emission wavelengths used for detection of released 4MU were 365 nm and 445 nm, respectively. Error bars represent the standard deviation from three independent experiments ($n = 3$).

particularly in the context of potential clinical applications and drug development strategies.

### 3.4. *Molecular dynamics simulations of the CHIT1 proteins*

The G102 residue that is mutated in the common variant and the substrate-binding site are both localized primarily within the catalytic domain of CHIT1. Next, therefore, we conducted MD simulations of the catalytic domain (residues 22–388) of the three CHIT1 variants with initial model building based on the corresponding AlphaFold model (Supplementary Fig. S2) [38,39]. Because our SDS-PAGE and mass analyses indicated partial *N*-glycosylation at N100 of G102S, we modeled scenarios with both *N*-glycosylated and non-glycosylated G102S proteins using the Glycan Modeler tool within CHARMM-GUI [40]. The G102S mutation in CHIT1 led to a new *N*-glycosylation site at N100 (Supplementary Fig. S2). Above, we found that the *N*-glycan structure was heterogenous (Supplementary Table S1); therefore, we used an *N*-glycan core structure ($Man_3GlcNAc_2$) in the MD simulation. All three proteins (WT, unglycosylated G102S and *N*-glycosylated G102S) showed almost constant RMSD values after 20 ns, suggesting that the MD simulation reached equilibrium at this time point (Supplementary Fig. S3A). The average RMSD values were 1.03 ± 0.11 Å, 1.38 ± 0.19 Å and 1.21 ± 0.13 Å for WT, unglycosylated G102S and *N*-glycosylated G102S, respectively. All proteins maintained similar and stable RG values, indicative of protein compactness (20.38 ± 0.06 Å, 20.46 ± 0.08 Å and 20.36 ± 0.07 Å, respectively) (Supplementary Fig. S3B), implying the proteins preserved a relatively compact 3D conformation throughout the simulation. Notably, unglycosylated G102S showed slightly higher RMSD and RG values relative to WT and *N*-glycosylated G102S, potentially indicating enhanced flexibility or slight relaxation in a specific region of G102S as compared with WT.

We superimposed 10 snapshots of WT, unglycosylated and *N*-glycosylated G102S, showing the overall structure (Fig. 7, left) and the N100–T103 region containing the mutation (Fig. 7, right). Whereas the 10 structures of WT almost all converged to a similar position, the 10 structures of unglycosylated G102S did not converge to the same position, indicating the presence of a more flexible region. Interestingly, the *N*-glycosylated G102S variant showed more convergence. It seems that the presence of *N*-glycans may be more conducive to stabilizing the protein conformation.

To investigate the effect of the G102S mutation and *N*-glycosylation on protein conformation and dynamics, we analyzed the main chain dihedral angles of the N100–T103 region using the MD simulation trajectory (Fig. 8). In WT, N100, F101 and T103 showed typical main chain dihedral angles with a small distribution. In contrast, G102 showed unusual dihedral angle distributions with $\varphi = 60°$ and $\psi = \pm 180°$; this irregular dihedral angle might due to the absence of side chain in Gly [52]. The main chain dihedral angles observed in MD simulations were similar to those in the crystal structure of CHIT1 including G102 (Fig. 8) [44]. Relative to WT, the main chain dihedral angles of F101 and S102 in unglycosylated and *N*-glycosylated G102S showed different dihedral angle distributions. Two conformations (major and minor) were found in F101 and S102 of unglycosylated and *N*-glycosylated G102S (Fig. 8), and the conformations changed at an early stage during the 100-ns simulation (Supplementary Fig. S4). The minor conformation of the S102 does not conform to the typical torsion angle distribution of serine in most structurally stable proteins [53]. We speculate that the initial structure of the G102S was not energetically favorable and the simulation rapidly induced G102S to adopt a stable conformation.

We then examined the conformation of the N100 side chain (Supplementary Fig. S5). As compared with WT, the N100 side chain unglycosylated G102S fluctuated more. In contrast, the fluctuation of the N100 side chain was limited in *N*-glycosylated G120S. This observation suggests that *N*-glycosylation affects the dynamics of asparagine side chains as previously indicated in a comparative analysis of *N*-glycosylated and unglycosylated proteins in the PDB [54].

Because *N*-glycosylation affected the dynamics of N100 and its vicinity, we examined the conformation of the *N*-glycan attached to G102S by comparing it with that of free *N*-glycan. For this purpose, glycosidic torsion angles were examined for the MD trajectories (Supplementary Fig. S6). Comparison of dihedral angles indicated that the distributions were almost similar except for the GlcNAcβ1–4GlcNAc linkage, where the distribution of ψ was limited in the protein-bound *N*-glycan. This observation indicates that intramolecular interactions exist between *N*-glycan and the G102S polypeptide, which in turn might explain the PNGaseF-resistant behavior of G102S variant under non-denaturing conditions (Fig. 2).

To gain further insights into differences in the conformations of the WT, unglycosylated and *N*-glycosylated G102S variants, we examined the MD trajectories focusing on hydrogen bonding around the G102/S102 site. We determined the percentage probability of hydrogen bond formation for each residue, as summarized in Table 1. We found that W99, an important substrate-binding residue on CHIT1, forms a hydrogen bond with G102 in WT CHIT1. In the G102S variant, this hydrogen bond is lost and S102 forms a new hydrogen bond with K105 (Table 1, Supplementary Fig. S7). In The *N*-glycan core structure in G102S also forms hydrogen bonds with S288, K296, E297, G298 and G299. Among them, E297 is one of the key sites in CHIT1 for substrate

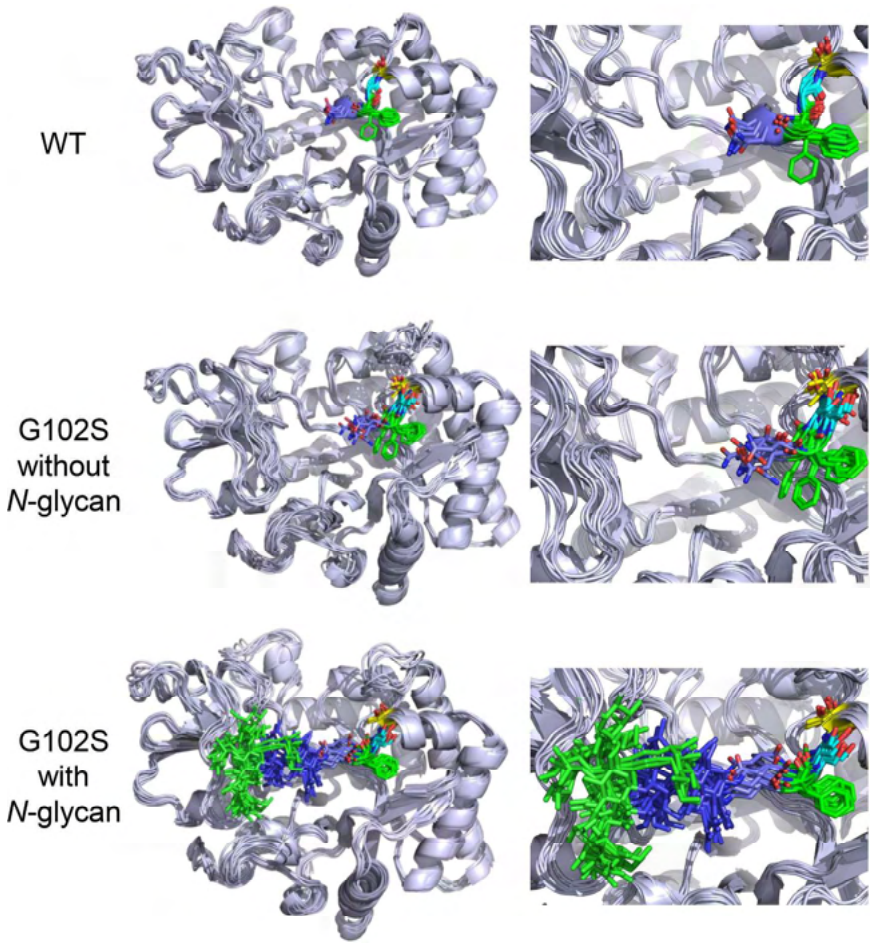


**Fig. 7.** MD simulation results of CHIT1 WT, unglycosylated G102S and *N*-glycosylated G102S at Asn100.
From top to bottom, 10 superimposed images of WT, unglycosylated G102S and *N*-glycosylated G102S proteins are shown as entire views (left) and close-up views of the N100–T103 region (right). Side chains of N100–T103 are shown as stick models in light purple (N100), green (F101), cyan (G/S102) and yellow (T103). The *N*-glycan attached on N100 of G102S is shown as a stick model in blue (GlcNAc) and green (Man). Figures were prepared using PyMOL software. (For interpretation of the references to colour in this figure legend, the reader is referred to the web version of this article.)

binding. Thus, both the G102S mutations and the presence of *N*-glycans have a clear effect on the substrate-binding site.

We also found that the T103 side chain forms hydrogen bonds with the neighboring loop (G143–A149). In unglycosylated G102S, this loop is rather disordered. Mark R et al. previously reported that *N*-glycan has a stabilizing effect on large-area main chain structures away from polysaccharides, probably by reducing the flexibility of the main chain [55]. The increased conformational flexibility caused by the G102S mutation and the loss of glycosylation further exacerbate this phenomenon, which may have a negative impact on substrate affinity, catalytic efficiency and the overall stability of CHIT1. This may explain why the N100Q+G102S protein, lacking the *N*-glycosylation site, consistently displayed lower enzymatic activity as compared with both WT and G102S.

Taking these observations together, we propose that the glycine to serine substitution at position 102 induces local conformational changes and reduces structural fluctuation of the CHIT1 protein. Furthermore, *N*-glycosylation at N100 significantly restricts conformational fluctuation around the *N*-glycosylation site, suggesting that the *N*-glycan in the G102S variant has a stabilizing effect. We speculate that the glycine to serine substitution is detrimental to the structural stability of the CHIT1 protein; however, the presence of *N*-glycan has a compensation effect to some extent.

To gain structural insight into ligand binding by CHIT1, we next built a docking model of the CHIT1 variants in complex with chitotriose. The crystal structure of CHIT1 bound to chitobiose (containing two GlcNAc units) (PDB ID: 4WKF) previously revealed that the binding site includes residues W99, N100, D138, E140, D213, R269, E297 and W358 [44] (Supplementary Table S2). Utilizing this crystal structure as a reference, we constructed the G102S variant with *N*-glycan in CHARMM-GUI and extended chitobiose to chitotriose to generate a protein–substrate docking simulation model (Fig. 9). We found that interactions occur between the chitotriose and the GlcNAc residues of the *N*-glycan (Supplementary Table S2). Analysis of dihedral angles and hydrogen bonds showed that the G102S mutation is not conducive to the stability of the binding site, but the presence of the *N*-glycan seems to have a stabilizing effect, consistent with our above speculations. The structural alterations at the binding site resulting from the glycine to serine mutation might lead to reduced substrate-binding affinity, potentially decreasing the enzyme's catalytic efficiency. Whether the instability in localized regions might propagate to affect the overall structure and function remains an open question.

It is now recognized that CHIT1 and its G102S variant are not directly implicated to the pathogenesis of Gaucher disease, which is caused by an accumulation of glucosylceramide in lysosomes due to a deficiency of lysosomal glucocerebrosidase. In light of our findings on

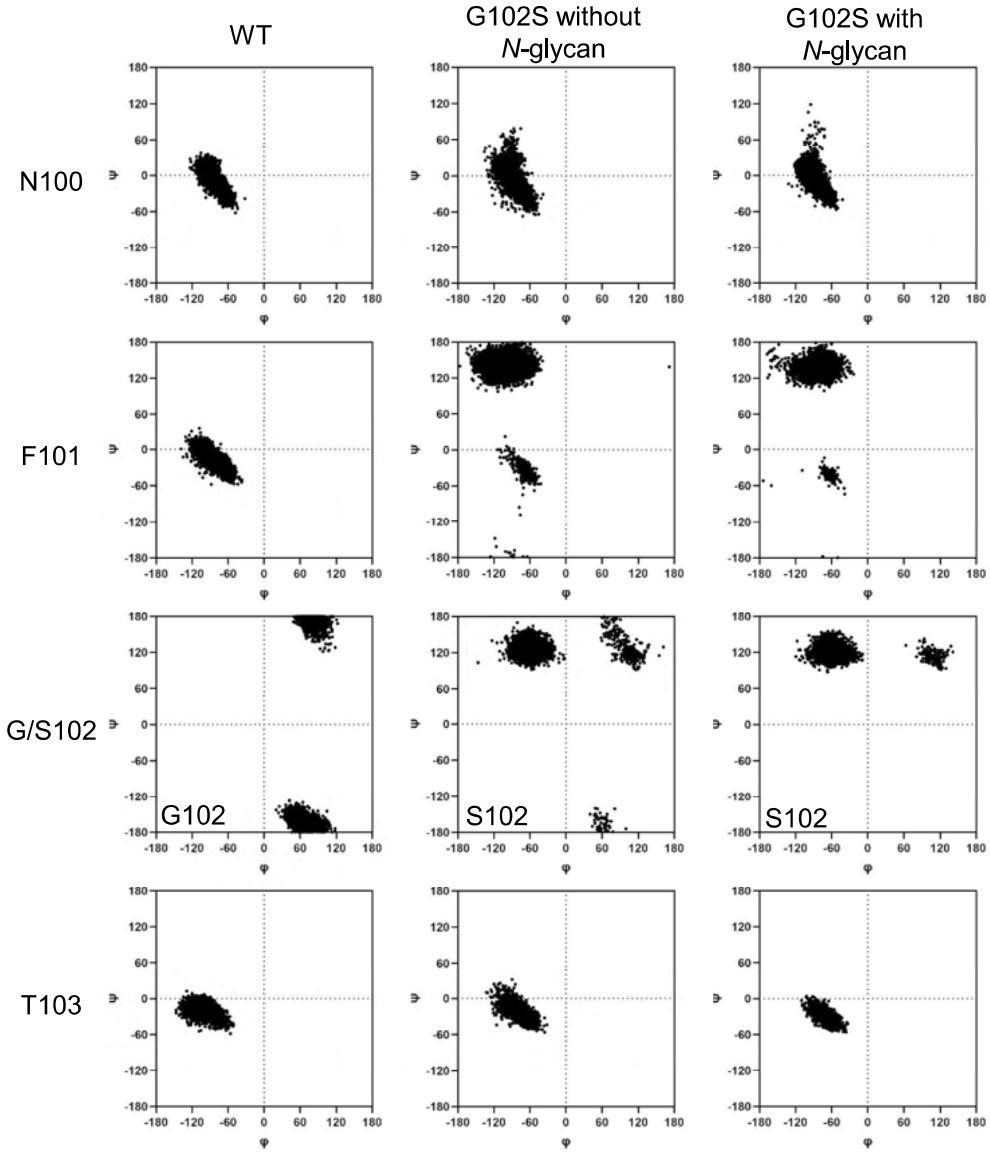


Crystal structure of CHIT1 (PDB ID: 4WKF)

| | N100 | F101 | G102 | T103 |
|---|---|---|---|---|
| φ | -68.5° | -66.4° | 71.4° | -118.8° |
| ψ | -24.6° | -28.4° | -160.0° | -23.1° |

**Fig. 8.** Ramachandran plots of the N100–T103 region the CHIT1 proteins determined from MD simulation results.
The distribution of the main chain dihedral angles (φ and ψ) at the N100–T103 site is shown for the WT, unglycosylated G102S and *N*-glycosylated G102S variants of CHIT1. The N100 side chain dihedral angles ($\chi_1$ and $\chi_2$) of the three proteins and glycosidic torsion angles (φ, ψ and ω) of the *N*-glycan attached to N100 of G102S are shown in Supplementary Fig. S5 and S6. Main chain dihedral angles of N100, F101, G102 and T103 from the crystal structure (PDB ID: 4WKF) are shown at the bottom for comparison.

the structure–function relationship of CHIT1 G102S, it is reasonable to hypothesize that the immunological response to the invasion of chitin-containing bacteria may differ between the wild-type and the G102S variant of CHIT1. Moreover, the presence of *N*-glycosylation at N100 may also influence the efficiency of CHIT1 degradation of exogenous chitin. It is therefore essential to exercise caution when monitoring CHIT1 activity in Gaucher's disease patients, taking into account the degree of *N*-glycosylation in the G102S variant.

**Table 1**
Probability of hydrogen bond formation in the WT, unglycosylated and *N*-glycosylated G102S variants of CHIT1.

| Site | Atom | Site | Atom | WT (%) | G102S-without-*N*-glycan (%) | G102S-with-*N*-glycan (%) |
|---|---|---|---|---|---|---|
| : | | | | | | |
| G/S102 | N | W99 | O | 39.7 | 0.2 | 0.0 |
| S102 | γO | K105 | N | 0.0 | 30.5 | 51.8 |
| : | | | | | | |
| T103 | γO1 | S144 | O | 0.34 | 31.4 | 6.1 |
| T103 | γO1 | S144 | γO | 0.0 | 9.0 | 5.3 |
| T103 | γO1 | Q145 | O | 6.78 | 1.0 | 4.7 |
| T103 | γO1 | Q145 | εO1 | 0.0 | 5.0 | 0.8 |
| T103 | γO1 | Q145 | εN2 | 0.0 | 4.0 | 0.6 |
| T103 | γO1 | G146 | N | 1.8 | 0.0 | 25.2 |
| T103 | γO1 | G146 | O | 0.24 | 0.1 | 0.1 |
| T103 | γO1 | S147 | N | 0.14 | 0.0 | 1.3 |
| T103 | γO1 | S147 | γO | 0.0 | 0.2 | 0.0 |
| : | | | | | | |
| S288 | γO | Man-4' | O3 | NA | NA | 12.1 |
| K296 | ηN | Man-4 | O2 | NA | NA | 13.7 |
| E297 | εO1 | GlcNAc-1 | O3 | NA | NA | 15.7 |
| E297 | εO2 | GlcNAc-1 | O3 | NA | NA | 16.8 |
| G298 | N | GlcNAc-2 | O3 | NA | NA | 44.6 |
| G299 | N | GlcNAc-2 | O | NA | NA | 69.3 |

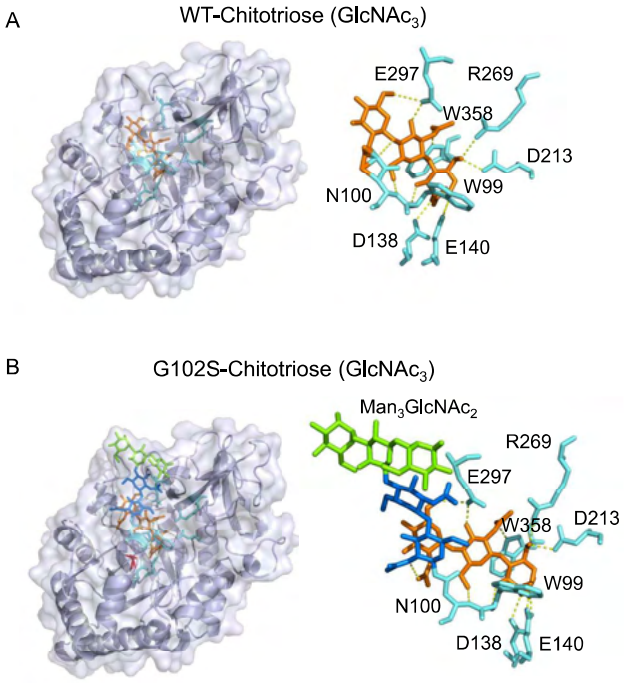


**Fig. 9.** Molecular docking simulations of CHIT1 proteins with chitotriose. Shown are docking simulations of the WT (A) and *N*-glycosylated G102S (B) CHIT1 proteins in complex with chitotriose. The entire structure (left) and substrate-binding site (right) are shown. In both cases, docking models were prepared based on the crystal structure of CHIT1 bound to chitobiose (PDB ID: 4WKF). Bound chitotriose ($GlcNAc_3$) is shown in orange in stick representation. The amino acid residues spatially close to the bound ligand are shown in light blue in stick representation. The N100 side chain of G102S was modified with the *N*-glycan core structure $Man_3GlcNAc_2$ (Man, green; GlcNAc, blue). Potential hydrogen bonds are shown as dotted yellow lines. (For interpretation of the references to colour in this figure legend, the reader is referred to the web version of this article.)

## 4. Conclusion

In summary, the G102S mutation found in the common variant of human CHIT1 induces local conformational changes and structural fluctuations. However, additional *N*-glycosylation at N100 of G102S reduces the conformational fluctuations, thereby stabilizing the G102S variant to some extent. These differences in conformation and dynamics are likely to explain the observed differences in the catalytic activity of CHIT1. Analysis of the composition of *N*-glycan at N100 of G102S newly identified *O*-glycosylation in the hinge region of CHIT1. The relationship between *N*- and *O*-glycan structures and the enzymatic activity should be explored in future studies.

## Funding and additional information

This work was financially supported by JSPS KAKENHI Grant Number 19H03362 and by the Tohoku Medical and Pharmaceutical University.

## CRediT authorship contribution statement

**Xiao Xu:** Investigation, Visualization, Writing – original draft, Writing – review & editing, Data curation. **Noriyoshi Manabe:** Investigation, Validation, Visualization, Writing – review & editing. **Shiho Ohno:** Investigation, Validation, Writing – review & editing. **Sachiko Komatsu:** Investigation, Writing – review & editing. **Tsutomu Fujimura:** Investigation, Validation, Writing – review & editing. **Yoshiki Yamaguchi:** Conceptualization, Data curation, Project administration, Supervision, Validation, Writing – original draft, Writing – review & editing.

## Declaration of competing interest

The authors declare that they have no known competing financial interests or personal relationships that could have influenced the work reported in this paper.

## Data availability

All data are contained within the manuscript.

## Acknowledgments

X.X. is a recipient of a scholarship from the Tohoku Kaihatsu Memorial Foundation. We express our thanks to Seizo Koshiba (Tohoku Medical Megabank Organization), and Tohoku University Technical Support Center for the NMR measurements conducted under the support of the NMR Platform (Grant Number Grant Number JPMXS0450100021,

MEXT). We also thank Re Suyong (National Institutes of Biomedical Innovation, Health and Nutrition) for technical advice on the MD simulations. The MD simulations were conducted using the supercomputing resources at the Cyberscience Center, Tohoku University. MALDI-MS measurements and the data analysis were kindly performed by Takashi Nishikaze, Kumiko Yamaguchi, and Takumi Tomita (Shimadzu Corporation).

## Appendix A. Supplementary data

Supplementary data to this article can be found online at https://doi.org/10.1016/j.bbagen.2024.130730.

## References

[1] C. Boscher, J.W. Dennis, I.R. Nabi, Glycosylation, galectins and cellular signaling, Curr. Opin. Cell Biol. 23 (4) (2011) 383–392, https://doi.org/10.1016/j.ceb.2011.05.001.
[2] F. Dall'olio, Protein glycosylation in cancer biology: an overview, Clin. Mol. Pathol. 49 (3) (1996) M126–M135, https://doi.org/10.1136/mp.49.3.m126.
[3] J.W. Dennis, I.R. Nabi, M. Demetriou, Metabolism, cell surface organization, and disease, Cell 139 (7) (2009) 1229–1241, https://doi.org/10.1016/j.cell.2009.12.008.
[4] R.A. Dwek, Glycobiology: toward understanding the function of sugars, Chem. Rev. 96 (2) (1996) 683–720, https://doi.org/10.1021/cr940283b.
[5] G.W. Hart, Glycosylation, Curr. Opin. Cell Biol. 4 (6) (1992) 1017–1023, https://doi.org/10.1016/0955-0674(92)90134-x.
[6] K. Marino, J. Bones, J.J. Kattla, P.M. Rudd, A systematic approach to protein glycosylation analysis: a path through the maze, Nat. Chem. Biol. 6 (10) (2010) 713–723, https://doi.org/10.1038/nchembio.437.
[7] R. Peracaula, S. Barrabes, A. Sarrats, P.M. Rudd, R. de Llorens, Altered glycosylation in tumours focused to cancer diagnosis, Dis. Markers 25 (4–5) (2008) 207–218, https://doi.org/10.1155/2008/797629.
[8] R. Mazumder, K.S. Morampudi, M. Motwani, S. Vasudevan, R. Goldman, Proteome-wide analysis of single-nucleotide variations in the N-glycosylation sequon of human genes, PLoS One 7 (5) (2012) e36212, https://doi.org/10.1371/journal.pone.0036212.
[9] A. Waite, M.C. De Rosa, A. Brancaccio, D.J. Blake, A gain-of-glycosylation mutation associated with myoclonus-dystonia syndrome affects trafficking and processing of mouse epsilon-sarcoglycan in the late secretory pathway, Hum. Mutat. 32 (11) (2011) 1246–1258, https://doi.org/10.1002/humu.21561.
[10] S.M. Firth, X. Yan, R.C. Baxter, D440N mutation in the acid-labile subunit of insulin-like growth factor complexes inhibits secretion and complex formation, Mol. Endocrinol. 25 (2) (2011) 307–314, https://doi.org/10.1210/me.2010-0295.
[11] P. Roll, G. Rudolf, S. Pereira, B. Royer, I.E. Scheffer, A. Massacrier, M.P. Valenti, N. Roeckel-Trevisiol, S. Jamali, C. Beclin, C. Seegmuller, M.N. Metz-Lutz, A. Lemainque, M. Delepine, C. Caloustian, A. de Saint Martin, N. Bruneau, D. Depetris, M.G. Mattei, E. Flori, A. Robaglia-Schlupp, N. Levy, B.A. Neubauer, R. Ravid, C. Marescaux, S.F. Berkovic, E. Hirsch, M. Lathrop, P. Cau, P. Szepetowski, SRPX2 mutations in disorders of language cortex and cognition, Hum. Mol. Genet. 15 (7) (2006) 1195–1207, https://doi.org/10.1093/hmg/ddl035.
[12] P. Goettig, Effects of glycosylation on the enzymatic activity and mechanisms of proteases, Int. J. Mol. Sci. 17 (12) (2016), https://doi.org/10.3390/ijms17121969.
[13] Y. Yasuda, S. Ikeda, H. Sakai, T. Tsukuba, K. Okamoto, K. Nishishita, A. Akamine, Y. Kato, K. Yamamoto, Role of N-glycosylation in cathepsin E, A comparative study of cathepsin E with distinct N-linked oligosaccharides and its nonglycosylated mutant, Eur. J. Biochem. 266 (2) (1999) 383–391, https://doi.org/10.1046/j.1432-1327.1999.00863.x.
[14] S. Ihara, E. Miyoshi, S. Nakahara, H. Sakiyama, H. Ihara, A. Akinaga, K. Honke, R. B. Dickson, C.Y. Lin, N. Taniguchi, Addition of beta1-6 GlcNAc branching to the oligosaccharide attached to Asn 772 in the serine protease domain of matriptase plays a pivotal role in its stability and resistance against trypsin, Glycobiology 14 (2) (2004) 139–146, https://doi.org/10.1093/glycob/cwh013.
[15] M.E. Dumez, N. Teller, F. Mercier, T. Tanaka, I. Vandenberghe, M. Vandenbranden, B. Devreese, A. Luxen, J.M. Frere, A. Matagne, A. Jacquet, M. Galleni, A. Chevigne, Activation mechanism of recombinant Der p 3 allergen zymogen: contribution of cysteine protease Der p 1 and effect of propeptide glycosylation, J. Biol. Chem. 283 (45) (2008) 30606–30617, https://doi.org/10.1074/jbc.M803041200.
[16] X. Liao, W. Wang, S. Chen, Q. Wu, Role of glycosylation in corin zymogen activation, J. Biol. Chem. 282 (38) (2007) 27728–27735, https://doi.org/10.1074/jbc.M703687200.
[17] K. Takao, S. Takai, N. Shiota, K. Song, K. Nishimura, T. Ishihara, M. Miyazaki, Lack of effect of carbohydrate depletion on some properties of human mast cell chymase, Biochim. Biophys. Acta 1427 (1) (1999) 74–81, https://doi.org/10.1016/s0304-4165(99)00002-1.
[18] P. Nelboeck, M. Fuchs, D. Bur, B.M. Loffler, Glycosylation of Asn-632 and Asn-651 is important for functional expression of endothelin-converting enzyme-1, J. Cardiovasc. Pharmacol. 31 (Suppl. 1) (1998) S4–S6, https://doi.org/10.1097/00005344-199800001-00003.
[19] B. Henrissat, A. Bairoch, New families in the classification of glycosyl hydrolases based on amino acid sequence similarities, Biochem. J. 293 (Pt 3) (1993) 781–788, https://doi.org/10.1042/bj2930781.
[20] R.G. Boot, G.H. Renkema, A. Strijland, A.J. van Zonneveld, J.M. Aerts, Cloning of a cDNA encoding chitotriosidase, a human chitinase produced by macrophages, J. Biol. Chem. 270 (44) (1995) 26252–26256, https://doi.org/10.1074/jbc.270.44.26252.
[21] G.H. Renkema, R.G. Boot, A.O. Muijsers, W.E. Donker-Koopman, J.M. Aerts, Purification and characterization of human chitotriosidase, a novel member of the chitinase family of proteins, J. Biol. Chem. 270 (5) (1995) 2198–2202, https://doi.org/10.1074/jbc.270.5.2198.
[22] Y. Guo, W. He, A.M. Boer, R.A. Wevers, A.M. de Bruijn, J.E. Groener, C.E. Hollak, J. M. Aerts, H. Galjaard, O.P. van Diggelen, Elevated plasma chitotriosidase activity in various lysosomal storage disorders, J. Inherit. Metab. Dis. 18 (6) (1995) 717–722, https://doi.org/10.1007/BF02436762.
[23] H. Michelakakis, E. Dimitriou, I. Labadaridis, The expanding spectrum of disorders with elevated plasma chitotriosidase activity: an update, J. Inherit. Metab. Dis. 27 (5) (2004) 705–706, https://doi.org/10.1023/b:boli.0000043025.17721.fc.
[24] A. Wajner, K. Michelin, M.G. Burin, R.F. Pires, M.L. Pereira, R. Giugliani, J. C. Coelho, Biochemical characterization of chitotriosidase enzyme: comparison between normal individuals and patients with Gaucher and with Niemann-pick diseases, Clin. Biochem. 37 (10) (2004) 893–897, https://doi.org/10.1016/j.clinbiochem.2004.06.008.
[25] F. Fusetti, H. von Moeller, D. Houston, H.J. Rozeboom, B.W. Dijkstra, R.G. Boot, J. M. Aerts, D.M. van Aalten, Structure of human chitotriosidase, Implications for specific inhibitor design and function of mammalian chitinase-like lectins, J. Biol. Chem. 277 (28) (2002) 25537–25544, https://doi.org/10.1074/jbc.M201636200.
[26] S. Chen, L.C. Francioli, J.K. Goodrich, R.L. Collins, M. Kanai, Q. Wang, J. Alfoldi, N. A. Watts, C. Vittal, L.D. Gauthier, T. Poterba, M.W. Wilson, Y. Tarasova, W. Phu, R. Grant, M.T. Yohannes, Z. Koenig, Y. Farjoun, E. Banks, S. Donnelly, S. Gabriel, N. Gupta, S. Ferriera, C. Tolonen, S. Novod, L. Bergelson, D. Roazen, V. Ruano-Rubio, M. Covarrubias, C. Llanwarne, N. Petrillo, G. Wade, T. Jeandet, R. Munshi, K. Tibbetts, C. Genome Aggregation Database, A. O'Donnell-Luria, M. Solomonson, C. Seed, A.R. Martin, M.E. Talkowski, H.L. Rehm, M.J. Daly, G. Tiao, B.M. Neale, D. G. MacArthur, K.J. Karczewski, A genomic mutational constraint map using variation in 76,156 human genomes, Nature 625 (7993) (2024) 92–100, https://doi.org/10.1038/s41586-023-06045-0.
[27] S. Tadaka, J. Kawashima, E. Hishinuma, S. Saito, Y. Okamura, A. Otsuki, K. Kojima, S. Komaki, Y. Aoki, T. Kanno, D. Saigusa, J. Inoue, M. Shirota, J. Takayama, F. Katsuoka, A. Shimizu, G. Tamiya, R. Shimizu, M. Hiratsuka, I.N. Motoike, S. Koshiba, M. Sasaki, M. Yamamoto, K. Kinoshita, jMorp: Japanese multi-omics reference panel update report 2023, Nucleic Acids Res. 52 (D1) (2024) D622–D632, https://doi.org/10.1093/nar/gkad978.
[28] D. Elstein, A. Abrahamov, I. Hadas-Halpern, A. Zimran, Gaucher's disease, Lancet 358 (9278) (2001) 324–327, https://doi.org/10.1016/S0140-6736(01)05490-3.
[29] C.E. Hollak, S. van Weely, M.H. van Oers, J.M. Aerts, Marked elevation of plasma chitotriosidase activity. A novel hallmark of Gaucher disease, J. Clin. Invest. 93 (3) (1994) 1288–1292, https://doi.org/10.1172/JCI117084.
[30] C.E. Hollak, M. Maas, J.M. Aerts, Clinically relevant therapeutic endpoints in type I Gaucher disease, J. Inherit. Metab. Dis. 24 (Suppl. 2) (2001) 97–105, discussion 87–8, https://doi.org/10.1023/a:1012492429191.
[31] P.K. Mistry, A. Abrahamov, A practical approach to diagnosis and management of Gaucher's disease, Baillieres Clin. Haematol. 10 (4) (1997) 817–838, https://doi.org/10.1016/s0950-3536(97)80042-x.
[32] D. Elstein, C. Hollak, J.M. Aerts, S. van Weely, M. Maas, T.M. Cox, R.H. Lachmann, M. Hrebicek, F.M. Platt, T.D. Butters, R.A. Dwek, A. Zimran, Sustained therapeutic effects of oral miglustat (Zavesca, N-butyldeoxynojirimycin, OGT 918) in type I Gaucher disease, J. Inherit. Metab. Dis. 27 (6) (2004) 757–766, https://doi.org/10.1023/B:BOLI.0000045756.54006.17.
[33] P.B. Deegan, M.T. Moran, I. McFarlane, J.P. Schofield, R.G. Boot, J.M. Aerts, T. M. Cox, Clinical evaluation of chemokine and enzymatic biomarkers of Gaucher disease, Blood Cells Mol. Dis. 35 (2) (2005) 259–267, https://doi.org/10.1016/j.bcmd.2005.05.005.
[34] M.E. Grace, M. Balwani, I. Nazarenko, A. Prakash-Cheng, R.J. Desnick, Type 1 Gaucher disease: null and hypomorphic novel chitotriosidase mutations-implications for diagnosis and therapeutic monitoring, Hum. Mutat. 28 (9) (2007) 866–873, https://doi.org/10.1002/humu.20524.
[35] J.V. Olsen, B. Macek, O. Lange, A. Makarov, S. Horning, M. Mann, Higher-energy C-trap dissociation for peptide modification analysis, Nat. Methods 4 (9) (2007) 709–712, https://doi.org/10.1038/nmeth1060.
[36] M. Bern, Y.J. Kil, C. Becker, Byonic: advanced peptide and protein identification software, Curr. Protoc. Bioinformatics 13 (1–13) (2012), https://doi.org/10.1002/0471250953.bi1320s40. Chapter 13. 20 14.
[37] S. Neelamegham, K. Aoki-Kinoshita, E. Bolton, M. Frank, F. Lisacek, T. Lutteke, N. O'Boyle, N.H. Packer, P. Stanley, P. Toukach, A. Varki, R.J. Woods, S.D. Group, Updates to the symbol nomenclature for Glycans guidelines, Glycobiology 29 (9) (2019) 620–624, https://doi.org/10.1093/glycob/cwz045.
[38] J. Jumper, R. Evans, A. Pritzel, T. Green, M. Figurnov, O. Ronneberger, K. Tunyasuvunakool, R. Bates, A. Zidek, A. Potapenko, A. Bridgland, C. Meyer, S.A. A. Kohl, A.J. Ballard, A. Cowie, B. Romera-Paredes, S. Nikolov, R. Jain, J. Adler, T. Back, S. Petersen, D. Reiman, E. Clancy, M. Zielinski, M. Steinegger, M. Pacholska, T. Berghammer, S. Bodenstein, D. Silver, O. Vinyals, A.W. Senior, K. Kavukcuoglu, P. Kohli, D. Hassabis, Highly accurate protein structure prediction with AlphaFold, Nature 596 (7873) (2021) 583–589, https://doi.org/10.1038/s41586-021-03819-2.

[39] M. Varadi, D. Bertoni, P. Magana, U. Paramval, I. Pidruchna, M. Radhakrishnan, M. Tsenkov, S. Nair, M. Mirdita, J. Yeo, O. Kovalevskiy, K. Tunyasuvunakool, A. Laydon, A. Zidek, H. Tomlinson, D. Hariharan, J. Abrahamson, T. Green, J. Jumper, E. Birney, M. Steinegger, D. Hassabis, S. Velankar, AlphaFold protein structure database in 2024: providing structure coverage for over 214 million protein sequences, Nucleic Acids Res. 52 (D1) (2024) D368–D375, https://doi.org/10.1093/nar/gkad1011.

[40] S.J. Park, J. Lee, Y. Qi, N.R. Kern, H.S. Lee, S. Jo, I. Joung, K. Joo, J. Lee, W. Im, CHARMM-GUI glycan modeler for modeling and simulation of carbohydrates and glycoconjugates, Glycobiology 29 (4) (2019) 320–331, https://doi.org/10.1093/glycob/cwz003.

[41] O. Guvench, E.R. Hatcher, R.M. Venable, R.W. Pastor, A.D. Mackerell, CHARMM additive all-atom force field for glycosidic linkages between hexopyranoses, J. Chem. Theory Comput. 5 (9) (2009) 2353–2370, https://doi.org/10.1021/ct900242e.

[42] C. Kobayashi, J. Jung, Y. Matsunaga, T. Mori, T. Ando, K. Tamura, M. Kamiya, Y. Sugita, GENESIS 1.1: a hybrid-parallel molecular dynamics simulator with enhanced sampling algorithms on multiple computational platforms, J. Comput. Chem. 38 (25) (2017) 2193–2206, https://doi.org/10.1002/jcc.24874.

[43] J. Jung, T. Mori, C. Kobayashi, Y. Matsunaga, T. Yoda, M. Feig, Y. Sugita, GENESIS: a hybrid-parallel and multi-scale molecular dynamics simulator with enhanced sampling algorithms for biomolecular and cellular simulations, Wiley Interdiscip. Rev. Comput. Mol. Sci. 5 (4) (2015) 310–323, https://doi.org/10.1002/wcms.1220.

[44] F. Fadel, Y. Zhao, A. Cousido-Siah, F.X. Ruiz, A. Mitschler, A. Podjarny, X-ray crystal structure of the full length human Chitotriosidase (CHIT1) reveals features of its chitin binding domain, PLoS One 11 (4) (2016) e0154190, https://doi.org/10.1371/journal.pone.0154190.

[45] E. Zurawska-Plaksej, E.M. Kratz, M. Ferens-Sieczkowska, M. Knapik-Kordecka, A. Piwowar, Changes in glycosylation of human blood plasma chitotriosidase in patients with type 2 diabetes, Glycoconj. J. 33 (1) (2016) 29–39, https://doi.org/10.1007/s10719-015-9629-z.

[46] J. Baenziger, S. Kornfeld, Structure of the carbohydrate units of IgA1 immunoglobulin. II. Structure of the O-glycosidically linked oligosaccharide units, J. Biol. Chem. 249 (22) (1974) 7270–7281.

[47] T.S. Mattu, R.J. Pleass, A.C. Willis, M. Kilian, M.R. Wormald, A.C. Lellouch, P. M. Rudd, J.M. Woof, R.A. Dwek, The glycosylation and structure of human serum IgA1, fab, and fc regions and the role of N-glycosylation on Fcalpha receptor interactions, J. Biol. Chem. 273 (4) (1998) 2260–2272, https://doi.org/10.1074/jbc.273.4.2260.

[48] Y. Hiki, H. Odani, M. Takahashi, Y. Yasuda, A. Nishimoto, H. Iwase, T. Shinzato, Y. Kobayashi, K. Maeda, Mass spectrometry proves under-O-glycosylation of glomerular IgA1 in IgA nephropathy, Kidney Int. 59 (3) (2001) 1077–1085, https://doi.org/10.1046/j.1523-1755.2001.0590031077.x.

[49] J. Mestecky, M. Tomana, P.A. Crowley-Nowick, Z. Moldoveanu, B.A. Julian, S. Jackson, Defective galactosylation and clearance of IgA1 molecules as a possible etiopathogenic factor in IgA nephropathy, Contrib. Nephrol. 104 (1993) 172–182, https://doi.org/10.1159/000422410.

[50] A.C. Allen, S.J. Harper, J. Feehally, Galactosylation of N- and O-linked carbohydrate moieties of IgA1 and IgG in IgA nephropathy, Clin. Exp. Immunol. 100 (3) (1995) 470–474, https://doi.org/10.1111/j.1365-2249.1995.tb03724.x.

[51] M. Tomana, K. Matousovic, B.A. Julian, J. Radl, K. Konecny, J. Mestecky, Galactose-deficient IgA1 in sera of IgA nephropathy patients is present in complexes with IgG, Kidney Int. 52 (2) (1997) 509–516, https://doi.org/10.1038/ki.1997.361.

[52] B.K. Ho, R. Brasseur, The Ramachandran plots of glycine and pre-proline, BMC Struct. Biol. 5 (2005) 14, https://doi.org/10.1186/1472-6807-5-14.

[53] S.A. Hollingsworth, P.A. Karplus, A fresh look at the Ramachandran plot and the occurrence of standard structures in proteins, Biomol. Concepts 1 (3–4) (2010) 271–283, https://doi.org/10.1515/BMC.2010.022.

[54] A.J. Petrescu, A.L. Milac, S.M. Petrescu, R.A. Dwek, M.R. Wormald, Statistical analysis of the protein environment of N-glycosylation sites: implications for occupancy, structure, and folding, Glycobiology 14 (2) (2004) 103–114, https://doi.org/10.1093/glycob/cwh008.

[55] M.R. Wormald, R.A. Dwek, Glycoproteins: glycan presentation and protein-fold stability, Structure 7 (7) (1999) R155–R160, https://doi.org/10.1016/s0969-2126(99)80095-1.

＜機能病態分子学＞
教授　稲森 啓一郎

## 糖脂質生合成に関わる糖転移酵素の新規バリアントの機能的評価

研究内容紹介：

スフィンゴ糖脂質は、セラミドに糖（鎖）が結合したもので、細胞膜外層でコレステロールや種々のタンパク質などとの相互作用を介して、細胞内シグナル伝達、細胞接着、細胞間相互作用などを制御している。特に、糖鎖部分にシアル酸を含む酸性スフィンゴ糖脂質はガングリオシドとよばれ、中枢神経系に多く存在し、神経細胞の機能と維持に重要な役割をもつ。哺乳類の脳では、GM1，GD1a，GD1b，GT1bの4分子種が主要なガングリオシドとして存在し、正常な脳の発達と神経細胞の機能と維持に必要である。これらの主要な4分子種の生合成には、シアル酸転移酵素であるGM3合成酵素（GM3S）と、*N*-アセチルガラクトサミン（GalNAc）転移酵素であるGM2/GD2合成酵素（GM2S）の両方が必須である（図1）。

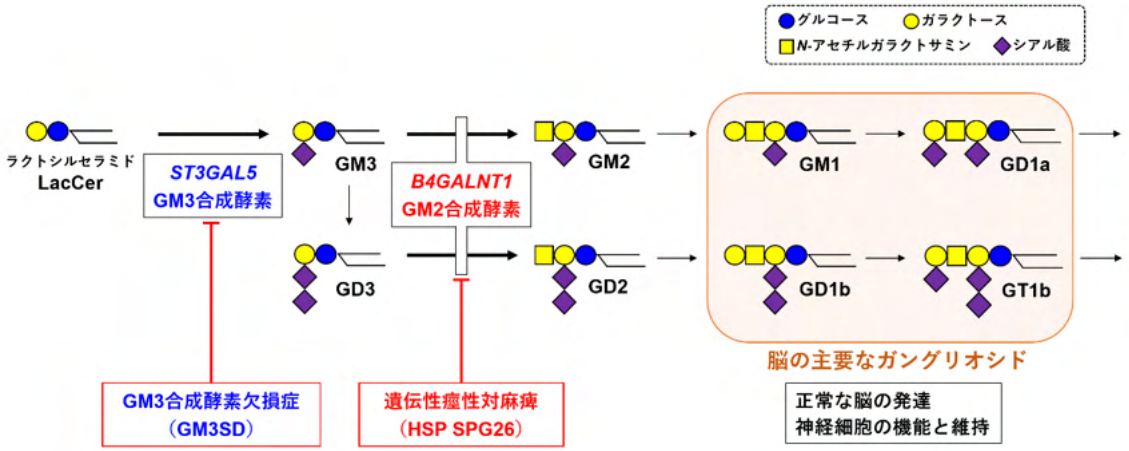


**図1. 糖脂質ガングリオシドの合成経路および生合成異常症**

GM3S遺伝子*ST3GAL5*とGM2S遺伝子*B4GALNT1*の病原性変異はそれぞれ、発達遅滞、異常運動、失明を伴う乳児期発症のてんかん症候群（GM3SD）、および，知的障害と末梢神経障害を伴う遺伝性痙性対麻痺（hereditary spastic paraplegia, HSP）の複合型であるSPG26を引き起こす。これまでに、*ST3GAL5*および*B4GALNT1*の各遺伝子変異によるGM3SDとSPG26の症例がそれぞれ報告されていたが、日本国内においては最近まで両疾患の患者の報告はなかった。我々は、GM3S酵素活性測定を通して国内で初めてとなるGM3SD患者の確定診断を行った（Watanabe et al. *Brain Dev* 2023）。今回は、信州大学において見出された神経変性症患者の新規*B4GALNT1*バリアントの機能解析によるSPG26の確定診断、さらに、日本人一般住民における新規*B4GALNT1*バリアントの機能評価による病的バリアントの同定を行った

（Inamori et al. *Front Neurosci* 2024）。

信州大学医学部附属病院において、進行性の神経変性症患者に新規 *B4GALNT1* 遺伝子変異（ホモ接合ミスセンス変異：D313N）が見出された。最初に、末梢血単核細胞（PBMC）を用いて *B4GALNT1* 遺伝子変異の影響を検討した。ヒトの PBMC は通常、ガングリオシドをほとんど発現していないが、抗 CD3/CD28 抗体による TCR 刺激で T 細胞を活性化させると *B4GALNT1* 遺伝子発現が特異的かつ顕著に誘導され、T 細胞表面のガングリオシド GM1 発現が顕著に上昇する。T 細胞活性化により、健常者コントロールと患者 T 細胞のどちらとも活性化マーカーCD69 の発現亢進が確認されたが、患者 T 細胞では GM1 発現の上昇がみられなかった。ヒト B4GALNT1（GM2S）とショウジョウバエの GalNAc 転移酵素 PGANT9A の両触媒ドメインのホモロジーモデリングからは、B4GALNT1 の D313 が UDP 結合に関わる可能性が予測された。GM2S を含む GalNAc 転移酵素は、UDP-GalNAc を供与体基質として利用し、受容体基質に対して GalNAc を転移する。D313N 変異によって UDP-GalNAc との結合が損なわれることで、GalNAc 転移活性に影響を及ぼす可能性が示唆された。そこで、B4GALNT1 を欠損させた HEK293 細胞への遺伝子導入により、D313N 変異体タンパク質の GM2S 活性を評価したところ、完全に酵素活性が消失していた。本例は、日本人で初めて SPG26 と診断された症例である。

さらに、東北大学東北メディカル・メガバンク機構（ToMMo）の日本人一般住民の全ゲノム参照パネルから、*B4GALNT1* のミスセンスバリアントのうち、PolyPhen2 と SIFT により有害と予測されるバリアントを抽出した。それらについて、前述と同様に機能解析を行ったところ、多くのバリアントにおいて細胞内局在変化と GM2S 酵素活性の減弱または消失がみられた（Table 1）。*ST3GAL5* も含め、日本人における糖脂質生合成遺伝子の病的バリアントの同定と機能解析をさらに進めることは、未診断疾患患者の診断、および国内患者・保因者状況の把握につながるものと考えられる。

**Table 1.** Summary of functional evaluation of B4GALNT1 missense variants

| B4GALNT1 variants | PolyPhen2 | SIFT | Allele frequency | | Localization | Relative activity to wild-type (SD) |
|---|---|---|---|---|---|---|
| | | | ToMMo 8.3KJPN | gnomAD v2.1.1 | | |
| T27N | D | T | 0.0001 | NF | Golgi | 1.30 (0.96) |
| L91P | D | D-LC | 0.0001 | 0.000003978 | Golgi | 0.19 (0.15) |
| Q221H | D | D-LC | 0.0001 | NF | Golgi | 0.21 (0.16) |
| R301H | D | D | 0.0002 | 0.000007953 | Golgi/ER | 0.87 (0.59) |
| D433A | D | D | 0.0001 | NF | Golgi/ER | ND |
| N437K | D | D | 0.0001 | NF | Golgi/ER | ND |
| F438L | D | D | 0.0001 | NF | Golgi | 0.04 (0.03) |
| A441E | D | D | 0.0002 | NF | Golgi/ER | ND |
| P453H | D | D | 0.0001 | NF | Golgi/ER | ND |
| R519W | D | D | 0.0001 | 0.000003976 | Golgi/ER | ND |
| R526W | D | T | 0.0001 | 0.000003976 | Golgi/ER | 0.14 (0.13) |

D, damaging; T, tolerated; LC, low confidence; NF, not found; ND, not detected.

＜論文発表＞

**Dietary gangliosides rescue GM3 synthase deficiency outcomes in mice accompanied by neurogenesis in the hippocampus.** Inokuchi JI, Go S, Suzuki A, Nakagawasai O, Odaira-Satoh T, Veillon L, Nitta T, McJarrow P, Kanoh H, Inamori KI, Tan-No K, Collett M. ***Front Neurosci.*** 18:1387221. doi: 10.3389/fnins.2024.1387221. 2024

**Functional evaluation of novel variants of B4GALNT1 in a patient with hereditary spastic paraplegia and the general population.** Inamori KI, Nakamura K, Shishido F, Hsu JC, Nagafuku M, Nitta T, Ikeda J, Yoshimura H, Kodaira M, Tsuchida N, Matsumoto N, Uemura S, Ohno S, Manabe N, Yamaguchi Y, Togayachi A, Aoki-Kinoshita KF, Nishihara S, Furukawa JI, Kaname T, Nakamura M, Shimohata T, Tadaka S, Shirota M, Kinoshita K, Nakamura Y, Ohno I, Sekijima Y, Inokuchi JI.. ***Front Neurosci.*** 18:1437668. doi: 10.3389/fnins.2024.1437668. 2024

**VarMeter2: An enhanced structure-based method for predicting pathogenic missense variants through Mahalanobis distance.** Ohno S, Ogura C, Yabuki A, Itoh K, Manabe N, Angata K, Togayachi A, Aoki-Kinoshita K, Furukawa J, Inamori K, Inokuchi J, Kaname T, Nishihara S, Yamaguchi Y. ***Comput. Struct. Biotechnol. J.*** 27:1034-1047. doi: 10.1016/j.csbj.2025.02.008. 2025

＜学会発表と講演＞

**神経変性症患者および一般住民に見出された新規 B4GALNT1（GM2 合成酵素）バリアントの機能解析**

稲森啓一郎, 宍戸史[a], 許家甄, 永福正和, 新田昂大[b], 中村勝哉[c], 土田奈緒美[d], 池田淳司[c], 小平農[c], 栂谷内晶[e], 古川潤一[f], 山口芳樹, 木下聖子[e], 要匡[g], 中村豊[a], 大野勲[a], 中村雅彦[h], 下畑享良[i], 松本直通[d], 古庄知己[c], 関島良樹[c], 木下賢吾[j], 西原祥子[e], 井ノ口仁一[k]

（東北医薬大医[a], 順天堂大院医[b], 信州大医[c], 横浜市大院医[d], 創価大 GaLSIC[e], 名古屋大 iGCORE[f], 国立成育医療研セ[g], 松本市立病院[h], 岐阜大院医[i], 東北大 ToMMo[j], 大阪大院理 FRC[k]）

第 66 回日本脂質生化学会, 静岡, 2024 年 6 月, 演題番号 2-38

**スフィンゴ糖脂質によるマクロファージのパイロトーシス促進機構**

新田昂大[a], 狩野裕考[b], 石川潮[b], 石田秀治[c], 今村彰宏[c], 稲森啓一郎, 宮崎哲朗[a], 岩渕和久[a], 井ノ口仁一[d]

(順天堂大院医 [a], 慶應大先端生命研 [b], 岐阜大応用生物科学 [c], 大阪大院理 FRC [d])
第 66 回日本脂質生化学会, 静岡, 2024 年 6 月, 演題番号 2-32

**ガングリオシド生合成酵素の新規バリアントの機能解析**
稲森啓一郎, 宍戸史 [a], 山口芳樹, 木下賢吾 [b], 西原祥子 [c], 井ノ口仁一 [d]
(東北医薬大医 [a], 東北大 ToMMo [b], 創価大 GaLSIC [c], 大阪大院理 FRC [d])
第 43 回日本糖質学会年会, 2024 年 9 月, 横浜, 演題番号 3C-08A

**日本人における SIGLEC ファミリー遺伝子多型と発症リスク**
井ノ口仁一 [a], 稲森啓一郎, 山口芳樹, 田高周 [b], 木下賢吾 [b], 山本雅之 [b], 西原祥子 [c], 木下聖子 [c], 栂谷内晶 [c], 安形清彦 [c], 佐藤ちひろ [d], 羽根正弥 [d], 古川潤一 [d], 石田秀治 [e], 矢木宏和 [f]
(大阪大院理 FRC [a], 東北大 ToMMo [b], 創価大 GaLSIC [c], 名古屋大 iGCORE [d], 岐阜大 iGCORE [e], 自然科学研究機構 ExCELLS [f])
第 18 回東北糖鎖研究会, 2024 年 10 月, 仙台, 演題番号 O-1

**ガングリオシド生合成に関わる糖転移酵素の新規ミスセンスバリアントの機能的評価**
稲森啓一郎, 宍戸史 [a], 山口芳樹, 木下賢吾 [b], 西原祥子 [c], 井ノ口仁一 [d]
(東北医薬大医 [a], 東北大 ToMMo [b], 創価大 GaLSIC [c], 大阪大院理 FRC [d])
第 18 回東北糖鎖研究会, 2024 年 10 月, 仙台, 演題番号 O-2

**Functional evaluation of novel missense variants of glycosyltransferases involved in ganglioside biosynthesis**
Kei-ichiro Inamori
2025 Academia Sinica – Tohoku Medical and Pharmaceutical University Bilateral Meeting, 2025 年 2 月, 台北, 演題番号 2

**神経疾患患者および一般住民に見出されたガングリオシド生合成酵素の新規バリアントの機能評価**
稲森啓一郎, 宍戸史 [a], 山口芳樹, 木下賢吾 [b], 要匡 [c], 西原祥子 [d], 井ノ口仁一 [e]
(東北医薬大医 [a], 東北大 ToMMo [b], 成育医療研セ [c], 創価大 GaLSIC [d], 大阪大院理 FRC [e])
第 18 回スフィンゴテラピィ研究会, 2025 年 3 月, 京都, 演題番号 3

frontiers | Frontiers in Neuroscience

TYPE Original Research
PUBLISHED 31 July 2024
DOI 10.3389/fnins.2024.1437668

Check for updates

OPEN ACCESS

EDITED BY
Suman Chowdhury,
The State University of New Jersey,
United States

REVIEWED BY
Yuki Ohkawa,
Osaka International Cancer Institute, Japan
Orhan Kerim İnci,
Izmir Institute of Technology, Türkiye
Alice Barbara Schindler,
National Institute of Neurological Disorders and Stroke (NIH), United States

*CORRESPONDENCE
Kei-ichiro Inamori
✉ kinamori@tohoku-mpu.ac.jp
Jin-ichi Inokuchi
✉ inokuchi@chem.sci.osaka-u.ac.jp

†These authors have contributed equally to this work and share first authorship

RECEIVED 24 May 2024
ACCEPTED 10 July 2024
PUBLISHED 31 July 2024

CITATION
Inamori K-i, Nakamura K, Shishido F, Hsu J-C, Nagafuku M, Nitta T, Ikeda J, Yoshimura H, Kodaira M, Tsuchida N, Matsumoto N, Uemura S, Ohno S, Manabe N, Yamaguchi Y, Togayachi A, Aoki-Kinoshita KF, Nishihara S, Furukawa J-i, Kaname T, Nakamura M, Shimohata T, Tadaka S, Shirota M, Kinoshita K, Nakamura Y, Ohno I, Sekijima Y and Inokuchi J-i (2024) Functional evaluation of novel variants of *B4GALNT1* in a patient with hereditary spastic paraplegia and the general population.
*Front. Neurosci.* 18:1437668.
doi: 10.3389/fnins.2024.1437668

COPYRIGHT
© 2024 Inamori, Nakamura, Shishido, Hsu, Nagafuku, Nitta, Ikeda, Yoshimura, Kodaira, Tsuchida, Matsumoto, Uemura, Ohno, Manabe, Yamaguchi, Togayachi, Aoki-Kinoshita, Nishihara, Furukawa, Kaname, Nakamura, Shimohata, Tadaka, Shirota, Kinoshita, Nakamura, Ohno, Sekijima and Inokuchi. This is an open-access article distributed under the terms of the Creative Commons Attribution License (CC BY). The use, distribution or reproduction in other forums is permitted, provided the original author(s) and the copyright owner(s) are credited and that the original publication in this journal is cited, in accordance with accepted academic practice. No use, distribution or reproduction is permitted which does not comply with these terms.

# Functional evaluation of novel variants of *B4GALNT1* in a patient with hereditary spastic paraplegia and the general population

Kei-ichiro Inamori[1*†], Katsuya Nakamura[2,3†], Fumi Shishido[4†], Jia-Chen Hsu[1], Masakazu Nagafuku[1], Takahiro Nitta[1,5,6], Junji Ikeda[2], Hidekane Yoshimura[7], Minori Kodaira[2], Naomi Tsuchida[8,9], Naomichi Matsumoto[8], Satoshi Uemura[10], Shiho Ohno[11], Noriyoshi Manabe[11], Yoshiki Yamaguchi[11], Akira Togayachi[12], Kiyoko F. Aoki-Kinoshita[12], Shoko Nishihara[12], Jun-ichi Furukawa[13], Tadashi Kaname[14], Masahiko Nakamura[15], Takayoshi Shimohata[16], Shu Tadaka[17], Matsuyuki Shirota[17], Kengo Kinoshita[17], Yutaka Nakamura[4], Isao Ohno[4], Yoshiki Sekijima[2] and Jin-ichi Inokuchi[18*]

[1]Division of Glycopathology, Institute of Molecular Biomembrane and Glycobiology, Tohoku Medical and Pharmaceutical University, Sendai, Japan, [2]Department of Medicine (Neurology and Rheumatology), Shinshu University School of Medicine, Matsumoto, Japan, [3]Center for Medical Genetics, Shinshu University Hospital, Matsumoto, Japan, [4]Faculty of Medicine, Center for Medical Education, Tohoku Medical and Pharmaceutical University, Sendai, Japan, [5]Laboratory of Bioregulatory Clinical Phamacology, Faculty of Pharmacy, Juntendo University, Urayasu, Japan, [6]Institute for Environmental and Gender Specific Medicine, Juntendo University Graduate School of Medicine, Urayasu, Japan, [7]Department of Otorhinolaryngology—Head and Neck Surgery, Shinshu University School of Medicine, Matsumoto, Japan, [8]Department of Human Genetics, Yokohama City University Graduate School of Medicine, Yokohama, Japan, [9]Department of Rare Disease Genomics, Yokohama City University Hospital, Yokohama, Japan, [10]Division of Medical Biochemistry, Faculty of Medicine, Tohoku Medical and Pharmaceutical University, Sendai, Japan, [11]Division of Structural Glycobiology, Institute of Molecular Biomembrane and Glycobiology, Tohoku Medical and Pharmaceutical University, Sendai, Japan, [12]Glycan and Life System Integration Center (GaLSIC), Soka University, Hachioji, Japan, [13]Institute for Glyco-core Research (iGCORE), Nagoya University, Nagoya, Japan, [14]Department of Genome Medicine, National Center for Child Health and Development, Tokyo, Japan, [15]Department of Neurosurgery, Matsumoto City Hospital, Matsumoto, Japan, [16]Department of Neurology, Gifu University Graduate School of Medicine, Gifu, Japan, [17]Tohoku Medical Megabank Organization, Tohoku University, Sendai, Japan, [18]Forefront Research Center, Graduate School of Science, Osaka University, Toyonaka, Japan

Hereditary spastic paraplegia (HSP) is a heterogeneous group of neurological disorders that are characterized by progressive spasticity and weakness in the lower limbs. SPG26 is a complicated form of HSP, which includes not only weakness in the lower limbs, but also cognitive impairment, developmental delay, cerebellar ataxia, dysarthria, and peripheral neuropathy, and is caused by biallelic mutations in the *B4GALNT1* (beta-1,4-*N*-acetylgalactosaminyltransferase 1) gene. The *B4GALNT1* gene encodes ganglioside GM2/GD2 synthase (GM2S), which catalyzes the transfer of *N*-acetylgalactosamine to lactosylceramide, GM3, and GD3 to generate GA2, GM2, and GD2, respectively. The present study attempted to characterize a novel *B4GALNT1* variant (NM_001478.5:c.937G>A p.Asp313Asn) detected in a patient with progressive multi-system neurodegeneration as well as deleterious variants found in the general population in Japan. Peripheral blood T cells from our patient lacked the ability for activation-induced ganglioside expression assessed by cell surface cholera toxin binding. Structural predictions suggested that the amino acid substitution,

p.Asp313Asn, impaired binding to the donor substrate UDP-GalNAc. An *in vitro* enzyme assay demonstrated that the variant protein did not exhibit GM2S activity, leading to the diagnosis of HSP26. This is the first case diagnosed with SPG26 in Japan. We then extracted 10 novel missense variants of *B4GALNT1* from the whole-genome reference panel jMorp (8.3KJPN) of the Tohoku medical megabank organization, which were predicted to be deleterious by Polyphen-2 and SIFT programs. We performed a functional evaluation of these variants and demonstrated that many showed perturbed subcellular localization. Five of these variants exhibited no or significantly decreased GM2S activity with less than 10% activity of the wild-type protein, indicating that they are carrier variants for HSP26. These results provide the basis for molecular analyses of *B4GALNT1* variants present in the Japanese population and will help improve the molecular diagnosis of patients suspected of having HSP.

KEYWORDS

**hereditary spastic paraplegia, gangliosides, *B4GALNT1*, GM2/GD2 synthase, glycosyltransferase, missense variant**

# 1 Introduction

Hereditary spastic paraplegia (HSP) is a progressive neurodegenerative disease that is characterized by axonal degeneration of the corticospinal tract of the spinal cord, leading to weakness and spasticity in the lower limbs (Shribman et al., 2019; Meyyazhagan and Orlacchio, 2022). It is divided into two main groups: uncomplicated HSP and complicated HSP. Uncomplicated HSP, also known as pure HSP, is characterized by gradual weakness in the legs. Complicated HSP is often accompanied by additional conditions, such as peripheral neuropathy, distal amyotrophy, intellectual disability, ataxia, extrapyramidal symptoms, epilepsy, dysarthria, optic neuropathy, dementia, ichthyosis, learning and developmental disturbances, hearing loss, and speech, breathing, or swallowing difficulties. To date, more than 80 genetic loci have been identified (Meyyazhagan and Orlacchio, 2022). Their genetic loci are referred to as SPG and the subtypes of HSP are designated by the ordinal numbers assigned to their discovery. Various subtypes of HSP exhibit distinct onset ages and disease progression, with some sharing similar conditions.

Glycosphingolipids (GSLs) are integral components of cellular membranes, and sialylated GSLs, which are gangliosides, play crucial roles in various cellular processes (Inokuchi et al., 2018). Ganglioside synthesis is initiated by glucosylceramide synthase (encoded by the *UGCG* gene) to add glucose to ceramide (Ichikawa et al., 1996), followed by the addition of galactose by lactosylceramide (LacCer) synthase (encoded by the *B4GALT5 or B4GALT6* gene; Nomura et al., 1998; Kumagai et al., 2010; Nishie et al., 2010). GM3 synthase (encoded by the *ST3GAL5* gene) adds a sialic acid to initiate the synthesis of a-, b-, and c-series gangliosides (Ishii et al., 1998). GM2/GD2 synthase (GM2S, encoded by the *B4GALNT1* gene) adds *N*-acetylgalactosamine (GalNAc) to LacCer, GM3, GD3, and GT3 to generate GA2, GM2, GD2, and GT2, respectively (Nagata et al., 1992). Other glycosyltransferases synthesize even more complex molecular species downstream (Figure 1). Gangliosides are highly expressed in neural tissues, with the four species, GM1, GD1a, GD1b, and GT1b predominating in the mammalian brain, particularly in the human brain, accounting for 99% of species (Schnaar, 2019). Pathogenic variants in the *ST3GAL5* gene may cause infantile-onset epilepsy syndrome, associated with developmental stagnation and blindness in humans (Simpson et al., 2004). In contrast, mice deficient in the orthologous gene *St3gal5* show no apparent neurological abnormalities, which may be attributed to alternatively expressed o-series gangliosides compensating for the loss of a- and b-series gangliosides (Yamashita et al., 2003; Inamori and Inokuchi, 2022). *B4galnt1* knockout (KO) mice, in which the expression of gangliosides, such as GM3 and GD3, is limited, grow apparently normal; however, myelination decreases as they age and they exhibit progressive axonal degeneration in both the central and peripheral nervous systems (Takamiya et al., 1996; Sheikh et al., 1999; Yao et al., 2014). Pathogenic variants in the human *B4GALNT1* gene cause SPG26, an autosomal recessive (OMIM #609195), complicated HSP, characterized not only by lower limb weakness, but also by cognitive impairment, developmental delay, cerebellar ataxia, dysarthria, and peripheral neuropathy, and these clinical phenotypes are similar to those of *B4galnt1* KO mice (Boukhris et al., 2013; Harlalka et al., 2013; Bhuiyan et al., 2019).

In the present study, we performed whole exome sequencing (WES) on our patient with progressive multi-system neurodegeneration and identified a novel, homozygous missense variant in the *B4GALNT1* gene (NM_001478.5:c.937G>A p.Asp313Asn). Functional analyses revealed that the Asp313Asn variant lost its enzyme activity, leading to the diagnosis of SPG26. Furthermore, we analyzed 10 novel missense variants of the *B4GALNT1* gene, which were predicted to be deleterious by the Polyphen-2 and SIFT programs, extracted from the general Japanese population using the whole-genome reference panel of the Tohoku Medical Megabank Organization (ToMMo), for their enzyme activity and subcellular localization.

# 2 Materials and methods

## 2.1 Clinical characterization and molecular testing

Since the clinical findings of our patient were suggestive of slowly progressive multi-system neurodegeneration, we performed WES, after obtaining informed consent. Genomic DNA was extracted from the patient's peripheral blood. WES was performed as previously

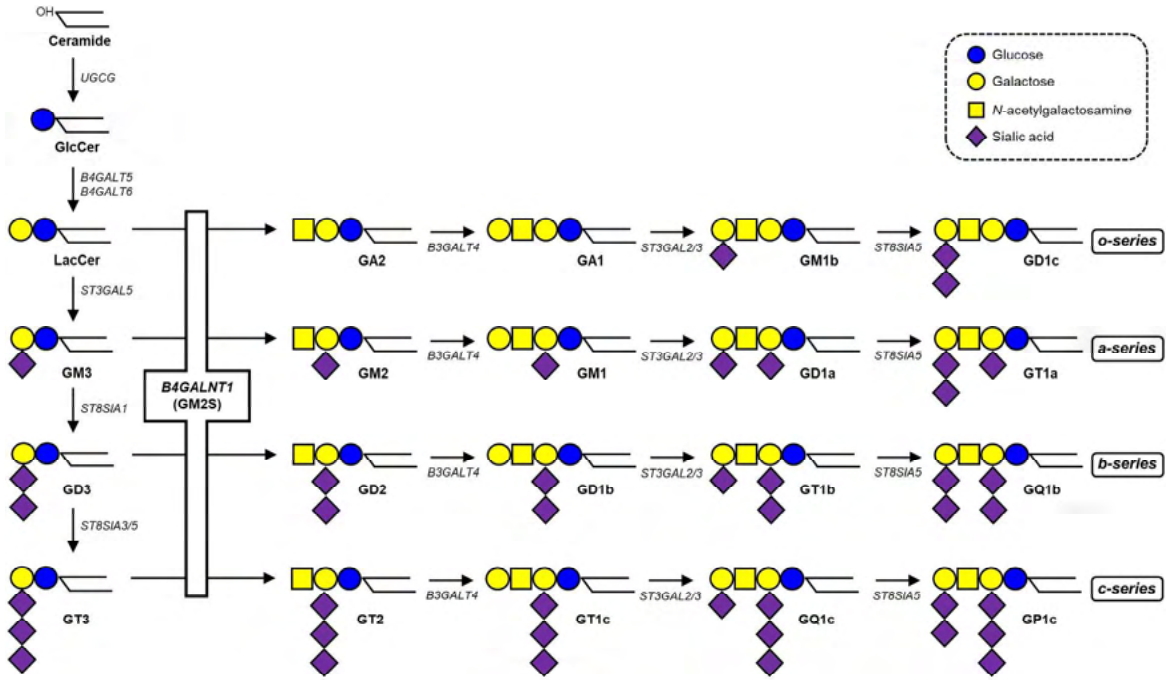


FIGURE 1
Biosynthetic pathway of gangliosides. See the text for details. The *B4GALNT1* gene encodes GM2/GD2 synthase (GM2S), which catalyzes the transfer of GalNAc to LacCer, GM3, GD3, and GT3 to generate GA2, GM2, GD2, and GT2, respectively.

described (Inoue et al., 2024). The present study was approved by the Institutional Review Board at Shinshu University. Written consent was obtained. Exome sequencing was conducted at Yokohama City University.

## 2.2 Homology modeling of the B4GALNT1 protein

Homology modeling of the human B4GALNT1 protein was performed using the SWISS-MODEL server (Waterhouse et al., 2018). The crystal structure of the *Drosophila melanogaster* polypeptide *N*-acetylgalactosaminyltransferase PGANT9A in complex with UDP and $Mn^{2+}$ (PDB ID: 6E4Q; Ji et al., 2018) was used as a template. A 3D model of the human structure was displayed using the PyMOL Molecular Graphics System, Version 2.5 Schrödinger, LLC.

## 2.3 Flow cytometry of activated T cells

Peripheral blood mononuclear cells (PBMCs) obtained from the proband, her father (mother's samples were not obtained), and an age-matched control were stimulated with anti-CD3 and anti-CD28, and the cell surface expression of GM1 on activated T cells was analyzed by flow cytometry using cholera toxin B subunit (CTX), as previously described (Tani-ichi et al., 2005). Briefly, PBMCs were cultured in the presence or absence of anti-CD3 and anti-CD28 for 48 h, and T cells were stained with a combination of antibodies including CD4-FITC, CD8-PE-Cy7, and CD69-APC (BioLegend), and with CTX-CF640R (Biotium).

## 2.4 B4GALNT1-KO HEK293T cells

To generate B4GALNT1-KO cells, human *B4GALNT1* gene-specific guide RNAs were designed using the online CRISPR design tool (Ran et al., 2013). Guide oligonucleotides (5′-CACCGACAAGCCAGAGCGCGTTAG-3′ and 5′-AAACCTAACGCGCTCTGGCTTGTC-3′) were synthesized, annealed, and subsequently inserted into the plasmid pSpCas9(BB)-2A-GFP (Addgene, Cambridge, MA). The resulting plasmid was transfected into HEK293T cells using Lipofectamine 2000 (Thermo Fisher Scientific), according to the manufacturer's protocol. Clonal cell lines were established through single-cell cloning, and the expression levels of gangliosides were assessed using thin-layer chromatography. In the GM2S enzyme assay, B4GALNT1-KO cells were transiently transfected with the N-terminal FLAG-tagged plasmid, pcDNA3 FLAG-hM2-B4GALNT1. Forty-eight hours after transfection, cells were collected and stored at −80°C until analyzed. In an immunocytochemical analysis, cells were transfected with the pCE puro-hM2-B4GALNT1-FLAG vector containing the C-terminal FLAG-tag, selected with puromycin, and the puromycin-resistant cells obtained were then examined.

## 2.5 GM2S enzyme assay

GM2S enzyme activity was assessed by an HPLC-based assay with a fluorescent-labeled acceptor substrate using microsomal membranes prepared from transfected cells (Inamori et al., 2023). Cells were homogenized in 20 mM

4-(2-hydroxyethyl)-1-piperazineethanesulfonic acid (HEPES) buffer, pH 7.2, and 250 mM sucrose containing 1 mM phenylmethylsulfonylfluoride (PMSF), 1× protease inhibitor cocktail (Nacalai Tesque Inc. Japan). After centrifugation at 6,000 rpm at 4°C for 10 min, the supernatant was ultracentrifuged at 100,000 × *g* at 4°C for 1 h and the resultant pellet (microsomal membranes) was solubilized in 50 mM HEPES buffer, pH 7.2 containing 1× protease inhibitor cocktail, 1 mM PMSF, and 1% Triton X-100. Solubilized microsomal membranes were incubated with 10 μM NBD-GM3 (Peptide Institute, Inc., Osaka, Japan), 1 mM UDP-GalNAc, 10 mM $MnCl_2$, 10 mM CDP-choline, and 50 mM HEPES buffer, pH 7.2 at 37°C for 15 min. The reaction was terminated by boiling for 5 min, and the supernatant was analyzed using an LC-18 column (TSKgel ODS-80TM, 5 μm, 4.6 × 250 mm, Tosoh Bioscience, Tokyo, Japan) equipped with an HPLC system (Jasco, Tokyo, Japan). The product was eluted with a gradient of acetonitrile in 50 mM ammonium acetate, pH 4.0. GM2S enzymatic activity was examined in triplicate, calculated as the peak area ratio (product peak area/product peak area + substrate peak area), normalized by the expression level of the B4GALNT1 protein evaluated by Western blotting with the FLAG antibody (DYKDDDDK tag antibody, Fujifilm Wako Pure Chemical Corporation, Osaka, Japan) and anti-calnexin antibody (MBL, Tokyo, Japan), and then calculated with the Volume Tools of ImageLab software (Bio-Rad).

## 2.6 Immunocytochemistry

Transfected cells were cultured on poly-L-lysine-coated coverslips (Sigma-Aldrich), fixed with 3.7% formaldehyde in PBS at room temperature for 15 min, and then rinsed with PBS. Cells were then permeabilized with 0.5% SDS in PBS and treated with Image-iT FX Signal Enhancer (Thermo Fisher Scientific) for 30 min. After that, cells were incubated with a 1:100 dilution of a FLAG antibody (Fujifilm Wako Pure Chemical Corporation) in 1% BSA/PBS for 1 h. Following three washes with PBS, cells were incubated for 30 min with Alexa 488-conjugated anti-mouse IgG antibodies (Thermo Fisher Scientific) diluted to 5 μg/mL in 1% BSA/PBS. Coverslips were then washed three times with PBS, mounted on glass slides using ProLong Gold antifade reagent (Thermo Fisher Scientific), and subjected to a fluorescence microscopy analysis (model spinSR10, Olympus; Tokyo, Japan).

## 2.7 Statistical analysis

Data were analyzed by Dunnett's multiple comparison test using GraphPad Prism version 7.0.

# 3 Results

## 3.1 Case presentation

The patient (III-4), a 44-year-old Japanese woman, was the second child of healthy first cousin parents (Figure 2A). Motor and intellectual development was delayed: she held her head up at the age of 8 months, walked without support at 20 months, and spoke words at 24 months. At the age of 3 years, she developed recurrent episodes of unconsciousness with generalized convulsions and, thus, was administered anti-epileptic drugs. At the age of 6 years, mild intellectual disability was noted. At the age of 15 years, she developed paroxysmal episodes of involuntary movement, showing dysesthesia, dysarthria, and the Trousseau sign in both of the upper limbs. At the age of 17 years, extensive neurological examinations were performed for the first time at a local hospital. The findings obtained revealed hypotonia, distal dominant muscle atrophy, and weakness. Tendon reflexes were absent in the upper and lower extremities. Pyramidal tract signs and sensory disturbance were not evident. She walked with a positive waddling gait. Intelligence assessed by the Wechsler Adult Intelligence Scale-Revised test revealed mild intellectual disability with a Full Scale IQ of 60, verbal IQ of 77, and performance IQ scale out. At the age of 19 years, she developed an anxiety disorder and hallucinations and was admitted to a psychiatric hospital. At that time, she was unable to walk without support. At the age of approximately 40 years, she first experienced hearing impairment, which gradually deteriorated. At the age of 42 years, she was referred to our hospital for a more detailed evaluation. Neurological examinations showed normal oculomotor movement. Although speech was slurred, dysphagia was absent. Distal muscle wasting and weakness, with foot deformities were evident. Hypoesthesia and decreases in position and vibration senses were also observed in the limbs. Deep tendon reflexes were absent in the upper and lower extremities. Babinski and Chaddock signs were both positive on both sides. Limb and truncal ataxia were evident. Brain MRI showed marked atrophy of the cerebellar hemispheres and vermis, but not the brainstem. Spinal MRI revealed atrophy of the spinal cord (Figure 2B). The results of nerve conduction studies showed normal motor conduction velocity and compound-muscle action potentials, whereas sensory nerve action potentials were not detected in the upper or lower limbs. The motor-evoked potential in the lower limbs had a prolonged central motor conduction time. Otoscopy revealed no abnormal findings. The results of pure tone audiometry and distortion product otoacoustic emissions indicated mild sensorineural deafness (Figures 2C,D).

## 3.2 Genetic testing and prediction of the impact of the variant

A homozygous missense variant in *B4GALNT1* (NM_001478.5:c.937G>A p.Asp313Asn) was identified. This result was confirmed using Sanger sequencing, and the patient's non-affected parents were both heterozygous for this variant (Figure 2A). The variant is registered in the Genome Aggregation Database (gnomAD v4.0.0, https://gnomad.broadinstitute.org/) with a minor allele frequency of 0.000007202 (6/833110 alleles). It has not been described in the disease-causing mutation databases, the Human Gene Mutation Database (HGMD) Professional 2024.1[1] and ClinVar.[2]

To predict whether the amino acid change, p.Asp313Asn, affected protein function, a theoretical 3D model of the catalytic domain of human B4GALNT1 (GM2S) was constructed with homology modeling using Swiss Model (Figure 3A). *D. melanogaster* polypeptide *N*-acetylgalactosaminyltransferase PGANT9A was used as the

1 http://www.hgmd.org/

2 http://www.ncbi.nlm.nih.gov/clinvar/

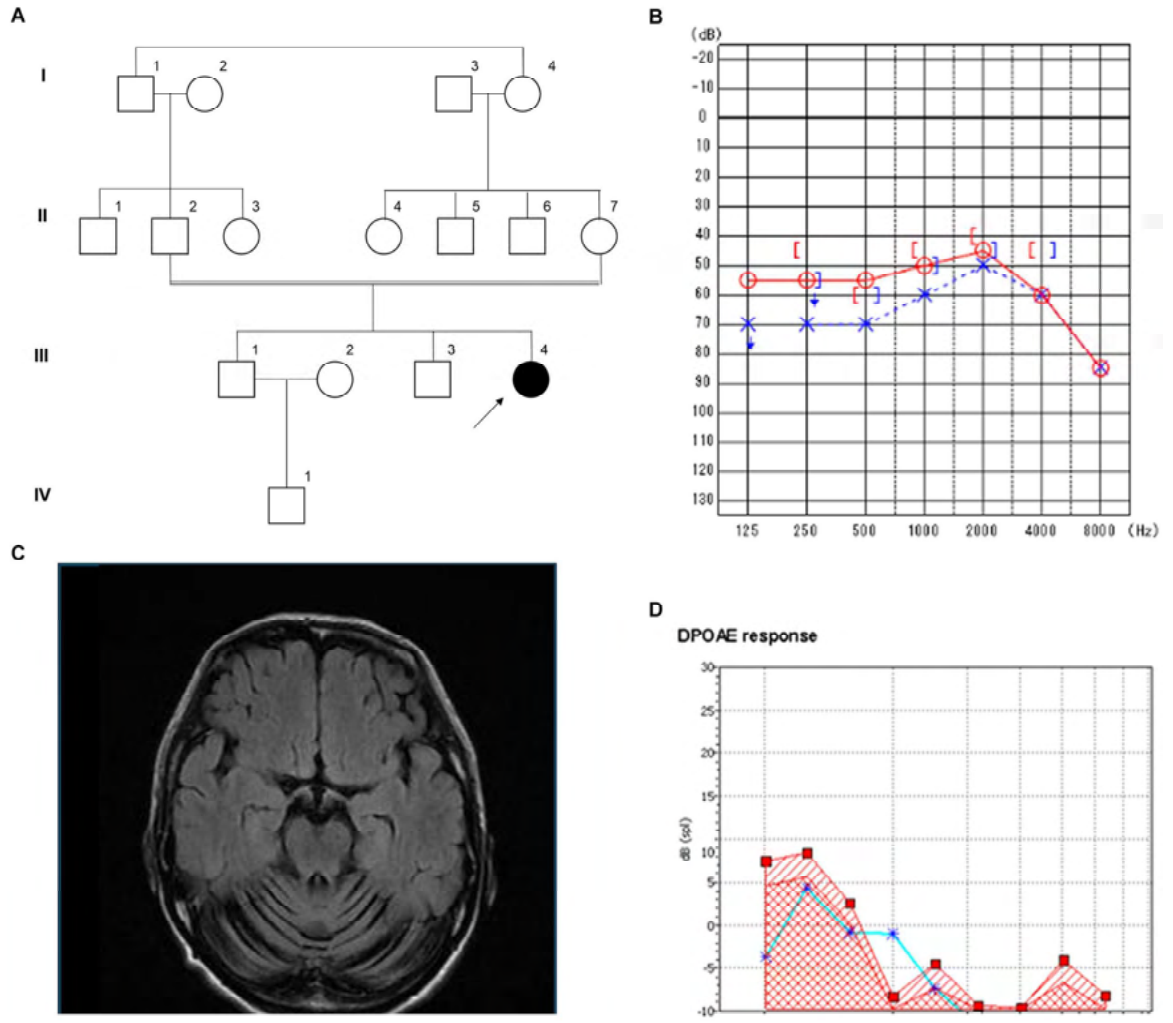


FIGURE 2
Clinical features of the patient with a novel *B4GALNT1* p.Asp313Asn variant. **(A)** Pedigree of the family. **(B)** Magnetic resonance imaging (MRI) of the brain showed severe cerebellar atrophy. **(C)** Pure tone audiometry. ○: Air conduction, right ear; ×: Air conduction, left ear; [: bone conduction, right ear;]: bone conduction, left ear. **(D)** Results of distortion product otoacoustic emissions of the left ear. From 1 to 8 kHz, with noise denoted by squares and the response denoted by asterisks.

template for modeling, and the sequence alignment of B4GALNT1 and the catalytic domain of PGANT9A (Figure 3B) indicated that Asp313 of B4GALNT1 corresponded to Asp249 of PGANT9A, which is a binding site for UDP (Figure 3C). Therefore, Asp313 of B4GALNT1 appeared to be involved in the binding of the donor substrate UDP-GalNAc and the enzyme activity of the p.Asp313Asn variant was predicted to be impaired by the loss of donor binding.

## 3.3 Analysis of cell surface GM1 expression on activated T cells from the patient with the p.Asp313Asn variant

In SPG26 patients, pathogenic mutations in the *B4GALNT1* gene result in the loss of GM2S enzyme activity and defective gangliosides biosynthesis (Bhuiyan et al., 2019). We analyzed patient-derived cells to establish whether this defect by the p.Asp313Asn substitution in the B4GALNT1 protein was present. Although human naive T cells express only low levels of GM1 on the cell surface, activation by anti-CD3 and anti-CD28 markedly up-regulates the expression of B4GALNT1, which increases surface GM1 expression (Tani-ichi et al., 2005). We used activation-induced ganglioside expression on T cells to analyze the cell surface expression of GM1 using CTX, which specifically binds to GM1. PBMCs from the patient, her father who is heterozygous for the p.Asp313Asn variant, and a healthy age-matched control male, were stimulated with anti-CD3 and anti-CD28 for 2 days. Surface staining for CD69, an activation marker of lymphocytes, confirmed that T cells were properly stimulated in the experiment (Figure 4). However, GM1 expression was completely impaired in patient T cells, indicating that the p.Asp313Asn substitution resulted in defective ganglioside synthesis.

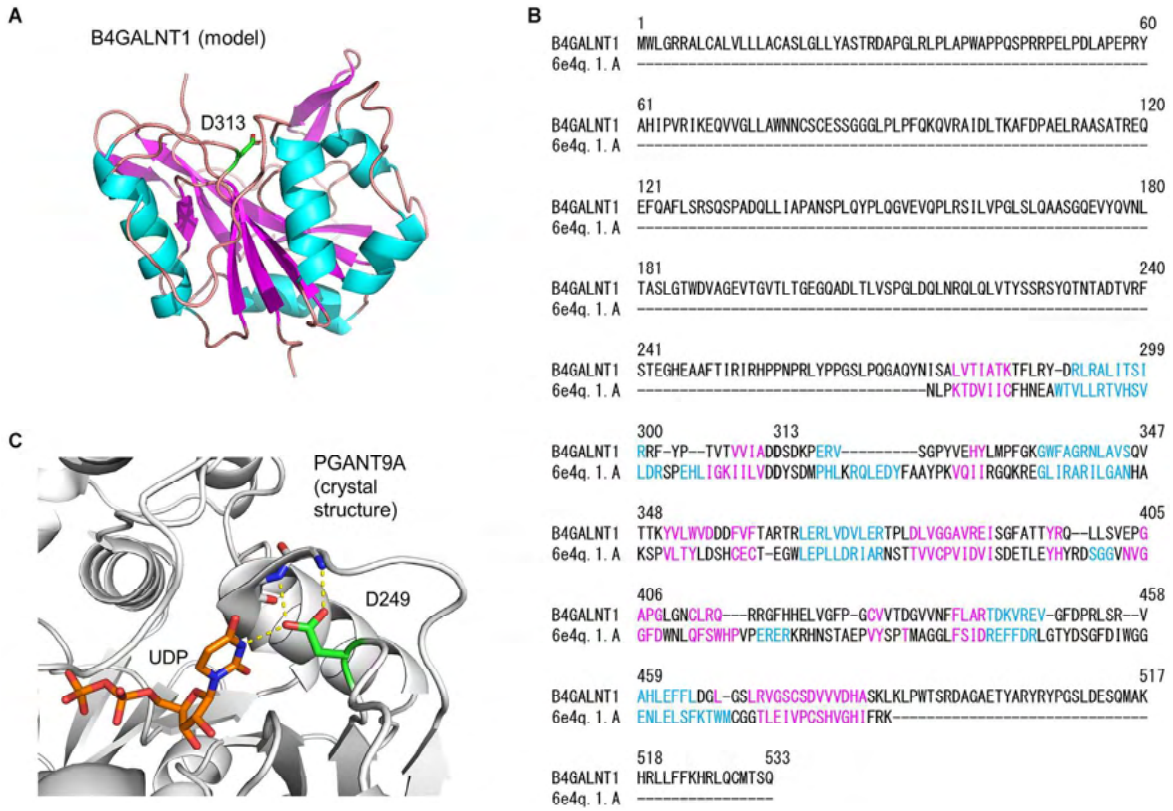


FIGURE 3
Homology modeling of the B4GALNT1 protein by Swiss Model. **(A)** A 3D model of the human B4GALNT1 catalytic domain. The α-helix (pink) and β-strand (blue) are shown in the ribbon model and Asp313 (D313) is shown in green with the stick representation. **(B)** Alignment of the B4GALNT1 protein sequence and that of the catalytic domain of the template 6E4Q, *Drosophila melanogaster* polypeptide *N*-acetylgalactosaminyltransferase PGANT9A. The sequences shown in pink and blue correspond to the α-helix and β-strand, respectively, in panel **(A)**. **(C)** The crystal structure of the catalytic domain of PGANT9A. The Asp249 (D249) side chain and bound UDP are shown with a stick model and intermolecular hydrogen bonds with dotted yellow lines.

## 3.4 Functional analysis of the p.Asp313Asn variant protein

We conducted a functional evaluation of the p.Asp313Asn variant of the B4GALNT1 protein. The N-terminal FLAG-tagged WT or p.Asp313Asn protein was transiently expressed in B4GALNT1-KO HEK293T cells, and GM2S activity was assayed using fluorescent-labeled GM3 (NBD-GM3) as the acceptor substrate and solubilized microsomal membranes as the enzyme source. The WT of B4GALNT1 exhibited GalNAc transferase activity toward GM3, as observed by the product peak (GM2) from the enzyme reaction being eluted earlier than the acceptor substrate peak (GM3; Figure 5A). In contrast, the reaction with p.Asp313Asn showed no product peak, even though the protein was expressed at a similar level to WT, as detected by the FLAG antibody on Western blotting (Figure 5B), demonstrating that the p.Asp313Asn mutant did not exhibit GM2S activity in a detectable range. Similar to numerous other glycosyltransferases, the B4GALNT1 protein localizes to the Golgi apparatus. We examined the subcellular localization of the p.Asp313Asn variant protein stably expressed in B4GALNT1-KO cells. Since the signal sequence required for the endoplasmic reticulum (ER) export and Golgi retention of B4GALNT1 exists at the N terminus (Uemura et al., 2015), a C-terminal FLAG-tagged version of the construct was used for a subcellular localization analysis. Immunocytochemistry for B4GALNT1 stably expressed in KO cells indicated that the p.Asp313Asn protein localized not only to the Golgi, but also to the ER (Figure 5C). This result indicates that Golgi localization was affected in the mutant protein.

## 3.5 Missense variants in the *B4GALNT1* gene extracted from jMorp

To evaluate the GM2S activity of B4GALNT1 variant proteins in the Japanese population, we searched for novel missense variants using the Japanese Multi Omics Reference Panel known as jMorp, a database that contains metabolome and proteome data for plasma obtained from healthy Japanese volunteers from ToMMo (Tadaka et al., 2018). Among the numerous missense variants in the *B4GALNT1* gene, we extracted 11 variants predicted to cause deleterious amino acid substitutions using SIFT and Polyphen2

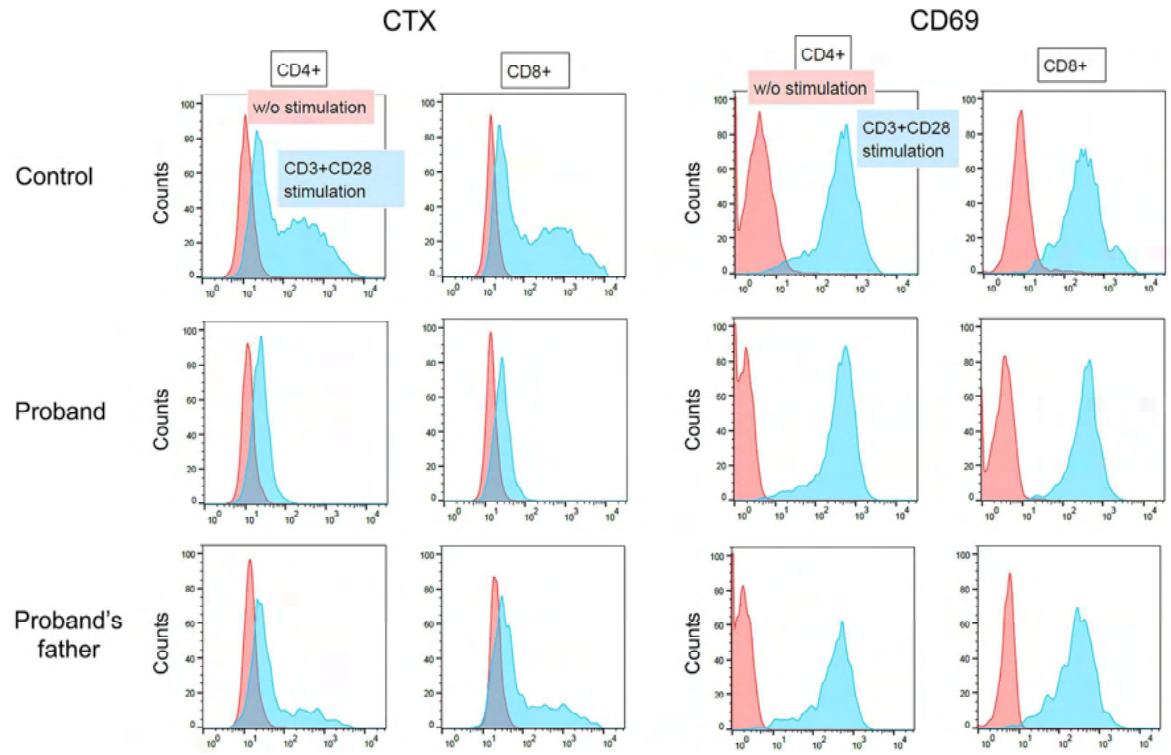


FIGURE 4
Flow cytometry of activated peripheral blood T cells. Peripheral blood mononuclear cells obtained from an age-matched control male, the patient (proband), and the patient's father, were cultured with or without anti-CD3 and anti-CD28. Two days later, cells were stained with a combination of antibodies including CD4-FITC, CD8-PE-Cy7, and CD69-APC. CD69 is an activation marker of T cells. The cells surface expression of GM1 was assessed by CTX staining.

prediction tools (Adzhubei et al., 2010; Vaser et al., 2016), as shown in Table 1. Ten of the missense variants have not been reported, while one variant, p.D433A, was previously detected in SPG26 patients (Boukhris et al., 2013). Based on the American College of Medical Genetics and Genomics (ACMG) guidelines (Richards et al., 2015), the p.D433A variant was classified as pathogenic, and the other variants were classified as uncertain significance.

### 3.6 Evaluation of the subcellular localization and GM2S activity of missense variants

To evaluate the functional impact of missense variants of B4GALNT1 extracted from jMorp, we examined the subcellular localization of the C-terminal FLAG-tagged variant proteins stably expressed in B4GALNT1-KO cells. B4GALNT1-expressing cells obtained by puromycin selection were initially analyzed by Western blotting for protein expression (Figure 6A). Expression levels varied in the variants, suggesting that some of the variants affected protein stability in cells. Interestingly, indirect immunostaining with the FLAG antibody revealed that many of the variants analyzed had both Golgi and ER staining patterns to different degrees (Figure 6B), similar to the p.Asp313Asn variant.

We then assessed the GM2S activities of these variants using microsomal membranes from transiently transfected HEK293T B4GALNT1-KO cells with N-terminal FLAG-tagged constructs. Enzyme activity was normalized by the expression levels of B4GALNT1 proteins assessed by Western blotting (Figure 6C). In the two sets of experiments, a known patients' mutation p.Asp433Ala showed the loss of enzyme activity as previously reported (Boukhris et al., 2013; Bhuiyan et al., 2019). The novel missense variants, p.Asn437Lys, p.Ala441Glu, p.Pro453His, and p.Arg519Trp, also showed no activity, while p.Phe438Leu exhibited a very weak activity at less than 10% that of WT activity. Since biallelic pathogenic mutations of B4GALNT1 cause SPG26, these novel variants may be carrier mutations.

## 4 Discussion

HSP is a highly heterogeneous group of genetic neurodegenerative disorders, and its pathogenic mechanisms and clinical features vary according to the gene responsible. Next generation sequencing is cost-effective and widely available for diagnoses, but has limitations, and a molecular diagnosis is required to identify the SPG subtype and offer the best therapeutic option to each HSP patient (Shribman et al., 2019; Meyyazhagan and Orlacchio, 2022). SPG26, a complicated form of HSP, is caused by biallelic *B4GALNT1* variants and the clinical phenotypes are similar to those observed in *B4galnt1* KO mice (Takamiya et al., 1996; Sheikh et al., 1999; Boukhris et al., 2013; Harlalka et al., 2013). The GM2S activity of the B4GALNT1 protein is required for the biosynthesis of the complex gangliosides GD1a and

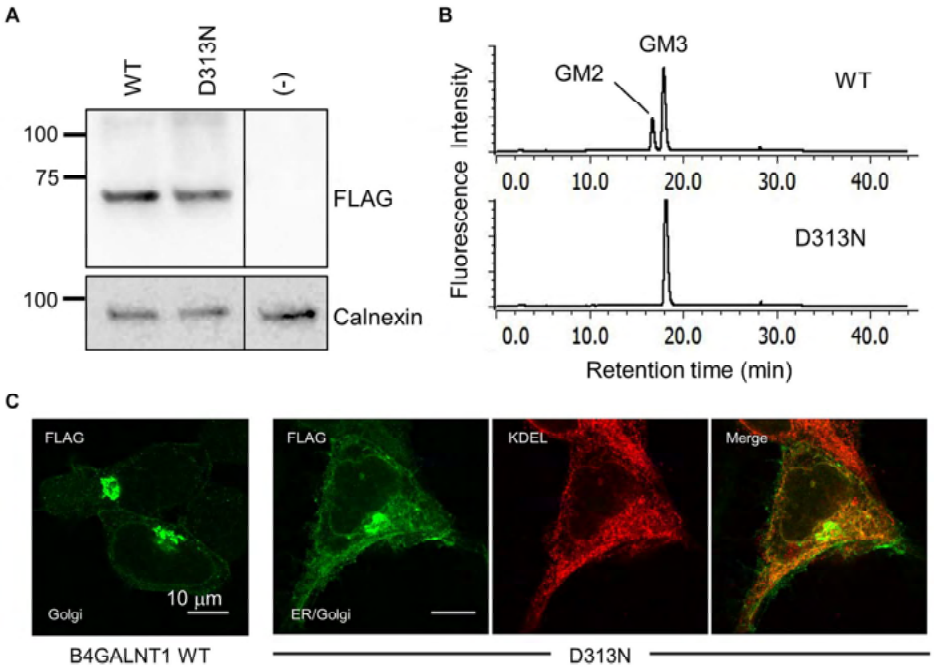


FIGURE 5
Enzyme activity assay and subcellular localization of the p.Asp313Asn mutant. **(A)** Western blotting for B4GALNT1 proteins transiently expressed in HEK293T/B4GALNT1-KO cells. Anti-FLAG blotting of microsomal membranes collected from cells transfected with B4GALNT1 WT and the p. Asp313Asn (D313N) mutant (upper). The same membrane was blotted with anti-calnexin antibody after stripping to assess the loading amount of membrane proteins (lower). The D313N protein was expressed at a similar level to the WT. **(B)** HPLC chromatograms of the GM2S reaction product. A reaction mixture using fluorescence-labeled GM3 as the substrate was analyzed by HPLC. The reaction was performed with solubilized microsomal membranes from B4GALNT1-KO cells transiently transfected with WT or D313N B4GALNT1. A product peak was not detected in the reaction with D313N. **(C)** Immunohistochemistry for the B4GALNT1 protein in B4GALNT1-KO cells stably expressing WT or D313N. The ER was visualized by staining with the anti-KDEL antibody.

TABLE 1 *B4GALNT1* missense variants extracted from jMorp 8.3KJPN.

| | | | | | | Allele frequency | |
|---|---|---|---|---|---|---|---|
| Position (GRCh37/hg19) | rsID | Transcript consequence | B4GALNT1 variants | PolyPhen2 | SIFT | ToMMo 8.3KJPN | gnomAD v2.1.1 Total |
| 12:58025836 | rs1408032467 | c.80C>A | T27N | D | T | 0.0001 | NF |
| 12:58025094 | rs775744221 | c.272T>C | L91P | D | D-LC | 0.0001 | 0.000003978 |
| 12:58023984 | N/A | c.663A>C | Q221H | D | D-LC | 0.0001 | NF |
| 12:58022596 | rs778379778 | c.902G>A | R301H | D | D | 0.0002 | 0.000007953 |
| 12:58021487 | rs879255242 | c.1298A>C | D433A | D | D | 0.0001 | NF |
| 12:58021474 | N/A | c.1311C>G | N437K | D | D | 0.0001 | NF |
| 12:58021471 | N/A | c.1314C>A | F438L | D | D | 0.0001 | NF |
| 12:58021463 | rs563575730 | c.1322C>A | A441E | D | D | 0.0002 | NF |
| 12:58021427 | N/A | c.1358C>A | P453H | D | D | 0.0001 | NF |
| 12:58020574 | rs755171392 | c.1555C>T | R519W | D | D | 0.0001 | 0.000003976 |
| 12:58020553 | rs1008314263 | c.1576C>T | R526W | D | T | 0.0001 | 0.000003976 |

D, damaging; T, tolerated; LC, low confidence; NF, not found.

GT1b, which are primarily expressed on axonal membranes and serve as receptors for myelin-associated glycoprotein (MAG; Yang et al., 1996; Collins et al., 1997). MAG is also known as Siglec-4, a member of the Siglec family that comprises sialic acid-binding immunoglobulin-like lectins (Macauley et al., 2014), is expressed on the innermost myelin sheath in oligodendrocytes and Schwann cells, and functions in bidirectional axon–glia signaling and inhibiting axon regeneration to maintain myelinated axons (Quarles, 2007; Lopez,

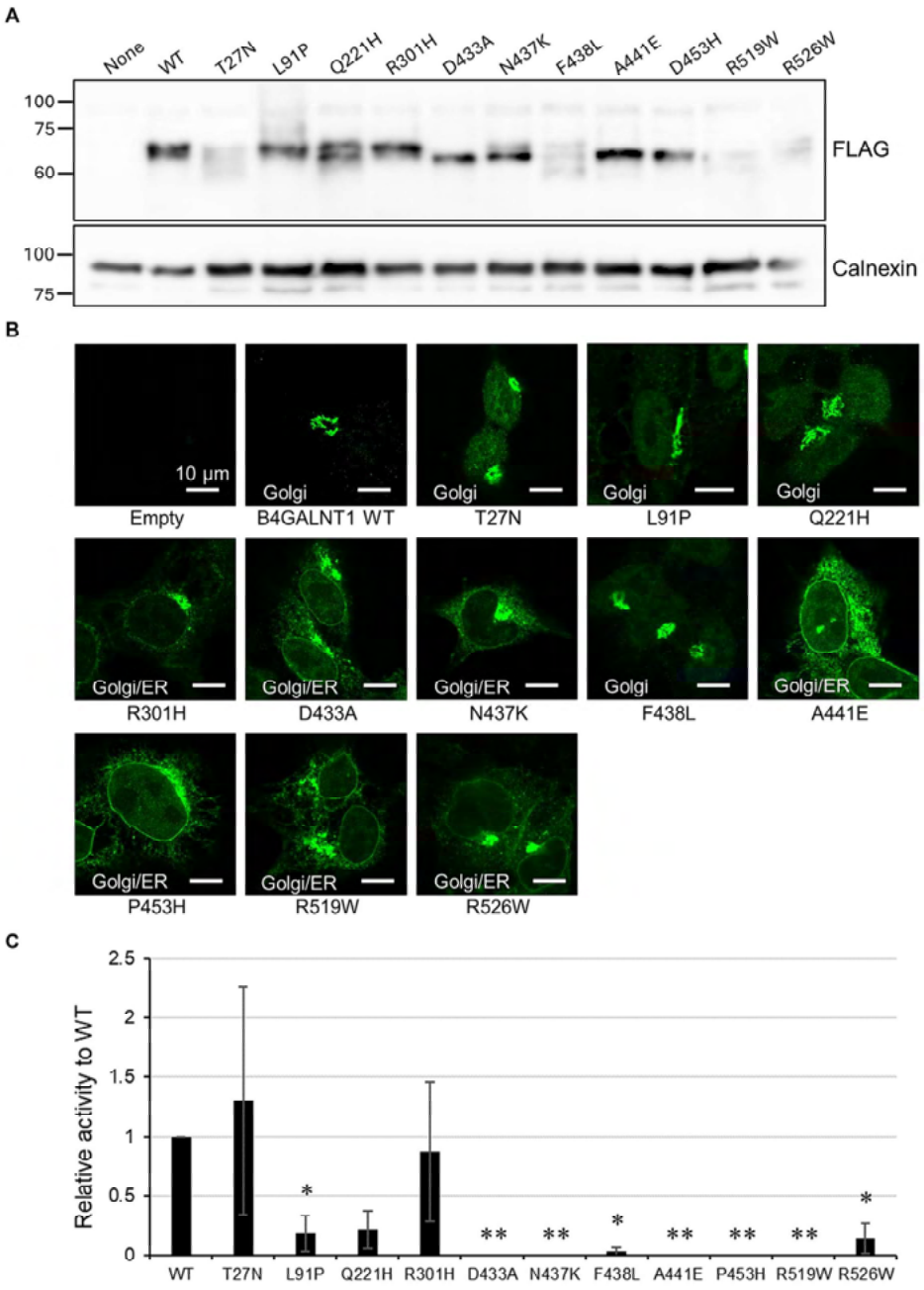


FIGURE 6
Subcellular localization and GM2S activity of B4GALNT1 variants. **(A)** Western blotting for B4GALNT1 proteins stably expressed in HEK293T/B4GALNT1-KO cells. Calnexin served as the loading control. **(B)** Immunohistochemistry for the B4GALNT1 protein in B4GALNT1-KO cells stably expressing the WT or each variant. **(C)** GM2S assay of the B4GALNT1 WT and variants. The assay was performed as three independent sets of experiments with triplicates in each set, and relative activity with respect to the WT, calculated as the peak area ratio as described in Materials and methods, and the standard deviation in the three experiments are shown. *$p < 0.05$ vs. WT; **$p < 0.01$ vs. WT, by Dunnett's test.

2014). MAG KO mice exhibited modest nervous system abnormalities, similar to *B4galnt1* KO mice (Li et al., 1994; Montag et al., 1994; Takamiya et al., 1996; Sheikh et al., 1999), while MAG/*B4galnt1* double KO mice had similar neuropathological phenotypes to single KO mice without exacerbation (Pan et al., 2005), supporting the contribution of the MAG-ganglioside interaction to axon-myelin stability. The combination of the *cis* homodimerization of MAG and *trans* interactions with gangliosides were identified as the mechanisms underlying MAG functions (Pronker et al., 2016).

In the present study, we found a novel missense variant (c.937G>A p.Asp313Asn) in the *B4GALNT1* gene from a patient with progressive multi-system neurodegeneration. The clinical features observed in our patient were similar to those in previously reported patients with HSP26 (Boukhris et al., 2013). Although the

crystal structure of the B4GALNT1 protein has not yet been reported, a prediction based on homology modeling suggested the involvement of the Asp313 residue in the binding of the donor substrate UDP-GalNAc, which is required for glycosyltransferase activity. A functional analysis, including the GM2S enzymatic assay, using patient-derived cells and the expression of the B4GALNT1 protein in cultured cells revealed that the amino acid substitution (p.Asp313Asn) caused the loss of GM2S enzyme activity, leading to the molecular diagnosis of SPG26. This is the first SPG26 case to be reported in Japan. To expand our understanding of SPG26 in the Japanese population, we extracted missense *B4GALNT1* variants from jMorp (ToMMo 8.3KJPN) that were predicted to be deleterious by the SIFT and PolyPhen2 programs performed a functional analysis of these variant proteins expressed in B4GALNT1-KO cells. In a previous study by Bhuiyan et al. (2019), the GM2S enzyme activity and subcellular localization of mutant B4GALNT1 proteins for 11 genetic mutations previously reported in SPG26 patients were examined. Four were missense variants, including p.Asp433Ala, which was also analyzed in the present study. They demonstrated that the majority of mutations resulted in the loss of enzyme activity, which may be responsible for the clinical features of HSP. One of the missense mutants, p.Arg300Cys, exhibited weak activity (approximately 10% that of the WT protein). In their study, these mutants as well as the WT protein exhibited similar Golgi localization patterns, evaluated by the transient transfection of HEK293T cells with C-terminal myc-$His_6$-tagged B4GALNT1 constructs (Bhuiyan et al., 2019). In the present study, among the novel variants extracted from jMorp, p.Asn437Lys, p.Ala441Glu, p.Pro453His and p.Arg519Trp did not exhibit enzyme activity and p.Phe438Leu showed less than 10% of the activity of the WT, indicating that these are pathogenic variants. A missense variant found in a HSP patient that caused the amino acid substitution of Arg519 to Pro has been also reported to result in the loss of enzyme activity (Alecu et al., 2022). The immunocytochemical analysis using stable cells expressing C-terminal FLAG-tagged B4GALNT1 proteins showed that most of the missense variants localized not only to the Golgi, but also the ER, as was the case with the p.Asp313Asn variant, indicating that each single amino acid substitution may affect export from the ER. Changes in protein folding due to the amino acid substitution may trigger the quality control of ER export, which monitors the folding status of proteins captured in COPII vesicles by cargo receptors (Phillips et al., 2020). Therefore, the missense B4GALNT1 variants examined in the present study may partially affect ER export.

Consistent with the previous findings (Tani-ichi et al., 2005) and as demonstrated in the present analysis of the peripheral blood T cells from our HSP patient and controls (Figure 3), activation by anti-CD3/CD28 markedly enhanced *B4GALNT1* gene expression and GM2S activity, resulting in the up-regulated expression of GM1 in T cells. Therefore, the use of activated peripheral blood T cells may contribute to a molecular diagnosis and facilitate carrier screening for deleterious *B4GALNT1* variants. In conclusion, our functional studies on novel *B4GALNT1* variants confirmed a loss-of-function, leading to a diagnosis of SPG26, and the identification of unaffected variant carriers. Our approach will contribute to the clinical diagnosis of patients with HSP.

## Data availability statement

The datasets presented in this article are not readily available because they contain personal data. Requests to access the datasets should be directed to the corresponding author.

## Ethics statement

The studies involving humans were approved by the Ethics Committee of Shinshu University School of Medicine/the Ethics Committee of Tohoku Medical and Pharmaceutical University. The studies were conducted in accordance with the local legislation and institutional requirements. The participants provided their written informed consent to participate in this study. Written informed consent was obtained from the individual(s) for the publication of any potentially identifiable images or data included in this article.

## Author contributions

K-iI: Conceptualization, Data curation, Funding acquisition, Investigation, Supervision, Writing – original draft, Writing – review & editing. KN: Data curation, Funding acquisition, Investigation, Resources, Writing – review & editing. FS: Investigation, Writing – review & editing. J-CH: Investigation, Writing – original draft. MNag: Investigation, Writing – review & editing. TN: Investigation, Writing – review & editing. JI: Investigation, Writing – review & editing. HY: Investigation, Writing – review & editing. MK: Investigation, Writing – review & editing. NT: Data curation, Funding acquisition, Investigation, Writing – review & editing. NaM: Funding acquisition, Supervision, Writing – review & editing. SU: Investigation, Writing – review & editing. SO: Formal analysis, Writing – review & editing. NoM: Formal analysis, Writing – review & editing. YY: Formal analysis, Writing – review & editing. AT: Writing – review & editing. KA-K: Resources, Software, Writing – review & editing. SN: Writing – review & editing. J-iF: Writing – review & editing. TK: Resources, Writing – review & editing. MNak: Resources, Writing – review & editing. TS: Resources, Writing – review & editing. ST: Software, Writing – review & editing. MS: Resources, Writing – review & editing. KK: Resources, Software, Writing – review & editing. YN: Project administration, Writing – review & editing. IO: Project administration, Writing – review & editing. YS: Supervision, Writing – review & editing. J-iI: Funding acquisition, Supervision, Writing – review & editing.

## Funding

The author(s) declare that financial support was received for the research, authorship, and/or publication of this article. This study was supported by JSPS KAKENHI, grant numbers JP21K06531 (K-iI), JP20H03452 (J-iI), JP23K15353 (NT), and JP24K02230 (NaM); AMED under grant numbers JP23ek0109674, JP23ek0109549, JP23ek0109617, JP23ek0109648 (NaM), and

JP22ek0109446 (SN, TK, YY, KA-K, J-iF, and J-iI); the Takeda Science Foundation (NaM); and the Ministry of Health, Labour and Welfare under grant number JPmh23fc1010 (KN).

## Acknowledgments

The authors thank the patient and her family for their understanding and consent. The authors also thank J. Fushimi for technical assistance. SN, KA-K, AT, and J-iF are supported by the "Human Glycome Atlas Project" as one of the "Large-Scale Academic Frontier Promotion Projects" of the Ministry of Education, Culture, Sports, Science and Technology (MEXT).

## Conflict of interest

The authors declare that the research was conducted in the absence of any commercial or financial relationships that could be construed as a potential conflict of interest.

## Publisher's note

All claims expressed in this article are solely those of the authors and do not necessarily represent those of their affiliated organizations, or those of the publisher, the editors and the reviewers. Any product that may be evaluated in this article, or claim that may be made by its manufacturer, is not guaranteed or endorsed by the publisher.

## References

Adzhubei, I. A., Schmidt, S., Peshkin, L., Ramensky, V. E., Gerasimova, A., Bork, P., et al. (2010). A method and server for predicting damaging missense mutations. *Nat. Methods* 7, 248–249. doi: 10.1038/nmeth0410-248

Alecu, J. E., Ohmi, Y., Bhuiyan, R. H., Inamori, K. I., Nitta, T., Saffari, A., et al. (2022). Functional validation of novel variants in B4GALNT1 associated with early-onset complex hereditary spastic paraplegia with impaired ganglioside synthesis. *Am. J. Med. Genet. A* 188, 2590–2598. doi: 10.1002/ajmg.a.62880

Bhuiyan, R. H., Ohmi, Y., Ohkawa, Y., Zhang, P., Takano, M., Hashimoto, N., et al. (2019). Loss of enzyme activity in mutated B4GALNT1 gene products in patients with hereditary spastic paraplegia results in relatively mild neurological disorders: similarity with phenotypes of B4galnt1 knockout mice. *Neuroscience* 397, 94–106. doi: 10.1016/j.neuroscience.2018.11.034

Boukhris, A., Schule, R., Loureiro, J. L., Lourenco, C. M., Mundwiller, E., Gonzalez, M. A., et al. (2013). Alteration of ganglioside biosynthesis responsible for complex hereditary spastic paraplegia. *Am. J. Hum. Genet.* 93, 118–123. doi: 10.1016/j.ajhg.2013.05.006

Collins, B. E., Yang, L. J., Mukhopadhyay, G., Filbin, M. T., Kiso, M., Hasegawa, A., et al. (1997). Sialic acid specificity of myelin-associated glycoprotein binding. *J. Biol. Chem.* 272, 1248–1255. doi: 10.1074/jbc.272.2.1248

Harlalka, G. V., Lehman, A., Chioza, B., Baple, E. L., Maroofian, R., Cross, H., et al. (2013). Mutations in B4GALNT1 (GM2 synthase) underlie a new disorder of ganglioside biosynthesis. *Brain* 136, 3618–3624. doi: 10.1093/brain/awt270

Ichikawa, S., Sakiyama, H., Suzuki, G., Hidari, K. I., and Hirabayashi, Y. (1996). Expression cloning of a cDNA for human ceramide glucosyltransferase that catalyzes the first glycosylation step of glycosphingolipid synthesis. *Proc. Natl. Acad. Sci. U. S. A.* 93, 4638–4643. doi: 10.1073/pnas.93.10.4638

Inamori, K. I., and Inokuchi, J. I. (2022). Ganglioside GM3 synthase deficiency in mouse models and human patients. *Int. J. Mol. Sci.* 23:368. doi: 10.3390/ijms23105368

Inamori, K. I., Nitta, T., Shishido, F., Watanabe, S., Ohno, I., and Inokuchi, J. I. (2023). Sialyltransferase activity assay for ganglioside GM3 synthase. *Methods Mol. Biol.* 2613, 101–110. doi: 10.1007/978-1-0716-2910-9_9

Inokuchi, J. I., Inamori, K. I., Kabayama, K., Nagafuku, M., Uemura, S., Go, S., et al. (2018). Biology of GM3 ganglioside. *Prog. Mol. Biol. Transl. Sci.* 156, 151–195. doi: 10.1016/bs.pmbts.2017.10.004

Inoue, Y., Tsuchida, N., Kim, C. A., de Oliveira Stephan, B., Castro, M. A. A., Honjo, R. S., et al. (2024). Novel compound heterozygous ABCA2 variants cause IDPOGSA, a variable phenotypic syndrome with intellectual disability. *J. Hum. Genet.* 69, 163–167. doi: 10.1038/s10038-024-01219-8

Ishii, A., Ohta, M., Watanabe, Y., Matsuda, K., Ishiyama, K., Sakoe, K., et al. (1998). Expression cloning and functional characterization of human cDNA for ganglioside GM3 synthase. *J. Biol. Chem.* 273, 31652–31655. doi: 10.1074/jbc.273.48.31652

Ji, S., Samara, N. L., Revoredo, L., Zhang, L., Tran, D. T., Muirhead, K., et al. (2018). A molecular switch orchestrates enzyme specificity and secretory granule morphology. *Nat. Commun.* 9:3508. doi: 10.1038/s41467-018-05978-9

Kumagai, T., Sato, T., Natsuka, S., Kobayashi, Y., Zhou, D., Shinkai, T., et al. (2010). Involvement of murine beta-1,4-galactosyltransferase V in lactosylceramide biosynthesis. *Glycoconj. J.* 27, 685–695. doi: 10.1007/s10719-010-9313-2

Li, C., Tropak, M. B., Gerlai, R., Clapoff, S., Abramow-Newerly, W., Trapp, B., et al. (1994). Myelination in the absence of myelin-associated glycoprotein. *Nature* 369, 747–750. doi: 10.1038/369747a0

Lopez, P. H. H. (2014). Role of myelin-associated glycoprotein (Siglec-4a) in the nervous system. *Adv Neurobiol.* 9, 245–262. doi: 10.1007/978-1-4939-1154-7_11

Macauley, M. S., Crocker, P. R., and Paulson, J. C. (2014). Siglec-mediated regulation of immune cell function in disease. *Nat. Rev. Immunol.* 14, 653–666. doi: 10.1038/nri3737

Meyyazhagan, A., and Orlacchio, A. (2022). Hereditary spastic paraplegia: an update. *Int. J. Mol. Sci.* 23:697. doi: 10.3390/ijms23031697

Montag, D., Giese, K. P., Bartsch, U., Martini, R., Lang, Y., Bluthmann, H., et al. (1994). Mice deficient for the myelin-associated glycoprotein show subtle abnormalities in myelin. *Neuron* 13, 229–246. doi: 10.1016/0896-6273(94)90472-3

Nagata, Y., Yamashiro, S., Yodoi, J., Lloyd, K. O., Shiku, H., and Furukawa, K. (1992). Expression cloning of beta 1,4 N-acetylgalactosaminyltransferase cDNAs that determine the expression of GM2 and GD2 gangliosides. *J. Biol. Chem.* 267, 12082–12089. doi: 10.1016/S0021-9258(19)49809-8

Nishie, T., Hikimochi, Y., Zama, K., Fukusumi, Y., Ito, M., Yokoyama, H., et al. (2010). Beta4-galactosyltransferase-5 is a lactosylceramide synthase essential for mouse extra-embryonic development. *Glycobiology* 20, 1311–1322. doi: 10.1093/glycob/cwq098

Nomura, T., Takizawa, M., Aoki, J., Arai, H., Inoue, K., Wakisaka, E., et al. (1998). Purification, cDNA cloning, and expression of UDP-gal: glucosylceramide beta-1,4-galactosyltransferase from rat brain. *J. Biol. Chem.* 273, 13570–13577. doi: 10.1074/jbc.273.22.13570

Pan, B., Fromholt, S. E., Hess, E. J., Crawford, T. O., Griffin, J. W., Sheikh, K. A., et al. (2005). Myelin-associated glycoprotein and complementary axonal ligands, gangliosides, mediate axon stability in the CNS and PNS: neuropathology and behavioral deficits in single- and double-null mice. *Exp. Neurol.* 195, 208–217. doi: 10.1016/j.expneurol.2005.04.017

Phillips, B. P., Gomez-Navarro, N., and Miller, E. A. (2020). Protein quality control in the endoplasmic reticulum. *Curr. Opin. Cell Biol.* 65, 96–102. doi: 10.1016/j.ceb.2020.04.002

Pronker, M. F., Lemstra, S., Snijder, J., Heck, A. J., Thies-Weesie, D. M., Pasterkamp, R. J., et al. (2016). Structural basis of myelin-associated glycoprotein adhesion and signalling. *Nat. Commun.* 7:13584. doi: 10.1038/ncomms13584

Quarles, R. H. (2007). Myelin-associated glycoprotein (MAG): past, present and beyond. *J. Neurochem.* 100, 1431–1448. doi: 10.1111/j.1471-4159.2006.04319.x

Ran, F. A., Hsu, P. D., Wright, J., Agarwala, V., Scott, D. A., and Zhang, F. (2013). Genome engineering using the CRISPR-Cas9 system. *Nat. Protoc.* 8, 2281–2308. doi: 10.1038/nprot.2013.143

Richards, S., Aziz, N., Bale, S., Bick, D., Das, S., Gastier-Foster, J., et al. (2015). Standards and guidelines for the interpretation of sequence variants: a joint consensus recommendation of the American College of Medical Genetics and Genomics and the Association for Molecular Pathology. *Genet. Med.* 17, 405–424. doi: 10.1038/gim.2015.30

Schnaar, R. L. (2019). The biology of gangliosides. *Adv. Carbohydr. Chem. Biochem.* 76, 113–148. doi: 10.1016/bs.accb.2018.09.002

Sheikh, K. A., Sun, J., Liu, Y., Kawai, H., Crawford, T. O., Proia, R. L., et al. (1999). Mice lacking complex gangliosides develop Wallerian degeneration and myelination defects. *Proc. Natl. Acad. Sci. U. S. A.* 96, 7532–7537. doi: 10.1073/pnas.96.13.7532

Shribman, S., Reid, E., Crosby, A. H., Houlden, H., and Warner, T. T. (2019). Hereditary spastic paraplegia: from diagnosis to emerging therapeutic approaches. *Lancet Neurol.* 18, 1136–1146. doi: 10.1016/S1474-4422(19)30235-2

Simpson, M. A., Cross, H., Proukakis, C., Priestman, D. A., Neville, D. C., Reinkensmeier, G., et al. (2004). Infantile-onset symptomatic epilepsy syndrome caused by a homozygous loss-of-function mutation of GM3 synthase. *Nat. Genet.* 36, 1225–1229. doi: 10.1038/ng1460

Tadaka, S., Saigusa, D., Motoike, I. N., Inoue, J., Aoki, Y., Shirota, M., et al. (2018). jMorp: Japanese multi omics reference panel. *Nucleic Acids Res.* 46, D551–D557. doi: 10.1093/nar/gkx978

Takamiya, K., Yamamoto, A., Furukawa, K., Yamashiro, S., Shin, M., Okada, M., et al. (1996). Mice with disrupted GM2/GD2 synthase gene lack complex gangliosides but exhibit only subtle defects in their nervous system. *Proc. Natl. Acad. Sci. U. S. A.* 93, 10662–10667. doi: 10.1073/pnas.93.20.10662

Tani-ichi, S., Maruyama, K., Kondo, N., Nagafuku, M., Kabayama, K., Inokuchi, J., et al. (2005). Structure and function of lipid rafts in human activated T cells. *Int. Immunol.* 17, 749–758. doi: 10.1093/intimm/dxh257

Uemura, S., Shishido, F., Kashimura, M., and Inokuchi, J. (2015). The regulation of ER export and Golgi retention of ST3Gal5 (GM3/GM4 synthase) and B4GalNAcT1 (GM2/GD2/GA2 synthase) by arginine/lysine-based motif adjacent to the transmembrane domain. *Glycobiology* 25, 1410–1422. doi: 10.1093/glycob/cwv071

Vaser, R., Adusumalli, S., Leng, S. N., Sikic, M., and Ng, P. C. (2016). SIFT missense predictions for genomes. *Nat. Protoc.* 11, 1–9. doi: 10.1038/nprot.2015.123

Waterhouse, A., Bertoni, M., Bienert, S., Studer, G., Tauriello, G., Gumienny, R., et al. (2018). SWISS-MODEL: homology modelling of protein structures and complexes. *Nucleic Acids Res.* 46, W296–W303. doi: 10.1093/nar/gky427

Yamashita, T., Hashiramoto, A., Haluzik, M., Mizukami, H., Beck, S., Norton, A., et al. (2003). Enhanced insulin sensitivity in mice lacking ganglioside GM3. *Proc. Natl. Acad. Sci. U. S. A.* 100, 3445–3449. doi: 10.1073/pnas.0635898100

Yang, L. J., Zeller, C. B., Shaper, N. L., Kiso, M., Hasegawa, A., Shapiro, R. E., et al. (1996). Gangliosides are neuronal ligands for myelin-associated glycoprotein. *Proc. Natl. Acad. Sci. U. S. A.* 93, 814–818. doi: 10.1073/pnas.93.2.814

Yao, D., McGonigal, R., Barrie, J. A., Cappell, J., Cunningham, M. E., Meehan, G. R., et al. (2014). Neuronal expression of GalNAc transferase is sufficient to prevent the age-related neurodegenerative phenotype of complex ganglioside-deficient mice. *J. Neurosci.* 34, 880–891. doi: 10.1523/JNEUROSCI.3996-13.2014

frontiers | Frontiers in Neuroscience

TYPE Original Research
PUBLISHED 25 July 2024
DOI 10.3389/fnins.2024.1387221

Check for updates

OPEN ACCESS

EDITED BY
Suman Chowdhury,
Rutgers, The State University of New Jersey, United States

REVIEWED BY
Shenzhao Lu,
Baylor College of Medicine, United States
Yuki Ohkawa,
Osaka International Cancer Institute, Japan

*CORRESPONDENCE
Jin-ichi Inokuchi
✉ inokuchi@chem.sci.osaka-u.ac.jp

RECEIVED 17 February 2024
ACCEPTED 10 July 2024
PUBLISHED 25 July 2024

CITATION
Inokuchi J-i, Go S, Suzuki A, Nakagawasai O, Odaira-Satoh T, Veillon L, Nitta T, McJarrow P, Kanoh H, Inamori K-i, Tan-No K and Collett M (2024) Dietary gangliosides rescue GM3 synthase deficiency outcomes in mice accompanied by neurogenesis in the hippocampus. *Front. Neurosci.* 18:1387221. doi: 10.3389/fnins.2024.1387221

COPYRIGHT
© 2024 Inokuchi, Go, Suzuki, Nakagawasai, Odaira-Satoh, Veillon, Nitta, McJarrow, Kanoh, Inamori, Tan-No and Collett. This is an open-access article distributed under the terms of the Creative Commons Attribution License (CC BY). The use, distribution or reproduction in other forums is permitted, provided the original author(s) and the copyright owner(s) are credited and that the original publication in this journal is cited, in accordance with accepted academic practice. No use, distribution or reproduction is permitted which does not comply with these terms.

# Dietary gangliosides rescue GM3 synthase deficiency outcomes in mice accompanied by neurogenesis in the hippocampus

Jin-ichi Inokuchi[1,2]*, Shinji Go[1], Akemi Suzuki[1], Osamu Nakagawasai[3], Takayo Odaira-Satoh[3], Lucas Veillon[1], Takahiro Nitta[1], Paul McJarrow[4], Hirotaka Kanoh[1], Kei-ichiro Inamori[1], Koichi Tan-No[3] and Michael Collett[4]

[1]Division of Glycopathology, Institute of Molecular Biomembranes and Glycobiology, Tohoku Medical and Pharmaceutical University, Sendai, Japan, [2]Forefront Research Centre, Graduate School of Science, Osaka University, Toyonaka, Japan, [3]Division of Pharmacology, Faculty of Pharmaceutical Sciences, Tohoku Medical and Pharmaceutical University, Sendai, Japan, [4]Fonterra Research and Development Centre, Palmerston North, New Zealand

Ganglioside GM3 synthase is a key enzyme involved in the biosynthesis of gangliosides. GM3 synthase deficiency (GM3SD) causes an absence of GM3 and all downstream biosynthetic derivatives, including all the a-, b-, c-series gangliosides, commonly found in neural tissues. The affected individuals manifest with severe irritability, intractable seizures, hearing loss, blindness, and profound intellectual disability. It has been reported that oral ganglioside supplementation has achieved some significant improvements in clinical symptoms, growth parameters, and developmental and cognitive scores in GM3SD patients. To gain insight into the molecular mechanisms of this supplementation, we performed supplementation of oral bovine milk gangliosides to GM3 synthase-deficient mice from early weaning periods. The oral milk ganglioside preparations were dominated by GM3 and GD3 gangliosides. Oral milk ganglioside supplementation improved the decreased cognitive function observed in GM3 synthase-deficient mice. The improvement in cognitive function was accompanied by increased ganglioside levels and neurogenesis in the hippocampus in the supplemented animals.

KEYWORDS

**GM3 synthase deficiency, milk gangliosides, GM3, GD3, oral supplementation, neurogenesis, hippocampus, cognitive function**

## 1 Introduction

In 1998, the human GM3 synthase gene (*GM3S*) was cloned (Ishii et al., 1998); 6 years later, the GM3S deficiency (GM3SD) was first reported by A. H. Crosby's group as an autosomal recessive infantile-onset epilepsy syndrome associated with developmental stagnation and blindness in Old Order Amish (Simpson et al., 2004). Biallelic pathogenic *ST3GAL5* variants led to the disrupted synthesis of a-, b- and c-series gangliosides and consequently to severe infantile-onset various neurological disorders (Table 1). Until today, GM3S deficiency has been found in many ethnic groups not only Old Order Amish (Simpson et al., 2004) but also French (Fragaki et al., 2013), Pakistani (Gordon-Lipkin et al., 2018), African American (Boccuto et al.,

TABLE 1 Clinical features of ST3GAL5 patients[a]

| Patient descent | Genotype | Disorder | | | | | | | | | | | Reference |
|---|---|---|---|---|---|---|---|---|---|---|---|---|---|
| | | Mc | Pd/r | MD | Ep | AEEG | SHI | VI | Ir | DD | Sc | AP | |
| Old Order Amish | c.862C > T<br>R288*<br>Homozygous | NR | 38/38 | 8/8 | 38/38 | 8/8 | NR | 8/8 | 8/8 | 8/8 | NR | 27/38 | Simpson et al. (2004) and Wang et al. (2013) |
| Old Order Amish | c.862C > T<br>R288*<br>Homozygous | 50/50 | 50/50 | 42/50 | 36/50 | 31/32 | 15/15 | 10/13 | 35/50 | 50/50 | 14/50 | Few | Bowser et al. (2019) |
| French | c.862C > T<br>R288*<br>Homozygous | NR | 2/2 | 2/2 | 2/2 | NR | 2/2 | 2/2 | 2/2 | 2/2 | NR | NR | Fragaki et al. (2013) |
| Pakistani | c.862C > T<br>R288*<br>Homozygous | 3/3 | 3/3 | 3/3 | 0/3 | 3/3 | 3/3 | 3/3 | 3/3 | 3/3 | NR | 2/3 | Gordon-Lipkin et al. (2018) |
| African-American | c.1063G > A<br>E355K<br>Homozygous | 4/4 | 4/4 | 3/3 | 1/4 | NR | NR | 0/1 | 1/1 | 4/4 | NR | 3/4 | Boccuto et al. (2014) |
| Korean | c.584G > C, c.601G > A<br>C195S,G201R<br>Comp het | 1/2 | 2/2 | 2/2 | 0/2 | NR | NR | 0/2 | 2/2 | 2/2 | NR | 1/2 | Lee et al. (2016) |
| Italian | c.1024G > A<br>G342S<br>Homozygous | 2/2 | 1/1 | 1/1 | 1/1 | 1/1 | 1/1 | 1/1 | 1/1 | 2/2 | NR | 1/1 | Indellicato et al. (2019) |
| Saudi Arabian | c.221 T > A<br>V74E<br>Homozygous | 3/3 | 3/3 | 3/3 | 3/3 | 3/3 | NR | 3/3 | 3/3 | 3/3 | NR | NR | Abdulkareem et al. (2023) |
| Chinese | c.1000delC, c.1214dupG<br>R334Efs*15, V406Sfs*10<br>Comp het | NR | 2/2 | 1/2 | 2/2 | 2/2 | 2/2 | 2/2 | 2/2 | 2/2 | 2/2 | 1/2 | Watanabe et al. (2023) |

*(Continued)*



10.3389/fnins.2024.1387221

10.3389/fnins.2024.1387221

TABLE 1 (Continued)

| Patient descent | Genotype | Disorder | | | | | | | | | | | Reference |
|---|---|---|---|---|---|---|---|---|---|---|---|---|---|
| | | Mc | Pd/r | MD | Ep | AEEG | SHI | VI | Ir | DD | Sc | AP | |
| Reunion Islander | c.740G > A G247D Homozygous; c.740G > A, c.1063G > A G247D, E355K Comp het | 9/16 | 16/16 | 14/14 | 12/16 | NR | 8/15 | 5/12 | 10/13 | 16/16 | NR | 5/16 | Heide et al. (2022) |
| Algerian | c.1255 T > C *419Rext*38 Homozygous | | | | | | | | | | | | |
| Italian | c.1000C > T, c.1166A > G R334X, H389R Comp het; c.1166A > G H389R Homozygous | | | | | | | | | | | | |
| Italian | c.1024G > A, c.1166A > G G342S, H389R Comp het | | | | | | | | | | | | |

[a]Mc, microcephaly; Pd/r, psychomotor delay/regression; MD, movement disorder; Ep, epilepsy; AEEG, abnormal EEG; SHI, sensorineural hearing impairment; VI, vision impairment; Ir, irritability; DD, developmental delay; Sc, scoliosis; AP, abnormal pigmentation; Comp Het, compound heterozygous; NR, not reported.

TABLE 2 Total analysis of ingredients of SuperZ and GL500.[a]

| Component | g/100 g sample | |
|---|---|---|
| | GL500 | SuperZ |
| Moisture | 2.8 | 3.0 |
| Lactose | 2.3 | 2.2 |
| Ash (minerals) | 12.3 | 11.2 |
| Total lipids | 82.6 | 83.6 |
| Neutral lipids | 28.41 | 27.74 |
| Glycerophospholipids | 47.59 | 47.06 |
| PC (phosphatidylcholine) | 6.32 | 5.73 |
| PI (phosphatidylinositol) | 9.11 | 8.98 |
| PS (phosphatidylserine) | 12.62 | 12.71 |
| LPC (lysophosphatidylcholine) | 0.17 | 0.00 |
| PE (phosphatidylethanolamine) | 13.50 | 14.84 |
| SM* (total sphingomyelin) | 5.32 | 4.46 |
| LPS (lysophosphatidylserine) | 0.15 | 0.18 |
| LPE (lysophosphatidylethanolamine) | 0.40 | 0.16 |
| Gangliosides | 6.6 | 8.8 |
| GM3 | 4.0 | 0.8 |
| GD3 | 2.6 | 8.0 |
| TN powder | 1.10 | 1.17 |
| Total (moisture + lactose + ash + total lipids) | 100.0 | 100.0 |

[a]Lactose calculated by difference. Neutral lipids are calculated as Total lipids – phospholipids – gangliosides. SM* is the sum of sphingomyelin + dihydrosphingomyelin. LPC, LPS, and LPE are minor lysophospholipids derived from partial hydrolysis of PC, PS, and PE. Phospholipids comprised all the total nitrogen in the protein test (N × 6.38); there was no significant level of protein in these samples.

2014), Korean (Lee et al., 2016), Italian (Indellicato et al., 2019), Reunion Islander and Algerian (Heide et al., 2022), Saudi Arabian (Abdulkareem et al., 2023), and Chinese (Watanabe et al., 2023). Various *ST3GAL5* mutations and symptoms in patients with GM3S deficiency are summarized in Table 1. This disease can cause severe neurodevelopmental defects characterized by progressive microcephaly, intellectual disability, choreoathetosis, blindness, deafness, intractable seizures, and/or pigment changes. Common features of these patients with GM3 synthase deficiency are delayed motor development, delayed language development, and reduced intellectual and memory abilities.

There have been several studies looking at the effects of exogenous and orally administered gangliosides on brain functions (Park et al., 2005; Liu et al., 2014; Reis et al., 2016; Wang et al., 2019). The supplementation of gangliosides to variously aged animals and humans and the outcomes measured (incorporation into plasma and brain; cognitive and disease/disorder states) were variable with some inconsistency. These results may be due to variations in the composition and amounts of gangliosides tested and the timing of feeding.

To solve these issues, the present study was designed to increase the amount of concentrated and purified complex milk lipids (CMLs) from milk given orally to normal weaned mice and GM3S KO mice. Two CMLs, SuperZ and GL500, were prepared with different amounts of gangliosides. As shown in Table 2, SuperZ contains a large amount of GD3 and GM3 is one-tenth of GD3. On the other hand, GL500 contains more GM3 than GD3. Pellets were prepared so that the daily oral intake of gangliosides by mice was approximately 18 mg/day (720 mg/kg bw/day) and fed from weaning at 3 weeks of age.

The memory assessment methods include the fear-conditioning test, passive avoidance test, and mazes such as the water maze and the eight radial maze. Unlike the fear-conditioning test or maze, the novel object recognition test (NORT) can be tested under more natural conditions; that is, the test can assess memory without introducing artificial rewards or punishments, such as electric shocks or food restrictions, that might affect behavior (Kudara et al., 2023). Our study aimed to determine whether GL500 or SuperZ diet feeding affected memory; the NORT allowed us to examine the memory performance of animals under conditions without external rewards or punishments. The NORT was tested, and ganglioside composition of the serum, liver, and brain regions was then measured. In addition, the effects of SuperZ and GL500 on neurogenesis in the hippocampus were also examined.

## 2 Materials and methods

### 2.1 Preparation of diets containing milk gangliosides GM3 and GD3 with different ratios

We utilized two bovine milk-derived powders called GL500 and SuperZ (Fonterra Co-operative Group Ltd) containing concentrated gangliosides GM3 and GD3 at different ratios. As indicated in Table 2, GL500 was enriched in GM3, and SuperZ was enriched in GD3. The rodent diet AIN-93G (CLEA Japan, Inc.[1]) was used as a basis for the diets. The supplementation target was to make diet pellets containing 18 mg gangliosides per 4 g (amounts of daily uptake by adult mice). Milk powders tend to weaken the hardness of pellets, but sufficient hardness can be achieved when the pellets contain 20% sucrose. We thereafter used AIN-93G containing 20% sucrose as the base diet. Pelletization involves a drying process that requires heating at 70°C for 4 h. As shown by thin-layer chromatography (TLC; Supplementary Figure S1), there were no signs of degradation or changes of GM3 and GD3 levels in the pellets compared to the respective original milk powder. Analysis of GM3 molecular species by LC–MS/MS demonstrated that molecules containing N-acyl chains C22:0, C23:0, C16:0, C24:0, and C21:0 are the major GM3 species (shown in Supplementary Figure S2). These results were consistent with the report by Fong et al. (2011).

### 2.2 Animals

GM3S KO mice were generated as described previously (Tsukamoto et al., 2005). In brief, the second exon of the 7-exon GM3 synthase gene was deleted and replaced with the neomycin resistance gene. Mutant mice were maintained on a BALB/c background by heterozygous mating to generate littermate controls. In this study, although the number of mice in each group was small, the study was performed among littermates because the experiments were conducted during the weaning period, which is affected by child-rearing. GM3S

1 https://www.clea-japan.com/products/special_diet/item_d0220

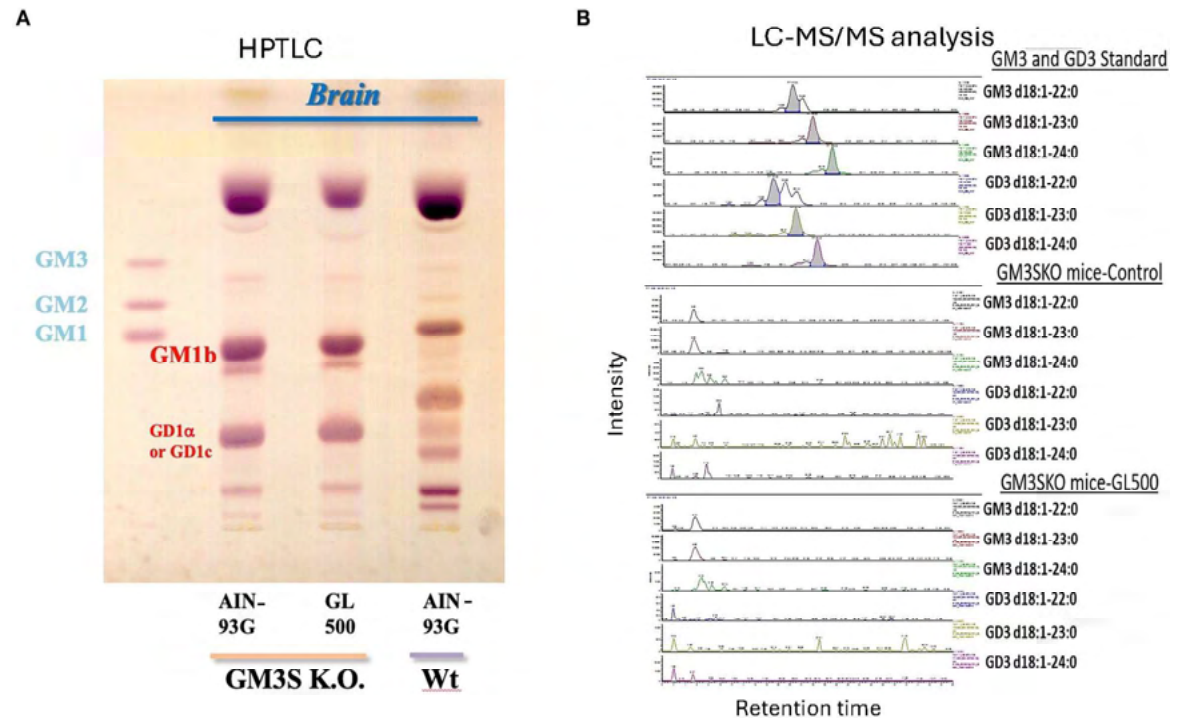


FIGURE 1
Brain gangliosides of wild-type (BALB/c) and GM3KO mice (♂) ($N = 3$/each group) fed a control diet (AIN-93G) or a diet supplemented with GL500 for 3 months from postnatal day 21. HPTLC analysis **(A)**. We do not have a standard for GD1α, but it has been reported that the brains of GM3S KO mice expressed GM1b and GD1α (Yoshikawa et al., 2009). There is a possibility to express GD1c, which migrates to the same position on HPTLC when we consider the metabolic pathway. LC–MS/MS analysis of GM3 and GD3 molecular species in the brain after feeding with GL500 **(B)**. There was no detectable milk-derived GM3 and GD3 in the whole brain of GM3S KO mice after 3 months of feeding of GL500.

genotypes were determined using the Southern blot and PCR analyses of genomic DNA isolated from tail biopsies. Primer pairs used for genotyping included 5′-GGAATCCATC-CCTTTTCTCACAGAG-3′ and 5′-TGAACTCACTTGGCATT-GCTGG-3′ for detection of the wild-type allele (exon 2) and 5′-ACTGGGCACAACAGACAATCGG-3′ and 5′-TGGATACTTTCTCGGCAGGAGC-3′ for the knockout allele (neomycin resistance gene). The GM3S KO (homozygotes) mice were unable to synthesize GM3 ganglioside and GM3-derived complex gangliosides such as a-, b- and c-series gangliosides and instead expressed o-series gangliosides in the brain such as GD1α or GD1c (Figure 1). Mice were housed under conditions of constant temperature (23 ± 1°C) and humidity (55 ± 5%), on a 12-h/12-h light–dark cycle (light from 07.00 to 19.00 h; dark from 19.00 to 07.00 h). The mice had free access to water throughout the experimental period; 3-week-old mice were then fed control (AIN-93G), GL500, or SuperZ diet for 2–3 weeks or 3 months. All animal handling procedures were approved by the Guide for Care and Use of Laboratory Animals at Tohoku Medical and Pharmaceutical University.

## 2.3 Novel object recognition test

Mice were individually habituated to the test box for 10 min over 3 consecutive days after 3 weeks or 3 months of feeding, in the absence of objects. On the fourth day, two objects were symmetrically fixed to the floor of the box, and each mouse was allowed to explore the box for 5 min (training session). Following a 24-h delay, mice were placed back in the box for 5 min where one of the familiar objects was replaced by a novel object (retention session). The percentage of exploratory preference (%EP) was calculated as the exploration time of the novel object (N) divided by the total exploration time of both novel (N) and familiar (F) objects [%EP=N/(N + F)*100].

## 2.4 Hearing tests by startle response

Startle responses were measured using the SR-LAB Startle Response System (San Diego Instruments). A Plexiglass cylinder was positioned on a piezoelectric transducer that detected the vibrations caused by the movements of the animals. Each test session began by placing a subject in the Plexiglass cylinder for 10 min to acclimatize to a background noise of 65 dB SPL.

To assess acoustic startle responses, each subject was exposed to five consecutive four blocks of eight acoustic stimuli of increasing intensity (70, 75, 80, 85, 90, 100, 110, and 120 dB SPL), each in 20-ms broadband burst and separated by a 40-s interval. The startle response was measured and recorded every 1 ms for 100 ms starting at the onset of each startle stimulus. Each experiment lasted ~30 min.

To measure startle responses to air puff, a 10-ms burst of compressed air (0.2 mPa) was delivered to the dorsal side of each animal through a pipe located 2 cm above the subject. Bursts were repeated five times per animal, and responses were recorded as above.

For each experiment, statistical significance within each group was estimated using an F-test followed by Student's *t*-test or the Aspin–Welch test.

Motor coordination and balance were measured using the Rota-Rod test. Mice were placed on a rotating rod (3 cm diameter; Neuroscience) with a non-skid surface, and the latency to fall was measured for up to 2 min. Rotation speed was 5, 10, and 15 rpm, and it increased 5 rpm every day. First, each mouse was trained until it achieved a criterion of staying on the rod for 2 min, three times in a row, at 5 rpm. The test was performed at 10 and 15 rpm, three times, for 2 days. The balance beam test was performed by using a 60-cm-long horizontal wooden dowel (1 cm diameter) placed at a height of 50 cm above a padded surface.

## 2.5 Analysis of GSLs

Lyophilized tissue was extracted twice with chloroform/methanol (2:1 and 1:1, v/v, consecutively). Total lipids were separated into acidic and neutral fractions on DEAE-Sephadex A-25 anion-exchange columns (GE Healthcare Life Sciences, Tokyo, Japan). Acidic and neutral lipids were de-esterified by mild alkaline hydrolysis and desalted using a Sep-Pak C18 Cartridge (Waters; Milford, MA). Acidic and neutral GSLs (protein equivalents of 1,000 μg and 200 μg, respectively) were spotted on HPTLC plates, developed with chloroform/methanol/0.2% $CaCl_2$ (55:45:10, by vol) and chloroform/methanol/water (60:25:4, by vol), respectively, and then visualized by orcinol/sulfuric acid staining.

## 2.6 Mass spectrometric (MS) analysis

The LC–MS/MS analysis was performed using the method described previously (Veillon et al., 2015; Go et al., 2017). Neu5Ac GM3 (d18:1-[$^{13}$C]16:0) was added to acidic GSL samples as the internal standard. GM3 molecular species were quantified using HPLC coupled with electrospray ionization tandem mass spectrometry (MS/MS) in multiple reaction-monitoring negative ionization mode. The triple-stage quadrupole (TSQ) Vantage AM instrument (Thermo Fisher, Waltham, MA) was calibrated by directly infusing a mixture of GM3 species extracted from milk, and all ion source parameters and ionization conditions were optimized to improve sensitivity. GSLs were dissolved in methanol, injected onto an HPLC pump (Accela 1,250, Thermo Fisher), and separated using a Develosil carbon 30 column (C30-UG-3–1 × 50 mm, Nomura Co., Aichi, Japan). The gradient program started with 100% solvent A (20% $H_2O$, 50% 2-propanol, 30% methanol containing 0.1% acetic acid, and 0.1% ammonia) for 5 min and then ramped to 100% solvent B (2% $H_2O$, 50% 2-propanol, 48% methanol containing 0.1% acetic acid, and 0.1% ammonia) over 30 min; 100% solvent B was maintained for 4 min, and then, the solvent was returned to 100% solvent A over 1 min and held there for 10 min. The flow was 50 μL/min throughout the chromatographic run, ~2,500 V potential was applied between the ion source and electrospray needle, and the carrier gas was nitrogen. Relative abundances of molecular species were assessed based on the relative percentage of internal standards. All GM3 molecular species may not necessarily have identical ionization efficiencies; however, because of the limited availability of pure molecular species standards, we assumed that all species have ionization efficiencies comparable with that of the internal standard. Thus, in evaluating relative abundances of molecular species, detected amounts are compared that may not necessarily represent absolute amounts (Veillon et al., 2015). The details for the assignment of ganglioside molecular species were described previously (Go et al., 2017).

## 2.7 Sialic acid analysis by fluorometric HPLC (DMB method)

Sialic acids were hydrolyzed from acidic GSL fractions using trifluoroacetic acid. An aliquot of the supernatant was lyophilized and then incubated with 1,2-diamino-4,5-methylene dioxybenzene (DMB) as described previously (Go et al., 2007). 1,2-Diamino-4,5-methylene dioxybenzene-labeled sialic acids were separated and detected using an HPLC system (JASCO; Tokyo, Japan) equipped with a reversed-phase C18 column (Wakopak Handy-ODS (4.6 mm × 250 mm); Wako Pure Chemical, Osaka, Japan).

## 2.8 Determination of neurogenesis in the dentate gyrus of the hippocampus

After 9 weeks of each diet feeding, 5-bromo-2′-deoxyuridine (BrdU) (50 mg/kg i.p.) was injected once daily for 5 days. After 3 months of feeding, animals were deeply anesthetized with sodium pentobarbital and intracardially perfused with phosphate-buffered saline (PBS), followed by paraformaldehyde (PFA). The brains were cut using a cryostat into 40 μm sections from bregma −2.20 mm to −2.80 mm, which included the dentate gyrus (DG). The sections were incubated with PBS containing 1% normal goat serum and 0.3% Triton X-100 (PBSGT) at room temperature. Then, the sections were incubated overnight with rat anti-BrdU monoclonal antibody (1:100) and mouse anti-NeuN monoclonal antibody (1:500). The sections were washed and then incubated with goat anti-rat IgG Alexa Fluor 568 (1:200) and goat anti-mouse IgG Alexa Fluor 488 (1:500) in PBSGT. Immunofluorescent images were analyzed using a confocal laser scanning microscope.

Three sections per mouse were used, and two images (left and right hemispheres, 640 × 640 μm) of the DG region of the hippocampus were obtained from each section. We calculated the BrdU/DCX-positive cells following methods outlined in our previous paper (Odaira et al., 2019). Positive cells were counted in the region observed under a fluorescence microscope. The positive cells in 2 images × 3 sections per mouse were added, and this total value is considered to be the total number of BrdU-/DCX-positive cells in the whole dorsal hippocampus. A total of six images were analyzed per mouse, and each group contained five to six mice.

## 2.9 Statistical analysis

The experimental results are presented as mean ± standard error of the mean (SEM). Significant differences were determined using one-way ANOVA, followed by a Tukey–Kramer test for multiple group comparisons. The criterion for a significant difference was set at $p < 0.05$.

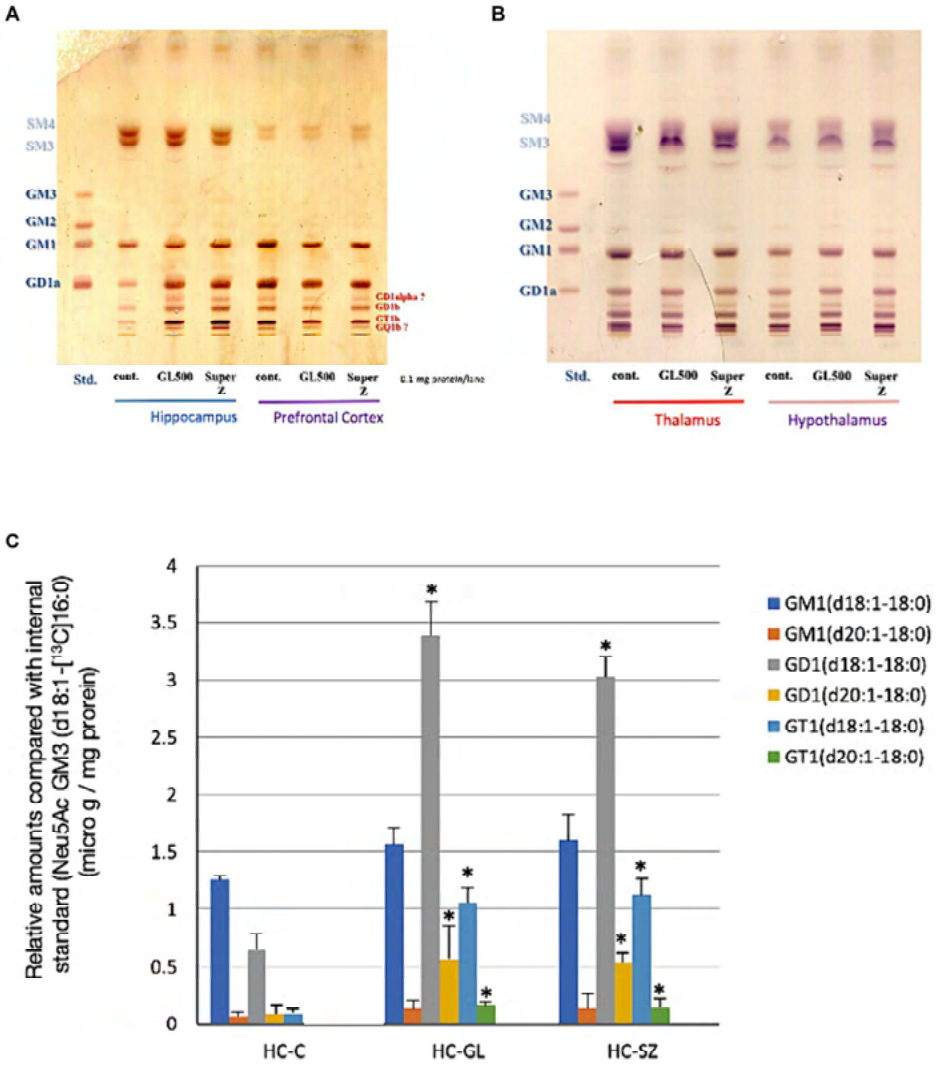


FIGURE 2
Selective increase of complex gangliosides in hippocampus from 3-week-old BALB/c mice (♂) ($N = 3$/group) fed for 2 weeks from postnatal day 21 with the control diet or a diet supplemented with GL500 or SuperZ. **(A,B)** Show HPTLC analyses of gangliosides in **(A)** the hippocampus and prefrontal cortex and **(B)** the thalamus and hypothalamus, while **(C)** shows the LC–MS/MS determination of complex ganglioside molecular species in the hippocampus (HC) of BALB/c mice (♂) fed with control diet (C), GL500 (GL), and SuperZ (SZ); an asterisk (*) indicates $p < 0.05$ vs. control (HC-C).

# 3 Results

## 3.1 Effects of oral GL500 and SuperZ supplementation on ganglioside contents in the serum, liver, and brain regions in mice

Three-week-old BALB/c male mice were fed control pellets (Cont) or pellets containing GM3-rich GL500 or GD3-rich SuperZ for 2 weeks; 5-week-old mice were euthanized, and the serum, liver, and brain regions (the prefrontal cortex, hippocampus, thalamus, and hypothalamus) were collected. Samples in the same group were combined, and the ganglioside fractions were purified for HPTLC and LC–MS/MS analyses. The major ganglioside in the serum and liver of this mouse strain (BALB/c) is GM2. When the mice ate GL500 and SuperZ for 2 weeks from weaning, there was no detectable GM3 and GD3 in the serum (Supplementary Figure S3A) or liver using HPTLC (Supplementary Figure S4A) and LC–MS/MS (Supplementary Figure S4B) analysis. The major sialic acid species in BALB/c mice are NeuGc species, but the sialic acid species in cow milk are NeuAc species (Takamizawa et al., 1986; Puente and Hueso, 1993). Therefore, we measured the levels of NeuGc and NeuAc sialic acids in serum from mice fed control, GL500, or SuperZ diets. There was no increase in NeuAc species in GL500 or SuperZ groups (Supplementary Figure S3C). Thus, there was no signature of appearance of milk-derived gangliosides, or derivative components such as NeuAc, in mice receiving oral supplementation of GL500 or SuperZ.

On the other hand, we observed a significant increase of complex gangliosides in the hippocampus of the same mice receiving GL500 or SuperZ but no increase in NeuAc or milk ganglioside components. As shown in Figure 2, the selective and significant increase in gangliosides

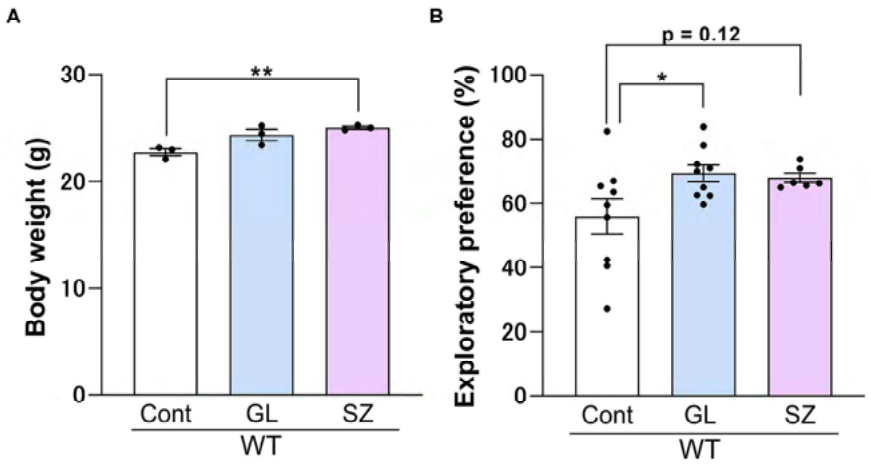


FIGURE 3
Influence of GL500 or SuperZ diet feeding on body growth **(A)** and cognitive function **(B)** of BALB/c mice (♂) fed from postnatal day 21 for 3 weeks with control diet (cont. diet) or diet supplemented with GL500 (GL) or SuperZ (SZ). **(A)** Shows an increase in the body weight of mice ($N = 3$ per group), and **(B)** shows the enhancement of the cognitive function of mice ($N = 6–9$ per group) fed with GL500 or SuperZ (asterisks indicate $p < 0.05$ vs. control diet-fed mice).

in the hippocampus, especially GD1 and GT1 species, was detected in mice fed with GL500 or SuperZ (Figure 2A). Increase in GD1 (d18:1–18:0 and d20:1–18:0) and GT1 (d18:1–18:0 and d20:1–18:0) was confirmed by LC–MS (Figure 2C). As C23 GM3 was abundantly contained in both pellets (Supplementary Figure S2), the ceramide parts of milk GM3 and GD3 were not utilized directly for the increased synthesis of complex gangliosides in the hippocampus. There were no increases of such complex gangliosides in the other regions of the brain (the prefrontal cortex, thalamus, and hypothalamus) of the same mice (Figures 2A,B).

## 3.2 Influences of ganglioside diet feeding on NORT behavior by wild-type mice

There were no significant differences in the exploratory preference for the training sessions after control, GL500, or SuperZ feeding for 3 weeks starting 3 weeks postpartum in WT mice (data not shown). Supplementation of GL500 to wild-type mice on early weaning periods significantly enhanced the exploratory preference in the retention session compared to the control diet (Figure 3B). SuperZ feeding also showed enhancements in growth (Figure 3A) and a trend in the exploratory preference in the retention session ($p = 0.12$) of WT mice (Figure 3B). These data indicated that supplementing the diet of WT mice with GL500 and SuperZ from the time of weaning (21 days after birth) for 2 weeks may enhance cognitive function by increasing gangliosides GD1 and GT1 in the hippocampus.

## 3.3 Influence of ganglioside diet feeding on GM3 synthase-deficient (KO) mice

In the training session, there were no significant differences in the exploratory preference between each group for 3 weeks or 3 months of feeding (Figures 4A,C). In the retention session, there were no significant differences in the exploratory preference between each group for 3 weeks of feeding (Figure 4B). Control diet-treated GM3S KO mice significantly decreased the exploratory preference on the retention session compared to control diet-treated WT mice ($p < 0.05$) after 3-month feeding (Figure 4D). GL500 ($p < 0.01$) and SuperZ ($p < 0.01$) treatments blocked the impairment of recognition memory in GM3S KO mice (Figure 4D).

However, analysis of gangliosides in whole brains of GM3S KO mice fed GL500 or SuperZ for 3 months did not confirm the presence of milk-derived GM3 and GD3 (Figure 1). Thus, ganglioside supplementation of GM3S-deficient mice did not normalize the ganglioside profile of the whole brain.

We reported for the first time that GM3S KO mice suffered from hearing loss (Yoshikawa et al., 2009); therefore, we performed "hearing tests" using the startle response on GM3S KO mice after 3 months of feeding GL500 and SuperZ. There was no improvement in hearing ability as assessed by startle response (Supplementary Figure S5).

## 3.4 Effects of GL500 and SuperZ on neurogenesis in the hippocampal dentate gyrus of GM3S KO mice

The experimental protocol is depicted in Figure 5A. BrdU and BrdU-/NeuN-positive cells in control diet-fed GM3S KO mice were fewer than in WT mice (BrdU-positive cells: $p = 0.052$, Figures 5B,C; BrdU-/NeuN-positive cells: $p < 0.05$, Figures 5B,D) at 3 months. In contrast, BrdU and BrdU-/NeuN-positive cells in the SuperZ-fed GM3S KO mice were significantly increased compared to control diet-fed GM3S KO mice (BrdU-positive cells: $p < 0.01$, Figure 5B,C; BrdU-/NeuN-positive cells: $p < 0.01$ Figures 5B,D). These results indicate that SuperZ feeding promotes neurogenesis in the hippocampal dentate gyrus of GM3S KO mice. GL500 feeding showed prevention of the decrease in neurogenesis in GM3S KO mice, but there was no increase.

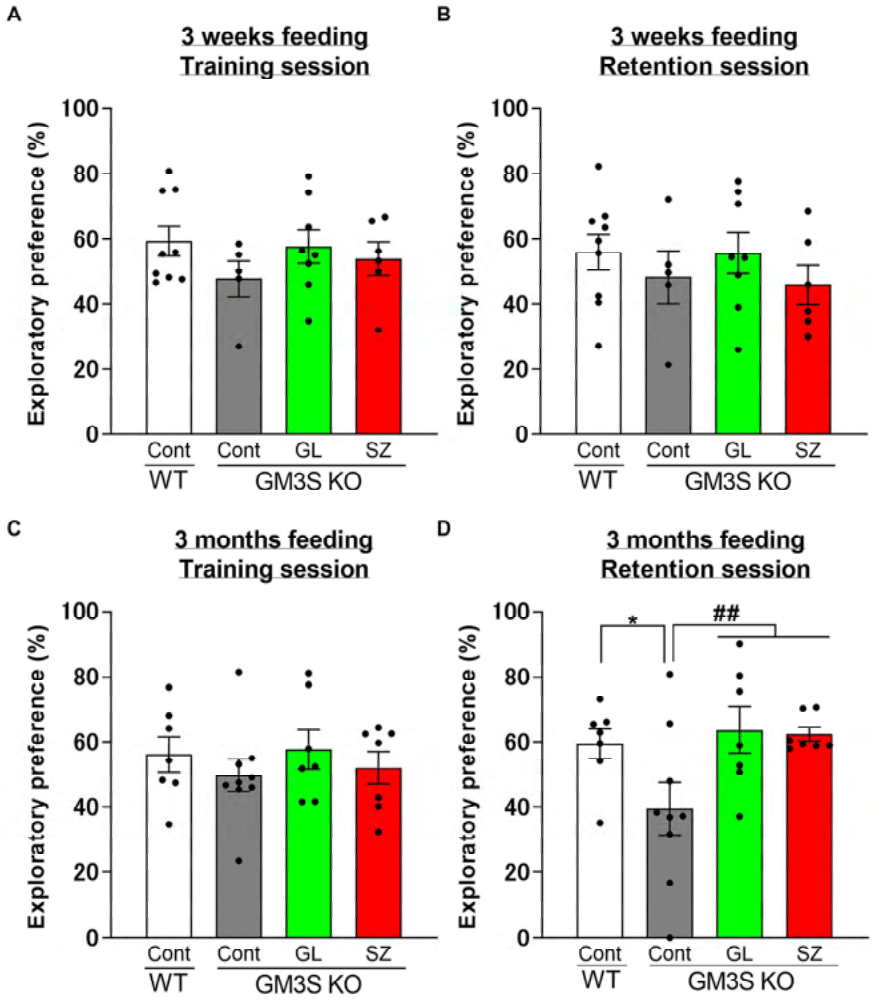


FIGURE 4
Influence of GL500 or SuperZ diet feeding for 3 weeks **(A,B)** and 3 months **(C,D)** from postnatal day 21 on cognitive function in WT and GM3S KO mice. Exploratory preferences for training **(A,C)** and retention **(B,D)** sessions are expressed as a percentage. $^{*}p < 0.05$ vs. control diet fed WT mice. $^{\#\#}p < 0.01$ vs. control diet fed GM3S KO mice. $n = 5–9$ per group.

## 4 Discussion

ST3GAL5 (GM3 synthase, GM3S) is located in the first step of the ganglioside biosynthetic pathway to the a-, b-, and c-series gangliosides commonly found in neural tissue. Inactivation of this enzyme by genetic mutation results in the loss of all complex gangliosides in the downstream a, b, and c pathways, causing severe damage to the central nervous system and other organs as shown in Table 1. B4GALNT1 (GM2 synthase, GM2S) synthesizes GM2 from GM3, but inactivation of the enzyme by mutation of the *B4GALNT1* gene results in only GM3 and GD3 gangliosides in the organism and none of the subsequent downstream a- and b-series gangliosides. GM2S deficiency was revealed when a mutation in the *B4GALNT1* gene was identified as the cause of hereditary spastic paraplegia 26 (SPG26) (Harlalka et al., 2013). Symptoms of SPG26 are substantially reduced compared to those seen in GM3S deficiency, suggesting that the severe symptoms of GM3S deficiency are mainly due to the additional loss of GM3 and GD3. GM3 and GD3 are known to be in higher concentrations and associated with early stages of neural development.

Therefore, we planned to investigate the effects of large oral doses of GM3 and GD3 on the central nervous system of weanling mice. The effects of oral administration of these gangliosides on learning performance have been studied in the past, but there are a number of variables, for example, dose, ganglioside composition, delivery method, animal age and developmental stage, and subsequently, the pharmacological effects on memory improvement also varied. In the present study, we performed NORT in wild-type and GM3 synthase-deficient mice orally ingesting 720 mg/kg bw/day of these gangliosides using two milk-derived formulations, GL500 and SuperZ, with different GM3 and GD3 ratios, prepared by Fonterra Cooperative Group Ltd. Our study utilizing NORT has revealed cognitive dysfunction in GM3S KO mice after 3 months of control diet feeding. This finding is consistent with a previous report that used the Y-maze in GM3S KO mice with C57/BL6 background (Niimi et al., 2011). These

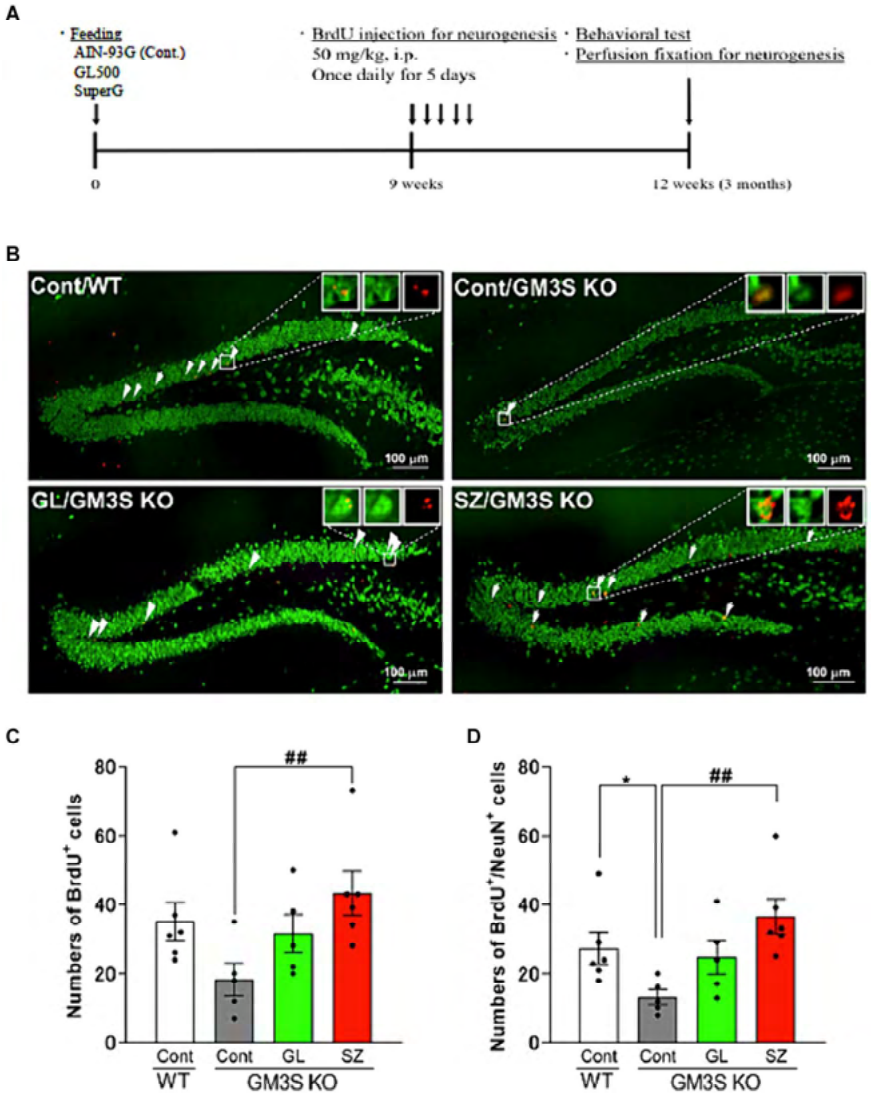


FIGURE 5
Effects of GL500 and SuperZ on neurogenesis in the hippocampal dentate gyrus of GM3S KO mice. **(A)** Shows the experimental protocol (details in Materials and methods). **(B)** shows immunohistochemistry images of brain slices stained with BrdU (red) and NeuN (green); the arrowhead point indicates double-positive cells. **(C,D)** Show quantification of the total number of BrdU **(C)** and BrdU-/NeuN-positive cells **(D)** in wild-type (WT) and GM3S KO mice fed 21 days postnatal for 3 months with control diet or control diet supplemented with GL500 (GL) or SuperZ (SZ); an asterisk (*) indicates $p < 0.05$ vs. control diet fed WT mice; a double hash (##) indicates $p < 0.01$ vs. control diet fed GM3S KO mice ($N = 5–6$ per group).

data suggest that GM3 may play a significant role in cognitive function.

There is a limited number of humans with GM3 synthase deficiency and the outcomes of the deficiency are more debilitating than that in the mouse model. The major impacts for human GM3 synthase deficiency within the study of Wang et al. (2019) were in decreasing irritability, improving interaction, and improving growth rates when supplementation in the range of 0.5–2 g of ingredient/kg, equivalent to 5.5–22 mg ganglioside/kg bw/day.

The use of the mouse model allows the use of cognitive testing and brain sample collection, which is very hard to undertake in the human cohort, and allows for the cohort to be of the same age and weight and the intervention to be times at a specific developmental time. The purpose of this study was to investigate the mouse model mechanism of changes with supplementation beginning at 21 days. The use of the mouse model also allowed for a larger dose of 720 mg gangliosides/kg bw/day.

Wang et al. (2019) investigated 13 individuals at different ages ranging from 0 to 115 months at the beginning of supplementation. This present study in GM3S KO mice confirmed the lack of impact of supplemented gangliosides on the serum ganglioside levels as in Wang et al. (2019).

Neurogenesis in the hippocampal dentate gyrus significantly contributes to central neuroplasticity mechanisms such as cognitive function (Massa et al., 2011). To determine the change in hippocampal neurogenesis in GM3S KO mice, the animals were injected with BrdU. Anti-NeuN antibody was then used to identify mature neurons in the dentate gyrus area. The incorporation of BrdU into a cell indicated that it was cycling at the time of BrdU injection. In the present study, GM3S KO mice with the BALB/c background showed

decreases in hippocampal neurogenesis. However, it has been previously reported that young ST3GAL5 KO mice with the C57BL/6 background were not impaired with respect to adult hippocampal neurogenesis (Tang et al., 2020). Mice of the C57BL/6 strain are known to have approximately twice as much ability for new cell proliferation in the hippocampus and for neural cell migration and differentiation compared to BALB/C strain mice (Pozniak and Pleasure, 2006; Kim et al., 2009). These differences in results may be due to strain differences in the mice used in the experiments.

The GL500 and SuperZ feeding protected against cognitive dysfunction in GM3S KO mice. Similarly, it has been reported that neurogenesis is reduced in the hippocampus of Alzheimer's disease patients (Lazarov and Marr, 2010). An increase in adult-born neurons is associated with the improvement of memory-related behavior in rodents (Oh et al., 2013).

Considering these reports, the present finding suggests that the enhancement of neurogenesis in the hippocampus by GL500 and SuperZ may be associated with the improvement of cognitive dysfunction in GM3S KO mice.

A recent study reported that IP administration of synthetic GM1 ganglioside to GM3S$^{-/-}$ and GM3S$^{-/+}$ mice was effective in preventing memory loss and the development of Parkinson's disease-like symptoms (Chowdhury et al., 2023). The details of the mechanism of the effect of synthetic GM1 on GM3S$^{-/-}$ and GM3S$^{-/+}$ mice are not clear. We expect that the protective effect of milk gangliosides (GM3 and GD3) on reversing the decrease in hippocampal neurogenesis seen in GM3S$^{-/-}$ mice may be related to the protective effect of synthetic GM1 on neuronal function.

## 5 Conclusion and perspectives

Oral supplementation of GM3 and GD3 to wild-type mice enhanced body weight gain and increased learning and memory abilities during early weaning periods, suggesting that oral ganglioside supplementation may be beneficial for infantile nutrition. Interestingly, the selective increase in complex gangliosides (GD1 and GT1) in the hippocampus (but no other regions of the brain) was observed in ganglioside-supplemented mice. For GM3S KO mice, GM3 and GD3 supplementation could block the decrease of cognitive function supporting the usefulness of the therapy of GM3SD patients performed by Wang et al. (2019). There was no evidence for the presence of milk-derived GM3 and GD3 molecules in the serum, liver, and brain after 3 months of feeding to wild-type mice and GM3S KO mice.

These results suggest that metabolites of GM3 and GD3 including sialic acids, ceramides, and fatty acids may positively affect infantile growth and brain development and improve symptoms of neurological disabilities for GM3SD patients. The lack of evidence in this study (and others) that the components of the oral gangliosides are incorporated into the brain gangliosides raises the question of what the mechanism is to achieve the functional outcome; this should be considered in future work.

## Data availability statement

The datasets presented in this study can be found in online repositories. The names of the repository/repositories and accession number(s) can be found in the article/Supplementary material.

## Ethics statement

All animal-handling procedures had been approved by the Guide for Care and Use of Laboratory Animals at Tohoku Medical and Pharmaceutical University. The study was conducted in accordance with the local legislation and institutional requirements.

## Author contributions

J-iI: Conceptualization, Data curation, Formal analysis, Funding acquisition, Investigation, Project administration, Supervision, Writing – original draft, Writing – review & editing. SG: Data curation, Formal analysis, Investigation, Methodology, Writing – original draft, Writing – review & editing. AS: Data curation, Investigation, Methodology, Writing – review & editing. ON: Investigation, Writing – original draft, Data curation, Formal analysis, Methodology, Writing – review & editing. TO-S: Investigation, Writing – original draft. LV: Data curation, Formal analysis, Investigation, Methodology, Writing – review & editing, Writing – original draft. TN: Data curation, Formal analysis, Investigation, Writing – review & editing, Methodology. PM: Conceptualization, Data curation, Formal analysis, Methodology, Writing – original draft, Writing – review & editing. HK: Data curation, Investigation, Writing – review & editing, Formal analysis. K-iI: Data curation, Investigation, Writing – review & editing. KT-N: Conceptualization, Data curation, Writing – review & editing, Investigation, Supervision. MC: Data curation, Formal analysis, Investigation, Writing – review & editing, Conceptualization, Project administration.

## Funding

The author(s) declare that financial support was received for the research, authorship, and/or publication of this article. This study was supported by grants-in-aid from Ministry of Education, Culture, Sports, Science and Technology of Japan [JSPS KAKENHI: Grants-in-Aid for Scientific Research (B) (JP20H03452 to J-iI).

## Acknowledgments

The authors are grateful to the Centre for Laboratory Animal Science, Tohoku Medical and Pharmaceutical University, for their services. The authors would like to thank Kohei Takahashi of the Tohoku Medical and Pharmaceutical University for his technical assistance.

## Conflict of interest

The authors declare that the research was conducted in the absence of any commercial or financial relationships that could be construed as a potential conflict of interest.

The authors declare that this study received funding from Fonterra co-operative Group Ltd. The funder had the following involvement in the study: study design, analysis and interpretation of data, the writing of this article and the decision to submit it for publication.

## Publisher's note

All claims expressed in this article are solely those of the authors and do not necessarily represent those of their affiliated organizations, or those of the publisher, the editors and the reviewers. Any product that may be evaluated in this article, or claim that may be made by its manufacturer, is not guaranteed or endorsed by the publisher.

## Supplementary material

The Supplementary material for this article can be found online at: https://www.frontiersin.org/articles/10.3389/fnins.2024.1387221/full#supplementary-material

## References

Abdulkareem, A. A., Shirah, B. H., and Naseer, M. I. (2023). Whole exome sequencing reveals a novel homozygous variant in the ganglioside biosynthetic enzyme, *ST3GAL5* gene in a Saudi family causing salt and pepper syndrome. *Genes (Basel)* 14:354. doi: 10.3390/genes14020354

Boccuto, L., Aoki, K., Flanagan-Steet, H., Chen, C. F., Fan, X., Bartel, F., et al. (2014). A mutation in a ganglioside biosynthetic enzyme, *ST3GAL5*, results in salt & pepper syndrome, a neurocutaneous disorder with altered glycolipid and glycoprotein glycosylation. *Hum. Mol. Genet.* 23, 418–433. doi: 10.1093/hmg/ddt434

Bowser, L. E., Young, M., Wenger, O. K., Ammous, Z., Brigatti, K. W., Carson, V. J., et al. (2019). Recessive GM3 synthase deficiency: natural history, biochemistry, and therapeutic frontier. *Mol. Gen. Met.* 126, 475–488. doi: 10.1016/j.ymgme.2019.01.013

Chowdhury, S., Kumar, R., Zepeda, E., DeFrees, S., and Ledeen, R. (2023). Synthetic GM1 improves motor and memory dysfunctions in mice with monoallelic or biallelic disruption of GM3 synthase. *FEBS Open Bio.* 13, 1651–1657. doi: 10.1002/2211-5463.13669

Fong, B., Ma, K., and McJarrow, P. (2011). Quantification of bovine milk oligosaccharides using liquid chromatography-selected reaction monitoring-mass spectrometry. *J. Agric. Food Chem.* 59, 9788–9795. doi: 10.1021/jf202035m

Fragaki, K., Ait-El-Mkadem, S., Chaussenot, A., Gire, C., Mengual, R., Bonesso, L., et al. (2013). Refractory epilepsy and mitochondrial dysfunction due to GM3 synthase deficiency. *Eur. J. Hum. Genet.* 21, 528–534. doi: 10.1038/ejhg.2012.202

Go, S., Sato, C., Yin, J., Kannagi, R., and Kitajima, K. (2007). Hypoxia-enhanced expression of free deaminoneuraminic acid in human cancer cells. *Biochem. Biophys. Res. Commun.* 357, 537–542. doi: 10.1016/j.bbrc.2007.03.181

Go, S., Veillon, L., Ciampa, M. G., Mauri, L., Sato, C., Kitajima, K., et al. (2017). Altered expression of ganglioside GM3 molecular species and a potential regulatory role during myoblast differentiation. *J. Biol. Chem.* 292, 7040–7051. doi: 10.1074/jbc.M116.771253

Gordon-Lipkin, E., Cohen, J. S., Srivastava, S., Soares, B. P., Levey, E., and Fatemi, A. (2018). ST3GAL5-related disorders: a deficiency in ganglioside metabolism and a genetic cause of intellectual disability and choreoathetosis. *J. Child Neurol.* 33, 825–831. doi: 10.1177/0883073818791099

Harlalka, G. V., Lehman, A., Chioza, B., Baple, E. L., Maroofian, R., Cross, H., et al. (2013). Mutations in *B4GALNT1* (GM2 synthase) underlie a new disorder of ganglioside biosynthesis. *Brain* 136, 3618–3624. doi: 10.1093/brain/awt270

Heide, S., Jacquemont, M. L., Cheillan, D., Renouil, M., Tallot, M., Schwartz, C. E., et al. (2022). GM3 synthase deficiency in non-Amish patients. *Genet. Med.* 24, 492–498. doi: 10.1016/j.gim.2021.10.007

Indellicato, R., Parini, R., Domenighini, R., Malagolini, N., Iascone, M., Gasperini, S., et al. (2019). Total loss of GM3 synthase activity by a normally processed enzyme in a novel variant and in all ST3GAL5 variants reported to cause a distinct congenital disorder of glycosylation. *Glycobiology* 29, 229–241. doi: 10.1093/glycob/cwy112

Ishii, A., Ohta, M., Watanabe, Y., Matsuda, K., Ishiyama, K., Sakoe, K., et al. (1998). Expression cloning and functional characterization of human cDNA for ganglioside GM3 synthase. *J. Biol. Chem.* 273, 31652–31655. doi: 10.1074/jbc.273.48.31652

Kim, J. S., Jung, J., Lee, H. J., Kim, J. C., Wang, H., Kim, S. H., et al. (2009). Differences in immunoreactivities of Ki-67 and doublecortin in the adult hippocampus in three strains of mice. *Acta Histochem.* 111, 150–156. doi: 10.1016/j.acthis.2008.05.002

Kudara, M., Kato-Ishikura, E., Ikegaya, Y., and Matsumoto, N. (2023). Ramelteon administration enhances novel object recognition and spatial working memory in mice. *J. Pharmacol. Sci.* 152, 128–135. doi: 10.1016/j.jphs.2023.04.002

Lazarov, O., and Marr, R. A. (2010). Neurogenesis and Alzheimer's disease: at the crossroads. *Exp. Neurol.* 223, 267–281. doi: 10.1016/j.expneurol.2009.08.009

Lee, J. S., Yoo, Y., Lim, B. C., Kim, K. J., Song, J., Choi, M., et al. (2016). GM3 synthase deficiency due to *ST3GAL5* variants in two Korean female siblings: masquerading as Rett syndrome-like phenotype. *Am. J. Med. Genet. A* 170, 2200–2205. doi: 10.1002/ajmg.a.37773

Liu, H., Radlowski, E. C., Conrad, M. S., Li, Y., Dilger, R. N., and Johnson, R. W. (2014). Early supplementation of phospholipids and gangliosides affects brain and cognitive development in neonatal piglets. *J. Nutr.* 144, 1903–1909. doi: 10.3945/jn.114.199828

Massa, F., Koehl, M., Wiesner, T., Grosjean, N., Revest, J. M., Piazza, P. V., et al. (2011). Conditional reduction of adult neurogenesis impairs bidirectional hippocampal synaptic plasticity. *Proc. Natl. Acad. Sci. USA* 108, 6644–6649. doi: 10.1073/pnas.1016928108

Niimi, K., Nishioka, C., Miyamoto, T., Takahashi, E., Miyoshi, I., Itakura, C., et al. (2011). Impairment of neuropsychological behaviors in ganglioside GM3-knockout mice. *Biochem. Biophys. Res. Commun.* 406, 524–528. doi: 10.1016/j.bbrc.2011.02.071

Odaira, T., Nakagawasai, O., Takahashi, K., Nemoto, W., Sakuma, W., Lin, J. R., et al. (2019). Mechanisms underpinning AMP-activated protein kinase-related effects on behavior and hippocampal neurogenesis in an animal model of depression. *Neuropharmacology* 150, 121–133. doi: 10.1016/j.neuropharm.2019.03.026

Oh, S. B., Park, H. R., Jang, Y. J., Choi, S. Y., Son, T. G., and Lee, J. (2013). Baicalein attenuates impaired hippocampal neurogenesis and the neurocognitive deficits induced by γ-ray radiation. *Br. J. Pharmacol.* 168, 421–431. doi: 10.1111/j.1476-5381.2012.02142.x

Park, E. J., Suh, M., Ramanujam, K., Steiner, K., Begg, D., and Clandinin, M. T. (2005). Diet-induced changes in membrane gangliosides in rat intestinal mucosa, plasma and brain. *J. Pediatr. Gastroenterol. Nutr.* 40, 487–495. doi: 10.1097/01.MPG.0000157199.25923.64

Pozniak, C. D., and Pleasure, S. J. (2006). Genetic control of hippocampal neurogenesis. *Genome Biol.* 7:207. doi: 10.1186/gb-2006-7-3-207

Puente, R., and Hueso, P. (1993). Lactational changes in the *N*-glycoloylneuraminic acid content of bovine milk gangliosides. *Biol. Chem. Hoppe Seyler* 374, 475–478. doi: 10.1515/bchm3.1993.374.7-12.475

Reis, M. M., Bermingham, E. N., Reis, M. G., Deb-Choudhury, S., MacGibbon, A., Fong, B., et al. (2016). Effect of dietary complex lipids on the biosynthesis of piglet brain gangliosides. *J. Agric. Food Chem.* 64, 1245–1255. doi: 10.1021/acs.jafc.5b05211

Simpson, M. A., Cross, H., Proukakis, C., Priestman, D. A., Neville, D. C., Reinkensmeier, G., et al. (2004). Infantile-onset symptomatic epilepsy syndrome caused by a homozygous loss-of-function mutation of GM3 synthase. *Nat. Genet.* 36, 1225–1229. doi: 10.1038/ng1460

Takamizawa, K., Iwamori, M., Mutai, M., and Nagai, Y. (1986). Gangliosides of bovine buttermilk. Isolation and characterization of a novel monosialoganglioside with a new branching structure. *J. Biol. Chem.* 261, 5625–5630. doi: 10.1016/S0021-9258(19)57260-X

Tang, F. L., Wang, J., Itokazu, Y., and Yu, R. K. (2020). Enhanced susceptibility to chemoconvulsant-induced seizures in ganglioside GM3 synthase knockout mice. *ASN Neuro* 12:175909142093817. doi: 10.1177/1759091420938175

Tsukamoto, K., Kohda, T., Mukamoto, M., Takeuchi, K., Ihara, H., Saito, M., et al. (2005). Binding of *Clostridium botulinum* type C and D neurotoxins to ganglioside and phospholipid. Novel insights into the receptor for clostridial neurotoxins. *J. Biol. Chem.* 280, 35164–35171. doi: 10.1074/jbc.M507596200

Veillon, L., Go, S., Matsuyama, W., Suzuki, A., Nagasaki, M., Yatomi, Y., et al. (2015). Identification of ganglioside GM3 molecular species in human serum associated with risk factors of metabolic syndrome. *PLoS One* 10, 1–15. doi: 10.1371/journal.pone.0129645

Wang, H., Bright, A., Xin, B., Bockoven, J. R., and Paller, A. S. (2013). Cutaneous dyspigmentation in patients with ganglioside GM3 synthase deficiency. *Am. J. Med. Gen. Part A.* 161, 875–879. doi: 10.1002/ajmg.a.35826

Wang, H., Sency, V., McJarrow, P., Bright, A., Huang, Q., Cechner, K., et al. (2019). Oral ganglioside supplement improves growth and development in patients with ganglioside GM3 synthase deficiency. *JIMD Rep.* 45, 9–20. doi: 10.1007/8904_2018_134

Watanabe, S., Lei, M., Nakagawa, E., Takeshita, E., Inamori, K. I., Shishido, F., et al. (2023). Neurological insights on two siblings with GM3 synthase deficiency due to novel compound heterozygous *ST3GAL5* variants. *Brain and Development* 45, 270–277. doi: 10.1016/j.braindev.2023.01.002

Yoshikawa, M., Go, S., Takasaki, K., Kakazu, Y., Ohashi, M., Nagafuku, M., et al. (2009). Mice lacking ganglioside GM3 synthase exhibit complete hearing loss due to selective degeneration of the organ of Corti. *Proc. Natl. Acad. Sci. U. S. A.* 106, 9483–9488. doi: 10.1073/pnas.0903279106

＜免疫学＞

教授　　中村　晃
准教授　海部　知則
助教　　武田　和也

## 中枢神経系自己免疫疾患モデルにおける免疫制御受容体の解析

研究内容紹介：

当研究室では主に中枢神経系自己免疫疾患モデルにおける免疫制御受容体の役割について解析を行なっている。我々は，システイニルロイコトリエン受容体の相同分子として単離された，オーファン G タンパク質共役型受容体（GPCR）・GPR141 の機能解析を行った．GPR141 の発現を mRNA レベルで検討してところ，ミエロイド系細胞に発現し T・B 細胞には発現していないことが判明した。次に *Gpr141*$^{-/-}$マウスを作成し，代表的な中枢神経系自己免疫疾患モデルである実験的自己免疫性脳脊髄炎を誘導した．その結果，*Gpr141*$^{-/-}$マウスは野生型マウスに比べて上行性麻痺など臨床スコアの増悪を認めた。また，血清中の抗原特異的抗体が有意に増加していた．誘導後のリンパ節細胞を抗原再刺激すると，*Gpr141*$^{-/-}$マウスにおいて，炎症性サイトカインや樹状細胞由来のサイトカイン産生が亢進していた．これの結果から，GPR141 は樹状細胞の機能を負に調節し，免疫反応を抑制的に制御することが示された [1)]．今後，リガンドの探索を行う予定である．また，同じく中枢神経系自己免疫疾患モデルであるタイラーマウス脳脊髄炎ウイルス感染による脱髄疾患モデルを誘導し，抑制型受容体 PIR-B の役割について欠損マウスを用いた解析を行なっている．この他，前立腺癌患者における免疫細胞の遺伝子発現解析に共同研究者として参画した [2)]．

**＜論文発表＞**

1. **The orphan G protein-coupled receptor 141 expressed in myeloid cells functions as a suppressor of inflammations.** Sawabe A, Nakamura A, Okazaki S, Goitsuka, R and Kaifu T. ***Journal of Leukocyte Biology***. 115:935. doi: 10.1093/jleuko/qiae009. 2024
2. **Transcriptome-Wide Association Study Identified Novel Blood Tissue Gene Biomarkers for Prostate Cancer Risk.** Sun Y, Zhu J, Zhong H, Zhang Z, Wang F, Nakamura A, Liu Y, Liu J, Yu J, Zeng G, Lin X, Zhou D, Wu C, Wang L, Deng Y, Wu L. ***Prostate.*** Jan 29:e24859. doi: 10.1002/pros.24859. 2025

＜学会発表と講演＞

- **タイラーマウス脳脊髄炎ウイルス感染における抑制型免疫グロブリン様受容体 PIR-B の役割**

  武田和也, 根本創史, 海部知則, 中村晃

  第 71 回日本ウイルス学会学術集会, 名古屋, 2024 年 11 月, 要旨集 p. 375

- **タイラーマウス脳脊髄炎ウイルス感染における抑制型免疫グロブリン様受容体 PIR-B の役割**

  武田和也, 根本創史, 海部知則, 中村晃

  第 36 回 日本神経免疫学会学術集会, 富山, 2024 年 10 月, 要旨集 p. 242

- **自然免疫受容体の機能理解に基づいた中枢神経系自己免疫疾患の病態解析**

  海部知則, 藤岡篤司, 清水謙次 [a], 中島一郎 [b], 城田祐子 [c], 岩倉洋一郎 [d], 中村晃

  第 200 回日仏生物学会例会, 日仏会館, 東京 2024 年 6 月, 要旨集 p7

  (東京大学・定量生命科学研究所 [a], 東北医科薬科大学・脳神経内科 [b], 同・血液・リウマチ科 [c], 東京理科大学・生命医科学研究所 [d])

- **免疫応答を負に制御する新規オーファン GPCR の解析**

  澤邊敦哉, 中村晃, 後飯塚遼 [a], 海部知則

  第 71 回日本実験動物学会総会, みやこめっせ・ロームシアター京都, 京都, 2024 年 5 月 要旨集 p89

  (東京理科大学・生命医科学研究所 [a])

OXFORD JLB JOURNAL OF LEUKOCYTE BIOLOGY

*Journal of Leukocyte Biology*, 2024, **115**, 935–945

**https://doi.org/10.1093/jleuko/qiae009**
Advance access publication 16 January 2024
**Article**

# The orphan G protein–coupled receptor 141 expressed in myeloid cells functions as an inflammation suppressor

Atsuya Sawabe,[1] Shogo Okazaki,[2] Akira Nakamura,[1] Ryo Goitsuka,[3] and Tomonori Kaifu[1,*]

[1]Division of Immunology, Faculty of Medicine, Tohoku Medical and Pharmaceutical University, 1-15-1, Fukumuro, Sendai 983-8536, Japan
[2]Department of Microbiology and Immunology, Nihon University School of Dentistry, 1-8-13, Surugadai, Kanda, Chiyoda-ku, Tokyo 101-8310, Japan
[3]Division of Cell Fate Regulations, Developmental Immmunology, Regenerative Biology, Research Institute for Biomedical Sciences, Tokyo University of Science, 2669 Yamazaki, Noda, Chiba 278-0022, Japan
*Corresponding author: Division of Immunology, Faculty of Medicine, Tohoku Medical and Pharmaceutical University, 1-15-1, Fukumuro, Sendai 983-8536, Japan. Email: kaifu@tohoku-mpu.ac.jp

## Abstract

G protein–coupled receptors (GPCRs) regulate many cellular processes in response to various stimuli, including light, hormones, neurotransmitters, and odorants, some of which play critical roles in innate and adaptive immune responses. However, the physiological functions of many GPCRs and the involvement of them in autoimmune diseases of the central nervous system remain unclear. Here, we demonstrate that GPR141, an orphan GPCR belonging to the class A receptor family, suppresses immune responses. High GPR141 messenger RNA levels were expressed in myeloid-lineage cells, including neutrophils ($CD11b^+Gr1^+$), monocytes ($CD11b^+Gr1^-Ly6C^+$ and $CD11b^+Gr1^-Ly6C^-$), macrophages ($F4/80^+$), and dendritic cells ($CD11c^+$). *Gpr141*$^{-/-}$ mice, which we independently generated, displayed almost no abnormalities in myeloid cell differentiation and compartmentalization in the spleen and bone marrow under steady-state conditions. However, *Gpr141* deficiency exacerbated disease conditions of experimental autoimmune encephalomyelitis, an autoimmune disease model for multiple sclerosis, with increased inflammation in the spinal cord. *Gpr141*$^{-/-}$ mice showed increased $CD11b^+Gr1^+$ neutrophils, $CD11b^+Gr1^-$ monocytes, $CD11c^+$ dendritic cells, and $CD4^+$ T cell infiltration into the experimental autoimmune encephalomyelitis–induced spinal cord compared with littermate control mice. Lymphocytes enriched from *Gpr141*$^{-/-}$ mice immunized with myelin oligodendrocyte glycoprotein 35–55 produced high amounts of interferon-γ, interleukin-17A, and interleukin-6 compared with those from wild-type mice. Moreover, $CD11c^+$ dendritic cells (DCs) purified from *Gpr141*$^{-/-}$ mice increased cytokine production of myelin oligodendrocyte glycoprotein 35–55–specific T cells. These findings suggest that GPR141 functions as a negative regulator of immune responses by controlling the functions of monocytes and dendritic cells and that targeting GPR141 may be a possible therapeutic intervention for modulating chronic inflammatory diseases.

**Keywords:** autoimmune disease, dendritic cells, experimental autoimmune encephalomyelitis, G protein–coupled receptor 141, monocytes, myeloid cells

## 1. Introduction

Multiple sclerosis (MS) is a chronic inflammatory disease characterized by demyelination of white matter in the central nervous system (CNS), leading to impaired neuronal function. Encephalitogenic T cells, capable of recognizing neuron-derived antigens, trigger neuroinflammation in the CNS and potential relapse. In addition, the therapeutic effect of B cell elimination in MS highlights the importance of other lymphocytes in this disease.[1] Experimental autoimmune encephalomyelitis (EAE), an autoimmune disease model of MS, has contributed to our understanding of MS pathogenesis, in which T helper 1 (Th1) cells producing interferon (IFN)-γ and Th17 cells producing interleukin (IL)-17 are involved in eliciting chronic inflammation.[2] In addition, Th cells producing granulocyte-macrophage colony-stimulating factor, an essential cytokine for monocyte-derived cell invasion in the CNS, are also required for neuroinflammation.[3,4] Therefore, dysregulated cytokine networks are associated with pathological conditions during the neuropathogenesis of MS.

Myeloid cell populations, including macrophages, DCs, and microglia, are heterogeneous in the CNS. These myeloid cell populations have diverse functions in health and disease. Microglia play a role in synaptic pruning during normal CNS development and may also play a vital role in synaptic loss in neuropathic diseases.[5,6] Microglia weakly present self-antigens to encephalitogenic T cells that cross the endothelial cell barrier. In contrast, $CD11c^+$ cells in the meninges and vessels can reactivate encephalitogenic T cells as antigen-presenting cells (APCs).[7] Although $CD11c^+$ is expressed in DCs, microglia, macrophages, and monocytes, $CD11b^+CD172a^+$ cDC2 has been identified as the primary APC that presents self-antigens to reactivate encephalitogenic T cells in EAE.[8] Moreover, $CCR2^+$ monocyte infiltration into the spinal cord is necessary for EAE progression.[9] $Ly6C^+CCR2^+$ monocytes require granulocyte-macrophage colony-stimulating factor to induce axonal demyelination, and monocyte-derived effector cells, including monocyte-derived DCs, initiate neuroinflammation.[4] Thus, myeloid cell populations in the CNS play distinct roles in encephalitogenic T cell reactivation, neuroinflammation initiation, and tissue damage to myelinated and neuronal cells, although they are necessary for EAE development and progression.

G protein–coupled receptors (GPCRs) are integral membrane proteins containing 7 transmembrane domains with clusters of hydrophobic amino acid residues. GPCRs mediate diverse cellular responses by interacting with several ligands, such as hormones, neurotransmitters, cytokines, and sensory stimuli, such as photons and odorants. More than 800 human genes and 1,300 murine genes have been identified, and these receptors have

**Received:** May 22, 2023. **Revised:** November 14, 2023. **Accepted:** December 27, 2023. **Corrected and Typeset:** February 20, 2024
© The Author(s) 2024. Published by Oxford University Press on behalf of Society for Leukocyte Biology. All rights reserved. For permissions, please e-mail: journals.permissions@oup.com

unique roles in processing various physiological functions in behavior, cognition, metabolism, hormone homeostasis, and immune responses.[10] GPCRs bind to these ligands and interact with and activate heterotrimeric G proteins in the cytoplasm, initiating signaling pathways to modulate cellular functions.[11,12] Because 30% to 60% of the present drugs act on GPCRs, these receptors are promising targets for drug development. Therefore, numerous studies have focused on hundreds of orphan GPCRs (oGPCRs) whose endogenous ligands are yet to be identified.[13]

GPR141 was identified in the human genome by searching an amino acid database containing the transmembrane domains of 254 GPCRs. GPR141 is a novel oGPCR categorized as a class A receptor, also known as a rhodopsin-like receptor.[14] GPR141 contains TRY residues instead of the DRY motif positioned near the membrane in the third transmembrane domain, a conserved motif in rhodopsin-like GPCRs. GPR141 does not have the NSxxNPxxY motif in the seventh transmembrane domain (i.e. conserved in rhodopsin-like GPCRs).[15] However, its physiological functions and endogenous ligands for GPR141 remain unclear.

GPCRs and oGPCRs are involved in the pathogenesis of MS and EAE.[16] The amino acid sequence of GPR141 is homologous to GPR17, the type 1 cysteinyl leukotriene (cys-LTs) receptor, and GPR34, a lysophosphatidylserine receptor. Cys-LTs are important proinflammatory mediators in chronic airway inflammation[17] and lysophosphatidylserine enhances the degranulation of mast cells.[18] These findings indicate that GPR141 may be associated with inflammatory responses for biological defenses or autoimmune diseases, such as MS. In the present study, we generated *Gpr141*$^{-/-}$ mice to understand the in vivo role of GPR141 in inflammatory diseases. Notably, GPR141 was expressed in myeloid cells, such as monocytes, macrophages, and DCs, and GPR141 may regulate the functions of APCs that are responsible for autoreactive T cells. Thus, our data point to a new suppressive immunomodulator of myeloid cells in demyelinating autoimmunity.

## 2. Methods

### 2.1 *Gpr141*$^{-/-}$ mice generation

*Gpr141*$^{-/-}$ mice were generated using homologous recombination in E14TG2a 129ola strain–derived embryonic stem (ES) cells. The targeting vector was designed by replacing the genomic fragment of the fifth exon of the *Gpr141* gene, containing the whole protein coding region and 3′ untranslated regions, with a DNA fragment containing a *neo*-resistance gene under the control of a phosphoglycerate kinase 1 promoter flanked by *lox*P. Diphtheria toxin subunit (DT-A), under the control of the MC1 promoter, was ligated to the 5′ ends of the targeting vector for negative selection. Two genomic fragments, including a 5.2 kb 5′ and a 7.5 kb 3′ homologous arm, were amplified from the RPCI-23-MM BAC clone (Thermo Fisher Scientific) via polymerase chain reaction (PCR) using KOD polymerase (Takara Bio). These fragments were assembled into a modified pBluescript II SK vector (Addgene) containing a phosphoglycerate kinase promoter–driven *loxP*-flanked *neo*-resistance gene and an MC1 promoter–driven *DT-A* gene. The targeting vector was electroporated into E14TG2a ES cells and selected using the G418. We screened 120 *neo*-resistant ES clones using Southern blotting and a 5′ probe, and 1 clone was identified as having undergone homologous recombination. The correct integration of the transgene was verified through Southern blotting using 5′ and 3′ probes.

Chimeras were generated via 8-cell aggregation, and the resultant chimeric mice were bred to produce progeny with germline transmission of the mutated allele. The F1 progeny harboring the targeted *Gpr141* allele were backcrossed for 11 generations onto a C57BL/6J background. Mice heterozygous for the *Gpr141* mutation, available from the Riken Bioresource Center (No. RBRC05742), were intercrossed to obtain homozygous mutant mice. All mice used in these experiments were male and 8- to 12-wk-old, and age- and sex-matched control C57BL/6J mice were purchased from Japan SLC, Inc. 2D2 TCR transgenic mice were purchased from the Jackson Laboratory. All mice were housed in the animal facilities of the Institute of Tokyo University of Science or Tohoku Medical and Pharmaceutical University. Animal experiments were carried out following the guidelines of each university and were approved by the Animal Experiment Committees (A22028-cn).

### 2.2 Quantitative real-time PCR

Total RNA was extracted using the ReliaPrep RNA Miniprep System (Promega). Total RNA was reverse-transcribed using Superscript II Reverse Transcriptase (Invitrogen) to synthesize the first complementary DNA. Quantitative PCR was performed in a total reaction volume of 10 µL including 5 ng of total RNA, TB Green Premix Ex TaqII (Takara Bio), and a set of forward and reverse primers (Operon) in duplicate or triplicate, according to the instruction of the manufacturer. The final concentration of each primer used was 800 nM. Quantification was performed using the CFX96 Real-Time system (Bio-Rad Laboratories). The cycling program was 1 cycle of 95 °C for 1 min, followed by 39 cycles of a set of 95 °C for 3 s and 60 °C for 30 s. The primer sets used to detect *Gpr141* and β-actin transcripts are described in Supplementary Table 1. β-actin was used as an internal housekeeping gene. The target and housekeeping genes were quantified simultaneously in one plate, with water samples as the negative reference. The differences in RNA quality and the initial sample quality were normalized to β-actin.

### 2.3 Flow cytometry

Single-cell suspensions from the spleen were prepared by grinding with gaskets of a 5 mL syringe (TERUMO CORPORATION, Tokyo, Japan) through 70 µm cell strainers (Corning). Bone marrow (BM) cells were isolated by flushing the BM cavity of the femurs with R10. The red blood cells were lysed on ice with hemolysis buffer (140 mM NH4Cl and 17 mM Tris-HCl, pH 7.2). These cells were washed twice with flow cytometry (FCM) staining buffer comprising 2% fetal bovine serum (FBS) in phosphate-buffered saline (PBS). Fc receptors on these cells were blocked with 2.4G2 at 4 °C for 10 min, followed by incubation with fluorescence-conjugated antibodies for 30 min on ice. Commercially available antibodies used in the experiments are listed in Supplementary Table 2. Dead cells were stained with BD Horizon Flexible Viability Stain 510 (BD Biosciences). The cells were washed twice with FCM buffer and analyzed using an Attune NxT flow cytometer (Thermo Fisher Scientific). The data were analyzed using FlowJo v10.8.2 software (FlowJo LLC).

### 2.4 Peptides

Mouse myelin oligodendrocyte glycoprotein 35–55 ($MOG_{35–55}$) (MEVGWYRSPFSRVVHLYRNGK) was synthesized by Kitayama Labes Co. Ltd.

### 2.5 EAE induction

Mice were subcutaneously immunized with 100 µg of $MOG_{35–55}$ peptide emulsified in 200 µL of incomplete Freund's adjuvant (Thermo Fisher Scientific) and PBS (1:1) supplemented with 250 µg of nonviable *Mycobacterium tuberculosis* H37RA (Difco

Laboratories) on days 0 and 7. Mice were intraperitoneally injected with 200 ng of pertussis toxin (PTX) (List Biological Labs) in PBS on days 0 and 2. Clinical EAE scores were monitored for 30 d according to the following grades: 0, no disease; 0.5, partially limp tail; 1, paralyzed tail; 1.5, paralyzed in 1 hind limb; 2, both hind limbs paralyzed; 2.5, weakness in 1 forelimb; 3, weakened forelimbs; 4, paralyzed forelimbs; and 5, moribund. The mean clinical score was determined by averaging the scores of all mice in each group. The cumulative score was the sum of the daily clinical scores of individual mice and was indicated as the average of each group. The average maximal score and onset were calculated as the average of the maximal clinical score or the date of EAE occurrence in individual mice of each group.

## 2.6 Histology

Mice were anesthetized with a combination of 3 types of anesthetic agents consisting of 0.3 mg/kg of medetomidine (Kyoritsu Seiyaku Corporation), 4 mg/kg of midazolam (Astellas Pharm), and 5 mg/kg of butorphanol (Meiji Seika Pharma) at the end of the induced disease. The mice were perfused with PBS to wash the blood from the spinal cord through the intracardiac route and continuously with a 10% formalin neutral buffer solution (pH 7.4) by gravity-driven perfusion. Amputated spinal cords were further fixed in 10% formalin solution for 24 h. Dissected spinal cords were dehydrated through 70%, 85%, 95%, and 100% alcohol, followed by xylene substitution for paraffinization. The tissues were embedded in paraffin blocks and sections (4 mm) between L3 and L5 position were prepared using microtome (Retoratome REM-710; Yamato). Paraffin-embedded sections were stained with hematoxylin and eosin and Luxol fast blue (LFB) (Muto Pure Chemicals). The sections were photographed using a NanoZoomer-SQ (Hamamatsu).

## 2.7 Histological encephalomyelitic severity evaluation

Three tissue sections were used to evaluate the severity of spinal cord inflammation. Encephalomyelitic severity was determined following the criteria used in previous reports.[19] The criteria for encephalomyelitic severity were as follows: 0, no inflammation; 1, cellular infiltration only in the perivascular areas and meninges; 2, mild cellular infiltration in the parenchyma (inflammatory cells infiltrating less than one-third of the white matter area); 3, moderate cellular infiltration in the parenchyma (inflammatory cells infiltrating more than one-third of the white matter area); and 4, severe cellular infiltration in the parenchyma. Demyelination conditions were assessed by LFB staining with following criteria: 0, no demyelination; 1, mild demyelination; 2, moderate demyelination; 3, severe demyelination.[20,21]

## 2.8 T cell response to $MOG_{35–55}$

Mice were subcutaneously immunized with 100 μg of the $MOG_{35–55}$ peptide, which was emulsified in 200 μL of incomplete Freund's adjuvant and PBS (1:1) supplemented with 250 μg of nonviable *M. tuberculosis* H37RA (Difco Laboratories). Mice were intraperitoneally injected with 200 ng of PTX in PBS on day 0. Single cells from the brachial and axillary lymph nodes (LNs) were harvested on day 7 after immunization and seeded at $5 \times 10^5$ cells/well in 96-well round-bottom plates with 10 μg/mL and 100 μg/mL of $MOG_{35–55}$ peptide for 72 h in RPMI supplemented with 0.1 mM of β-mercaptoethanol, 100 U/mL of penicillin, 100 μg/mL of streptomycin, and 10% heat-inactivated FBS (the culture medium is called R10). These cells were centrifuged at 1500 rpm for 5 min, and the supernatant was stocked at −80 °C until used.

## 2.9 Cytokine enzyme-linked immunosorbent assay

The concentration of cytokines in the culture supernatants was determined using enzyme-linked immunosorbent assay (ELISA), according to the manufacturer's instructions. The concentrations of IFN-γ and IL-17 were measured using mouse ELISA sets (R&D Systems) and those of IL-6 and tumor necrosis factor α (TNF-α) were determined using mouse ELISA MAX (BioLegend). IL-12 (p40) was assayed with BD OptEIA Set (BD Biosciences).

## 2.10 Magnetic cell sorting

For the coculture of 2D2T cells and DCs, splenic cells were prepared from wild-type (WT) and *Gpr141*$^{-/-}$ mice and red blood cells were removed by a hemolysis buffer. Resuspended cells were treated with 2.4G2 at 4 °C for 15 min to block Fc receptors. After washing with an FCM buffer, the cells were incubated with 15 μL of CD11b- and CD11c-MicroBeads per 10 million cells for 30 min at 4 °C. CD11b- and CD11c-positive fractions were separated with an auto MACS Pro separator (Miltenyi Biotec), and these cells were used as APCs.

Cells from the spleens and the axillary, branchial, cervical, inguinal, and mesenteric LNs were treated with a hemolysis buffer to remove red blood cells. The Fc receptors on these cells were blocked with 2.4G2 at 4 °C for 15 min and the cells were incubated with 10 μL of Thy1.2 MicroBeads (Miltenyi Biotec) per 10 million total cells for 30 min at 4 °C. Thy1.2-positive fractions were separated with an auto MACS Pro separator, and these cells were used as 2D2T cells.

## 2.11 2D2T cell-DC coculture

2D2T cells ($2 \times 10^5$ cells) were cultured either with WT or *Gpr141*$^{-/-}$ DCs ($2 \times 10^4$ cells) with or without pMOG (10 and 100 mg/mL) for 3 d in a 96-well round-bottom plate in RPMI supplemented with 0.1 mM of β-mercaptoethanol, 100 U/mL of penicillin, 100 μg/mL of streptomycin, and 10% heat-inactivated FBS (R10). 2D2T cells and DCs were sorted with the auto MACS Pro separator described previously. The cells were subjected to the cell surface and intracellular staining for FCM analysis.

## 2.12 Anti-$MOG_{35–55}$ antibody measurement

On day 30 after EAE induction, whole-blood samples were collected via cardiac puncture under anesthesia. The blood samples were stored at 4 °C overnight, and sera were collected by centrifugation at 3000 rpm for 10 min. $MOG_{35–55}$ peptides (1 μg/well of a 96-well plate in PBS) were coated on a 96-well plate at 4 °C overnight. The wells were blocked with 10% FBS in PBS at room temperature for 1 h. Serum samples were diluted at 100-fold, and 30 μL of diluted samples was incubated at 4 °C overnight. Horseradish peroxidase –conjugated goat anti-mouse immunoglobulin G (IgG) (0.8 μg/mL) (Jackson ImmunoResearch) or 0.4 μg/mL alkaline phosphatase–conjugated anti-mouse IgG1, IgG2a, IgG2b, and IgG3 (Santa Cruz Biotechnology) were added and incubated at room temperature for 1 h. Then, 3,3′,5,5′-tetramethylbenzidine solution (Dako) for IgG or p-nitrophenyl phosphate solution (Sigma-Aldrich) for IgG1, IgG2a, IgG2b, and IgG3 was added as substrate, and 1 N HCl or 1 N NaOH was used to stop color development. Antibody concentrations were determined by measuring the absorbance at 450 nm for IgG and 405 nm for the other subclasses.

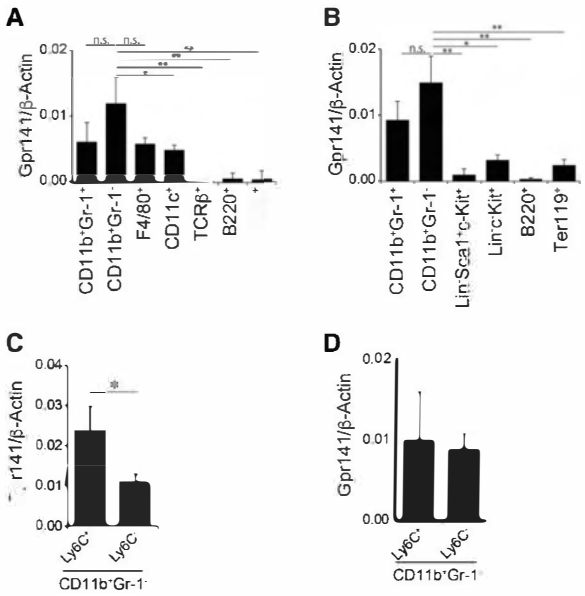
A
B
C
D
Gpr141/β-Actin
0.02
0.01
0.00
n.s.
*
**
CD11b+Gr-1+
CD11b+Gr-1-
F4/80+
CD11c+
TCRβ+
B220+
Lin-Sca1+c-Kit+
Lin-c-Kit+
Ter119+
0.04
0.03
Ly6C+
Ly6C-
CD11b+Gr-1-
CD11b+Gr-1+

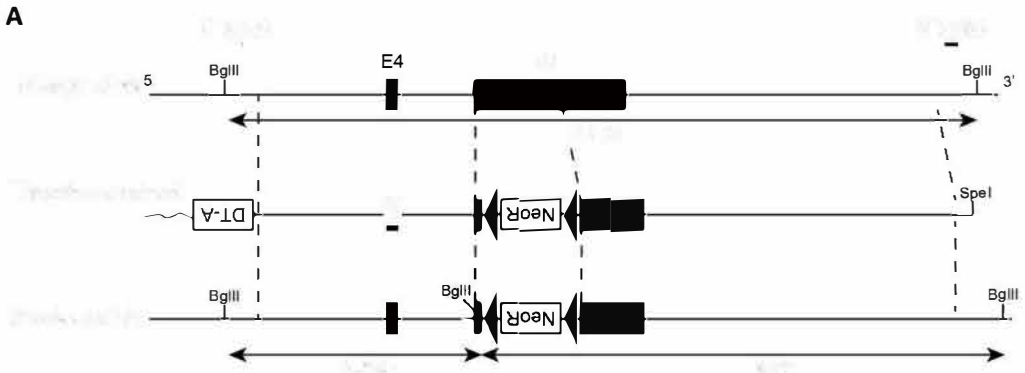
A
5
BglII
E4
BglII
3'
DT-A
NeoR
SpeI
BglII
BglII
NeoR
BglII

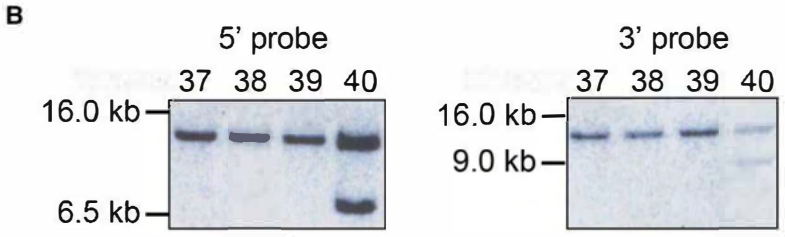
B
5' probe
37 38 39 40
16.0 kb
6.5 kb
3' probe
37 38 39 40
16.0 kb
9.0 kb

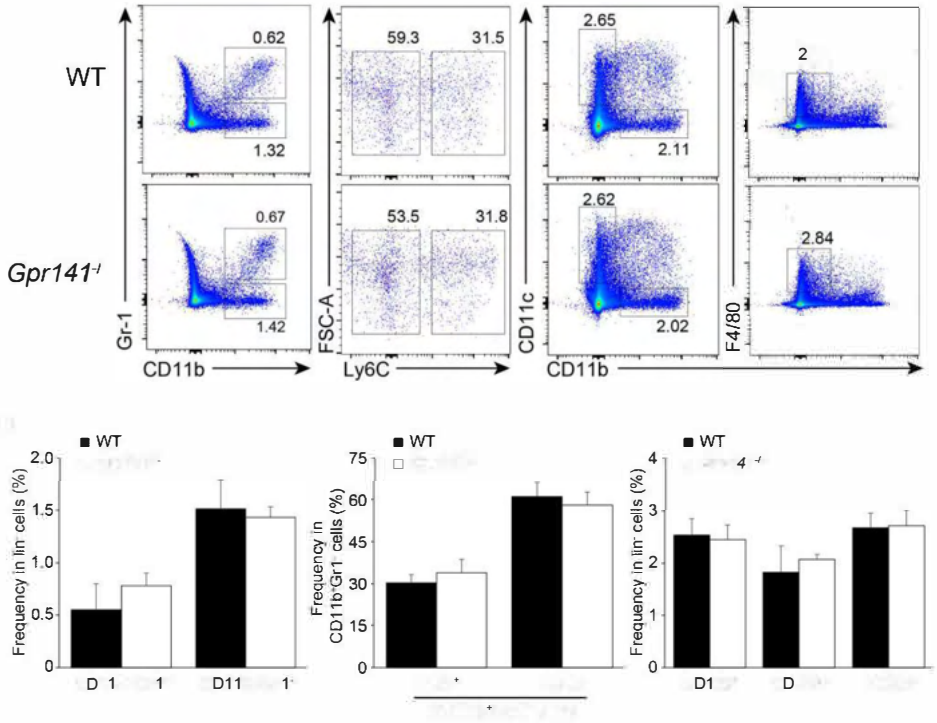
WT
Gpr141-/-
0.62
1.32
0.67
1.42
59.3
31.5
53.5
31.8
2.65
2.11
2.62
2.02
2
2.84
Gr-1
CD11b
FSC-A
Ly6C
CD11c
CD11b
F4/80
WT
Frequency in lin- cells (%)
Frequency in CD11b+Gr1+ cells (%)
D1
D11

C

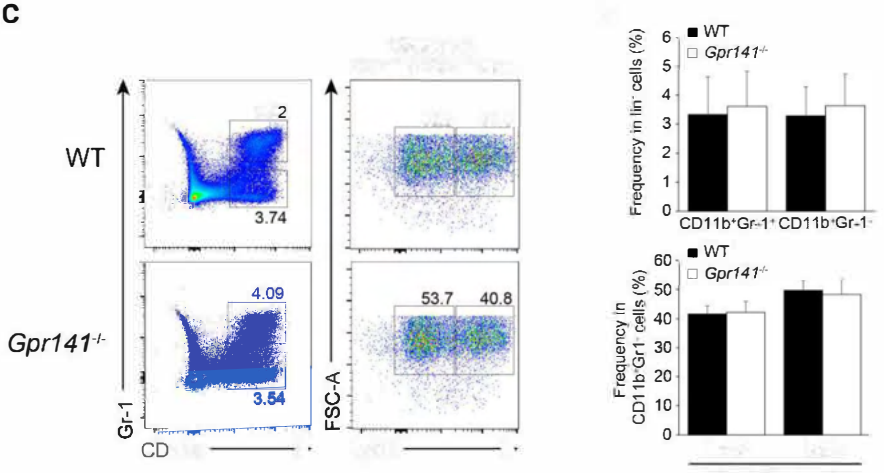
WT
Gpr141-/-
2
3.74
4.09
3.54
53.7
40.8
Gr-1
FSC-A
WT
Gpr141-/-
Frequency in lin- cells (%)
CD11b+Gr-1+
CD11b+Gr-1-
Frequency in CD11b+Gr1+ cells (%)

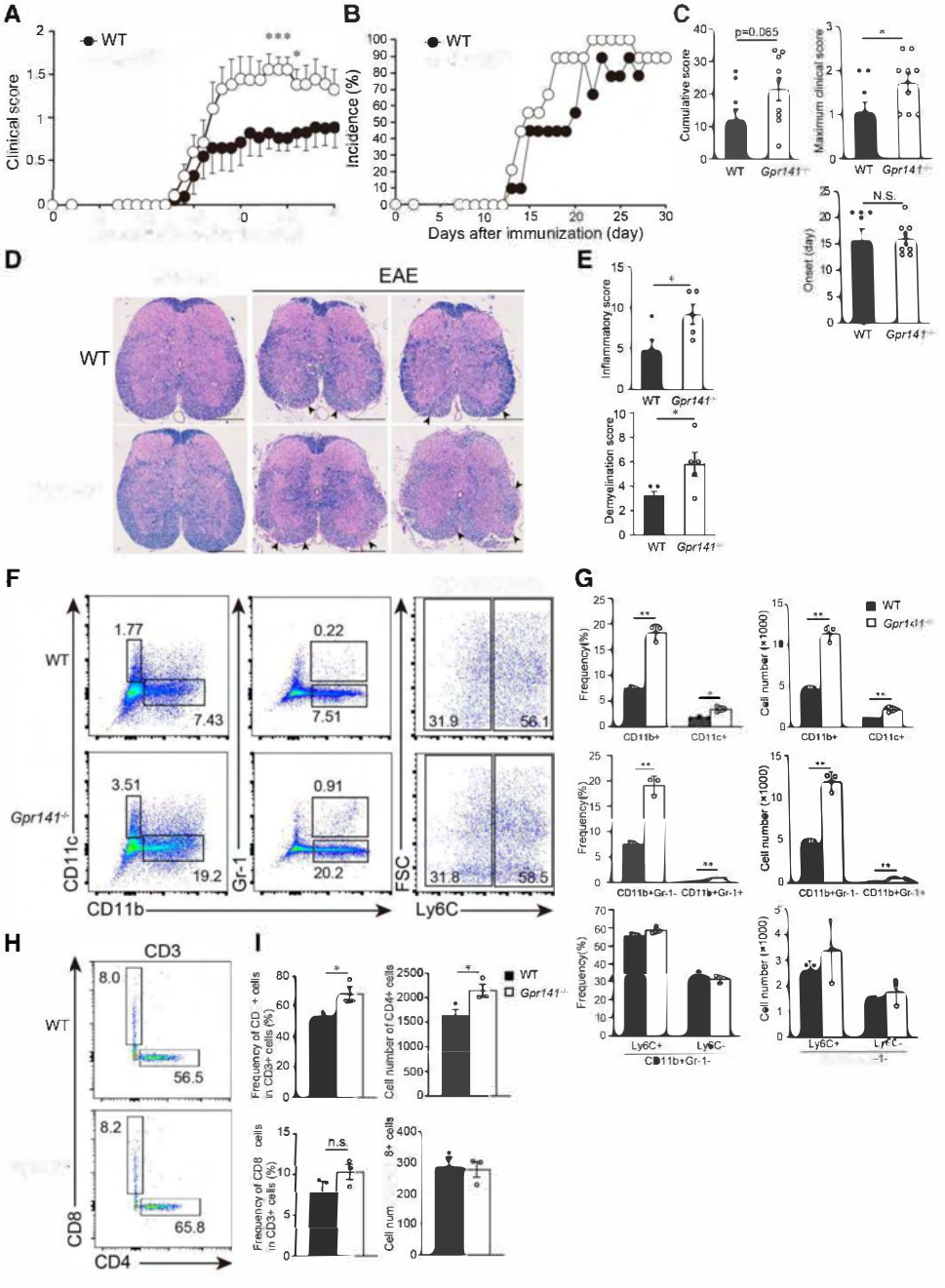
A
WT
Clinical score
B
WT
Incidence (%)
Days after immunization (day)
C
p=0.065
Cumulative score
Maximum clinical score
N.S.
Onset (day)
WT
Gpr141-/-
D
EAE
WT
E
Inflammatory score
Demyelination score
F
WT
Gpr141-/-
1.77
7.43
0.22
7.51
31.9
56.1
3.51
19.2
0.91
20.2
31.8
58.5
CD11c
CD11b
Gr-1
FSC
Ly6C
G
Frequency(%)
Cell number (×1000)
CD11b+
CD11c+
CD11b+Gr-1-
CD11b+Gr-1+
Ly6C+
Ly6C-
H
CD3
8.0
56.5
8.2
65.8
CD8
CD4
I
Frequency of CD + cells in CD3+ cells (%)
Cell number of CD4+ cells
Frequency of CD8 cells in CD3+ cells (%)
Cell num
8+ cells
n.s.

35 55

<

=

=

<

<

±

+ +

+ +

±

=

Table 1. EAE disease course.

| Strain | Incidence | Cumulative score | Maximum clinical score | Day of onset |
|---|---|---|---|---|
| WT | 8/9 (89%) | 109 ± 9.8 | 1.1 ± 0.7 (affected mice) | 17.6 ± 3.4 |
| *Gpr141*$^{-/-}$ | 9/9 (100%) | 194 ± 12.2 | 1.7 ± 0.6 (affected mice)[a] | 16.0 ± 3.1 |

Values are n/n (%) or mean ± SD.
[a]$P < 0.05$, 2-tailed unpaired Student's *t* test.

cytokine secretion, such as IFN- γ, IL-17, and TNF-α, compared with WT DCs (Fig. 5D). In addition, p40, mainly produced by DCs, and IL-6, produced by T cells and DCs, were higher in the co-culture with *Gpr141*$^{-/-}$ DCs than WT DCs (Fig. 5E), suggesting that GPR141 deficiency heightens the DC functions, such as antigen presentation and cytokine production. These data show that GPR141 deficiency facilitates adaptive immune responses to MOG antigens, including antibody and cytokine production, suggesting that GPR141 indirectly modulates B and T cells by negatively regulating myeloid cells, at least, and DCs.

## 4. Discussion

In this study, we demonstrated the physiological roles of GPR141, an orphan rhodopsin-like GPCR, in the immune system. The *Gpr141* transcripts were detected in myeloid cells, including DCs, monocytes (inflammatory and patrolling monocytes), macrophages, and neutrophils but were barely detectable in lymphocytes, such as T, B, and NK cells. *Gpr141*$^{-/-}$ mice, generated by targeting homologous recombination in ES cells, proved that GPR141 deficiency does not affect myeloid cell development and compartmentalization under steady-state conditions.

However, *Gpr141*$^{-/-}$ mice were more susceptible to EAE, and cellular infiltration into the spinal cord increased in *Gpr141*$^{-/-}$ mice. GRP141 deficiency enhanced adaptive immune responses against the lymphocyte recall response to the $MOG_{35–55}$ peptide. Although further studies are needed to understand the molecular mechanisms underlying the GPR141-mediated regulation of immune responses, these data suggest that GPR141 is a negative immune response regulator, possibly by modifying the myeloid cell function, especially DCs, which dictates naïve T cell differentiation into effector T cells and reactivates effector cells at the site where T cells exert their functions.

Several oGPCRs are expressed in immune-related cells, including lymphocytes and myeloid cells.[24] In our study, immune cell subsets were sorted from the spleen, and BM and *Gpr141* transcripts were detected in neutrophils ($CD11b^+Gr1^+$), inflammatory monocytes ($CD11b^+Gr1^-Ly6C^+$), patrolling monocytes ($CD11b^+Gr1^-Ly6C^-$), macrophages ($F4/80^+$), and DCs ($CD11c^+$). The Immunological Genome Project database provides the *Gpr141* messenger RNA expression profiles (ProbeSet ID:10407985). In the database, *Gpr141* is highly expressed in splenic $CD11c^+CD4^+$ cells and $F4/80^{hi}$ macrophages, $CD115^+Ly6C^+$ monocytes from the blood and LNs, and $CD11b^+Gr1^+$ neutrophils from the BM. In contrast, $NK1.1^+$ NK, $CD4^+TCR\beta^+$T, $CD8^+TCR\beta^+$T, and $CD19^+$ $B220^+$ B cells sorted from the spleen showed low *Gpr141* expression. Although the lymphoid organs from which each immune cell was sorted differed between our analyses and the Immunological Genome Project, our data provided convincing evidence that GPR141 is expressed in myeloid cells. However, we could not confirm GPR141 at the protein level due to lacking GPR141-specific antibodies. However, *Gpr141* expression profiles suggest that GPR141 should be involved in innate immunity, in which neutrophils and monocytes or macrophages sense and eliminate pathogens.

The mechanisms underlying the GPR141 immunomodulation of myeloid cells remain unknown. Our data in Fig. 3 show that myeloid cell development and compartmentalization in the BM and spleen were comparable between *Gpr141*$^{-/-}$ and WT mice, indicating that GPR141 deficiency does not affect the developmental process of myeloid cells at a steady state.

Chemokine receptors belong to the class A GPCRs and inflammatory and patrolling monocytes migrate from the BM and are guided by the chemokine receptor CCR2.[25] GPR141 deficiency showed that the cellular infiltration of $CD11c^+$ DCs, $CD11b^+$ $Gr1^-$ monocytes, and $CD11b^+Gr1^+$ neutrophils into the spinal cord increased in *Gpr141*$^{-/-}$ mice 7 days after immunization, possibly indicating that GPR141 may regulate myeloid cell migration. In addition, $CD11b^+Ly6C^+$ inflammatory monocytes are recruited in the CNS during inflammatory conditions, in which they differentiate into monocyte-derived DCs characterized by CD11c and major histocompatibility complex class II expression. Therefore, the increasing $CD11c^+$ DCs may contribute to antigen presentation to infiltrating T cells to initiate excessive immune responses in *Gpr141*$^{-/-}$ mice, and as a result, CD4+ T cell infiltration into the spinal cord was increased in *Gpr141*$^{-/-}$ mice. However, the myeloid cell increase in the CNS during EAE may be a secondary effect of enhanced inflammatory responses, which increase chemokine production from tissues and chemokine receptor expression in myeloid cells.

Although the role of neutrophils in autoimmune neuroinflammation is not well understood, increasing evidence suggests that neutrophils are involved in EAE. Neutrophils may be involved in the breakdown of the blood-brain barrier, glial limitans, and inflammatory cytokines secretion.[26] In addition, Th17, a pathogenic Th cell subset, induces the expression of neutrophil-activating molecules, such as granulocyte colony-stimulating factor, CXCL5, and IL-17. *Csf3r* deficiency ameliorated EAE clinical scores and decreased neutrophil infiltration in the CNS.[27]

DCs are APCs that prime naïve T cells in peripheral lymphoid tissues. During DC maturation, they produce IL-1, IL-6, IL-12, and IL-23 and induce naïve T cell differentiation into Th1 and Th17 cells. In EAE, encephalitogenic T cells are required for reactivation by APCs to infiltrate the parenchyma and cause immunopathology.[8] The lymphocyte recall response showed that GPR141 deficiency substantially increased IFN-γ– and IL-17 secretion in response to the $MOG_{35–55}$ peptide, indicating that GPR141 could be involved in DC functions, such as antigen processing and presentation, costimulatory molecule expression, and cytokine secretion. Furthermore, we detected an increased IL-6 concentration, a proinflammatory cytokine secreted by DCs and macrophages responsible for Th17 differentiation. Our data on the coculture of MACS-sorted splenic WT and *Gpr141*$^{-/-}$ DCs with T cells with TCR specific for$MOG_{35–55}$ peptide in the presence of $MOG_{35–55}$ peptide strongly support the idea that GPR141 regulates DC functions in a negative manner because *Gpr141* deficiency enhanced not only the secretion of T cell–derived cytokines and proinflammatory cytokines from DCs. The enhanced Th1 and Th17 responses in *Gpr141*$^{-/-}$ mice may have increased antibody titers against the $MOG_{35–55}$ peptide during EAE. Although further experiments are required to understand GPR141-mediated suppressive regulation of immune responses, GPR141 inhibits T cell-dependent autoimmune responses by modulating DC functions.

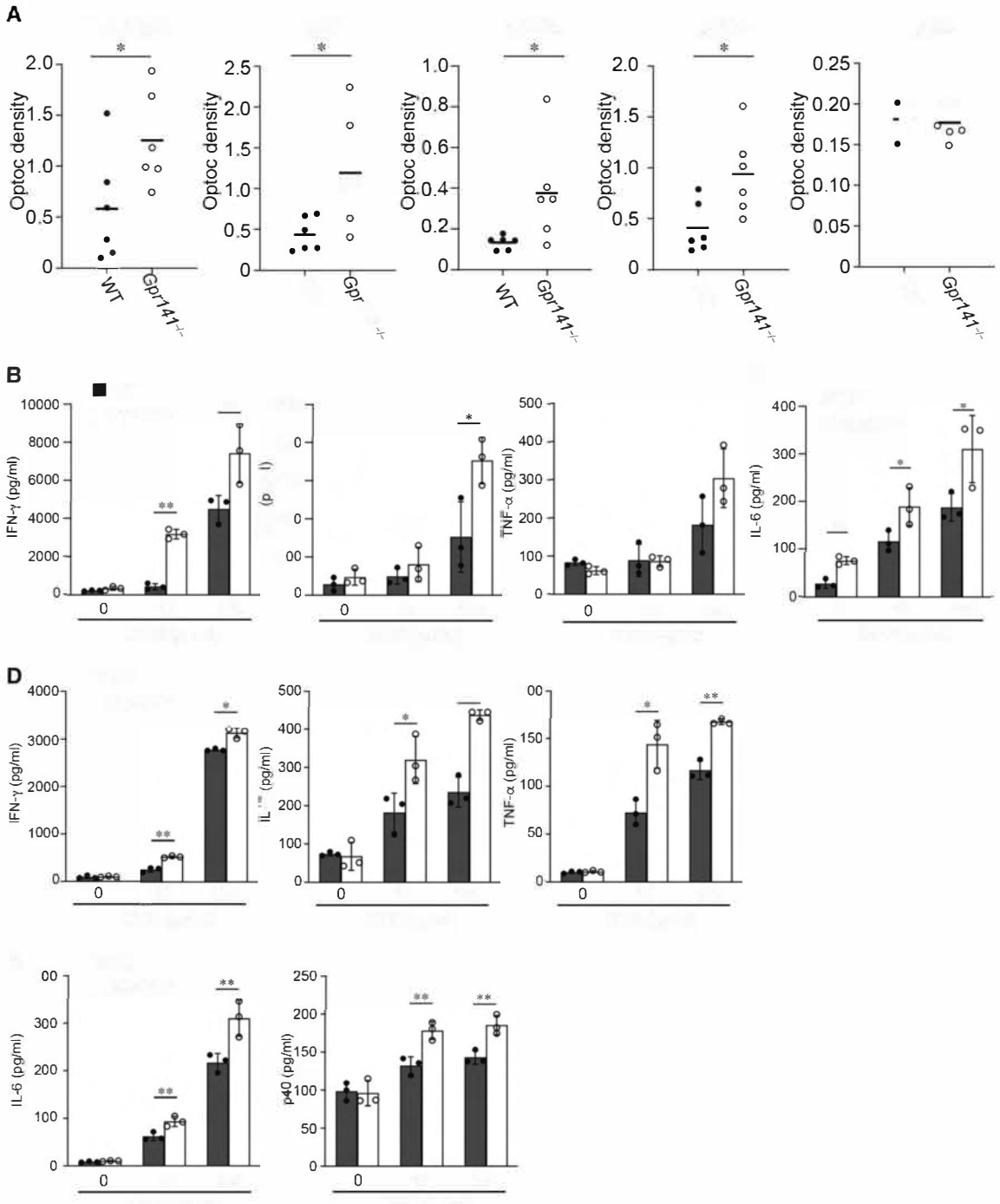


35 55

35 55

35 55

35 55

35 55

35 55

5 5

8

9 29 30

–/–

3 33

5

–/

5

– – – –

–/
+

30

35 55
35 55

## Acknowledgments

–/–

## Author contributions

–/–

## Supplementary material

## Funding

5 8

## References


1. 5 88
8 5 88

5 5 5 5 558
8 8

3.

5 5 8

4.

5 3 3 5 5
5 8

5.

5 8
8

6.

8 5 – 58
5

7.

5 8 38

8.

8 8
838

9.

derived macrophages are vital cells playing an anti-inflammatory role in recovery from spinal cord injury in mice. *PLoS Med*. 2009:6(7):e1000113. https://doi.org/10.1371/journal.pmed.1000113
10. Pierce KL, Premont RT, Lefkowitz RJ. Seven-transmembrane receptors. *Nat Rev Mol Cell Biol*. 2002:3(9):639–650. https://doi.org/10.1038/nrm908
11. Weis WI, Kobilka BK. The molecular basis of G protein-coupled receptor activation. *Annu Rev Biochem*. 2018:87(1):897–919. https://doi.org/10.1146/annurev-biochem-060614-033910
12. Wootten D, Christopoulos A, Marti-Solano M, Babu MM, Sexton PM. Mechanisms of signalling and biased agonism in G protein-coupled receptors. *Nat Rev Mol Cell Biol*. 2018:19(10):638–653. https://doi.org/10.1038/s41580-018-0049-3
13. Basith S, Cui M, Macalino SJY, Park J, Clavio NAB, Kang S, Choi S. Exploring G protein-coupled receptors (GPCRs) ligand space via cheminformatics approaches: impact on rational drug design. *Front Pharmacol*. 2018:9:128. https://doi.org/10.3389/fphar.2018.00128
14. Vassilatis DK, Hohmann JG, Zeng H, Li F, Ranchalis JE, Mortrud MT, Brown A, Rodriguez SS, Weller JR, Wright AC, *et al*. The G protein-coupled receptor repertoires of human and mouse. *Proc Natl Acad Sci U S A*. 2003:100(8):4903–4908. https://doi.org/10.1073/pnas.0230374100
15. Fredriksson R, Hoglund PJ, Gloriam DE, Lagerstrom MC, Schioth HB. Seven evolutionarily conserved human rhodopsin G protein-coupled receptors lacking close relatives. *FEBS Lett*. 2003:554(3):381–388. https://doi.org/10.1016/S0014-5793(03)01196-7
16. Du C, Xie X. G protein-coupled receptors as therapeutic targets for multiple sclerosis. *Cell Res*. 2012:22(7):1108–1128. https://doi.org/10.1038/cr.2012.87
17. Maekawa A, Balestrieri B, Austen KF, Kanaoka Y. GPR17 is a negative regulator of the cysteinyl leukotriene 1 receptor response to leukotriene D4. *Proc Natl Acad Sci U S A*. 2009:106(28):11685–11690. https://doi.org/10.1073/pnas.0905364106
18. Horigome K, Tamori-Natori Y, Inoue K, Nojima S. Effect of serine phospholipid structure on the enhancement of concanavalin A-induced degranulation in rat mast cells. *J Biochem*. 1986:100(3):571–579. https://doi.org/10.1093/oxfordjournals.jbchem.a121748
19. Kaifu T, Yabe R, Maruhashi T, Chung SH, Tateno H, Fujikado N, Hirabayashi J, Iwakura Y. DCIR and its ligand asialo-biantennary N-glycan regulate DC function and osteoclastogenesis. *J Exp Med*. 2021:218(12):e20210435. https://doi.org/10.1084/jem.20210435
20. Seno A, Maruhashi T, Kaifu T, Yabe R, Fujikado N, Ma G, Ikarashi T, Kakuta S, Iwakura Y. Exacerbation of experimental autoimmune encephalomyelitis in mice deficient for DCIR, an inhibitory C-type lectin receptor. *Exp Anim*. 2015:64(2):109–119. https://doi.org/10.1538/expanim.14-0079
21. Okuda Y, Okuda M, Bernard CC. The suppression of T cell apoptosis influences the severity of disease during the chronic phase but not the recovery from the acute phase of experimental autoimmune encephalomyelitis in mice. *J Neuroimmunol*. 2002:131(1-2):115–125. https://doi.org/10.1016/S0165-5728(02)00267-9
22. Ginhoux F, Jung S. Monocytes and macrophages: developmental pathways and tissue homeostasis. *Nat Rev Immunol*. 2014:14(6):392–404. https://doi.org/10.1038/nri3671
23. Zhou D, Srivastava R, Nessler S, Grummel V, Sommer N, Bruck W, Hartung HP, Stadelmann C, Hemmer B. Identification of a pathogenic antibody response to native myelin oligodendrocyte glycoprotein in multiple sclerosis. *Proc Natl Acad Sci U S A*. 2006:103(50):19057–19062. https://doi.org/10.1073/pnas.0607242103
24. Zhao M, Wang Z, Yang M, Ding Y, Zhao M, Wu H, Zhang Y, Lu Q. The roles of orphan G protein-coupled receptors in autoimmune diseases. *Clin Rev Allergy Immunol*. 2021:60(2):220–243. https://doi.org/10.1007/s12016-020-08829-y
25. Dominguez PM, Ardavin C. Differentiation and function of mouse monocyte-derived dendritic cells in steady state and inflammation. *Immunol Rev*. 2010:234(1):90–104. https://doi.org/10.1111/j.0105-2896.2009.00876.x
26. Carlson T, Kroenke M, Rao P, Lane TE, Segal B. The Th17-ELR+ CXC chemokine pathway is essential for the development of central nervous system autoimmune disease. *J Exp Med*. 2008:205(4):811–823. https://doi.org/10.1084/jem.20072404
27. RumbleJM, Huber AK, Krishnamoorthy G, Srinivasan A, Giles DA, Zhang X, Wang L, Segal BM. Neutrophil-related factors as biomarkers in EAE and MS. *J Exp Med*. 2015:212(1):23–35. https://doi.org/10.1084/jem.20141015
28. Civelli O, Nothacker HP, Saito Y, Wang Z, Lin SH, Reinscheid RK. Novel neurotransmitters as natural ligands of orphan G-protein-coupled receptors. *Trends Neurosci*. 2001:24(4):230–237. https://doi.org/10.1016/S0166-2236(00)01763-X
29. Xing R, Liu F, Yang Y, Cui X, Wang T, Xie L, Zhao Y, Fang L, Yi T, Zheng B, *et al*. GPR54 deficiency reduces the Treg population and aggravates experimental autoimmune encephalomyelitis in mice. *Sci China Life Sci*. 2018:61(6):675–687. https://doi.org/10.1007/s11427-017-9269-8
30. WangJ, Wang X, Chen X, Lu S, Kuang Y, FeiJ, Wang Z. Gpr97/Adgrg3 ameliorates experimental autoimmune encephalomyelitis by regulating cytokine expression. *Acta Biochim Biophys Sin (Shanghai)*. 2018:50(7):666–675. https://doi.org/10.1093/abbs/gmy060
31. Huang H, Tao YX. Functions of the DRY motif and intracellular loop 2 of human melanocortin 3 receptor. *J Mol Endocrinol*. 2014:53(3):319–330. https://doi.org/10.1530/JME-14-0184
32. Han X, Feng Y, Chen X, Gerard C, Boisvert WA. Characterization of G protein coupling mediated by the conserved D134(3.49) of DRY motif, M241(6.34), and F251(6.44) residues on human CXCR1. *FEBS Open Bio*. 2015:5(1):182–190. https://doi.org/10.1016/j.fob.2015.03.001
33. Guo S, Zhang J, Zhang S, Li J. A single amino acid mutation (R104P) in the E/DRY motif of GPR40 impairs receptor function. *PLoS One*. 2015:10(10):e0141303. https://doi.org/10.1371/journal.pone.0141303
34. Wirasinha RC, Vijayan D, Smith NJ, Parnell GP, Swarbrick A, Brink R, King C, Stewart G, Booth DR, Batten M. GPR65 inhibits experimental autoimmune encephalomyelitis through CD4(+) T cell independent mechanisms that include effects on iNKT cells. *Immunol Cell Biol*. 2018:96(2):128–136. https://doi.org/10.1111/imcb.1031

Check for updates

*The Prostate*

WILEY

The Prostate

ORIGINAL ARTICLE

# Transcriptome-Wide Association Study Identified Novel Blood Tissue Gene Biomarkers for Prostate Cancer Risk

Yanfa Sun[1,2] | Jingjing Zhu[3] | Hua Zhong[2] | Zichen Zhang[4] | Fubo Wang[5] | Akira Nakamura[6] | Yanhui Liu[1] | Jiawen Liu[1] | Jie Yu[1] | Guanghua Zeng[1] | Xin Lin[1] | Dan Zhou[7] | Chong Wu[4,8] | Liang Wang[9] | Youping Deng[3] | Lang Wu[2]

[1]College of Life Science, Fujian Provincial Key Laboratory for the Prevention and Control of Animal Infectious Diseases and Biotechnology, Fujian Provincial Universities Key Laboratory of Preventive Veterinary Medicine and Biotechnology (Longyan University), Longyan University, Longyan, Fujian, P. R. China | [2]Cancer Epidemiology Division, Population Sciences in the Pacific Program, University of Hawaii Cancer Center, University of Hawaii at Manoa, Honolulu, Hawaii, USA | [3]Department of Quantitative Health Sciences, John A. Burns School of Medicine, University of Hawaii at Manoa, Honolulu, Hawaii, USA | [4]Department of Biostatistics, The University of Texas MD Anderson Cancer Center, Houston, Texas, USA | [5]Department of Urology, Shanghai Changhai Hospital, Naval Medical University (Second Military Medical University), Shanghai, P. R. China | [6]Division of Immunology, Faculty of Medicine, Tohoku Medical and Pharmaceutical University, Sendai, Japan | [7]School of Public Health and the Second Affiliated Hospital, Zhejiang University School of Medicine, Hangzhou, China | [8]Institute for Data Science in Oncology, The University of Texas MD Anderson Cancer Center, Houston, Texas, USA | [9]Department of Tumor Biology, Moffitt Cancer Center, Tampa, Florida, USA

**Correspondence:** Youping Deng (dengy@hawaii.edu) | Lang Wu (lwu@cc.hawaii.edu)

**Received:** 28 August 2024 | **Revised:** 10 December 2024 | **Accepted:** 17 January 2025

**Funding:** This study was supported by University of Hawaii Cancer Center and Teacher Training Project of Longyan University.

**Keywords:** biomarker | blood tissue | prostate cancer | susceptibility gene | TWAS

## ABSTRACT

**Objective:** A number of susceptibility genes in prostate tissue have been identified to be associated with prostate cancer (PCa) risk. However, the reported genes based on assessing prostate tissue could not fully explain PCa genetic susceptibility. It is believed that genes functioning in the immune system may fill in the gap of some missing heritability.

**Methods:** To study potential susceptibility genes acting in such pathways, we performed a transcriptome-wide association study (TWAS) of 79,194 PCa cases and 61,112 control of European ancestry by using three sets of gene expression prediction models of blood tissue.

**Results:** A total of 470 genes were associated at false discovery rates-corrected $p$-value $< 0.05$, of which 51 were implicated as likely causal genes based on fine-mapping analysis. Compared with previous literature, 133 novel genes were reported for the first time. Of the identified genes, five (*CREB3L4*, *GSTP1*, *MAPK3*, *NKX3*-1, and *PIK3C2B*) were enriched in a PCa signaling pathway, and 128 genes were enriched in five PCa categories. Importantly, 13 genes (*SCP2*, *LMNA*, *ZNF148*, *H2AFV*, *TACC1*, *FLII*, *SUPT4H1*, *CD300LF*, *MYO9B*, *COX6B1*, *CTSA*, *EP300*, and *TSPO*) showed consistent effect directions for the measured levels in circulating immune cells between PCa cases and controls, and 14 genes (*SLC39A1*, *ZBTB7B*, *TRIM59*, *NCEH1*, *N4BP2*, *TAGAP*, *TACC1*, *TRAF1*, *AIP*, *SECTM1*, *C18orf54*, *ZNF793*, *YIF1B*, and *TSPO*) showed consistency for levels in blood exosomes between PCa patients and controls.

**Conclusion:** The identified blood-based candidate susceptibility genes provide further insights into the genetic basis of PCa risk.

Yanfa Sun and Jingjing Zhu contributed equally and are co-first authors.

© 2025 Wiley Periodicals LLC.

## | Introduction

Prostate cancer (PCa) is one of the most common adult malignancies worldwide, and a major leading cause of cancer-related death in men in Western societies [1]. It is estimated that there are 299,010 new PCa cases and 35,250 PCa deaths in 2024 [2]. It is also expected that they will grow to almost 2.3 million new cases and 740,000 deaths by 2040 due to the growth and aging of the population [3]. The mortality rate of PCa can be decreased through effective early detection, prevention and treatment strategies [4].

Genetic factors are known to contribute to the etiology of PCa [5]. Genome-wide association studies (GWAS) have identified 451 genetic risk variants for PCa [6]. Also, many susceptibility loci and genes for PCa risk have been identified in transcriptome-wide association studies (TWAS) or splicing TWAS [7–14], which integrate GWAS and gene expression reference datasets to identify gene/splicing-trait associations to gain insights into the genetic basis of PCa [15]. These GWAS-identified loci along with prostate-tissue-based TWAS/splicing TWAS-identified genes/splicing events could not fully explain the genetic susceptibility to this common malignancy. Genes that function in the immune system may fill in the gaps of some missing heritability [16]. Therefore, it is critical to conduct a well-designed TWAS using information from blood tissue. However, this is insufficiently explored.

Blood sampling through venesection is a noninvasive and cost-effective approach that can provide high-throughput diagnostic information [17]. Blood-based biomarker panels have been used to identify men with aggressive PCa [18] and commercially available gene expression tests for PCa prognosis have been used [19]. Protein-coding genes, mRNA in blood [20], blood exosomes [21], circulating myeloid-derived suppressor cells (MDSCs) [22], and the noncoding transcripts, such as long noncoding RNAs (lncRNAs) [23, 24], have been shown to potentially serve as diagnostic, prognostic and/or predictive biomarkers and therapeutic targets for PCa.

Herein, to comprehensively assess blood-based gene markers for PCa risk, we conducted a comprehensive TWAS leveraging a large reference data set from the Genotype-Tissue Expression (GTEx) for blood tissue with three modeling strategies, including the statistical framework PrediXcan [25], modifying the unified test for molecular signatures (UTMOST) [26], and joint-tissue imputation (JTI) [27]. GWAS summary statistics generated from 79,194 PCa cases and 61,112 controls of European ancestry in the Prostate Cancer Association Group to Investigate Cancer Associated Alterations in the Genome (PRACTICAL) consortium (http://practical.icr.ac.uk/blog/) were used to test the associations between predicted gene expression in blood and PCa risk. Through TWAS analysis, we report the results of novel candidate susceptibility loci and genes in the blood tissue for PCa risk.

## 2 | Materials and Methods

### 2.1 | Transcriptome and Genome Data From the GTEx Project

Transcriptome and genome data from the GTEx v8 were used to build the genetic prediction models for genes expressed in blood tissue. Details of the GTEx v8 data set have been described elsewhere (https://gtexportal.org/home/documentationPage). More than 98% of the samples were European American or African American. The RNA sequencing experiments, quality control (QC) of the gene expression data, and genomic data have been described elsewhere [28, 29]. In brief, RNA and DNA were isolated from 670 whole blood samples. The library preparation and RNA sequencing were performed at the Broad Institute using a large-scale, automated variant of the Illumina TruSeq™ RNA sample preparation protocol. RNA-seq data were aligned to the human reference genome GRCh37/hg19. QC of samples was performed as following: low-quality samples were identified and removed based on alignment metrics like $< 10$ million mapped reads, read mapping rate $< 0.2$, intergenic mapping rate $> 0.3$, base mismatch rate $> 0.008$, and rRNA read rate $> 0.3$. Outlier samples were also identified by expression profile (using a correlation-based statistic) and sex incompatibility checks. Among technical replicates, the sample with the most reads was kept for analysis. Samples from donors with cytogenetic anomalies (two with Klinefelter syndrome and one transgender donor found after sequencing) were excluded from analyses. Genomic information of 670 subjects was obtained using whole genome sequencing (WGS) with a median depth of 32×, as performed by the Broad Institute's Genomics Platform, with the SNPs QC and phasing, minor allele frequency and small indels $\geq 0.01$, resulting in the detection of 43,066,422 SNPs.

### 2.2 | Building Blood Tissue Gene Expression Prediction Models

Three separate sets of blood tissue expression genetic prediction models were constructed using the PrediXcan, modified UTMOST, and JTI statistical frameworks. The details of model development have been described elsewhere [25–27]. Briefly, the residuals of the normalized gene expression levels were corrected through regressing covariates, including sex, platform, top five principal components (PCs), and probabilistic estimation of expression residuals (PEER) factors [30]. In the model, SNPs within 1 Mb upstream and downstream of the gene body were used as predictor variables. Before model training, SNPs were removed using linkage disequilibrium (LD)-pruning ($r^2 = 0.9$) to reduce the computational burden, and there was no significant difference in prediction quality after applying LD pruning.

For the PrediXcan model, an elastic net regression was applied to the model training. To evaluate their prediction performance, the gene expression prediction model was built using five-fold cross-validation. For the modified UTMOST model, the effect size is estimated by minimizing the loss function, which minimizes the LASSO penalty for within-tissue effects and the group LASSO penalty for within-tissue effects in the joint tissue prediction model. The information from the feature (SNP) selection was shared by the group penalty term across all the tissues. Five-fold cross-validation of hyperparameter tuning was performed using two hyperparameters, $\lambda_1$ and $\lambda_2$, for within- and cross-tissue penalties, respectively. The original script of UTMOST was modified using uniform hyper-parameters across different folds to make the hyper-parameters directly comparable. The modified UTMOST that gave an unbiased estimate of

prediction performance was confirmed using empirical datasets. For details on the modification can be found at https://github.com/gamazonlab/MR- JTI/tree/master/model_training/UTMOST/main_modified.r. For the JTI model, the gene expression profile similarity and the regulatory profile similarity were estimated for each tissue-tissue pair. Five-fold cross-validation was used to tune the hyper-parameters, by which the two similarity measures were combined. For all the prediction models, from five-fold cross-validation (the correlation between the observed and the predicted expression, $r > 0.1$ and $p < 0.05$), genes with a good prediction quality were defined as imputable genes and used for downstream analyses.

### 2.3 | Associations Between Genetically Predicted Gene Expression and PCa Risk

Associations of genetically predicted gene expression in blood tissue with PCa risk were examined using the GWAS summary statistics generated from 79,194 PCa cases and 61,112 controls of European ancestry in the PRACTICAL consortium. The detailed information of this GWAS meta-analysis has been described elsewhere [8, 14, 31–33]. Briefly, 46,939 cases and 27,910 controls were genotyped by Infinium OncoArray-500k BeadChip with 570,000 SNPs (http://epi.grants.cancer.gov/oncoarray/). These SNPs were imputed using the 1000 Genomes Project (2014 June release) data as a reference. The data from several previous PCa GWAS or high-density SNP panels imputed to the 1000 Genomes Project of European ancestry was also included, UK stage 1 (1854 cases and 1894 controls) and stage 2 (3650 cases and 3940 controls), CaPS 1 (478 cases and 428 controls) and CaPS 2 (1458 cases and 512 controls), BPC3 (2068 cases and 2993 controls), NCI PEGASUS (4600 cases and 2941 controls), and iCOGS (20,219 cases and 20,440 controls). The logistic regression summary statistics were meta-analyzed using an inverse variance fixed effect approach. The associations of predicted gene expression with PCa risk were further estimated based on gene expression prediction weights, and summary statistics of SNP-PCa risk associations using the S-PrediXcan framework [15] with an SNP-correlation (LD) matrix with 1000G EUR population as reference. The false discovery rate (FDR) method was used for corrected multiple comparisons (FDR $p$ value $< 0.05$).

Putative causal genes for PCa risk were determined by FOCUS (Fine-mapping Of CaUsal gene Sets) fine-mapping analysis, as described elsewhere [34]. TWAS results and blood gene expression prediction model were used as inputs, and the posterior probability for each gene was outputted. For FOCUS, putative causal genes were prioritized by the default 90% credible gene set.

### 2.4 | Expression Levels of TWAS-Identified Genes in Blood Immune Cell and Exosomes

For our TWAS-identified genes, we compared their measured expression in blood immune cells of 31 PCa patients vs 11 controls [22] and exosomes of 31 PCa patients vs 17 controls [21] of previous studies. Details of these datasets have been described elsewhere [21, 22]. For one of the datasets, information about scRNA-seq and data analysis can be found in the original publication [22]. In detail, all patients were diagnosed with metastatic prostate cancer as metastatic findings were found in lymph nodes outside pelvis, bones, and viscera. Diagnosis was based on pathological & clinical tests including biopsy Gleason score, counts of neutrophils, lymphocytes, monocytes, and levels of prostate-specific antigen (PSA), ALP, LDH, Hb, and Alb. Patients without pathological PCa diagnosis via prostatic biopsy or consenting were excluded. PSA progression was defined as per Prostate Cancer Clinical Trials Working Group 3 (18): first increase $> 25\%$ and $> 2$ ng/mL above nadir. PSA-PFS was the time from ADT start to PSA progression. Patients with normalized PSA after 3 months of ADT (with degarelix) were diagnosed with mHSPC and included in the study. Blood samples were collected, and red blood cells were removed. The fractions of MDSCs in the peripheral blood were tested by using Flow cytometry, and then a scRNA-seq of gene expression and immune cell profiling analysis were performed using the 10X Genomics Chromium Single Cell platform on samples from 31 metastatic-hormone sensitive PCa patients and 11 healthy controls. The differentially expressed genes (DEGs) of the MDSCs were selected based on $|\log2\text{FoldChange}| > 1$ and $p$ value $< 0.05$. For the other data set, the method of circulating exosomes RNA sequencing has been described elsewhere [21]. In detail, samples of 31 PCa patients (median age; 67, range; 45–78, gender; males) and 17 benign prostatic hyperplasia (BPH) (median age; 65, range; 54–74, gender; males) were verified through prostate biopsy. Subsequently, two pathologists examined the pathology of the biopsy tissues to confirm the diagnosis as well as to determine the Gleason score. For patients who underwent biopsy, they were evaluated based on the condition that either their PSA levels had increased to be greater than 4 ng/mL or, even if their PSA was not elevated, their rectal examination showed a nodule or there was an abnormality detected in the imaging examination. Blood samples were collected, and serum exosomes were extracted with the exoEasy Maxi Kit (Qiagen 76064) and then purified using the exoRNeasy Serum/Plasma Maxi Kit (Qiagen 77064). Strand-specific RNA-seq libraries were prepared by the NEBNext Ultra II Directional RNA Library Prep Kit for Illumina (NEB). The quality of the libraries was checked by a Bioanalyzer 2100 (Agilent). These libraries were sequenced on the HiSeq X10 platform. All samples reached similar sequencing depths (10 Gb of raw data for cells, cell-derived exosomes, PCa and BPH serum exosomes). After QC, the sequencing reads were mapped to the reference human genome. Exosomal RNA profiles were obtained in the blood tissue of 31 PCa patients and 17 BPH individuals (negative prostate biopsy). DEGs in circulating exosomes were selected for those genes with $\log2|\text{FoldChange}| > 1$ and $p$ value $< 0.05$.

### 2.5 | Ingenuity Pathway Analysis (IPA) of TWAS-Identified Genes

"Ingenuity canonical pathways," "Diseases and Bio Functions" and "Networks" of our TWAS identified PCa risk genes were performed using "Core Analysis" function of IPA version 01-22-01 (Ingenuity System Inc, USA). Canonical pathways and

**3**

**3.1**

$^{2}) \geq$

|

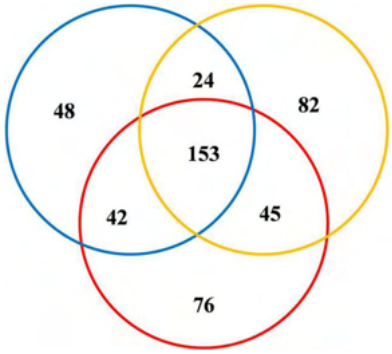


-

−6

5

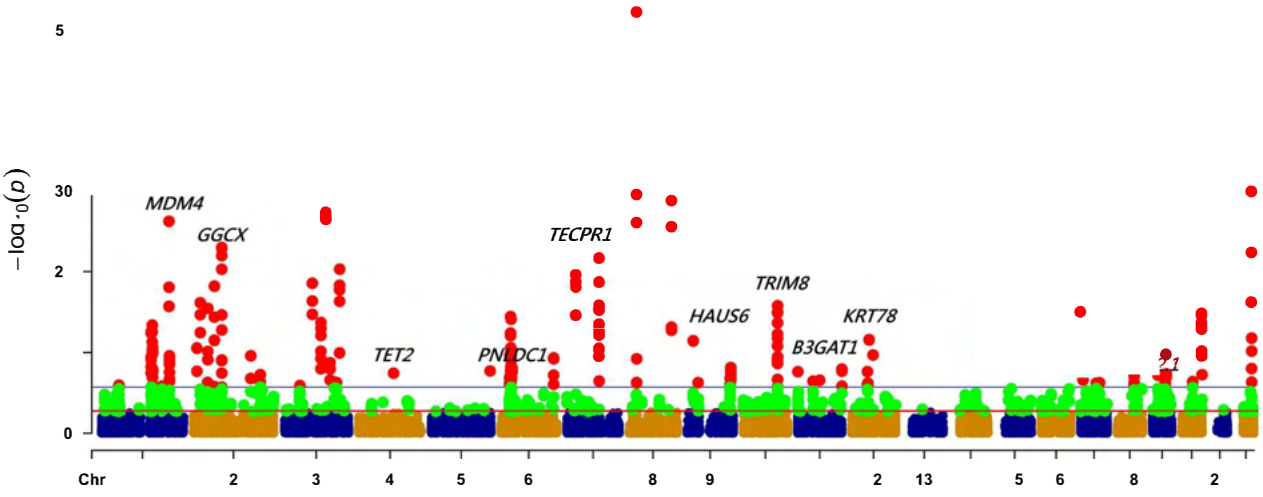


-

−3

−6

(Supporting Information S1: Tables 3 and 5) [7–14], and 102 were located at genomic loci within 500 kb of GWAS-identified PCa risk variants (Supporting Information S1: Table 4).

Through fine-mapping analysis using FOCUS, 109 identified associations were further prioritized as likely causal associations for PCa risk (Supporting Information S1: Table 6), involving 51 causal genes (Table 1). These 51 likely causal genes for PCa risk were also reported in previous TWAS or splicing TWAS studies [7–14] or located at known loci for PCa [31, 35–37].

### 3.3 | Expression Levels of TWAS-Identified Genes in Blood Immune Cells and Exosomes

For a total of 25 TWAS-identified genes, they showed consistent directions of effort on PCa when comparing their overall measured expression in blood immune cell and/or exosomes of PCa cases vs controls (Tables 2 and 3). Specifically, 13 genes showed consistent effects for measured expression levels in blood immune cells in PCa patients and controls (Table 2). And 14 showed consistent effects for expression in blood exosomes (Table 3). Two of the genes, *TACC1* (8p11.22) and *TSPO* (22q13.2) were found in both datasets and demonstrated consistent expression directions for both scenarios. For these 25 genes, higher expression levels of 21 genes were observed in PCa patients compared with controls, including *SCP2* (1p32.3), *SLC39A1* (1q21.3), *ZBTB7B* (1q21.3), *LMNA* (1q22), *ZNF148* (3q21.2), *TRIM59* (3q25.33), *NCEH1* (3q26.2), *N4BP2* (4p14), *H2AFV* (7p13), *TACC1* (8p11.22), *TRAF1* (9q33.2), *FLII* (17p11.2), *SUPT4H1* (17q22), *C18orf54* (18q21.2), *CD300LF* (17q25.1), *MYO9B* (19p13.11), *COX6B1* (19q13.12), *ZNF793* (19q13.12), *CTSA* (20q13.12), *EP300* (22q13.2), and *TSPO* (22q13.2); the expression levels of four genes were lower in PCa cases, containing *TAGAP* (6q25.3), *AIP* (11q13.2), *SECTM1* (17q25.3), and *YIF1B* (19q13.12). Importantly, ten of them were firstly reported as PCa risk genes in the current work, namely, *SCP2*, *N4BP2*, *H2AFV*, *TAGAP*, *FLII*, *CD300LF*, *SECTM1*, *CTSA*, *ZNF793*, and *EP300*.

### 3.4 | IPA Analysis Results

From the IPA analysis, 44 ingenuity canonical pathways for 80 TWAS-identified genes (including 20 novel genes) for PCa risk were obtained (Supporting Information S1: Table 7). The top five pathways were involved in amino acid metabolism (methionine and cysteine), fatty acid metabolism (colanic acid and mevalonate), and ataxia telangiectasia mutated kinase (ATM) signaling. Particularly, PCa signaling ($P = 4.68 \times 10^{-2}$) was also identified. Five genes were enriched in this pathway, including *CREB3L4* (1q21.3), *PIK3C2B* (1q32.1), *NKX3-1* (8p21.3), *GSTP1* (11q13.2), and *MAPK3* (16p11.2).

Of the "Diseases and Bio Functions" analysis, 129 TWAS-identified genes for PCa risk were enriched in five PCa-related categories, including 36 novel genes (Supporting Information S1: Table 8). Functions of these categories were involved in PCa, cell viability, hormone-sensitive malignant neoplasm of the prostate, and metastatic castration-resistant PCa. These categories and risk genes may have key roles in the development, proliferation and metastasis of the PCa.

A total of 242 genes (71 novel genes) were enriched in the top ten networks of IPA analysis (Supporting Information S1: Figure 1 and Table 9). Four cancer-related networks are shown in Figure 3. Our TWAS identified novel genes, such as *MRPL10* (17q21.32), *ECHDC2* (1p32.3) (Figure 1A), *LIMA1* (12q13.12) (Figure 1B), *EP300* (22q13.2), *KAT5* (11q13.1), *SMAD2* (18q21.1), *SMC4* (3q25.33) (Figure 1C), *CBX1* (17q21.32), and *GLYR1* (16p13.3) (Figure 1D), were in core nodes or nodes of these cancer-related networks, indicating that these genes may influence PCa development.

## 4 | Discussion

In this study, state-of-the-art modeling strategies of PrediXcan modified UTMOST, and JTI was used to comprehensively evaluate the associations of genetically predicted gene expression for PCa risk across the human blood tissue transcriptome. Four hundred and seventy genes with genetically determined expression were identified to be associated with PCa risk (FDR-corrected $p$ value $< 0.05$), including 51 prioritized as potential causal genes by FOCUS fine-mapping analysis. It is remarkable that 25 genes have consistent effect directions for measured expression in blood immune cells and/or exosomes between PCa patients and controls. Moreover, 135 genes were reported as PCa risk genes for the first time, most of which (128/135) were enriched in PCa disease and bio-functional categories. Our study could provide important new information for potential blood-based candidate susceptibility genes for PCa risk, which can substantially improve insights into the genetic basis of this common malignancy.

To achieve high statistical power for identifying PCa risk genes, three complementary modeling strategies were leveraged. Similar to our previous study using such three modeling strategies focusing on prostate tissue [12], of the genes that showed a significant association in two or three sets of models, a majority (396/411) demonstrated consistent directions (Supporting Information S1: Table 10). This further supports the robustness of our findings regardless of the type of prediction modeling method used.

Most of our identified PCa risk genes (335/470) in blood tissue have been reported in previous GWAS and/or TWAS (Supporting Information S1: Tables 3–5). Of these genes, 51 were verified as likely causal genes for PCa risk by FOCUS fine-mapping analysis (Table 1). These putatively causal genes are already shown to play important roles in the progression and metastasis of PCa, such as *ARNT* (1q21.3) [38], *UGP2* (2p15) [39], and *PDK1* (2q31.1) [40]. Of our TWAS-identified genes, 26 were already found in a previous TWAS using blood tissues [7], and they demonstrated consistent direction effects, including *ENSA*, *CTSK*, *ARNT*, *SLC39A1*, *TPM3*, and *PBXIP1* (1q21.3), *MDM4* and *SLC41A1* (1q32.1), *WDPCP* (2p15), *GGCX* and *VAMP8* (2p11.2), *CHMP2B* (3p11.2), *SIDT1* (3q13.2), *ZBTB38* (3q23), *UHRF1BP1* (6p21.31), *HIBADH* and *TAX1BP1* (7p15.2), *TECPR1* (7q21.3), *BAIAP2L1* (7q21.3-q22.1), *NKX3-1* (8p21.3),

Fifty-one causal genes in blood tissue for PCa risk identified using FOCUS fine mapping analysis.

| | Gene | Type[a] | Model[b] | R[b,c] | Number of SNPs in model | OR | | [d] | TWAS *p* value | TWAS *p* value after FDR correction | FOCUS |
|---|---|---|---|---|---|---|---|---|---|---|---|
| 21 3 | *ARNT* | protein | | 17 | 7 | 9 87 | | 92 | 4 33 1 $^{-}$ | 1 53 1 $^{-10}$ | 1 |
| | | | PrediXcan | 17 | 15 | 89 | 86 | 91 | 2 76 1 $^{-}$ | 1 5 1 $^{-10}$ | 1 |
| | | | UTMOST | 14 | 59 | 88 | 84 | 91 | 3 38 1 $^{-10}$ | 7 84 1 $^{-}$ | 1 |
| | | protein | | 9 | 12 | 1 16 | 1 11 | 1 2 | 4 24 1 $^{-14}$ | 1 85 1 $^{-}$ | 1 |
| | | | PrediXcan | 7 | 8 | 1 25 | 1 18 | 1 33 | 2 93 1 $^{-}$ | 1 1 1 $^{-10}$ | 1 |
| | | | UTMOST | 8 | 15 | 1 91 | 1 59 | 2 29 | 5 21 1 $^{-12}$ | 1 63 1 $^{-}$ | 1 |
| | | protein | UTMOST | 2 | 5 | 46 | 36 | 58 | 1 14 1 $^{-10}$ | 2 95 1 $^{-}$ | 1 |
| | | protein | | 0.01 | 5 | 65 | 57 | 74 | 1 1 1 $^{-10}$ | 2 67 1 $^{-}$ | 1 |
| | | lncRNA | | 5 | 5 | 82 | 77 | 88 | 1 34 1 $^{-}$ | 2 25 1 $^{-}$ | 1 |
| | | | PrediXcan | 3 | 6 | 79 | 73 | 86 | 2 76 1 $^{-}$ | 4 28 1 $^{-}$ | 99 |
| | | | UTMOST | 3 | 9 | 65 | 56 | 75 | 1 2 1 $^{-}$ | 2 3 1 $^{-}$ | 1 |
| 32 1 | *MDM4* | protein | | 5 | 1 | 75 | 7 | 8 | 2 4 1 $^{-16}$ | 1 37 1 $^{-}$ | 1 |
| | | | PrediXcan | 2 | 6 | 53 | 47 | 59 | 5 69 1 $^{-}$ | 1 86 1 $^{-23}$ | 1 |
| | | | UTMOST | 4 | 11 | 52 | 45 | 6 | 8 77 1 $^{-19}$ | 8 2 1 $^{-16}$ | 1 |
| | | protein | | 1 | 1 | 76 | 66 | 89 | 3 73 1 $^{-4}$ | 1 52 1 $^{-2}$ | 1 |
| | | protein | | 29 | 12 | 92 | 9 | 95 | 2 98 1 $^{-10}$ | 7 9 1 $^{-}$ | 97 |
| | | | PrediXcan | 27 | 14 | 92 | 9 | 95 | 2 52 1 $^{-10}$ | 6 5 1 $^{-8}$ | 96 |
| 2 25 | | lncRNA | | 0.01 | 4 | 1 48 | 1 29 | 1 69 | 2 8 1 $^{-}$ | 3 34 1 $^{-}$ | 1 |
| | | | UTMOST | 2 | 14 | 1 64 | 1 41 | 1 89 | 2 89 1 $^{-}$ | 8 51 1 $^{-}$ | 1 |
| 2 24 1 | | protein | | 11 | 14 | 91 | 89 | 93 | 3 62 1 $^{-}$ | 1 34 1 $^{-10}$ | 1 |
| | | | PrediXcan | 9 | 6 | 8 | 76 | 85 | 2.20 × 1 $^{-15}$ | 1 2 1 $^{-12}$ | 1 |
| | | | UTMOST | 1 | 14 | 83 | 79 | 87 | 7 25 1 $^{-17}$ | 5 28 1 $^{-14}$ | 1 |
| 2 21 | | protein | | 9 | 26 | 91 | 88 | 95 | 4 91 1 $^{-}$ | 5 9 1 $^{-5}$ | 96 |
| | | | PrediXcan | 8 | 16 | 88 | 84 | 93 | 6 68 1 $^{-}$ | 7 64 1 $^{-5}$ | 1 |
| | *THADA* | protein | UTMOST | 3 | 9 | 1 94 | 1 65 | 2 27 | 3 54 1 $^{-16}$ | 2 32 1 $^{-}$ | 1 |
| 2 5 | *OTX1* | protein | | 21 | 8 | 95 | 92 | 97 | 1 2 1 $^{-5}$ | 9 55 1 $^{-}$ | 1 |
| | | | PrediXcan | 2 | 12 | 96 | 93 | 98 | 6 16 1 $^{-}$ | 2 25 1 $^{-}$ | 1 |
| | | protein | PrediXcan | 5 | 9 | 1 26 | 1 18 | 1 34 | 3 15 1 $^{-12}$ | 1 1 1 $^{-}$ | 1 |
| | | | UTMOST | 5 | 83 | 1 29 | 1 22 | 1 37 | 6 36 1 $^{-19}$ | 6 17 1 $^{-16}$ | 1 |

(Continues)

| (Continued)

| Loci | Gene | Type | Model[b] | R[b,c] | Number of SNPs in model | | [d] | TWAS *p* value | TWAS *p* value after correction | |
|---|---|---|---|---|---|---|---|---|---|---|
| | | protein | PrediXcan | | 14 | 8 | | – | – | 8 |
| | | protein | PrediXcan | | 10 | 8 | 8 | – | – | |
| | *GGCX* | protein | | 3 | 15 | 88 8 | 3 | $-22$ | 3 $-19$ | |
| | | | PrediXcan | 3 | 19 | 8 8 | 3 | $-23$ | 3 3 $-20$ | |
| | | | | 3 | 17 | 8 85 | 8 | $-24$ | 3 $-20$ | |
| | | protein | PrediXcan | | 28 | 88 8 | 5 8 3 | – | 8 – | |
| | | protein | | | 11 | 8 | 3 | – | 5 – | |
| | | protein | | | 16 | 8 8 | 3 3 35 | $-15$ | 5 $-12$ | |
| | | protein | | 3 | 19 | 38 | 5 | – | 8 $-11$ | |
| 3 | | protein | | | 15 | | 3 | – | – | |
| | | | | | 15 | 3 | 3 5 | – | 5 – | |
| 3 3 | | protein | | 8 | 25 | 3 8 | | – | – | |
| | | | PrediXcan | 5 | 38 | | 5 3 | – | – | |
| | | | | 8 | 99 | 8 | 8 | $-11$ | 8 – | |
| 3 3 | | protein | PrediXcan | 5 | 11 | | 3 | $-27$ | $-23$ | |
| | | | | | 77 | 5 | | $-28$ | 3 $-24$ | |
| 3 3 | | protein | | 8 | 17 | 3 | 3 | – | 85 – | |
| 3 | | protein | PrediXcan | | 24 | | 8 | $-18$ | 5 $-15$ | |
| 3 | | protein | PrediXcan | 3 | 38 | | 8 3 | – | 35 – | |
| 5 | | protein | | | 3 | | 5 | $-19$ | 8 $-16$ | |
| | | | PrediXcan | | 5 | 5 | 58 | $-19$ | $-16$ | |
| | | | | 3 | 49 | 55 8 | 8 | $-20$ | $-17$ | |
| 3 | | protein | | 3 | 8 | | 3 | – | – | |
| | | | PrediXcan | | 5 | 5 53 | 5 | $-16$ | 3 5 – | |
| | | | | 3 | 41 | 3 | 53 | $-19$ | 5 $-16$ | |
| | | lncRNA | JTI | | 12 | | 5 | $-11$ | 3 – | |
| | | | PrediXcan | | 18 | 88 | 3 3 35 | $-11$ | 5 – | |
| | | | | 3 | 24 | 88 85 | 3 8 | $-14$ | 5 $-11$ | |
| 8 3 | | protein | | | 21 | | 5 | $-30$ | $-26$ | |

(Continues)

| a | b | b c | | d | | | | | |
|---|---|---|---|---|---|---|---|---|---|
| | | 7 | 39 | 8 ± 22 | 7 99 | −27 | 2 2 | − | |
| | | 2 | 9 | 44 2 4 | 7 | −53 | | − | |
| 8 24 2 | | | 35 | 9 | 2 4 | −26 | | − | |
| | | | 15 | | 49 | − | 9 7 | −26 | |
| | | 22 | 2 | 4 89 | 8 | − | 7 29 | − | |
| 9 22 | | | 9 | 48 4 ± 9 | 7 | − | 7 | − | |
| 9 4 | | 7 | 14 | 4 4 7 | | −7 | 2 9 | − | 94 |
| | | 24 | 31 | 9 88 ± 94 | | −7 | 79 | − | |
| | | 9 | 34 | 9 87 94 | 2 | −8 | 78 | − | |
| | | 2 | 51 | 2 74 | 2 4 | −8 | 9 | − | 97 |
| 2 | | | 17 | 88 84 ± 92 | 2 | −8 | | − | |
| | | 9 | 7 | 84 8 89 | | − | 9 | − | 98 |
| 7 | | 2 | 4 | 7 | | −8 | | − | 97 |
| | | | 9 | 9 ± | 4 79 | − | 9 | − | |
| 7 | | | 17 | 7 8 8 | 2 9 | − | 2 89 | −4 | |
| 8 2 2 | | 4 | 7 | 78 7 8 | 9 | − | 2 | − | 97 |
| | | 2 | 12 | 7 84 | | − | 24 | − | |
| | | 28 | 12 | 9 9 9 | | −7 | 98 | − | 9 |
| 9 | | | 31 | 8 ± 22 | 2 99 | − | 2 97 | − | 9 |
| | | 4 | 23 | 8 2 | | − | 9 7 | − | 99 |
| 9 2 | | 7 | 8 | 48 ± | | − | 2 | − | |
| | | 9 | 29 | 8 ± | 2 | − | | − | |
| | | 4 | 12 | 4 9 | 8 | −7 | 2 4 | − | |
| | | 8 | 46 | 9 92 ± 97 | 2 98 | − | 28 | − | |
| | | | 19 | 2 7 | 9 | − | 4 29 | −8 | |
| | | | 15 | 7 | | −7 | | − | |
| | | | 19 | 7 | 4 7 | −8 | 4 | − | |
| 2 22 | | | 12 | 8 8 | 98 | −7 | 4 9 | − | 92 |

2

**TABLE 2** | Thirteen genes with differential expression in prostate cancer patients and controls for circulating immune cell levels consistent with association directions observed in TWAS.

| | | TWAS study | | | Single-cell RNA-seq study | | |
|---|---|---|---|---|---|---|---|
| **Loci** | **Gene** | **Model**[a] | **OR (95% CI)**[b] | **FDR *p*-value** | **Log2Fold change** | **Cell type**[c] | ***p*-value** |
| 1p32.3 | ***SCP2*** | PrediXcan | 1.06 (1.03 ± 1.10) | $2.34 \times 10^{-2}$ | 1.47 | M-MDSCs | < 0.05 |
| | | UTMOST | 1.21 (1.11 ± 1.32) | $1.29 \times 10^{-3}$ | | | |
| | | JTI | 1.31 (1.17 ± 1.47) | $3.12 \times 10^{-4}$ | | | |
| 1q22 | *LMNA* | JTI | 1.13 (1.06 ± 1.20) | $6.03 \times 10^{-3}$ | 1.60 | Basophils | < 0.05 |
| | | PrediXcan | 1.18 (1.10 ± 1.27) | $4.17 \times 10^{-4}$ | | | |
| 3q21.2 | ***ZNF148*** | UTMOST | 1.64 (1.21 ± 2.22) | $3.66 \times 10^{-2}$ | 2.68 | cDC2 | < 0.05 |
| 7p13 | ***H2AFV*** | UTMOST | 1.21 (1.08 ± 1.35) | $3.50 \times 10^{-2}$ | 1.42 | cDC2 | < 0.05 |
| | | PrediXcan | 1.21 (1.09 ± 1.34) | $1.09 \times 10^{-2}$ | | | |
| | | JTI | 1.14 (1.07 ± 1.21) | $4.89 \times 10^{-3}$ | | | |
| 8p11.22 | *TACC1* | UTMOST | 1.28 (1.12 ± 1.45) | $1.05 \times 10^{-2}$ | 1.05 | PMN-MDSCs | < 0.05 |
| | | PrediXcan | 1.07 (1.04 ± 1.11) | $6.14 \times 10^{-3}$ | 2.10 | M-MDSCs | < 0.05 |
| | | JTI | 1.07 (1.04 ± 1.11) | $6.03 \times 10^{-3}$ | 1.95 | e-MDSCs | < 0.05 |
| 17p11.2 | ***FLII*** | UTMOST | 1.59 (1.20 ± 2.10) | $3.62 \times 10^{-2}$ | 1.21 | PMN-MDSCs | < 0.05 |
| 17q22 | *SUPT4H1* | UTMOST | 1.32 (1.17 ± 1.49) | $8.59 \times 10^{-4}$ | 1.68 | cDC2 | |
| | | JTI | 1.13 (1.07 ± 1.20) | $7.57 \times 10^{-4}$ | | | |
| 17q25.1 | ***CD300LF*** | UTMOST | 1.74 (1.24 ± 2.45) | $3.76 \times 10^{-2}$ | 1.42 | cDC2 | < 0.05 |
| 19p13.11 | *MYO9B* | PrediXcan | 1.22 (1.12 ± 1.33) | $5.05 \times 10^{-4}$ | 1.04 | cDC2 | < 0.05 |
| | | JTI | 1.15 (1.08 ± 1.22) | $2.97 \times 10^{-4}$ | | | |
| | | UTMOST | 1.38 (1.23 ± 1.55) | $9.17 \times 10^{-6}$ | | | |
| 19q13.12 | *COX6B1* | JTI | 1.09 (1.04 ± 1.14) | $4.74 \times 10^{-3}$ | 1.48 | M-MDSCs | < 0.05 |
| | | PrediXcan | 1.16 (1.08 ± 1.24) | $3.47 \times 10^{-3}$ | | | |
| | | UTMOST | 1.13 (1.07 ± 1.19) | $1.37 \times 10^{-3}$ | | | |
| 20q13.12 | ***CTSA*** | UTMOST | 2.40 (1.52 ± 3.79) | $8.72 \times 10^{-3}$ | 2.00 | M-MDSCs | < 0.05 |
| 22q13.2 | ***EP300*** | JTI | 1.14 (1.05 ± 1.23) | $3.09 \times 10^{-2}$ | 1.53 | cDC2 | < 0.05 |
| | *TSPO* | PrediXcan | 1.12 (1.07 ± 1.16) | $5.53 \times 10^{-5}$ | 1.02 | Effector, memory CD8 T cells | < 0.05 |
| | | JTI | 1.11 (1.08 ± 1.15) | $5.83 \times 10^{-10}$ | 1.11 | γδ T cells | < 0.05 |

[a]The statistical framework PrediXcan, a modified version of the unified test for molecular signatures (UTMOST), and a Joint-Tissue Imputation (JTI) model.
[b]OR, odds ratio; CI, confidence interval.
[c]M-MDSCs, monocytic myeloid-derived suppressor cells; cDC2, CD11b, CD14+CD163+CLEC10A+NOTCH2+ cells; PMN-MDSCs, polymorphonuclear myeloid-derived suppressor cells; e-MDSCs, Lineage-CD11b + CD33+ cells; Effector Memory CD8 T cells, CD27–CCR7–CD62L–CD3e+CD8+TRAC+ cells; γδ T cells, CD3e+TRDC +TRGC1,2+CD4-CD8-TRAC-cells. Results of 470 TWAS identified FDR-significant genes based on analysis of three sets of models were used.

*ACTR1A* and *TRIM8* (10q24.32), *DIS3L* (15q22.31), *MPHOSPH6* (16q23.3), *PPP1R14A* (19q13.2), and *LIME1* (20q13.33) (Supporting Information S1: Table 11). Moreover, for four of the genes, namely, *CTSS* (1q21.3), *LAMC1* (1q25.3), *ARL3* (10q24.32) and *TNFRSF6B* (20q13.33), their protein expression levels in plasma also showed consistent directions of effect on PCa risk [41].

Importantly, most of our identified novel genes (128/135) for PCa risk were enriched in PCa disease and bio-functional categories, and 25 showed differential expression in blood immune cells and/or exosomes between PCa patients and controls. Some of these novel genes have been reported to play key roles in PCa-associated processes, such as *SCP2*, *FLII*, *SECTM1*, *CTSA*, and *EP300*. *SCP2* encodes sterol carrier protein 2, which was shown to be involved in intracellular fatty acid transport and metabolism [42]. Its expression is higher in the primary PCa versus metastatic androgen-independent PCa [43]. *FLII* encodes FLII actin remodeling protein, a member of the gelsolin superfamily of actin-remodeling proteins, whose mRNA expression was downregulated in PCa tumor tissue compared with normal tissue [44]. *SECTM1* encodes secreted and transmembrane 1, a transmembrane and secreted protein with characteristics of a type 1a transmembrane protein, which was downregulated in urine between PCa patients and cancer-free individuals [45]. *CTSA* encodes cathepsin A, a member of the peptidase S10 family of serine carboxypeptidases. Compared with normal prostate tissue, its expression was significantly higher in the prostate tissues of PCa patients [46]. *EP300* encodes E1A binding protein p300, an adenovirus E1A-associated cellular

**TABLE 3** | Fourteen genes with differential expression in prostate cancer patients and benign prostatic hyperplasia individuals for exosomal mRNA levels consistent with association directions observed in TWAS.

| | | TWAS study | | | Exosomes RNA-seq study | | |
|---|---|---|---|---|---|---|---|
| Loci | Gene | Model[a] | OR (95% CI)[b] | FDR *p*-value | Transcript ID | Log2Fold Change | *p*-value |
| 1q21.3 | *SLC39A1* | PrediXcan | 1.25 (1.18 ± 1.33) | $1.10 \times 10^{-10}$ | ENST00000368623 | 2.92 | $4.67 \times 10^{-2}$ |
| | | UTMOST | 1.91 (1.59 ± 2.29) | $1.63 \times 10^{-9}$ | | | |
| | | JTI | 1.16 (1.11 ± 1.20) | $1.85 \times 10^{-11}$ | | | |
| | *ZBTB7B* | JTI | 1.25 (1.17 ± 1.33) | $6.79 \times 10^{-9}$ | ENST00000417934 | 2.13 | $2.55 \times 10^{-2}$ |
| 3q25.33 | *TRIM59* | PrediXcan | 1.21 (1.13 ± 1.31) | $6.11 \times 10^{-5}$ | ENST00000309784 | 2.33 | $8.32 \times 10^{-3}$ |
| | | JTI | 1.19 (1.11 ± 1.28) | $2.82 \times 10^{-4}$ | ENST00000543469 | 3.52 | $9.81 \times 10^{-3}$ |
| | | UTMOST | 1.40 (1.21 ± 1.61) | $4.62 \times 10^{-4}$ | | | |
| 3q26.2 | *NCEH1* | JTI | 1.42 (1.20 ± 1.69) | $4.18 \times 10^{-3}$ | ENST00000475381 | 2.86 | $1.00 \times 10^{-3}$ |
| 4p14 | ***N4BP2*** | UTMOST | 1.16 (1.06 ± 1.27) | $4.34 \times 10^{-2}$ | ENST00000261435 | 1.99 | $5.45 \times 10^{-3}$ |
| | | JTI | 1.10 (1.04 ± 1.15) | $1.01 \times 10^{-2}$ | | | |
| | | PrediXcan | 1.13 (1.05 ± 1.21) | $1.82 \times 10^{-2}$ | | | |
| 6q25.3 | ***TAGAP*** | JTI | 0.85 (0.77 ± 0.93) | $3.08 \times 10^{-2}$ | ENST00000367066 | −0.71 | $3.39 \times 10^{-2}$ |
| 8p11.22 | *TACC1* | PrediXcan | 1.07 (1.04 ± 1.11) | $6.14 \times 10^{-3}$ | ENST00000524193 | 5.48 | $4.02 \times 10^{-2}$ |
| | | UTMOST | 1.28 (1.12 ± 1.45) | $1.05 \times 10^{-2}$ | | | |
| | | JTI | 1.07 (1.04 ± 1.11) | $6.03 \times 10^{-3}$ | | | |
| 9q33.2 | *TRAF1* | PrediXcan | 1.07 (1.03 ± 1.12) | $2.51 \times 10^{-2}$ | ENST00000373887 | 2.13 | $4.51 \times 10^{-2}$ |
| 11q13.2 | *AIP* | PrediXcan | 0.85 (0.78 ± 0.94) | $3.52 \times 10^{-2}$ | ENST00000525341 | −3.95 | $3.37 \times 10^{-3}$ |
| | | JTI | 0.87 (0.81 ± 0.94) | $9.18 \times 10^{-3}$ | | | |
| 17q25.3 | ***SECTM1*** | UTMOST | 0.69 (0.57 ± 0.84) | $1.07 \times 10^{-2}$ | ENST00000269389 | −2.72 | $1.03 \times 10^{-3}$ |
| 18q21.2 | *C18orf54* | JTI | 1.05 (1.02 ± 1.08) | $3.94 \times 10^{-2}$ | ENST00000620105 | 2.76 | $4.14 \times 10^{-2}$ |
| | | UTMOST | 1.13 (1.05 ± 1.21) | $1.81 \times 10^{-2}$ | | | |
| 19q13.12 | ***ZNF793*** | UTMOST | 1.10 (1.05 ± 1.16) | $1.35 \times 10^{-2}$ | ENST00000445217 | 4.12 | $7.40 \times 10^{-3}$ |
| | | PrediXcan | 1.08 (1.03 ± 1.14) | $4.66 \times 10^{-2}$ | | | |
| | | JTI | 1.10 (1.05 ± 1.16) | $3.37 \times 10^{-3}$ | | | |
| 19q13.2 | *YIF1B* | JTI | 0.93 (0.89 ± 0.96) | $4.07 \times 10^{-3}$ | ENST00000587039 | −4.89 | $1.23 \times 10^{-2}$ |
| | | UTMOST | 0.48 (0.35 ± 0.65) | $3.23 \times 10^{-4}$ | | | |
| | | PrediXcan | 0.93 (0.91 ± 0.96) | $2.11 \times 10^{-3}$ | | | |
| 22q13.2 | *TSPO* | JTI | 1.11 (1.08 ± 1.15) | $5.83 \times 10^{-10}$ | ENST00000396265 | 3.76 | $3.05 \times 10^{-2}$ |
| | | PrediXcan | 1.12 (1.07 ± 1.16) | $5.53 \times 10^{-5}$ | | | |

Abbreviations: CI, confidence interval; OR, odds ratio.
[a]The statistical framework PrediXcan, a modified version of the unified test for molecular signatures (UTMOST), and a Joint-Tissue Imputation (JTI) model;
[b]Results of 470 TWAS identified FDR-significant genes based on analysis of three sets of models were used.

p300 transcriptional co-activator protein. High levels of *EP300* were identified to be associated with PCa progression [47].

Despite the advantages of this study, potential limitations need to be considered for the appropriate interpretation of our findings. Like all conventional TWAS designs, the identified associated genes for PCa risk may not necessarily imply causality [48]. To pinpoint the most likely causal genes, we further conducted FOCUS fine-mapping analysis to prioritize 51 potential causal genes. Future functional studies are needed to better understand the exact roles of the identified potential causal genes in prostate tumor development. In addition, the observed association directions of some of the genes identified in our TWAS were inconsistent with those of these genes identified in previous TWAS/spTWAS using blood tissue models (Supporting Information S1: Table 11) [7, 16]. This may be due to the different modeling strategies and different GTEx reference datasets used for establishing genetic prediction models. Future work is needed to determine their exact relationships. Furthermore, the current study largely focused on analyses of the European population. It is unclear whether the findings may be generalizable to other populations. Specific populations such as African American men have higher PCa burden and may have increased prostate inflammation. Further work focusing on those non-European populations would be needed to better characterize PCa etiology in those understudied populations. Lastly, although our validation analyses focusing on overall measured expression generated meaningful information. The design of leveraging data from patients with metastatic disease is suboptimal for our goal of assessing PCa risk-associated genes. Future work using ideal datasets with the most appropriate subject characteristics would be helpful in providing more relevant information for our research question of interest.

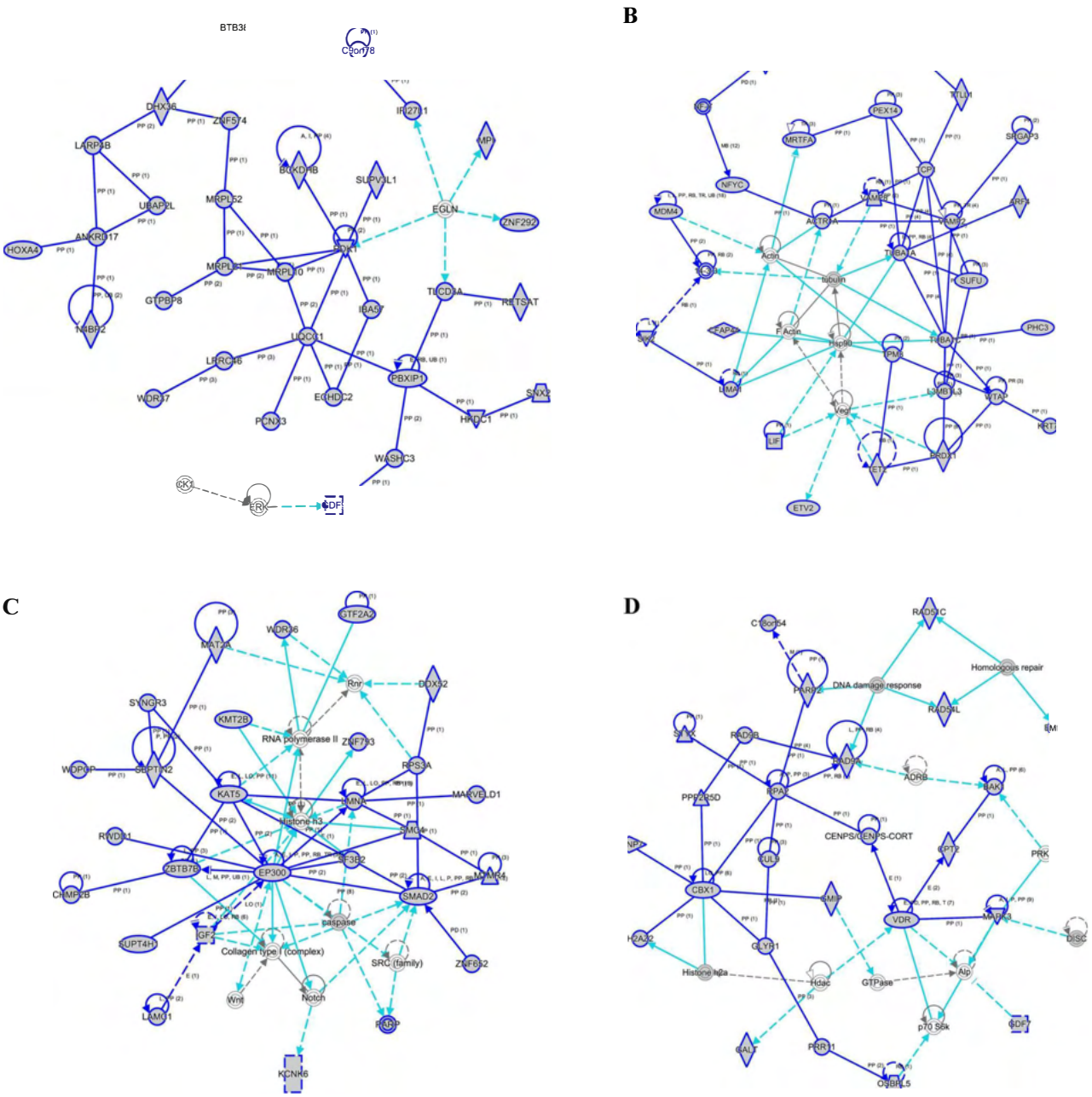


**FIGURE 3** | Cancer-related networks for blood tissue TWAS identified genes for prostate cancer risk. (A) Network 1: Cancer, Cell-To-Cell Signaling and Interaction, Cellular Assembly and Organization; (B) Network 3: Cancer, Hematological Disease, Immunological Disease; (C) Network 5: Cancer, Organismal Injury and Abnormalities, Cellular Assembly and Organization; (D) Network 6: DNA Replication, Recombination, and Repair, Cancer, Hereditary Disorder. The data set used all TWAS-identified FDR-significant genes for three models, the statistical framework PrediXcan, a modified version of the unified test for molecular signatures (UTMOST), and a joint-tissue imputation (JTI). [Color figure can be viewed at wileyonlinelibrary.com]

## 5 Conclusions

In conclusion, in a comprehensive TWAS study leveraging three complementary modeling strategies, we identified 470 genes (including 51 putatively causal genes) in blood tissue associated with PCa risk. Of them, 25 genes showed consistent effect directions for their measured overall expression in blood immune cells and/or exosomes when comparing PCa patients with controls. Our study provides new knowledge for potential blood candidate susceptibility genes for PCa risk and contributes to a better understanding of the genetic basis of PCa risk.


### Acknowledgments

This study is supported by the University of Hawaii Cancer Center and the Teacher Training Project of Longyan University.

## Conflicts of Interest

L.W. provided consulting service to Pupil Bio Inc. and reviewed manuscripts for *Gastroenterology Report*, not related to this study, and received honorarium. No potential conflicts of interest were disclosed by the other authors.

## Data Availability Statement

The PCa GWAS summary statistics can be accessed at PRACTICAL consortium website (http://practical.icr.ac.uk/blog/?page_id=8164). The transcriptome and genome data from the GTEx project are available in dbGaP web site (www.ncbi.nlm.nih.gov/gap; dbGaP Study Accession: phs000424.v8.p2). The code and the results from our TWAS are available from the corresponding author upon request.

## References


1. R. Iacovelli, C. Ciccarese, G. Schinzari, et al., "Biomarkers of Response to Advanced Prostate Cancer Therapy," *Expert Review of Molecular Diagnostics* 20 (2020): 195–205.

2. R. L. Siegel, A. N. Giaquinto, and A. Jemal, "Cancer Statistics, 2024," *CA: A Cancer Journal for Clinicians* 74 (2024): 12–49.

3. M. B. Culp, I. Soerjomataram, J. A. Efstathiou, F. Bray, and A. Jemal, "Recent Global Patterns in Prostate Cancer Incidence and Mortality Rates," *European Urology* 77 (2020): 38–52.

4. J. Cuzick, M. A. Thorat, G. Andriole, et al., "Prevention and Early Detection of Prostate Cancer," *Lancet Oncology* 15 (2014): e484–e492.

5. E. Mohamed Abd Ellatif, G. Basiouny El Gamal, M. Adel Osman Musaam, A. Malik, and T. Mohammed, "An Update on Genetic Predisposition for Prostate Cancer: Perspectives and Prospects," *Cellular and Molecular Biology* 69 (2023): 1–7.

6. A. Wang, J. Shen, A. A. Rodriguez, et al., "Characterizing Prostate Cancer Risk Through Multi-Ancestry Genome-Wide Discovery of 187 Novel Risk Variants," *Nature Genetics* 55 (2023): 2065–2074.

7. N. Mancuso, S. Gayther, A. Gusev, et al., "Large-Scale Transcriptome-Wide Association Study Identifies New Prostate Cancer Risk Regions," *Nature Communications* 9 (2018): 4079.

8. L. Wu, J. Wang, Q. Cai, et al., "Identification of Novel Susceptibility Loci and Genes for Prostate Cancer Risk: A Transcriptome-Wide Association Study in Over 140,000 European Descendants," *Cancer Research* 79 (2019): 3192–3204.

9. N. C. Emami, L. Kachuri, T. J. Meyers, et al., "Association of Imputed Prostate Cancer Transcriptome With Disease Risk Reveals Novel Mechanisms," *Nature Communications* 10 (2019): 3107.

10. A. Gusev, K. Lawrenson, X. Lin, et al., "A Transcriptome-Wide Association Study of High-Grade Serous Epithelial Ovarian Cancer Identifies New Susceptibility Genes and Splice Variants," *Nature Genetics* 51 (2019): 815–823.

11. P. N. Fiorica, R. Schubert, J. D. Morris, M. Abdul Sami, and H. E. Wheeler, "Multi-Ethnic Transcriptome-Wide Association Study of Prostate Cancer," *PLoS One* 15 (2020): e0236209.

12. D. Liu, J. Zhu, D. Zhou, et al., "A Transcriptome-Wide Association Study Identifies Novel Candidate Susceptibility Genes for Prostate Cancer Risk," *International Journal of Cancer* 150 (2022): 80–90.

13. J. He, W. Wen, A. Beeghly, et al., "Integrating Transcription Factor Occupancy With Transcriptome-Wide Association Analysis Identifies Susceptibility Genes in Human Cancers," *Nature Communications* 13 (2022): 7118.

14. Y. Sun, Y. E. Bae, J. Zhu, et al., "A Splicing Transcriptome-Wide Association Study Identifies Candidate Altered Splicing for Prostate Cancer Risk," *OMICS: A Journal of Integrative Biology* 27 (2023): 372–380.

15. A. Gusev, A. Ko, H. Shi, et al., "Integrative Approaches for Large-Scale Transcriptome-Wide Association Studies," *Nature Genetics* 48 (2016): 245–252.

16. E. E. Eichler, J. Flint, G. Gibson, et al., "Missing Heritability and Strategies for Finding the Underlying Causes of Complex Disease," *Nature Reviews Genetics* 11 (2010): 446–450.

17. Y. Pang, M. V. Holmes, Z. Chen, and C. Kartsonaki, "A Review of Lifestyle, Metabolic Risk Factors, and Blood-Based Biomarkers for Early Diagnosis of Pancreatic Ductal Adenocarcinoma," *Journal of Gastroenterology and Hepatology* 34 (2019): 330–345.

18. M. L. Liong, C. R. Lim, H. Yang, et al., "Blood-Based Biomarkers of Aggressive Prostate Cancer," *PLoS One* 7 (2012): e45802.

19. J. H. Creed, A. E. Berglund, R. J. Rounbehler, et al., "Commercial Gene Expression Tests for Prostate Cancer Prognosis Provide Paradoxical Estimates of Race-Specific Risk," *Cancer Epidemiology, Biomarkers & Prevention* 29 (2020): 246–253.

20. B. C. Thomas, J. D. Kay, S. Menon, et al., "Whole Blood mRNA in Prostate Cancer Reveals a Four-Gene Androgen Regulated Panel," *Endocrine-Related Cancer* 23 (2016): 797–812.

21. J. Ji, R. Chen, L. Zhao, et al., "Circulating Exosomal mRNA Profiling Identifies Novel Signatures for the Detection of Prostate Cancer," *Molecular Cancer* 20 (2021): 58.

22. Y. Kohada, A. Kuromoto, K. Takeda, et al., "Circulating PMN-MDSC Level Positively Correlates With a Poor Prognosis in Patients With Metastatic Hormone-Sensitive Prostate Cancer," *Frontiers in Urology* 2 (2022): 967480.

23. R. Das, F. Y. Feng, and L. A. Selth, "Long Non-Coding RNAs in Prostate Cancer: Biological and Clinical Implications," *Molecular and Cellular Endocrinology* 480 (2019): 142–152.

24. Y. H. Xu, J. L. Deng, G. Wang, and Y. S. Zhu, "Long Non-Coding RNAs in Prostate Cancer: Functional Roles and Clinical Implications," *Cancer Letters* 464 (2019): 37–55.

25. E. R. Gamazon, H. E. Wheeler, K. P. Shah, et al., "A Gene-Based Association Method for Mapping Traits Using Reference Transcriptome Data," *Nature Genetics* 47 (2015): 1091–1098.

26. Y. Sun, J. Zhu, D. Zhou, et al., "A Transcriptome-Wide Association Study of Alzheimer's Disease Using Prediction Models of Relevant Tissues Identifies Novel Candidate Susceptibility Genes," *Genome Medicine* 13 (2021): 141.

27. D. Zhou, Y. Jiang, X. Zhong, N. J. Cox, C. Liu, and E. R. Gamazon, "A Unified Framework for Joint-Tissue Transcriptome-Wide Association and Mendelian Randomization Analysis," *Nature Genetics* 52 (2020): 1239–1246.

28. K. G. Ardlie, D. S. Deluca, A. V. Segrè, et al., "The Genotype-Tissue Expression (Gtex) Pilot Analysis: Multitissue Gene Regulation in Humans," *Science* 348 (2015): 648–660.

29. G. T. Consortium, D. A. Laboratory, G. Coordinating Center -Analysis Working, et al., "Genetic Effects on Gene Expression Across Human Tissues," *Nature* 550 (2017): 204–213.

30. F. Aguet, S. Anand, K. G. Ardlie, et al., "The GTEx Consortium Atlas of Genetic Regulatory Effects Across Human Tissues," *Science* 369 (2020): 1318–1330.

31. F. R. Schumacher, A. A. Al Olama, S. I. Berndt, et al, "Association Analyses of More Than 140,000 Men Identify 63 New Prostate Cancer Susceptibility Loci," *Nature Genetics* 50 (2018): 928–936.

32. L. Wu, X. Shu, J. Bao, et al., "Analysis of Over 140,000 European Descendants Identifies Genetically Predicted Blood Protein Biomarkers Associated With Prostate Cancer Risk," *Cancer Research* 79 (2019): 4592–4598.

33. L. Wu, Y. Yang, X. Guo, et al., "An Integrative Multi-Omics Analysis to Identify Candidate DNA Methylation Biomarkers Related to Prostate Cancer Risk," *Nature Communications* 11 (2020): 3905.

34. N. Mancuso, M. K. Freund, R. Johnson, et al., "Probabilistic Fine-Mapping of Transcriptome-Wide Association Studies," *Nature Genetics* 51 (2019): 675–682.

35. S. N. Thibodeau, A. J. French, S. K. McDonnell, et al., "Identification of Candidate Genes for Prostate Cancer-Risk Snps Utilizing a Normal Prostate Tissue eQTL Data Set," *Nature Communications* 6 (2015): 8653.

36. A. A. Al Olama, Z. Kote-Jarai, S. I. Berndt, et al., "A Meta-Analysis of 87,040 Individuals Identifies 23 New Susceptibility Loci for Prostate Cancer," *Nature Genetics* 46 (2014): 1103–1109.

37. R. A. Eeles, A. A. A. Olama, S. Benlloch, et al., "Identification of 23 New Prostate Cancer Susceptibility Loci Using the iCOGS Custom Genotyping Array," *Nature Genetics* 45 (2013): 385–391.

38. G. Chen, Z. Cai, Z. Lin, et al., "Arnt-Dependent CCR8 Reprogrammed LDH Isoform Expression Correlates With Poor Clinical Outcomes of Prostate Cancer," *Molecular Carcinogenesis* 59 (2020): 897–907.

39. P. Liu, W. Wang, F. Wang, et al., "Alterations of Plasma Exosomal Proteins and Motabolies Are Associated With the Progression of Castration-Resistant Prostate Cancer," *Journal of Translational Medicine* 21 (2023): 40.

40. W. Li, L. Qian, J. Lin, et al., "CD44 Regulates Prostate Cancer Proliferation, Invasion and Migration via PDK1 and PFKFB4," *Oncotarget* 8 (2017): 65143–65151.

41. H. Zhong, J. Zhu, S. Liu, et al., "Identification of Blood Protein Biomarkers Associated With Prostate Cancer Risk Using Genetic Prediction Models: Analysis of Over 140,000 Subjects," *Human Molecular Genetics* 32 (2023): 3181–3193.

42. H. Zhao, B. R. Pflug, X. Lai, and M. Wang, "Metabolic and Molecular Regulation of Dietary Polyunsaturated Fatty Acids on Prostate Cancer," *Proteomics – Clinical Applications* 10 (2016): 267–279.

43. M. Stanbrough, G. J. Bubley, K. Ross, et al., "Increased Expression of Genes Converting Adrenal Androgens to Testosterone in Androgen-Independent Prostate Cancer," *Cancer Research* 66 (2006): 2815–2825.

44. T. Wang, W. Song, Y. Chen, et al., "Flightless I Homolog Represses Prostate Cancer Progression Through Targeting Androgen Receptor Signaling," *Clinical Cancer Research* 22 (2016): 1531–1544.

45. T. Lima, A. S. Barros, F. Trindade, et al., "Application of Proteogenomics to Urine Analysis Towards the Identification of Novel Biomarkers of Prostate Cancer: An Exploratory Study," *Cancers* 14 (2022): 2001.

46. S. Park, W. Kwon, J. K. Park, et al., "Suppression of Cathepsin a Inhibits Growth, Migration, and Invasion by Inhibiting the p38 MAPK Signaling Pathway in Prostate Cancer," *Archives of Biochemistry and Biophysics* 688 (2020): 108407.

47. M. Gruber, L. Ferrone, M. Puhr, et al., "p300 Is Upregulated by Docetaxel and Is a Target in Chemoresistant Prostate Cancer," *Endocrine-Related Cancer* 27 (2020): 187–198.

48. M. Wainberg, N. Sinnott-Armstrong, N. Mancuso, et al., "Opportunities and Challenges for Transcriptome-Wide Association Studies," *Nature Genetics* 51 (2019): 592–599.

**Supporting Information**

Additional supporting information can be found online in the Supporting Information section.

＜内科学第二（消化器内科）＞

教授　佐藤　賢一
教授　廣田　衛久
准教授　小暮　高之
准教授　遠藤　克哉
講師　上野　正道
講師　高須　充子
助教　支倉　さやか
助教　福士　大介
助教　小岩井　昭信
助教　佐々木　義輝
助教　佐藤　麻里
助教　吉野　祐貴
助教　永井　千菜津
助手　金　諒
助手　片山　智文
助手　伊藤　豪仁
助手　宮下　優輝

## 消化器疾患の病態解明を目指して

多数の臨床症例を解析し、新たな診断法や治療法の確立を目指した臨床研究と臨床検体を用いて遺伝子の変異、分子の発現などを検討する基礎的研究を行い、消化器(食道、胃、小腸、大腸、肝臓、胆道、膵臓)疾患の病態解明につながる新たな知見を発見することを目指している。多くの症例を解析することによって、その疾病の病態・病因を明らかにする臨床研究とともに、病理検体や細胞、動物を用いた実験から病態を追求する基礎研究も行っている。

具体的な臨床研究として、胃や食道癌の発生や長期予後に関連する因子を同定できるかを検討し、同様に急性膵炎・慢性膵炎、膵癌、肝癌・肝硬変、炎症性腸疾患の治療法の妥当性の検討、新しい診断法の開発を目指した研究を行っている。

基礎研究に関しては、宮城県立がんセンター研究所や東北大学と共同して、消化器癌の浸潤・転移に関わる分子の網羅的遺伝子解析による同定を試みている。さらに、メタボローム解析によって、癌転移に関与している代謝物や代謝経路を明らかにすることを目指している。

また、肝癌増殖の分子機構・薬剤感受性の新規メカニズムの解明を目指して機能性 RNA やエキソソーム、肝癌幹細胞の腫瘍微小環境の解析ならびに、B 型肝炎の新規の治療法開発を目指して細胞内・細胞外のウイルス転写産物を解析している。

＜論文発表＞

**・Delta-6 desaturase FADS2 is a tumor-promoting factor in cholangiocarcinoma**

Hasegawa K, Fujimori H, Nakatani K, Takahashi M, Izumi Y, Bamba T, Nakamura-Shima M, Shibuya-Takahashi R, Mochizuki M, Wakui Y, Abue M, Iwai W, Fukushi D, Satoh K, Yamaguchi K, Shindo N, Yasuda J, Asano N, Imai T, Asada Y, Katori Y, Tamai K.Cancer Sci. 115(10). 3346—3357. (2024)

**・Real-world NUDT15 genotyping and thiopurine treatment optimization in inflammatory bowel disease: a multicenter study**

Makuuchi M, Kakuta Y, Umeno J, Fujii T, Takagawa T, Ibuka T, Miura M, Sasaki Y, Takahashi S, Nakase H, Kiyohara H, Tominaga K, Shimodaira Y, Hiraoka S, Ueno N, Yanai S, Yoshihara T, Kakimoto K, Matsuoka K, Hayashi R, Nanjo S, Iwama I, Ishiguro Y, Chiba H, Endo K, Kagaya T, Fukuda T, Sakata Y, Kudo T, Takagi T, Takahashi K, Naganuma M, Shinozaki M, Ogata N, Tanaka H, Narimatsu K, Miyazaki H, Ishige T, Onodera M, Hashimoto Y, Nagai H, Shimoyama Y, Naito T, Moroi R, Shiga H; Post-MENDEL study group; Kinouchi Y, Andoh A, Hisamatsu T, Masamune A.　J Gastroenterol. 59(6). 468-482. (2024)

**・Peribiliary gland hyperplasia that required differentiation from extrahepatic bile duct cancer: A case report**

Takami K, Yamamoto K, Sakurai H, Sato Y, Kondo N, Nakano T, Tsujinaka S, Koiwai A, Hirota M, Murakami K, Murakami K, Shibata C, Katayose Y.
Case Rep Gastroenterol. 18(1). 279-285. (2024)

**・Postprocedure serum amylase or lipase levels predict postendoscopic retrograde cholangiopancreatography pancreatitis: Meta-analysis of diagnostic test accuracy studies and utility assessment**

Hirota M, Itoi T, Morizane T, Koiwai A, Yasuda I, Ryozawa S, Mukai S, Ikeura T, Irisawa T, Iwasaki E, Katanuma A, Kitamura K, Takenaka M, Ito T, Masamune A, Mayumi T, Takeyama Y. Dig Endosc. 36(6). 670-687. (2024)

**・Early detection of necrosis in low-enhanced pancreatic parenchyma using contrast-enhanced computed tomography was a better predictor of clinical outcomes than pancreatic inflammation: A multicenter cohort study of severe acute pancreatitis**

Yamamoto T, Horibe M, Sanui M, Sasaki M, Mizobata Y, Esaki M, Sawano H, Goto T, Ikeura T, Takeda T, Oda T, Yasuda H, Namiki S, Miyazaki D, Kitamura K, Chiba N, Ozaki T, Yamashita T, Oshima T, Hirota M, Moriya T, Shirai K, Yamamoto S, Kobayashi M, Saito K, Saito S, Iwasaki E, Kanai T, Mayumi T.

Pancreatology. 24(6). 827-833. (2024)

**・Comprehensive analysis of peripheral blood free amino acids in MASLD: the impact of glycine-serine-threonine metabolism. Amino Acids**

Mino M, Kakazu E, Sano A, Tsuruoka M, Matsubara H, Kakisaka K, Kogure T, Sekine K, Aoki Y, Imamura M, Matsuda M, Yamazoe T, Mori T, Yoshio S, Inoue J, Masamune A, Kanto T. Amino Acids. 57(1):3 (2024)

**・Differences in branched-chain amino acid to tyrosine ratio (BTR) among etiologies of chronic liver disease progression compared to healthy adults**

Mino M, Sano A, Kakazu E, Matsubara H, Kakisaka K, Kogure T, Sekine K, Aoki Y, Imamura M, Matsuda M, Yamazoe T, Mori T, Yoshio S, Inoue J, Masamune A, Kanto T. J Gastroenterol. 59(6):483-493 (2024)

**・A case of relapsed pan-colonic ulcerative colitis accompanied with gastroduodenal lesions immediately after COVID-19**

Endo K, Satoh T, Yoshino Y, Kondo S, Kawakami Y, Fukushi D, Takasu A, Kogure T, Hirota M, Satoh K. Clin J Gastroenterol. doi: 10.1007/s12328-025-02107-0. (2025)

**・ERCP 後膵炎ガイドライン 2023**

糸井隆夫, 池浦司, 入澤篤志, 岩崎栄典, 潟沼朗生, 北村勝哉, 竹中完, 竹山宜典, 廣田衛久, 正宗淳, 真弓俊彦, 向井俊太郎, 森實敏夫, 安田一朗, 良沢昭銘, 吉田雅博, 伊藤鉄英, 安田健治朗, 伊藤嵩志, 岩野光佑, 鎌田研, 茅島敦人, 小岩井明信, 谷坂優樹, 中丸洸, 永島一憲, 林伸彦, 堀部昌靖, 本間俊裕, 水出雅文, 三長孝輔, 山宮知.

膵臓, 39 巻 2 号, 79-158 (2024.04)

**・膵癌早期診断を目指した新規バイオマーカーの進歩と今後の展望**

小岩井明信, 廣田衛久, 高須充子, 佐藤賢一.

膵臓, 39 巻 4 号, 255-262 (2024.08)

**・胆嚢癌内に右肝動脈瘤破裂をきたした 1 例**

宮下優輝, 小岩井明信, 廣田衛久, 佐藤賢一.

胆道, 39 巻 1 号, 64-70 (2025.03)

**・6. 膵疾患**

廣田衛久, 下瀬川徹.

臨床検査ガイド 2025 年改訂版. 文光堂. 東京. 31-38. (2024.12)

**・40. 膵臓疾患治療薬**

廣田衛久.

Pocket Drugs. 医学書院. 東京. 331-334. (2025.01)

**・4-2-20. 急性肝不全と人工肝補助療法**

小暮高之, 廣田衛久.

ER・ICU の適正輸液. MEDICAL VIEW. 東京. 251-255. (2025.03)

**・【胆膵 Interventional Endoscopy を極める】トラブルシューティング ERCP 後膵炎**

小岩井明信, 廣田衛久, 猪股奈々, 高須充子, 佐藤賢一.

胆と膵, 45 巻臨時特大, 1365-1370. (2024.10)

**・【膵外分泌機能障害を極める】 膵外分泌機能障害の病態**

廣田衛久.

胆と膵, 46 巻 1 号, 23-28. (2025.01)

<学会発表＞

**・当科クローン病の生物学的製剤新規導入例に対する T2T 戦略の実践と治療予後**

遠藤克哉, 吉野祐貴, 川上瑶子, 近藤史帆, 佐藤賢一

第 107 回 日本消化器内視鏡学会総会, 東京, 2024 年 6 月, 演題番号 P-353

**・5-ASA 治療抵抗性の潰瘍性大腸炎に対するカロテグラストメチルの治療成績**
遠藤克哉, 吉野祐貴, 近藤史帆, 川上瑶子, 佐藤賢一
日本消化器病学会東北支部第 217 回例会, 仙台, 2024 年 7 月, 演題番号 O-13

**・アメーバ性大腸炎の臨床的・内視鏡的特徴に関する検討**
沼田燿孝, 遠藤克哉, 近藤史帆, 佐々木義輝,
川上瑶子, 吉野祐貴, 佐藤賢一
日本消化器病学会東北支部第 217 回例会, 仙台, 2024 年 7 月, 演題番号 O-15

**・潰瘍性大腸炎における 5-ASA 不耐の臨床的特徴と治療方針についての検討**
吉野祐貴, 遠藤克哉, 川上瑶子, 近藤史帆, 佐藤賢一
日本消化器病学会東北支部第 217 回例会, 仙台, 2024 年 7 月, 演題番号 WS1-02

**・内視鏡的摘除により保存的に治療をしえた爪楊枝による S 状結腸穿通の一例**
大沼創, 遠藤克哉, 三浦智也, 辻中眞康, 高橋良平, 佐々木義輝,
吉野祐貴, 佐藤賢一
日本消化器病学会東北支部第 217 回例会, 仙台, 2024 年 7 月, 演題番号 A-05

**・急性膵炎診療の最前線**
廣田衛久
日本消化器病学会東北支部第 217 回例会, 仙台, 2024 年 7 月, 日本消化器病学会東北支部第 26 回専門医セミナー講演 1.

**・肝胆膵疾患診療:予後改善にむけた早期診断と治療　膵癌診断前の CT 画像における特徴的画像所見に対する検討**
小岩井明信, 廣田衛久, 猪股奈々, 高須充子, 佐藤賢一.
日本消化器病学会東北支部第 217 回例会, 仙台, 2024 年 7 月, 演題番号 S2-01

**・EUS-FNB で診断した, 術後 24 年での淡明細胞型腎細胞癌膵転移の一例**
片山智文, 小岩井明信, 廣田衛久, 猪股奈々, 高須充子, 佐藤賢一.
日本消化器病学会東北支部第 217 回例会, 仙台, 2024 年 7 月, 演題番号 O-25

**・門脈圧亢進症による難治性腹水を来した全身性アミロイドーシスの一例**
中谷拓朗, 小暮高之, 廣田衛久, 高須充子, 小岩井明信, 片山智文, 猪股奈々, 伊藤豪仁,

山崎ゆうか, 佐藤賢一.
日本消化器病学会東北支部第 217 回例会, 仙台, 2024 年 7 月, 演題番号 O-30

**・悪性遠位胆管狭窄に対する Multi-hole SEMS の有用性**
小岩井明信, 廣田衛久, 猪股奈々, 高須充子, 佐藤賢一.
日本消化器内視鏡学会東北支部第 172 回例会, 仙台, 2024 年 7 月, 演題番号 SS-07

**・当院での良性胆管空腸吻合部狭窄に対する治療成績と金属ステントの有用性の検討**
猪股奈々, 小岩井明信, 廣田衛久, 高須充子, 佐藤賢一.
日本消化器内視鏡学会東北支部第 172 回例会, 仙台, 2024 年 7 月, 演題番号 SS-07

**・心嚢液貯留による呼吸苦を契機に診断に至った膵体部癌,癌性心膜炎の一例**
猪股奈々, 小岩井明信, 廣田衛久, 高須充子, 村上一宏, 佐藤賢一.
第 55 回日本膵臓学会大会, 宇都宮, 2024 年 7 月, 演題番号 O-38-3.

**・Zn 結合不全型 CRY1 発現マウスの特異な膵 管病変における TFF2 の発現と膵 α 細胞の新生**
岡野 聡 , 安井 明 , 菅野新一郎, 佐々木 悠, 佐藤 賢一, 五十嵐雅彦, 中島 修.
第 55 回日本膵臓学会大会, 宇都宮, 2024 年 7 月, 演題番号 P7-1.

**・EUS-FNB で診断した胆嚢原発悪性リンパ腫の一例**
猪股奈々, 小岩井明信, 廣田衛久, 佐藤賢一.
第 60 回日本胆道学会学術集会, 名古屋, 2024 年 10 月, 演題番号 P34-3.

**・The involvement of microRNA-1297 in lenvatinib resistance in hepatocellular carcinoma cells**
Takayuki Kogure, Mari Satoh, Takehito Ito, Kennichi Satoh
The Liver Meeting 2024, San Diego, Nov 2024

**・Functional role of microRNA-491 in lenvatinib resistance in hepatocellular carcinoma**
Mari Satoh, Takayuki Kogure, Kennichi Satoh
The Liver Meeting 2024, San Diego, Nov 2024

**・無症候性アメーバ性大腸炎の臨床的・内視鏡的特徴に関する検討**

沼田燿孝, 遠藤克哉, 吉野祐貴, 佐藤賢一
第 32 回日本消化器病関連学会週間 JDDW2024, 神戸, 2024 年 11 月, 演題番号 内 P-143

**・当科における潰瘍性大腸炎に対するカロテグラストメチルの治療成績**
遠藤克哉, 吉野祐貴, 近藤史帆, 川上瑶子, 佐藤賢一
第 15 回日本炎症性腸疾患学会, 東京, 2024 年 11 月, 演題番号 O7-3

**・潰瘍性大腸炎の治療方針 ～今改めて考える抗 TNFα 抗体製剤の位置付け～**
遠藤克哉
第 113 回日本消化器内視鏡学会近畿支部例会, 大阪, 2024 年 12 月, ランチョンセミナー2

**・不明熱を主訴に受診し回腸生検培養検査にて確定診断しえたエルシニア腸炎の一例**
高橋良平, 遠藤克哉, 吉野祐貴, 近藤史帆, 佐藤賢一
第 173 回 日本消化器内視鏡学会東北支部例会, 仙台, 2025 年 2 月, 演題番号 O-027

**・終末回腸の主病変と回腸重複腸管との間に内瘻を形成し、術後に確定診断しえた小腸型クローン病の一例**
金諒, 遠藤克哉, 吉野祐貴, 佐々木義輝, 近藤史帆, 小岩井明信, 羽根田祥,
高橋賢一, 佐藤賢一
第 218 回日本消化器病学会東北支部例会, 仙台, 2025 年 2 月, 演題番号 O-17

**・当院における潰瘍性大腸炎に対するミリキズマブの使用経験**
吉野祐貴, 遠藤克哉, 近藤史帆, 佐藤賢一
第 218 回日本消化器病学会東北支部例会, 仙台, 2025 年 2 月, 演題番号 O-23

**・閉塞性黄疸を契機に発見された, 門脈輪状膵と膵管非融合の複数膵奇形を背景とする膵頭部癌の一例**
五十嵐滉平, 小岩井明信, 髙橋良平, 猪股奈々, 片山智文, 高須充子, 廣田衛久, 佐藤賢一.
日本消化器病学会東北支部第 218 回例会, 仙台, 2025 年 2 月, 演題番号 PL2-10.

**・悪性遠位胆道狭窄に対する金属ステント留置による ERCP 後膵炎発症の危険因子の検討**
猪股奈々, 小岩井明信, 廣田衛久, 高須充子, 佐藤賢一.
日本消化器内視鏡学会東北支部第 173 回例会, 仙台, 2025 年 2 月, 演題番号 S2-02.

**・悪性肝門部胆管狭窄に対する inside stent 留置時の乳頭処置の必要性に関する検討**

宮下優輝, 小岩井明信, 高須充子, 廣田衛久, 佐藤賢一.

日本消化器内視鏡学会東北支部第 173 回例会, 仙台, 2025 年 2 月, 演題番号 S2-06.

**・急速に増大する巨大腹腔内腫瘍による悪性輸入脚閉塞症に対して plastic stent を用いた内視鏡的減圧が有効であった一例**

石川慶, 小岩井明信, 宮下優輝, 猪股奈々, 片山智文, 高須充子, 廣田衛久, 佐藤賢一.

日本消化器内視鏡学会東北支部第 173 回例会, 仙台, 2025 年 2 月, 演題番号 O-044.

**・Multi-option 時代の UC 治療を考える ～抗 TNFα 抗体 ゴリムマブの強みをどう生かすか～**

遠藤克哉

GI WEEK 2025 第 21 回日本消化管学会総会学術集会, 東京, 2025 年 2 月, ランチョンセミナー7

Clinical Journal of Gastroenterology
https://doi.org/10.1007/s12328-025-02107-0

CASE REPORT

# A case of relapsed pan-colonic ulcerative colitis accompanied with gastroduodenal lesions immediately after COVID-19

Katsuya Endo[1] · Tomonori Satoh[1] · Yuki Yoshino[1] · Shiho Kondo[1] · Yoko Kawakami[1] · Daisuke Fukushi[1] · Atsuko Takasu[1] · Takayuki Kogure[1] · Morihisa Hirota[1] · Kennichi Satoh[1]

Received: 26 August 2024 / Accepted: 16 February 2025
© The Author(s) 2025

**Abstract**
Some patients with ulcerative colitis (UC) suffer from complicated UC-associated upper gastrointestinal lesions. However, the trigger of these lesions has not been clarified. Herein, we present a 28-year-old man with relapsed pan-colonic UC accompanied by gastroduodenal lesions immediately after contracting coronavirus disease 2019 (COVID-19). In this patient, UC relapsed approximately 7 days after the COVID-19 onset, despite being in remission for 3 years. The patient also developed symptoms such as epigastric pain and nausea on day 19 of COVID-19. The endoscopic and pathologic findings of the stomach and duodenum closely resembled colorectal lesions of UC; accordingly, we diagnosed the patient with UC-associated gastroduodenal lesions. Corticosteroids were significantly effective in the colorectal and upper gastrointestinal lesions, leading to remission. This report is the first to describe UC-associated upper GI lesions that developed right after COVID-19 infection. Therefore, COVID-19 can be a possible trigger of UC-associated upper gastrointestinal lesion. Further studies are needed to understand the relationship between the onset of UC or UC-associated upper GI lesions and COVID-19.

**Keywords** Ulcerative colitis · UC-associated gastroduodenal lesion · COVID-19

## Introduction

Ulcerative colitis (UC) is a chronic inflammatory disease of the large intestine with unknown etiology. However, some reports have described UC cases accompanied by upper gastrointestinal (GI) tract inflammation. UC-associated upper GI lesions are characterized by diffuse inflammatory lesions in the stomach, duodenum, and/or intestine that resemble colonic lesions of UC in terms of endoscopic and pathological findings [1]. However, the trigger of UC-associated upper GI lesions remains unclear.

The novel coronavirus disease 2019 (COVID-19) induced by severe acute respiratory syndrome coronavirus-2 (SARS-CoV-2) has spread worldwide since the end of 2019. However, only a few reports have described cases of UC triggered by COVID-19 [2–4].

Herein, we report for the first time a rare case of relapsed pan-colonic UC accompanied by UC-associated gastroduodenal lesions immediately after contracting COVID-19.

## Case report

A 28-year-old man presented to our hospital complaining of fever, sore throat, and cough. He was diagnosed with COVID-19.

The patient had a history of pancolitis-type ulcerative colitis diagnosed three years earlier at another hospital. Colonoscopic findings at the time of initial diagnosis are shown in Fig. 1. According to medical records from that institution, the patient had an allergy to 5-aminosalicylic acid (5-ASA) and experienced spontaneous remission upon its discontinuation. Subsequently, the patient independently discontinued follow-up visits, and no further detailed evaluations, including endoscopy, were performed. However, he remained asymptomatic for UC for 3 years.

Then, he was diagnosed with COVID-19, but his fever and upper respiratory tract symptoms improved on day 5 of infection by restful recuperation and symptomatic treatment.

✉ Katsuya Endo
kendo@tohoku-mpu.ac.jp

[1] Division of Gastroenterology, Tohoku Medical and Pharmaceutical University School of Medicine, 1-15-1 Fukumuro, Miyagino-ku, Sendai, Miyagi 983-8536, Japan

Published online: 01 March 2025

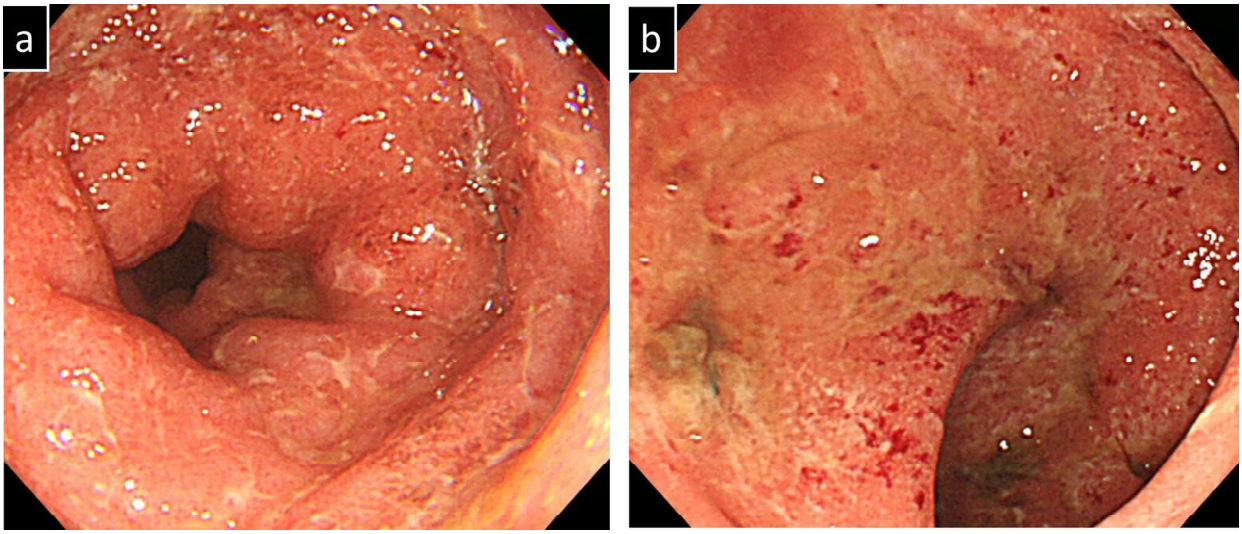


**Fig. 1** Features observed in colonoscopy at the time of initial diagnosis of UC. (**a**) Sigmoid colon. (**b**) Rectum. Continuous extension of erythema, edema, and erosion with adherent pus from the rectum to the oral side was observed. These findings were consistent with moderate ulcerative colitis

However, on day 7, he developed a fever of 38℃, abdominal pain, and bloody stool. On day 19, he also developed severe epigastric pain and nausea, prompting admission to our hospital. The laboratory findings indicated elevated white blood cell count, decreased hemoglobin level, increased platelet count, marked hypoalbuminemia, and elevated C-reactive protein level (Table 1). Contrast-enhanced computed tomography of the abdomen showed marked wall thickening of the entire colon and duodenum (Fig. 2). In contrast to the marked thickening observed in the duodenum and large intestine, the CT scan showed no wall thickening in the jejunum and ileum. On day 21, a colonoscopy was performed, inserting an endoscope into the transverse colon for observation. The colonoscopy revealed edematous mucosa, erythema, obliterated vascular pattern, luminal mild bleeding, and erosions, indicating moderately active UC (Fig. 3). Pathological findings of biopsy specimens from the rectum showed neutrophilic infiltration, cryptitis, and crypt abscess, which were also consistent with UC (Fig. 4). To exclude bacterial enteritis, we performed a stool culture, which did not reveal any significant bacterial growth. Additionally, both the *Clostridioides difficile* antigen and toxin tests were negative, ruling out *Clostridioides difficile* infection. According to these findings, we diagnosed the patient with relapsed pan-colonic UC with moderate severity. On day 22, the patient underwent esophagogastroduodenoscopy (EGD) because the patient complained of severe epigastric pain and nausea. Erythema, edema, and granular mucosa were noted in the stomach, mainly in the lower gastric body and antrum (Fig. 5 a, b). Additionally, the duodenum exhibited erythema, edema, erosion, and coarse mucosa with pus adhesion (Fig. 5 c,d). Biopsy specimens from the duodenum showed histopathologic findings suggestive of colonic lesions of UC, including inflammatory cell infiltration, glandular duct atrophy, disorganized arrangement, and crypt abscess (Fig. 6). After ruling out intestinal infection

**Table 1** Laboratory data on admission

| | | | | | |
|---|---|---|---|---|---|
| WBC | 11,200 | /μL | BUN | 10 | mg/dL |
| RBC | 440 | $\times 10^4$/μL | Cr | 0.59 | mg/dL |
| Hb | 13 | g/dL | Na | 134 | mEq/L |
| Ht | 38.1 | % | K | 3.1 | mEq/L |
| MCV | 86.5 | fL | Cl | 67 | mEq/L |
| MCH | 29.6 | pg | Ca | 8.3 | mg/dL |
| MCHC | 34.2 | % | TP | 5.2 | g/dL |
| Plt | 63.8 | $\times 10^4$/μL | Alb | 2.1 | g/dL |
| AST | 10 | IU/L | T-Chol | 94 | mg/dL |
| ALT | 7 | IU/L | TG | 89 | mg/dL |
| LDH | 145 | IU/L | FBS | 100 | mg/dL |
| T-Bil | 0.28 | mg/dL | CRP | 6.53 | mg/dL |
| ALP | 55 | U/L | | | |
| gGTP | 19 | IU/L | | | |

*WBC* white bold cells, *RBC* red blood cells, *Hb* hemoglobin, *Ht* hematocrit, *MCV* mean corpuscular volume, *MCH* mean corpuscular hemoglobin, *MCHC* mean corpuscular hemoglobin concentration, *Plt* platelets, *AST* aspartate aminotransferase, *ALT* alanine aminotransferase, *LDH* lactate dehydrogenase, *T-Bil* total bilirubin, *ALP* alkaline phosphatase, *gGTP* gamma-glutamyltranspeptidase, *S-AMY* serum amylase, *BUN* blood urea nitrogen, *Cr* creatinine, *Na* sodium, *K* potassium, *Cl* chloride, *Ca* calcium, *TP* total protein, *Alb* albumin, *T-Chol* total cholesterol, *TG* triglycerides, *FBS* fasting blood sugar, *CRP* C-reactive protein

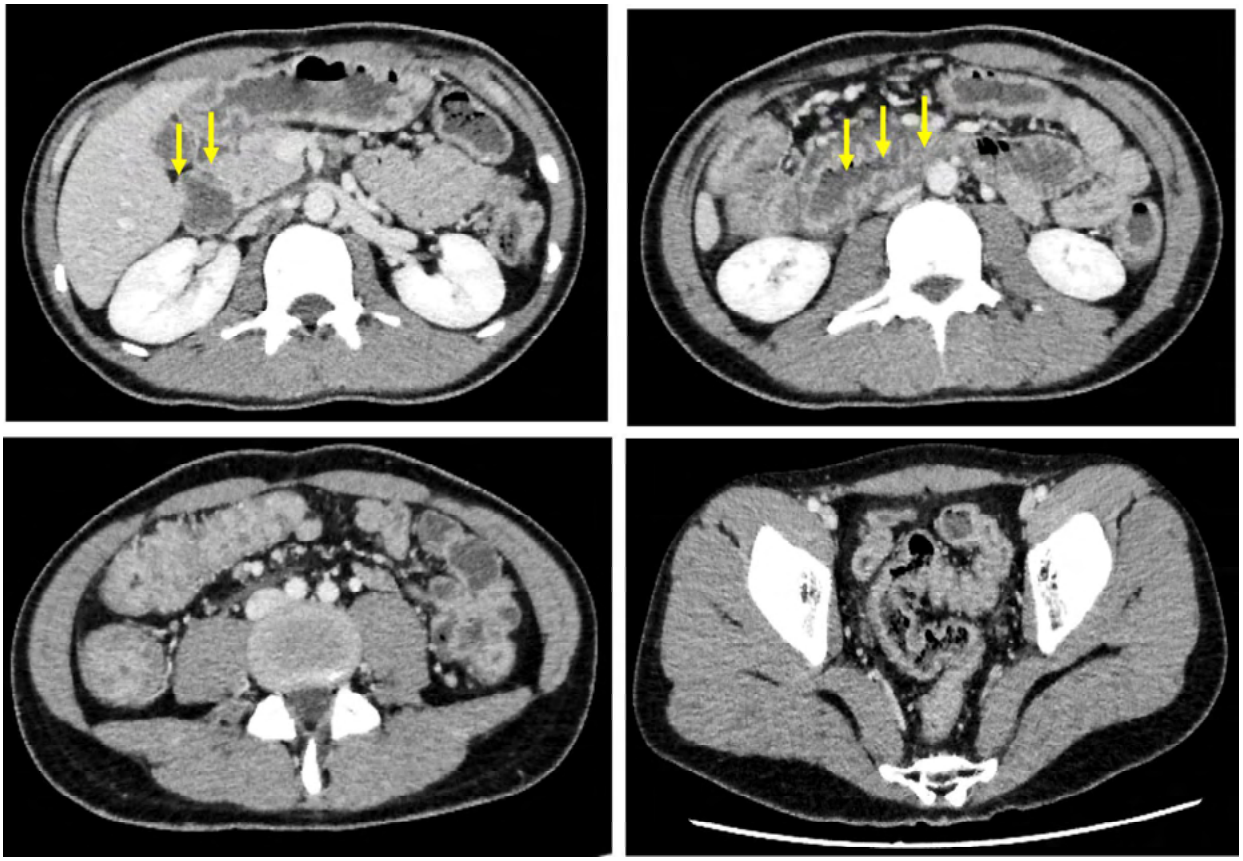

**Fig. 2** Contrast-enhanced computed tomography of the abdomen.The entire colon and the duodenum showed enhanced marked wall thickening (arrow)

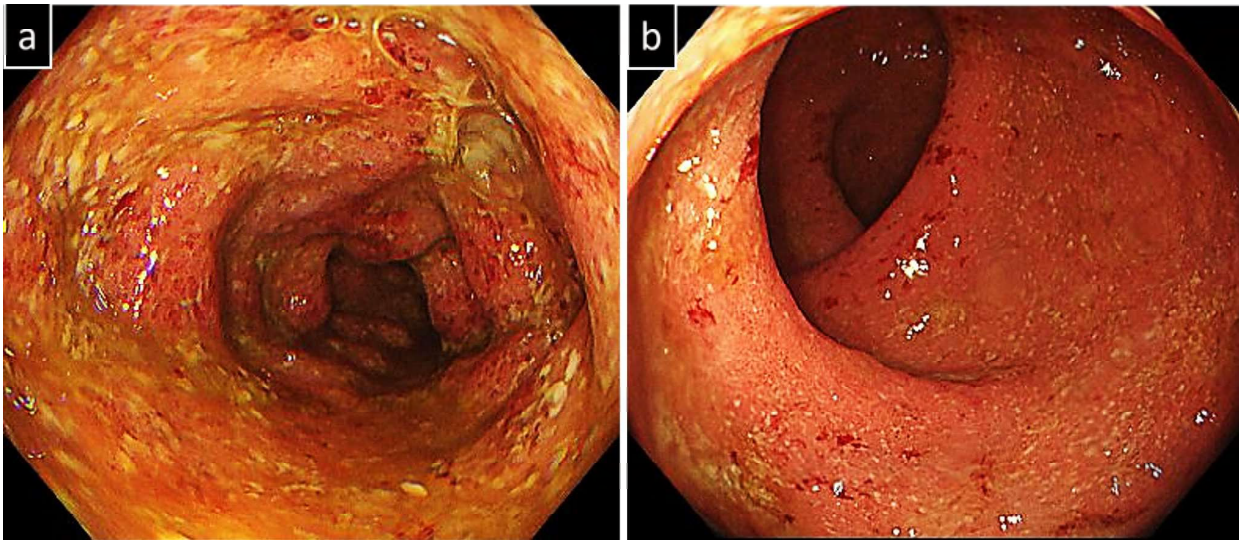


**Fig. 3** Features observed in colonoscopy on day 21 of COVID-19 onset. **a** Descending colon. **b** Rectum. Colonoscopy revealed edematous mucosa, erythema, obliterated vascular pattern, luminal mild bleeding, and erosions, which all indicate moderately active UC. These appearances were circumferential and continuous from the rectum to the transverse colon

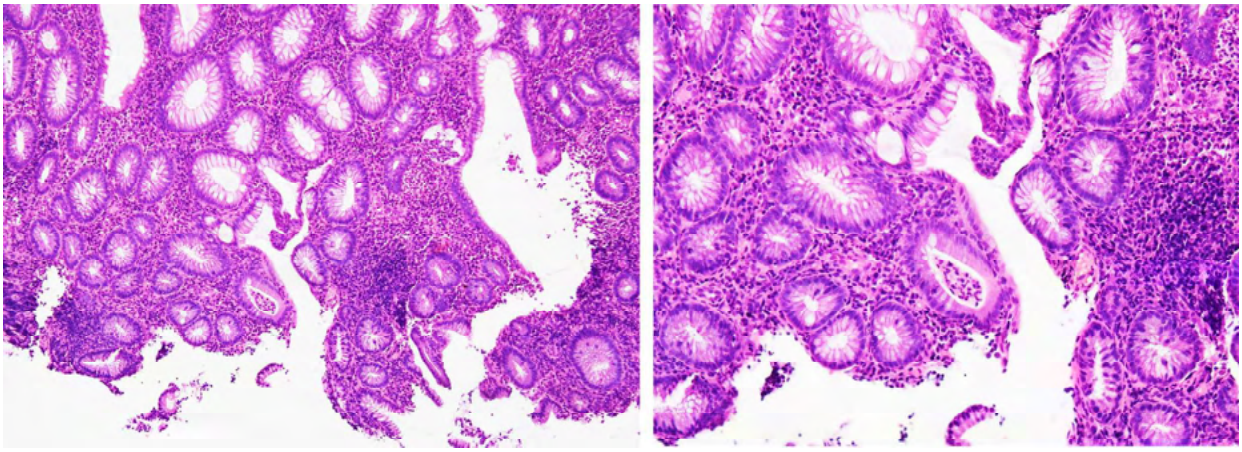

**Fig. 4** Pathological findings of the mucosal biopsies from the rectum. The biopsy specimens extracted from the rectum showed inflammatory findings including neutrophilic infiltration, cryptitis, and crypt abscess

such as cytomegalovirus (CMV) infection and vasculitis, we diagnosed him with UC-associated gastroduodenal lesion according to the upper GI findings.

We initiated remission induction therapy by intravenously injecting prednisolone (PSL, 60 mg/day). The upper and lower GI tract symptoms improved rapidly after PSL administration, and clinical remission was achieved after 2 weeks. SCS and EGD performed 2 weeks after PSL administration showed significantly improved mucosal findings (Fig. 7, 8). On day 18 of PSL administration, he was discharged with outpatient management. PSL was systematically tapered, and adalimumab was started for remission maintenance because of 5-aminosalicylic acid allergy. With the introduction of adalimumab, he became steroid-free, and his UC and duodenal lesions have not relapsed for more than 1 year on either therapy. The clinical course after the COVID-19 onset is presented in Fig. 9.

## Discussion

The disease extent of UC is usually confined to the colon and the rectum. However, the involvement of the upper GI tract has been recently reported [1, 5–11]. UC-associated upper GI lesions are characterized by diffuse inflammatory lesions in the stomach, duodenum, and/or intestine that resemble colonic lesions of UC on the basis of both endoscopic and pathological findings. In the present case, we suspected upper GI lesions because of the presence of epigastric pain and nausea, which are not usually seen as UC symptoms. The endoscopic and pathologic findings of the stomach and duodenum in our case are closely similar to the colorectal lesions of UC and consistent with UC-associated upper GI lesions. In the diagnosis of UC-associated upper GI lesions, other diseases, such as infectious disease and systemic vasculitis, must be excluded [8, 12, 13]. In the present case, CMV infection was ruled out according to the negative histopathology specimen and negative blood CMV antigenemia. Systemic IgA vasculitis was also ruled out because of the absence of systemic symptoms such as purpura, arthralgia, and renal involvement. Small bowel inflammation caused by COVID-19 is also an important consideration in the differential diagnosis. The CT scan of this patient showed no wall thickening in the jejunum and ileum, in contrast to the marked thickening observed in the duodenum and large intestine. Therefore, endoscopic examination of the small intestine distal to the duodenum was not performed. The colorectal lesions exhibited typical relapsing UC features, while the gastroduodenal lesions demonstrated UC-like endoscopic and histopathologic findings. Given these observations, we concluded that enteritis related to COVID-19 was deemed unlikely, and the diagnosis was consistent with upper GI involvement of UC.

While the treatment strategy for UC-associated upper GI lesions remains poorly established, these lesions are empirically known to improve by treatment for UC. Similar to treatment for colitis in UC, 5-aminosalicylic acid, corticosteroid, and anti-TNF alfa antibody can be used for UC-associated upper GI lesions or enteritis [7, 12–17]. In the present case, the good response to steroid treatment strongly supports that these lesions are UC-associated upper GI lesions. In this case, adalimumab was initiated following corticosteroid

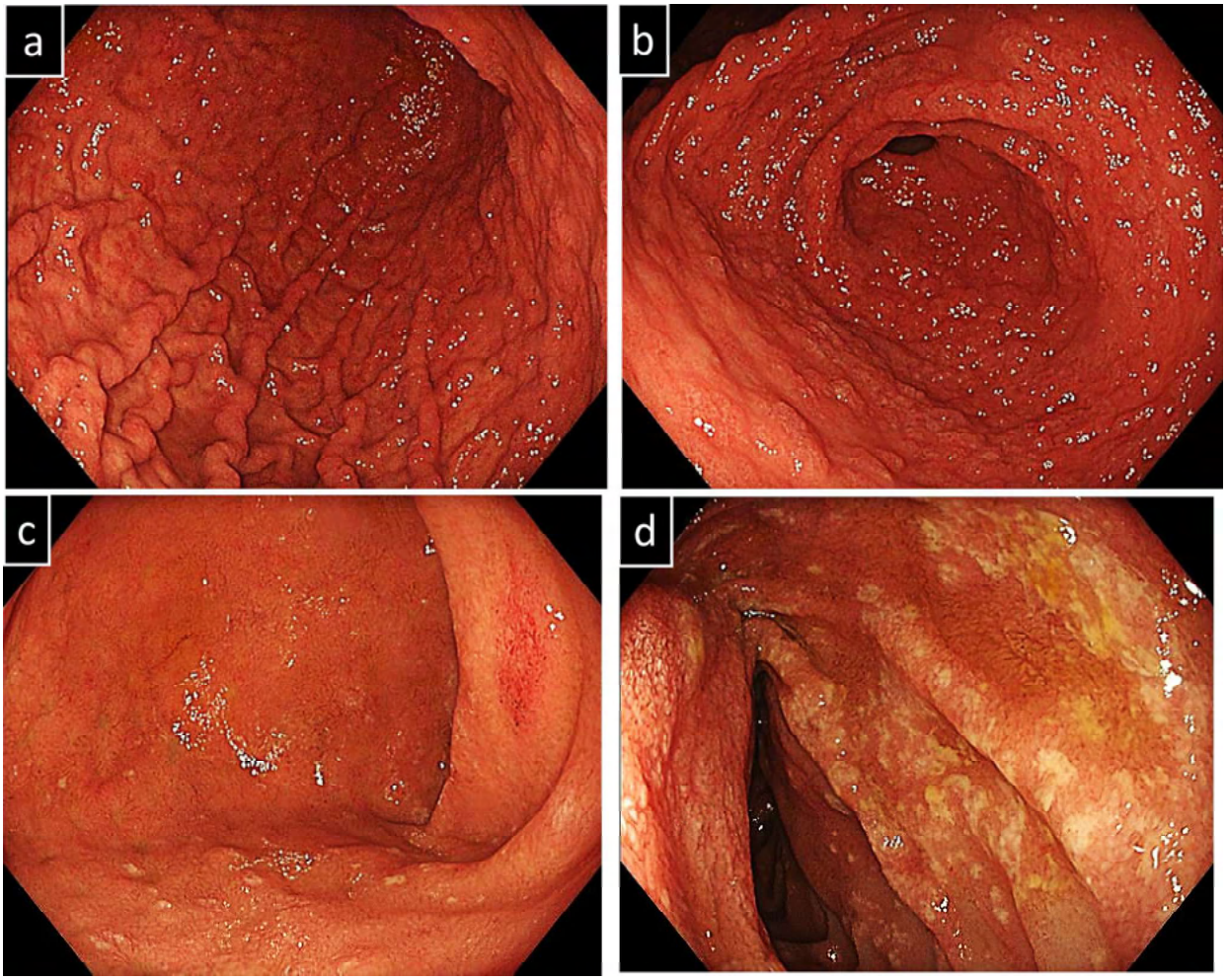


**Fig. 5** Features observed in esophagogastroduodenoscopy on day 22 of COVID-19 onset. Erythema, edema, and granular mucosa were detected in the stomach, mainly in the lower gastric body and antrum (**a**,**b**). Erythema, edema, erosion, and coarse mucosa with pus adhesion were noted in the duodenum (**c**,**d**)

treatment. There were two primary reasons for selecting anti-TNF-α therapy. First, the patient had a history of 5-ASA allergy, which limited the available options for effective maintenance therapy. In the absence of 5-ASA treatment, the patient was considered at high risk for relapse. Therefore, we opted for an anti-TNF-α agent to ensure sustained remission. Second, anti-TNF-α antibodies are an appropriate treatment for active UC complicated by COVID-19 infection and are not considered a significant risk factor requiring special precautions. According to recent evidence, Nakase et al. analyzed Japanese IBD patients with COVID-19 and reported that immunosuppressive therapies other than corticosteroids (including thiopurines and anti-TNF-α agents) are associated with a relatively low risk of severe COVID-19 infection [18]. Furthermore, the British Society of Gastroenterology (BSG) guidelines recommend the combination of corticosteroids and infliximab for patients with severe UC during COVID-19 infection [19]. Based on these findings, we determined that anti-TNF-α antibody therapy would be appropriate for managing COVID-19-induced UC relapse. In the present case, the introduction of adalimumab proved to be an effective therapeutic strategy, as it did not exacerbate COVID-19 infection and successfully induced and maintained remission of UC with upper GI involvement.

The triggers of upper GI inflammation in UC are still unclear. Most of the reported cases of UC-associated GI

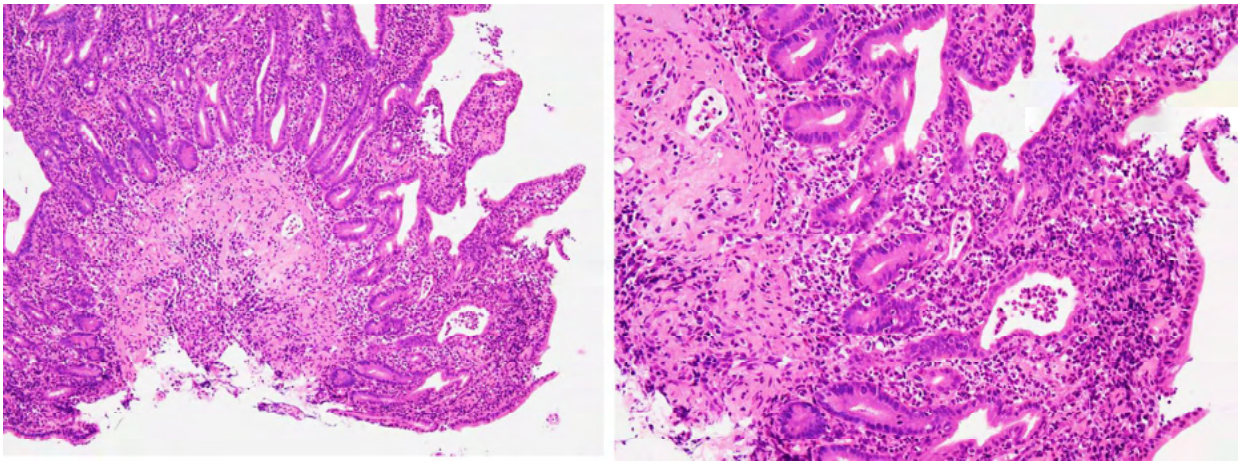

**Fig. 6** Pathological findings of the mucosal biopsies from the duodenum. The biopsy specimens from the duodenum showed inflammatory findings similar to those in the rectum, including neutrophilic infiltration, cryptitis, and crypt abscesses

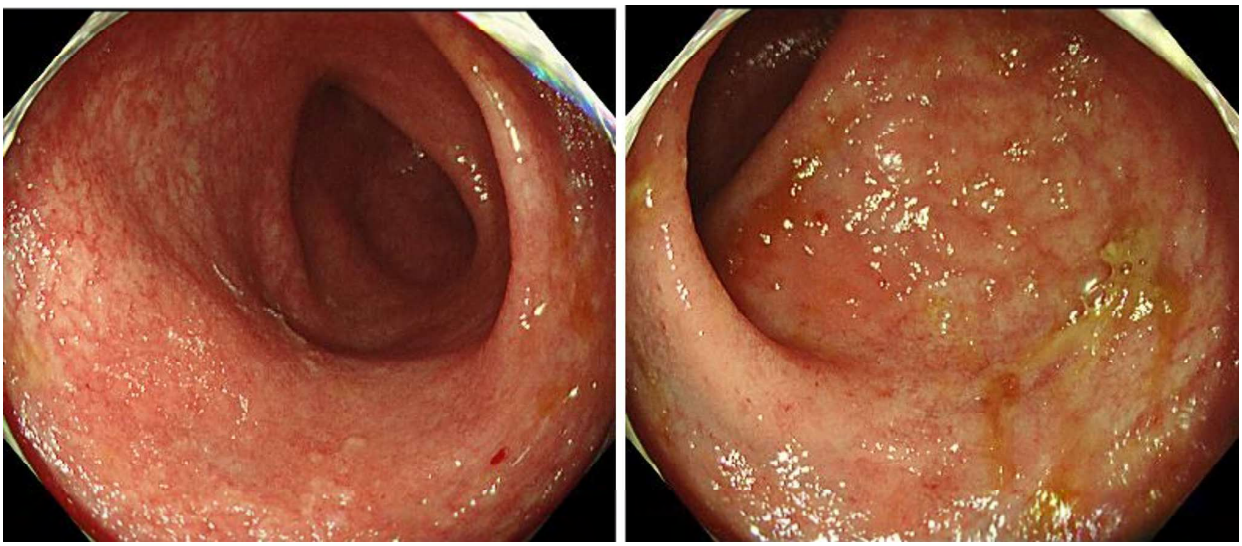

**Fig. 7** Features observed in colonoscopy 2 weeks after PSL administration. Sigmoid colonoscopy performed 2 weeks after PSL administration showed significantly improved mucosal findings.

lesions were accompanied by pan-colonic UC, indicating that pan-colonic inflammation is strongly associated with upper GI inflammation [5, 6, 10]. A lower dose of prednisolone has been also reported as a possible risk factor for developing UC-associated upper GI lesions [5]. In addition, total or subtotal colectomy is one of the important triggers for the development of UC-associated upper GI lesions and small bowel lesions [8, 9, 11, 20]. Kohyama et al. reported that 42 (0.8%) out of 5284 UC cases had been diagnosed with UC-related postoperative enteritis [9]. However, the other triggers of UC-associated upper GI lesions remain largely unknown. The total colitis observed in our patient is similar to that seen in previously reported cases. Of note, in our case, the relapse of UC and the appearance of upper GI lesions occurred almost concurrently, immediately after COVID-19. A recent European cohort study has reported that COVID-19 has a slight impact on the course of inflammatory bowel disease (IBD) [21]. However, a multicenter

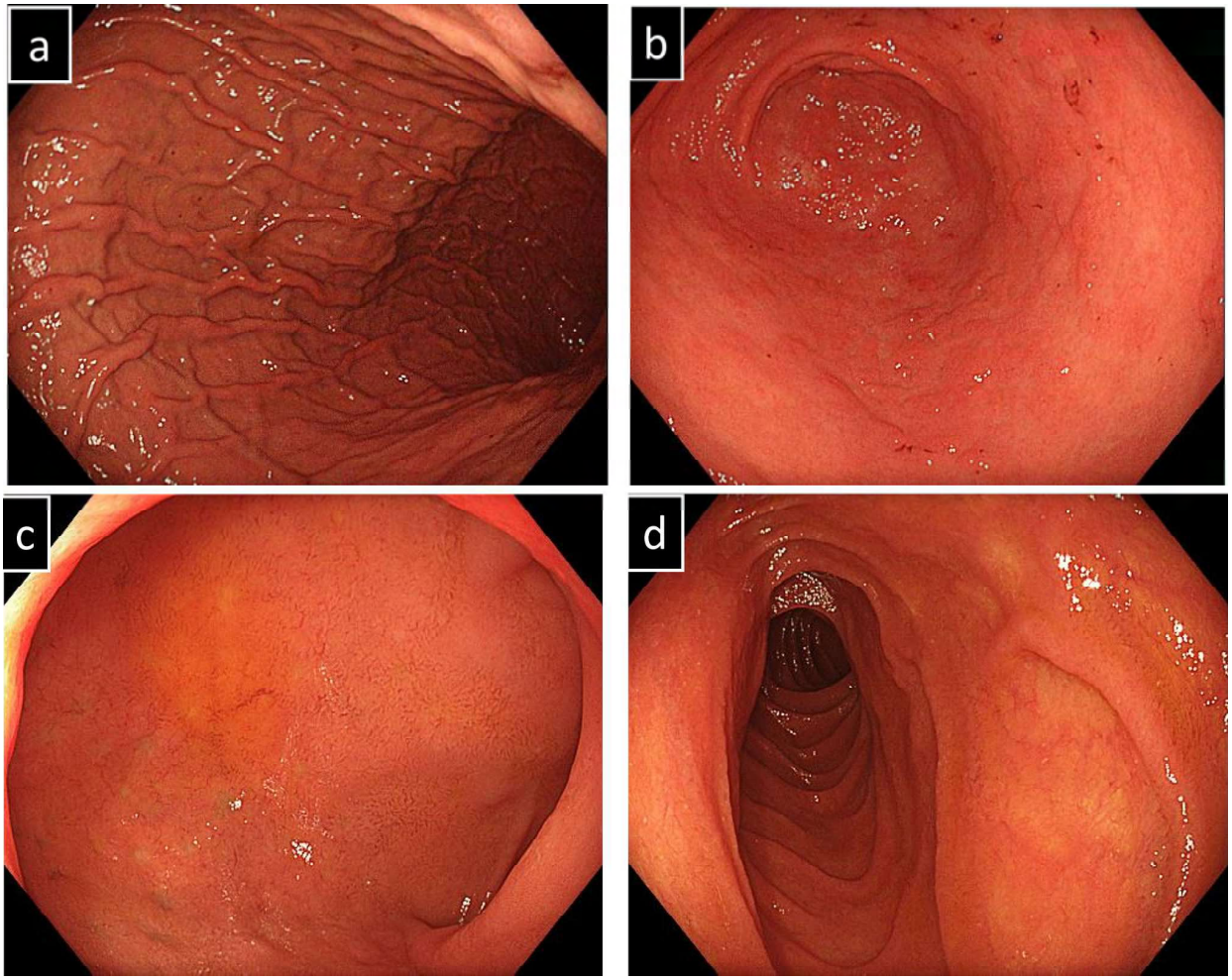


**Fig. 8** Features observed in esophagogastroduodenoscopy 2 weeks after PSL administration. Esophagogastroduodenoscopy performed 2 weeks after PSL administration showed significantly improved mucosal findings

study from Japan has described that COVID-19 changed the course of IBD in approximately 10% of patients [22]. Furthermore, the onset of UC triggered by COVID-19 has been reported in some patients [2–4]. Although evidence is still limited, these reports suggest that COVID-19 amplifies UC or causes UC by revealing masked inflammation. In the present case, UC relapsed approximately 7 days after the COVID-19 onset, despite being in remission for 3 years. The patient also developed UC-associated gastroduodenal lesions almost at the same time as the UC recurrence. Thus, the activation of the systemic immune system by COVID-19 may have caused the recurrence of UC and the development of UC-related upper GI lesions.

In conclusion, this report describes for the first time a rare case of relapsed pan-colonic UC accompanied by UC-associated GI lesions immediately after contracting COVID-19. COVID-19 can be a possible trigger of UC-associated upper GI lesion. In patients with UC infected with COVID-19, we should be aware of the development of upper GI lesions and the relapse or worsening of UC. Further studies are needed to understand the relationship between UC or UC-associated upper GI lesion onset and COVID-19.

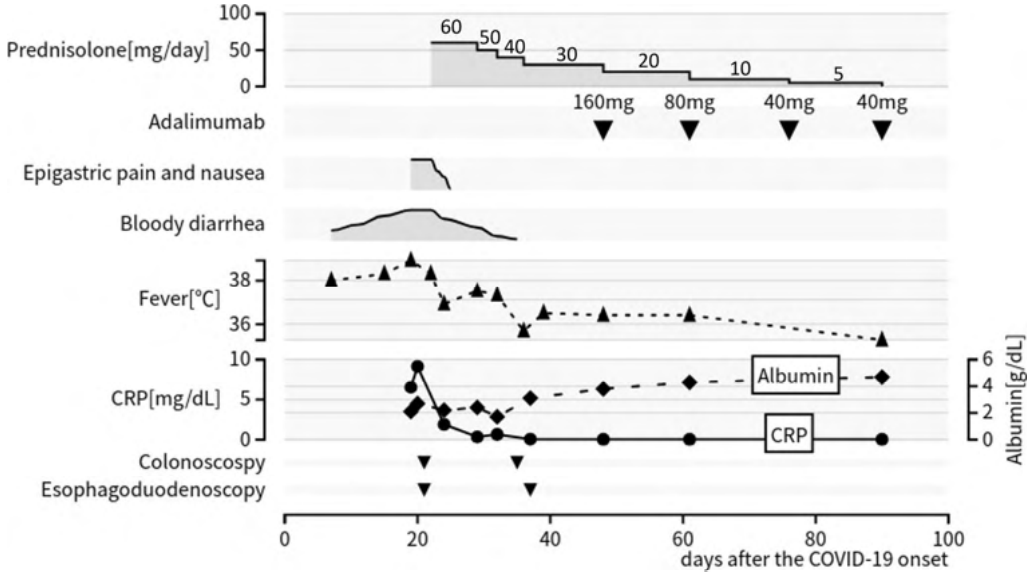


**Fig. 9** Clinical course after the COVID-19 onset

**Acknowledgements** We sincerely appreciate Dr. Keiichiro Hiramoto for providing the endoscopic images taken at the time of UC diagnosis.

**Funding** Open Access funding provided by Tohoku Medical and Pharmaceutical University.

## Declarations

**Conflict of interest** The authors have no conflict of interest to declare.

**Human and animal rights** This study was conducted in accordance with the ethical principles of the Declaration of Helsinki for medical research involving human participants.

**Informed consent** Informed consent was obtained from the patient to be included in this study.

**Open Access** This article is licensed under a Creative Commons Attribution 4.0 International License, which permits use, sharing, adaptation, distribution and reproduction in any medium or format, as long as you give appropriate credit to the original author(s) and the source, provide a link to the Creative Commons licence, and indicate if changes were made. The images or other third party material in this article are included in the article's Creative Commons licence, unless indicated otherwise in a credit line to the material. If material is not included in the article's Creative Commons licence and your intended use is not permitted by statutory regulation or exceeds the permitted use, you will need to obtain permission directly from the copyright holder. To view a copy of this licence, visit http://creativecommons.org/licenses/by/4.0/.

## References

1. Hisabe T, Matsui T, Miyaoka M, et al. Diagnosis and clinical course of ulcerative gastroduodenal lesion associated with ulcerative colitis: possible relationship with pouchitis. Dig Endosc. 2010;22:268–74.
2. Aydin MF, Tasdemir H. Ulcerative colitis in a COVID-19 patient: a case report. Turk J Gastroenterol. 2021;32:543–7.
3. Nawghare P, Jain S, Chandnani S, et al. A case of acute severe ulcerative colitis triggered by COVID-19 infection. Cureus. 2023;15: e34369.
4. Cayley WE Jr. New-onset ulcerative colitis in patients with COVID-19. Am Fam Physician. 2022;106:362.
5. Hori K, Ikeuchi H, Nakano H, et al. Gastroduodenitis associated with ulcerative colitis. J Gastroenterol. 2008;43:193–201.
6. Endo K, Kuroha M, Shiga H, et al. Two cases of diffuse duodenitis associated with ulcerative colitis. Case Rep Gastrointest Med. 2012;2012: 396521.
7. Choi YS, Kim JK, Kim WJ, et al. Remission of diffuse ulcerative duodenitis in a patient with ulcerative colitis after infliximab therapy: a case study and review of the literature. Intest Res. 2019;17:273–7.
8. Horio Y, Uchino M, Hori K, et al. Clinical features and therapeutic outcomes of post-colectomy enteritis with ulcerative colitis. J Anus Rectum Colon. 2021;5:405–13.
9. Kohyama A, Watanabe K, Sugita A, et al. Ulcerative colitis-related severe enteritis: an infrequent but serious complication after colectomy. J Gastroenterol. 2021;56:240–9.
10. San Aye K, Lin Htun L, Win TM, et al. Gastroduodenal ulcerative colitis in association with ulcerative pancolitis. Case Rep Gastrointest Med. 2021;2021:6684806.
11. Shimoda F, Kuroha M, Chiba H, et al. Ulcerative colitis-related postoperative enteritis treated with anti-tumor necrosis factor therapy: two case reports and a literature review. Clin J Gastroenterol. 2021;14:1396–403.
12. Hoentjen F, Hanauer SB, Hart J, et al. Long-term treatment of patients with a history of ulcerative colitis who develop gastritis and pan-enteritis after colectomy. J Clin Gastroenterol. 2013;47:52–7.
13. Uchino M, Ikeuchi H, Bando T, et al. Diffuse gastroduodenitis and enteritis associated with ulcerative colitis and concomitant

cytomegalovirus reactivation after total colectomy: report of a case. Surg Today. 2013;43:321–4.
14. Mitomi H, Atari E, Uesugi H, et al. Distinctive diffuse duodenitis associated with ulcerative colitis. Dig Dis Sci. 1997;42:684–93.
15. Chiba M, Ono I, Wakamatsu H, et al. Diffuse gastroduodenitis associated with ulcerative colitis: treatment by infliximab. Dig Endosc. 2013;25:622–5.
16. Okabayashi S, Kobayashi T, Sujino T, et al. Steroid-refractory extensive enteritis complicated by ulcerative colitis successfully treated with adalimumab. Intest Res. 2017;15:535–9.
17. Akitake R, Nakase H, Tamaoki M, et al. Modulation of Th1/Th2 balance by infliximab rescues postoperative occurrence of small-intestinal inflammation associated with ulcerative colitis. Dig Dis Sci. 2010;55:1781–4.
18. Nakase H, Hayashi Y, Yokoyama Y, et al. Final analysis of COVID-19 patients with inflammatory bowel disease in japan (J-COSMOS): a multicenter registry cohort study. Gastro Hep Adv. 2023;2:1056–65.
19. Din S, Kent A, Pollok RC, et al. Adaptations to the British Society of Gastroenterology guidelines on the management of acute severe UC in the context of the COVID-19 pandemic: a RAND appropriateness panel. Gut. 2020;69:1769–77.
20. Feuerstein JD, Shah S, Najarian R, et al. A fatal case of diffuse enteritis after colectomy for ulcerative colitis: a case report and review of the literature. Am J Gastroenterol. 2014;109:1086–9.
21. Amiot A, Rahier JF, Baert F, et al. The Impact of COVID-19 on patients with IBD in a prospective european cohort study. J Crohns Colitis. 2023;17:37–48.
22. Nakase H, Hayashi Y, Hirayama D, et al. Interim analysis of a multicenter registry study of COVID-19 patients with inflammatory bowel disease in Japan (J-COSMOS). J Gastroenterol. 2022;57:174–84.

**Publisher's Note** Springer Nature remains neutral with regard to jurisdictional claims in published maps and institutional affiliations.

Check for updates

Received: 8 February 2024 | Revised: 17 July 2024 | Accepted: 25 July 2024

DOI: 10.1111/cas.16306

ORIGINAL ARTICLE

Cancer Science WILEY

# Delta-6 desaturase FADS2 is a tumor-promoting factor in cholangiocarcinoma

Kohsei Hasegawa[1,2,3] | Haruna Fujimori[1] | Kohta Nakatani[4] | Masatomo Takahashi[4] | Yoshihiro Izumi[4] | Takeshi Bamba[4] | Mao Nakamura-Shima[1] | Rie Shibuya-Takahashi[1] | Mai Mochizuki[1] | Yuta Wakui[5] | Makoto Abue[5] | Wataru Iwai[5] | Daisuke Fukushi[6] | Kennichi Satoh[6] | Kazunori Yamaguchi[7] | Norihisa Shindo[8] | Jun Yasuda[7] | Naoki Asano[1,9] | Takayuki Imai[2] | Yukinori Asada[2] | Yukio Katori[3] | Keiichi Tamai[1]

[1]Division of Cancer Stem Cell, Miyagi Cancer Center Research Institute, Natori, Miyagi, Japan

[2]Department of Head and Neck Surgery, Miyagi Cancer Center, Natori, Miyagi, Japan

[3]Department of Otolaryngology-Head and Neck Surgery, Tohoku University Graduate School of Medicine, Sendai, Miyagi, Japan

[4]Division of Metabolomics, Medical Research Center for High Depth Omics, Medical Institute of Bioregulation, Kyushu University, Fukuoka, Japan

[5]Division of Gastroenterology, Miyagi Cancer Center, Natori, Miyagi, Japan

[6]Division of Gastroenterology, Tohoku Medical and Pharmaceutical University, Sendai, Miyagi, Japan

[7]Division of Molecular and Cellular Oncology, Miyagi Cancer Center Research Institute, Natori, Miyagi, Japan

[8]Division of Cancer Chromosome Biology Unit, Miyagi Cancer Center Research Institute, Natori, Miyagi, Japan

[9]Division of Gastroenterology, Tohoku University Graduate School of Medicine, Sendai, Japan

**Correspondence**
Haruna Fujimori, Division of Cancer Stem Cell, Miyagi Cancer Center Research Institute, 47-1, Medeshima-Shiote, Natori, Miyagi, 981-1293, Japan.
Email: fuji.spr.na@gmail.com

**Funding information**
Takeda Medical Research Foundation; Kobayashi Foundation for Cancer Research; Japan Agency for Medical Research and Development, Grant/Award Number: JP22ama121055; Japan Society for the Promotion of Science, Grant/Award Number: 19K08430, 20K09701, 21H02396, 21K07137, 21K07186, 21K07973, 22K07974, 22K08085, 22K09678 and 22K09696; MEXT Cooperative Research Project Program, Medical Research Center Initiative for High Depth Omics, and CURE, Grant/Award Number: JPMXP1323015486

## Abstract

Cholangiocarcinoma is a fatal disease with limited therapeutic options. We screened genes required for cholangiocarcinoma tumorigenicity and identified FADS2, a delta-6 desaturase. FADS2 depletion reduced in vivo tumorigenicity and cell proliferation. In clinical samples, FADS2 was expressed in cancer cells but not in stromal cells. FADS2 inhibition also reduced the migration and sphere-forming ability of cells and increased apoptotic cell death and ferroptosis markers. Lipidome assay revealed that triglyceride and cholesterol ester levels were decreased in FADS2-knockdown cells. The oxygen consumption ratio was also decreased in FADS2-depleted cells. These data indicate that FADS2 depletion causes a reduction in lipid levels, resulting in decrease of energy production and attenuation of cancer cell malignancy.

KEYWORDS
cholangiocarcinoma, cholesterol esters, delta-6 desaturase, FADS2, triglyceride

**Abbreviations:** BSA, bovine serum albumin; CCA, cholangiocarcinoma; ELOVL2, elongation of very-long-chain fatty acids protein 2; FA, fatty acid; FADS2, fatty acid desaturase 2; FBS, fetal bovine serum; GSH, glutathione; GSSG, oxidized glutathione; PDX, patient-derived xenograft; SCD1, stearoyl-CoA desaturase 1

Kohsei Hasegawa and Haruna Fujimori contributed equally to this work.

This is an open access article under the terms of the Creative Commons Attribution-NonCommercial License, which permits use, distribution and reproduction in any medium, provided the original work is properly cited and is not used for commercial purposes.
© 2024 The Author(s). *Cancer Science* published by John Wiley & Sons Australia, Ltd on behalf of Japanese Cancer Association.

## 1 | INTRODUCTION

Cholangiocarcinoma (CCA) is a disease entity that comprises diverse epithelial tumors with features of cholangiocyte differentiation.[1] CCA is difficult to treat and has an incidence of <6 cases per 100,000 people[2] and the mortality rate is 1 per 100,000 people worldwide.[3] Most patients are diagnosed at an advanced stage, and there are consequently few therapeutic options, including targeted therapies.

Cholangiocarcinoma tumor tissues consist of heterogeneous cell populations,[2] comprising a mixture of highly and minimally malignant cells. This heterogeneity involves several cell characteristics, including chemoresistance, stemness, and tumorigenicity.[4] Patient-derived xenografts (PDX) in mice are an appropriate experimental model for reproducing tumor heterogeneity in the tumor microenvironment.[5,6] The xenografted tissue is similar to the original human cancerous tissue[7] and is widely used in preclinical research.[8] Proliferating xenografted cancer cells originate from a highly tumorigenic subpopulation, which is enriched in serially transplanted xenografts in mice.[9] Thus, highly tumorigenic, therapy-resistant cells can be identified using this model.

Fatty acids (FAs) consist of a terminal carboxyl group and a hydrocarbon chain, mostly with an even number of carbon atoms that can be either saturated or unsaturated.[10] Unsaturated lipids are produced by FA desaturases, such as SCD1 and FADS2. Alterations in FA metabolism have been increasingly reported in cancer cells. Unsaturated lipids are increased in ovarian cancer stem cells.[11] The expression of SCD1 and FADS2 are increased in metastatic tumors, and SCD1/FADS2 inhibitors in combination with cisplatin synergistically repress tumor cell dissemination.[12] In glioblastoma, ELOVL2, which is a key polyunsaturated FA synthesis enzyme, is upregulated in cancer stem cells through EGFR signaling.[13] However, little is known regarding unsaturated enzyme-dependent mechanisms, especially in CCA.

In this study, we aimed to identify a gene required for tumorigenicity using a xenograft model, which led to the identification of the delta-6 desaturase FADS2.

## 2 | MATERIALS AND METHODS

### 2.1 | Ethics statements

This study was conducted in accordance with the principles of the Declaration of Helsinki and approved by the ethics committee of the Miyagi Cancer Center Research Institute (Natori, Japan). The animal experimental protocols were approved by the Miyagi Cancer Center Animal Care and Use Committee (permit number AE.22.01).

### 2.2 | Cell lines

The CCA PDX cell line, CHOL1, was established using serial xenografts of tumor tissues derived from a human CCA patient with written informed consent (50-year-old male), as described previously.[14] TFK-1 cells were provided by the Cell Resource Center for Biomedical Research, Institute of Development, Aging, and Cancer, Tohoku University. Both cell lines were maintained in RPMI medium supplemented with 10% FBS.

### 2.3 | Quantitative real-time PCR

Total RNA was extracted from cells using the RNeasy Mini Kit (Qiagen), reverse transcribed using a PrimeScript II cDNA Synthesis Kit (Takara Bio) and then real-time PCR was performed using the Brilliant III Ultra-Fast SYBR Green QPCR Master Mix (Agilent Technologies). ß-Actin was used as the housekeeping gene, and data were analyzed using the ΔΔCt method. The primer sequences were as follows: ß-Actin forward primer 5′-ccaaccgcgagaagatga-3′, ß-actin reverse primer 5′-tccatcacgatgccagtg-3′, FADS2 forward primer 5′-ttcagtggacaccttaacttcc, and FADS2 reverse primer 5′- cacatagagacttcaccagcg.

### 2.4 | Cell proliferation assay

Cells were plated in 96-well plates, and the relative cell number was determined by image analysis using an Incucyte Zoom device (Sartorius) or by MTT assay. For the MTT assay, MTT (5 mg/mL, 1:10) was added to the medium, and after 2 h, an equal volume of 10% sodium dodecyl sulfate (SDS) in 0.01 M HCl was added, and further incubated overnight, after which the absorbance at 550 nm was measured.[15]

### 2.5 | Sphere-formation assay

On day 0, $1\times10^4$ cells were plated in DMEM/F12 (Fujifilm Wako Pure Chemical Corporation) supplemented with B27 (1:50; Thermo Fisher Scientific), epidermal growth factor (20 ng/mL; PeproTech), and fibroblast growth factor-2 (20 ng/mL; PeproTech) in 96-well Nunclon Sphera plates (Thermo Fisher Scientific). For FADS2 knockdown, small interfering RNA (siRNA) was transfected on day 0, as described below. On day 6, MTT (5 mg/mL, 1:10) was added to the medium, and after 2 h, an equal volume of 10% SDS in 0.01 M HCl was added and further incubated overnight, after which the absorbance at 550 nm was measured.[15]

### 2.6 | Small interfering RNA

Negative control siRNA (12935-300), FADS2 siRNAs FADS2#23 (s18023), FADS2#24 (s18024), and FADS2#25 (s18025) were purchased from Thermo Fisher Scientific. siRNA transfection was performed using lipofectamine RNAiMAX Reagent (Life Technologies).[16]



13497006, 2024, 10, Downloaded from https://onlinelibrary.wiley.com/doi/10.1111/cas.16306 by Tohoku Ika Yakka Daigaku, Wiley Online Library on [20/04/2025]. See the Terms and Conditions (https://onlinelibrary.wiley.com/terms-and-conditions) on Wiley Online Library for rules of use; OA articles are governed by the applicable Creative Commons License

## 2.7 | In vivo tumorigenesis assay

Tumor formation was assayed as previously described.[17] Briefly, the cells were suspended in 50 μL of phosphate-buffered saline (PBS) and an equal volume of Matrigel matrix (BD Biosciences) on ice and then injected into immunodeficient NOD/Shi-scid, IL-2Rγnull (NOG) mice using a 1-mL syringe. Tumor formation was monitored weekly, and the tumor volumes were calculated using the following formula: 1/2 (length × width$^2$).

## 2.8 | Apoptosis assay

For flow cytometry, cells were harvested using 0.25% trypsin. The cells were resuspended in annexin-binding buffer (BioLegend) and stained with FITC-conjugated annexin V (BioLegend) and propidium iodide. After incubation for 15 min, the cells were analyzed using an SA3800 spectral flow cytometer (SONY). For the luminescence assay, caspase-Glo 3/7 (Promega) was used according to the manufacturer's protocol.

## 2.9 | Scratch assay

The scratch-wound assay was performed as described previously.[18] Cells were seeded in 24-well plates in medium containing 3% FBS, incubated until confluent, and then treated with 2.5 μg/mL mitomycin C (Fujifilm-Wako) for 4 h. A yellow pipette tip was used to create straight scratch wounds in the cell monolayer. The medium was replaced with serum-free medium, and after 24 h of incubation, the area occupied by cells that had migrated into the scratch wound area was measured using ImageJ software. To inhibit FADS2, SC26196 (Cayman Chemical) was added to the medium 3 days before scratching.

## 2.10 | Western blot analysis

Western blotting was performed as previously described, with minor modifications.[15] Cells were washed once with Dulbecco's PBS or plain medium, suspended in SDS-loading buffer (100 mM Tris–Cl pH 6.8, 4% SDS, 0.2% bromophenol blue, 20% glycerol, and 2% β-mercaptoethanol), sonicated for 5 min, heated to 100°C for 5 min, and then subjected to SDS-PAGE. The separated proteins were transferred onto an Immun-Blot Low Fluorescence PVDF Membrane (Bio-Rad) and blocked with 2% BSA in Tris-buffered saline containing 0.1% Tween® 20 (TTBS) for 30 min at room temperature. The membrane was then incubated with primary antibody, washed, and incubated with secondary antibody. Primary antibody binding was detected using Clarity Western ECL Substrate (Bio-Rad) and images were captured using a FUSION-SOLO.7S.EDGE imaging system (Vilber Bio Imaging). The antibodies used in this study were anti-glutathione peroxidase 4 (AB125066, Abcam), anti-pan-Akt (C67E7, rabbit mAb #4691, Cell Signaling Technology), and anti-phospho-AKT (Ser473) (#4069, Cell Signaling Technology).

## 2.11 | In situ hybridization

A CCA tissue-array (#GA802a) was purchased from TissueArray Co. FADS2 mRNA in the tissue microarray was detected by RNAscope 2.5 HD Assay-BROWN assay (Advanced Cell Diagnostics) according to the manufacturer's protocol. The probes used were Hs-FADS2 (#569811; Advanced Cell Diagnostics), a positive control probe (Hs-PPIB #313901), and a negative control probe (dapB #310043).

## 2.12 | Microarray analysis

Expression profiling of xenografted tumors and FADS2-knockdown cells was performed using a microarray (SurePrint G3 8 × 60 k, Agilent).[15] Data processing was performed using R statistical software (version 4.2.0),[19] and GSEA was performed as described previously.[20] A time-series analysis was conducted using maSigPro.[21]

## 2.13 | Quantification of the glutathione/oxidized glutathione (GSH/GSSG) ratio

Detection and quantification of total glutathione (GSH + GSSG), GSSG, and GSH/GSSG ratios were performed using the GSH/GSSG-Glo assay (Promega). Cells were cultured and treated in white assay plates (SPL). The media were discarded and replaced with either total GSH lysis reagent or GSSG lysis reagent, and the cells were agitated for 5 min. Both plates were kept at room temperature for 30 min before luciferin generation reagent was added. The plates were briefly agitated on an orbital shaker and allowed to equilibrate at room temperature for 15 min. The luminescence was measured using a Synergy LX plate reader (Agilent), and the GSH/GSSG ratio was calculated according to the manufacturer's guidelines.

## 2.14 | Quantification of intracellular lipid droplets

Cells were treated with siRNA or SC26196. After 2 days (CHOL1) or 3 days (TFK-1), cells were stained with Lipi-Green (1:1000, Dojindo) for 1 h at 37°C. The cells were then trypsinized, and the Lipi-Green intensity was measured by flow cytometry (SA3800, SONY). Images were obtained using a fluorescence microscope (IX73; EVIDENT).



13497006, 2024, 10, Downloaded from https://onlinelibrary.wiley.com/doi/10.1111/cas.16306 by Tohoku Ika Yakka Daigaku, Wiley Online Library on [20/04/2025]. See the Terms and Conditions (https://onlinelibrary.wiley.com/terms-and-conditions) on Wiley Online Library for rules of use; OA articles are governed by the applicable Creative Commons License

## 2.15 | Flux analyzer assay

The oxygen consumption ratio was measured using a flux analyzer (Seahorse XF96, Agilent).[22] CHOL1 and TFK-1 cells were plated on Seahorse XFe96 V3 PS plates. The cells were cultured under standard 5% $CO_2$ and 37°C conditions. Seahorse XF base medium enriched with 10 mM glucose, 2 mM L-glutamine, and 1 mM sodium pyruvate was equilibrated to 37°C and an adjusted pH of 7.35 ± 0.05. All wells were carefully washed three times with the Seahorse XF base medium and then incubated for 1 h in assay medium in a 37°C $CO_2$-free incubator before the measurement. Values were normalized to the relative cell number measured using an Incucyte device (Sartorius). Basal respiration was measured at the time point without the mitochondria inhibitor treatment. Maximal respiration was measured at the time point after the carbonyl cyanide 4-(trifluoromethoxy) phenylhydrazone (FCCP, Sigma Aldrich), a potent uncoupler of mitochondrial oxidative phosphorylation, treatment.

## 2.16 | Gas chromatography–mass spectrometry (GC-MS)

Gas chromatography–mass spectrometry analysis was performed at Shimadzu Techno-Research. Briefly, CHOL1 cells were harvested and sonicated on ice. Lipids were extracted from the lysate with chloroform/methanol. The extracted organic layer was evaporated to dryness, followed by methyl esterification with 4% methanolic HCl at 90°C for 2 h. After quenching with distilled water, palmitic acid-$d_{31}$ was added as an internal standard (IS). The ISs and the resulting FA methyl esters were extracted with *n*-hexane. The extracted *n*-hexane layer was analyzed by GC-MS (GCMS-QP2020, Shimadzu). TC-70 column (60 m × 0.25 mm i.d., 0.25 μm film thickness; GL Sciences) was used for the analysis.

## 2.17 | Lipidomic analysis

CHOL1 cell samples (approximately $2.3 \times 10^5$ cells) were prepared for extracting lipids using the Bligh and Dyer method[23] with minor modifications.[24] Briefly, the CHOL1cells were washed twice with 10 mL of PBS and quenched with 1 mL of ice-cold methanol. After scraping, the cell suspension (~1 mL) was transferred into a 2-mL Eppendorf tube and mixed with 10 μL of IS solution A (Mouse SPLASH Lipidomix Mass Spec Standard, Avanti Polar Lipids Inc.) containing phosphatidylcholine (PC) 15:0/[$^2H_7$]18:1 (1.0 nmol), phosphatidylethanolamine (PE) 15:0/[$^2H_7$]18:1 (0.070 nmol), phosphatidylserine (PS) 15:0/[$^2H_7$]18:1 (0.20 nmol), phosphatidylglycerol (PG) 15:0/[$^2H_7$]18:1 (0.050 nmol), phosphatidylinositol (PI) 15:0/[$^2H_7$]18:1 (0.20 nmol), phosphatidic acid (PA) 15:0/[$^2H_7$]18:1 (0.10 nmol), lysophosphatidylcholine (LPC) [$^2H_7$]18:1 (0.45 nmol), lysophosphatidylethanolamine (LPE) [$^2H_7$]18:1 (0.020 nmol), cholesteryl ester (ChE) [$^2H_7$]18:1 (2.5 nmol), diacylglycerol (DG) 15:0/[$^2H_7$]18:1 (0.15 nmol), triacylglycerol (TG) 15:0/[$^2H_7$]18:1/15:0 (0.35 nmol), and sphingomyelin (SM) d18:1/[$^2H_9$]18:1 (0.20 nmol), and 10 μL of IS solution B (Avanti Polar Lipids Inc.) containing ceramide (Cer) d[$^2H_7$]18:1/15:0 (0.10 nmol), hexosylceramide (HexCer) d[$^2H_5$]18:1/18:1 (0.10 nmol), free FA [$^{13}C_{16}$]16:0 (0.10 nmol), monoacylglycerol (MG) [$^2H_7$]18:1 (1.0 nmol), and [$^2H_7$]cholesterol (3.0 nmol). The samples were vigorously mixed by vortexing for 1 min followed by 5 min of sonication. The samples were centrifuged at 16,000 × *g* at 4°C for 5 min, and the supernatant (400 μL) was collected in clean tubes for lipidomic analysis. After mixing with 400 μL of chloroform and 360 μL of water, phase separation of aqueous and organic layers was performed via centrifugation (16,000 × *g*, 4°C, 5 min). The organic layer (bottom, 280 μL) obtained by phase separation was dried under a nitrogen stream and stored at −80°C until analysis. Prior to lipidomic analysis, the dried sample was reconstituted in methanol/chloroform (1/1, v/v, 100 μL).

The analytical conditions for lipidomics using supercritical fluid chromatography–tandem mass spectrometry (SFC-MS/MS) were performed as previously described.[24,25] The SFC (Nexera UC system, Shimadzu Co.) conditions were as follows: an ACQUITY UPC$^2$ Torus DEA column (3.0 mm i.d. × 100 mm, 1.7 μm particle size, Waters); injection volume, 1 μL; column temperature, 50°C; mobile phase A, supercritical carbon dioxide; mobile phase B (modifier) and make-up pump solvent; methanol/water (95/5, v/v) with 0.1% (w/v) ammonium acetate; flow rate of mobile phase, 1.0 mL/min; flow rate of make-up pump, 0.1 mL/min; and back pressure regulator, 10 MPa. The gradient conditions were as follows: 1% B, 0–1 min; 1–75% B, 1–24 min; 75% B, 24–26 min; and 1% B, 26–30 min. The triple quadrupole mass spectrometry (TQMS, LCMS-8060NX, Shimadzu Co.) analysis conditions were as follows: polarity, positive and negative ionization; electrospray voltage, 4 kV in the positive ion mode and − 3.5 kV in the negative ion mode; nebulizer gas flow rate, 3.0 L/min; drying gas flow rate, 10.0 L/min; desolvation line temperature, 250°C; heat block temperature, 400°C; and detector voltage, 2.16 kV. The multiple reaction monitoring (MRM) parameters per one time period were as follows: limit on number of MRM transitions, 150; dwell time, 2 ms; pause time, 2 ms; and polarity switching time, 5 ms. The analytical platform for lipidomic analysis was controlled using LabSolutions (version 5.99 SP2, Shimadzu Co.), and data analysis was performed using Multi-ChromatoAnalysT (Beforce).

## 2.18 | Fluorescence recovery after photobleaching (FRAP) analysis

The specific methods are described in the Supporting Information (Data S1).

## 2.19 | Reactive oxygen species (ROS) generation

The specific methods are described in the Supporting Information (Data S1).



13497006, 2024, 10, Downloaded from https://onlinelibrary.wiley.com/doi/10.1111/cas.16306 by Tohoku Iku Yakka Daigaku, Wiley Online Library on [20/04/2025]. See the Terms and Conditions (https://onlinelibrary.wiley.com/terms-and-conditions) on Wiley Online Library for rules of use; OA articles are governed by the applicable Creative Commons License

### 2.20 | Statistical analysis

The statistical analyses were performed using GraphPad Prism version 10.0.2 (GraphPad Software). Differences between two groups were analyzed using an unpaired *t*-test. One-way ANOVA tests were used for three or more groups. $^{*}p<0.05$, $^{**}p<0.01$, $^{***}p<0.001$, and $^{****}p<0.0001$ were considered to indicate statistical significance. All data were expressed as means ± the SEM and represent the results of three independent experiments.

## 3 | RESULTS

### 3.1 | FADS2 is required for CCA tumorigenesis

To identify genes required for tumorigenicity, we investigated serially transplanted xenografts in immunodeficient mice, which were enriched in a subset of the cell population that possesses tumor reconstruction activity. Patient-derived human CCA cells (CHOL1) were subcutaneously implanted into NOG mice and serially passaged into new mice as previously described (Figure 1A), resulting in shorter passage intervals for each generation. Tumor samples were collected at each passage, and an expression microarray was performed. A time-series analysis revealed clusters with an upward trend. We selected genes in clusters that were not previously reported to be associated with CCA. We focused on *FADS2* because *FADS2* mRNA expression increased with serial passaging (Figure 1B). FADS2 knockdown in CHOL1 and TFK-1 cells (Figure 1C) suppressed tumor development in NOG mice (Figure 1D,E). In vitro proliferation capability was also decreased under the treatment of FADS2 knockdown in both two cell lines (Figure 1F). We examined the FADS2 expression in human CCA specimens. Because no anti-FADS2 antibody was available for immunohistochemistry, we performed in situ hybridization of *FADS2* mRNA in FFPE human CCA specimens. *FADS2* mRNA was observed in CCA tumor cells but not in the stroma (Figure 1G). These data suggest that FADS2 is required for tumorigenesis.

### 3.2 | FADS2 inhibitor attenuated cancer cell malignancy

SC26196 is a well-known FADS2 inhibitor.[26] Next, we confirmed that inhibition of FADS2 by SC26196 reduced cell proliferation in both two cell lines (Figure 2A). AKT signaling is known to be involved in cell proliferation.[27] We found that inhibition of FADS2 reduced AKT phosphorylation under the 2-μM SC26196 treatment in both CCA cell lines (Figure 2B).

We performed a sphere-formation assay, which is known to reflect stemness characteristics.[28] Treatment of CHOL1 cells with the FADS2 inhibitor SC26196 (2 μM) reduced their sphere-forming ability by 34.8% compared with controls (Figure 2C). Similar results were obtained in TFK-1 cells (Figure 2C).

Migration activity is one of the hallmarks of cancer.[29] To test the cell migration activity following FADS2 inhibitor treatment, we performed a scratch assay. Treatment with the FADS2 inhibitor reduced the migration capacity by 24% in CHOL1 cells and 50% in TFK-1 cells (Figure 2D).

### 3.3 | Inhibition of FADS2 promoted apoptosis and ferroptosis

Cell death is a factor that determines cancer cell viability, resulting in tumorigenicity. Therefore, we tested whether FADS2 is involved in apoptosis. The early and late apoptotic rates of the two cell lines were increased by FADS2 inhibition (Figure 3A). We measured caspase 3/7 activity, which is a key player in apoptosis,[30] and we found that the apoptotic cell death increased 1.64-fold in CHOL1 cells and 1.32-fold in TFK-1 cells upon treatment with the FADS2 inhibitor compared with the control (Figure 3B and Figure S1A).

Ferroptosis is another form of programmed cell death, characterized by intracellular iron accumulation and lipid peroxidation, and previous studies identified glutathione peroxidase 4 (GPX4) as an essential regulator of this process.[31] Given the crucial role of GPX4 in ferroptosis, we evaluated its expression level in relation to CCA tumorigenicity. Treatment with the FADS2 inhibitor or siFADS2s decreased GPX4 protein expression in both cell lines (Figure 3C and Figure S1B). To confirm this, we measured the GSH/GSSG ratio, which is a marker of ferroptosis.[32] Using a GSH assay, inhibition of FADS2 led to a reduction in the GSH/GSSG ratio by approximately 50.9% in CHOL1 cells and 24.4% in TFK-1 cells compared with the DMSO controls (Figure 3D). These findings suggest that FADS2 inhibition attenuates GPX4 expression and activity in CCA.

### 3.4 | Triglyceride alteration in FADS2-depleted cells

FADS2 is a delta-6 desaturase. We hence measured the saturated and unsaturated FA levels by GC-MS. Both FAs were not significantly changed between FADS2-depleted cells and control cells (Figure S2A,B). To investigate whether the composition of lipids other than FAs was altered, we performed a lipidomics assay. The levels of various lipids, including triglycerides and cholesterol esters, were decreased in FADS2 knockdown cells (Figure 4A,B). To confirm this, we measured the number of lipid droplets, which mainly consist of triglycerides and cholesterol esters, in the cells.[33] The intracellular lipid droplets were stained with Lipi-Green, and the Lipi-Green intensity was measured by flow cytometry. In CHOL1 cells, the number of lipid droplets was reduced by 20.9% by FADS2 knockdown and by 12.0% by FADS2 inhibition (Figure 4C). In TFK-1 cells, the number of lipid droplets was reduced by 17.6% following FADS2 knockdown and by 14.6% following FADS2 inhibition (Figure 4C). These data suggest that depletion of FADS2 reduces intracellular lipids, especially triglycerides.



13497006, 2024, 10, Downloaded from https://onlinelibrary.wiley.com/doi/10.1111/cas.16306 by Tohoku Iku Yakka Daigaku, Wiley Online Library on [20/04/2025]. See the Terms and Conditions (https://onlinelibrary.wiley.com/terms-and-conditions) on Wiley Online Library for rules of use; OA articles are governed by the applicable Creative Commons License

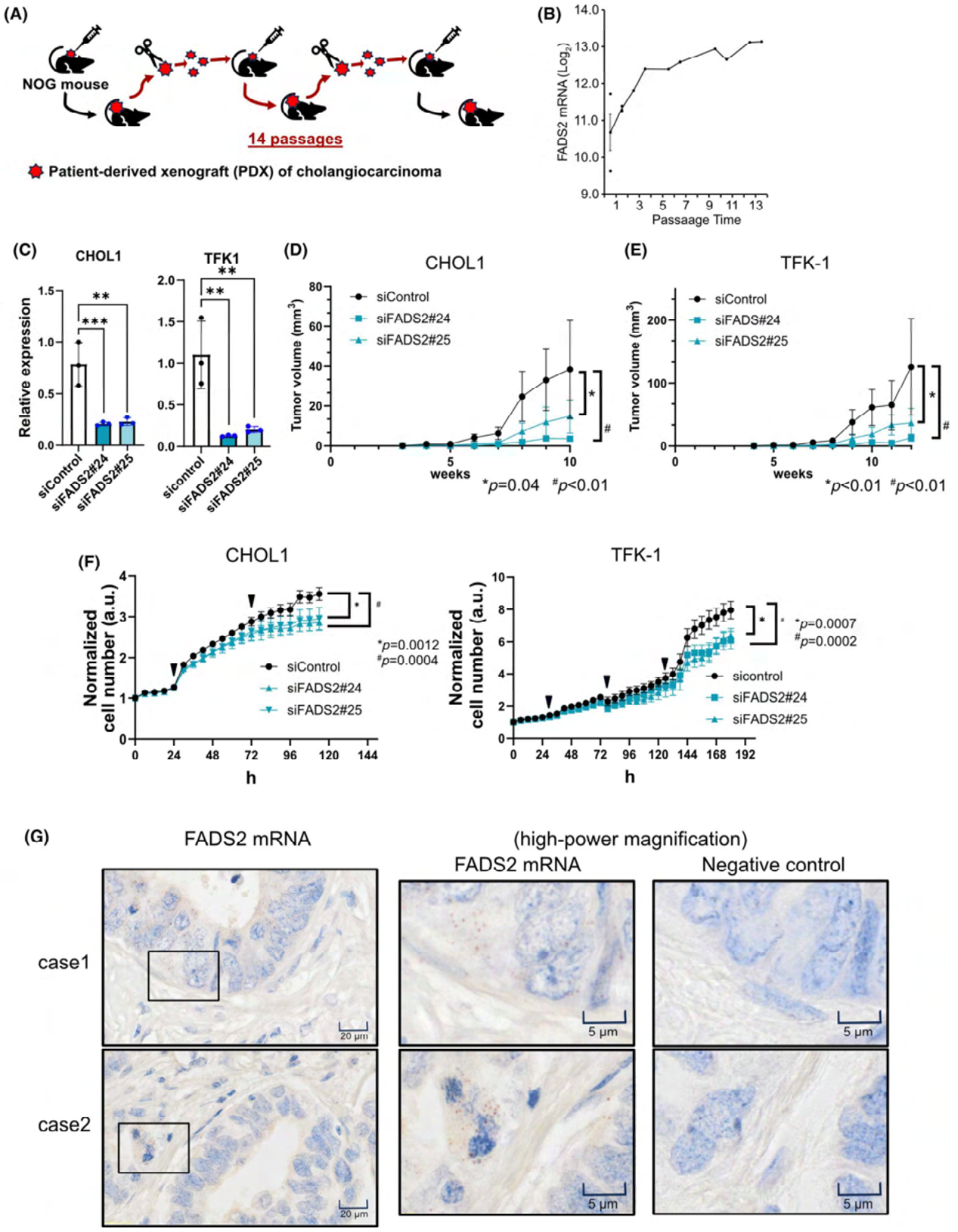


13497006, 2024, 10, Downloaded from https://onlinelibrary.wiley.com/doi/10.1111/cas.16306 by Tohoku Ika Yakka Daigaku, Wiley Online Library on [20/04/2025]. See the Terms and Conditions (https://onlinelibrary.wiley.com/terms-and-conditions) on Wiley Online Library for rules of use; OA articles are governed by the applicable Creative Commons License

FIGURE 1 Fatty acid desaturase 2 (FADS2) is enriched in serially transplanted xenograft cancer cells (A) Schematic outline of the serially transplanted xenograft model. (B) *FADS2* mRNA at each passage point was determined by microarray analysis. (C) FADS2 was knocked down by siRNA, and *FADS2* mRNA expression was measured by real-time PCR. $^{**}p < 0.01$, $^{***}p < 0.001$. (D, E) FADS2 knockdown and control cells were transplanted into NOG mice, and the tumor volumes were measured weekly. (D) CHOL1 cells; (E) TFK-1 cells. *p*-Values were calculated by comparing the nonlinear regression curves of the two groups. (F) Cell proliferation was measured after treatment with siFADS2 using an Incucyte system. Arrowheads indicate the treatment of siRNA. (G) Representative images of *FADS2* mRNA expression in cholangiocarcinoma tissues based on RNAscope assay. *FADS2* positive appeared as brown spots. Bar (low-magnification images), 20 μm. Bar (high-magnification images), 5 μm.

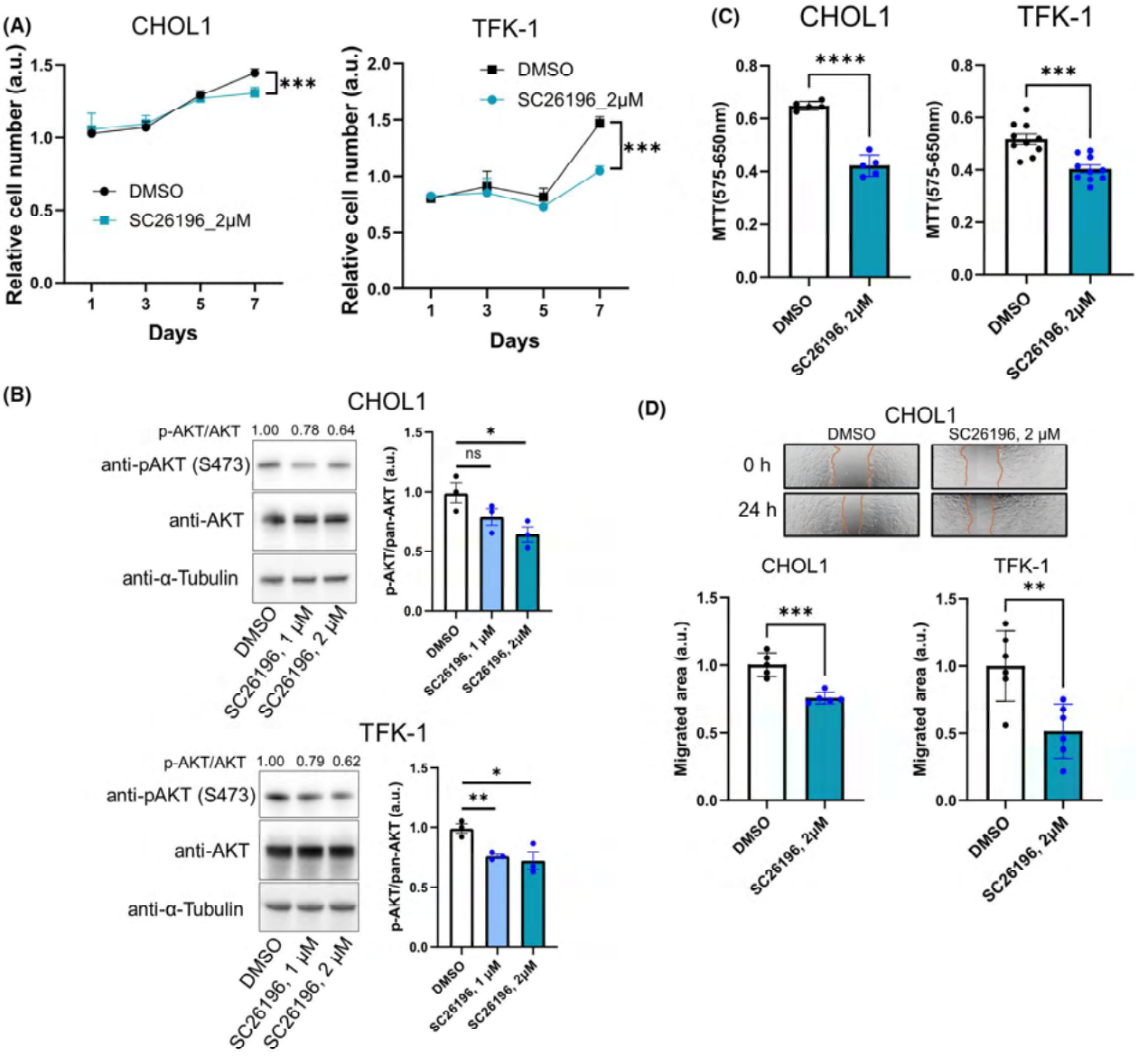


FIGURE 2 Fatty acid desaturase 2 (FADS2) depletion reduces cell proliferation activity. (A) Cell proliferation was measured after treatment with FADS2 inhibitor SC26196 using MTT assay. (B) Western blotting. CHOL1 and TFK-1 cells were harvested at 9 and 4 days after SC26196 addition, respectively. The values indicate the band densities quantified using ImageJ software. (C) Sphere formation assay with SC26196 in CHOL1 and TFK-1 cells using MTT assay. (D) Scratch-wound assay. The migrated areas were measured after 24 h with or without SC26196 treatment. The wound-healing size was quantified using ImageJ software and is shown in the bar graphs. $^{*}p < 0.05$, $^{**}p < 0.01$, $^{***}p < 0.001$, $^{****}p < 0.0001$.



13497006, 2024, 10, Downloaded from https://onlinelibrary.wiley.com/doi/10.1111/cas.16306 by Tohoku Ika Yakka Daigaku, Wiley Online Library on [20/04/2025]. See the Terms and Conditions (https://onlinelibrary.wiley.com/terms-and-conditions) on Wiley Online Library for rules of use; OA articles are governed by the applicable Creative Commons License

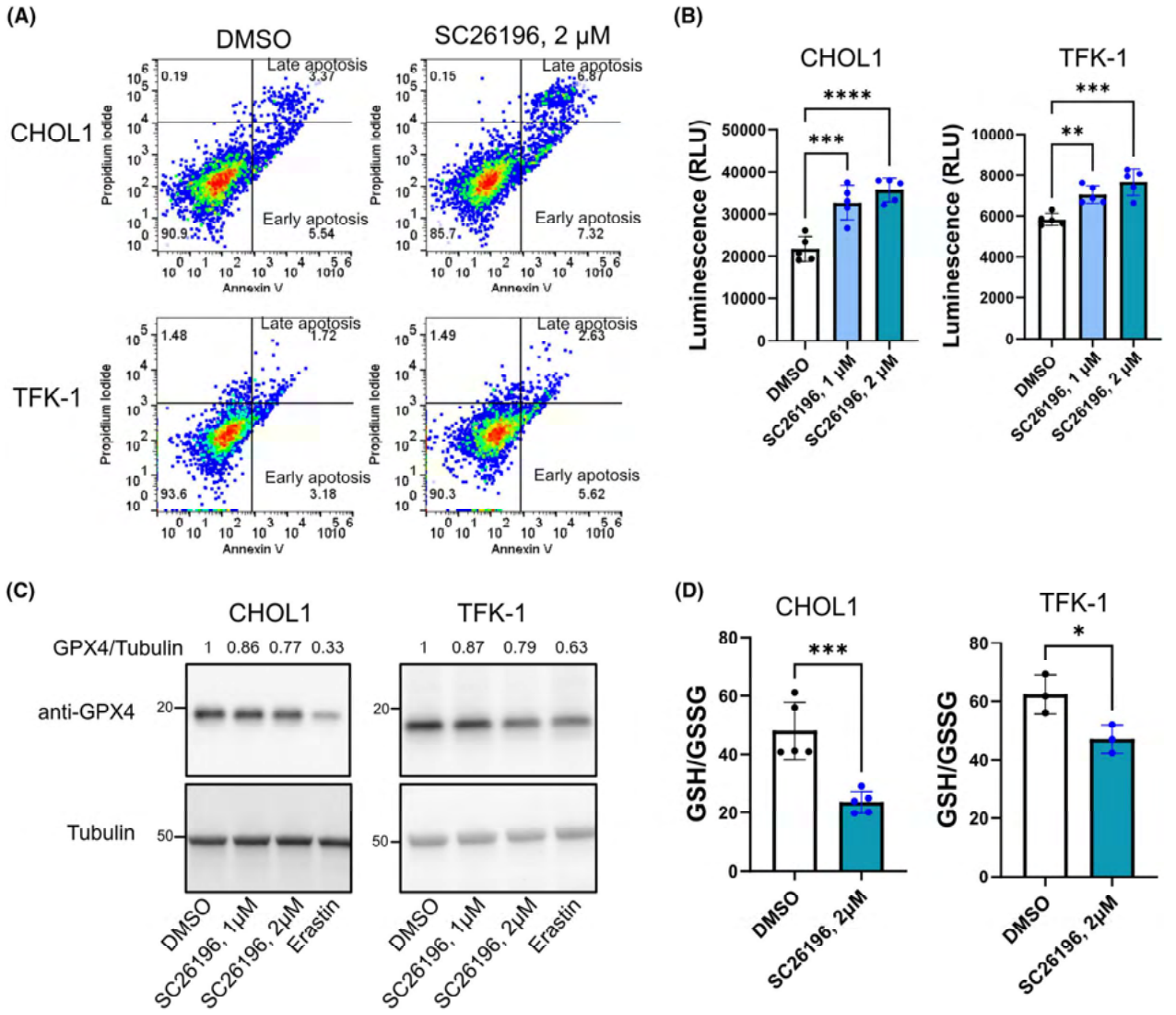


FIGURE 3 Fatty acid desaturase 2 (FADS2) inhibitor alters characteristics of cancer cells. (A) Apoptotic cells were counted by flow cytometry. Apoptotic cells were detected by propidium iodide and/or annexin V-positive staining. (B) Apoptosis assay. Caspase 3/7 activity was measured with a luminometer. (C) Western blotting. Cells were treated with FADS2 inhibitor or erastin (a ferroptosis inducer) for 3 days, and GPX4 protein expression was determined by Western blotting. The values indicate the band densities quantified using ImageJ software. (D) The GSH/GSSG ratio was measured. $^{*}p<0.05$, $^{**}p<0.01$, $^{***}p<0.001$, $^{****}p<0.0001$.

### 3.5 | FADS2 inhibition reduced mitochondrial oxygen consumption ratio in CCA

Fatty acids are released from triglycerides by lipase, and mitochondrial FA beta-oxidation is a major pathway fueling the tricarboxylic acid cycle.[34] To test whether FADS2 depletion alters the beta-oxidation pathway, we measured the mitochondrial oxygen consumption ratio. We found that basal and maximal respiration in CHOL1 and TFK-1 cells was decreased by FADS2 inhibition (Figure 4D). Microarray analysis demonstrated that oxidative phosphorylation pathway was negatively correlated with FADS2-depleted cells (Figure S2C). These data suggested that the beta-oxidation pathway is attenuated by FADS2 inhibition.

## 4 | DISCUSSION

FADS2 is a desaturase that plays an important role in polyunsaturated FA synthesis.[35] Recently, however, other roles of FADS2 have been reported. In adipocytes, FADS2 deficiency promotes TG lipolysis, resulting in a decrease in lipid droplets.[36,37] In mouse liver, ablation of FADS2 increases TG and cholesterol accumulation.[38] SCD1 is an enzyme that catalyzes the synthesis of monounsaturated fatty acids (MUFAs), but it is also known to affect lipid pathways other than desaturation, such as FA uptake, lipogenesis, and β-oxidation.[39] We found that FADS2 knockdown or inhibition did not alter the ratio of unsaturated FAs but significantly reduced the total lipids including triglycerides and cholesterol esters. Our data also demonstrated that the oxygen



13497006, 2024, 10, Downloaded from https://onlinelibrary.wiley.com/doi/10.1111/cas.16306 by Tohoku Ika Yakka Daigaku, Wiley Online Library on [20/04/2025]. See the Terms and Conditions (https://onlinelibrary.wiley.com/terms-and-conditions) on Wiley Online Library for rules of use; OA articles are governed by the applicable Creative Commons License

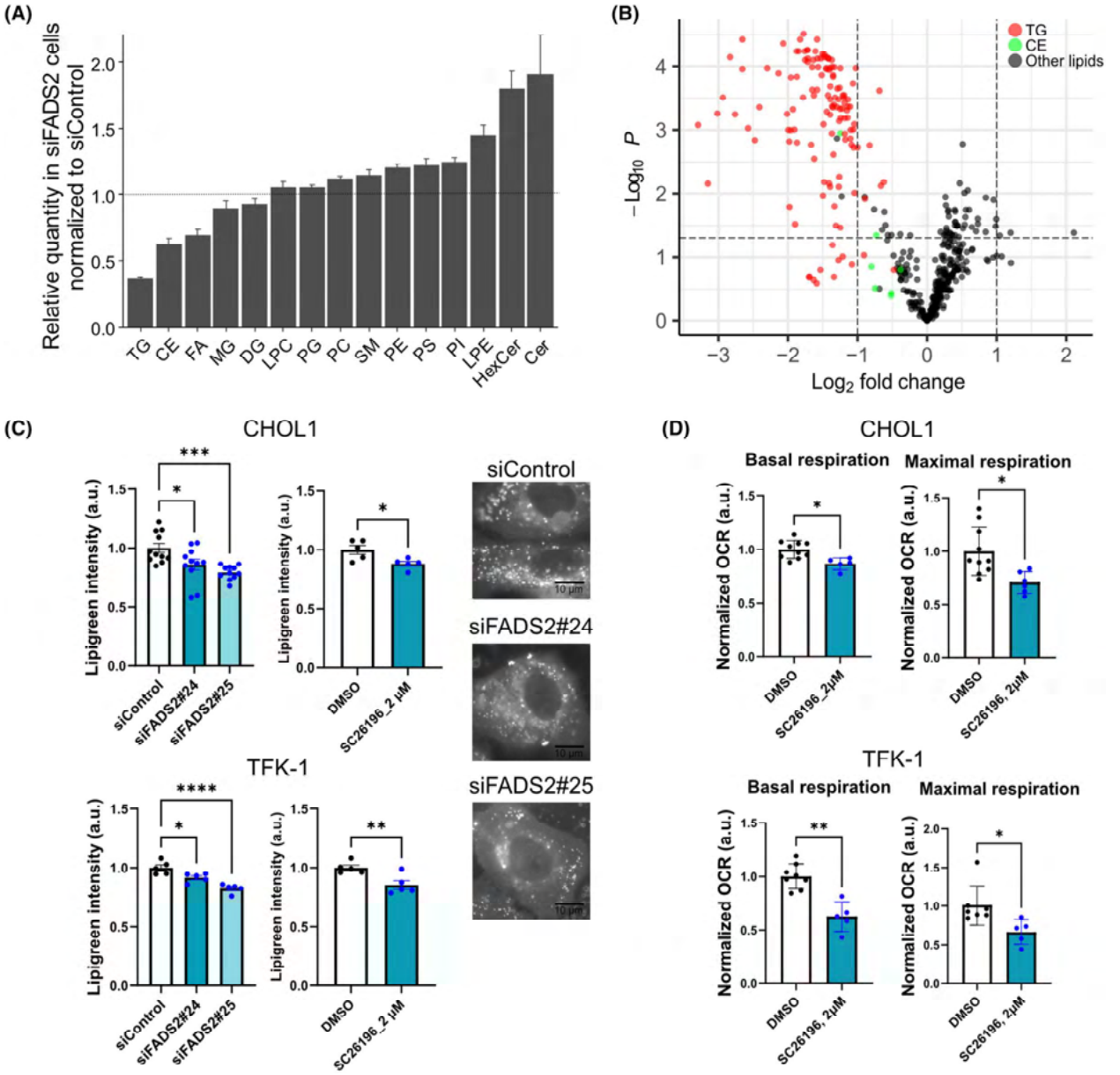


FIGURE 4 Triglyceride is altered in fatty acid desaturase 2 (FADS2)-depleted cells. (A) Lipidomics in FADS2 knockdown CHOL1 cells. Lipids were quantitatively identified by supercritical fluid chromatography–tandem mass spectrometry (SFC-MS/MS) spectrometry and the relative expression of siFADS2s ($n = 9$) to siControl ($n = 3$) was calculated. TG, triglycerides; CE, cholesterol esters; FA, free fatty acids; MG, monoglycerides; DG, diglycerides; LPC, lysophosphatidylcholine; PG, phosphatidylglycerol; PC, phosphatidylcholines; SM, sphingomyelin; PE; phosphatidylethanolamine; PS, phosphatidylserine; PI, phosphatidylinositol; LPE, lysophophatidylethanolamine; HexCer, hexosylceramine; Cer, ceramide. (B) Volcano plot. Fold change was calculated based on the values of siFADS2 to siControl samples. Triglycerides are marked with red circles, and the others are gray. (C) CHOL1 and TFK-1 cells were stained by Lipi-Green, and the intensity was measured by flow cytometry. Representative images of CHOL1 cells are shown (scale bar = 10 μm). (D) The oxygen consumption ratio was measured with a flux analyzer. $^{*}p < 0.05$, $^{**}p < 0.01$, $^{***}p < 0.001$, $^{****}p < 0.0001$.

consumption ratio was decreased in FADS2-depleted cells, suggesting that β-oxidation and ATP production are also decreased.[40] Collectively, FADS2 depletion reduced lipid storage and energy production, resulting in the attenuation of cancer malignancy by reduction of cell proliferation and migration. Although precise mechanisms are still unknown, FADS2 might have a function other than desaturase.

FADS2 is a desaturase enzyme and synthesizes unsaturated FAs, such as ω3, ω6, and ω9. However, in this study, we found no alteration in the amount of unsaturated FAs (Figure S2A,B). Because many biochemical systems including FA synthesis have functional redundancy,[41] other desaturases could recover the pathway in CCA cells. Another possibility is the involvement of a subtle amount of



13497006, 2024, 10, Downloaded from https://onlinelibrary.wiley.com/doi/10.1111/cas.16306 by Tohoku Ika Yakka Daigaku, Wiley Online Library on [20/04/2025]. See the Terms and Conditions (https://onlinelibrary.wiley.com/terms-and-conditions) on Wiley Online Library for rules of use; OA articles are governed by the applicable Creative Commons License

metabolites which are produced by FADS2 but could not be detected in this study and could act as a ligand for the nuclear receptor.[42] In this study, membrane fluidity was reduced in FADS2-depleted cells (Figure S2D). Membrane fluidity is controlled by the lipid composition in membranes, and unsaturated FAs contribute to a greater disorder of membranes than saturated FAs at equal absolute temperatures.[43] In glioma stem cells, knockdown of ELOVL2, a key enzyme in the synthesis of long polyunsaturated FAs, reduced membrane fluidity.[13] In this study, saturated/unsaturated FAs in total cell lysates showed no alteration; nonetheless, it is possible that the proportion of unsaturated FAs located in plasma membrane was altered in FADS2-depleted cells.

We demonstrated that FADS2 depletion reduced the content of triglyceride and cholesterol ester, but how FADS2 is involved in the lipid storage is still unclear. SCD1 affect FA transport proteins, resulting in the decrease of TG in the heart.[39] It is possible that the uptake of FAs and lipoproteins is reduced in FADS2 depletion cells. Another possibility is that lipid storage is degraded (lipolysis) by autophagy.[44] Further study is required to identify the new function of FADS2.

In this study, apoptosis and ferroptosis are increased by FADS2 depletion. In ovarian cancer cells, apoptosis and ferroptosis are also increased by SCD1/FADS2 inhibitors.[12] SCD1/FADS2 inhibitors reduced GPX4 expression and increased reactive oxygen species and lipid peroxidation, resulting in ferroptosis.[32] We also demonstrated the reduction of GPX4 expression, but total cellular and mitochondrial ROS were not altered by FADS2 inhibition (Figure S3). Previous studies showed that SCD1 contributes to resistance to ferroptosis by producing MUFAs,[45,46] but our data showed that FADS2 depletion did not alter the FA composition. Therefore, FADS2 might regulate the ferroptosis via unknown mechanisms. Recent studies demonstrated that FADS2 protein interacts with proteins such as STING, ACSL, and SLC27A2.[47,48] The FADS2–protein complex may play a novel role and further studies are needed to elucidate the mechanisms of cell death by FADS2 depletion.

## AUTHOR CONTRIBUTIONS

**Kohsei Hasegawa:** Formal analysis; investigation; validation; visualization; writing – original draft; writing – review and editing. **Haruna Fujimori:** Formal analysis; funding acquisition; investigation; project administration; validation; visualization; writing – original draft; writing – review and editing. **Kohta Nakatani:** Data curation; methodology; software. **Masatomo Takahashi:** Methodology; software. **Yoshihiro Izumi:** Data curation; methodology; software. **Takeshi Bamba:** Methodology; software. **Mao Nakamura-Shima:** Funding acquisition; resources. **Rie Shibuya-Takahashi:** Validation. **Mai Mochizuki:** Funding acquisition; writing – original draft. **Yuta Wakui:** Funding acquisition; resources. **Makoto Abue:** Resources. **Wataru Iwai:** Resources. **Daisuke Fukushi:** Resources. **Kennichi Satoh:** Funding acquisition; resources. **Kazunori Yamaguchi:** Funding acquisition; writing – original draft. **Norihisa Shindo:** Funding acquisition; writing – original draft. **Jun Yasuda:** Funding acquisition; writing – original draft. **Naoki Asano:** Writing – review and editing. **Takayuki Imai:** Resources. **Yukinori Asada:** Resources. **Yukio Katori:** Resources. **Keiichi Tamai:** Conceptualization; formal analysis; funding acquisition; investigation; project administration; supervision; validation; visualization; writing – original draft; writing – review and editing.

## ACKNOWLEDGMENTS

This study was supported in part by the Biomedical Research Core of the Tohoku University Graduate School of Medicine.

## FUNDING INFORMATION

This study was supported by JSPS KAKENHI (grant no. JP:22K09696, 22K09678, 22K08085, 22K07974, 21K07137, 21K07973, 21K07186, 21H02396, 20K09701, and 19K08430), the Takeda Medical Foundation, the Kobayashi Foundation for Cancer Research, and AMED-BINDS (JP22ama121055 for T.B.) from the Japan Agency for Medical Research and Development (AMED). This work was also partly performed in the MEXT Cooperative Research Project Program, Medical Research Center Initiative for High Depth Omics, and CURE: JPMXP1323015486.

## CONFLICT OF INTEREST STATEMENT

The authors declare no conflict of interest.

## ETHICS STATEMENT

Approval of the research protocol by an Institutional Reviewer Board: Yes (approval number: 2018-010).

Informed Consent: Cholangiocarcinoma tissues were obtained from the Tohoku University Hospital (Sendai, Japan) with written informed consent.

Registry and the Registration No. of the study/trial: NA.

Animal Studies: Approved by the Miyagi Cancer Center Animal Care and Use Committee (approval number: AE.22.01).

## ORCID

*Haruna Fujimori* https://orcid.org/0009-0008-8855-1216

*Keiichi Tamai* https://orcid.org/0000-0003-0813-5885

## REFERENCES

1. Rizvi S, Khan SA, Hallemeier CL, Kelley RK, Gores GJ. Cholangiocarcinoma—evolving concepts and therapeutic strategies. *Nat Rev Clin Oncol*. 2018;15(2):95-111.
2. Banales JM, Cardinale V, Carpino G, et al. Expert consensus document: Cholangiocarcinoma: current knowledge and future perspectives consensus statement from the European network for the study of Cholangiocarcinoma (ENS-CCA). *Nat Rev Gastroenterol Hepatol*. 2016;13(5):261-280.
3. Bertuccio P, Malvezzi M, Carioli G, et al. Global trends in mortality from intrahepatic and extrahepatic cholangiocarcinoma. *J Hepatol*. 2019;71(1):104-114.
4. Kreso A, Dick JE. Evolution of the cancer stem cell model. *Cell Stem Cell*. 2014;14(3):275-291.
5. Afify SM, Seno M. Conversion of stem cells to cancer stem cells: undercurrent of cancer initiation. *Cancer*. 2019;11(3):345.
6. Anderson NM, Simon MC. The tumor microenvironment. *Curr Biol*. 2020;30(16):921-925.



13497006, 2024, 10, Downloaded from https://onlinelibrary.wiley.com/doi/10.1111/cas.16306 by Tohoku Ika Yakka Daigaku, Wiley Online Library on [20/04/2025]. See the Terms and Conditions (https://onlinelibrary.wiley.com/terms-and-conditions) on Wiley Online Library for rules of use; OA articles are governed by the applicable Creative Commons License

7. Fujii E, Suzuki M, Matsubara K, et al. Establishment and characterization of in vivo human tumor models in the NOD/SCID/gamma(c) (null) mouse. *Pathol Int*. 2008;58(9):559-567.
8. Brown KM, Xue A, Mittal A, Samra JS, Smith R, Hugh TJ. Patient-derived xenograft models of colorectal cancer in pre-clinical research: a systematic review. *Oncotarget*. 2016;7(40):66212-66225. Accessed October,13. https://www.ncbi.nlm.nih.gov/pmc/articles/PMC5323228/
9. Kobayashi S, Yamada-Okabe H, Suzuki M, et al. LGR5-positive colon cancer stem cells interconvert with drug-resistant LGR5-negative cells and are capable of tumor reconstitution. *Stem Cells*. 2012;30(12):2631-2644.
10. Currie E, Schulze A, Zechner R, Walther TC, Farese RV. Cellular fatty acid metabolism and cancer. *Cell Metab*. 2013;18(2):153-161.
11. Li J, Condello S, Thomes-Pepin J, et al. Lipid desaturation is a metabolic marker and therapeutic target of ovarian cancer stem cells. *Cell Stem Cell*. 2017;20(3):303-314.
12. Xuan Y, Wang H, Yung MM, et al. SCD1/FADS2 fatty acid desaturases equipoise lipid metabolic activity and redox-driven ferroptosis in ascites-derived ovarian cancer cells. *Theranostics*. 2022;12(7):3534-3552.
13. Gimple RC, Kidwell RL, Kim LJY, et al. Glioma stem cell-specific Superenhancer promotes polyunsaturated fatty-acid synthesis to support EGFR signaling. *Cancer Discov*. 2019;9(9):1248-1267.
14. Imai T, Tamai K, Oizumi S, et al. CD271 defines a stem cell-like population in hypopharyngeal cancer. *PLoS One*. 2013;8(4):e62002.
15. Yasumoto A, Fujimori H, Mochizuki M, et al. BEX2 is poor prognostic factor and required for cancer stemness in gastric cancer. *Biochem Biophys Res Commun*. 2023. Accessed March, 16. https://www.sciencedirect.com/science/article/pii/S0006291X23003029;655:59-67.
16. Tamai K, Nakamura-Shima M, Shibuya-Takahashi R, et al. BEX2 suppresses mitochondrial activity and is required for dormant cancer stem cell maintenance in intrahepatic cholangiocarcinoma. *Sci Rep*. 2020;10(1):21592. doi:10.1038/s41598-020-78539-0
17. Fukushi D, Shibuya-Takahashi R, Mochizuki M, et al. BEX2 is required for maintaining dormant cancer stem cell in hepatocellular carcinoma. *Cancer Sci*. 2021;112:4580-4592.
18. Katayama H, Tamai K, Shibuya R, et al. Long non-coding RNA HOTAIR promotes cell migration by upregulating insulin growth factor-binding protein 2 in renal cell carcinoma. *Sci Rep*. 2017;7(1):12016.
19. R Core Team. *R: A Language and Environment for Statistical Computing*. R Foundation for Statistical Computing; 2019. https://www.R-project.org/
20. Subramanian A, Tamayo P, Mootha VK, et al. Gene set enrichment analysis: a knowledge-based approach for interpreting genome-wide expression profiles. *Proc Natl Acad Sci USA*. 2005;102(43):15545-15550.
21. Nueda MJ, Tarazona S, Conesa A. Next maSigPro: updating maSigPro bioconductor package for RNA-seq time series. *Bioinformatics*. 2014;30(18):2598-2602.
22. Corenblum M, McRobbie-Johnson A, Carruth E, et al. Parallel neurodegenerative phenotypes in sporadic parkinson's disease fibroblasts and midbrain dopamine neurons. *Prog Neurobiol*. 2023;229:102501.
23. Bligh EG, Dyer WJ. A rapid method of total lipid extraction and purification. *Can J Biochem Physiol*. 1959;37(8):911-917.
24. Fushimi T, Izumi Y, Takahashi M, Hata K, Murano Y, Bamba T. Dynamic metabolome analysis reveals the metabolic fate of medium-chain fatty acids in AML12 cells. *J Agric Food Chem*. 2020;68(43):11997-12010.
25. Takeda H, Izumi Y, Takahashi M, et al. Widely-targeted quantitative lipidomics method by supercritical fluid chromatography triple quadrupole mass spectrometry. *J Lipid Res*. 2018;59(7):1283-1293.
26. Harmon SD, Kaduce TL, Manuel TD, Spector AA. Effect of the delta6-desaturase inhibitor SC-26196 on PUFA metabolism in human cells. *Lipids*. 2003;38(4):469-476.
27. Revathidevi S, Munirajan AK. Akt in cancer: mediator and more. *Semin Cancer Biol*. 2019;59:80-91.
28. Ishiguro T, Ohata H, Sato A, Yamawaki K, Enomoto T, Okamoto K. Tumor-derived spheroids: relevance to cancer stem cells and clinical applications. *Cancer Sci*. 2017;108(3):283-289.
29. Hanahan D. Hallmarks of cancer: new dimensions. *Cancer Discov*. 2022;12(1):31-46.
30. McIlwain DR, Berger T, Mak TW. Caspase functions in cell death and disease. *Cold Spring Harb Perspect Biol*. 2013;5(4):a008656.
31. Ma T, Du J, Zhang Y, Wang Y, Wang B, Zhang T. GPX4-independent ferroptosis—a new strategy in disease's therapy. *Cell Death Dis*. 2022;8(1):434.
32. Ursini F, Maiorino M. Lipid peroxidation and ferroptosis: the role of GSH and GPx4. *Free Radic Biol Med*. 2020;152:175-185.
33. Zhang C, Liu P. The lipid droplet: a conserved cellular organelle. *Protein Cell*. 2017;8(11):796-800.
34. Houten SM, Violante S, Ventura FV, Wanders RJA. The biochemistry and physiology of mitochondrial fatty acid β-oxidation and its genetic disorders. *Annu Rev Physiol*. 2016;78:23-44.
35. Glaser C, Heinrich J, Koletzko B. Role of FADS1 and FADS2 polymorphisms in polyunsaturated fatty acid metabolism. *Metabolism*. 2010;59(7):993-999.
36. Wang C, Hucik B, Sarr O, et al. Delta-6 desaturase (Fads2) deficiency alters triacylglycerol/fatty acid cycling in murine white adipose tissue. *J Lipid Res*. 2023;64(6):100376.
37. Wang C, MacIntyre B, Mutch DM. Inhibition of Δ-6 desaturase reduces fatty acid re-esterification in 3T3-L1 adipocytes independent of changes in n3-PUFA cellular content. *Biochim Biophys Acta Mol Cell Biol Lipids*. 2022;1867(7):159160.
38. Hayashi Y, Lee-Okada HC, Nakamura E, et al. Ablation of fatty acid desaturase 2 (FADS2) exacerbates hepatic triacylglycerol and cholesterol accumulation in polyunsaturated fatty acid-depleted mice. *FEBS Lett*. 2021;595(14):1920-1932.
39. Dobrzyn P, Bednarski T, Dobrzyn A. Metabolic reprogramming of the heart through stearoyl-CoA desaturase. *Prog Lipid Res*. 2015;57:1-12.
40. Fukaya M, Sato Y, Kondo S, Adachi SI, Yoshizawa F, Sato Y. Quercetin enhances fatty acid β-oxidation by inducing lipophagy in AML12 hepatocytes. *Heliyon*. 2021;7(6):e07324.
41. Ruppe S, Mains K, Fox JM. A kinetic rationale for functional redundancy in fatty acid biosynthesis. *Proc Natl Acad Sci USA*. 2020;117(38):23557-23564.
42. Sampath H, Ntambi JM. Polyunsaturated fatty acid regulation of gene expression. *Nutr Rev*. 2004;62(9):333-339.
43. Holte LL, Peter SA, Sinnwell TM, Gawrisch K. 2H nuclear magnetic resonance order parameter profiles suggest a change of molecular shape for phosphatidylcholines containing a polyunsaturated acyl chain. *Biophys J*. 1995;68(6):2396-2403.
44. Grabner GF, Xie H, Schweiger M, Zechner R. Lipolysis: cellular mechanisms for lipid mobilization from fat stores. *Nat Metab*. 2021;3(11):1445-1465.
45. Luis G, Godfroid A, Nishiumi S, et al. Tumor resistance to ferroptosis driven by Stearoyl-CoA Desaturase-1 (SCD1) in cancer cells and fatty acid biding Protein-4 (FABP4) in tumor microenvironment promote tumor recurrence. *Redox Biol*. 2021;1(43):102006.
46. *Long noncoding RNA LINC01606 protects colon cancer cells from ferroptotic cell death and promotes stemness by SCD1–Wnt/β-catenin–TFE3 feedback loop signalling—Luo—2022—clinical and translational medicine—wiley online library*. 2024. https://onlinelibrary.wiley.com/doi/full/10.1002/ctm2.752.
47. Vila IK, Chamma H, Steer A, et al. STING orchestrates the crosstalk between polyunsaturated fatty acid metabolism and inflammatory responses. *Cell Metab*. 2022;34(1):125-139.




13497006, 2024, 10, Downloaded from https://onlinelibrary.wiley.com/doi/10.1111/cas.16306 by Tohoku Iku Yakka Daigaku, Wiley Online Library on [20/04/2025]. See the Terms and Conditions (https://onlinelibrary.wiley.com/terms-and-conditions) on Wiley Online Library for rules of use; OA articles are governed by the applicable Creative Commons License

48. Chu H, Zhao Q, Liu J, et al. Ionic liquid-based extraction system for in-depth analysis of membrane protein complexes. *Anal Chem*. 2022;94(2):758-767.

## SUPPORTING INFORMATION

Additional supporting information can be found online in the Supporting Information section at the end of this article.

**How to cite this article:** Hasegawa K, Fujimori H, Nakatani K, et al. Delta-6 desaturase FADS2 is a tumor-promoting factor in cholangiocarcinoma. *Cancer Sci*. 2024;115:3346-3357. doi:10.1111/cas.16306



13497006, 2024, 10, Downloaded from https://onlinelibrary.wiley.com/doi/10.1111/cas.16306 by Tohoku Ika Yakka Daigaku, Wiley Online Library on [20/04/2025]. See the Terms and Conditions (https://onlinelibrary.wiley.com/terms-and-conditions) on Wiley Online Library for rules of use; OA articles are governed by the applicable Creative Commons License

＜脳神経内科学＞
教授　　中島　一郎
教授　　藤盛　寿一
講師　　中村　正史
講師　　小林　理子
講師　　宮澤　康一
助教　　石垣　あや
助教　　市川　大
助教　　東野　将志
助教　　八木橋　崇仁
助手　　萩野　琢郎

## 神経免疫疾患の病態解析

神経免疫疾患とは、自己免疫学機序によって生じる神経筋疾患の総称である。多発性硬化症（Multiple sclerosis: MS）、視神経脊髄炎、重症筋無力症、HTLV-1 関連脊髄症、炎症性筋疾患、慢性炎症性脱髄性多発神経炎などの指定難病や、ギラン・バレー症候群、自己免疫性脳炎、MOG 抗体関連疾患、急性散在性脳脊髄炎、膠原病などの内科的疾患に伴う神経疾患、腫瘍随伴症候群としての神経筋疾患、薬剤性の神経筋疾患などが含まれる。

当科は、多発性硬化症、視神経脊髄炎、MOG 抗体関連疾患を主たる対象疾患とし、病態解析ならびに、予後改善に向けた様々な臨床研究を行っている。

### MS における脳萎縮解析

MS は若年者に好発する中枢神経系の炎症性脱髄疾患である。発症後しばらくは再発期と寛解期を繰り返す再発寛解型 MS として経過するが、約半数は次第に再発の有無にかかわらず病状が進行する二次進行型 MS に移行する。再発寛解期には炎症に伴う脱髄が病態の主体をなすが、進行期に入ると神経変性が病態の主体をなすようになり脳萎縮が目立つようになる。脳萎縮が不可逆的に進行すると身体機能障害や高次脳機能障害といった障害が出現し後遺症として残存する。

我々はこれまで、MS 症例の脳 MRI 画像を FreeSurfer とよばれる画像解析ソフトを用いて横断的に解析してきたが、今回、各脳領域における容積変化を 2 年間にわたり縦断的に観察した。その結果、11 領域における脳容積の変化率は、異なる領域間で近似し、再発性の再発寛解型 MS、再発のない再発寛解型 MS、二次進行型 MS の 3 群間で類似していた（図1）。これらのことから、脳萎縮は MS 脳内でびまん性に進行すること、再発寛解型 MS と二次進行型 MS

は、同一スペクトラム上にある連続帯であり、MS では早期から脳萎縮が持続的に生じていることが示された。

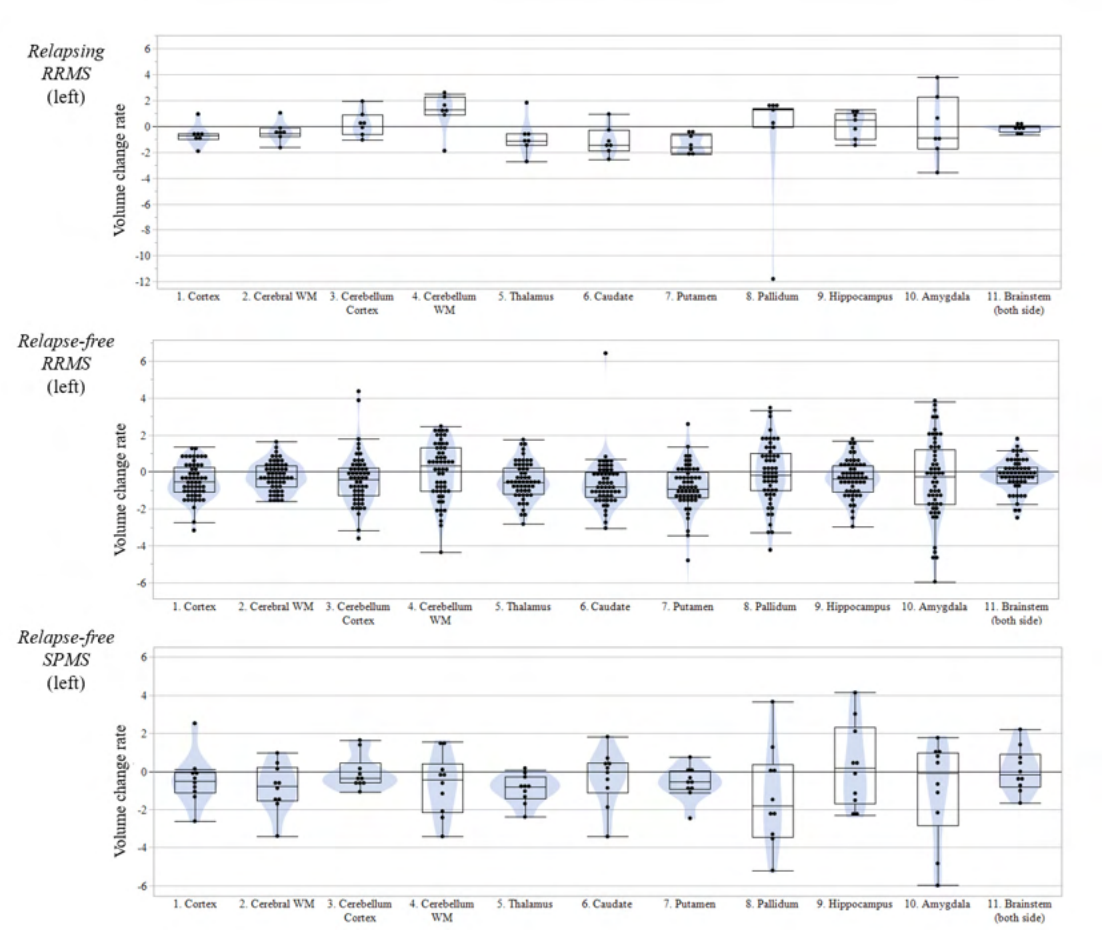


図1. 領域別にみた局所脳容積の変化率。上段は、再発を認めた再発寛解型 MS (n = 7)、中段は、再発を認めなかった再発寛解型 MS (n = 56)、下段は再発を認めなかった二次進行型 MS (n = 10) における脳容積変化率をそれぞれ示している。

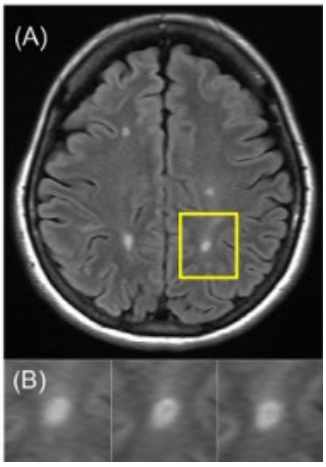


また、MS では, slowly expanding lesion (SEL)と呼ばれる脳 MRI 画像所見が認められ, 慢性炎症を反映すると考えられている. 日本人 MS 患者では 35%の症例で SEL が認められ, その増加は灰白質萎縮と相関することを報告した。慢性的な脳内炎症が脳萎縮に結び付くことが示された。

図2. Slowly expanding lesion (SEL)。(A) 左頭頂葉の SEL。(B) 黄色ボックス内病変の拡大図. ベースライン (左)、12 ヶ月後 (中央)、24 か月後 (右)

論文（英文）

1. **Stochastic models for the onset and disease course of multiple sclerosis**. Akaishi T, Misu T, Takahashi T, Fujihara K, Fujimori J, Nakashima I, et al. ***Clin Neurol Neurosurg***. 239: 108224. doi: 10.1016/j.clineuro.2024.108224. 2024

2. **Real-world management of patients with neuromyelitis optica spectrum disorder using satralizumab: Results from a Japanese claims database**. Nakashima I, Nakahara J, Yasunaga H, Yamashita M, Nishijima N, Satomura A, et al. ***Mult Scler Relat Disord***. 84: 105502. doi: 10.1016/j.msard.2024.105502. 2024

3. **Continuous diffuse brain atrophy independent of relapse as a hallmark of multiple sclerosis beginning from relapsing-remitting stage**. Akaishi T, Fujimori J, Yokote H, Nakashima I. ***Clin Neurol Neurosurg***. 242: 108342. doi: 10.1016/j.clineuro.2024.108342. 2024

4. **Primary Angiitis of the Central Nervous System with Pathological Findings of Eosinophilic Granulomatosis with Polyangiitis**. Yamashita K, Miyazawa K, Murakami K, Nakashima I. ***Intern Med***. 63: 1939. doi: 10.2169/internalmedicine.2793-23. 2024

5. **Different Complement Activation Patterns Following C5 Cleavage in MOGAD and AQP4-IgG+NMOSD**. Kaneko K, Kuroda H, Matsumoto Y, Sakamoto N, Yamazaki N, Yamamoto N, et al. ***Neurol Neuroimmunol Neuroinflamm***. 11: e200293. doi: 10.1212/NXI.0000000000200293. 2024

6. **Statistical evaluation of cluster formation of relapse in neuromyelitis optica spectrum disorder**. Akaishi T, Nakashima I. ***Neural Regen Res***. 19: 1888. doi: 10.4103/1673-5374.390980. 2024

7. **Characterization of Japanese multiple sclerosis patients with progression independent of relapse activity: A 2-year multicenter cohort study**. Yokote H, Miyazaki Y, Fujimori J, Nishida Y, Toru S, Niino M, et al. ***J Neuroimmunol***. 394: 578407. doi: 10.1016/j.jneuroim.2024.578407. 2024

8. **Clinical practice guidelines for multiple sclerosis, neuromyelitis optica spectrum disorder, and myelin oligodendrocyte glycoprotein antibody-associated disease 2023 in Japan**. Niino M, Isobe N, Araki M, Ohashi T, Okamoto T, Ogino M, et al. ***Mult Scler Relat Disord***. 90: 105829. doi: 10.1016/j.msard.2024.105829. 2024

9. **Efficacy and Safety of Ravulizumab in Adults With Anti-Aquaporin-4 Antibody-Positive (AQP4-Ab+) Neuromyelitis Optica Spectrum Disorder (NMOSD): Interim Analysis From the Ongoing Phase 3 CHAMPION-NMOSD Trial**. Pittock S, Barnett M, Bennett J, Berthele A, De Seze J, Levy M, et al. ***Neurology***. 103: S99. doi:

10.1212/01.wnl.0001051664.43530.b7. 2024

10. **Safety and Effectiveness of Satralizumab in Japanese Patients with Neuromyelitis Optica Spectrum Disorder: A 6-month Interim Analysis of Post-marketing Surveillance**. Yamamura T, Isobe N, Kawachi I, Nohara C, Miyazaki Y, Tomita M, et al. ***Neurol Ther***. 13: 1361. doi: 10.1007/s40120-024-00640-7. 2024

11. **Cryptococcal Choroid Plexitis and Ependymitis in Progressive Dementia**. Okajima N, Ogawa R, Fujimori J, Nakashima I. Intern Med. doi: 10.2169/internalmedicine.4547-24. 2024

12. **Prevalence of, and Disability Due to, Multiple Sclerosis and Neuromyelitis Optica Spectrum Disorder in Japan by the Fifth Nationwide Survey**. Watanabe M, Isobe N, Niino M, Nakashima I, Matsushita T, Sakai Y, et al. ***Neurology***. 103: e209992. doi: 10.1212/WNL.0000000000209992. 2024

13. **Slowly expanding lesions are associated with disease activity and gray matter loss in relapse-onset multiple sclerosis**. Yokote H, Miyazaki Y, Fujimori J, Nishida Y, Toru S, Niino M, et al. ***J Neuroimaging***. 34: 758. doi: 10.1111/jon.13243. 2024

14. **The real-world impact of biologics for NMOSD: A retrospective single-center study compared with natural course and conventional treatments in Japanese**. Yamazaki N, Misu T, Matsumoto Y, Takai Y, Namatame C, Ono H, et al. ***Mult Scler Relat Disord***. 92: 106176. doi: 10.1016/j.msard.2024.106176. 2024

15. **Employment status of multiple sclerosis patients in Japan**. Nakashima I, Tanaka N. ***J Med Econ***. 27: 1507. doi: 10.1080/13696998.2024.2427510. 2024

16. **Clinical value of the Japanese version of patient-reported multiple sclerosis neuropsychological screening questionnaire**. Muryoi A, Nei M, Fujimori J, Nakashima I. ***Clinical and Experimental Neuroimmunology***. n/a. doi: 10.1111/cen3.12829. 2025

論文（和文）

1. **【リウマチ性疾患診療における自己抗体アップデート】視神経脊髄炎関連疾患関連自己抗体**. 中村 正史, 中島 一郎. *リウマチ科*. 71: 396. 2024

2. **各種疾患 脱髄・免疫性疾患 本邦における MOG 抗体関連疾患の疫学と実態**. 中村 正史, 中島 一郎. Annual Review 神経. 2024: 199. 2024

3. **初診時出血性病変が検出されず,髄軟膜病変と血管周囲腔拡大のみ呈したアミロイド β 関連血管炎の 1 例**. 市川 大, 柳澤 俊晴, 大森 泰文, 鎌田 幸子. *脳卒中*. 46: 239. 2024

4. **疾患修飾薬未治療の多発性硬化症患者におけるフマル酸ジメチル(テクフィデラ)の安全性と有効性 国内使用成績調査中間報告**. 大橋 高志, 中島 一郎, 深澤 俊行, 佐藤 竜介, 牧岡 大器, 土屋 文, et al. *診療と新薬*. 61: 401. 2024

5. **「精神神経医学」を再考する 精神医学と神経医学のボーダーランド**. 曾根 大地, 品川 俊一郎, 藤盛 寿一, 高尾 昌樹, 兼本 浩祐. *精神神経学雑誌*. 126: 577. 2024

6. **【神経疾患治療の進歩2023】脱髄疾患(中枢神経系)の治療の進歩**. 中村 正史, 中島 一郎. *神経治療学*. 41: 725. 2024

学会発表（海外）

1. **Effectiveness and Safety of Satralizumab in a Real-world Clinical Setting in Japan: Interleukin-6 Receptor Inhibition in Neuromyelitis Optica Spectrum Disorders: A Six-month Interim Analysis of Multicenter Medical Chart Review**. Fujihara K, Isobe N, Miyamoto K, Niino M, Nakahara J, Hattori S, Yamamoto M, Kawachi I, Matsui N, Nohara C, Kokubun N, Chihara N, Misu T, Okada K, Yamashita K, Nagatsuka T, Adachi H, Nakashima I. The 40th Congress of the European Committee for Treatment and Research in Multiple Sclerosis. Copenhagen, Denmark. September 2024. Multiple Sclerosis Journal. 2024;30(3):663-4.
2. **Quality of life in patients with multiple sclerosis**. Fujimori J, Nei M, Nakashima I. The 40th Congress of the European Committee for Treatment and Research in Multiple Sclerosis. Copenhagen, Denmark. September 2024. Multiple Sclerosis Journal. 2024;30(3):728-.
3. **Distinct CSF complement activation pattern following C5 cleavage in MOGAD and AQP4-IgG+NMOSD**. Kaneko K, Kuroda H, Matsumoto Y, Sakamoto N, Yamazaki N, Yamamoto N, Umezawa S, Namatame C, Ono H, Takai Y, Takahashi T, Fujimori J, Nakashima I, Harigaya Y, Fujihara K, Misu T, Aoki M. The 40th Congress of the European Committee for Treatment and Research in Multiple Sclerosis. Copenhagen, Denmark. September 2024. Multiple Sclerosis Journal. 2024;30(3):134-5.
4. **Long-term safety, effectiveness, and corticosteroid sparing effects of eculizumab in patients with AQP4Ab+neuromyelitis optica spectrum disorder: realworld data from Japan.** Nakahara J, Nakashima I, Yokote H, Isobe N, Yajima T, Hasegawa K, Fujihara K. The 40th Congress of the European Committee for Treatment and Research in Multiple Sclerosis. Copenhagen, Denmark. September 2024. Multiple Sclerosis Journal. 2024;30(3):143-4.
5. **Analyzing the Impact of Blood-Brain Barrier Dysfunction on Clinical Phenotypes in Multiple Sclerosis**. Nishihara H, Matsuo K, Fujisawa M, Engelhardt B, Miyazaki Y, Niino M, Fujimori J, Nakashima I, Nakamori M. The 40th Congress of the European Committee for Treatment and Research in Multiple Sclerosis. Copenhagen, Denmark. September 2024. Multiple Sclerosis Journal. 2024;30(3):1149-.
6. **Mapping myelin oligodendrocyte glycoprotein antibodyassociated disease (MOGAD) and neuromyelitis optica spectrum disorder (NMOSD) global registries: A comprehensive review of publicly listed patient disease registries**. Palace J, Marignier R, Abend A, Banwell B, Broadley S, Contentti E C, Chitnis T, deFiebre G, Flanagan E, Filippi

M, Fujihara K, Galleguillos L, Geraldes R, Gonzalez A, Greenberg B M, Hamid S, Hor J Y, Huda S, Kim H J, Kister I, Lefelar J, Levy M, Messina S, Mochan A, Nakashima I, Panahloo Z, Pandit L, Patsa S, Podlecka-Pietowska A, Ramanathan S, Rojas J I, Sadiq E, Santoro J, Sotirchos E, Tenembaum S, Tian D C, Shi F D, Yeaman M, Paul F. The 40th Congress of the European Committee for Treatment and Research in Multiple Sclerosis. Copenhagen, Denmark. September 2024. Multiple Sclerosis Journal. 2024;30(3):148-50.

7. **Time-series analysis of information processing speed indicates white matter integrity changes in patients with multiple sclerosis**. Umezawa S, Matsumoto Y, Tatewaki Y, Sakamoto N, Yamamoto N, Yamazaki N, Namatame C, Ono H, Kaneko K, Takai Y, Kuroda H, Fujihara K, Fujimori J, Misu T, Taki Y, Aoki M. The 40th Congress of the European Committee for Treatment and Research in Multiple Sclerosis. Copenhagen, Denmark. September 2024. Multiple Sclerosis Journal. 2024;30(3):931-2.
8. **Different activation pattern of late complement pathway in the CSF between MOGAD and AQP4+NMOSD**. Kaneko K, Kuroda H, Ono H, Matsumoto Y, Yamazaki N, Yamamoto N, Umezawa S, Namatame C, Takai Y, Takahashi T, Fujimori J, Fujimori I, Harigaya Y, Fujihara K, Misu T, Aoki M. The 16th Congress of the Pan-Asian Committee for Treatment and Research in Multiple Sclerosis. Bangkok, Thailand. October 2024. Multiple Sclerosis Journal. 2024;30(9):NP5-NP.
9. **Immunosuppressive Therapy Used For Patients With NMOSD Treated With Satralizumab In Japan: A RealWorld Study**. Nakashima I, Nakahara J, Yasunaga H, Yamashita M, Nishijima N, Satomura A, Nio M, Fujihara K. The 16th Congress of the Pan-Asian Committee for Treatment and Research in Multiple Sclerosis. Bangkok, Thailand. October 2024. Multiple Sclerosis Journal. 2024;30(9):NP14-NP.
10. **Satralizumab for Relapse In Patients With NMOSD In Japan: Analysis Of Real-World Data**. Nakashima I, Nakahara J, Yasunaga H, Yamashita M, Nishijima N, Satomura A, Nio M, Fujihara K. The 16th Congress of the Pan-Asian Committee for Treatment and Research in Multiple Sclerosis. Bangkok, Thailand. October 2024. Multiple Sclerosis Journal. 2024;30(9):NP13-NP.
11. **A Multicentre Retrospective Observational Study To Investigate The Current Natalizumab Treatment Status In Japan -REFIND Study**. Nakashima I, Ohashi T, Kanda M, Tani Y, Yokoyama K. The 16th Congress of the Pan-Asian Committee for Treatment and Research in Multiple Sclerosis. Bangkok, Thailand. October 2024. Multiple Sclerosis Journal. 2024;30(9):NP14-NP5.

学会発表(国内)

1. **質問表を利用した多発性硬化症患者への面談介入による QOL 変化の分析(第 1 報)**. 根井 道子, 及川 寛未, 阿部 美和子, 鳥居 みえ, 中村 正史, 藤盛 寿一, 半田 厚子, 中島 一郎. 第 65 回日本神経学会学術大会, 東京, 2024 年 5 月, 臨床神経学. 64: S433. 2024
2. **多発性硬化症における COVID-19 感染に対する疾患修飾療法の影響**. 小川 泰佑, 藤盛 寿一, 菊池 大輔, 中島 一郎. 第 65 回日本神経学会学術大会, 東京, 2024 年 5 月, 臨床神経学. 64: S439. 2024
3. **日本人多発性硬化症患者における認知機能と QOL,疲労,抑うつの縦断的解析**. 新野 正明, 福元 尚子, 宮崎 雄生, 三條 伸夫, 大橋 高志, 竹内 英之, 藤盛 寿一, 奥野 龍禎, 深浦 彦彰, 清水 優子, 高橋 恵里, 三船 恒裕. 第 65 回日本神経学会学術大会, 東京, 2024 年 5 月, 臨床神経学. 64: S236. 2024
4. Functional Neurological Disorders **多発性硬化症と FND**. 中島 一郎. 第 65 回日本神経学会学術大会, 東京, 2024 年 5 月, 臨床神経学. 64: S130. 2024
5. Progression independent of relapse activity in patients with relapsing multiple sclerosis in Japan. 横手裕明, 宮﨑雄生, 藤盛寿一, 西田陽一郎, 融 衆太, 三浦義治, 新野正明, 中島一郎, 横田隆徳. 第 65 回日本神経学会学術大会, 東京, 2024 年 5 月
6. Different activation pattern of late complement pathway in the CSF between MOGAD and AQP4+NMOSD. 金子仁彦, 黒田 宙, 松本勇貴, 阪本直広, 梅澤周, 山本尚輝, 山﨑直也, 生田目知尋, 小野紘彦, 高井良樹, 高橋利幸, 藤盛寿一, 中島一郎, 針谷康夫, 藤原一男, 三須建郎, 青木正志. 第 65 回日本神経学会学術大会, 東京, 2024 年 5 月
7. **抗発作薬で加療した持続性認知障害**. 安藤 賀子, 市川 大, 猪股 拓海, 大川 聡. 第113回日本神経学会東北地方会, 仙台, :2024年9月, 臨床神経学. 64: 908. 2024
8. **対麻痺で発症したリウマチ性髄膜炎の一例**. 岡島 なるみ, 中村 正史, 萩野 琢郎, 東野 将志, 市川 大, 石垣 あや, 小林 理子, 宮澤 康一, 藤盛 寿一, 中島 一郎. 第113回日本神経学会東北地方会, 仙台, :2024年9月, 臨床神経学. 64: 909. 2024
9. Claustrum sign **を呈した** febrile infection-related epilepsy syndrome(FIRES)**の一例**. 赤尾 剛, 中村 正史, 岡島 なるみ, 東野 将志, 萩野 琢郎, 市川 大, 石垣 あや, 小林 理子, 宮澤 康一, 藤盛 寿一, 中島 一郎. 第113回日本神経学会東北

地方会, 仙台, :2024 年 9 月, 臨床神経学. 64: 910. 2024

10. **「上着が着られない」を主訴とした大脳皮質基底核症候群の 1 例**. 天野 尚美, 虎岩 辰弥, 目黒 祐子, 木川田 雅子, 高橋 泰地, 萩野 琢朗, 藤盛 寿一, 中島 一郎. 第 48 回日本神経心理学会学術集会, 京都, 2024 年 9 月, 日本神経心理学会総会プログラム・予稿集. 48 回: 76. 2024

11. **尾状核頭部の出血後に作話を呈した高次脳機能障害の 1 症例**. 目黒 祐子, 浜谷 圭佑, 吉田 祐子, 大野 美和子, 藤盛 寿一, 中島 一郎. 第 48 回日本神経心理学会学術集会, 京都, 2024 年 9 月, 日本神経心理学会総会プログラム・予稿集. 48 回: 84. 2024

12. **抗発作薬で加療された譫妄における通常短時間脳波所見と治療転帰の検討**. 大川 聡, 猪股 拓海, 市川 大, 深谷 浩史. 第 57 回日本てんかん学会学術集会, 福岡, 2024 年 9 月, てんかん研究. 42: 585. 2024

13. **MS【WS3】日本人多発性硬化症患者における slowly expanding lesion と疾患活動性・脳萎縮進行の関連性**. 横手 裕明, 宮崎 雄生, 藤盛 寿一, 融 衆太, 三浦 義治, 新野 正明, 中島 一郎, 西田 陽一郎, 横田 隆徳. 第 36 回日本神経免疫学会学術集会, 富山, 2024 年 10 月, 神経免疫学. 29: 222. 2024

14. **脳炎・肥厚性硬膜炎【CCS】リウマチ性髄膜炎の 2 例**. 岡島 なるみ, 東野 将志, 中村 正史, 藤盛 寿一, 中島 一郎. 第 36 回日本神経免疫学会学術集会, 富山, 2024 年 10 月, 神経免疫学. 29: 185. 2024

15. **脳炎・肥厚性硬膜炎【WS】奇形腫合併急性脳炎における AMPA 型 GluR subunit 抗体の意義**. 高橋 幸利, 西村 成子, 高尾 恵美子, 笠井 理沙, 榎田 かおる, 大村 泰史, 田中 淳, 佐藤 秀樹, 橋本 侑, 水谷 あかね, 大喜多 賢治, 新田 永俊, 上田 周一, 軸丸 美香, 中村 晋之, 藤盛 寿一, 岡田 久. 第 36 回日本神経免疫学会学術集会, 富山, 2024 年 10 月, 神経免疫学. 29: 219. 2024

16. **血液脳関門破綻が多発性硬化症の臨床病型に与える影響の解析**. 西原 秀昭, 松尾 欣哉, Fujisawa Miwako, Engelhardt Britta, 宮崎 雄生, 新野 正明, 藤盛 寿一, 中島 一郎, 中森 雅之. 第 36 回日本神経免疫学会学術集会, 富山, 2024 年 10 月, 神経免疫学. 29: 171. 2024

17. **MOG 抗体関連疾患診療の現在地(2024 年) 小児科・眼科・脳神経内科の視点から**. 中村 正史, 藤盛 寿一, 中島 一郎. 第 36 回日本神経免疫学会学術集会, 富山, 2024 年 10 月, 神経免疫学. 29: 125. 2024

18. **視神経脊髄炎と重症筋無力症の合併例に生じた結節性リンパ組織過形成の病理学的解析**. 東野 将志, 藤盛 寿一, 佐々木 高信, 菅原 崇史, 藤島 史喜, 金子 仁彦, 中島 一郎. 第 36 回日本神経免疫学会学術集会, 富山, 2024 年 10 月, 神

経免疫学. 29: 269. 2024

19. **Real-world Effectiveness of Satralizumab for AQP4( )NMOSD: Interim Analysis of SAkuraBeyond**. 藤原 一男, 磯部 紀子, 宮本 勝一, 新野 正明, 中原 仁, 服部 聡, 山本 真守, 河内 泉, 松井 尚子, 野原 千洋子, 國分 則人, 千原 典夫, 三須 建郎, 岡田 和将, 山下 勝久, 長塚 匡史, 安達 宏紀, 中島 一郎. 第 36 回日本神経免疫学会学術集会, 富山, 2024 年 10 月, 神経免疫学. 29: 175. 2024

20. **NMOSD 患者における症状と経口グルココルチコイドの有害事象が日常生活へ与える影響に関する質的研究**. 清水 優子, 中島 一郎, 池口 亮太郎, 長塚 匡史, 山下 勝久, 福岡 勇太, 村田 達教, 藤原 一男. 第 42 回日本神経治療学会学術集会, 千葉, 2024 年 11 月, 神経治療学. 41: S278. 2024

21. **神経免疫疾患のレジストリ研究 神経免疫疾患レジストリ構築の意義と挑戦 CIDPを事例として**. 大森 茂樹, 三澤 園子, 桑原 聡, 竹内 英之, 中島 一郎, JANIMA study group. 第 42 回日本神経治療学会学術集会, 千葉, 2024 年 11 月, 神経治療学. 41: S163. 2024

22. **MG・NMOSD における生物学的製剤の使い分けについて考える NMOSD に対する生物学的製剤の使い分け**. 中島 一郎. 第 42 回日本神経治療学会学術集会, 千葉, 2024 年 11 月, 神経治療学. 41: S234. 2024

23. **神経眼科と免疫～診療科ネットワーク～ NMOSDとMOGADの診療連携**. 中島 一郎. 第 62 回日本神経眼科学会総会, 金沢, 2024 年 11 月, 神経眼科. 41: 48. 2024

24. **SARS-CoV-2感染後に長大な両側錐体路病変を呈した一例**. 千葉優響ほか. 第 114回日本神経学会東北地方会, 仙台, 2025 年 3 月.

25. **重症筋無力症と鑑別を要した抗 GQ1b抗体症候群の1例**. 赤尾剛ほか. 第 114回日本神経学会東北地方会, 仙台, 2025 年 3 月.

Clinical Neurology and Neurosurgery 242 (2024) 108342

Contents lists available at ScienceDirect

Clinical Neurology and Neurosurgery

journal homepage: www.elsevier.com/locate/clineuro

# Continuous diffuse brain atrophy independent of relapse as a hallmark of multiple sclerosis beginning from relapsing-remitting stage

Tetsuya Akaishi [a], Juichi Fujimori [b,*], Hiroaki Yokote [c], Ichiro Nakashima [b]

[a] Department of Neurology, Tohoku University Graduate School of Medicine, Sendai, Japan
[b] Division of Neurology, Tohoku Medical and Pharmaceutical University, Sendai, Japan
[c] Department of Neurology and Neurological Science, Tokyo Medical and Dental University, Tokyo, Japan

ARTICLE INFO

*Keywords:*
Multiple sclerosis
MRI
Volumetric analysis
FreeSurfer

ABSTRACT

*Background:* Neurodegenerative changes are observed in relapsing-remitting multiple sclerosis (RRMS) and are prominent in secondary progressive MS (SPMS). However, whether neurodegenerative changes accelerate and are altered after the transition into SPMS or in the presence of relapses remains uncertain.
*Methods:* In this study, 73 patients with MS (seven with *relapsing RRMS*, 56 with *relapse-free RRMS*, and 10 with *relapse-free SPMS*) were evaluated for brain segmental volume changes over a 2-year follow-up period. Volume change was calculated using a within-subject unbiased longitudinal image analysis model.
*Results:* The rates of brain volume change in the 11 brain regions evaluated were relatively similar among different brain regions. Moreover, they were similar among the relapsing RRMS, relapse-free RRMS, and SPMS groups, even after adjusting for age.
*Conclusions:* The relatively constant brain segmental atrophy rate throughout the disease course, regardless of relapse episodes, suggests that RRMS and SPMS are continuous, uniform, and silent progressing brain atrophy diseases on a spectrum.

## 1. Introduction

Multiple sclerosis (MS) is an autoimmune disease of unknown aetiology affecting the central nervous system [1,2]. In most patients, the disease course is characterised by repeated relapses associated with disease progression [3]. Traditionally, in relapsing MS, the accrual of irreversible disability has been attributed to incomplete recovery from relapse, whereas relapse-independent mechanisms are considered the hallmark of the progressive forms of the disease [4,5]. However, accumulating evidence suggests that progression unrelated to relapses is not restricted to patients diagnosed with the progressive forms of MS. In the earliest phases of MS and in patients classified as having a typical relapsing-remitting disease, a substantial proportion of disability accumulation occurs independent of relapse activity. Despite the lack of concomitant clinically evident relapses, clinical deterioration has been termed *progression independent of relapse activity (PIRA)* or *silent progression*, in contrast to *relapse-associated disability worsening (RAW)* [5–10]. Recently, a systematic review reported that in the context of the variable definitions of PIRA, along with other methodological differences related to disease modifying therapy (DMT) use and follow-up duration, the reported proportion of MS patients experiencing PIRA varied from 4% to 24% [11]. However, few studies have investigated the neural substrates of the PIRA in relapse-free relapse remitting MS (RRMS) or secondary progressive MS (SPMS). Moreover, it has not been fully elucidated how the regional brain atrophy silently (*i.e,*. without relapse) progressed over the course of MS, with or without disability progression. Therefore, this retrospective 2-year follow-up study evaluated and compared the longitudinal relapse-free brain segmental atrophy rate in specific brain regions of patients with RRMS and SPMS.

## 2. Materials and methods

### 2.1. Enrollment

All patients with MS treated at the Tohoku Medical and Pharmaceutical University Hospital were initially recruited. Among them, those who underwent brain magnetic resonance imaging (MRI) for volumetric measurements at two time points within a 2-year interval were enrolled in the study. Participants were categorised into one of the following three groups: [1] *relapsing RRMS* with at least one relapse during the

* Correspondence to: Division of Neurology, Tohoku Medical and Pharmaceutical University, 1-15-1 Fukumuro, Miyagino-ku, Sendai 983-8536, Japan.
*E-mail address:* j-fujimori@tohoku-mpu.ac.jp (J. Fujimori).

https://doi.org/10.1016/j.clineuro.2024.108342
Received 1 April 2024; Received in revised form 13 May 2024; Accepted 14 May 2024
Available online 17 May 2024
0303-8467/© 2024 Elsevier B.V. All rights are reserved, including those for text and data mining, AI training, and similar technologies.

**Table 1**
Demographic, clinical, and radiological profiles of the patient in each disease group.

| Characteristics | *Relapsing RRMS* | *Relapse-free RRMS* | *Relapse-free SPMS* |
|---|---|---|---|
| Numbers | 7 | 56 | 10 |
| Male, n (%) | 2 (29%) | 13 (23%) | 4 (40%) |
| Age [years] * | 43 (33.5–49) years | 39 (34–44.5) years | 45.5 [42–52] years |
| Disease duration at enrollment [years] * | 3.6 (0.6–10.6) years | 7.2 (4.3–12.1) years | 19.6 (11.7–24) years |
| Baseline EDSS * | 2.0 (1.5–3.0) | 1.5 (1.0–2.0) | 6.0 (4.5–7.0) |
| Final EDSS * | 2.0 (1.0–2.5) | 1.0 (0.0–2.0) | 5.5 (4.5–7.0) |
| PIRA, n (%) | 0 (0.0%) | 2 (3.6%) | 0 (0.0%) |
| *Disease-modifying therapies, n (%)* | | | |
| Dimethyl fumarate | 4 (57%) | 20 (36%) | 0 (0.0%) |
| Fingolimod | 0 (0.0%) | 25 (45%) | 8 (80%) |
| Natalizumab | 0 (0.0%) | 5 (8.9%) | 1 (10%) |
| Interferon $\beta$ | 0 (0.0%) | 2 (3.6%) | 0 (0.0%) |
| Glatiramer acetate | 0 (0.0%) | 1 (1.8%) | 0 (0.0%) |
| No DMTs | 3 (43%) | 3 (5.4%) | 1 (10%) |
| Baseline whole-brain volume/eTIV* | 0.72 (0.71–0.73) | 0.72 (0.71–0.74) | 0.67 (0.63–0.69) |
| Baseline total gray matter volume/eTIV | 0.39 (0.38–0.39) | 0.40 (0.39–0.42) | 0.36 (0.33–0.38) |

DMTs, disease-modifying therapies; EDSS, the Kurtzke Expanded Disability Status Scale; PIRA, progression independent of relapse activity; RRMS, relapsing-remitting multiple sclerosis; SPMS, secondary progressive multiple sclerosis; eTIV, estimated total intracranial volume.
* Median and interquartile range.

2-year follow-up period, [2] *relapse-free RRMS* with no relapses during the follow-up period, and [3] *relapse-free SPMS*. As none of the patients with SPMS relapsed during the follow-up period, *relapsing SPMS* group was not prepared.

### 2.2. Segmental brain regions

Volumes of the following brain segments on each side of the brain were measured in this study: the cerebral cortex, cerebral white matter (WM), cerebellar cortex, cerebellar WM, thalamus, caudate, putamen, pallidum, hippocampus, and amygdala. In addition, brainstem volumes were measured longitudinally.

### 2.3. MRI data acquisition

A whole-body 1.5 Tesla MRI system (MAGNETOM Aera, Siemens, Germany) was used in this study. A high-resolution sagittal 3D T1-weighted magnetisation-prepared rapid gradient-echo (MPRAGE) sequence was obtained using the following parameters: repetition time [TR]: 2730 ms; echo time: 3.3 ms; inversion time [TI]: 1000 ms; 176 slices; field of view [FoV]: 256 mm; and measured isotropic voxel size: 1 × 1 × 1 $mm^3$. The sagittal 3D fluid-attenuated inversion recovery sequence was obtained using the following parameters: TR: 5000 ms; TE: 335 ms; TI: 1800 ms; 176 slices; FoV: 256 mm; and measured isotropic voxel size: 1 × 1 × 1 $mm^3$. The brain segmental volumes were estimated by using the automated FreeSurfer stream (version 7.1.1; https://surfer.nmr.mgh.harvard.edu/) [12–16].

### 2.4. Calculation of longitudinal brain volume change rates

Longitudinal brain segmental volume change rates over the 2-year follow-up period were estimated with the 3D T1-weighted images using FreeSurfer and Lin4Neuro [17,18]. First, cross-sectional analyses using the regular FreeSurfer processing stream "recon-all" were performed as reported previously [19]. The second step was performed to create base images, which were the average images of the patients over time. Longitudinal images were created and the symmetrised percent change (SPC) was calculated using the long_stats_ slope function in FreeSurfer to evaluate changes in regional brain volume and cortical thickness, as previously described [19]. The SPC is defined as the rate of volume change divided by the average volume at two time points. SPC is considered a statistically useful and robust tool [20].

### 2.5. Assessment of PIRA

The association between the presence of PIRA during the 2-year study period and each brain segment volume change rate was evaluated. The presence of PIRA was assessed using the Kurtzke Expanded Disability Status Scale (EDSS) at the beginning and end of the study period. PIRA was defined as an EDSS score increase of [1] ≥1.5 when baseline EDSS was 0, [2] ≥1.0 when baseline EDSS was 1.0–5.5, and [3] ≥0.5 when baseline EDSS was ≥6.0 [8,21].

### 2.6. Statistical analysis

The distributions of the quantitative variables are described using the median and interquartile range (IQR: 25–75 percentiles). Comparisons of quantitative variables between the two groups were performed using the Mann-Whitney U test. The effect size $r$ was calculated as $Z/\sqrt{N}$. To evaluate the difference in the brain volume change rate between the RRMS and SPMS groups after adjusting for demographic confounders, an analysis of covariance (ANCOVA) was performed. In the ANCOVA, the brain volume change rate in each brain segment was used as the dependent variable, and MS disease type (categorical data) and demographic confounders (continuous data) were used as covariates. P-values $< 0.05$ were considered statistically significant. The alpha level was not adjusted for multiple comparisons because of the exploratory nature of the study. Statistical analyses were performed using the R statistical software version 4.1.3 (R Foundation for Statistical Computing, Vienna, Austria).

### 2.7. Ethics

This study was approved by the Institutional Review Board of the Tohoku Medical and Pharmaceutical University Graduate School of Medicine (approval number: 2023–2–002). All participants provided written informed consent. The study was conducted in accordance with the latest version of the Declaration of Helsinki, which was revised in 2013.

## 3. Results

### 3.1. Study participants

A total of 73 patients with RRMS (n = 63) or SPMS (n = 10) were assessed in the study and their longitudinal segmental brain volume change rates over two years were calculated using within-subject unbiased longitudinal image analysis [22]. Seven patients with RRMS had at least one relapse during the 2-year follow-up period and were categorised into the *relapsing RRMS* group. The remaining 56 patients who did not relapse during the follow-up period were categorised into the *relapse-free RRMS* group. The remaining 10 patients were categorised into the *relapse-free SPMS* group. The demographic and clinical profiles of the participants and the administered DMTs for relapse prevention in each group are summarised in Table 1.

### 3.2. EDSS and PIRA

Among the 7 patients with *relapsing RRMS*, the median (IQR) of the baseline EDSS was 2.0 (1.5–3.0) and that of the final EDSS at the end of the 2-year follow-up period was 2.0 (1.0–2.5). This change was not significant (Cohen's d = 0.391; p = 0.1775, Wilcoxon signed-rank test).

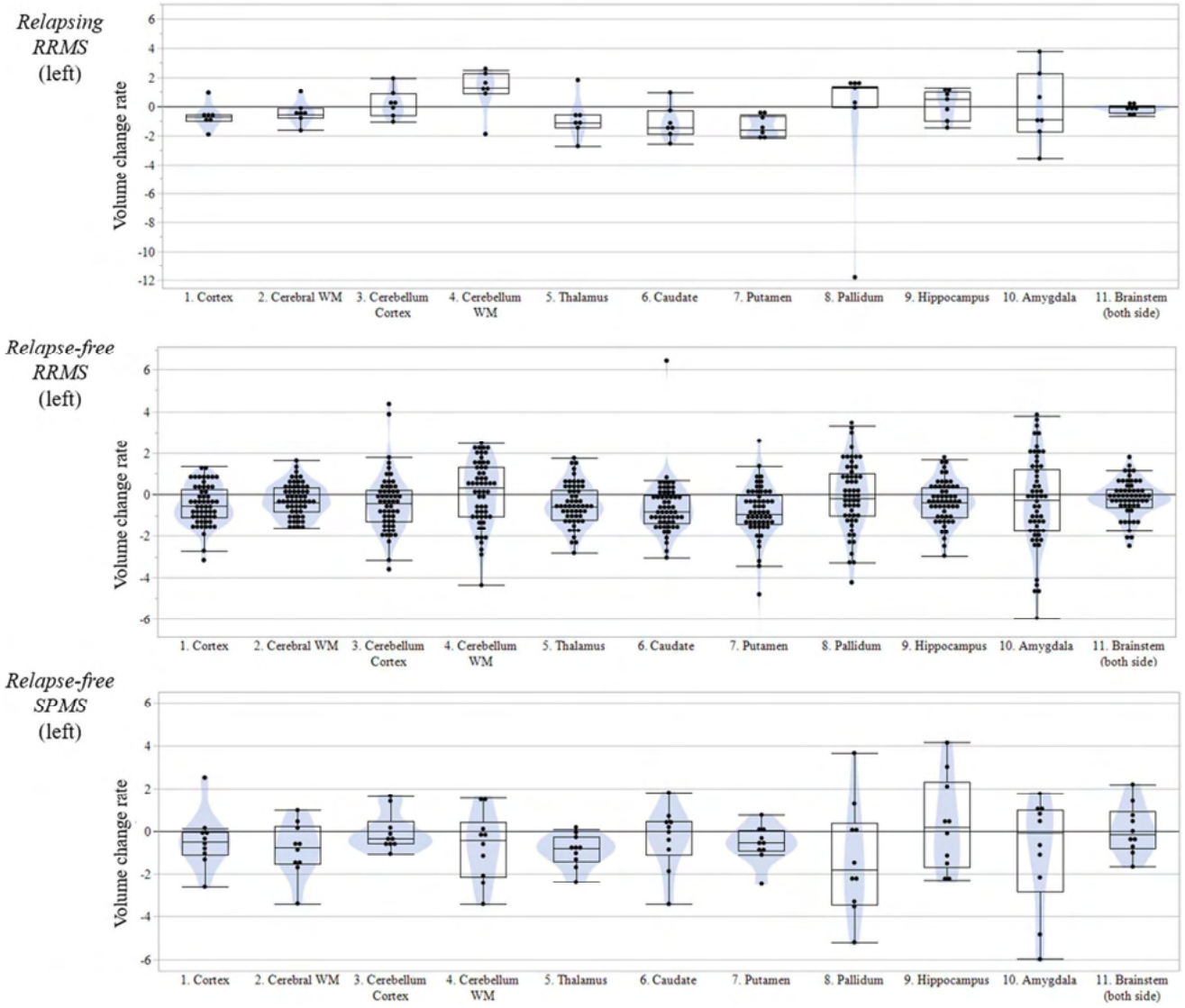


**Fig. 1.** Segmental brain volume changes over two years in the left hemisphere. Segmental longitudinal brain volume change rates, calculated using within-subject unbiased longitudinal image analysis, on the left side of the brain in relapsing RRMS (top; n = 7), relapse-free RRMS (middle; n = 56), and relapse-free SPMS (bottom; n = 10). RRMS, relapsing-remitting multiple sclerosis; SPMS, secondary progressive multiple sclerosis; WM, white matter.

None of the 10 patients in the *relapsing RRMS* group had a PIRA. Among the 56 patients with *relapse-free RRMS*, the median (IQR) of the baseline EDSS was 1.5 (1.0–2.0) and that of the final EDSS was 1.0 (0.0–2.0). This change was not significant (Cohen's d = 0.133; p = 0.1613). Two of the 56 patients in the *relapse-free RRMS* group underwent PIRA. Among the 10 patients with *relapse-free SPMS*, the median (IQR) of the baseline EDSS was 6.0 (4.5–7.0) and that of the final EDSS was 5.5 (4.5–7.0). The change in EDSS during the study period in the SPMS group was not significant (Cohen's d = 0.079; p = 0.2789). None of the 10 patients with SPMS had PIRA.

### 3.3. Segmental brain volume change rate

The longitudinal segmental brain volume change rates were calculated and compared among the *relapsing RRMS*, *relapse-free RRMS*, and *relapse-free SPMS* groups. The rate of change observed in the left hemisphere is shown in Fig. 1. The distributions suggest that volume decreases over two years were present in broad brain segments, with no predominant atrophic regions. The volume change rates were similar in all evaluated brain segments among the three groups. The rate of change in the right hemisphere is shown in Fig. 2. Similar to the changes observe in the right hemisphere, the volume decreases over two years were present in broad brain segments, and the change rates appeared to be similar among the three groups. To statistically evaluate the difference in volume change rates between *relapse-free RRMS* and *relapse-free SPMS*, Mann-Whitney U tests were performed for each of the evaluated brain segments in each hemisphere (Table 2). We observed no accelerated brain volume decrease rates in *relapse-free SPMS* group compared to those in the *relapse-free RRMS* group in the evaluated brain segments in either side of the brain.

### 3.4. ANCOVA adjusting for age

Next, to evaluate the difference in the brain volume change rate between *relapsing RRMS*, *relapse-free RRMS*, and *relapse-free SPMS* groups after adjusting for age, ANCOVA was performed using baseline

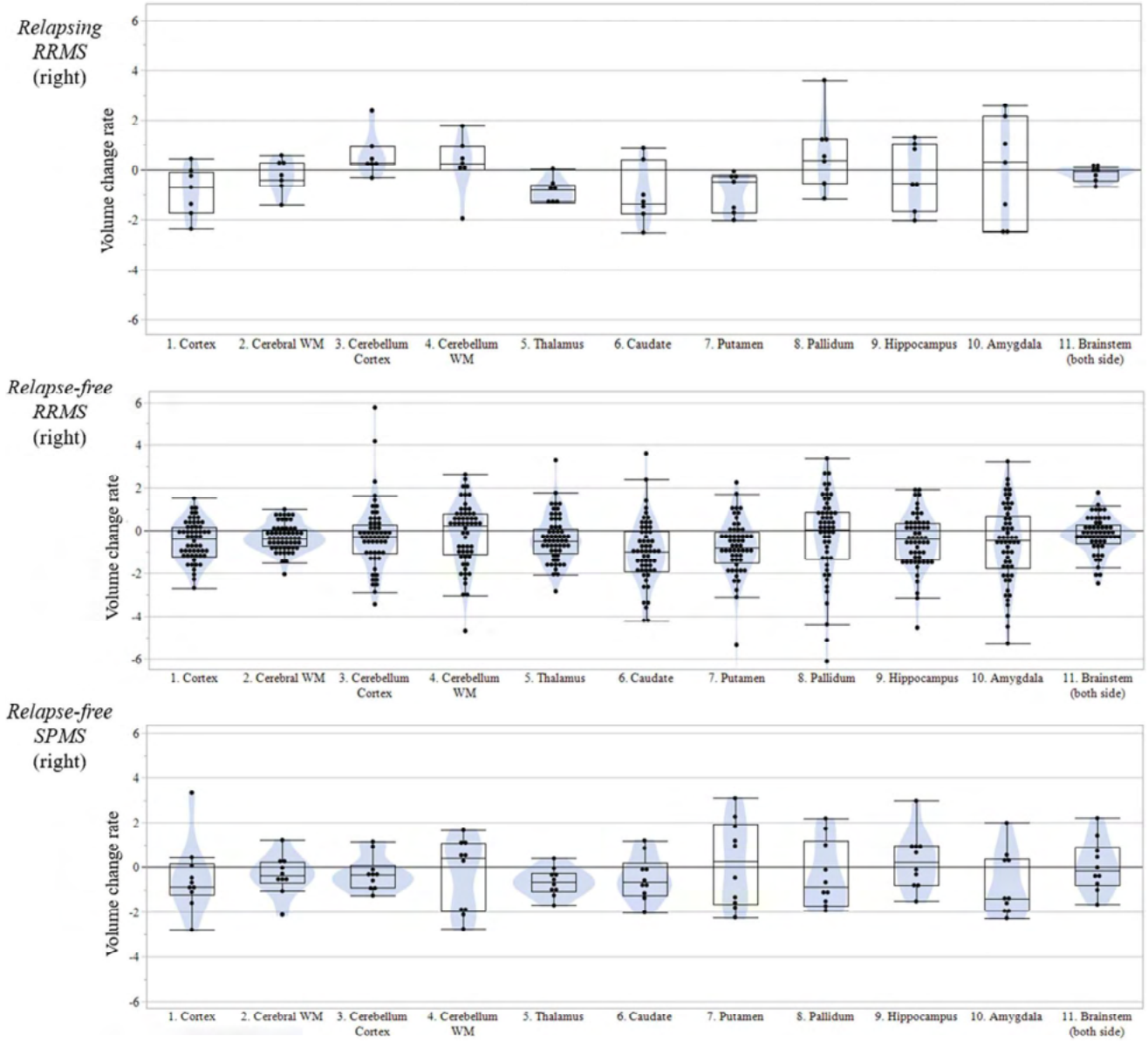


**Fig. 2.** Segmental brain volume changes over two years in the right hemisphere. Segmental longitudinal brain volume change rates, calculated using within-subject unbiased longitudinal image analysis, on the right side of the brain in *relapsing RRMS* (top, n = 7), *relapse-free RRMS* (middle, n = 56), and *relapse-free SPMS* (bottom, n = 10). RRMS, relapsing-remitting multiple sclerosis; SPMS, secondary progressive multiple sclerosis; WM, white matter.

age as the covariate (Table 3). None of the evaluated brain segments on either side of the brain showed a significant difference in brain volume change rate between the three groups; thus, suggesting that the brain segmental atrophy rate was almost constant in patients with MS, irrespective of age, relapse activity, or disease stage.Fig. 3

### 3.5. ANCOVA among stable MS

Next, we adjusted for baseline age and performed ANACOVA after excluding two patients with PIRA; thus, creating two patient populations: *stable relapse-free RRMS* and *stable relapse-free SPMS groups*. The results are summarised in Table 4. Only the left cerebral WM volume change rate was slightly lower (i.e. faster atrophy) in *stable relapse-free SPMS* than that in *stable relapse-free RRMS* (p = 0.0282), whereas the volume change rates in the other evaluated segments did not show any difference between the two groups.

### 3.6. DMTs and brain segmental atrophy in relapse-free RRMS

Finally, to estimate the differences in the volume change rates of the cerebral cortex and cerebral WM according to the administered DMTs, scatterplots grouped by the types of DMTs during the follow-up period were generated among the 56 patients with *relapse-free RRMS* (Fig. 4). For both volume change rates in the cerebral cortex (upper panels) and

**Table 2**
Comparisons of the segmental brain volume changes over two years in each side between *relapse-free RRMS* and *relapse-free SPMS*.

| Brain region | MS type | Left side | | Right side | |
|---|---|---|---|---|---|
| | | Volume change rate * | *P* (ES) | Volume change rate * | *P* (ES) |
| Cerebral cortex | RRMS | –0.539 (–1.090; 0.226) | 0.9786 (r<0.01) | –0.391 (–1.218; 0.124) | 0.6940 (r=0.05) |
| | SPMS | –0.527 (–1.006; –0.091) | | –0.881 (–1.080; –0.109) | |
| Cerebral WM | RRMS | –0.372 (–0.775; 0.315) | 0.1135 (r=0.19) | –0.391 (–0.737; 0.018) | 0.9216 (r=0.01) |
| | SPMS | –0.785 (–1.490; –0.029) | | –0.390 (–0.574; 0.135) | |
| Cerebellum cortex | RRMS | –0.427 (–1.288; 0.198) | 0.3956 (r=0.10) | –0.298 (–1.065; 0.240) | 0.9359 (r<0.01) |
| | SPMS | –0.371 (–0.588; 0.068) | | –0.341 (–0.816; –0.216) | |
| Cerebellum WM | RRMS | 0.319 (–1.045; 1.293) | 0.1551 (r=0.18) | 0.223 (–1.103; 0.716) | 0.8933 (r=0.02) |
| | SPMS | –0.417 (–1.854; 0.033) | | 0.394 (–1.894; 0.930) | |
| Brainstem (both sides) | RRMS | –0.221 (–0.596; 0.177) | 0.6808 (r=0.05) | – | – |
| | SPMS | –0.181 (–0.658; 0.658) | | – | |
| Thalamus | RRMS | –0.580 (–1.205; 0.222) | 0.1798 (r=0.17) | –0.502 (–1.061; 0.072) | 0.5372 (r=0.08) |
| | SPMS | –0.804 (–1.256; –0.401) | | –0.659 (–1.020; –0.352) | |
| Caudate | RRMS | –0.809 (–1.336; –0.074) | 0.1948 (r=0.16) | –1.012 (–1.932; –0.034) | 0.2274 (r=0.15) |
| | SPMS | –0.028 (–0.758; 0.322) | | –0.675 (–1.118; –0.074) | |
| Putamen | RRMS | –0.934 (–1.389; –0.065) | 0.3760 (r=0.11) | –0.808 (–1.472; –0.222) | 0.1769 (r=0.17) |
| | SPMS | –0.565 (–0.885; –0.089) | | 0.247 (–1.521; 1.654) | |
| Pallidum | RRMS | –0.163 (–1.013; 0.926) | 0.0860 (r=0.21) | 0.042 (–1.310; 0.826) | 0.6874 (r=0.05) |
| | SPMS | –1.809 (–3.127; 0.058) | | –0.883 (–1.540; 0.718) | |
| Hippocampus | RRMS | –0.372 (–1.071; 0.313) | 0.5082 (r=0.08) | –0.426 (–1.327; 0.332) | 0.1176 (r=0.19) |
| | SPMS | 0.162 (–1.426; 1.689) | | 0.210 (–0.661; 0.934) | |
| Amygdala | RRMS | –0.275 (–1.750; 1.198) | 0.7885 (r=0.03) | –0.500 (–1.702; 0.564) | 0.7139 (r=0.05) |
| | SPMS | –0.105 (–1.901; 0.915) | | –1.408 (–1.853; 0.320) | |

Segmental longitudinal brain volume change rates on each side of the brain were compared between patients with relapse-free RRMS (n = 56) and those with relapse-free SPMS (n = 10). No significant differences were observed in any of the evaluated brain segments on either side of the brain.

ES, effect size; RRMS, relapsing-remitting multiple sclerosis; SPMS, secondary progressive multiple sclerosis; WM, white matter.
* Median and interquartile range (25–75 percentiles)

**Table 3**
ANCOVA of brain volume change rates between the three groups adjusted for age.

| Brain segments | Left side | | | Right side | | |
|---|---|---|---|---|---|---|
| | Mean square | *F*-ratio | *P* | Mean square | *F*-ratio | *P* |
| Cerebral cortex | 0.0970 | 0.0980 | 0.9067 | 0.3582 | 0.3276 | 0.7218 |
| Cerebral WM | 1.7171 | 2.3985 | 0.0984 | 0.0182 | 0.0397 | 0.9611 |
| Cerebellum cortex | 1.5896 | 0.9053 | 0.4092 | 2.4405 | 1.1922 | 0.3097 |
| Cerebellum WM | 5.9060 | 2.5037 | 0.0892 | 0.7570 | 0.3488 | 0.7068 |
| Brainstem (both sides) | 0.7122 | 1.0006 | 0.3729 | – | – | – |
| Thalamus | 1.0868 | 1.0597 | 0.3521 | 0.6878 | 0.6619 | 0.5191 |
| Caudate | 1.1503 | 0.6694 | 0.5153 | 0.9026 | 0.4596 | 0.6334 |
| Putamen | 0.9876 | 0.4879 | 0.6160 | 4.4009 | 1.6644 | 0.1968 |
| Pallidum | 5.0958 | 1.0188 | 0.3664 | 4.6102 | 0.7914 | 0.4573 |
| Hippocampus | 2.4547 | 1.6383 | 0.2018 | 3.1097 | 1.9244 | 0.1537 |
| Amygdala | 1.3815 | 0.2677 | 0.7659 | 0.4190 | 0.1288 | 0.7207 |

The brain segmental volume change rate in each segment was compared between patients with relapsing RRMS (n = 7), relapse-free RRMS (n = 56), and relapse-free SPMS (n=10) by performing ANCOVA adjusted for age at enrolment. The volume of each brain segment was used as the outcome variable, and the disease groups and ages were used as covariates.

cerebral WM (lower panels), the distributions did not differ according to the type of DMT administered. The distributions of dimethyl fumarate (n = 20) and fingolimod (n = 25) were not significantly different in the left cerebral cortex (effect size $r = 0.09$; p = 0.5450, Mann-Whitney U test), right cerebral cortex (effect size $r = 0.05$; p = 0.7578), or right cerebral WM (effect size $r = 0.14$; p = 0.3317); however, there was a slight difference in the left cerebral WM (effect size $r = 0.33$; p = 0.0275).

## 4. Discussion

In this study, the rate of brain volume change in 11 brain regions was shown to be relatively similar among the different brain regions and to remain constant throughout the disease course (before and after the transition to SPMS), regardless of relapse activity. This finding highlights the importance of continuous diffuse brain atrophy underlying MS-associated neurodegeneration, which begins during earlier disease stages.

To date, similar findings of a relatively uniform progression of MS throughout the brain over longer time periods in has been reported in several studies [23–26]. For example, one study suggested that the rate of whole-brain volume loss is relatively constant throughout the course of RRMS [23]. A few studies have also suggested that whole-brain atrophy proceeds at a rate largely independent of the MS subtype [24,25]. Alternatively, the rates of whole-brain volume loss have been suggested to be accelerated during the first 5 years after disease onset, followed by subsequent stabilisation [26]. Therefore, the present study shows that a relatively constant brain volume change throughout the MS disease stages is observed even after excluding the effects of RAW. Although age-dependent acceleration of brain volume loss is present in both healthy individuals and patients with MS, the brain volume loss rate is higher in patients with MS than that in healthy individuals [27]. However, in our study, the aforementioned conclusions did not change, even after excluding the effect of age. Unchanged common mechanisms underlying brain volume loss throughout the disease course, both in earlier and later disease stages, may exist; hence, suggesting that RRMS and

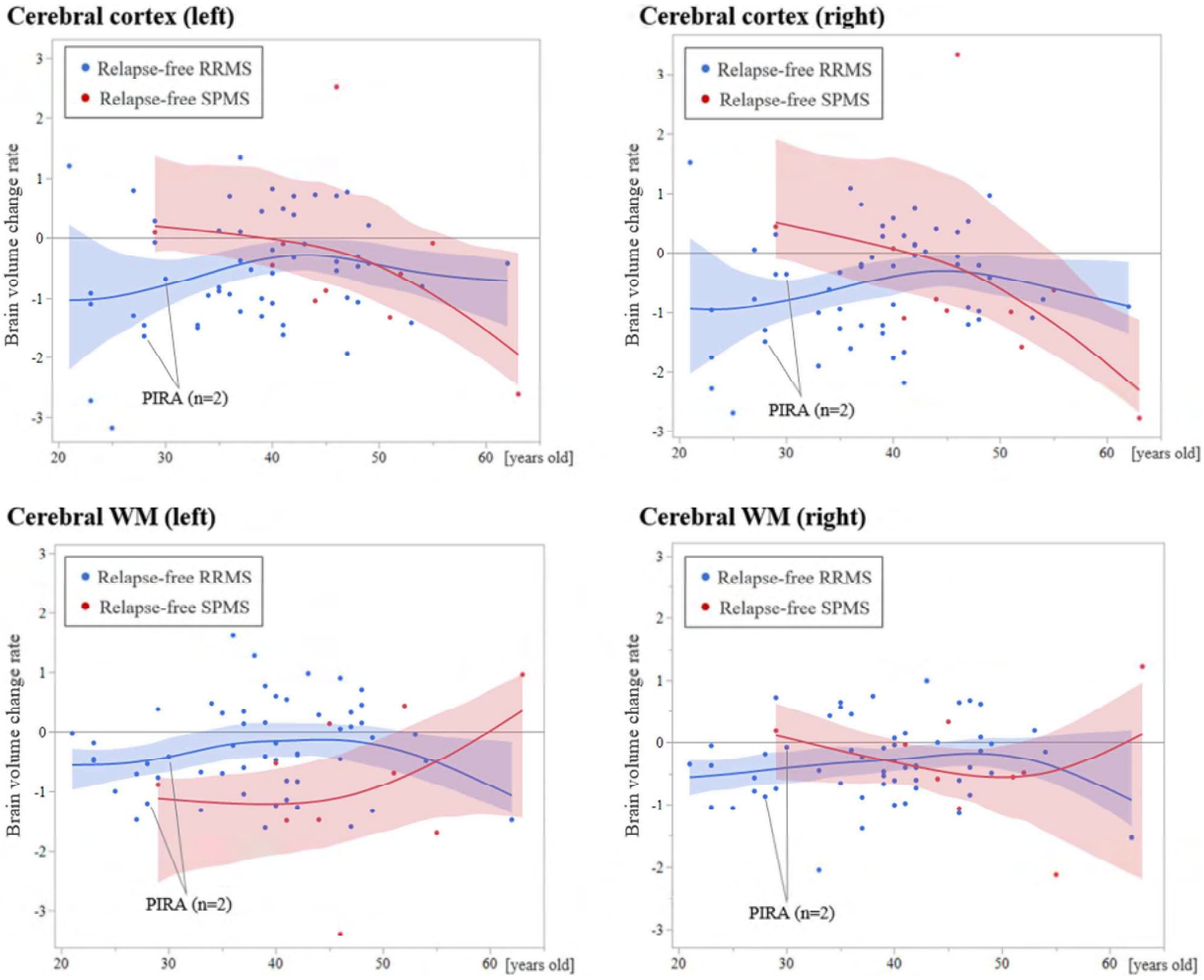


**Fig. 3.** Scatterplots with age and brain volume change rates in cerebral cortex and cerebral WM. The confidence interval ranges overlapped considerably between *relapse-free RRMS* (blue plots; n = 56) and *relapse-free SPMS* (red plots; n = 10) patients; thus, suggesting that the relapse-free brain volume change rate remains relatively stable after the transition to SPMS, even after adjusting for age. The lambda value of the smooth lines was set to 2.0. RRMS, relapsing-remitting multiple sclerosis; SPMS, secondary progressive multiple sclerosis; WM, white matter.

SPMS are on a continuous disease spectrum with a uniform silent progression of brain atrophy.

However, careful interpretation is needed here, as the presence of accelerated cortical atrophy in the later stages still remains unclear [28, 29]. The SPMS sample size in the present study was not large enough to confirm this. Future studies with larger sample sizes are needed to evaluate whether the brain segmental volume change rate is accelerated after the transition to SPMS, even after excluding confounding effects from age-dependent acceleration of brain atrophy in the general population.

The frequency of PIRA infection in our study (3%) was relatively low. Although similar results have been reported previously [11], we assume that several factors may be associated with these results. First, as reported in a recent study, variability in the definition of PIRA, DMT use, or exclusion of patients with relapse can contribute to PIRA outcomes [11]. In our study, most patients (90%) received DMTs including fingolimod. Interestingly, a recent study that included 1640 patients (64% interferon-beta/glatiramer acetate (IFN/GA), 36% fingolimod, median total follow-up time = 4–5 years) reported that disability progression was observed in 155 patients (8.8%) on IFN/GA and 51 (7.6%) on fingolimod, of whom 44 and 23 were relapse-free during the initial DMT, respectively [30]. Second, Japanese patients with MS have been reported to present with a milder clinical course [31] and lower proportions of secondary progressive MS [32] than Caucasian patients. Finally, although we could not include SPMS patients with PIRA, lower relapse rates and greater time on high-efficacy DMTs after reaching EDSS steps 3, 4, and 6 were associated with a decreased risk of accumulating further disability [33]. Thus, our results might also suggest that even in progressive MS patients with higher EDSS scores, brain atrophy and cortical atrophy might not progress rapidly if appropriate treatment is administered, and recurrence as well as PIRA are suppressed.

This study has several limitations. First, the follow-up period of two years may not be sufficient to evaluate the rate of change in brain volume. However, considering the relatively narrow distribution of the volume change rates with median values below 0.0, the rates shown in this study can be considered reliable. Another limitation was that the number of patients with *relapsing RRMS* and *relapse-free SPMS* was small. Although the absence of an apparent difference in the brain volume change rate among the three groups can be visually confirmed from the grouped scatterplots, revealing the absence of a difference between the three groups might be difficult with the number of patients in this study. Further studies with larger numbers of patients with SPMS and healthy volunteers are required to confirm the presence or absence of

**Table 4**
ANCOVA of brain volume change rates between patients with *stable relapse-free RRMS* and *stable relapse-free SPMS*.

| Brain segments | Left side | | | Right side | | |
|---|---|---|---|---|---|---|
| | Mean square | *F*-ratio | *P* | Mean square | *F*-ratio | *P* |
| Cerebral cortex | 0.0018 | 0.0017 | 0.9668 | 0.0026 | 0.0023 | 0.9615 |
| Cerebral WM | 3.6844 | 5.0546 | 0.0282 | 0.0268 | 0.0576 | 0.8112 |
| Cerebellum cortex | 1.6133 | 0.8585 | 0.3578 | 0.0095 | 0.0042 | 0.9483 |
| Cerebellum WM | 2.3905 | 1.0115 | 0.3185 | 0.0771 | 0.0349 | 0.8524 |
| Brainstem (both sides) | 1.4663 | 1.8419 | 0.1797 | – | – | – |
| Thalamus | 1.4150 | 1.4672 | 0.2305 | 0.4930 | 0.4530 | 0.5034 |
| Caudate | 0.4829 | 0.2696 | 0.6055 | 2.2284 | 1.0968 | 0.2991 |
| Putamen | 0.0861 | 0.0385 | 0.8451 | 8.9630 | 3.0576 | 0.0854 |
| Pallidum | 9.1929 | 3.0626 | 0.0851 | 0.0155 | 0.0024 | 0.9609 |
| Hippocampus | 4.0357 | 2.5589 | 0.1148 | 6.9369 | 4.4768 | 0.0384 * |
| Amygdala | 1.4078 | 0.2746 | 0.6021 | 0.0429 | 0.0133 | 0.9086 |

The brain segmental volume change rate in each segment was compared between patients with stable relapse-free RRMS (n = 54) and stable relapse-free SPMS (n = 10) using ANCOVA after adjusting for age at enrolment. The volume of each brain segment was used as the outcome variable, and the disease group and age were used as covariates.
* Higher volume change rate in the left hippocampus (*i.e.* slower atrophy) in the *stable relapse-free SPMS* group compared to than in the *stable relapse-free RRMS* group.

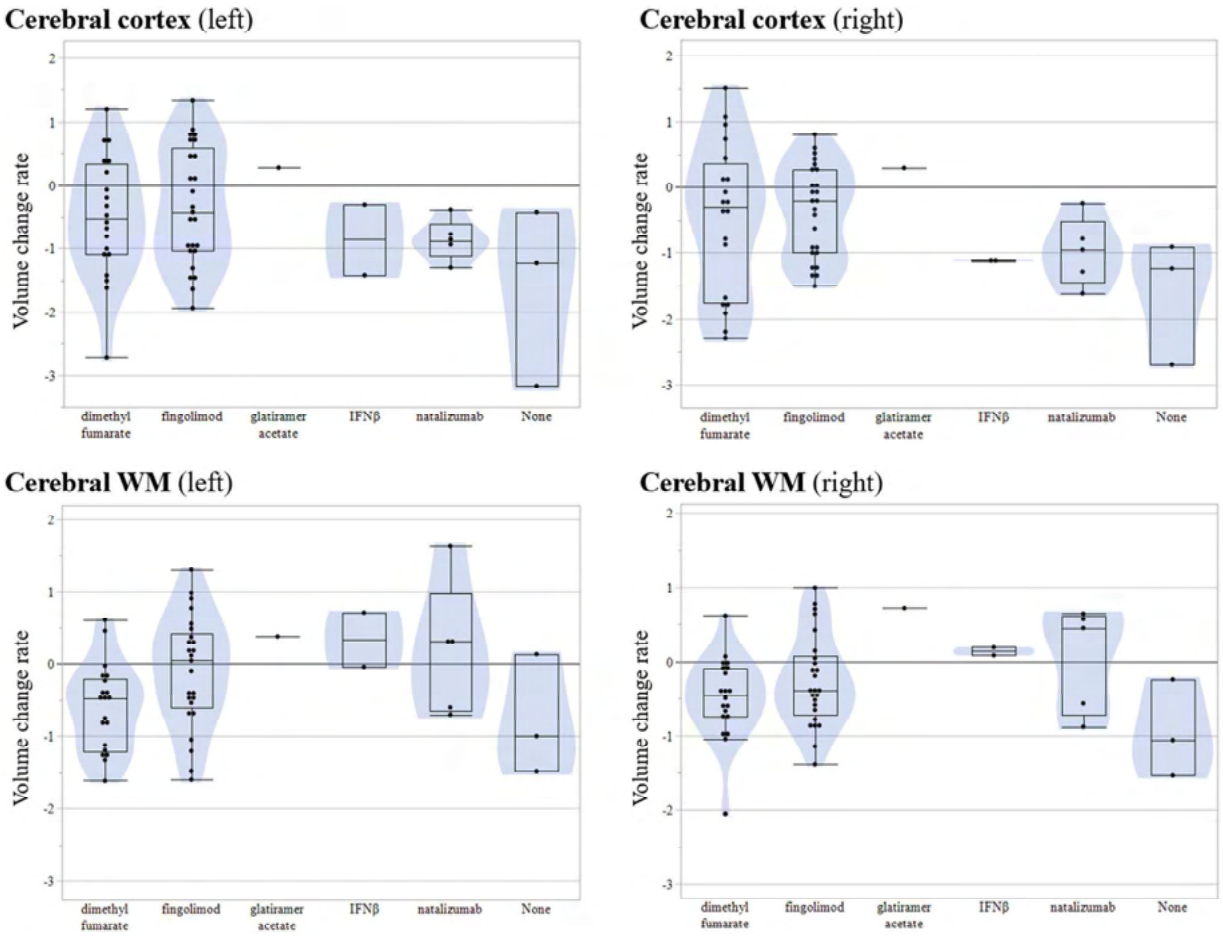


**Fig. 4.** Grouped scatterplots of volume change rate in relapse-free RRMS by the types of DMTs. The upper two panels show the distributions of brain volume change rates in the cerebral cortex, and the lower panels show those in the cerebral WM according to the types of DMTs administered during the two-year follow-up period. The distributions did not show remarkable differences among the different DMTs. DMTs, disease-modifying therapies; IFN β, interferon β; WM, white matter; RRMS, relapsing-remitting multiple sclerosis.

accelerated PIRA after the transition to SPMS, even when considering the age-dependent acceleration of brain atrophy in the general population. Finally, all participants in this study were of Japanese ancestry in whom it has been related with a less severe clinical course of MS [31]. Therefore, the generalisability of these findings to patients of other ethnicities remains uncertain.

## 5. Conclusions

The brain volume loss due to MS-associated neurodegeneration was diffuse, as observed during the earlier disease stages, and remained relatively constant throughout the disease course (before and after the transition to SPMS). Relapse activity in RRMS did not significantly affect

the rate of change in brain volume. These findings indicate the importance of relapse-independent brain atrophy during earlier disease stages of the RRMS form, and that RRMS and SPMS are on a continuous spectrum of brain atrophy.

## Author contributions

Study design: T.A., J.F., H.Y., and I.N.; data collection: J.F. and I.N.; calculation of brain volume change rates: H. Y.; analysis and interpretation of results: T.A. and J.F.; drafting: T.A. and J.F.; resources: I.N.; and supervision: I.N. All authors critically reviewed and approved the final version of the manuscript.

## Funding

This study was funded by the Japanese Ministry of Health, Labor, and Welfare Program (grant numbers 23FC1009 and 20K07892).

## CRediT authorship contribution statement

**Ichiro Nakashima:** Supervision, Resources, Funding acquisition, Conceptualization. **Hiroaki Yokote:** Writing – review & editing, Methodology, Investigation, Formal analysis, Conceptualization. **Juichi Fujimori:** Writing – review & editing, Project administration, Conceptualization. **Tetsuya Akaishi:** Writing – original draft, Project administration, Methodology, Investigation, Formal analysis, Data curation, Conceptualization.

## Declaration of Competing Interest

The authors declare no conflict of interest to disclose for this study.

## Data Availability

Individual-level data are not publicly available because of legal restrictions. However, some anonymised data supporting the findings of this study are available upon request from the corresponding author.

## References

[1] W.J. Huang, W.W. Chen, X. Zhang, Multiple sclerosis: pathology, diagnosis and treatments, Exp. Ther. Med. 13 (6) (2017) 3163–3166.
[2] A.J. Thompson, B.L. Banwell, F. Barkhof, W.M. Carroll, T. Coetzee, G. Comi, et al., Diagnosis of multiple sclerosis: 2017 revisions of the McDonald criteria, Lancet Neurol. 17 (2) (2018) 162–173.
[3] C. Confavreux, A. Compston, The natural history of multiple sclerosis, McAlpine's Mult. Scler. (2006) 183–272.
[4] F.D. Lublin, S.C. Reingold, J.A. Cohen, G.R. Cutter, P.S. Sørensen, A.J. Thompson, et al., Defining the clinical course of multiple sclerosis: the 2013 revisions, Neurology 83 (3) (2014) 278–286.
[5] J. Müller, A. Cagol, J. Lorscheider, C. Tsagkas, P. Benkert, Ö. Yaldizli, et al., Harmonizing definitions for progression independent of relapse activity in multiple sclerosis: a systematic review, JAMA Neurol. 80 (11) (2023) 1232–1245.
[6] A. Cagol, P. Benkert, L. Melie-Garcia, S.A. Schaedelin, S. Leber, C. Tsagkas, et al., Association of spinal cord atrophy and brain paramagnetic rim lesions with progression independent of relapse activity in people with MS, Neurology 102 (1) (2024) e207768.
[7] C. Tur, M.A. Rocca, Progression independent of relapse activity in multiple sclerosis: closer to solving the pathologic puzzle, Neurology 102 (1) (2024) e207936.
[8] L. Kappos, J.S. Wolinsky, G. Giovannoni, D.L. Arnold, Q. Wang, C. Bernasconi, et al., Contribution of relapse-independent progression vs relapse-associated worsening to overall confirmed disability accumulation in typical relapsing multiple sclerosis in a pooled analysis of 2 randomized clinical trials, JAMA Neurol. 77 (9) (2020) 1132–1140.
[9] N. Molazadeh, T. Akaishi, G. Bose, S. Nishiyama, T. Chitnis, M. Levy, Progression independent of relapses in aquaporin4-IgG-seropositive neuromyelitis optica spectrum disorder, myelin oligodendrocyte glycoprotein antibody-associated disease, and multiple sclerosis, Mult. Scler. Relat. Disord. 80 (2023) 105093.
[10] B.A.C. Cree, J.A. Hollenbach, R. Bove, G. Kirkish, S. Sacco, E. Caverzasi, et al., Silent progression in disease activity-free relapsing multiple sclerosis, Ann. Neurol. 85 (5) (2019) 653–666.
[11] D. Sharrad, P. Chugh, M. Slee, S. Bacchi, Defining progression independent of relapse activity (PIRA) in adult patients with relapsing multiple sclerosis: a systematic review(, Mult. Scler. Relat. Disord. 78 (2023) 104899.
[12] J. Fujimori, K. Fujihara, R. Ogawa, T. Baba, M. Wattjes, I. Nakashima, Patterns of regional brain volume loss in multiple sclerosis: a cluster analysis, J. Neurol. 267 (2) (2020) 395–405.
[13] J. Fujimori, K. Fujihara, M. Wattjes, I. Nakashima, Patterns of cortical grey matter thickness reduction in multiple sclerosis, Brain Behav. 11 (4) (2021) e02050.
[14] J. Fujimori, K. Uryu, K. Fujihara, M.P. Wattjes, C. Suzuki, I. Nakashima, Measurements of the corpus callosum index and fractional anisotropy of the corpus callosum and their cutoff values are useful to assess global brain volume loss in multiple sclerosis, Mult. Scler. Relat. Disord. 45 (2020) 102388.
[15] K. Nishizawa, J. Fujimori, I. Nakashima, Two-dimensional measurements with cut-off values are useful for assessing brain volume, physical disability, and processing speed in multiple sclerosis, Mult. Scler. Relat. Disord. 59 (2022) 103543.
[16] T. Akaishi, J. Fujimori, I. Nakashima, Enlarged choroid plexus in multiple sclerosis is associated with increased lesion load and atrophy in white matter but not gray matter atrophy, Mult. Scler. Relat. Disord. 82 (2024) 105424.
[17] B. Fischl, D.H. Salat, E. Busa, M. Albert, M. Dieterich, C. Haselgrove, et al., Whole brain segmentation: automated labeling of neuroanatomical structures in the human brain, Neuron 33 (3) (2002) 341–355.
[18] K. Nemoto, I. Dan, C. Rorden, T. Ohnishi, D. Tsuzuki, M. Okamoto, et al., Lin4Neuro: a customized Linux distribution ready for neuroimaging analysis, BMC Med. Imaging 11 (2011) 3.
[19] H. Yokote, Y. Miyazaki, S. Toru, Y. Nishida, T. Hattori, M. Niino, et al., High-efficacy therapy reduces subcortical grey matter volume loss in Japanese patients with relapse-onset multiple sclerosis: a 2-year cohort study, Mult. Scler. Relat. Disord. 67 (2022) 104077.
[20] D.A. Berry, G.D. Ayers, Symmetrized percent change for treatment comparisons, Am. Stat. 60 (1) (2006) 27–31.
[21] A. Cagol, S. Schaedelin, M. Barakovic, P. Benkert, R.A. Todea, R. Rahmanzadeh, et al., Association of brain atrophy with disease progression independent of relapse activity in patients with relapsing multiple sclerosis, JAMA Neurol. 79 (7) (2022) 682–692.
[22] M. Reuter, N.J. Schmansky, H.D. Rosas, B. Fischl, Within-subject template estimation for unbiased longitudinal image analysis, Neuroimage 61 (4) (2012) 1402–1418.
[23] T. Uher, J. Krasensky, C. Malpas, N. Bergsland, M.G. Dwyer, E. Kubala Havrdova, et al., Evolution of brain volume loss rates in early stages of multiple sclerosis, Neurol. Neuroimmunol. Neuroinflamm. 8 (3) (2021).
[24] N. De Stefano, A. Giorgio, M. Battaglini, M. Rovaris, M.P. Sormani, F. Barkhof, et al., Assessing brain atrophy rates in a large population of untreated multiple sclerosis subtypes, Neurology 74 (23) (2010) 1868–1876.
[25] N.F. Kalkers, N. Ameziane, J.C. Bot, A. Minneboo, C.H. Polman, F. Barkhof, Longitudinal brain volume measurement in multiple sclerosis: rate of brain atrophy is independent of the disease subtype, Arch. Neurol. 59 (10) (2002) 1572–1576.
[26] M. Andorra, K. Nakamura, E.J. Lampert, I. Pulido-Valdeolivas, I. Zubizarreta, S. Llufriu, et al., Assessing biological and methodological aspects of brain volume loss in multiple sclerosis, JAMA Neurol. 75 (10) (2018) 1246–1255.
[27] T. Akaishi, I. Nakashima, S. Mugikura, M. Aoki, K. Fujihara, Whole brain and grey matter volume of Japanese patients with multiple sclerosis, J. Neuroimmunol. 306 (2017) 68–75.
[28] A.J.C. Eijlers, I. Dekker, M.D. Steenwijk, K.A. Meijer, H.E. Hulst, P.J.W. Pouwels, et al., Cortical atrophy accelerates as cognitive decline worsens in multiple sclerosis, Neurology 93 (14) (2019) e1348–e1359.
[29] A. Eshaghi, F. Prados, W.J. Brownlee, D.R. Altmann, C. Tur, M.J. Cardoso, et al., Deep gray matter volume loss drives disability worsening in multiple sclerosis, Ann. Neurol. 83 (2) (2018) 210–222.
[30] V. von Wyl, P. Benkert, A. Moser, J. Lorscheider, B. Décard, P. Hänni, et al., Disability progression in relapse-free multiple sclerosis patients on fingolimod versus interferon-beta/glatiramer acetate, Mult. Scler. 27 (3) (2021) 439–448.
[31] L. Piccolo, G. Kumar, I. Nakashima, T. Misu, Y. Kong, B. Wakerley, et al., Multiple sclerosis in Japan appears to be a milder disease compared to the UK, J. Neurol. 262 (4) (2015) 831–836.
[32] H. Houzen, K. Kondo, K. Horiuchi, M. Niino, Consistent increase in the prevalence and female ratio of multiple sclerosis over 15 years in northern Japan, Eur. J. Neurol. 25 (2) (2018) 334–339.
[33] N. Lizak, A. Lugaresi, R. Alroughani, J. Lechner-Scott, M. Slee, E. Havrdova, et al., Highly active immunomodulatory therapy ameliorates accumulation of disability in moderately advanced and advanced multiple sclerosis, J. Neurol. Neurosurg. Psychiatry 88 (3) (2017) 196–203.

Check for updates

Received: 8 August 2024 | Revised: 25 September 2024 | Accepted: 28 September 2024

DOI: 10.1111/jon.13243

JOURNAL OF NEUROIMAGING
THE OFFICIAL JOURNAL OF THE AMERICAN SOCIETY OF NEUROIMAGING
WILEY

CLINICAL INVESTIGATIVE STUDY

# Slowly expanding lesions are associated with disease activity and gray matter loss in relapse-onset multiple sclerosis

Hiroaki Yokote[1,2] | Yusei Miyazaki[3] | Juichi Fujimori[4] | Yoichiro Nishida[2] | Shuta Toru[5] | Masaaki Niino[3] | Ichiro Nakashima[4] | Yoshiharu Miura[1] | Takanori Yokota[2]

[1]Department of Neurology, Tokyo Metropolitan Komagome Hospital, Tokyo, Japan

[2]Department of Neurology and Neurological Science, Tokyo Medical and Dental University, Tokyo, Japan

[3]Department of Clinical Research, National Hospital Organization Hokkaido Medical Center, Sapporo, Japan

[4]Division of Neurology, Tohoku Medical and Pharmaceutical University, Sendai, Japan

[5]Department of Neurology, Nitobe Memorial Nakano General Hospital, Tokyo, Japan

**Correspondence**
Hiroaki Yokote, Department of Neurology, Tokyo Metropolitan Komagome Hospital, 3-18-20, Honkomagome, Bunkyo-ku, Tokyo 113–8677, Japan.
Email: yktenuro@tmd.ac.jp

**Funding information**
Health and Labour Sciences Research Grant on Intractable Diseases (Neuroimmunological Diseases); Ministry of Health, Labour, and Welfare of Japan, Grant/Award Number: 23FC1009; Scientific Research on Innovative Areas-Platforms for Advanced Technologies and Research Resources; JSPS KAKENHI, Grant/Award Number: JP22H04926; Grant-in-Aid for Scientific Research (C) JSPS KAKENHI, Grant/Award Number: 24K10632

## Abstract

**Background and Purpose:** Slowly expanding lesions (SELs) have been proposed as novel MRI markers of chronic active lesions in multiple sclerosis (MS). However, the mechanism through which SELs affect brain volume loss in patients with MS remains unknown. Additionally, the prevalence and significance of SELs in Asian patients with MS remain unclear. This study aimed to investigate the association between SELs and no evidence of disease activity (NEDA)-3 status as well as brain volume loss in Japanese patients.

**Methods:** A total of 99 patients with relapse-onset MS were retrospectively evaluated. SELs were identified on brain MRI based on local deformation when consecutive scans were registered longitudinally. We developed a logistic regression model and generalized linear mixed models (GLMMs) to evaluate the association between the number of SELs and disease activity and changes in brain volume.

**Results:** During the observation period (2.0 ± 0.22 years), 35 patients developed at least one SEL. Multivariable logistic regression analysis showed that ≥2 SELs were associated with 0.2 times the risk of achieving a NEDA-3 status. GLMMs revealed that the number of SELs was negatively associated with volume changes in the cortex ($p = .00169$) and subcortical gray matter ($p = .00964$) after correction for multiple comparisons.

**Conclusion:** SELs were identified in Japanese patients with MS during the 2-year observation period. The number of SELs is associated with disease activity and brain volume loss, suggesting that the number of SELs could be a biomarker of disease activity in MS.

KEYWORDS
brain atrophy, high-efficacy therapy, Japanese, multiple sclerosis, slowly expanding lesion

## INTRODUCTION

Slowly expanding lesions (SELs), also known as smoldering or chronic active lesions, are histopathologically characterized by activated peripheral iron-rich macrophages/microglia associated with myelin breakdown.[1,2] These lesions reflect chronic inflammatory activity and substantial axonal injury and are associated with neurodegeneration markers.[2–6]

SELs can be identified on brain MRI based on local deformations when consecutive scans are longitudinally registered and have been proposed as novel MRI markers of chronic active lesions.[7,8] Some of these lesions overlap with lesions with iron or paramagnetic

rims.[5,6,9–18] Although SELs are more frequently observed compared to paramagnetic rim lesions,[19] the reason for this discrepancy is not fully clear as of now. Recent studies have shown that SELs are relevant in not only progressive multiple sclerosis (MS),[20,21] but also relapsing and remitting MS.[22]

However, there have been no studies on SELs in Asian patients with MS. Furthermore, it remains unclear how the development of SELs affects brain volume loss in patients with MS. Additionally, the association between treatment strategies such as high- versus moderate-efficacy therapy and the development of SELs remains unknown, although fingolimod could reduce the number of chronic active lesions in primary progressive MS.[23]

This study aimed to investigate the association between SELs and no evidence of disease activity (NEDA)-3 status and the reduction of brain volume including the whole brain, cortex, and subcortical gray matter in Japanese patients with MS. Additionally, we evaluated whether the development of SELs differs with the administration of high- versus moderate-efficacy drugs.

## METHODS

### Study centers and patient recruitment

This multicenter retrospective observational study included patients with relapse-onset MS who visited the Nitobe Memorial Nakano General Hospital (NMNGH), Tokyo Medical and Dental University Hospital (TMDUH), Hokkaido Medical Centre (HMC), or Tohoku Medical and Pharmaceutical University Hospital (TMPUH) between April 2016 and September 2022. Patients or their legally authorized representatives provided informed consent for participation. All procedures were conducted in accordance with the World Medical Association Declaration of Helsinki and were approved by the local ethics committees of NMNGH (30-3), TMDUH (M2018-105), HMC (2019-6-2), and TMPU (2023-2-002).

The inclusion criteria were aged ≥18 years and diagnosed with relapse-onset MS according to the McDonald 2017 criteria. The exclusion criteria were enough follow-up brain MRIs after the baseline scan, use of corticosteroid within 3 months prior to the MRI scan, and no use of disease-modifying drugs. Participants were followed up every 2 months, and their neurological findings including Expanded Disability Status Scale (EDSS) score and the presence or absence of relapse were monitored. MRI scans were conducted every 6 months, including at baseline and at the end of the observation period. According to the definition in the previous study,[24,25] if participants did not have relapses or new or enlarging T2 lesions on MRI (not including SELs) during the observation period, the condition was defined as NEDA-3.

### High- and moderate-efficacy therapy administration

High-efficacy therapy comprised natalizumab and fingolimod, while moderate-efficacy therapy comprised injectables such as interferon-$\beta$, glatiramer acetate, and dimethyl fumarate. Treatment was administered based on disease activity, future progression risk, patient's choice, and fertility concerns.

### Brain MRI and T2 lesion volume

All patients underwent 3-dimensional (3D) T1-weighted and fluid-attenuated inversion recovery brain MRI between April 2016 and September 2022, during the remission phase, which lasted at least 3 months. Images obtained at NMNGH, TMDUH, HMC, and TMPUH were acquired using a 1.5-Tesla (T) Vantage Titan (Canon), 3T MAGNETOM Spectra (Siemens), 3T Discovery MR750w (GE Healthcare), and 1.5T MAGNETOM Aera (Siemens), respectively.

Three-dimensional T1-weighted images (repetition time [TR]/echo time [TE] = 155/5.5 ms, 240 × 240 matrix, flip angle 8°, field of view [FOV] 23 × 23, 190 slices of 1-mm thickness, sagittal orientation for Vantage Titan; TR/TE = 1800/2.42 ms, 256 × 256 matrix, flip angle 9°, FOV 250 × 250, 192 slices of 1-mm thickness, sagittal orientation for MAGNETOM Spectra; TR/TE = 6.6/2.6 ms, 256 × 256 matrix, flip angle 14°, FOV 25.6 × 25.6, 176 slices of 1-mm thickness, sagittal orientation for Discovery MR750w; TR/TE = 2730/3.3 ms, 256 × 256 matrix, FOV 256 × 256, 176 slices of 1-mm thickness, sagittal orientation for MAGNETOM Aera) were used to determine brain volumes. Fluid-attenuated inversion recovery images (TR/TE = 9000/120 ms, 224 × 256 matrix, flip angle 8°, FOV 23 × 23, 44 slices of 3-mm thickness, axial orientation for Vantage Titan; TR/TE = 10,000/103 ms, 256 × 256 matrix, flip angle 150, FOV 250 mm, 48 slices of 3.3-mm thickness, axial orientation for MAGNETOM Spectra; TR/TE = 6000/95 ms, 192 × 288 matrix, flip angle 160°, FOV 23 × 23, 22 slices of 5-mm thickness, axial orientation for Discovery MR750w; TR/TE = 5000/335 ms, inversion time = 1800 ms, FOV 256 mm, 176 slices of 1-mm thickness, sagittal orientation for MAGNETOM Aera) were used to evaluate T2 lesion volumes using nicMSlesions (Figure 1B), which facilitated accurate segmentation of white matter lesions on MRI using supervised deep learning.[26] These MRI protocols were consistent throughout the observation period.

### Longitudinal regional brain volume change

Longitudinal changes in brain volume were evaluated with 3D T1-weighted images using FreeSurfer (version 7.1.1, Athinoula A. Martinos Center for Biomedical Imaging, Boston, Massachusetts, USA, http://surfer.nmr.mgh.harvard.edu)[27,28] and Lin4Neuro (version L4N 20.04, K-Lab, Tsukuba, Japan, https://www.nemotos.net/?page_id=29).[29] We performed cross-sectional analyses using the regular FreeSurfer processing stream "recon-all," followed by longitudinal processing "two stage model" as previously described.[30] The symmetrized percentage change (SPC) is defined as the rate of volume change divided by the average volume at two time points.[31] SPC is considered statistically useful and robust.[32] Since lesion filling does not change the output of



15526569, 2024, 6, Downloaded from https://onlinelibrary.wiley.com/doi/10.1111/jon.13343 by Iuichi Fujimori - Tohoku Ika Yakka Daigaku , Wiley Online Library on [30/03/2025]. See the Terms and Conditions (https://onlinelibrary.wiley.com/terms-and-conditions) on Wiley Online Library for rules of use; OA articles are governed by the applicable Creative Commons License

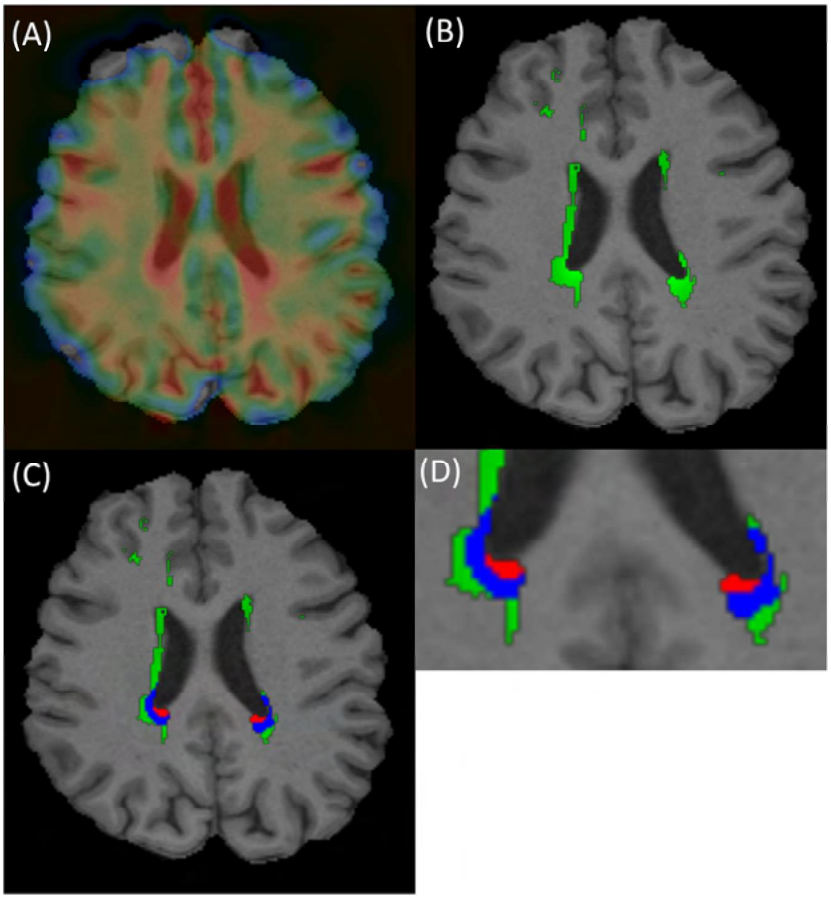


**FIGURE 1** Jacobian analysis and identification of slowly expanding lesions (SELs). (A) The Jacobian determinant of the nonlinear deformation field between a reference and follow-up scan computed. Blue indicates local contraction, while red denotes local expansion. (B) T2 lesion segmentation performed using nicMSlesions (green). (C) Voxels within existing T2 lesions obtained by masking panel A with panel B. Voxels within existing T2 lesions with a minimum expansion rate ≥8% (blue) and those with a minimum expansion rate ≥12% (red) obtained. (D) Enlarged view of (C).

FreeSurfer,[33] we did not perform lesion filling prior to the analyses. Moreover, we used FreeSurfer because it has more robust normalized brain and gray matter volumes on different scanners than FMRIB Software Library-Structural Image Evaluation, using Normalization, of Atrophy Cross-sectional.[33]

## Identification of SELs

SELs were identified using a previously described method with slight modifications in the threshold of lesion expansion.[7] First, the Jacobian determinant of the nonlinear deformation field between the reference and follow-up T1-weighted images was computed (Figure 1A). T2 lesion segmentation was made using FLAIR images. Subsequently, voxels within existing T2 lesions with a minimum rate of expansion ≥12% were identified (Figure 1C). Group voxels were identified based on 3D-connected component analysis using 26 connections. Any identified SELs less than 10 voxels in size were discarded. Second, potential SELs were subselected based on their concentricity, with a central core and neighboring voxels with minimum expansion ≥8% (Figure 1C). The constancy of all SELs was confirmed using MRIs from at least three time points, showing that they increased in size gradually rather than rapidly.

## Statistical analysis

All statistical analyses were performed using R (version 4.2.2, R Foundation, Vienna, Austria, https://www.r-project.org/). Continuous data are presented as mean ± standard deviation and compared using one-way analysis of variance, whereas discrete data were presented as median ± interquartile and compared using Fisher's exact test or the Kruskal-Wallis test. We developed a logistic regression model predicting the NEDA-3 status during the observation period. The final model included age, sex, baseline Multiple Sclerosis Severity Score (MSSS), number of SELs, and classification of disease-modifying therapies. Additionally, we developed generalized linear mixed models (GLMMs) to predict regional brain volume changes in the whole brain volume without ventricles, cortical volume, and subcortical volume among patients with no SEL, 1 SEL, and ≥2 SELs. All models were adjusted for facility-level (MRI scanner) clustering. The full models included age, sex, classification of disease-modifying therapies, presence or absence of disease activity including relapses or new or enlarging T2 lesions, baseline MSSS, duration between MRI scans, and baseline T2 lesion volumes as fixed effects and MRI scanner as a random effect. We then calculated the coefficient of the number of SELs and its *p* value in each GLMM and corrected for multiple comparisons using the false discovery rate.[34] GLMM is widely used for analyzing nonnormal data when



15526569, 2024, 6, Downloaded from https://onlinelibrary.wiley.com/doi/10.1111/jon.13343 by Iuichi Fujimori - Tohoku Ika Yakka Daigaku , Wiley Online Library on [30/03/2025]. See the Terms and Conditions (https://onlinelibrary.wiley.com/terms-and-conditions) on Wiley Online Library for rules of use; OA articles are governed by the applicable Creative Commons License

JOURNAL OF NEUROIMAGING
THE OFFICIAL JOURNAL OF THE AMERICAN SOCIETY OF NEUROIMAGING
WILEY



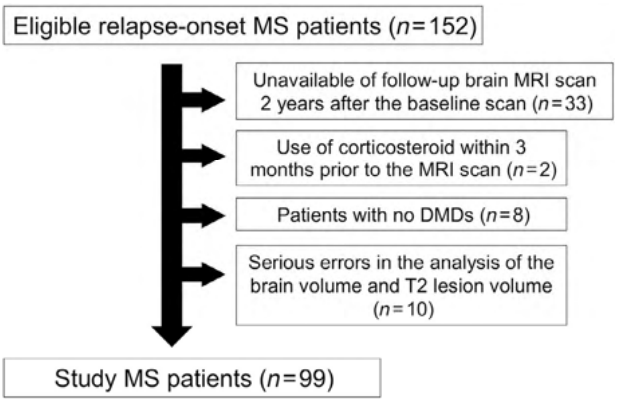


**FIGURE 2** Flow chart of study patients. MS, multiple sclerosis; *n*, number of patients; DMD, disease-modifying drugs.

**TABLE 1** Distribution of patients with slowly expanding lesions among MRI scanners.

| | No SEL | 1 SEL | ≥2 SELs | *p* |
|---|---|---|---|---|
| *N* | 64 | 23 | 12 | .43 |
| 1.5 Tesla Vantage Titan (*N* = 16) | 13 (81.3%) | 3 (18.8%) | 0 (0%) | |
| 3 Tesla MAGNETOM Spectra (*N* = 11) | 5 (45.5%) | 3 (27.3%) | 3 (27.3%) | |
| 3 Tesla Discovery MR750w (*N* = 13) | 8 (61.5%) | 3 (23.1%) | 2 (15.4%) | |
| 1.5 Tesla MAGNETOM Aera (*N* = 59) | 38 (64.4%) | 14 (23.7%) | 7 (11.9%) | |

Abbreviation: *N*, number of patients; SEL, slowly expanding lesion.

random effects are present.[35] We used GLMM because no-normal data were included in our analyses.

## RESULTS

Of the 152 patients, 99 with MS were enrolled in this study (Figure 2). During the observation period, 35 (35%) had at least 1 SEL (median = 1, range = 1-11) according to the definition of SELs in this study. The mean SEL volume was 24.96 (0-571.02) $mm^3$. No SEL was found in 64 patients, whereas at least 1 SEL was observed in 35 patients. The distribution of these patients was similar among the four MS centers with different MRI scanners (Table 1). Representative SELs are shown in Figure 3. We confirmed that the SELs have enlarged steadily. Baseline characteristics of the participants are summarized in Table 2. Age, female ratio, baseline EDSS score, and MSSS were similar between patients with no SEL, 1 SEL, and ≥2 SELs. The volumes of the whole brain without the ventricles, cortex, and subcortical gray matter were similar among the three groups. However, there was a trend that patients with 1 or ≥2 SELs also had larger T2 lesion volumes than those with no SEL. Additionally, the proportion of patients with ≥2 SELs on high-efficacy drugs was smaller than that of those with no SEL or 1 SEL. During the observation period (2.0 ± 0.22 years), the annualized relapse rate and occurrence rate of new T2 lesions in patients with ≥2 SELs were higher than those in patients with no or 1 SEL, although not significant (Table 3). The proportion of patients with worsening EDSS scores was marginally higher among those with 1 and ≥2 SELs than among those with no SEL (Table 3). The proportion of patients who achieved a NEDA-3 status was significantly lower among those with ≥2 SELs than among those with no or 1 SEL ($p = .012$; Figure 4). Logistic regression analysis revealed that having ≥2 SELs was a significant risk factor for loss of the NEDA-3 status after adjusting for confounding factors such as age, sex, baseline MSSS, and disease-modifying therapy (Table 4). Additionally, patients receiving high-efficacy therapy were approximately five times more likely to achieve a NEDA-3 status (Table 4). Finally, we found that volume change rates of the cortex and subcortical gray matter, but not of the lateral ventricles, negatively correlated with the number of SELs after adjusting for covariates in the GLMM (Table 5).

## DISCUSSION

This study found that 35% of patients with relapse-onset MS from four Japanese MS centers developed at least one SEL during the 2-year observation period. An increased number of SELs was associated with the loss of the NEDA-3 status, independent of disease-modifying therapy use, in these patients. Conversely, high-efficacy therapy was a strong indicator for achieving the NEDA-3 status. Moreover, the volume loss of the cortex or subcortical gray matter correlated with the number of SELs after adjusting for eight covariates, including disease-modifying therapy classification, suggesting that the number of SELs was a clinical and radiological prognostic biomarker for relapse-onset MS independent of disease-modifying therapy use. Consistent with our results, SELs are associated with disability progression in patients with relapse-onset MS,[22] secondary progressive MS,[21] and primary progressive MS.[20]

The strength of this study lies in demonstrating that having ≥2 SELs was a risk factor independent of disease-modifying therapy use, implying that some patients may not be well managed even with the high-efficacy therapy currently available.

Our observations indicated that the number of SELs was associated with subcortical gray matter and cortical atrophy, suggesting that SELs contributed to central and peripheral atrophy. Considering that the associations remained significant after adjusting for the disease activity including relapses and new or enlarging T2 lesions, SELs could lead to brain volume loss independent of the disease activity. An earlier study showed that the expansion of chronic lesions evaluated using the JIM software was associated with central brain atrophy progression, as assessed on SIENAX and VIENA.[36] This discrepancy might be due to multiple factors, including the different methods used to evaluate SELs and brain volume loss, as well as the small sample size. However, it is likely that the relatively short observation period of 2 years and the age range of this study participants also played a significant role. A previous 2-year observational study showed that the rate of the lateral



15526569, 2024, 6, Downloaded from https://onlinelibrary.wiley.com/doi/10.1111/jon.13343 by Iwate Fujimori - Tohoku Ika Yakka Daigaku , Wiley Online Library on [30/03/2025]. See the Terms and Conditions (https://onlinelibrary.wiley.com/terms-and-conditions) on Wiley Online Library for rules of use; OA articles are governed by the applicable Creative Commons License

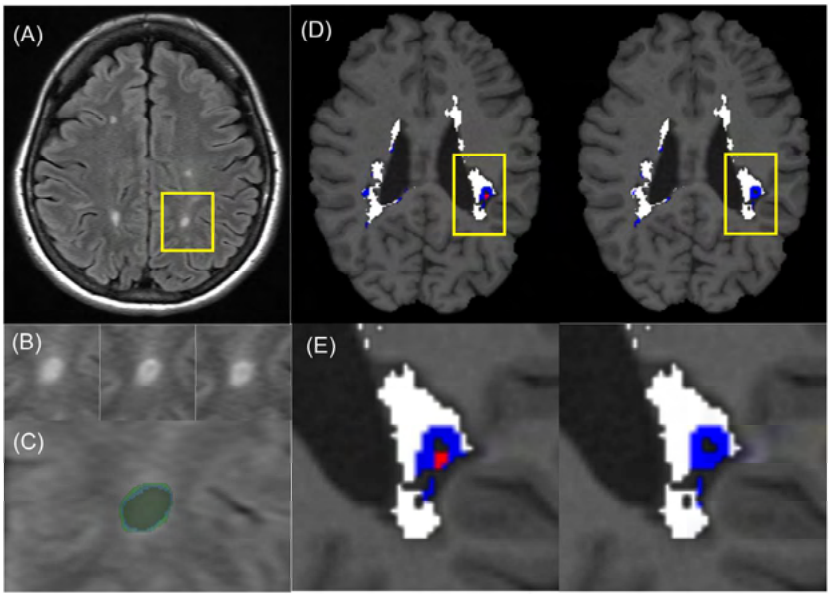


**FIGURE 3** Representative slowly expanding lesions (SELs). (A) An SEL in the left parietal lobe. (B) An enlarged view at baseline (left), 12 months (middle), and 24 months (right) inside yellow box in panel A. (C) A diagram with panel B overlaid. The baseline is shown in red, 12 months in blue, and 24 months in green. While there is significant overlap among the three lesions and the rate of expansion is relatively small, the color gradient from a tricolored innermost layer to a blue intermediate layer and a green outermost layer indicates a nearly uniform radial expansion of the lesion. (D) SELs in the periventricular lesions; >12% expanded legions (red), >4% expanded legions (blue), and all T2 lesions (white) over 2 years (left) and over a year (right). The lesion with expansion >12% in the left image (red) appeared blue in the right image, suggesting that this lesion had enlarged gradually over 2 years. (E) Enlarged views inside each yellow box in (D).

**TABLE 2** Baseline characteristics of study patients.

| | No SEL | 1 SEL | ≥2 SELs | *p* |
|---|---|---|---|---|
| *N* | 64 | 23 | 12 | |
| Age (years) | 41 ± 9.1 | 39 ± 6.6 | 39 ± 9.3 | .61 |
| Female sex ratio (%) | 73.4% | 65.2% | 83.3% | .59 |
| Baseline EDSS score | 2.0 (1.0, 3.125) | 2.0 (1.0, 3.5) | 2.0 (1.0, 3.25) | .98 |
| Disease duration (years) | 9.7 ± 7.4 | 10 ± 7.1 | 8.1 ± 5.1 | .53 |
| Baseline MSSS | 3.1 ± 2.6 | 3.4 ± 3.7 | 3.4 ± 2.6 | .93 |
| Disease-modifying drugs | | | | .33 |
| High-efficacy drugs, *N* (%) | 34 (53.1%) | 14 (60.9%) | 4 (33.3%) | |
| Moderate-efficacy drugs, *N* (%) | 30 (46.9%) | 9 (39.1%) | 8 (66.7%) | |
| BrainSegVolNotVent ($cm^3$) | 1063 ± 110 | 1045 ± 123 | 1024 ± 148 | .62 |
| CortexVol ($cm^3$) | 446 ± 47.9 | 440 ± 48.7 | 430 ± 56.7 | .63 |
| SubCortGrayVol ($cm^3$) | 51.5 ± 5.94 | 49.9 ± 5.95 | 51.3 ± 7.54 | .53 |
| T2 lesion volume ($cm^3$) | 9.09 ± 8.80 | 12.1 ± 10.0 | 16.4 ± 11.0 | .084 |
| Estimated intracranial volume ($cm^3$) | 1509 ± 153 | 1495 ± 162 | 1469 ± 144 | .68 |

*Note*: Continuous variables are presented as mean ± standard deviation and discrete variables as median ($25^{th}$ percentile, $75^{th}$ percentile). Objective variables are listed as the original FreeSurfer-output name. BrainSegVolNotVent = whole brain volume without the ventricles; CortexVol = cortical volume; SubCortGrayVol = subcortical gray matter volume.
Abbreviations: EDSS, Expanded Disability Status Scale; MSSS, Multiple Sclerosis Severity Score; *N*, number of patients; SEL, slowly expanding lesion.

ventricle enlargement in patients with MS during the first year was not substantially different from that of healthy individuals. Even over the total 2-year period, the difference in enlargement between patients and healthy individuals appeared to be smaller compared to the rate of gray matter atrophy.[37] Another study reported that over a 2-year observation period, gray matter atrophy was more pronounced than white matter atrophy.[38] Therefore, over the 2-year period, gray matter atrophy may have had a greater impact than ventricular enlargement.

Moreover, research into the link between the growth of T2 lesions and whole brain and central brain atrophy had revealed that, although the rates of increase in T2 lesions and lateral ventricular enlargement were uncorrelated over the initial 2-year period, a correlation trend became apparent in the subsequent years.[39] Given the established link between increased white matter lesions and more pronounced cortical atrophy,[40] as well as the inverse correlation between the volume of periventricular white matter lesions and cortical thickness,[41] it is



15326569, 2024, 6, Downloaded from https://onlinelibrary.wiley.com/doi/10.1111/jon.13243 by Iuichi Fujimori - Tohoku Ika Yakka Daigaku , Wiley Online Library on [30/03/2025]. See the Terms and Conditions (https://onlinelibrary.wiley.com/terms-and-conditions) on Wiley Online Library for rules of use; OA articles are governed by the applicable Creative Commons License

JOURNAL OF NEUROIMAGING
THE OFFICIAL JOURNAL OF THE AMERICAN SOCIETY OF NEUROIMAGING
WILEY



**TABLE 3** Disease activity during the observation period between MRI scans.

| | No SEL | 1 SEL | ≥2 SELs | *p* |
|---|---|---|---|---|
| *N* | 64 | 23 | 12 | |
| Duration between MRI scans (years) | 2.05 ± 0.23 | 2.04 ± 0.18 | 1.96 ± 0.23 | .43 |
| Annualized relapse rate (%) | 3.84% | 2.35% | 7.53% | .39 |
| Occurrence of new T2 lesions (%) | 23.4% | 17.4% | 50.0% | .12 |
| EDSS score worsening (%) | 4.69% | 17.4% | 16.7% | .076 |

*Note*: Duration between MRI scans is presented as mean ± standard deviation.
Abbreviations: EDSS, Expanded Disability Status Scale; *N*, number of patients; SEL, slowly expanding lesion.

reasonable to conclude that SEL exerted a greater influence on gray matter atrophy than on lateral ventricular enlargement in our study. Age-related effects on ventricular enlargement must also be considered. The rate of lateral ventricular enlargement was similar in patients with MS and healthy controls after the age of 40.[42] As the average age of our participants was around 40, the observed ventricular enlargement may not be specific to MS pathology.

Another highlight is that we investigated SEL development in Asian people with MS, an area that has not been previously studied. MS disease activity was milder in a Japanese cohort than in a UK cohort.[43,44] Thus, it is important to observe SELs as they are associated with milder disability progression in Japanese than in Caucasian patients.

This study has a few limitations, including a relatively small sample size, short follow-up period, and lack of healthy controls. Additionally, the number of SELs depended on the definition of SELs, as well as the number of T2 lesion volumes. In this study, we used a different definition of SELs, where the expansion rate of lesions was smaller than that in Elliott's study because we found no SEL based on Elliott's definition. This is partly because MS disease activity might be milder in this cohort as discussed earlier. However, the expansion rate of SELs varies between studies. For example, in the study by Calvi et al,[21] the average expansion rate was 1.5%-3.0%, which is lower than that observed in our study. The definition of SELs is not yet definitive and may vary depending on the study population and the MRI scanner used. The bias of T2 lesion volume was statistically adjusted for GLMMS. Finally, the use of different MRI scanners at the four study sites and limited spatial resolution of FLAIR images in some protocols may have confounded our results. Nevertheless, GLMMs were adjusted for facility-level clustering.

In summary, the results of this study suggest that the presence of SELs can be a marker of disease activity as well as cortical and subcortical gray matter atrophy in Japanese patients with relapse-onset MS. Considering that high-efficacy therapy is a strong indicator of the NEDA-3 status, more efficacious drugs will be suitable for patients with a high number of SELs that can lead to brain atrophy and disability progression.

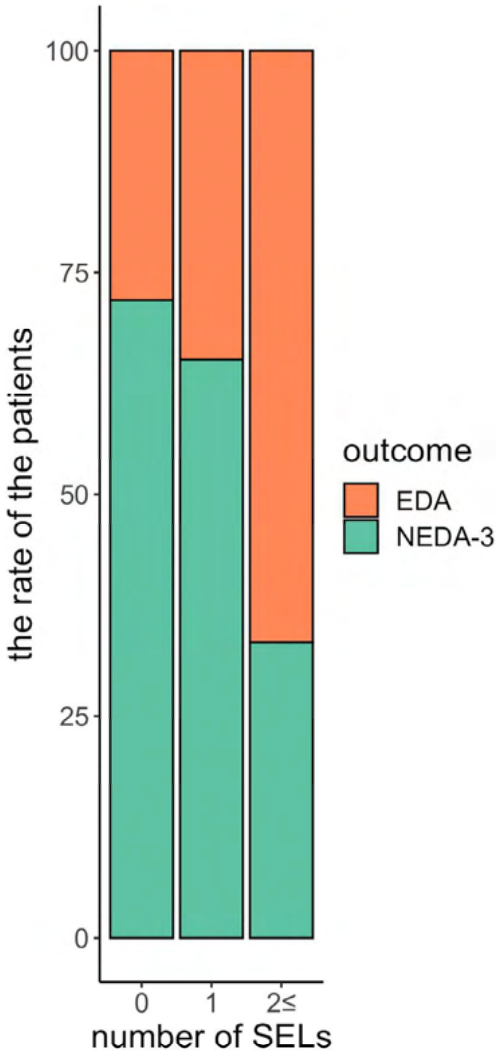


**FIGURE 4** Proportion of patients who achieved the no evidence of disease activity (NEDA)-3 status during the observation period. Patients with ≥2 slowly expanding lesions (SELs) were less likely to achieve the NEDA-3 status than those with no or 1 SEL ($p = .012$). EDA, evidence of disease activity.

**TABLE 4** Logistic regression analysis modeling no evidence of disease activity-3 for slowly expanding lesions.

| Variable | Odds ratio (95% confidence interval) | *p* |
|---|---|---|
| Age | 1.00 (0.95, 1.06) | .877 |
| Male sex | 0.44 (0.14, 1.37) | .157 |
| Baseline MSSS | 1.00 (0.851, 1.18) | .98 |
| Number of SELs (reference: no SEL) | | |
| 1 | 0.64 (0.21, 1.92) | .425 |
| ≥2 | 0.2 (0.05, 0.83) | .027 |
| High-efficacy therapy | 5.48 (1.96, 15.36) | .0012 |

Abbreviation: MSSS, Multiple Sclerosis Severity Score.



15326569, 2024, 6, Downloaded from https://onlinelibrary.wiley.com/doi/10.1111/jon.13343 by Iuichi Fujimori - Tohoku Ika Yakka Daigaku , Wiley Online Library on [30/03/2025]. See the Terms and Conditions (https://onlinelibrary.wiley.com/terms-and-conditions) on Wiley Online Library for rules of use; OA articles are governed by the applicable Creative Commons License

**TABLE 5** General linear mixed model analysis modeling regional volume change for number of slowly expanding lesions.

| Objective variables | Coefficient (95% confidence interval) | *p* | Adjusted *p* |
|---|---|---|---|
| CortexVol | −0.273 (−0.465, −0.0818) | .00846 | .0169 |
| SubCortGrayVol | −0.303 (−0.487, −0.120) | .00241 | .00964 |
| Lateral.Ventricle | −0.00667 (−0.206, 0.192) | .95 | .95 |
| BrainSegVolNotVent | 0.0334 (−0.152, 0.254) | .753 | .95 |

*Note*: Objective variables are listed as the original FreeSurfer-output name. BrainSegVolNotVent = whole brain volume without the ventricles; CortexVol = cortical volume; SubCortGrayVol = Subcortical gray matter volume.

## ACKNOWLEDGMENTS

This work was supported in part by a Health and Labour Sciences Research Grant on Intractable Diseases (Neuroimmunological Diseases) from the Ministry of Health, Labour, and Welfare of Japan (23FC1009), Grant-in-Aid for Scientific Research on Innovative Areas-Platforms for Advanced Technologies and Research Resources "Advanced Bioimaging Support" from JSPS KAKENHI (JP22H04926), and Grant-in-Aid for Scientific Research (C) from JSPS KAKENHI (24K10632).

## CONFLICT OF INTEREST STATEMENT

HY has received speaker honoraria from Biogen, Mitsubishi-Tanabe Pharma, Alexion Pharma Godo Kaisha, Chugai Pharma, and Novartis. YM has received speaker honoraria from Mitsubishi-Tanabe Pharma, Alexion Pharma Godo Kaisha, Chugai Pharma, and Novartis. MN has received speaker honoraria from Novartis Pharma, Biogen Japan, Mitsubishi Tanabe Pharma, Chugai Pharma, and Alexion Pharma Godo Kaisha. IN serves on the scientific advisory boards for Biogen Japan and Novartis Pharma; receives honoraria for speaking engagements with Biogen Japan, Mitsubishi Tanabe Pharma, Novartis Pharma, Takeda Pharmaceutical, and Eisai; and has been granted funding by the Japanese Ministry of Health, Labour, and Welfare Program Grant Number 23FC1009. TY has received personal fees from Mitsubishi Tanabe Pharma and Takeda, outside the submitted work, and holds a patent with Takeda that includes paid royalties. The other authors declare no conflicts of interest.

## ORCID

*Hiroaki Yokote* https://orcid.org/0000-0001-8620-5063
*Masaaki Niino* https://orcid.org/0000-0001-5722-920X

## REFERENCES

1. Kuhlmann T, Ludwin S, Prat A, et al. An updated histological classification system for multiple sclerosis lesions. Acta Neuropathol. 2017;133:13-24.
2. Frischer JM, Bramow S, Dal-Bianco A, et al. The relation between inflammation and neurodegeneration in multiple sclerosis brains. Brain. 2009;132:1175-89.
3. Luchetti S, Fransen NL, van Eden CG, et al. Progressive multiple sclerosis patients show substantial lesion activity that correlates with clinical disease severity and sex: a retrospective autopsy cohort analysis. Acta Neuropathol. 2018;135:511-28.
4. Popescu BFG, Lucchinetti CF. Pathology of demyelinating diseases. Annu Rev Pathol. 2012;7:185-217.
5. Absinta M, Sati P, Masuzzo F, et al. Association of chronic active multiple sclerosis lesions with disability in vivo. JAMA Neurol. 2019;76:1474-83.
6. Dal-Bianco A, Grabner G, Kronnerwetter C, et al. Slow expansion of multiple sclerosis iron rim lesions: pathology and 7 T magnetic resonance imaging. Acta Neuropathol. 2017;133:25-42.
7. Elliott C, Wolinsky JS, Hauser SL, et al. Slowly expanding/evolving lesions as a magnetic resonance imaging marker of chronic active multiple sclerosis lesions. Mult Scler. 2019;25:1915-25.
8. Calvi A, Haider L, Prados F, et al. In vivo imaging of chronic active lesions in multiple sclerosis. Mult Scler. 2022;28:683-90.
9. Pitt D, Boster A, Pei W, et al. Imaging cortical lesions in multiple sclerosis with ultra–high-field magnetic resonance imaging. Arch Neurol. 2010;67:812-18.
10. Bagnato F, Hametner S, Yao B, et al. Tracking iron in multiple sclerosis: a combined imaging and histopathological study at 7 Tesla. Brain. 2011;134:3602-15.
11. Yao B, Bagnato F, Matsuura E, et al. Chronic multiple sclerosis lesions: characterization with high-field-strength MR imaging. Radiology. 2012;262:206-15.
12. Hagemeier J, Heininen-Brown M, Poloni GU, et al. Iron deposition in multiple sclerosis lesions measured by susceptibility-weighted imaging filtered phase: a case control study. J Magn Reson Imaging. 2012;36:73-83.
13. Hammond KE, Metcalf M, Carvajal L, et al. Quantitative in vivo magnetic resonance imaging of multiple sclerosis at 7 Tesla with sensitivity to iron. Ann Neurol. 2008;64:707-13.
14. Bian W, Harter K, Hammond-Rosenbluth KE, et al. A serial in vivo 7T magnetic resonance phase imaging study of white matter lesions in multiple sclerosis. Mult Scler. 2012;19:69-75.
15. Walsh AJ, Lebel RM, Eissa A, et al. Multiple sclerosis: validation of MR imaging for quantification and detection of iron. Radiology. 2013;267:531-42.
16. Wisnieff C, Ramanan S, Olesik J, et al. Quantitative susceptibility mapping (QSM) of white matter multiple sclerosis lesions: interpreting positive susceptibility and the presence of iron. Magn Reson Med. 2015;74:564-70.
17. Harrison DM, Li X, Liu H, et al. Lesion heterogeneity on high-field susceptibility MRI is associated with multiple sclerosis severity. Am J Neuroradiol. 2016;37:1447.
18. Absinta M, Sati P, Fechner A, et al. Identification of chronic active multiple sclerosis lesions on 3T MRI. Am J Neuroradiol. 2018;39:1233.
19. Calvi A, Clarke MA, Prados F, et al. Relationship between paramagnetic rim lesions and slowly expanding lesions in multiple sclerosis. Mult Scler. 2023;29:352-62.
20. Elliott C, Belachew S, Wolinsky JS, et al. Chronic white matter lesion activity predicts clinical progression in primary progressive multiple sclerosis. Brain. 2019;142:2787-99.
21. Calvi A, Carrasco FP, Tur C, et al. Association of slowly expanding lesions on MRI with disability in people with secondary progressive multiple sclerosis. Neurology. 2022;98:e1783-93.
22. Calvi A, Tur C, Chard D, et al. Slowly expanding lesions relate to persisting black-holes and clinical outcomes in relapse-onset multiple sclerosis. Neuroimage Clin. 2022;35:103048.
23. Calvi A, Mendelsohn Z, Hamed W, et al. Treatment reduces the incidence of newly appearing multiple sclerosis lesions evolving into chronic active, slowly expanding lesions: a retrospective analysis. Eur J Neurol. 2024;31:e16092.
24. Nixon R, Bergvall N, Tomic D, et al. No evidence of disease activity: indirect comparisons of oral therapies for the treatment of relapsing-remitting multiple sclerosis. Adv Ther. 2014;31:1134-54.



15526569, 2024, 6, Downloaded from https://onlinelibrary.wiley.com/doi/10.1111/jon.13343 by Iuichi Fujimori - Tohoku Ika Yakka Daigaku , Wiley Online Library on [30/03/2025]. See the Terms and Conditions (https://onlinelibrary.wiley.com/terms-and-conditions) on Wiley Online Library for rules of use; OA articles are governed by the applicable Creative Commons License

25. Havrdova E, Galetta S, Stefoski D, et al. Freedom from disease activity in multiple sclerosis. Neurology. 2010;74 Suppl 3:S3-S7.
26. Valverde S, Salem M, Cabezas M, et al. One-shot domain adaptation in multiple sclerosis lesion segmentation using convolutional neural networks. Neuroimage Clin. 2019;21:101638.
27. Fischl B, Dale AM. Measuring the thickness of the human cerebral cortex from magnetic resonance images. Proc Natl Acad Sci USA. 2000;97:11050-55.
28. Fischl B, Salat DH, Busa E, et al. Whole brain segmentation: automated labeling of neuroanatomical structures in the human brain. Neuron. 2002;33:341-55.
29. Nemoto K, Dan I, Rorden C, et al. Lin4Neuro: a customized Linux distribution ready for neuroimaging analysis. BMC Med Imaging. 2011;11:3.
30. Yokote H, Miyazaki Y, Toru S, et al. High-efficacy therapy reduces subcortical grey matter volume loss in Japanese patients with relapse-onset multiple sclerosis: a 2-year cohort study. Mult Scler Relat Disord. 2022;67:104077.
31. Curran-Everett D, Williams CL. Explorations in statistics: the analysis of change. Adv Physiol Educ. 2015;39:49-54.
32. Ammon B. Longitudinal Two Stage Model. Available from: https://surfer.nmr.mgh.harvard.edu/fswiki/LongitudinalTwoStageModel. Accessed 28 Aug 2024.
33. Guo C, Ferreira D, Fink K, et al. Repeatability and reproducibility of FreeSurfer, FSL-SIENAX and SPM brain volumetric measurements and the effect of lesion filling in multiple sclerosis. Eur Radiol. 2019;29:1355-64.
34. Glickman ME, Rao SR, Schultz MR. False discovery rate control is a recommended alternative to Bonferroni-type adjustments in health studies. J Clin Epidemiol. 2014;67:850-57.
35. Bolker BM, Brooks ME, Clark CJ, et al. Generalized linear mixed models: a practical guide for ecology and evolution. Trends Ecol Evol. 2009;24:127-35.
36. Klistorner S, Barnett MH, Klistorner A. Mechanisms of central brain atrophy in multiple sclerosis. Mult Scler. 2022;28:2038-45.
37. Horakova D, Cox JL, Havrdova E, et al. Evolution of different MRI measures in patients with active relapsing-remitting multiple sclerosis over 2 and 5 years: a case-control study. J Neurol Neurosurg Psychiatry. 2008;79:407-14.
38. Tedeschi G, Dinacci D, Comerci M, et al. Brain atrophy evolution and lesion load accural in multiple sclerosis: a 2-year follow-up study. Mult Scler. 2009;15:204-11.
39. Lukas C, Minneboo A, de Groot V, et al. Early central atrophy rate predicts 5 year clinical outcome in multiple sclerosis. J Neurol Neurosurg Psychiatry. 2010;81:1351-56.
40. Lie I, Weeda M, Mattiesing R, et al. Relationship between white matter lesions and gray matter atrophy in multiple sclerosis. Neurology. 2022;98:e1562-73.
41. Jehna M, Pirpamer L, Khalil M, et al. Periventricular lesions correlate with cortical thinning in multiple sclerosis. Ann Neurol. 2015;78:530-39.
42. Ghione E, Bergsland N, Dwyer M, et al. Aging and brain atrophy in multiple sclerosis. J Neuroimaging. 2019;29:527-35.
43. Piccolo L, Kumar G, Nakashima I, et al. Multiple sclerosis in Japan appears to be a milder disease compared to the UK. J Neurol. 2015;262:831-36.
44. Akaishi T, Nakashima I, Mugikura S, et al. Whole brain and grey matter volume of Japanese patients with multiple sclerosis. J Neuroimmunol. 2017;306:68-75.


**How to cite this article:** Yokote H, Miyazaki Y, Fujimori J, Nishida Y, Toru S, Niino M, et al. Slowly expanding lesions are associated with disease activity and gray matter loss in relapse-onset multiple sclerosis. J Neuroimaging. 2024;34:758–65. https://doi.org/10.1111/jon.13243

15526569, 2024, 6, Downloaded from https://onlinelibrary.wiley.com/doi/10.1111/jon.13243 by Iuichi Fujimori - Tohoku Ika Yakka Daigaku , Wiley Online Library on [30/03/2025]. See the Terms and Conditions (https://onlinelibrary.wiley.com/terms-and-conditions) on Wiley Online Library for rules of use; OA articles are governed by the applicable Creative Commons License

＜耳鼻咽喉科学＞

教授　太田伸男
准教授　鈴木貴博
講師　佐藤輝幸
助教　舘田豊

## 耳鼻咽喉科領域疾患におけるペリオスチンの発現

研究内容紹介：

好酸球性副鼻腔炎は、典型例は成人発症で、両側性かつ多発性の鼻茸を有する。この鼻茸や副鼻腔粘膜組織には好酸球優位な炎症細胞浸潤が認められる。上顎洞に比較して篩骨洞病変が強いため嗅覚障害を訴えることが多く進行すると汎副鼻腔炎となる。また、気管支喘息の合併頻度が高く、アスピリン喘息を合併する場合は特に難治性である。好酸球性副鼻腔炎（ECRS）の病理病態はまだ十分に解明されていないが、その病態や病理像は気管支喘息と類似していることから“上気道の喘息(asthma of the upper airway)”としての理解が重要である。したがって、ECRSに対する治療は、喘息に対する治療指針と同様に急性増悪時の対応と長期管理療法に分けたマネージメントが重要で疾患活動性のバイオマーカーの開発が求められている。ペリオスチンは近年、多くの炎症性疾患の病態形成に重要な役割を果たしていることが報告されている。病変部位に大量に沈着したペリオスチンが気管支喘息のリモデリングやアトピー性皮膚炎の炎症の重症化と遷延化に関与していることが明らかとなりその病態における役割が注目されている。ペリオスチンの好酸球性副鼻腔炎、唾液腺腫瘍、中耳疾患等における役割と臨床的意義について検討している。

**＜論文発表＞**

1)　Tateda Y, Suzuki T, Sato T, Izuhara K, Ise K, Shimada H, Murakami K, Murakami K, Nakamura Y, Ohta N.　Expression of Periostin in Benign Salivary Gland Tumors.　Tohoku J Exp Med. 2024 Feb 27;262(2):105-113. doi: 10.1620/tjem.2023.J099. Epub 2023 Dec 14.

2)　Tateda Y, Ikeda R, Kakuta R, Izuhara K, Ogawa T, Ise K, Shimada H, Murakami K, Murakami K, Nakamura Y, Katori Y, Ohta N.　Expression of Vascular and Tissue Repair Factors in Laryngeal Granulomas.　Tohoku J Exp Med. 2024 Jun 27. doi: 10.1620/tjem.2024.J056.

3)　Suzuki J, Hemmi T, Ida T, Ogata S, Yoshitake J, Matsunaga T, Ishida T, Numano Y, Kusano Y, Ikeda R, Nomura K, Sugawara M, Ohta N, Akaike T, Katori Y.　Supersulfide formation in the sinus mucosa of chronic rhinosinusitis.
Laryngoscope Investig Otolaryngol. 2024 Jul 27;9(4):e1261. doi: 10.1002/lio2.1261. eCollection

2024 Aug.

4) Miyabe Y, Fukuchi M, Tomizawa H, Nakamura Y, Jikei M, Matsuwaki Y, Arima M, Konno Y, Moritoki Y, Takeda M, Tanabe N, Shima H, Shiraishi Y, Hirai T, Ohta N, Takahata J, Matsubara A, Yamada T, Asano K, Miyairi I, Melo RCN, Weller PF, Ueki S. Aggregated eosinophils and neutrophils characterize the properties of mucus in chronic rhinosinusitis. J Allergy Clin Immunol. 2024 May;153(5):1306-1318. doi: 10.1016/j.jaci.2023.11.925. Epub 2024 Jan 4.

5) Yamada T, Yanagaki S, Satani N, Kagaya Y, Sato T, Matsuura T, Sato T, Noguchi N, Ohta N . Spontaneous cervical and mediastinal hematoma due to rupture of inferior thyroid artery. Radiol Case Rep. 2024 :1145-1149. doi: 10.1016/j.radcr.2024.11.014. eCollection 2025 Feb.

6) 權太浩一, 太田伸男, 東海林 史, 鈴木 貴博 顔面神経麻痺評価法のあるべき姿と、新旧整合的な柳原法の修正. Nacial N Res Jpn 2024;43:165-169

7) 館田豊, 鈴木貴博, 佐藤輝幸, 山﨑宗治, 野口直哉, 太田伸男 経鼻胃管挿入を契機に血腫・気道狭窄をきたした高齢者の 1 例. 口咽科 2024;37(1):81-88

8) 太田 伸男, 岡野光博, 湯田厚司;【スギ・ヒノキ花粉症診療の現況と展望 2024 年、そして 10 年先の未来へ】. 鼻アレルギーフロンティア 2024;24(1):7－14

9) 太田伸男:実践！花粉症治療マニュアル 2024 小児花粉症への対応. 耳鼻咽喉科・頭頚部外科 2024;96(2);166-172

10) 太田伸男;ポストコロナ時代のアレルギー性鼻炎診療 【ポストコロナ時代の耳鼻咽喉科医の役割】ANCA 関連血管炎, IgG4 関連疾患. JOHNS 2024;40(5):515-520

11) 太田伸男;【治療法の再整理とアップデートのために】専門家による私の治療 副鼻腔嚢胞. 日本医事新報 2024;5253:52-53

12) 鈴木貴博, 太田伸男;必携！唾液腺診療虎の巻 非腫瘍性失火の診断と治療 ガマ腫 耳鼻咽喉科・頭頸部外科 2024;96(8):630-632

13) 舘田豊, 鈴木貴博, 佐藤輝幸, 山﨑宗治, 野口直哉, 太田 伸男;【てこずった症例・難治例にどう対応するのか】喉頭気管食道領域 呼吸苦を反復した成人発症の喉頭軟弱症例. JOHNS 2024;40(9):1085-1088

14) 佐藤輝幸, 太田伸男:【好酸球細胞外トラップと疾患】好酸球性中耳炎 これまでとこれから. 医学の歩み 2024;291(3):183－186

**＜学会発表と講演＞**

1) 太田伸男:シンポジウム 花粉症重症化ゼロ作戦. 宮城県の取り組み 第 125 回日本耳鼻咽喉科頭頸部外科学会, 大阪; 2024 年 5 月 16 日

2)　太田伸男: モーニングセミナー　アレルギー性鼻炎の UP TO DATE　診療のノウハウ･ドウハウ　押さえておきたい！スギ花粉症の診療のコツと落とし穴.　第 125 回日本耳鼻咽喉科頭頸部外科学会, 大阪; 2024 年 5 月 16 日

3)　舘田勝, 佐藤輝幸, 池田怜吉, 角田梨紗子,　小川武則, 香取幸夫, 太田伸男: リサーチフォーラム　声帯ポリープにおける免疫組織化学的検討.　第 72 回日本耳鼻咽喉科頭頸部外科学会東北地方部会連合学術講演会, 秋田;2024 年 7 月 13 日

4)　太田伸男:シンポジウム　アレルギン免疫療法の現状と展望　アレルゲン免疫療法のバイオマーカーの可能性.　第 73 回日本アレルギー学会, 京都;2024 年 10 月 20 日

5)　太田伸男; 特別講演　耳鼻咽喉科免疫関連疾患のパラダイムシフト　鼻アレルギーを中心に.　KETNET クロスカンファランス, 倉敷:2024 年 10 月 26 日

6)　太田伸男: 教育セミナー　難治性好酸球炎症性疾患-マネージメントの新展開.　第 38 回日本耳鼻咽喉科頭頸部学会秋季大会, 京都:204 年 12 月 1 日-

ii)一般演題

1)　鈴木貴博, 東海林史, 舘田豊, 野口直哉, 佐藤輝幸, 太田伸男:顔面神経麻痺の原因の鑑別に苦慮した耳下腺癌症例.　第 33 回日本頭頸部外科学会, 愛媛; 2024 年 2 月 1 日

2)　白鳥秋菜, 鈴木貴博, 佐藤輝幸, 野口直哉, 山﨑宗治, 舘田豊, 今井悠,太田伸男: 急性扁桃炎から Lemierre 症候群をきたした 1 例.　第 196 回日本耳鼻咽喉科頭頸部外科学会　宮城県地方部会, 仙台; 2024 年 3 月 4 日

3)　中角美穂, 東海林史, 池田怜吉, 齋藤雄太郎, 太田伸男　当科における口蓋扁桃摘出術の合併症の検討.　第 196 回日本耳鼻咽喉科頭頸部外科学会　宮城県地方部会, 仙台; 2024 年 3 月 4 日

4)　早河勇毅, 鈴木貴博, 野口直哉, 佐藤輝幸, 館田豊, 山﨑宗治, 白鳥秋菜, 中角美穂, 東海林史, 太田伸男　呼吸困難を呈したバセドウ病の 3 例.　第 196 回日本耳鼻咽喉科頭頸部外科学会　宮城県地方部会, 仙台; 2024 年 3 月 4 日

5)　Sato T, Ohta N　Periostin as a predictor of postoperative nasal polyps recurrence.　42nd Congress of the international Society of Inflammation and Allergy of the Nose.　Tokyo 2024 April 4

6)　Saito Y, Ohta N　Endoscopic treatment of sinonasal glomagiopericytoma; A case report in light of the literature.　42nd　Congress of the international Society of Inflammation and Allergy of the Nose.　Tokyo 2024 April 4

7)　舘田 豊, 佐藤 輝幸, 香取 幸夫, 太田 伸男　帯ポリープにおける CD31, CD34 とペリオスチンの発現の検討.　第 4 回日本耳鼻咽喉科免疫アレルギー感染症学会, 枚

方:2024 年 4 月 13 日

8） 太田伸男, 鈴木貴博, 野口直哉, 佐藤輝幸, 山﨑宗治, 舘田豊, 中角美穂, 東海林史: Facelift 法による副咽頭腫瘍摘出術. 第 125 回日本耳鼻咽喉科頭頸部外科学会, 大阪; 2024 年 5 月 18 日

9） 佐藤輝幸, 池田浩己, 鈴木貴博, 野口直哉, 山﨑宗治, 舘田豊, 太田伸男: 術後鼻茸再発予測因子としてのペリオスチン. 第 125 回日本耳鼻咽喉科頭頸部外科学会, 大阪; 2024 年 5 月 18 日

10） 舘田豊, 鈴木貴博, 佐藤輝幸, 太田伸男: 良性耳下腺腫瘍におけるペリオスチンの免疫組織学的検討. 第 125 回日本耳鼻咽喉科頭頸部外科学会, 大阪; 2024 年 5 月 16 日

11） 佐藤輝幸, 鈴木貴博, 野口直哉, 山﨑宗治, 舘田豊, 太田伸男: 切除範囲決定に苦慮した耳垢腺癌の 1 症例. 第 86 回日本耳鼻咽喉科臨床学会, 福井; 2024 年 6 月 28 日

12） 舘田豊, 佐藤輝幸, 香取幸夫, 太田伸男:声帯ポリープにおける CD31,CD34 の発現. 第 86 回日本耳鼻咽喉科臨床学会, 福井; 2024 年 6 月 28 日

13） 佐藤輝幸, 野口直哉, 山﨑宗治, 舘田 豊, 原陽介, 佐藤克海, 鈴木貴博, 太田伸男 副甲状腺腫瘍破裂により引き起こされた頸・縦隔血腫及び血胸を認めた 1 例. 第 72 回日本耳鼻咽喉科頭頸部外科学会東北地方部会連合学術講演会, 秋田;2024 年 7 月 13 日

14） 佐藤克海, 太田伸男, 鈴木貴博, 佐藤輝幸, 野口直哉, 山﨑宗治, 館田豊, 加藤雅士, 藤原 デュピルマブ投与後に好酸球性多発血管炎性肉芽腫症を発症した好酸球性副鼻腔炎例. 第 72 回日本耳鼻咽喉科頭頸部外科学会東北地方部会連合学術講演会, 秋田;2024 年 7 月 13 日

15） 太田伸男, 早河勇毅, 鈴木貴博, 野口直哉, 佐藤輝幸, 舘田勝, 山﨑宗治, 佐藤克海, 中角美穂, 東海林史, 中村はな, 吉田明子, 長屋慶 呼吸困難を呈したバセドウ病に対するマネージメント. 第 72 回日本耳鼻咽喉科頭頸部外科学会東北地方部会連合学術講演会, 秋田;2024 年 7 月 13 日

16） 舘田豊, 鈴木貴博, 佐藤輝幸, 太田伸男 唾液腺腫瘍におけるペリオスチンの発現様式の検討. 第 37 回日本口腔・咽頭科学会, 和歌山;2024 年 9 月 6 日

17） 鈴木貴博, 野口直哉, 舘田豊, 太田伸男 ワルトン管粘膜下に埋没した唾石症の 1 例. 第 37 回日本口腔咽頭科学会, 和歌山;2024 年 9 月 6 日

18） 佐藤克海, 野口直哉, 佐藤輝幸, 太田伸男 Dupilumab 投与後に好酸球性多発血管炎性肉芽腫症を発症した好酸球性副鼻腔炎例. 第 63 回日本鼻科学会, 東京;2024 年 9 月 28 日

19） 太田伸男, 佐藤輝幸, 佐藤克海, 野口直哉, 野口直哉, 鈴木貴博, 東海林史 ステロイド抵抗性鼻アレルギーにおける 11 beta-hydroxxysteroid dehydrogenase の発現. 第 63 回日本鼻科学会, 東京;2024 年 9 月 28 日

20)　中角美穂, 野口直哉, 佐藤輝幸, 佐藤克海, 東海林史, 太田伸男　頸部リンパ節転移をきたした嗅神経芽細胞腫の 1 例.　第 63 回日本鼻科学会, 東京;2024 年 9 月 28 日

21)　藤枝重治, 高林哲司, 太田伸男, 吉川衛, 木部友貴, 石田雅人, 鈴木勝人, 高橋康則, Maloey Jennifer, Wright Lakiera, Robinson Lacey, 八幡憲治　既存治療で効果不十分な鼻茸を伴う慢性副鼻腔炎患者に対するデュピルマブの有効性と安全性:第IV相試験.　第 63 回日本鼻科学会, 東京;2024 年 9 月 28 日

22)　太田伸男, WJ Fokkens, Ede CORSO, P Geraert, SE Lee, 藤枝重治, A Praestgaard, S Nash, M Corbet, H Sacks, JA Jacob-nara　鼻茸を伴う慢性副鼻腔炎患者における Dupilumab の客観的,患者報告アウトマムの改善順序.　第 73 回日本アレルギー学会, 京都;2024 年 10 月 20 日

23)　山﨑宗治, 川瀬哲明, 太田伸男　脳脊髄液漏出症を合併した機能性難聴の検討. 第 69 回日本聴覚医学会, 東京:2024 年 10 月 24 日

24)　佐藤克海　太田伸男; 当初甲状腺が疑われた甲状腺内胸腺癌の一例.　KETNET クロスカンファランス, 倉敷:2024 年 10 月 26 日

25)　舘田豊, 佐藤克海　太田伸男; 声帯ポリープにおける CD31.CD34 とペリオスチンの免疫組織学的局在.　KETNET クロスカンファランス, 倉敷:2024 年 10 月 26 日

26)　佐藤輝幸, 佐藤克海　太田伸男; アレルギー性鼻炎緩徐あの睡眠に対する脳内ヒスタミン H1 受容体占拠率の差が及ぼす影響.　KETNET クロスカンファランス, 倉敷:2024 年 10 月 26 日

27)　鈴木貴博, 舘田豊, 太田伸男　耳下腺良性腫瘍の形態および進展方向についての検討.　第 68 回日本唾液腺学会, 東京、2024 年 12 月 7 日　一般演題臨床 2－7

28)　舘田豊, 鈴木貴博, 佐藤輝幸, 太田伸男　良性耳下腺腫瘍における D-β-アスパラギン酸の発現　第 68 回日本唾液腺学会, 東京、2024 年 12 月 7 日　一般演題基礎 3－10

29)　山﨑宗治、川瀬哲明、太田伸男　脳脊髄液漏出症を合併した機能性難聴の検討. 日本耳鼻美咽喉科頭頚部外科学会　199 回宮城県地方部会, 仙台, 2024 年 12 月 7 日　一般演題　II-4

30)　河上和, 鈴木貴博, 野口直哉, 佐藤輝幸, 館田豊, 山﨑宗治, 佐藤克海, 神林友紀, 東海林史, 太田伸男、山方俊弘, 鈴木清寿, 長尾宗紀, 児山香, 安田勝洋, 工藤千枝子, 下平秀樹　化学放射線性咽喉頭炎に対する半夏瀉心湯の使用経験.　日本耳鼻美咽喉科頭頚部外科学会　199 回宮城県地方部会, 仙台, 2024 年 12 月 7 日　一般演題　I-1

31)　小川恭平, 鈴木貴博, 野口直哉, 佐藤輝幸, 館田豊, 山﨑宗治, 佐藤克海, 神林友紀, 東海林史, 太田伸男中村はな, 吉田明子, 長屋慶, 黒澤伸　バセドウ病に対する甲状腺全摘出術の臨床的検討.　日本耳鼻美咽喉科頭頚部外科学会　199 回宮城県地方部会, 仙台, 2024 年 12 月 7 日　一般演題　II-1

32）　佐藤克海, 鈴木貴博, 野口直哉, 佐藤輝幸, 館田豊, 山﨑宗治, 太田伸男、加藤雅士, 藤島史喜, 清水拓也日本耳鼻美咽喉科頭頚部外科学会　199 回宮城県地方部会, 仙台, 2024 年 12 月 7 日　一般演題　I-2

Tohoku J. Exp. Med., 2024, **262**, 105-113

# Expression of Periostin in Benign Salivary Gland Tumors

**Yutaka Tateda,[1] Takahiro Suzuki,[1] Teruyuki Sato,[1] Kenji Izuhara,[2] Kazue Ise,[3,4] Hiroki Shimada,[4] Keigo Murakami,[4] Kazuhiro Murakami,[4] Yasuhiro Nakamura[4] and Nobuo Ohta[1]**

[1]Division of Otolaryngology, Tohoku Medical and Pharmaceutical University Hospital, Sendai, Miyagi, Japan
[2]Division of Medical Biochemistry, Department of Biomolecular Sciences, Saga Medical School, Otsu, Saga, Japan
[3]Division of Technical Services, Tohoku Medical and Pharmaceutical University, Sendai, Miyagi, Japan
[4]Division of Pathology, Tohoku Medical and Pharmaceutical University, Sendai, Miyagi, Japan

Parotid tumors present a wide range of histological features, from benign to malignant. Periostin, an extracellular matrix protein specifically expressed in the periosteum and periodontal ligament, is isolated from osteoblast cell lines. It regulates fibrosis and collagen deposition and plays an important role in myocardial repair after myocardial infarction. It is also known to be involved in otorhinolaryngological-diseases. This study included 36 patients [38 specimens; 16 men and 20 women, mean age 59.2 (range 26-82) years] who underwent parotid tumor resection at the Division of Otorhinolaryngology, Tohoku Medical and Pharmaceutical University, between April 2017 and March 2022 and were clinically and pathologically diagnosed as having benign parotid tumors. Formalin-fixed, paraffin-embedded sections from the surgical specimens were autoclaved and immunostained with anti-periostin antibodies to evaluate the expression and distribution of periostin. Histologically, the tumors were diagnosed as pleomorphic adenomas in 15 cases (15 specimens), Warthin's tumors in 13 cases (15 specimens), basal cell adenomas in 2 cases (2 specimens), oncocytomas in 4 cases (4 specimens), and myoepitheliomas in 2 cases (2 specimens). An increased expression of periostin was found in 32 of 38 samples (84.2%) in the stroma of benign parotid tumors. Four distinct patterns of periostin expression were observed in benign parotid gland tumors: negative, superficial, infiltrative, and diffuse. Statistically significant differences were found between periostin expression patterns and histological classification of the tumors. Our results suggest that periostin may be involved in the pathogenesis of benign parotid tumors and could serve as a new biomarker for these tumors.

**Keywords:** benign salivary gland tumors; biomarker; capsule; patterns of periostin expression; periostin
Tohoku J. Exp. Med., 2024 February, **262** (2), 105-113.
doi: 10.1620/tjem.2023.J099

## Introduction

Infra-auricular masses can be attributed to salivary gland diseases as well as diseases originating from the surrounding soft tissues, such as lymph nodes. In addition, the inside of the parotid gland is in contact with the parapharyngeal space, and it is necessary to differentiate masses arising from this area. Salivary gland diseases encompass a wide variety of diseases, including inflammatory diseases and degenerative diseases in addition to neoplastic diseases. However, it is not always easy to differentiate between them as the main symptom is often just a mass.

Parotid gland tumors histologically range from benign to malignant and exhibit a variety of histological patterns. According to the WHO 2017 classification, there are 11 types of benign tumors and 23 types of malignant tumors. Treatment is tailored according to histological findings, indicating that no uniform treatment policy has been established. Approximately 85% of salivary gland tumors occur in the parotid gland, and the majority of parotid tumors are pleomorphic adenomas. Warthin's tumor is a benign tumor of the parotid gland and is the second most common tumor after pleomorphic adenoma. In the early 1900s, enucleation was the preferred surgery for benign parotid gland tumors.

Received November 8, 2023; revised and accepted December 5, 2023; J-STAGE Advance online publication December 14, 2023
Correspondence: Yutaka Tateda, Division of Otolaryngology, Tohoku Medical and Pharmaceutical University Hospital, 1-15-1 Fukumuro, Miyagino-ku, Sendai, Miyagi 983-8536, Japan.
e-mail: ytateda@tohoku-mpu.ac.jp
©2024 Tohoku University Medical Press. This is an open-access article distributed under the terms of the Creative Commons Attribution-NonCommercial-NoDerivatives 4.0 International License (CC-BY-NC-ND 4.0). Anyone may download, reuse, copy, reprint, or distribute the article without modifications or adaptations for non-profit purposes if they cite the original authors and source properly.
https://creativecommons.org/licenses/by-nc-nd/4.0/

However, it has been reported that the recurrence rate for parotid pleomorphic adenomas was as high as 45% (Rawson et al. 1950). Because of the high recurrence rate, total parotidectomy (TP) and superficial parotidectomy (SP) were proposed in the 1940s, which significantly reduced the recurrence rate (Guntinas-Lichius et al. 2006; Zernial et al. 2007). However, TP and SP are associated with complications such as a high rate of postoperative facial nerve paralysis and Frey syndrome.

Subsequently, partial superficial parotidectomy (PSP) was proposed, which preserves a portion of the normal parotid gland tissue and minimizes the dissection of facial nerve branches. This method is associated with fewer complications compared to SP and does not lead to a high recurrence rate (O'Brien 2003; Witt 2005). In terms of surgical approach, enucleation is selected for Warthin's tumor, whereas PSP is often performed for pleomorphic adenoma.

Periostin is an extracellular matrix protein that is specifically expressed in the periosteum and periodontal ligament and has been isolated from osteoblast cell lines. This protein regulates fibrosis and collagen deposition, and also plays an important role in myocardial repair after myocardial infarction. It is also known to be involved in various otorhinolaryngological diseases (Ohta et al. 2013, 2014; Tateda et al. 2022, 2023; Sato et al. 2023). According to recent studies, periostin expression is significantly higher in cardiac disease and tumor tissues in the majority of cancers compared to normal tissues (Hoersch and Andrade-Navarro 2010). Periostin is overexpressed in a variety of solid epithelial tumors, and its interaction with cell-surface receptor integrins, which modulates intracellular signaling pathways, has a direct effect on the hallmarks of cancer (Gonzalez-Gonzalez and Alonso 2018). It is upregulated in metastasis and can influence the size and number of metastatic lesions, underscoring its critical role in the formation and remodeling of cancer tissue microenvironments (Gonzalez-Gonzalez and Alonso 2018).

To the best of our knowledge, no studies focusing on the role of periostin in benign parotid tumors have been reported. Given the suggested involvement of periostin in tumorigenesis, our study investigated the expression sites of periostin in benign parotid gland tumors.

## Materials and Methods

*Subjects*

The patient group consisted of 38 patients [mean age ± standard deviation (SD) 59.2 ± 14.1 (range 26-82) years] with benign salivary gland tumors. These were all new cases without any instances of recurrence or signs of infection. All patients underwent benign parotid tumor surgery at the Division of Otolaryngology, Tohoku Medical and Pharmaceutical University Hospital from April 2017 to March 2022. Out of these patients, 36 presented with single lesions and two had double lesions. Only patients with typical clinical and histological findings were included in the patient group. The benign parotid gland tumors included in this study were of five different histologic types. Tumors were histologically diagnosed as pleomorphic adenomas in 15 cases (15 specimens) (Fig. 1A), Warthin's tumors in 13 cases (15 specimens) (Fig. 1B), basal cell adenomas in 2 cases (2 specimens) (Fig. 1C), oncocytomas in 4 cases (4 specimens) (Fig. 1D), and myoepitheliomas in 2 cases (2 specimens) (Fig. 1E). As a control group, normal parotid tissue specimens were obtained from patients aged 31 to 78 (mean age ± SD; 54.1 ± 15.1) years who had undergone PSP for pleomorphic adenoma. Histopathological diagnoses of benign salivary gland tumors were conducted at the Division of Pathology, Tohoku Medical and Pharmaceutical University Hospital. The study was approved by the ethics review committee of Tohoku Medical University Hospital (approval no. 2021-2-115). The requirement for obtaining informed consent was waived because of the adoption of an opt-out policy in the study.

*Immunohistochemistry analysis for detection of periostin*

Exactly 4-$\mu$m sections were cut from paraffin-embedded tissue blocks, deparaffinized, and rehydrated in a graded series of alcohols. Endogenous peroxidase activity was blocked using 3% $H_2O_2$ in absolute methanol at room temperature for 10 minutes. All sections were preincubated in Protein Block Serum-Free (Dako Cat No. X0909, Agilent Technologies Inc., Santa Clara, CA, USA) at room temperature for 20 minutes to block nonspecific background staining. The sections were then incubated with a polyclonal antibody (diluted 1:2,730) against polyclonal anti-periostin antibody and kept at 4°C overnight, followed by incubation with a secondary antibody, EnVision+ Dual Link System-HRP (Dako Cat No. K4063), for 60 minutes at room temperature. Finally, the sections were incubated with liquid diaminobenzidine + Substrate Chromogen System (Cat No. K3468 Dako) and counterstained with hematoxylin.

*Assessment of slides*

The immunostained sections were assessed at × 40 and × 100 magnifications under a light microscope equipped with an eyepiece reticle. Cell counts were expressed as means per high-power field (0.202 $mm^2$). At least two sections were immunostained, and more than five fields per section were evaluated via the reticle.

*Statistical analysis*

Variables were compared using one-way analysis of variance, Chi-square test for independence, or Fisher's exact test, as appropriate. A *P*-value of less than 0.05 was considered statistically significant. All statistical analyses were performed using EZR (Saitama Medical Center, Jichi Medical University, Saitama, Japan), a graphical user interface for R (The R Foundation for Statistical Computing, Vienna, Austria). More precisely, EZR is a modified version of R Commander designed to add statistical functions frequently used in biostatistics (Kanda 2013).

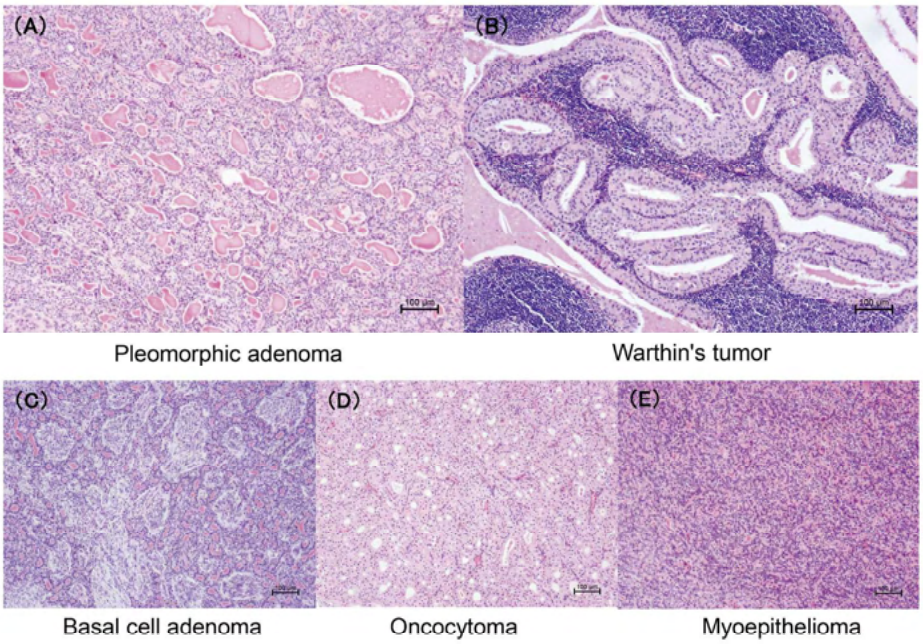


Fig. 1. Hematoxylin and eosin (HE) staining of benign parotid gland tumors.
(A) Pleomorphic adenomas showed a proliferation of the epithelial component in tubular, sheet-like, cord-like, or reticular arrangements. The mesenchymal component migrated from the epithelial component and was observed to be myxomatous, chondroid, fibrous, or vitreous. Osteogenesis was also observed (original magnification × 100). (B) Warthin's tumors demonstrated papillary, cystic, or tubular structures of the epithelium and a dense lymphocytic stromal component. The epithelial cells were organized in two layers of cylindrical, acidophilic cells (oncocytes) found on the luminal side of the ducts or cysts and small cuboidal or flattened basal-type cells located on the basement membrane side (original magnification × 100). (C) In basal cell adenomas, complex jigsaw-like nests of tumor cells were observed. The boundary between the foci and the stroma was distinct, and each foci was bordered by a basal lamina, which was sometimes thick and raised. A fenestrated array of tumor cells in a row was observed at the margins of the foci (original magnification × 100). (D) In oncocytomas, tumor cells grew in solid or cord-like nests, and conduit-like structures were observed in some areas (original magnification × 100). (E) In myoepitheliomas, tumor cells were mixed, and four morphologic types were observed: spindle cell, epithelioma, vitreous-like, and pale clear cell type (original magnification × 100).

Table 1. Periostin expression patterns and histopathological typing of benign salivary gland tumors.

| Histopathological typing of benign salivary gland tumors | Periostin expression patterns | | | | |
|---|---|---|---|---|---|
| | Negative type (n = 6) | Superficial type (n = 10) | Infiltrate type (n = 17) | Diffuse type (n = 5) | *P*-value |
| Pleomorphic adenoma (n = 15) | 1 | 0 | 9 | 5 | |
| Warthin's tumor (n = 15) | 3 | 10 | 2 | 0 | |
| Basal cell adenoma (n = 2) | 0 | 0 | 2 | 0 | < 0.001 |
| Oncocytoma (n = 4) | 0 | 0 | 4 | 0 | |
| Myoepithelioma (n = 2) | 2 | 0 | 0 | 0 | |

Chi-square test for independence test; $P < 0.001$

## Results

*Expression of periostin in benign parotid gland tumors*

Periostin expression was investigated in 38 samples of benign parotid gland tumors from 36 patients (Table 1). It was present in 32 (84.2%) samples obtained from patients with benign parotid gland tumors. The following four patterns of periostin expression were observed: negative (Fig. 2; A-1, A-2), superficial (Fig. 2; B-1, B-2), infiltrative (Fig. 2; C-1, C-2), and diffuse (Fig. 2; D-1, D-2). In the superficial pattern, periostin was detected only in the subepithelial layers between the basal-type cell and the stromal tissue

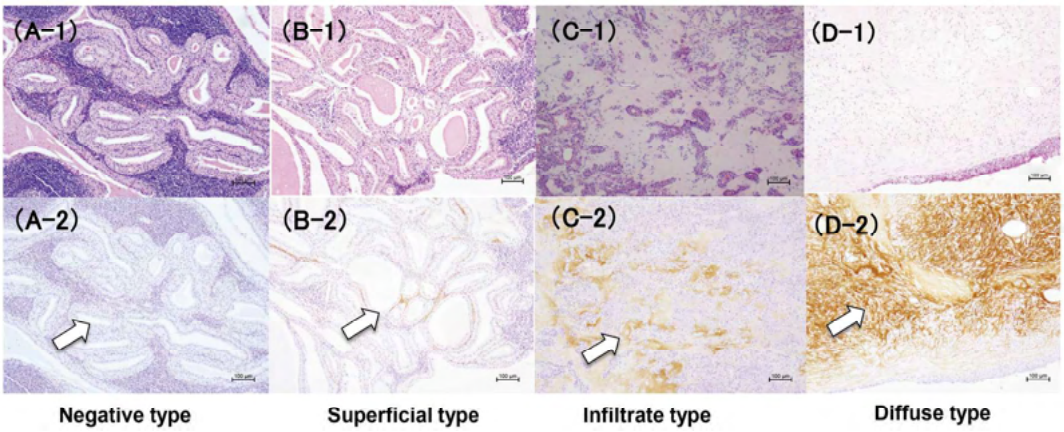


Fig. 2. Immunohistochemical staining for periostin in benign parotid gland tumors.
Immunohistochemical staining was categorized into the following four patterns: negative (n = 6), superficial (n = 10), infiltrative (n = 17), and diffuse (n = 5) (original magnification × 100) . (A-1) A Warthin's tumor was histologically identified by HE staining. (A-2) Immunohistochemical staining for periostin in a Warthin's tumor revealed no periostin, indicating a negative expression pattern (arrow). (B-1) A Warthin's tumor was histologically diagnosed by HE staining. (B-2) Immunohistochemical staining for periostin in a Warthin's tumor showed periostin only in the subepithelial layers between the basal-type cell and the stromal tissue, reflecting a superficial expression pattern (arrow). (C-1) A pleomorphic adenoma was histologically diagnosed by HE staining. (C-2) Immunohistochemical staining for periostin in pleomorphic adenoma showed variable expression in parts of the tumor stroma, indicating an infiltrative expression pattern (arrow). (D-1) A pleomorphic adenoma was histologically diagnosed by HE staining. (D-2) Immunohistochemical staining for periostin in pleomorphic adenoma showed widespread expression throughout the tumor stroma, indicating a diffuse expression pattern (arrow).

Table 2. Periostin expression patterns of the tumor capsules.

| | Periostin expression patterns of the tumor capsules | | |
|---|---|---|---|
| | Negative type (n = 18) | Positive type (n = 20) | *P*-value |
| Pleomorphic adenoma (n = 15) | 0 | 15 | |
| Warthin's tumor (n = 15) | 12 | 3 | |
| Basal cell adenoma (n = 2) | 2 | 0 | < 0.001 |
| Oncocytoma (n = 4) | 4 | 0 | |
| Myoepithelioma (n = 2) | 0 | 2 | |

Chi-square test for independence test; $P < 0.001$

(Fig. 2; B-2); in the infiltrative pattern, periostin was observed in parts of the tumor stroma to varying degrees (Fig. 2; C-2); and in the diffuse pattern, periostin was diffusely expressed in the tumor stroma (Fig. 2; D-2). No periostin expression was observed in the normal parotid tissue samples.

*Expression of periostin in the capsule of benign parotid gland tumors*

The expression of periostin was investigated in the same 38 samples (Table 2), out of which 20 (52.6%) showed increased periostin expression in the tumor capsule. The breakdown of periostin-positive cases of tumor capsules was pleomorphic adenoma in all 15 cases (100%), myoepithelioma in 2 cases (100%), and Warthin's tumor in 3 out of 15 cases (20%). Two distinct patterns of periostin expression were observed in the tumor capsule: positive type (Fig. 3; A-1, A-2, A-3) and negative type (Fig. 3; B-1, B-2, B-3). A significant association was found between the pattern of periostin expression in the tumor capsule and the histology of benign parotid tumors (Table 2).

*Expression of periostin, and clinical and histological factors*

An association was observed between the periostin expression pattern and the histological types of the benign parotid gland tumors (Table 1). The Warthin's tumor was

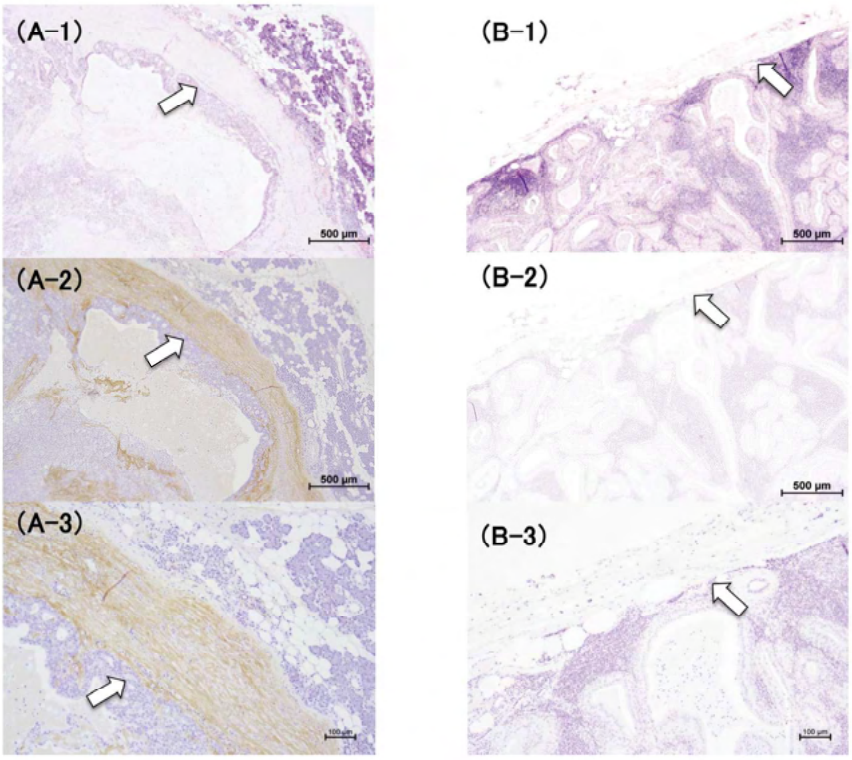


Fig. 3. Immunohistochemical staining patterns of periostin in the capsules of benign parotid gland tumors, categorized into two types: positive (n = 20) and negative (n = 18) (original magnification × 40 and × 100, respectively).
Case A. A 78-year-old Japanese woman presented with a parotid gland tumor. (A-1) Histological analysis identified a pleomorphic adenoma (HE staining). (A-2, A-3) Immunohistochemical staining revealed the presence of periostin in the capsule of the pleomorphic adenoma (arrow). Case B. A 77-year-old Japanese man was evaluated for a parotid gland tumor. (B-1) Histological examination revealed a Warthin's tumor (HE staining). (B-2, B-3) Immunohistochemical staining showed no periostin in the capsule of the tumor (arrow).

Table 3. Clinical characteristics and expression of periostin in 38 samples of benign salivary gland tumors.

| | | Negative type | Positive type | *P*-value | Superficial type | Infiltrate type | Diffuse type | *P*-value |
|---|---|---|---|---|---|---|---|---|
| Total | 38 | 6 | 32 | | 10 | 17 | 5 | |
| Male, n (%) | 17 (44.7%) | 2 (5.3%) | 15 (39.5%) | 0.54 | 8 (21.1%) | 6 (15.8%) | 1 (8.5%) | 0.0338 |
| Female, n (%) | 21 (55.3%) | 4 (10.5%) | 17 (44.7%) | | 2 (5.3%) | 11 (29.0%) | 4 (10.5%) | |
| Mean age ± SD (years) | 59.2 ± 14.1 | 54.0 ± 7.9 | 60.1 ± 14.9 | 0.336 | 66.1 ± 8.4 | 55.9 ± 16.2 | 62.6 ± 18.3 | 0.222 |
| Tumor site | | | | | | | | |
| Superficial lobe, n (%) | 27 (71.1%) | 5 (13.2%) | 22 (57.9%) | 0.47 | 9 (23.7%) | 9 (23.7%) | 4 (10.5%) | 0.165 |
| Deep lobe, n (%) | 11 (28.9%) | 1 (2.6%) | 10 (26.3%) | | 1 (2.6%) | 8 (21.1%) | 1 (2.6%) | |
| Pain, n (%) | 1 (2.6%) | 1 (2.6%) | 0 (0%) | 0.0192 | 0 (0%) | 0 (0%) | 0 (0%) | 1 |
| Mobility | | | | | | | | |
| Good mobility, n (%) | 36 (94.7%) | 5 (13.2%) | 31 (81.6%) | 0.172 | 10 (26.3%) | 16 (42.1%) | 5 (13.2%) | 0.492 |
| No palpable tumor, n (%) | 2 (5.3%) | 1 (2.6%) | 1 (2.6%) | 0.173 | 0 (0%) | 1 (2.6%) | 0 (0%) | 0.492 |

significantly dominant in the superficial periostin expression pattern (Table 1). Furthermore, a sex-related difference was found between the patterns of periostin expression in parotid gland tumors. Females were significantly more likely than males to exhibit the infiltrative and diffuse patterns of periostin expression (Table 3). Conversely, the superficial pattern was significantly more common in males than in females (Table 3). No association was found

Table 4. Tumor size and expression of periostin in 38 samples of benign salivary gland tumors.

| | | Negative type | Positive type | *P*-value | Superficial type | Infiltrate type | Diffuse type | *P*-value |
|---|---|---|---|---|---|---|---|---|
| Total | 38 | 6 | 32 | | 10 | 17 | 5 | |
| Size (cm) | | | | | | | | |
| Tumor ≦ 2 | 7 (18.4%) | 1 (2.6%) | 6 (15.8%) | | 2 (5.3%) | 3 (7.9%) | 1 (2.6%) | |
| 2 < Tumor ≦ 4 | 24 (63.2%) | 5 (13.2%) | 19 (50%) | $P = 0.235$ | 5 (13.2%) | 11 (28.9%) | 3 (7.9%) | $P = 0.862$ |
| Tumor > 4 | 7 (18.4%) | 0 (0%) | 7 (18.4%) | | 3 (7.9%) | 3 (7.9%) | 1 (2.6%) | |

Table 5. Dynamic MRI pattern and expression of periostin in 18 samples of benign salivary gland tumors.

| | | Negative type | Positive type | *P*-value | Superficial type | Infiltrate type | Diffuse type | *P*-value |
|---|---|---|---|---|---|---|---|---|
| Total | 18 | 3 | 15 | | 4 | 9 | 2 | |
| Dynamic MRI pattern | | | | | | | | |
| Persistent pattern, n (%) | 6 (33.3%) | 1 (5.6%) | 5 (27.8%) | | 1 (5.6%) | 3 (16.7%) | 1 (5.6%) | |
| Plateau pattern, n (%) | 4 (22.2%) | 0 (0%) | 4 (22.2%) | 0.549 | 0 (0%) | 3 (16.7%) | 1 (5.6%) | 0.504 |
| Washout pattern, n (%) | 8 (44.4%) | 2 (11.1%) | 6 (33.3%) | | 3 (16.7%) | 3 (16.7%) | 0 (0%) | |

Table 6. Clinical characteristics and histopathological typing of benign salivary gland tumors.

| | | Pleomorphic adenoma | Warthin's tumor | Basal cell adenoma | Oncocy toma | Myoepithe lioma | *P*-value |
|---|---|---|---|---|---|---|---|
| Total | 38 | 15 | 15 | 2 | 4 | 2 | |
| Male | 17 (44.7%) | 4 (10.5%) | 10 (26.3%) | 0 (0%) | 2 (5.3%) | 1 (2.6%) | 0.159 |
| Female | 21 (55.3%) | 11 (29.0%) | 5 (13.2%) | 2 (5.3%) | 2 (5.3%) | 1 (2.6%) | |
| Mean age ± SD (years) | 59.2 ± 14.1 | 54.1 ± 15.3 | 65.8 ± 8.68 | 62.0 ± 9.9 | 55.5 ± 22.9 | 51.5 ± 12.0 | |

between the periostin expression pattern and other clinical characteristics, including the involvement of the superficial and deep lobes (Table 3). Furthermore, no association was found between periostin expression pattern and tumor size (Table 4), or between periostin expression pattern and dynamic MRI pattern (Table 5). Finally, no association was found between clinical characteristics and the histopathological typing of benign salivary gland tumors (Table 6).

## Discussion

Periostin was cloned by Takeshita et al. as osf-2, a gene specifically expressed in osteoblasts and similar to midline fasciclin-1, an intercellular adhesion factor of Drosophila melanogaster, and subsequently localized specifically to the outer bone membrane and periodontal ligament. It was later renamed periostin because of its specific localization in the epiphyseal and periodontal ligaments and its involvement in cell adhesion (Takeshita et al. 1993; Horiuchi et al. 1999). Recent studies have reported the expression of periostin not only in the epiphyseal and periodontal ligaments but also in embryogenesis; various pathological conditions such as myocardial infarction, cancer, myelofibrosis, and muscular dystrophy; and in the healing and regeneration-related processes including wound healing and skeletal muscle regeneration (Urasawa et al. 1996; Stanton et al. 2000; Kruzynska-Frejtag et al. 2001; Goetsch et al. 2003; Wang et al. 2003; Katsuragi et al. 2004; Norris et al. 2007; Hamilton 2008; Oku et al. 2008). In otorhinolaryngology, periostin expression has been reported in chronic sinusitis, vocal folds polyps, IgG4-related diseases, organized hematoma, and eosinophilic otitis media (Ohta et al. 2013, 2014; Tateda et al. 2022, 2023; Sato et al. 2023). Studies on tumors and periostin have reported periostin overexpression in thymoma and non-small-cell lung cancer (Sasaki et al. 2001a, b). Subsequently, it has been reported in ovarian cancer, neuroblastoma, breast cancer, colorectal cancer, bladder cancer, squamous cell carcinoma of the head and neck, pancreatic cancer, thyroid cancer, and other cancer types, highlighting a close relationship between periostin expression and malignant transformation and progression of cancer, including invasion, metastasis, and prognosis (Sasaki et al. 2001a, b, 2002, 2003; Gillan et al. 2002; Bao et al. 2004; Kudo et al. 2006; Fukushima et al. 2008; Puppin et al. 2008; Kim et al. 2011; Li et al. 2015; Ratajczak-Wielgomas et al. 2017; Kujawa et al. 2020; Yue et al. 2021). To the best of our knowledge, no studies have

reported on the role of periostin in parotid tumors.

Benign parotid tumors are classified into 11 types according to the 2017 WHO classification. The current study included five types of benign parotid tumors: pleomorphic adenoma, Warthin's tumor, basal cell adenoma, oncocytoma, and myoepithelioma. In the four histological types (pleomorphic adenoma, Warthin's tumor, basal cell adenoma, and oncocytoma) analyzed in the present study, various levels and patterns of periostin expression were observed in the stroma of the tumors. In a previous study, Tateda et al. (2022, 2023) reported that periostin was overexpressed in vocal fold polyps, which are non-neoplastic lesions of the larynx. In these polyps, periostin expression was found in the interstitial spaces, and the pattern of expression was classified into four types: negative, superficial, infiltrate, and diffuse (Tateda et al. 2022, 2023).

Based on these findings, we investigated the expression pattern of periostin in benign parotid tumors in this study. None of the parotid tumors included in this study showed periostin expression in the epithelium.

The four histological types and the expression patterns of periostin were examined in this study. In cases of pleomorphic adenoma, periostin exhibited the following expression patterns: negative in one case, infiltrate in nine cases, and diffuse in five cases. High expression of periostin was noted in spindle-shaped cells and areas of fibrosis in the stroma. In Warthin's tumor, periostin expression was categorized as follows: negative in three cases, superficial in ten cases, and infiltrative in two cases. In the superficial type, the most common periostin phenotype in Warthin's tumors, periostin was detected only in the subepithelial layer between basal-type cells and the stromal tissue. The superficial pattern was consistently observed in all 10 cases within Warthin's tumors, marking it as a characteristic finding. The rates of recurrence and malignant transformation for this tumor are low. In all cases of basal cell adenoma, periostin expression was of the infiltrative type, with high expression observed in spindle-shaped cells and the fibrotic stroma. In all four cases of oncocytoma, periostin expression was of the infiltrative type, with high expression observed in spindle-shaped cells and stromal fibrosis. In myoepithelioma cases, periostin expression was negative. Previous studies have reported the expression of periostin in the fibrous stroma of invasive carcinomas and the fibrous capsules found in tumors (Shimazaki and Kudo 2008).

Among benign parotid tumors, pleomorphic adenomas are clinically characterized by the possibility of recurrence; hence, enucleation is not the surgical technique of choice. Instead, partial lobectomy is preferred, which involves excision of the tumor along with the normal parotid gland. Most tumors have a low risk of recurrence if surgical margins are negative, with postoperative recurrence rates of approximately 7%. However, this is not the case for tumors that extend histologically outside the capsule in a finger-like or pseudopodial pattern. In addition, about 6% of polymorphous adenomas develop into cancer. In our study, out of the 15 cases of pleomorphic adenoma, 14 exhibited periostin expression of infiltrative or diffuse type. Conversely, in Warthin's tumors, which do not recur frequently, 13 of the 15 cases were of the negative or superficial type in terms of periostin expression. The only significant factor was the sex (Table 3). We think that it simply means the difference in material number of pleomorphic adenoma and Warthin's tumor.

In terms of parotid tumor capsules, pathological examinations revealed that pleomorphic adenoma, Warthin's tumor, basal cell adenoma, oncocytoma, and myoepithelioma showed capsules. Among these, pleomorphic adenoma was found to be carcinomatous in about 6% of cases, and myoepithelioma was reported to be malignant in a few cases. The capsules of pleomorphic adenoma and myoepithelioma, which have been reported to be potentially carcinomatous, were positive for periostin expression in all cases. Significant differences were observed between the histological types of benign parotid tumors and the expression pattern of periostin. For the tumor capsule, significant differences were observed between the histological type of benign parotid tumor and the presence or absence of periostin expression in the tumor capsule. This suggests a possible association between pleomorphic adenoma, and increased expression and localization of periostin and the possibility of recurrence. Our study has several limitations. First, the number of patients with salivary gland tumors recruited in this study was relatively small because the samples were collected from only a single center. Second, we should investigate the relationship between benign salivary gland tumors and malignant salivary gland tumors to ascertain differences in periostin expression between benign salivary gland tumors and malignant salivary gland tumors, which were not investigated in this study. Further research with many more samples is required to reveal the mechanism of expression of periostin in salivary gland tumors. Third, the relationship between periostin expression and benign salivary gland tumors growth was not investigated in this study. In conclusion, our results indicate that overexpression of periostin is likely involved in the pathogenesis of benign parotid tumors. We propose that periostin could serve as a novel biomarker for these tumors and might offer a new avenue for therapeutic intervention.

In conclusion, our results indicate that overexpression of periostin is likely involved in the pathogenesis of benign salivary gland tumors. Based on these findings, periostin emerges as a potential novel biomarker and therapeutic target for these tumors.

## Acknowledgments

We sincerely thank Mr. Junya Ono for his assistance.

## Conflict of Interest

The authors declare no conflict of interest.

## References


Bao, S., Ouyang, G., Bai, X., Huang, Z., Ma, C., Liu, M., Shao, R., Anderson, R.M., Rich, J.N. & Wang, X.F. (2004) Periostin potently promotes metastatic growth of colon cancer by augmenting cell survival via the Akt/PKB pathway. *Cancer Cell*, **5**, 329-339.

Fukushima, N., Kikuchi, Y., Nishiyama, T., Kudo, A. & Fukayama, M. (2008) Periostin deposition in the stroma of invasive and intraductal neoplasms of the pancreas. *Mod. Pathol.*, **21**, 1044-1053.

Gillan, L., Matei, D., Fishman, D.A., Gerbin, C.S., Karlan, B.Y. & Chang, D.D. (2002) Periostin secreted by epithelial ovarian carcinoma is a ligand for alpha(V)beta(3) and alpha(V)beta(5) integrins and promotes cell motility. *Cancer Res.*, **62**, 5358-5364.

Goetsch, S.C., Hawke, T.J., Gallardo, T.D., Richardson, J.A. & Garry, D.J. (2003) Transcriptional profiling and regulation of the extracellular matrix during muscle regeneration. *Physiol. Genomics*, **14**, 261-271.

Gonzalez-Gonzalez, L. & Alonso, J. (2018) Periostin: a matricellular protein with multiple functions in cancer development and progression. *Front. Oncol.*, **8**, 225.

Guntinas-Lichius, O., Klussmann, J.P., Wittekindt, C. & Stennert, E. (2006) Parotidectomy for benign parotid disease at a university teaching hospital: outcome of 963 operations. *Laryngoscope*, **116**, 534-540.

Hamilton, D.W. (2008) Functional role of periostin in development and wound repair: implications for connective tissue disease. *J. Cell Commun. Signal.*, **2**, 9-17.

Hoersch, S. & Andrade-Navarro, M.A. (2010) Periostin shows increased evolutionary plasticity in its alternatively spliced region. *BMC Evol. Biol.*, **10**, 30.

Horiuchi, K., Amizuka, N., Takeshita, S., Takamatsu, H., Katsuura, M., Ozawa, H., Toyama, Y., Bonewald, L.F. & Kudo, A. (1999) Identification and characterization of a novel protein, periostin, with restricted expression to periosteum and periodontal ligament and increased expression by transforming growth factor beta. *J. Bone Miner. Res.*, **14**, 1239-1249.

Kanda, Y. (2013) Investigation of the freely available easy-to-use software 'EZR' for medical statistics. *Bone Marrow Transplant.*, **48**, 452-458.

Katsuragi, N., Morishita, R., Nakamura, N., Ochiai, T., Taniyama, Y., Hasegawa, Y., Kawashima, K., Kaneda, Y., Ogihara, T. & Sugimura, K. (2004) Periostin as a novel factor responsible for ventricular dilation. *Circulation*, **110**, 1806-1813.

Kim, C.J., Sakamoto, K., Tambe, Y. & Inoue, H. (2011) Opposite regulation of epithelial-to-mesenchymal transition and cell invasiveness by periostin between prostate and bladder cancer cells. *Int. J. Oncol.*, **38**, 1759-1766.

Kruzynska-Frejtag, A., Machnicki, M., Rogers, R., Markwald, R.R. & Conway, S.J. (2001) Periostin (an osteoblast-specific factor) is expressed within the embryonic mouse heart during valve formation. *Mech. Dev.*, **103**, 183-188.

Kudo, Y., Ogawa, I., Kitajima, S., Kitagawa, M., Kawai, H., Gaffney, P.M., Miyauchi, M. & Takata, T. (2006) Periostin promotes invasion and anchorage-independent growth in the metastatic process of head and neck cancer. *Cancer Res.*, **66**, 6928-6935.

Kujawa, K.A., Zembala-Nozynska, E., Cortez, A.J., Kujawa, T., Kupryjanczyk, J. & Lisowska, K.M. (2020) Fibronectin and periostin as prognostic markers in ovarian cancer. *Cells*, **9**, 149.

Li, Z., Zhang, X., Yang, Y., Yang, S., Dong, Z., Du, L., Wang, L. & Wang, C. (2015) Periostin expression and its prognostic value for colorectal cancer. *Int. J. Mol. Sci.*, **16**, 12108-12118.

Norris, R.A., Damon, B., Mironov, V., Kasyanov, V., Ramamurthi, A., Moreno-Rodriguez, R., Trusk, T., Potts, J.D., Goodwin, R.L., Davis, J., Hoffman, S., Wen, X., Sugi, Y., Kern, C.B., Mjaatvedt, C.H., et al. (2007) Periostin regulates collagen fibrillogenesis and the biomechanical properties of connective tissues. *J. Cell. Biochem.*, **101**, 695-711.

O'Brien, C.J. (2003) Current management of benign parotid tumors--the role of limited superficial parotidectomy. *Head Neck*, **25**, 946-952.

Ohta, N., Ishida, A., Kurakami, K., Suzuki, Y., Kakehata, S., Ono, J., Ikeda, H., Okubo, K. & Izuhara, K. (2014) Expressions and roles of periostin in otolaryngological diseases. *Allergol. Int.*, **63**, 171-180.

Ohta, N., Kurakami, K., Ishida, A., Furukawa, T., Suzuki, Y., Aoyagi, M., Matsubara, A., Izuhara, K. & Kakehata, S. (2013) Roles of TGF-beta and periostin in fibrosclerosis in patients with IgG4-related diseases. *Acta Otolaryngol.*, **133**, 1322-1327.

Oku, E., Kanaji, T., Takata, Y., Oshima, K., Seki, R., Morishige, S., Imamura, R., Ohtsubo, K., Hashiguchi, M., Osaki, K., Yakushiji, K., Yoshimoto, K., Ogata, H., Hamada, H., Izuhara, K., et al. (2008) Periostin and bone marrow fibrosis. *Int. J. Hematol.*, **88**, 57-63.

Puppin, C., Fabbro, D., Dima, M., Di Loreto, C., Puxeddu, E., Filetti, S., Russo, D. & Damante, G. (2008) High periostin expression correlates with aggressiveness in papillary thyroid carcinomas. *J. Endocrinol.*, **197**, 401-408.

Ratajczak-Wielgomas, K., Grzegrzolka, J., Piotrowska, A., Matkowski, R., Wojnar, A., Rys, J., Ugorski, M. & Dziegiel, P. (2017) Expression of periostin in breast cancer cells. *Int. J. Oncol.*, **51**, 1300-1310.

Rawson, A.J., Howard, J.M., Royster, H.P. & Horn, R.C. Jr. (1950) Tumors of the salivary glands; a clinicopathological study of 160 cases. *Cancer*, **3**, 445-458.

Sasaki, H., Dai, M., Auclair, D., Fukai, I., Kiriyama, M., Yamakawa, Y., Fujii, Y. & Chen, L.B. (2001a) Serum level of the periostin, a homologue of an insect cell adhesion molecule, as a prognostic marker in nonsmall cell lung carcinomas. *Cancer*, **92**, 843-848.

Sasaki, H., Dai, M., Auclair, D., Kaji, M., Fukai, I., Kiriyama, M., Yamakawa, Y., Fujii, Y. & Chen, L.B. (2001b) Serum level of the periostin, a homologue of an insect cell adhesion molecule, in thymoma patients. *Cancer Lett.*, **172**, 37-42.

Sasaki, H., Sato, Y., Kondo, S., Fukai, I., Kiriyama, M., Yamakawa, Y. & Fuji, Y. (2002) Expression of the periostin mRNA level in neuroblastoma. *J. Pediatr. Surg.*, **37**, 1293-1297.

Sasaki, H., Yu, C.Y., Dai, M., Tam, C., Loda, M., Auclair, D., Chen, L.B. & Elias, A. (2003) Elevated serum periostin levels in patients with bone metastases from breast but not lung cancer. *Breast Cancer Res. Treat.*, **77**, 245-252.

Sato, T., Ikeda, H., Murakami, K., Murakami, K., Shirane, S. & Ohta, N. (2023) Periostin is an aggravating factor and predictive biomarker of eosinophilic chronic rhinosinusitis. *Allergol. Int.*, **72**, 161-168.

Shimazaki, M. & Kudo, A. (2008) Impaired capsule formation of tumors in periostin-null mice. *Biochem. Biophys. Res. Commun.*, **367**, 736-742.

Stanton, L.W., Garrard, L.J., Damm, D., Garrick, B.L., Lam, A., Kapoun, A.M., Zheng, Q., Protter, A.A., Schreiner, G.F. & White, R.T. (2000) Altered patterns of gene expression in response to myocardial infarction. *Circ. Res.*, **86**, 939-945.

Takeshita, S., Kikuno, R., Tezuka, K. & Amann, E. (1993) Osteoblast-specific factor 2: cloning of a putative bone adhesion protein with homology with the insect protein fasciclin I. *Biochem. J.*, **294** ( Pt 1), 271-278.

Tateda, Y., Ikeda, R., Kakuta, R., Izuhara, K., Ogawa, T., Ise, K., Shimada, H., Murakami, K., Murakami, K., Nakamura, Y., Katori, Y. & Ohta, N. (2023) Immunohistochemical localization of D-beta-aspartic acid and periostin in vocal fold polyps. *Tohoku J. Exp. Med.*, **260**, 223-230.

Tateda, Y., Ikeda, R., Kakuta, R., Ono, J., Izuhara, K., Ogawa, T., Ise, K., Shimada, H., Murakami, K., Murakami, K., Naka-

mura, Y., Katori, Y. & Ohta, N. (2022) Expression of periostin in vocal fold polyps. *Tohoku J. Exp. Med.*, **258**, 55-62.
Urasawa, K., Yoshida, I., Takagi, C., Onozuka, H., Mikami, T., Kawaguchi, H. & Kitabatake, A. (1996) Enhanced expression of beta-adrenergic receptor kinase 1 in the hearts of cardiomyopathic Syrian hamsters, BIO53.58. *Biochem. Biophys. Res. Commun.*, **219**, 26-30.
Wang, D., Oparil, S., Feng, J.A., Li, P., Perry, G., Chen, L.B., Dai, M., John, S.W. & Chen, Y.F. (2003) Effects of pressure overload on extracellular matrix expression in the heart of the atrial natriuretic peptide-null mouse. *Hypertension*, **42**, 88-95.
Witt, R.L. (2005) Minimally invasive surgery for parotid pleomorphic adenoma. *Ear Nose Throat J.*, **84**, 308, 310-311.
Yue, H., Li, W., Chen, R., Wang, J., Lu, X. & Li, J. (2021) Stromal POSTN induced by TGF-beta1 facilitates the migration and invasion of ovarian cancer. *Gynecol. Oncol.*, **160**, 530-538.
Zernial, O., Springer, I.N., Warnke, P., Harle, F., Risick, C. & Wiltfang, J. (2007) Long-term recurrence rate of pleomorphic adenoma and postoperative facial nerve paresis (in parotid surgery). *J. Craniomaxillofac. Surg.*, **35**, 189-192.

Tohoku J. Exp. Med., 2024, **264**, 93-99

# Expression of Vascular and Tissue Repair Factors in Laryngeal Granulomas

**Yutaka Tateda[1], Ryoukichi Ikeda[2,3], Risako Kakuta[2], Kenji Izuhara[4], Takenori Ogawa[2,5], Kazue Ise [6,7], Hiroki Shimada[7], Keigo Murakami[7], Kazuhiro Murakami[7], Yasuhiro Nakamura[7], Yukio Katori[2] and Nobuo Ohta[1]**

[1]Division of Otolaryngology, Tohoku Medical and Pharmaceutical University Hospital, Sendai, Miyagi, Japan
[2]Department of Otolaryngology-Head and Neck Surgery, Tohoku University Graduate School of Medicine, Sendai, Miyagi, Japan
[3]Department of Otolaryngology, Iwate Medical University, Morioka, Iwate, Japan
[4]Division of Medical Biochemistry, Department of Biomolecular Sciences, Saga Medical School, Saga, Saga, Japan
[5]Department of Otolaryngology, Gifu University Graduate School of Medicine, Gifu, Gifu, Japan
[6]Technical Services Division, Tohoku Medical and Pharmaceutical University, Sendai, Miyagi, Japan
[7]Division of Pathology, Tohoku Medical and Pharmaceutical University, Sendai, Miyagi, Japan

Voice abuse, chronic cough, laryngeal surgery, and tracheal intubation may lead to injury and subsequent repair/remodeling in the vocal fold mucosa. Periostin is known to be involved in airway remodeling and is also associated with various otolaryngological diseases. D-β-aspartic acid is the major isomer of D-aspartic acid found in tissues of elderly individuals. In ischemic heart disease, increased CD31 expression has been observed around cardiomyocytes during remodeling, and endothelial proliferation has been reported at these sites. In this study, we investigated the expression and role of CD31, CD34, D-β-aspartic acid, and periostin in the formation of laryngeal granulation tissue. This retrospective study involved five patients who underwent surgical treatment for laryngeal granulation tissue. The expressions of CD31, CD34, D-β-aspartic acid, and periostin in surgical samples were investigated by immunohistochemistry. Histologically, the specimens showed inflammatory cell infiltration, fibrin exudation, fibrosis, and neovascularization, but no tumor cells. No stratified squamous epithelial covering was observed. The expression of periostin and D-β-aspartic acid was also observed in the specimens. CD31-positive cells (endothelial cells) and CD34-positive cells (progenitors of endothelial cells) were observed in the specimens. Our results indicate that the overexpression of CD31, CD34, D-β-aspartic acid, and periostin may play a role in the pathogenesis of laryngeal granulation tissue, and we speculate that D-β-aspartic acid and periostin could serve as novel biomarkers and therapeutic targets for laryngeal granulation tissue.

**Keywords:** CD31; CD34; D-β-aspartic acid; laryngeal granulation tissue; periostin
Tohoku J. Exp. Med., 2024 October, **264** (2), 93-99.
doi: 10.1620/tjem.2024.J056

## Introduction

Granulation tissue is a newly formed mass of connective tissue and capillaries that appear on a wound. Laryngeal granulation tissue is an inflammatory mass that tends to occur near the vocal fold process in the posterior part of the median portal, and is classified according to its cause into four categories: that resulting from laryngeal surgery, that occurring after endotracheal intubation, that caused by contact with the voice through overuse or force, and that of unknown cause (Kleinsasser 1969). The formation of this tissue can be attributed to voice overuse or forceful generation of voice, where the epithelium is damaged by friction caused by coughing or strenuous raising of the voice, resulting in an inflammatory mass at the site of the injury. Conditions occurring after endotracheal intuba-

Received March 26, 2024; revised and accepted June 18, 2024; J-STAGE Advance online publication June 27, 2024
Correspondence: Yutaka Tateda, Division of Otolaryngology, Tohoku Medical and Pharmaceutical University Hospital, 1-15-1 Fukumuro, Miyagino-ku, Sendai, Miyagi 983-8536, Japan.
e-mail: ytateda@tohoku-mpu.ac.jp
©2024 Tohoku University Medical Press. This is an open-access article distributed under the terms of the Creative Commons Attribution-NonCommercial-NoDerivatives 4.0 International License (CC-BY-NC-ND 4.0). Anyone may download, reuse, copy, reprint, or distribute the article without modifications or adaptations for non-profit purposes if they cite the original authors and source properly.
https://creativecommons.org/licenses/by-nc-nd/4.0/

tion are similar, caused by irritation from the intubation. Recently, this condition has also been associated with gastric acid reflux into the pharynx. Pathologically, it is characterized by chronic inflammation and is not considered a tumor.

In the context of laryngeal diseases, the expressions of CD31, CD34, D-$\beta$-aspartic acid, and periostin have been reported in vocal polyps, which are non-neoplastic masses (Tateda et al. 2022, 2023a, b). Immunological studies on periostin and D-$\beta$-aspartic acid in laryngeal granulation tissue, including CD31 and CD34, which are thought to be involved in neovascularization in chronic inflammation, have not yet been performed. In the present study, we immunohistochemically examined the expression of periostin, CD31, and CD34 in seven samples from five patients undergoing surgical treatment for laryngeal granulation tissue, and D-$\beta$-aspartic acid in three samples.

## Materials and Methods

*Subjects*

The patient group consisted of five individuals with laryngeal granulation tissue, aged 54–84 (mean age ± standard deviation (SD) 72.8 ± 11.2) years, who did not respond to at least three months of conservative therapy, necessitating surgical removal of the laryngeal granulation tissue by endolaryngeal microsurgery at the Division of Otolaryngology, Tohoku Medical and Pharmaceutical University Hospital, between January 2016 and November 2018. All patients had single lesions, and only cases with typical clinical and histological findings were included in this study.

The laryngeal granulation tissues were histologically diagnosed at the Division of Pathology, Tohoku Medical and Pharmaceutical University Hospital. The study was approved by the ethics review committees of both Tohoku Medical University Hospital (Approval no. 2016-2-058) and Tohoku University Graduate School of Medicine (Approval no. 2017-1-321), and the requirement for informed consent was waived owing to the opt-out policy adopted in the study.

*Immunohistochemistry analysis to detect CD31, CD34, and periostin*

Sections (4 $\mu$m thick) were prepared from paraffin-embedded tissue blocks and deparaffinized, followed by rehydration in alcohols. Endogenous peroxidase activity was blocked using 3% $H_2O_2$ in absolute methanol at room temperature for 10 min. All sections were preincubated in Protein Block Serum-Free (Cat. No. X0909; Dako, Santa Clara, CA, United States) at room temperature for 20 min to block nonspecific background staining. The sections were then treated with monoclonal antibodies (diluted 1:100) against CD31 (Cat. No. M0823, Clone: JC70A; Dako, Santa Clara, CA, United States) and CD34 (Cat No. 413361, Clone: NU-4A1; Nichirei Biosciences Inc., Chuo, Tokyo, Japan), and with a polyclonal anti-periostin antibody (diluted 1:2730), and kept at 4°C overnight. The sections were then incubated with biotin-conjugated anti-mouse antibody (Cat. No. 42402, N-Histofine SABPO (M); Nichirei Biosciences Inc.) for 30 min and then with streptavidin-labeled peroxidase for another 30 min at room temperature. Finally, they were incubated with liquid diaminobenzidine (DAB) and counterstained with hematoxylin for CD31 and CD34 immunostaining. For periostin immunostaining, after the primary antibody incubation, sections were incubated with a secondary antibody, the EnVision+ Dual Link System-HRP (Cat. No. K4063; Dako) for 60 min at room temperature and finally with DAB + Substrate Chromogen System (Cat. No. K3468; Dako). They were counterstained with hematoxylin.

*Immunohistochemistry analysis to detect Dβ-aspartic acid*

About 4-$\mu$m thick sections were prepared from paraffin-embedded tissue blocks, deparaffinized, and rehydrated. Antigen retrieval was performed by heating the sections in antigen retrieval solution (pH 9.0) at 121°C in an autoclave for 5 min. Endogenous peroxidase activity was blocked by treating the sections with 3% $H_2O_2$ in absolute methanol at room temperature for 10 min. Before antibody incubation, all sections were preincubated with normal goat serum (Cat. No. MP-7444, ImmPRESS HRP REAGENT Kit Anti-Rat; Vector Laboratories, Newark, CA, United States) at room temperature for 20 min to block nonspecific background staining. The sections were then treated with a polyclonal antibody (diluted 1:800) against D-aspartic acid (Cat. No. AB-T047, Advanced Targeting Systems, Carlsbad, CA, United States) and kept at 4°C overnight. Thereafter, the sections were incubated with a secondary antibody (Cat. No. MP-7444, ImmPRESS HRP REAGENT Kit Anti-Rat; Vector Laboratories) for 30 min at room temperature and finally incubated with liquid DAB+ Substrate Chromogen System and counterstained with hematoxylin.

*Assessment of slides*

Immunostained sections were examined under a light microscope at × 20, × 40, and × 100 magnifications using an eyepiece reticle. Cell counts were expressed as means per high-power field, corresponding to an area of 0.202 $mm^2$. At least two sections were immunostained, and more than five areas per section were evaluated using the reticle. Results are expressed as the presence or absence of positive cells as follows: (–): Negative. (+): Positive.

## Results

*Histological subtypes of laryngeal granulation tissue*

A characteristic feature of laryngeal granulation tissue is the absence of epithelium.

Fig. 1 shows control samples (A1–5), vocal fold polyps (B1–6), and laryngeal granulation tissue samples (C1–6, D1–6, E1–6).

Fig. 1 A1–5 Images of a 73-year-old Japanese man with hypopharyngeal cancer are presented as the control. A

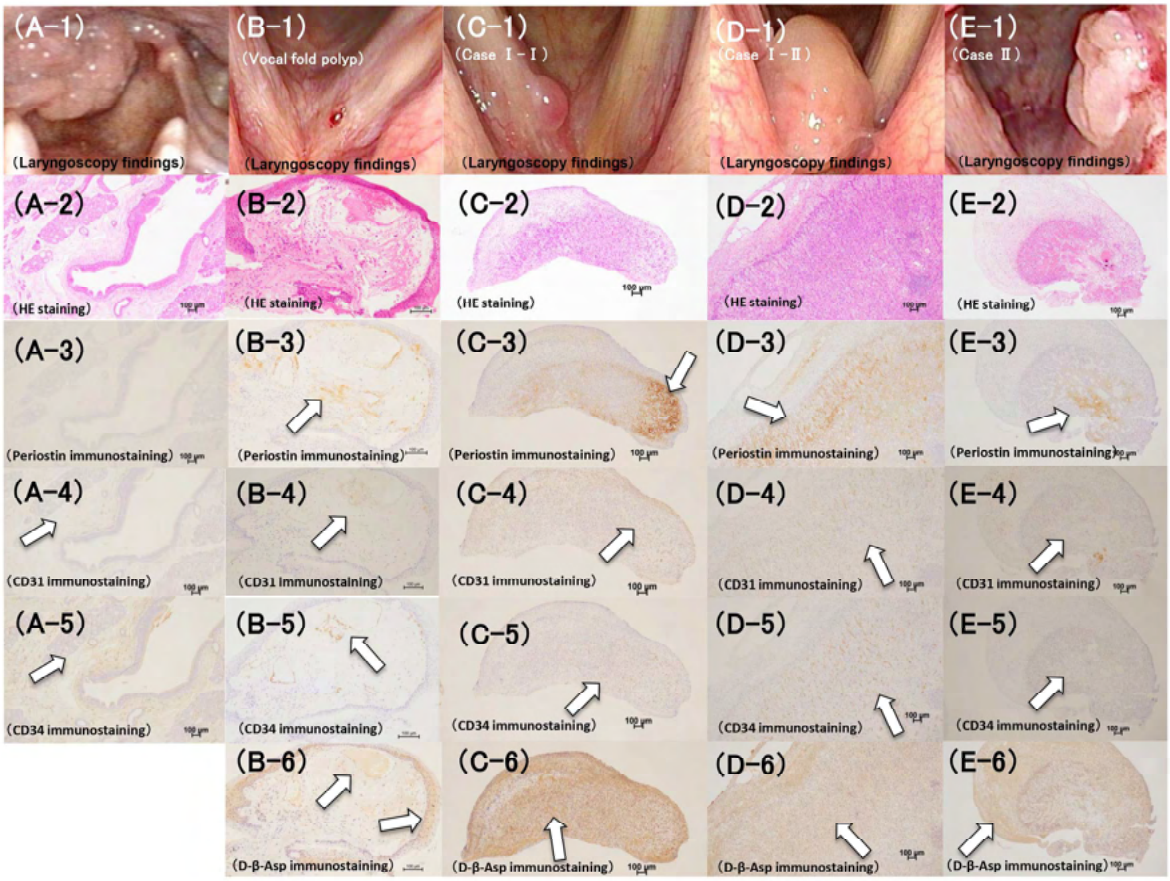


Fig. 1. Laryngeal findings, hematoxylin and eosin (HE) staining and immunohistochemical staining of periostin, CD31, and CD34 in control specimens, vocal fold polyps, and laryngeal granulation tissue (A-1) A 73-year-old Japanese man with hypopharyngeal cancer is presented as the control. A hypopharyngeal mass is observed in the right pyriform sinus. A normal vocal fold mucosa specimen was used. (A-2) Mucosal epithelium and lamina propria (HE staining, original magnification × 40).
(A-3) Expression of periostin was not detected (immunostaining, original magnification × 40).
(A-4) Minimal expression of CD31 and (A-5) CD34 was detected (corresponding arrows) (immunostaining, original magnification × 40).
(B-1) A 73-year-old Japanese man with red polyps on the left vocal fold. (B-2) This case is a typical vascular-hyaline type. Dense eosinophilic submucosal deposition of fibrin material closely apposed to a vascular space is observed (HE staining, original magnification × 100). (B-3) Periostin was observed from the basement membrane to the lamina propria in varying degrees (arrow) (immunostaining, original magnification × 100). (B-4) Noticeable expression of CD31 and (B-5) CD34 was detected (corresponding arrows) (immunostaining, original magnification × 100). (B-6) D-*β*-aspartic acid was detected in the epithelium and stroma (arrow) (immunostaining, original magnification × 100).
(C-1) An 84-year-old Japanese man with red laryngeal granulation tissue on the right vocal fold. (C-2) The specimens consisted of inflammatory cell infiltration, edema, fibrin exudation, fibrosis, and neovascularization, without epithelium and tumor cells. (HE staining, original magnification × 40 ). (C-3) Expression of periostin (C-4) CD31, (C-5) CD34, and (C-6) D-*β*-aspartic acid was detected (corresponding arrows) (immunostaining, original magnification × 40 for all).
(D-1) An 84-year-old Japanese man with white laryngeal granulation tissue on the right vocal fold. (D-2) The specimens consisted of inflammatory cell infiltration, edema, fibrin exudation, fibrosis, and neovascularization, without epithelium and tumor cells. (HE staining, original magnification × 40).
(D-3) Expression of periostin, (C-4) CD31, (C-5) CD34, and (C-6) D-*β*-aspartic acid was detected (corresponding arrows) (immunostaining, original magnification × 40 for all).
(E-1) A 54-year-old Japanese man with white laryngeal granulation tissue on the left vocal cord cartilage area. (E-2) The specimens consisted of inflammatory cell infiltration, edema, fibrin exudation, fibrosis, and neovascularization, without epithelium and tumor cells. (HE staining, original magnification × 40 ). (E-3) Expression of periostin, (E-4) CD31, (E-5) CD34, and (E-6) D-*β*-aspartic acid was detected (corresponding arrows) (immunostaining, original magnification × 40 for all).

Table 1. Patient demographics, Clinical features and Pathological findings.

| Case | age/gender | Chief complaint | Side | Period illness (month) | Tobacco | Alchohol | Reflex esophagitis | Periostin | CD31 | CD34 | D-β-Asp |
|---|---|---|---|---|---|---|---|---|---|---|---|
| I-I | 84/M | Hoarseness | R | 12M | (+) | (+) | (–) | (+) | (+) | (+) | (+) |
| I-II | 84/M | Hoarseness | R | 1M | (+) | (+) | (–) | (+) | (+) | (+) | (+) |
| II | 54/M | Laryngeal discomfort | L | 7M | (+) | (+) | (–) | (+) | (+) | (+) | (+) |
| III | 77/M | Hoarseness | L | 12M | (–) | (+) | (–) | (+) | (+) | (+) | ND |
| IV-I | 74/F | Hoarseness | L | 7M | (–) | (–) | (–) | (+) | (+) | (+) | ND |
| IV-II | 74/F | Hoarseness | L | 2M | (–) | (–) | (–) | (+) | (+) | (+) | ND |
| V | 75/F | Hoarseness | L | 4M | (–) | (–) | (–) | (+) | (+) | (+) | ND |

M: male; F: female; R: right; L: left, ND: not done.

hypopharyngeal mass is observed in the right pyriform sinus, and a normal vocal fold mucosa specimen was used for comparison. Fig. 1A-2 shows the mucosal epithelium and lamina propria.

Vocal fold polyps were categorized into four histological types (edematous type, vascular-hyaline type, fibrous type, and myxoid type). Fig. 1B1–6 Images of a 73-year-old Japanese man with red polyps on the left vocal fold, which is a case of the vascular-hyaline type. Dense eosinophilic submucosal deposition of fibrin material closely adjacent to a vascular space is observed.

Specimens of laryngeal granulation tissue consisted of inflammatory cell infiltrate, edema, fibrous exudation, fibrosis, and neovascularization, with no epithelial or tumor cells (Fig. 1C-2, D-2, E-2).

*Expression of periostin in laryngeal granulation tissue*

The expression of periostin was investigated in seven samples of laryngeal granulation tissue from five patients. It was detected in all 7 (100%) samples obtained from patients with laryngeal granulation tissue (Fig. 1C-3, D-3, E-3) (Table 1). In the laryngeal granulation tissue, periostin was found to be expressed internally, near the surface, or in a mixed distribution of internal and near-surface areas.

*Expression of D-β-aspartic acid in laryngeal granulation tissue*

The expression of D-β-aspartic acid was investigated in the same three samples. All three cases showed diffuse staining, ranging from the interior to near the surface areas (Fig. 1 C-6, D-6, E-6) (Table 1).

*Expression of CD31 in laryngeal granulation tissue*

The expression of CD31 was investigated in seven samples of laryngeal granulation tissue from five patients. It was detected in all 7 (100%) samples obtained from patients with laryngeal granulation tissue (Fig. 1C-4, D-4, E-4) (Table 1). The CD31-positive structures showed a vascular appearance and were distant from each other, with some having point-positive structures.

*Expression of CD34 in laryngeal granulation tissue*

The expression of CD34 was investigated in seven samples of laryngeal granulation tissue from five patients. It was detected in all 7 (100%) samples obtained from patients with laryngeal granulation tissue (Fig. 1C-5, D-5, E-5) (Table 1). The CD34-positive structures had a vascular appearance and were distant from each other, with some having point-positive structures.

*Patient characteristics and the clinical features of laryngeal granulation tissue*

Patient characteristics and the clinical features of the five cases are summarized in Table 1. The age of the patients ranged from 54 to 84 (mean age 72.8) years. The distribution of lesions was predominantly unilateral, with four cases presenting on the left side and one case on the right side; no cases involved both sides. The majority of cases occurred on one side, more frequently on the left side. Three of the patients were male, and two were female. Two patients had a history of smoking, and three had a history of alcohol consumption. No patient had a history of reflux esophagitis. The clinical features resembled those of vocal fold polyps. The most commonly observed primary symptom was recurrent hoarseness, although a wide variety of clinical features were observed, including laryngeal discomfort, pharyngodynia, and chronic cough.

In all cases, the laryngeal granulation tissue eventually resolved.

## Discussion

Laryngeal granulation tissues are elevated lesions caused by nonspecific inflammation that may occur unilaterally or bilaterally. These lesions are particularly important in the diagnosis of laryngeal granulomatosis, typically localized to the vocal fold process or cartilage areas. Morphologically, granulation tissues appear smooth, spherical, hemispherical, or lobulated, and vary in size and shape. Their color ranges from white to red, depending on the degree of inflammation. Historically, lesion etiology has been classified into four categories: those resulting from laryngeal surgery, those occurring after endotracheal intu-

bation, those caused by voice overuse or excessive force generation, and those with no apparent cause (Kleinsasser 1969). Recently, these lesions have also been associated with gastric acid reflux into the pharynx, i.e., pharyngolaryngeal gastric acid reflux disease. Despite their infrequent occurrence, some cases of laryngeal granulation tissue recur and are refractory to treatment. The primary clinical manifestations are hoarseness and an abnormal sensation in the pharynx, although pharyngotracheal irritation and chronic cough may also be present. In some instances, the condition remains asymptomatic and may be detected incidentally during upper gastrointestinal endoscopy. During patient interview, in addition to smoking, alcohol consumption, and voice use, the patient's coughing habits, conditions that result in coughing, history of tracheal intubation, and symptoms of gastric acid reflux (e.g., heartburn) should be assessed. It is also important to check for the presence of drug-induced cough, such as that associated with the use of angiotensin-converting enzyme inhibitors.

Periostin is a type of extracellular matrix protein that has been reported to be strongly expressed in lesions of airway inflammatory diseases such as bronchial asthma, allergic rhinitis, and chronic sinusitis. Recent studies have shown that periostin may be differentially involved in various otolaryngological diseases such as vocal cord polyps, allergic rhinitis, chronic rhinosinusitis with nasal polyps, IgG4-related diseases, tissue hematomas, eosinophilic otitis media, and eosinophilic otitis media (Ishida et al. 2012; Ohta et al. 2013a, 2014; Shiono et al. 2015; Tateda et al. 2022). However, the role of periostin in laryngeal granulation tissue has not been previously reported. Periostin is characterized not only by its role as an extracellular matrix structural protein that regulates fibrosis and collagen deposition but also as a matrix protein that regulates the Th2-mediated inflammatory cascade (Ishida et al. 2012; Ohta et al. 2013a; Shiono et al. 2015). In vocal polyps, periostin is expressed in the stroma but not in the epithelium. Four patterns of periostin expression have been reported: negative, superficial, infiltrate, and diffuse. In the present cases of laryngeal granulation tissue, periostin expression varied; in some cases, it was localized around the base of the mass, while in other cases, it was centered on the superficial layer of the mass. Notably, TGF-$\beta$, but not IL-13, expression was found in the same region as periostin expression, suggesting that TGF-$\beta$ may be involved in the induction of periostin expression in vocal polyps (Tateda et al. 2022). This observation raises the prospect of further investigating the inducer of periostin expression in laryngeal granulation tissue.

Contrary to popular belief that all proteins that make up living organisms are composed of L-amino acids, recent findings highlight the accumulation of D-aspartic acid, which should not be present in the body, in various tissues such as the ligaments (Ritz-Timme et al. 2003), brain (Shapira and Chou 1987), aorta (Powell et al. 1992), cataracts (Masters et al. 1977), lens (Fujii et al. 1999; Kaji et al. 2007), skin (Fujii et al. 2002), and teeth (Helfman and Bada 1976) due to aging and UV light exposure. The presence of D-$\beta$-aspartic acid is thought to be the result of the racemization of L-$\beta$-aspartic acid in proteins (Kaji et al. 2007), making it a novel indicator of aging-related damage (Fujii et al. 1999; Kaji et al. 2007). UV irradiation of the skin is closely associated with the formation of D-$\beta$-aspartic acid in elastic fibers of the skin (Miura et al. 2004). In vocal polyps, D-$\beta$-aspartic acid was reported to be upregulated in the epithelium and stroma. It has also been reported that increased D-$\beta$-aspartic acid expression in the vocal polyp stroma was associated with the expression pattern of periostin (Tateda et al. 2023a). In the present study, D-$\beta$-aspartic acid expression was detected in laryngeal granulation tissue, even though the laryngeal cavity was not exposed to UV irradiation. These results indicate that racemization of L-amino acids may occur due to reasons other than aging or UV irradiation.

CD31 plays important roles in leukocyte trafficking, mechanotransduction, angiogenesis, vascular permeability, and regulation of cellular responsiveness. In previous reports, CD31 expression was found to be upregulated during myocardial remodeling following ischemic injury; however, this upregulation disappeared once the remodeling process was complete (Kondo et al. 2022). Furthermore, CD31 expression in human ischemic heart disease is not upregulated in complete fibrotic foci in the myocardium (Kondo et al. 2022). CD34+ cells, which are multipotent hematopoietic stem cells also known as endothelial progenitor cells, migrate to target sites, where they enhance angiogenesis, neovascularization, and tissue regeneration. Increased expression of CD31 and CD34 was observed in the stroma of vocal fold polyps, with three different expression patterns reported (negative, vascular, and diffuse). Three histological subtypes of vocal polyps were observed: edematous, vascular-hyaline, and fibrous, highlighting a potential correlation between CD31 expression patterns and the histological subtypes of the polyps (Tateda et al. 2023b).

CD31 is a marker of endothelial cells, with CD31 revealing that these cells maintain their structural integrity and a dilated pattern in limited areas (Ohta et al. 2013b). CD31 immunostaining showed that these endothelial cells were present in laryngeal granulation tissue. Interestingly, this study also highlighted the absence of a correlation between increased CD31 expression and areas of periostin expression in laryngeal granulation tissue.

CD34 is a crucial marker of endothelial cell progenitors and neovascularization. In the field of otorhinolaryngology, CD34-positive connective tissue is presumed to appear at sites of recovery or regeneration after pathology or injury. The regular vascular arrangement of CD34-positive structures along the epithelium underscores the role of the epithelium in differentiation, suggesting a sequential recovery where blood vessel restoration precedes or accompanies the regeneration of the epithelial tissue in the otorhi-

nolaryngological region (Katori et al. 2011). CD34 is expressed on the progenitors of endothelial cells and might play an important role in neovascularization and wound healing (Dreger et al. 2002; Pleşea et al. 2005; Oe et al. 2007). Immunostaining for CD34 has shown that these endothelial cell progenitors were present in laryngeal granulation tissues.

Periostin is a regulator of fibrosis and collagen deposition, marking its significance in the domain of myocardial repair/remodeling following myocardial infarction (Kondo et al. 2022). Also, evidence suggests that its overexpression in the nasal mucosa and vocal fold polyps contributes to tissue repair and fibrosis. These findings may support the negative spiral theory immunohistopathologically.

Laryngeal granulation tissues are thought to begin forming at the epithelial defect site after epithelial damage. Laryngeal granulation tissues are formed by direct stimulation of the epithelial defect site, but the characteristic feature of laryngeal granulation tissue is the absence of epithelium. Vocal fold polyps are thought to cause edema, hematoma, neovascularization, and fibrosis due to local interstitial circulation disorder after irritation is applied to the vocal folds due to vocal abuse. In vocal fold polyps, periostin was expressed only in the stroma. It has been reported that there are four periostin staining patterns in vocal fold polyps: negative type, superficial type, infiltrative type, and diffuse type (Tateda et al. 2022, 2023a).

Periostin expression was observed in all cases of laryngeal granulation tissues. However, the site of high expression varies depending on the case, such as on the surface layer or near the base, and the mode of expression was considered to be a subject for future investigation.

In vocal fold polyps, CD31 and CD34 were expressed only in the stroma. It has been reported that there are three staining patterns for CD31 and CD34 in vocal fold polyps: negative type, vascular type, and diffuse type (Tateda et al. 2023b). In laryngeal granulation tissues, expression of CD31 and CD34 was observed in all cases. However, the site of high expression varies depending on the case, such as on the surface layer or near the base, and the mode of expression was considered to be a subject for future investigation.

In vocal fold polyps, D-$\beta$-aspartic acid was expressed in the epithelium and stroma.

In vocal fold polyp epithelium, the expression rate of D-$\beta$-aspartic acid is reported to be 100% (Tateda et al. 2023a). It has been reported that there are two D-$\beta$-aspartic acid staining patterns in vocal fold polyps stroma: negative and positive (Tateda et al. 2023a).

In laryngeal granulation tissues, D-$\beta$-aspartic acid was expressed in all cases. High expression of D-$\beta$-aspartic acid in laryngeal granulation tissues was observed throughout the granulation tissues, from the superficial layer to the base. Due to the small number of cases, the mode of expression was considered to be a subject for future investigation.

Laryngeal granulation tissue presents a significant clinical challenge due to its high recurrence rate, rendering it a difficult condition to treat. It is important to accurately determine the cause of the disease and provide appropriate treatment by combining drug therapy, voice therapy, lifestyle modifications, and surgical interventions. It is believed that a deeper understanding of its pathology is crucial for developing strategies to reduce the recurrence rate.

*Conclusion*

Our results indicate that overexpression of CD31, CD34, D-$\beta$-aspartic acid, and periostin is likely involved in the pathogenesis of laryngeal granulation tissue. The presence of D-$\beta$-aspartic acid and periostin, in particular, presents a promising avenue for research, potentially serving as novel biomarkers for diagnosis and therapeutic targets of laryngeal granulation tissue.

## Acknowledgment

This work was supported by a Grant-in-Aid for Scientific Research (C) (17K11363) from the Ministry of Education, Science, Sports and Culture of Japan. We express our sincere gratitude to Mr. Junya Ono for his assistance.

## Funding

This work was supported by a Grant-in-Aid for Scientific Research (C) (17K11363) from the Ministry of Education, Science, Sports and Culture of Japan.

## Conflict of Interest

The authors declare no conflict of interest.

## References

Dreger, S.A., Taylor, P.M., Allen, S.P. & Yacoub, M.H. (2002) Profile and localization of matrix metalloproteinases (MMPs) and their tissue inhibitors (TIMPs) in human heart valves. *J. Heart Valve Dis.*, **11**, 875-880; discussion 880.

Fujii, N., Harada, K., Momose, Y., Ishii, N. & Akaboshi, M. (1999) D-amino acid formation induced by a chiral field within a human lens protein during aging. *Biochem. Biophys. Res. Commun.*, **263**, 322-326.

Fujii, N., Tajima, S., Tanaka, N., Fujimoto, N., Takata, T. & Shimo-Oka, T. (2002) The presence of D-beta-aspartic acid-containing peptides in elastic fibers of sun-damaged skin: a potent marker for ultraviolet-induced skin aging. *Biochem. Biophys. Res. Commun.*, **294**, 1047-1051.

Helfman, P.M. & Bada, J.L. (1976) Aspartic acid racemisation in dentine as a measure of ageing. *Nature*, **262**, 279-281.

Ishida, A., Ohta, N., Suzuki, Y., Kakehata, S., Okubo, K., Ikeda, H., Shiraishi, H. & Izuhara, K. (2012) Expression of pendrin and periostin in allergic rhinitis and chronic rhinosinusitis. *Allergol. Int.*, **61**, 589-595.

Kaji, Y., Oshika, T., Takazawa, Y., Fukayama, M., Takata, T. & Fujii, N. (2007) Localization of D-beta-aspartic acid-containing proteins in human eyes. *Invest. Ophthalmol. Vis. Sci.*, **48**, 3923-3927.

Katori, Y., Kiyokawa, H., Kawase, T., Murakami, G. & Cho, B.H. (2011) CD34-positive primitive vessels and other structures in human fetuses: an immunohistochemical study. *Acta Otolaryngol.*, **131**, 1086-1090.

Kleinsasser, O. (1969) Microlaryngoscopy and Endolaryngeal Microsurgery Techniques and Typical Cases. W.B. Suanders Publishing, Philadelphia, pp. 46-48.

Kondo, T., Takahashi, M., Yamasaki, G., Sugimoto, M., Kuse, A., Morichika, M., Nakagawa, K., Sakurada, M., Asano, M. & Ueno, Y. (2022) Immunohistochemical analysis of CD31 expression in myocardial tissues from autopsies of patients with ischemic heart disease. *Leg. Med.* (*Tokyo*), **59**, 102127.

Masters, P.M., Bada, J.L. & Zigler, J.S. Jr. (1977) Aspartic acid racemisation in the human lens during ageing and in cataract formation. *Nature*, **268**, 71-73.

Miura, Y., Fujimoto, N., Komatsu, T., Tajima, S., Kawada, A., Saito, T. & Fujii, N. (2004) Immunohistochemical study of chronological and photo-induced aging skins using the antibody raised against D-aspartyl residue-containing peptide. *J. Cutan. Pathol.*, **31**, 51-56.

Oe, K., Miwa, M., Sakai, Y., Lee, S.Y., Kuroda, R. & Kurosaka, M. (2007) An in vitro study demonstrating that haematomas found at the site of human fractures contain progenitor cells with multilineage capacity. *J. Bone Joint Surg. Br.*, **89**, 133-138.

Ohta, N., Ishida, A., Kurakami, K., Suzuki, Y., Kakehata, S., Ono, J., Ikeda, H., Okubo, K. & Izuhara, K. (2014) Expressions and roles of periostin in otolaryngological diseases. *Allergol. Int.*, **63**, 171-180.

Ohta, N., Kurakami, K., Ishida, A., Furukawa, T., Suzuki, Y., Aoyagi, M., Matsubara, A., Izuhara, K. & Kakehata, S. (2013a) Roles of TGF-beta and periostin in fibrosclerosis in patients with IgG4-related diseases. *Acta Otolaryngol.*, **133**, 1322-1327.

Ohta, N., Watanabe, T., Ito, T., Kubota, T., Suzuki, Y., Ishida, A., Aoyagi, M., Matsubara, A., Izuhara, K. & Kakehata, S. (2013b) Clinical and pathological characteristics of organized hematoma. *Int. J. Otolaryngol.*, **2013**, 539642.

Pleşea, I.E., Camenita, A., Georgescu, C.C., Enache, S.D., Zaharia, B., Georgescu, C.V. & Tenovici, M. (2005) Study of cerebral vascular structures in hypertensive intracerebral haemorrhage. *Rom. J. Morphol. Embryol.*, **46**, 249-256.

Powell, J.T., Vine, N. & Crossman, M. (1992) On the accumulation of D-aspartate in elastin and other proteins of the ageing aorta. *Atherosclerosis*, **97**, 201-208.

Ritz-Timme, S., Laumeier, I. & Collins, M. (2003) Age estimation based on aspartic acid racemization in elastin from the yellow ligaments. *Int. J. Legal Med.*, **117**, 96-101.

Shapira, R. & Chou, C.H. (1987) Differential racemization of aspartate and serine in human myelin basic protein. *Biochem. Biophys. Res. Commun.*, **146**, 1342-1349.

Shiono, O., Sakuma, Y., Komatsu, M., Hirama, M., Yamashita, Y., Ishitoya, J. & Oridate, N. (2015) Differential expression of periostin in the nasal polyp may represent distinct histological features of chronic rhinosinusitis. *Auris Nasus Larynx*, **42**, 123-127.

Tateda, Y., Ikeda, R., Kakuta, R., Izuhara, K., Ogawa, T., Ise, K., Shimada, H., Murakami, K., Murakami, K., Nakamura, Y., Katori, Y. & Ohta, N. (2023a) Immunohistochemical Localization of D-beta-Aspartic Acid and Periostin in Vocal Fold Polyps. *Tohoku J. Exp. Med.*, **260**, 223-230.

Tateda, Y., Ikeda, R., Kakuta, R., Ono, J., Izuhara, K., Ogawa, T., Ise, K., Shimada, H., Murakami, K., Murakami, K., Nakamura, Y., Katori, Y. & Ohta, N. (2022) Expression of Periostin in Vocal Fold Polyps. *Tohoku J. Exp. Med.*, **258**, 55-62.

Tateda, Y., Sato, T., Ikeda, R., Kakuta, R., Izuhara, K., Ogawa, T., Ise, K., Shimada, H., Katoh, M., Murakami, K., Murakami, K., Nakamura, Y., Katori, Y. & Ohta, N. (2023b) Immunohistochemical localization of CD31, CD34, and periostin in vocal fold polyps. *Acta Otolaryngol.*, **143**, 806-813.

＜臨床検査医学＞

教授　髙橋 伸一郎
助教　遠藤 康弘
助教　鈴木 歩

## 造血器腫瘍の病態解明とより良い臨床検査を目指した研究

研究内容紹介：

当教室では、急性骨髄性白血病（Acute Myeloid Leukemia: AML）を中心とした造血器腫瘍の病態解明を進めています。顧建国教授研究室と共同研究を行い、白血病における糖鎖の役割について明らかにしようとしています。このような知見に基づいた、効果的な治療法の開発を目指しています。今年度は、抗がん剤の一種でシグナル伝達阻害剤でもあるTriciribine（TCN）という化合物がAML細胞に対し効果的であること、糖鎖の中でも、フコシル化阻害剤（6-alkynylfucose: 6AF）が、全トランス型レチノイン酸（all-trans retinoic acid: ATRA）による骨髄系細胞分化を促進すること（図）を明らかにしました。

また、悪性腫瘍は、脂質代謝の異常が認められます。現在、血液リウマチ科の協力を頂きながら、様々な造血器腫瘍患者さんの残余血清検体を収集中です。それを元に、主に脂質代謝の異常に注目して、造血器腫瘍の病勢を把握できる、効果的な血清マーカーの開発を目指しています。さらに、より良い検査指標の開発や、検査業務改善への取り組みなども行なっています。

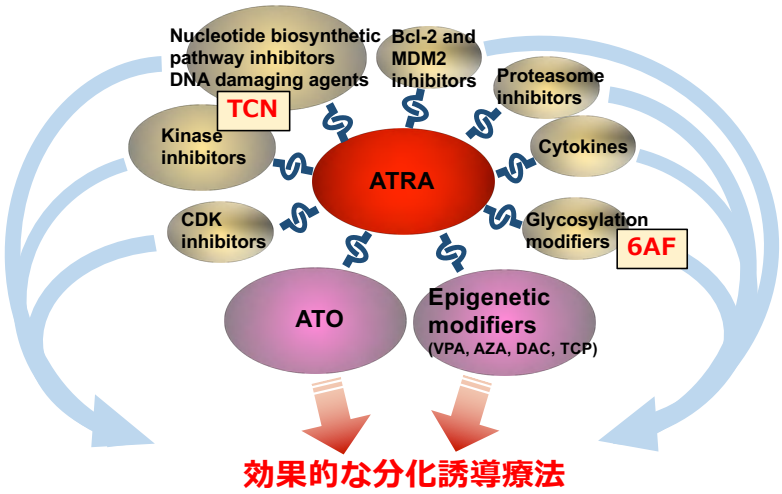


TCN (Triciribine)、6AF (6-alkynylfucose) は、それぞれ効果的な分化誘導 (PLoS ONE 2024) 及び分化誘導促進 (BBRC 2024) 薬物である。

＜論文発表＞

**BBRC36 specifically associates with FLT3-ITD to regulate its protein stability and intracellular signaling in acute myeloid leukemia.** Liu J, Isaji T, Komatsu S, Sun Y, Xu X, Fukuda T, Fujimura T, Takahashi S, Gu J. ***Cancer Sci***, 115, 1196-1208. doi.org/10.1111/cas.16090. 2024

**Fucosylation inhibitor 6-alkynylfucose enhances the ATRA-induced differentiation effect on acute promyelocytic leukemia cells.** Suzuki S, Liu J, Sato Y, Miyake R, Suzuki S, Okitsu Y, Fukuda T, Isaji T, Gu J, Takahashi S. ***Biochem Biophys Res Commun*****,** 710, 149541. doi.org/10.1016/j.bbrc.2024.149541. 2024

**Identification of triciribine as a novel myeloid cell differentiation inducer.** Suzuki S, Suzuki S, Sato-Nagaoka Y, Ito C and Takahashi S. ***PLOS ONE*****,** 19, e0303428. 10.1371/journal.pone.0303428. 2024

**全自動便尿分析装置 AA01 を用いたネスコート®Cp オートの基礎的性能評価.** 三浦りり佳, 小堺利恵, 土居洋介, 福本祐子, 若生望, 阿部成晃, 星くに子, 髙橋伸一郎**.** ***医学と薬学***, 81, p351-357. 2024

**全自動便尿分析装置 AA01 を用いたネスコート®Hb オートの基礎的性能評価**. 三浦りり佳, 小堺利恵, 土居洋介, 福本祐子, 若生望, 阿部成晃, 星くに子, 髙橋伸一郎. ***医学と薬学***, 81, p359-364. 2024

**OC センサーCeres を用いた OC-カルプロテクチン‘栄研’の基礎的性能評価.** 若生望, 小堺利恵, 三浦りり佳, 阿部成晃, 星くに子, 髙橋伸一郎**.** ***医療と検査機器・試薬***, 47, p375-381. 2024

**Signaling effect, combinations, and clinical applications of triciribine.** Takahashi S. ***J Chemother,*** **14**:1-9. 10.1080/1120009X.2024.2403050. 2024

**Combination of triciribine and p38 MAPK inhibitor PD169316 enhances the differentiation effect on myeloid leukemia cells.** Sato-Nagaoka Y, Suzuki S, Suzuki S and Takahashi S. ***PLOS ONE*****,** 19, e0312406. 10.1371/journal.pone.0312406. 2024

＜学会発表と講演＞

**感染性粉瘤の膿汁から Facklamia hominis を分離した 1 症例**

川端きり, 甲谷由香里, 正路舞, 小堺利恵, 松尾幾, 髙橋伸一郎

第 73 回日本医学検査学会, 金沢, 2024 年 5 月, 演題番号 269

**骨髄検査所見により診断が確定した Myeloid sarcoma with CBFB-MYH11 の一例**

加賀淑子, 阿部正理, 梅木彩, 長岡裕李, 伊藤智咲, 浅野裕子, 大場祐輔, 齊藤梨絵, 櫻田明美, 小堺利恵, 亀岡淳一, 髙橋伸一郎

第 73 回日本医学検査学会, 金沢, 2024 年 5 月, 演題番号 312

**稀な染色体異常を伴う急性骨髄性白血病に BCR-ABL1 融合遺伝子が認められた一例**

大場祐輔, 野村順, 梅木彩, 長岡裕李, 伊藤智咲, 浅野裕子, 加賀淑子, 齊藤梨絵, 櫻田明美, 亀岡淳一, 髙橋伸一郎

第 13 回日本検査血液学会東北支部学術集会, 盛岡, 2024 年 6 月, 演題番号 2

**東北医科薬科大学病院検査部における臨床と基礎研究の紹介**

髙橋伸一郎

第 43 回田沢湖セミナー, 秋田県仙北市, 2024 年 7 月, 特別講演

**血中薬物濃度測定における精度管理の実際について**

髙橋瑞恵, 小堺利恵, 髙橋伸一郎

第 40 回日本 TDM 学会学術大会, 札幌, 2024 年 7 月

**LA 陽性検体における APTT 試薬の反応性の違い:4 社 5 試薬を用いた検討**

加賀淑子, 松田将門, 小堺利恵, 沖津庸子, 髙橋伸一郎

第 25 回日本検査血液学会, 広島, 2024 年 7 月, 日本検査血液学会雑誌　(検査と血液) 25(学術集会)号, S208.

**全自動電気泳動装置ミニキャップ FLEX PIERCING におけるイムノタイピングの評価**

髙橋瑞恵, 小堺利恵, 髙橋伸一郎

第 64 回日本臨床化学会年次学術集会, 宇都宮, 2024 年 8 月, 演題番号 O17-3

**CRP が異常高値となった重症急性膵炎の 1 症例**

小堺利恵, 片山智文, 髙橋瑞恵, 髙橋伸一郎

第 64 回日本臨床化学会年次学術集会, 宇都宮, 2024 年 8 月, 演題番号 O2-5

**採血管変更における生化学検体の再採血に関する調査**

佐藤美空, 小堺利恵, 鈴木歩, 髙橋瑞恵, 髙橋伸一郎

第 64 回日本臨床化学会年次学術集会, 宇都宮, 2024 年 8 月, 演題番号 YIA-2

**東北科薬科大学病院検査部・教室における教育活動の紹介**

髙橋伸一郎

第 56 回日本臨床検査医学会東北支部総会, 第 35 回日本臨床化学会東北支部総会, 秋田, 2024 年 9 月, 演題番号 S1-2

**東北医科薬科大学病院検査部におけるパニック値報告の運用と今後の課題**

髙橋昂希, 梅木彩, 千田和, 小堺利恵, 髙橋伸一郎

第 56 回日本臨床検査医学会東北支部総会, 第 35 回日本臨床化学会東北支部総会, 秋田, 2024 年 9 月, 演題番号 O1-5

**血中薬物濃度測定における精度管理について**

小堺利恵, 髙橋瑞恵, 髙橋伸一郎

第 56 回日本臨床検査医学会東北支部総会, 第 35 回日本臨床化学会東北支部総会, 秋田, 2024 年 9 月, 演題番号 S2-5

**当院における新 MEQNET MINILAB の導入効果**

千田 和, 小堺 利恵, 葛西 恵里香, 佐藤 美空, 奥 明日香, 髙橋 瑞恵, 岩渕 淑子, 髙橋伸一郎

第 56 回日本医療検査科学会, 横浜, 2024 年 10 月, 演題番号 51

**LA 陽性検体における 5 種の APTT 試薬の反応性の違い:免疫血清学的抗リン脂質抗体検査との関連**

加賀淑子, 松田将門, 小堺利恵, 沖津庸子, 髙橋伸一郎

第 56 回日本医療検査科学会, 横浜, 2024 年 10 月, 演題番号 86

**分化誘導促進剤としての Triciribine の効果検討**

長岡裕李, 鈴木歩, 髙橋伸一郎

第 71 回日本臨床検査医学会学術集会, 大阪, 2024 年 11 月, 演題番号 O-039

**当院における採血室待ち時間調査からみえる課題**

長岡裕李, 浅野裕子, 岩渕淑子, 小堺利恵, 髙橋伸一郎

第 12 回日臨技北日本支部医学検査学会, 仙台, 2024 年 12 月, 演題番号 51

検査室マネジメントからみた臨床検査の新しい価値

髙橋伸一郎

第 12 回日臨技北日本支部医学検査学会, 仙台, 2024 年 12 月, 特別講演Ⅱ

**Vasospastic AnginaMaintains HDL Function with Elevated Sphingosine-1-phosphate**

佐々木慧, 江崎裕敬, 遠藤康弘, 綾織誠人, 桜田 真己, 池脇克則

第 89 回日本循環器学会学術集会, 横浜, 2025 年 3 月, 演題番号 PJ01-6

PLOS ONE

RESEARCH ARTICLE

# Identification of triciribine as a novel myeloid cell differentiation inducer

**Souma Suzuki[1], Susumu Suzuki[1,2], Yuri Sato-Nagaoka[2], Chisaki Ito[2], Shinichiro Takahashi[1,2]***

**1** Faculty of Medicine, Division of Laboratory Medicine, Tohoku Medical and Pharmaceutical University, Sendai, Miyagi, Japan, **2** Department of Clinical Laboratory, Tohoku Medical and Pharmaceutical University Hospital, Sendai, Miyagi, Japan

* shintakahashi@tohoku-mpu.ac.jp

Check for updates

OPEN ACCESS

**Citation:** Suzuki S, Suzuki S, Sato-Nagaoka Y, Ito C, Takahashi S (2024) Identification of triciribine as a novel myeloid cell differentiation inducer. PLoS ONE 19(5): e0303428. https://doi.org/10.1371/journal.pone.0303428

**Editor:** Tanay Chaubal, International Medical University, MALAYSIA

**Received:** July 18, 2023

**Accepted:** April 24, 2024

**Published:** May 14, 2024

**Peer Review History:** PLOS recognizes the benefits of transparency in the peer review process; therefore, we enable the publication of all of the content of peer review and author responses alongside final, published articles. The editorial history of this article is available here: https://doi.org/10.1371/journal.pone.0303428

**Copyright:** © 2024 Suzuki et al. This is an open access article distributed under the terms of the Creative Commons Attribution License, which permits unrestricted use, distribution, and reproduction in any medium, provided the original author and source are credited.

**Data Availability Statement:** All relevant data are within the article and its Supporting Information files. The data for microarray analysis are openly available in the NCBI Gene Expression Omnibus (http://www.ncbi.nlm.nih.gov/geo/) at the GEO

## Abstract

Differentiation therapy using all-trans retinoic acid (ATRA) for acute promyelocytic leukemia (APL) is well established. However, because the narrow application and tolerance development of ATRA need to be improved, we searched for another efficient myeloid differentiation inducer. Kinase activation is involved in leukemia biology and differentiation block. To identify novel myeloid differentiation inducers, we used a Kinase Inhibitor Screening Library. Using a nitroblue tetrazolium dye reduction assay and real-time quantitative PCR using NB4 APL cells, we revealed that, PD169316, SB203580, SB202190 (p38 MAPK inhibitor), and triciribine (TCN) (Akt inhibitor) potently increased the expression of CD11b. We focused on TCN because it was reported to be well tolerated by patients with advanced hematological malignancies. Nuclear/cytoplasmic (N/C) ratio was significantly decreased, and myelomonocytic markers (*CD11b* and *CD11c*) were potently induced by TCN in both NB4 and acute myeloid leukemia (AML) M2 derived HL-60 cells. Western blot analysis using NB4 cells demonstrated that TCN promoted ERK1/2 phosphorylation, whereas p38 MAPK phosphorylation was not affected, suggesting that activation of the ERK pathway is involved in TCN-induced differentiation. We further examined that whether ATRA may affect phosphorylation of ERK and p38, and found that there was no obvious effect, suggesting that ATRA induced differentiation is different from TCN effect. To reveal the molecular mechanisms involved in TCN-induced differentiation, we performed microarray analysis. Pathway analysis using DAVID software indicated that "hematopoietic cell lineage" and "cytokine-cytokine receptor interaction" pathways were enriched with high significance. Real-time PCR analysis demonstrated that components of these pathways including IL1β, CD3D, IL5RA, ITGA6, CD44, ITGA2B, CD37, CD9, CSF2RA, and IL3RA, were upregulated by TCN-induced differentiation. Collectively, we identified TCN as a novel myeloid cell differentiation inducer, and trials of TCN for APL and non-APL leukemia are worthy of exploration in the future.

## Introduction

Acute myeloid leukemia (AML) is a fatal disease characterized by the proliferation of clonal and abnormally differentiated cells of the hematopoietic system, which infiltrate into the bone

series accession number GSE235632, as well as in the supplementary material of this article.

**Funding:** This work was supported in part by a Grant-in-Aid for Scientific Research (21K07346) from the Ministry of Education, Science and Culture, Japan to ST, Kyowa-Kirin Research Support (Kyowa-Kirin Co. Ltd.) to ST, and Daiichi-Sankyo Research Support (Daiichi-Sankyo Inc.) to ST. The funders had no role in study design, data collection and analysis, decision to publish, or preparation of the manuscript.

**Competing interests:** The authors have declared that no competing interests exist.

marrow, peripheral blood, and other tissues [1]. Cytarabine-based standard chemotherapy is widely used to treat all types of AML, although it can cause severe side effects. All-trans retinoic acid (ATRA) is well established as a differentiation therapy because it is very effective and has few side effects for a specific type of AML, acute promyelocytic leukemia (APL). However, the development of tolerance and narrow application of ATRA need to be improved. The activation of kinase signal transduction pathways contribute to the biology of AML through aberrant cell proliferation and differentiation blockade [2]. Furthermore, kinase inhibitors have been proposed as differentiation agents for acute leukemia [3,4]. Therefore, targeting these signaling pathways might be useful for the molecular-targeted treatment of AML.

Many kinase inhibitors have been reported to induce differentiation, including cyclin-dependent kinase inhibitors, glycogen synthesis kinase 3 inhibitors, Akt inhibitors, p38 mitogen-activated protein kinase (MAPK) inhibitors [5]. In the current study, we identified novel myeloid differentiation inducers using a Kinase Inhibitor Screening Library and found that triciribine (TCN) was an effective myeloid differentiation inducer.

TCN is a tricyclic nucleoside, whose synthesis was first described in 1971 by Shram and Townsen [6]. Subsequent studies indicated that TCN inhibits DNA synthesis, although the precise mechanisms involved remain unclear [7]. Wotring *et al.* [8] reported TCN might inhibit Okazaki fragment initiation and/or DNA polymerase delta. Thereafter, it was revealed that TCN had activity against the Akt enzyme, and had higher selectivity for Akt compared with other kinases, including phosphoinositide 3-kinase (PI3K), protein kinase C, protein kinase A, and extracellular signal-regulated kinase (ERK) 1/2 [9,10]. We revealed that the addition of TCN to APL NB4 cells led to the induction of "hematopoietic cell lineage" and "cytokine-cytokine receptor interaction" pathways, which might activate the ERK/MAPK pathway leading to myeloid differentiation.

## Materials and methods

### Cell culture and reagents

NB4 and HL-60 cells were cultured in RPMI medium containing 10% heat-inactivated fetal bovine serum under 5% $CO_2$ at 37˚C in a humidified atmosphere. Cell cultures were performed using an authenticated technique (https://www.sigmaaldrich.com/japan/ordering/technical-service/recipe-cc.html). The following kinase inhibitors were used for flow cytometry (FCM), morphological analysis, and western blotting in this study: Kinase Inhibitor Screening Library (Cayman, MI, USA), TCN (Cayman), and U0126 (Cayman).

### Nitroblue tetrazolium reduction test (NBT)

For the NBT reduction test, $5\times10^5$ cells were incubated in 0.5 ml of a freshly prepared solution containing PBS, NBT (Sigma; 1 tablet/10 ml of PBS), and 0.33 μM phorbol myristate acetate for 30 min at 37˚C. After the blind labeling of each sample, at least 200 cells were counted and the percentage of NBT-positive cells was calculated.

### Surface marker expression analysis by FCM

For FCM analysis, approximately $2–3\times10^5$ cells were washed with PBS, and 30 μl aliquots of the cell suspensions were protected from light and incubated with 1 μl of a phycoerythrin (PE)-conjugated mouse anti-human CD11b antibody (BioLegend, San Diego, CA) for 30 min at room temperature. An isotype-matched PE-conjugated mouse IgG (BioLegend) antibody was used as a negative control. After incubation, the samples were analyzed on an LSR Fortessa X-20 Flow cytometer (BD Biosciences, San Jose, CA).

## Morphological analysis

In each experiment, NB4 and HL-60 cells in the logarithmic growth phase were seeded at $2\times10^5$ cells/ml, and induced to differentiate with or without ATRA or TCN. The differentiated cells were collected for analysis at specified times. Differentiation was evaluated by morphology after Wright–Giemsa staining. After the blind labeling of each sample, the nucleus/cytoplasm ratio of at least 200 cells was objectively evaluated, and the data were analyzed statistically and presented as a violin plot using Prism software (version 9.0; GraphPad Software Inc., La Jolla, CA, USA).

## Western blotting

We used a nuclear extract and cytosol preparation kit (Apro Science, Naruto, Tokushima, Japan) following the manufacturer's protocol. An appropriate amount of 1× phosphatase inhibitor cocktail (Roche, Indianapolis, IN) and 1× protease inhibitor cocktail (Roche)) was added and the protein concentration was measured by a Pierce protein assay kit (Thermo Fisher, Waltham, MA, USA). Aliquots of supernatants containing 20–30 μg of protein were separated and immunoblotted. Image was captured by WSE-6300H-CS LuminoGraph III (ATTO, Tokyo, Japan). Total cellular extracts were prepared and immunoblotted as described. Signaling pathway molecules were examined using anti-phospho-p44/42 MAPK ERK1/2 (Thr202/Tyr204), anti-phospho p38(T180/Y182), and p44/42 MAPK mouse monoclonal antibodies (all from Cell Signaling Technology, Beverly, MA, USA). Anti-p38α/stress-activated protein kinase (SAPK)2α mouse monoclonal antibody was obtained from BD Biosciences. Rabbit monoclonal β–actin (Cell Signaling Technology) was employed to access the equal loading of the protein.

## Microarray and mRNA expression analyses

For RNA preparation for real-time PCR analyses, NB4 cells treated with TCN and their control cells were seeded at a density of 2–3×105 cells/ml. For microarray analyses, total cellular RNA was isolated from controls and cells treated with 10 μM TCN for 72 hours, using an RNA Mini Purification Kit (Qiagen, Miami, FL) according to the manufacturer's protocol. The samples were subjected to microarray analyses using a Filgen Clariom™ D Assay (Filgen, Nagoya, Japan). Data were analyzed by Transcriptome Analysis Console (TAC) Software (Thermo Fisher Scientific). KEGG pathway analysis was performed by the Database for Annotation, Visualization and Integrated Discovery (DAVID) (https://david.ncifcrf.gov). The gene expression datasets were deposited in the NCBI Gene Expression Omnibus (http://www.ncbi.nlm.nih.gov/geo/) and are accessible through the GEO series (accession number GSE235632). For RNA preparation for real-time PCR analyses, cells were seeded at a density of $2–3\times10^5$ cells/ml and treated with 10 μM or the indicated amount of TCN. The cells were harvested after 72 h, or at the specified times. For mRNA expression analyses, cDNAs were prepared from cells using a ReverTra Ace® qPCR RT Kit (Toyobo, Tokyo, Japan). Quantitative PCR was performed using the Thunderbird SYBR qPCR Mix (Toyobo) according to the manufacturer's protocol, an Opticon Mini Real-time PCR Instrument (Bio-Rad, Hercules, CA), and a CFX Connect Real-Time PCR Detection System (Bio-Rad) as previously described [11]. The sequences of the primers are listed in S1 Table. The thermal cycling conditions for all genes were: 95˚C for 15 sec, 35 cycles of 95˚C for 10 s, 60˚C for 45 s, and 72˚C for 3 min.

## Results

### Identification of TCN as a novel myeloid differentiation inducer

To identify novel myeloid differentiation inducers, we used a Kinase Inhibitor Screening Library. The NBT assay using NB4 cells showed there was an increase in the percentage of NBT-positive cells after incubation with 18 of 152 inhibitors (Fig 1A).

Next, we examined the expressions of *CD11b* gene by real-time quantitative PCR. We found that TCN (Akt inhibitor), SB202190, PD169316, CAY10571, SB203580 (p38 MAPK inhibitor) and several other inhibitors increased the expression of *CD11b* (Fig 1B), and this was confirmed by FCM analysis (Fig 2A). p38 MAPK inhibitors were reported to be involved in myeloid differentiation [5]; therefore, we focused on TCN because it has not been identified as a myeloid differentiation inducer, and is well tolerated in patients with advanced hematological malignancies [12]. We assessed the time-course effect of TCN on NB4 cells. As shown in Fig 2B, maximal CD11b expression was observed 72 hours after incubation with TCN.

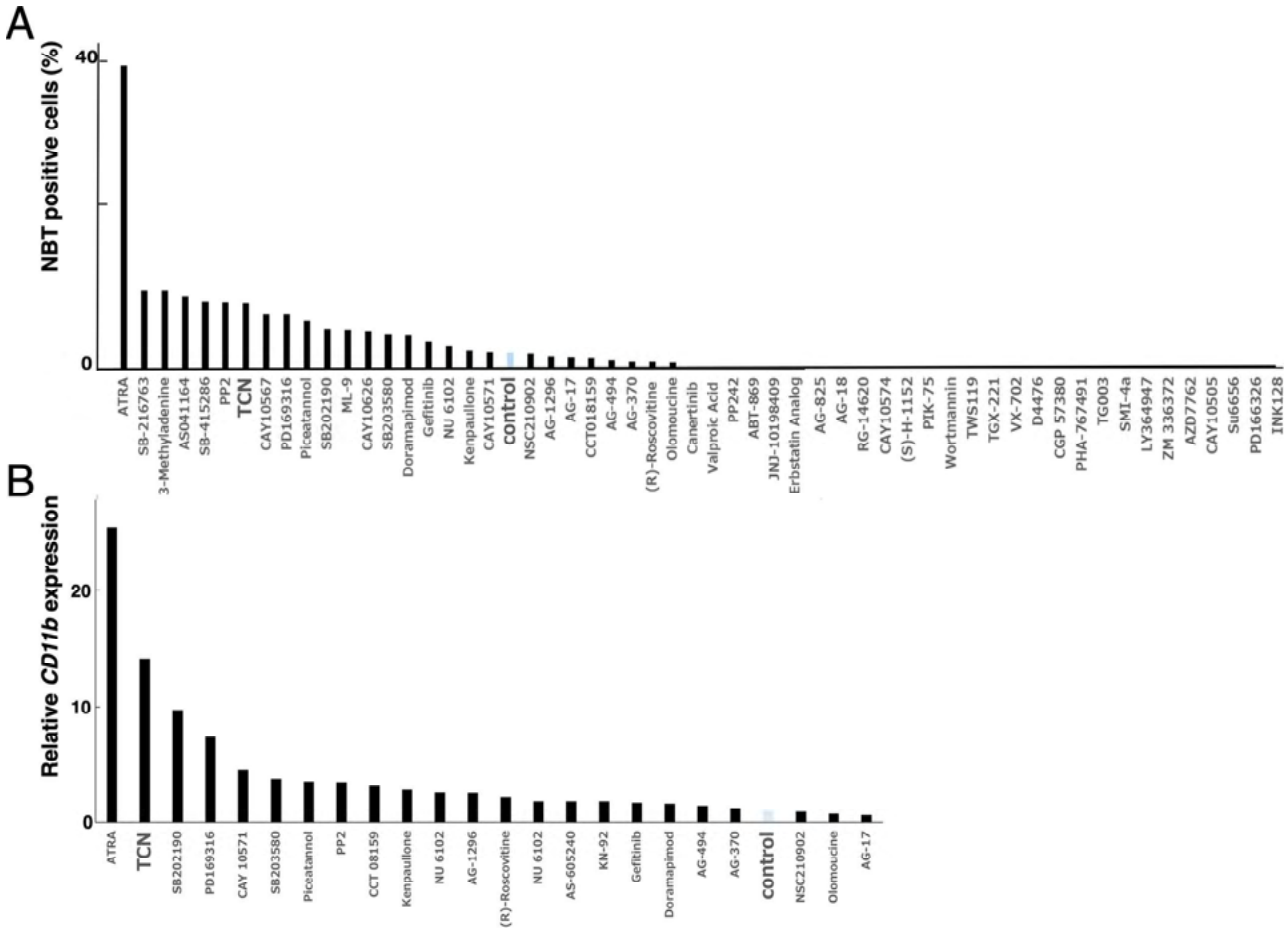


**Fig 1. Identification of TCN as a novel myeloid differentiation inducer.** (A) Effects of ATRA and components of the kinase inhibitor screening library on NBT positive cells. ATRA was used at a final concentration of 100 nM and kinase inhibitors were used at 10 μM, unless noted otherwise. The NBT assay was performed 72 hours after the addition of these agents. (B) Summary of *CD11b* gene expressions by real-time PCR. The relative *CD11b* expression was calculated from the fold expression of *CD11b*, determined by the copy number of *CD11b* divided by the copy number of the internal control, *GAPDH*, compared with control values. The data shown are the mean values of experiments performed in triplicate.

https://doi.org/10.1371/journal.pone.0303428.g001

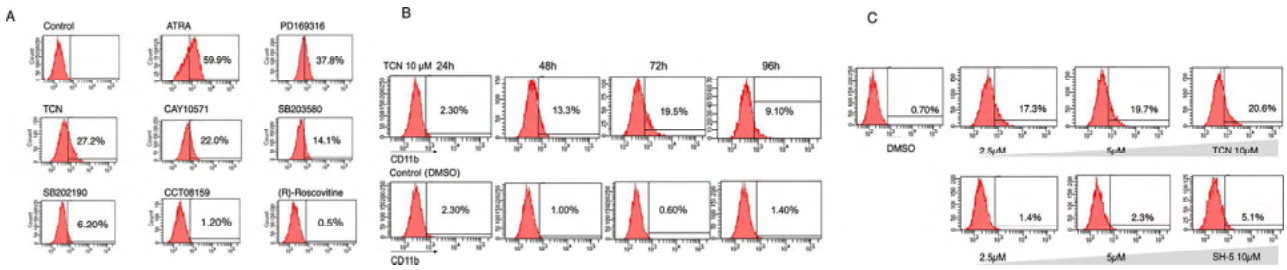


**Fig 2. Effects of ATRA and kinase inhibitors on the expression of CD11b in NB4 cells analyzed by FCM.** (A) The percentages of CD11b positive cells after the addition of the indicated kinase inhibitors are shown as representative histograms of at least three independent experiments. (B) Time course FCM experiment to examine CD11b positive cells after the addition of TCN. Lower panels are controls, to which the solvent dimethylsulfoxide (DMSO) was added. (C) The expression of CD11b in the presence of the indicated doses of TCN and controls (upper panels). The indicated amount of Akt inhibitor SH-5 was added as a comparative experiment (lower panels).

https://doi.org/10.1371/journal.pone.0303428.g002

## TCN changes the morphology and potently decreases the nuclear/cytoplasmic ratio of NB4 and HL-60 cells

We next examined the morphology of cells with or without TCN. To prove the efficiency of TCN in inducing cell differentiation in other AML cell types other than NB4, we examined an AML (M2) derived [13] cell line HL-60. As shown in Fig 3A, 72 hours after the addition of TCN, the cytoplasm of NB4 cells was enlarged with slight budding of the plasma membrane region, which was morphologically similar to the effect of 100 nM of ATRA, at the concentration we observed similar nuclear/cytoplasmic (N/C) ratio to 10 μM of TCN (Fig 3B). This indicates that partial myelomonocytic differentiation rather than full myeloid differentiation was achieved [14,15]. Next, we evaluated N/C ratio, which was analyzed statistically and presented as a violin plot. In the absence of TCN, the mean N/C ratio was 70%, which was significantly decreased to 60% in the presence of TCN, which was similar to the effect of the addition of 100 nM ATRA (16) (Fig 3B). In HL-60 cells, the cytoplasm was enlarged like which was seen in NB4 cells (Fig 3C), however, the effect of TCN was even more efficient than 100 nM of ATRA (Fig 3D).

## TCN potently induces myelomonocytic and other differentiation markers in NB4 and HL-60 cells

To characterize the features of TCN-induced NB4 and HL-60 cells, we examined the dose-dependent effect of TCN on several differentiation markers including *CD11b*, *CD11c*, *CD14*, *and myeloperoxidase (MPO)* genes. As shown in Fig 4A–4D, in NB4 cells, real-time PCR analyses demonstrated that TCN potently increased the expressions of myelomonocytic markers *CD11b* and *CD11c* in a dose-dependent manner. In contrast, monocytic *CD14* expression was highest at 2.5 μM TCN and was decreased at a higher concentration (10 μM), whereas *MPO* expression was decreased regardless of the TCN concentration. Similar effect was also observed in HL-60 cells. We next examined the effect of ATRA on *CD11b*, *CD11c*, *CD14*, *and myeloperoxidase (MPO)* genes. Real-time PCR analyses demonstrated that ATRA potently increased the expressions of myelomonocytic markers *CD11b*, *CD11c*, whereas *MPO* expression was decreased, in a dose-dependent manner in both NB4 and HL-60 cells (Fig 4E–4H), which was similar to the TCN effect we observed (Fig 4A–4D). In addition, CD14 expression is induced by ATRA in both lineages.

These results suggest that a high concentration of TCN efficiently induces myelomonocytic markers (*CD11b* and *CD11c*) in NB4 and HL-60 cells.

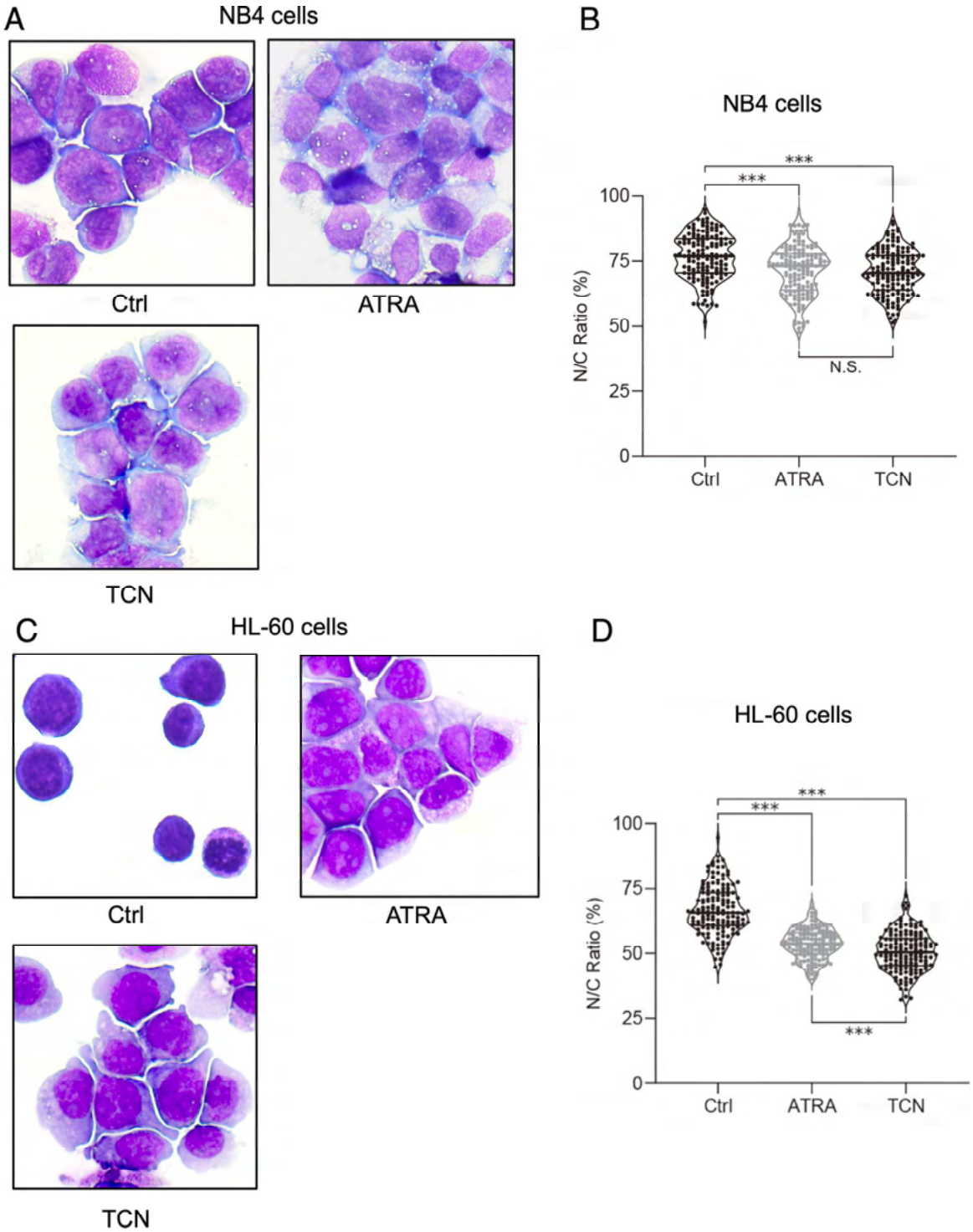


**Fig 3. Morphologic analyses of NB4 and HL-60 cells in the presence or absence of TCN or ATRA.** (A, C) NB4 cells (A) or HL-60 cells (C) were collected and subjected to Wright-Giemsa staining, with and without ATRA (100 nM) or TCN (10 μM) treatment. Magnification = ×400. (B, D) A violin plot of the percentages of the N/C ratio of each cell type, using NB4 cells (B) or HL-60 cells (D). Result of ATRA [16], shown in gray, is presented for comparison (***$p<0.001$; N.S. not significant).

https://doi.org/10.1371/journal.pone.0303428.g003

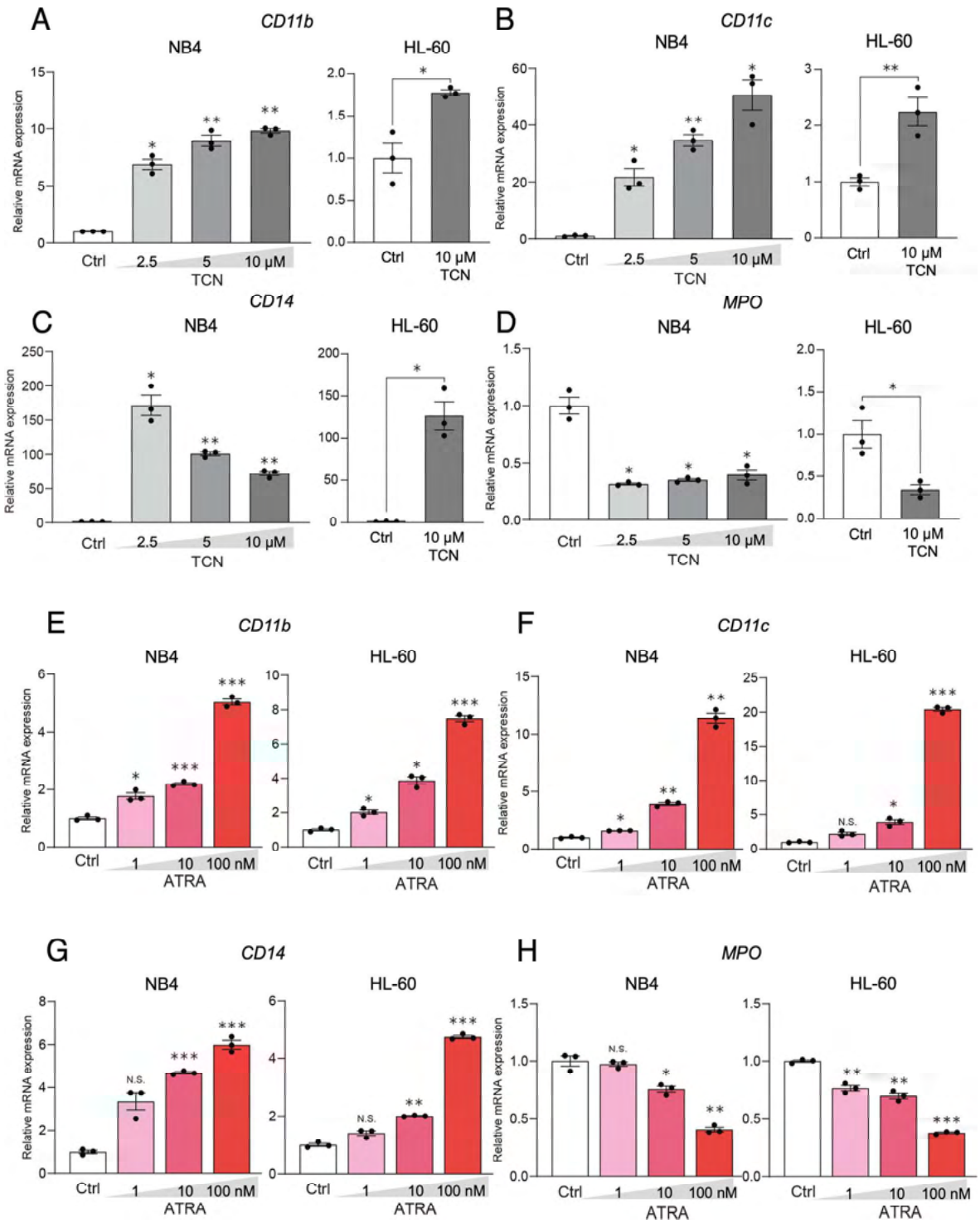


**Fig 4. Analyses of TCN-induced differentiation by differentiation markers.** The TCN-induced differentiation of NB4 and HL-60 cells and control cells was examined by the real-time PCR analysis of several markers. The expressions of (A, E) *CD11b*, (B, F) *CD11c*, (C, G) *CD14*, and (D, H) *MPO*, were examined in the presence of the indicated doses of TCN (A-D) or ATRA (E-H). Relative mRNA expression was calculated from the copy number of the target gene adjusted by *GAPDH*, in each TCN-treated sample (2.5, 5, 10 μM), or ATRA-treated sample (1, 10, 100 nM), which was then divided by the control sample values. The data shown were obtained from three independent PCR amplifications (average ± SD; $^{*}p<0.05$; $^{**}p<0.01$; $^{***}p<0.001$ vs. Ctrl).

https://doi.org/10.1371/journal.pone.0303428.g004

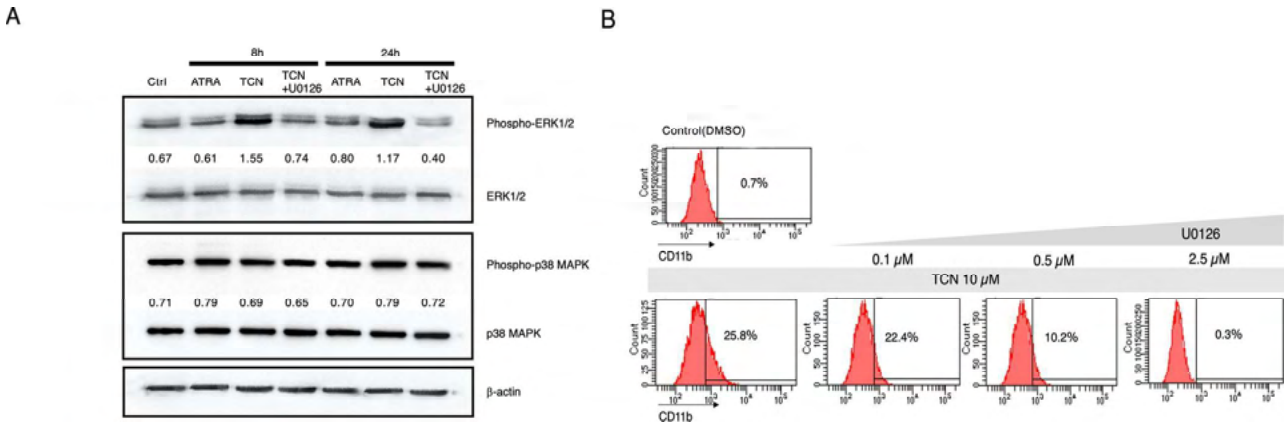


**Fig 5. TCN activates ERK, and the MEK inhibitor U0126 diminishes the induction of CD11b expression by TCN.** (A) Cells were cultured in the presence or absence of TCN or ATRA, for indicated periods, and analyzed for ERK and p38 MAPK activity by western blotting. MEK inhibitor U0126 is also added in the indicated sample. The membranes were probed with an anti-phospho-ERK rabbit polyclonal antibody or anti-phospho-p38 mouse monoclonal antibody. Next, the membranes were stripped and re-probed with an anti-total-ERK mouse monoclonal antibody or anti-total-p38 mouse monoclonal antibody to verify equal protein loading. Indicated numbers are relative density, calculated by Image J 1.54 software, obtained from the amount of density from the band of phospho-ERK, or phosphor-p38, divided by total-ERK, or total-p38. (B) FCM experiment of the effect of TCN on CD11b expression in the presence (0.1, 0.5, 2.5 μM) or absence of the U0126.

https://doi.org/10.1371/journal.pone.0303428.g005

## Phosphorylation of ERK is induced by TCN, and the MEK inhibitor U0126 diminishes the induction of CD11b expression on NB4 cells by TCN

We next examined the signaling pathways in NB4 cells affected by TCN. As shown in Fig 5A, Western blot analysis using NB4 cells demonstrated that TCN promoted ERK1/2 phosphorylation, whereas p38 MAPK phosphorylation was not affected, suggesting that activation of the ERK pathway is involved in TCN-induced differentiation. We also examined that whether ATRA may affect phosphorylation of ERK and p38, and found that there was no obvious effect, suggesting that mechanisms of ATRA induced differentiation is different from TCN effect. In addition, TCN induced phosphorylation of ERK was completely abrogated by the addition of MEK inhibitor U0126, suggesting that the involvement of MEK/ERK pathway. We further examined the combination effect of TCN and ATRA for the induction of CD11b expression, and found that there was no enhancement effect (S1 Fig), may also suggest the difference of the mechanisms of these agents. To verify whether the ERK pathway has a role in TCN induced differentiation, we confirmed that the induction of CD11b expression was efficiently reduced by the addition of U0126 (Fig 5B). Collectively, activation of the MEK/ERK pathway is involved in TCN-induced differentiation and this is distinctly different from ATRA induced differentiation.

## Gene expression profiling reveals the effect of TCN on NB4 cell differentiation

To clarify the molecular mechanisms involved in TCN-induced NB4 cell differentiation, we performed microarray analysis. Control NB4 cells and cells incubated with 10 μM TCN were harvested after 72 hours because the maximal effect of TCN was observed at this time point (Fig 2B). When defined to greater than 3-fold changes, TCN upregulated 348 genes and downregulated 83 genes (Fig 6A). We subjected these 348 genes to pathway analysis using DAVID software, and revealed that "hematopoietic cell lineage" and "cytokine-cytokine receptor interaction" were enriched with high significance (Fig 6B). Therefore, we focused on these

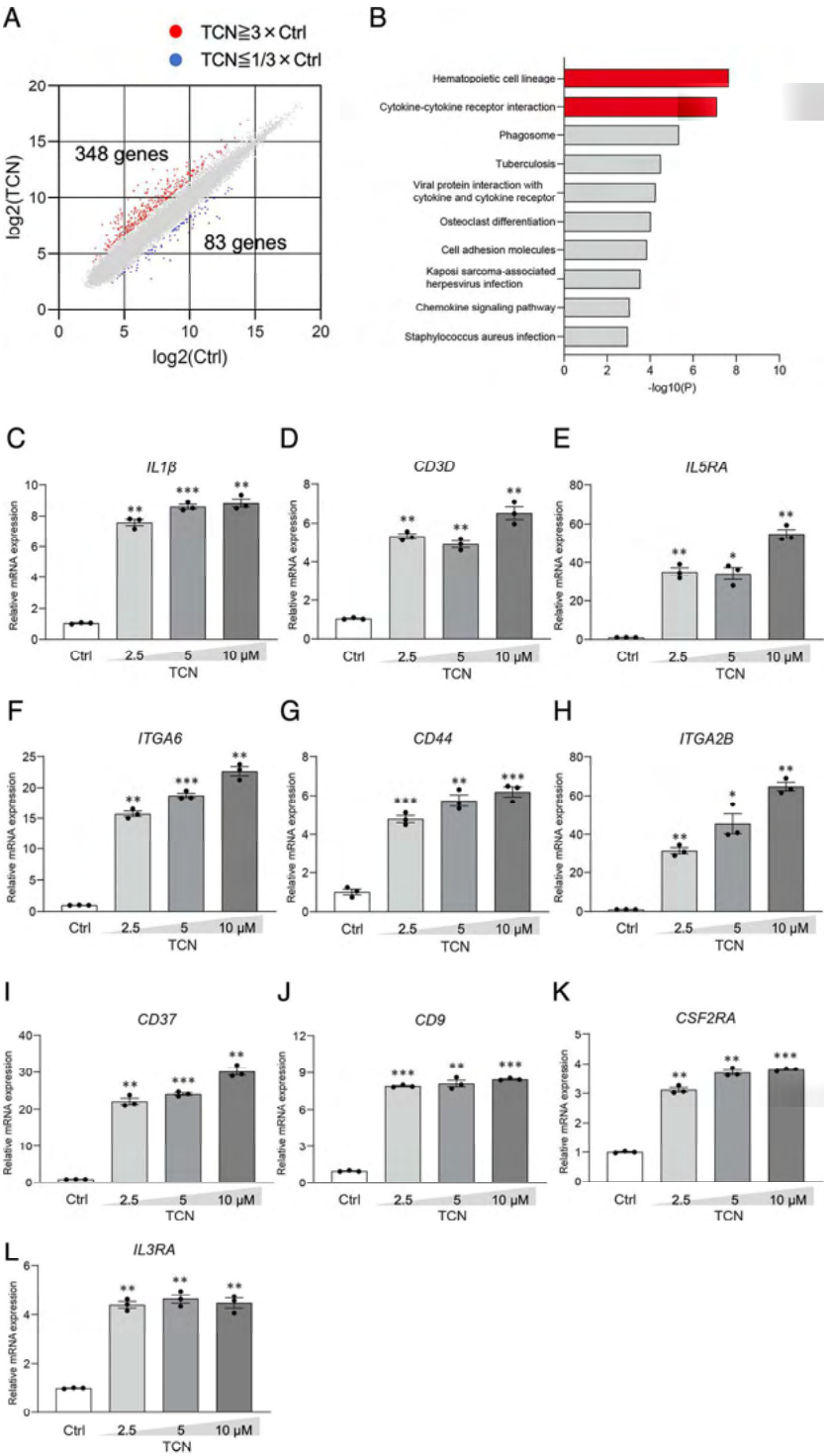


**Fig 6. Results of the microarray analysis.** (A) Gene expression profile of NB4 cells comparing TCN treated vs control cells. (B) Result of pathway analysis using DAVID (https://david.ncifcrf.gov/home.jsp) software from 348 genes. The x-axis shows the negative log base 10 p-value. The higher the number, the higher the significance. (C-L) Total RNAs from NB4 cells cultured in the presence or absence of ATRA and/or TCN for 72 h were analyzed by real-time PCR with specific primers for (C) *IL-1β*, (D) *CD3D*, (E) *IL5RA*, (F) *ITGA6*, (G) *CD44*, (H) *ITGA2B*, (I) *CD37*, (J) *CD9*, (K)

*CSF2RA*, and (L) *IL3RA*. Relative mRNA expressions were calculated from the copy number of the target gene adjusted by *GAPDH*, in each TCN-treated sample (2.5, 5, 10 μM), which were divided by the control sample values. The data presented were obtained from three independent PCR amplifications and reproducibility was confirmed using different batches of cDNA. Statistical significance was determined by one-way ANOVA followed by Dunnett's test. $^{*}p<0.05$, $^{**}p<0.01$, $^{***}p<0.001$ vs control.

https://doi.org/10.1371/journal.pone.0303428.g006

pathways. The results of pathway analysis using the KEGG pathway database and DAVID software are shown in S2 and S3 Figs. A list of the genes related to "hematopoietic cell lineage" and "cytokine-cytokine receptor interaction" are shown in S2 and S3 Tables, respectively. From this list, we selected 11 genes including *CD11b* (S2 and S3 Tables, bold), and verified them by real-time PCR. The other genes were *IL1β*, *CD3 delta subunit of T-cell receptor complex (CD3D)*, *interleukin 5 receptor subunit alpha (IL5RA)*, *integrin subunit alpha 6 (ITGA6)*, *CD44*, *integrin subunit alpha 2b (ITGA2B)*, *CD37*, *CD9*, *colony stimulating factor 2 receptor subunit alfa (CSF2RA) and interleukin 3 receptor subunit alfa (IL3RA)*. These genes are related to hematopoietic cell development, signal transduction, cell adhesion, immunity, and inflammatory responses. All gene expressions were significantly upregulated by TCN (Fig 6C–6L), suggesting that TCN-induced NB4 cell differentiation is dependent, at least in part, on these genes.

## Discussion

The PI3K/Akt-mammalian target of rapamycin (mTOR) pathway is one of the intracellular pathways aberrantly upregulated in cancers including hematopoietic malignancies [17]. Recently, it was reported that targeting the PI3K/Akt/mTOR signaling pathway had some benefit, even in clinical settings [18–21]. The PI3K/Akt axis is aberrantly activated in T-cell acute lymphoblastic leukemia (T-ALL). The therapeutic potential of TCN for T-ALL was reported by Evangelisti *et al* [22], who showed that TCN, a highly specific Akt inhibitor, induced autophagy and synergized with vincristine, a chemotherapeutic drug for T-ALL patients.

The inhibition of Akt was reported to activate the Raf/MEK/ERK pathway [23]. Bertacchini *et al.* [24]. examined 80 samples of primary cells from AML patients and revealed that the inhibition of Akt and mTOR resulted in the paradoxical activation of growth factor receptor tyrosine kinases (RTKs). In accordance with this, the dual inhibition of RTKs and Akt had synergistic cytotoxic effects in a pre-clinical model [24]. This is consistent with our current result of the activation of ERK pathway by TCN. In the current study, we demonstrated that the signaling effect to ERK, are completely different between TCN and ATRA in NB4 ells. This fact may suggest that synergistic interactions cannot be expected for these two agents. In fact, there was no obvious positive combinational effect for CD11b expression in NB4 cells (data not shown).

In addition, it was previously reported that the MEK/ERK pathway was activated in the early stage of the 1,25-dihydroxyvitamin D-induced monocytic differentiation of HL-60 cells [25]. The Raf/MEK/ERK pathway is considered to control the balance between the expansion and differentiation of hematopoietic progenitors [26,27], and have a critical role during the monocytic and granulocytic differentiation of several myeloid cell lines, including HL-60 and U937 [27]. Therefore, the activation of this pathway by an Akt inhibitor may be critical for myeloid differentiation.

Indeed, many potent myeloid differentiation inducers including ursolic acid [28], Jasmonates, potent lipid regulators in plants [29], *Momordica charantia* seeds [30], Vibsanin A, a novel protein kinase C activator [31], diptoindonesin G (Dip G), a natural resveratrol aneuploid [32], human epidermal growth factor receptor 2 (HER2) inhibitor TAK165 [33], and

staurosporine, a protein kinase C pan-inhibitor [34], were reported to activate the Raf/MEK/ERK pathway. These agents mainly activate ERK/MAPK [28–34] and the downstream STAT1 [32,33], either alone or in combination with ATRA [34], to induce the monocytic and/or granulocytic differentiation of myeloid cell lines including HL-60 [28–32], NB4 [33], U937 [34], or primary AML samples [32].

Inflammatory cytokines, such as IL-1β, tumor necrosis factor (TNF)-α, and the adhesion molecules, L-selectin and intercellular adhesion molecule-1 are upregulated during APL cell differentiation [35,36]. In the current microarray study, we found that the expressions of IL-1β and several integrins were increased (Fig 6), suggesting the TCN-induced differentiation effect may partially overlap with ATRA-induced myeloid differentiation.

Clinical trials of TCN-related agents have been reported in various malignancies including solid tumors [37], metastatic breast cancer [38], and squamous carcinoma of the cervix [39]. However, these trials have reported the limited activity of TCN. Sampath *et al.* [12] reported that TCN phosphate monohydrate therapy was well tolerated in patients with advanced hematological malignancies. In their study, 32 of 41 treated patients were considered evaluable for responses. Among these, 3 patients had decreased marrow blast counts, 1 had a marked reduction in leukocytosis and spleen size, and 17 had stable disease with acceptable toxicities. Because TCN had limited toxicity in these malignancies [12,37–39], basic and clinical research, including combination trials of TCN for APL and non-APL leukemia are worthy of exploration. Further clarification of the role of TCN for myeloid differentiation should be elucidated.

## Supporting information

**S1 Fig. Effect of TCN and ATRA for CD11b expression in NB4 cells, examined by the real-time PCR analysis.** Relative mRNA expression was calculated from the copy number of the target gene adjusted by *GAPDH*, in each TCN-treated sample (10 μM), or ATRA-treated sample (1, 10, 100 nM), which was then divided by the control sample values. The data shown were obtained from three independent PCR amplifications Statistical significance was determined by two-way ANOVA followed by Tukey's multiple comparisons test (*** $p<0.001$ vs. ctrl, δδ $p<0.01$, δδδ $p<0.001$ vs. ATRA).
(TIFF)

**S2 Fig. The pathway analysis of 348 genes in the hematopoietic cell lineage pathway (Fig 6A) using the KEGG pathway database and DAVID software.** Red stars are genes with expressions induced more than 3-fold by TCN compared with controls.
(TIFF)

**S3 Fig. The pathway analysis of 348 genes in the cytokine-cytokine receptor interaction pathway (Fig 6A) using the KEGG pathway database and DAVID software.** Red stars are genes with expressions induced more than 3-fold by TCN compared with controls.
(TIFF)

**S1 Raw images. Western blot raw images for Fig 5A.**
(PDF)

**S1 Table. Sequences of primers used for real-time quantitative PCR.**
(XLSX)

**S2 Table. List of genes in the hematopoietic cell lineage pathway from pathway analysis using the KEGG pathway database and DAVID software.** Bold text indicates genes selected and verified by real-time PCR.
(XLSX)

**S3 Table. List of genes in the cytokine-cytokine receptor interaction pathway from pathway analysis using the KEGG pathway database and DAVID software.** Bold text indicates genes selected and verified by real-time PCR.
(XLSX)

## Acknowledgments

We thank J. Ludovic Croxford, PhD, from Edanz (https://jp.edanz.com/ac) for editing a draft of this manuscript.

## Author Contributions

**Conceptualization:** Shinichiro Takahashi.

**Data curation:** Shinichiro Takahashi.

**Formal analysis:** Susumu Suzuki, Shinichiro Takahashi.

**Funding acquisition:** Shinichiro Takahashi.

**Investigation:** Souma Suzuki, Susumu Suzuki, Yuri Sato-Nagaoka, Chisaki Ito, Shinichiro Takahashi.

**Methodology:** Shinichiro Takahashi.

**Project administration:** Shinichiro Takahashi.

**Resources:** Shinichiro Takahashi.

**Supervision:** Shinichiro Takahashi.

**Validation:** Susumu Suzuki.

**Visualization:** Shinichiro Takahashi.

**Writing – original draft:** Shinichiro Takahashi.

**Writing – review & editing:** Shinichiro Takahashi.

## References

1. Dohner H, Weisdorf DJ, Bloomfield CD. Acute Myeloid Leukemia. N Engl J Med. 2015; 373(12):1136–52. https://doi.org/10.1056/NEJMra1406184 PMID: 26376137
2. Steelman LS, Pohnert SC, Shelton JG, Franklin RA, Bertrand FE, McCubrey JA. JAK/STAT, Raf/MEK/ERK, PI3K/Akt and BCR-ABL in cell cycle progression and leukemogenesis. Leukemia. 2004; 18 (2):189–218. https://doi.org/10.1038/sj.leu.2403241 PMID: 14737178
3. Koeffler HP. Is there a role for differentiating therapy in non-APL AML? Best Pract Res Clin Haematol. 2010; 23(4):503–8. https://doi.org/10.1016/j.beha.2010.09.014 PMID: 21130414
4. Sell S. Leukemia: stem cells, maturation arrest, and differentiation therapy. Stem Cell Rev. 2005; 1 (3):197–205. https://doi.org/10.1385/SCR:1:3:197 PMID: 17142856
5. Takahashi S. Kinase Inhibitors and Interferons as Other Myeloid Differentiation Inducers in Leukemia Therapy. Acta Haematol. 2022; 145(2):113–21. https://doi.org/10.1159/000519769 PMID: 34673646
6. Karl H. Schram LBT. The synthesis of 6-amino-4-methyl-8-(β-D-ribofuranosyl) (4-H,8-H)pyrrolo-[4,3,2-de]pyrimido[4,5-c]pyridazine, a new tricyclic nucleoside. Tetrahedron Letters. 1971; 12(49):4757–60.
7. Wotring LL, Passiatore JE, Roti Roti JL, Hudson JL, Townsend LB. Effects of the tricyclic nucleoside 6-amino-4-methyl-8-(beta-D-ribofuranosyl)- pyrrolo[4,3,2-de]pyrimido[4,5-c]pyridazine on the viability and cell cycle distribution of L1210 cells in vitro. Cancer Res. 1985; 45(12 Pt 1):6355–61.
8. Wotring LL, Townsend LB, Jones LM, Borysko KZ, Gildersleeve DL, Parker WB. Dual mechanisms of inhibition of DNA synthesis by triciribine. Cancer Res. 1990; 50(16):4891–9. PMID: 2379153

9. Yang L, Dan HC, Sun M, Liu Q, Sun XM, Feldman RI, et al. Akt/protein kinase B signaling inhibitor-2, a selective small molecule inhibitor of Akt signaling with antitumor activity in cancer cells overexpressing Akt. Cancer Res. 2004; 64(13):4394–9. https://doi.org/10.1158/0008-5472.CAN-04-0343 PMID: 15231645

10. Toson B, Fortes IS, Roesler R, Andrade SF. Targeting Akt/PKB in pediatric tumors: A review from preclinical to clinical trials. Pharmacol Res. 2022; 183:106403. https://doi.org/10.1016/j.phrs.2022.106403 PMID: 35987481

11. Hirako N, Nakano H, Takahashi S. A PU.1 suppressive target gene, metallothionein 1G, inhibits retinoic acid-induced NB4 cell differentiation. PLoS One. 2014; 9(7):e103282. https://doi.org/10.1371/journal.pone.0103282 PMID: 25072246

12. Sampath D, Malik A, Plunkett W, Nowak B, Williams B, Burton M, et al. Phase I clinical, pharmacokinetic, and pharmacodynamic study of the Akt-inhibitor triciribine phosphate monohydrate in patients with advanced hematologic malignancies. Leuk Res. 2013; 37(11):1461–7. https://doi.org/10.1016/j.leukres.2013.07.034 PMID: 23993427

13. Dalton WT, Jr., Ahearn MJ, McCredie KB, Freireich EJ, Stass SA, Trujillo JM. HL-60 cell line was derived from a patient with FAB-M2 and not FAB-M3. Blood. 1988; 71(1):242–7.

14. Drexler HG, Quentmeier H, MacLeod RA, Uphoff CC, Hu ZB. Leukemia cell lines: in vitro models for the study of acute promyelocytic leukemia. Leuk Res. 1995; 19(10):681–91. https://doi.org/10.1016/0145-2126(95)00036-n PMID: 7500643

15. Khanna-Gupta A, Kolibaba K, Zibello TA, Berliner N. NB4 cells show bilineage potential and an aberrant pattern of neutrophil secondary granule protein gene expression. Blood. 1994; 84(1):294–302. PMID: 7517212

16. Suzuki S LJ, Sato Y, Miyake R, Suzuki S, Okitsu Y, Fukuda T, Isaji T, Gu J, Takahashi S. Fucosylation inhibitor 6-alkynylfucose enhances the ATRA-induced differentiation effect on acute promyelocytic leukemia cells. Biochemical and Biophysical Research Communications. 2024;in press. https://doi.org/10.1016/j.bbrc.2024.149541 PMID: 38608490

17. Nepstad I, Hatfield KJ, Gronningsaeter IS, Reikvam H. The PI3K-Akt-mTOR Signaling Pathway in Human Acute Myeloid Leukemia (AML) Cells. Int J Mol Sci. 2020; 21(8). https://doi.org/10.3390/ijms21082907 PMID: 32326335

18. Park S, Chapuis N, Saint Marcoux F, Recher C, Prebet T, Chevallier P, et al. A phase Ib GOELAMS study of the mTOR inhibitor RAD001 in association with chemotherapy for AML patients in first relapse. Leukemia. 2013; 27(7):1479–86. https://doi.org/10.1038/leu.2013.17 PMID: 23321953

19. Amadori S, Stasi R, Martelli AM, Venditti A, Meloni G, Pane F, et al. Temsirolimus, an mTOR inhibitor, in combination with lower-dose clofarabine as salvage therapy for older patients with acute myeloid leukaemia: results of a phase II GIMEMA study (AML-1107). Br J Haematol. 2012; 156(2):205–12. https://doi.org/10.1111/j.1365-2141.2011.08940.x PMID: 22082314

20. Kasner MT, Mick R, Jeschke GR, Carabasi M, Filicko-O'Hara J, Flomenberg N, et al. Sirolimus enhances remission induction in patients with high risk acute myeloid leukemia and mTORC1 target inhibition. Invest New Drugs. 2018; 36(4):657–66. https://doi.org/10.1007/s10637-018-0585-x PMID: 29607465

21. Takahashi S. Combination Therapies with Kinase Inhibitors for Acute Myeloid Leukemia Treatment. Hematology Reports. 2023; 15(2):331–46. https://doi.org/10.3390/hematolrep15020035 PMID: 37367084

22. Evangelisti C, Ricci F, Tazzari P, Chiarini F, Battistelli M, Falcieri E, et al. Preclinical testing of the Akt inhibitor triciribine in T-cell acute lymphoblastic leukemia. J Cell Physiol. 2011; 226(3):822–31. https://doi.org/10.1002/jcp.22407 PMID: 20857426

23. Wang J, Zhao Y, Kauss MA, Spindel S, Lian H. Akt regulates vitamin D3-induced leukemia cell functional differentiation via Raf/MEK/ERK MAPK signaling. Eur J Cell Biol. 2009; 88(2):103–15. https://doi.org/10.1016/j.ejcb.2008.05.003 PMID: 19058874

24. Bertacchini J, Guida M, Accordi B, Mediani L, Martelli AM, Barozzi P, et al. Feedbacks and adaptive capabilities of the PI3K/Akt/mTOR axis in acute myeloid leukemia revealed by pathway selective inhibition and phosphoproteome analysis. Leukemia. 2014; 28(11):2197–205. https://doi.org/10.1038/leu.2014.123 PMID: 24699302

25. Wang X, Studzinski GP. Inhibition of p38MAP kinase potentiates the JNK/SAPK pathway and AP-1 activity in monocytic but not in macrophage or granulocytic differentiation of HL60 cells. J Cell Biochem. 2001; 82(1):68–77. https://doi.org/10.1002/jcb.1141 PMID: 11400164

26. Geest CR, Coffer PJ. MAPK signaling pathways in the regulation of hematopoiesis. J Leukoc Biol. 2009; 86(2):237–50. https://doi.org/10.1189/jlb.0209097 PMID: 19498045

27. Miranda MB, McGuire TF, Johnson DE. Importance of MEK-1/-2 signaling in monocytic and granulocytic differentiation of myeloid cell lines. Leukemia. 2002; 16(4):683–92. https://doi.org/10.1038/sj.leu.2402400 PMID: 11960350

28. Zhang T, He YM, Wang JS, Shen J, Xing YY, Xi T. Ursolic acid induces HL60 monocytic differentiation and upregulates C/EBPbeta expression by ERK pathway activation. Anticancer Drugs. 2011; 22 (2):158–65.

29. Ishii Y, Kiyota H, Sakai S, Honma Y. Induction of differentiation of human myeloid leukemia cells by jasmonates, plant hormones. Leukemia. 2004; 18(8):1413–9. https://doi.org/10.1038/sj.leu.2403421 PMID: 15229618

30. Sharma J, Prabha P, Sharma R, Gupta S, Dixit A. Anti-leukemic principle(s) from Momordica charantia seeds induce differentiation of HL-60 cells through ERK/MAPK signalling pathway. Cytotechnology. 2022; 74(5):591–611.

31. Shen X, Xing S, Zhang L, Wang F, Ou H, Shan Y, et al. Vibsanin A sensitizes human acute myeloid leukemia cells to tyrosine kinase inhibitor-induced myeloid differentiation via activation of PKC and upregulation of Lyn. Biochem Biophys Res Commun. 2018; 502(1):110–5. https://doi.org/10.1016/j.bbrc.2018.05.129 PMID: 29787755

32. Gao J, Fan M, Xiang G, Wang J, Zhang X, Guo W, et al. Diptoindonesin G promotes ERK-mediated nuclear translocation of p-STAT1 (Ser727) and cell differentiation in AML cells. Cell Death Dis. 2017; 8 (5):e2765.

33. Shao X, Liu Y, Li Y, Xian M, Zhou Q, Yang B, et al. The HER2 inhibitor TAK165 Sensitizes Human Acute Myeloid Leukemia Cells to Retinoic Acid-Induced Myeloid Differentiation by activating MEK/ERK mediated RARalpha/STAT1 axis. Sci Rep. 2016; 6:24589.

34. Shi L, Weng XQ, Sheng Y, Wu J, Ding M, Cai X. Staurosporine enhances ATRA-induced granulocytic differentiation in human leukemia U937 cells via the MEK/ERK signaling pathway. Oncol Rep. 2016; 36 (5):3072–80. https://doi.org/10.3892/or.2016.5123 PMID: 27665842

35. Matikainen S, Tapiovaara H, Vaheri A, Hurme M. Activation of interleukin-1 beta gene expression during retinoic acid-induced granulocytic differentiation of promyeloid leukemia cells. Cell Growth Differ. 1994; 5(9):975–82. PMID: 7819135

36. Hsu HC, Tsai WH, Chen PG, Hsu ML, Ho CK, Wang SY. In vitro effect of granulocyte-colony stimulating factor and all-trans retinoic acid on the expression of inflammatory cytokines and adhesion molecules in acute promyelocytic leukemic cells. Eur J Haematol. 1999; 63(1):11–8. https://doi.org/10.1111/j.1600-0609.1999.tb01844.x PMID: 10414449

37. Garrett CR, Coppola D, Wenham RM, Cubitt CL, Neuger AM, Frost TJ, et al. Phase I pharmacokinetic and pharmacodynamic study of triciribine phosphate monohydrate, a small-molecule inhibitor of AKT phosphorylation, in adult subjects with solid tumors containing activated AKT. Invest New Drugs. 2011; 29(6):1381–9. https://doi.org/10.1007/s10637-010-9479-2 PMID: 20644979

38. Hoffman K, Holmes FA, Fraschini G, Esparza L, Frye D, Raber MN, et al. Phase I-II study: triciribine (tricyclic nucleoside phosphate) for metastatic breast cancer. Cancer Chemother Pharmacol. 1996; 37 (3):254–8. https://doi.org/10.1007/BF00688325 PMID: 8529286

39. Feun LG, Blessing JA, Barrett RJ, Hanjani P. A phase II trial of tricyclic nucleoside phosphate in patients with advanced squamous cell carcinoma of the cervix. A Gynecologic Oncology Group Study. Am J Clin Oncol. 1993; 16(6):506–8.

Contents lists available at ScienceDirect

Biochemical and Biophysical Research Communications

journal homepage: www.elsevier.com/locate/ybbrc

# Fucosylation inhibitor 6-alkynylfucose enhances the ATRA-induced differentiation effect on acute promyelocytic leukemia cells

Susumu Suzuki [a,b], Jianwei Liu [c], Yuri Sato [b], Rikuto Miyake [a], Souma Suzuki [a], Yoko Okitsu [d], Tomohiko Fukuda [c], Tomoya Isaji [c], Jianguo Gu [c,**], Shinichiro Takahashi [a,b,*]

[a] Division of Laboratory Medicine, 4Rheumatology and Hematology, Faculty of Medicine, Tohoku Medical and Pharmaceutical University, 1-15-1 Fukumuro, Miyagino-ku, Sendai, 983-8536, Japan
[b] Department of Clinical Laboratory, Tohoku Medical and Pharmaceutical University Hospital, 1-12-1 Fukumuro, Miyagino-ku, Sendai, 983-8512, Japan
[c] Division of Regulatory Glycobiology, Institute of Molecular Biomembrane and Glycobiology, Tohoku Medical and Pharmaceutical University, 4-4-1 Komatsushima, Aoba-ku, Sendai, Miyagi, 981-8558, Japan
[d] Division of Rheumatology and Hematology, Faculty of Medicine, Tohoku Medical and Pharmaceutical University, 1-15-1 Fukumuro, Miyagino-ku, Sendai, 983-8536, Japan

ARTICLE INFO

*Keywords:*
6-Alkynylfucose
All-trans retinoic acid
Myeloid differentiation
C-type lectin receptor signaling pathway
IL-1β

ABSTRACT

For acute promyelocytic leukemia (APL), differentiation therapy with all-trans retinoic acid (ATRA) is well established. However, the narrow application and tolerance development of ATRA remain to be improved. In this study, we investigated the effects of combinations of glycosylation inhibitors with ATRA to achieve better efficiency than ATRA alone. We found that the combination of fucosylation inhibitor 6-alkynylfucose (6AF) and ATRA had an additional effect on cell differentiation, as revealed by expression changes in two differentiation markers, CD11b and CD11c, and significant morphological changes in NB4 and HL-60 APL cells. In AAL lectin blot analyses, ATRA or 6AF alone could decrease fucosylation, while their combination decreased fucosylation more efficiently. To clarify the molecular mechanism for the 6AF effect on ATRA-induced differentiation, we performed microarray analyses using NB4 cells. In a pathway analysis using DAVID software, we found that the C-type lectin receptor (CLR) signaling pathway was enriched with high significance. In real-time PCR analyses using NB4 and HL-60 cells, *FcεRIγ*, *CLEC6A*, *CLEC7A*, *CASP1*, *IL-1β*, and *EGR3*, as components of the CLR pathway, as well as *CD45* and *AKT3* were upregulated by 6AF in ATRA-induced differentiation. Taken together, the present findings suggest that the CLR signaling pathway is involved in the 6AF effect on ATRA-induced differentiation.

## 1. Introduction

Acute myeloid leukemia (AML) is a fatal disease. It is characterized by infiltration of bone marrow, peripheral blood, and other tissues by clonal, proliferative, and abnormally differentiated hematopoietic cells [1]. Differentiation therapy with all-trans retinoic acid (ATRA) is well established for acute promyelocytic leukemia (APL), a specific type of AML. However, the narrow application and tolerance development of ATRA require improvement.

The genetic hallmark of APL is the reciprocal translocation of t (15:17)(q22; q11-12) leading to a fusion of the promyelocytic (PML) gene on chromosome 15 and the retinoic acid receptor a (RARα) on chromosome 17 [2]. The PML-RARα is an aberrant repressor of RA signaling. PML-RARα fusion gene binds histone deacetylase complex (HDAC)-recruiting co-repressor complex with high affinity [3]. PML-RARα is also able to bind the DNA methylating enzymes Dnmt 1 and Dnmt 3a, result in the methylation of RA target genes [4]. Wild type RARα forms heterodimers with the retinoid X receptor (RXR) and forms repressor complex with HDAC, bears transcriptional repression. Physiological concentrations of RA ($1 \times 10$-9 M) are able to release repressor

* Corresponding author. Division of Laboratory Medicine, 4Rheumatology and Hematology, Faculty of Medicine, Tohoku Medical and Pharmaceutical University, 1-15-1 Fukumuro, Miyagino-ku, Sendai. 983-8536, Japan.
** Corresponding author.
*E-mail addresses:* jgu@tohoku-mpu.ac.jp (J. Gu), shintakahashi@tohoku-mpu.ac.jp (S. Takahashi).

https://doi.org/10.1016/j.bbrc.2024.149541
Received 26 October 2023; Received in revised form 8 January 2024; Accepted 15 January 2024

**Table 1**
Primer sequences for real-time quantitative PCR.

| | | |
|---|---|---|
| hGAPDH | Forward | 5′-GAAGGTGAAGGTCGGAGT-3′ |
| | Reverse | 5′-GAAGATGGTGATGGGATTTC-3′ |
| hCD11b | Forward | 5′-GCCGGTGAAATATGCTGTCT-3′ |
| | Reverse | 5′-GCGGTCCCATATGACAGTCT-3′ |
| hCD11c | Forward | 5′-ACCACAAGCAGTAGCTCCTTC-3′ |
| | Reverse | 5′-AAGTAGGAGCCGATCTGAGTC-3′ |
| hCD14 | Forward | 5′-GTCTGCAACTTCTCCGAACC-3′ |
| | Reverse | 5′-CCAGTAGCTGAGCAGGAACC-3′ |
| hMPO | Forward | 5′-TCCTTCGTCACTGGCGTCA-3′ |
| | Reverse | 5′-ATGCAGTCGGCTTGGTTCTT-3′ |
| hFcεR1ϒ | Forward | 5′-GGAGAGCCTCAGCTCTGCTA-3′ |
| | Reverse | 5′-TGGTGGTTTCTCATGCTTCA-3′ |
| hEGR2 | Forward | 5′-CCTCCTTATTCTGGCTGTGC-3′ |
| | Reverse | 5′-CTGGGATCATTGGGAAGAGA-3′ |
| hEGR3 | Forward | 5′-GCGTTGGACAGCAATCTCTT-3′ |
| | Reverse | 5′-AATGCCTTGATGGTCTCCAG-3′ |
| hLSP1 | Forward | 5′-AGCACCAGAAATGTCAGCAG-3′ |
| | Reverse | 5′-TCTGGCTGGGATTTCTTCAC-3′ |
| hCCL22 | Forward | 5′-ACTGCACTCCTGGTTGTCCT-3′ |
| | Reverse | 5′-CGGCACAGATCTCCTTATCC-3′ |
| hVAV1 | Forward | 5′-TGGTGTCCTTCTGTGTCAGC-3′ |
| | Reverse | 5′-CTTGAGGCCGAACTTCTCAC-3′ |
| hKSR1 | Forward | 5′-CCCAGAGCTCAACAGCTACC-3′ |
| | Reverse | 5′-CTGGAGTCCTCCTTGTGCTC-3′ |
| hIRF1 | Forward | 5′-AGCTCAGCTGTGCGAGTGTA-3′ |
| | Reverse | 5′-TAGCTGCTGTGGTCATCAGG-3′ |
| hIRF9 | Forward | 5′-CAAGGCCTGGGCAATATTTA-3′ |
| | Reverse | 5′-ACTGTGCTGTCGCTTTGATG-3′ |
| hCASP1 | Forward | 5′-GCTTTGTGCTCTTCCACACC-3′ |
| | Reverse | 5′-CATCTGGCTGCTCAAATGAA-3′ |
| hIL-1β | Forward | 5′-GGGCCTCAAGGAAAAGAATC-3′ |
| | Reverse | 5′-TTCTGCTTGAGAGGTGCTGA-3′ |
| hPIK3CD | Forward | 5′-AAGATCGGCCACTTCCTTTT-3′ |
| | Reverse | 5′-TGAGAGCTCAGCTTGACGAA-3′ |
| hCD45 | Forward | 5′-ACTCTTGGCATTTGGCTTTG-3′ |
| | Reverse | 5′-CCAAGTTCCTCAGCTTTTGG-3′ |
| hAKT3 | Forward | 5′-GGTTCGAGAGAAGGCAAGTG-3′ |
| | Reverse | 5′-CGGTCTTTTGTCTGGAAGGA-3′ |
| hRAC2 | Forward | 5′-GCAAGACCTGCCTTCTCATC-3′ |
| | Reverse | 5′-GAAGACGTCCGTCTGTGGAT-3′ |
| hCLEC6A | Forward | 5′-ATGGTGAAACTGGCAAAAGG-3′ |
| | Reverse | 5′-ACCAAATGTGCTCCCATCTC-3′ |
| hCLEC7A | Forward | 5′-CTGGCAACTGGGCTCTAATC-3′ |
| | Reverse | 5′-TTGGAGATGGGTTTTCTTGG-3′ |

complex and recruit activators with histone acetyltransferase activities, result in the up-regulation of RARα target genes [5], which, in turn, can induce terminal differentiation and growth arrest of cells including normal myeloid hemopoietic cells [6,7]. In contrast, mechanisms of the action of the ATRA towards fusion protein PML-RARα are different from wild type RARα. Higher concentration of RA (1 × 10-6 M) is required to release transcriptional repression of PML-RARα, since PML-RARα chimeric fusion binds to the HDAC recruiting co-repressor complex with higher affinity [3]. Watts et al. reported a case of relapsed AML, a non-APL patient, failed with two lines of salvage chemotherapy followed with continuous dose of ATRA [8]. The patient died from rapid disease progression after eight days of ATRA treatment. Therefore, the use of ATRA in patients who have other subtypes of AML then M3 is usually not beneficial and may be even harmful, and this may be due to the differences of the mechanisms of action between wild type and chimeric fusion RARα.

Many studies have demonstrated that the structures of oligosaccharide chains (glycans) on the cell surface are changed during cancer cell differentiation [9] and in leukemia cell lines [10–12]. For example, it was reported that the asparagine-linked sugar chains were changed in human AML cells (HL-60) during monocytoid and myeloid differentiation [11]. Specifically, high-molecular-weight oligosaccharides were initially predominant in HL-60 cells, but were slightly decreased during myeloid differentiation and markedly decreased during monocytoid differentiation, with a concomitant increase in biantennary oligosaccharides.

The above structural alterations were reported to be caused by expression level changes in the corresponding glycosyltransferases [9,10,13]. The two main glycosyltransferases responsible for the synthesis of poly-N-acetyllactosamine (polyLacNAc) in glycans, β1,3-N-acetylglucosamonyltransferase (β3GnT)-2 and β3GnT-8, were investigated in leukemia cell lines during differentiation [14]. The study revealed that the expression levels of β3GnT-2, β3GnT-2-8, and polyLacNAc were increased during myeloid differentiation. The expression level of polyLacNAc was also increased on the HL-60 cell surface after treatment with myeloid differentiation inducers, ATRA, and dimethylsulfoxide. Similar findings were noted for NB4 cells, an APL [15] line. However, the expression level of polyLacNAc remained unchanged after treatment with phorbol 12-myristate 13-acetate (PMA), an inducer of monocytic differentiation.

In a study involving HL-60 cells, Li et al. [10] reported that the content of bisected N-glycans catalyzed by

N-acetylglucosaminyltransferase III (GnT-III) was decreased in ATRA-treated cells, but increased in PMA-treated cells. Notably, N-glycans containing α-1,6-fucose catalyzed by α-1,6-fucosyltransferase (Fut8) were decreased during differentiation. Furthermore, Fut8 activity was reduced in ATRA- and PMA-treated cells. Collectively, these findings suggest that glycosylation plays an important role in myeloid differentiation.

To understand whether the above changes are functional for myeloid differentiation, the present study investigated the effects of fucosylation on APL cell differentiation using 6-alkynyl fucose (6AF), a specific inhibitor of Fut8 [16].

## 2. Materials and methods

### 2.1. Culture of HL-60 and NB4 cells

AML (M2)-derived HL-60 [17] and AML (M3)-derived NB4 cells [15] were cultured in RPMI medium containing 10 % heat-inactivated fetal bovine serum under 5 % $CO_2$ at 37 °C in a humidified atmosphere. The cells were cultured using an authenticated technique (https://www.sigmaaldrich.com/japan/ordering/technical-service/recipe-cc.html).

### 2.2. Surface marker analysis by flow cytometry (FCM)

HL-60 and NB4 cells in the exponential growth phase were seeded at 2 × 105 cells/mL, cultured in the presence of 100 nM ATRA and/or 10 μM 6AF, and collected for analysis at 72 h. Briefly, 2–3 × 105 cells were washed with phosphate-buffered saline and resuspended. Aliquots of the cell suspensions (30 μL) were incubated with 1 μL of PE-conjugated mouse anti-human CD11b antibody (BioLegend, San Diego, CA) in the dark for 30 min at room temperature. An isotype-matched PE-conjugated mouse IgG antibody (BioLegend) was used as a negative control. For FCM analysis, the cell samples were applied to an LSR Fortessa X-20 Flow Cytometer (BD Biosciences, San Jose, CA).

### 2.3. Morphological analysis

HL-60 and NB4 cells in the exponential growth phase were seeded at 2 × 105 cells/mL, and induced to differentiate by treatment with ATRA and/or 6AF for 72 h. After the incubation, the cells were collected and smeared on glass slides for analysis. Wright–Giemsa staining was conducted, and the cell differentiation was evaluated by the morphology. Images were taken using a NIKON ECLIPSE Ni microscope and a DS-Fi3 digital camera with NIS-Elements D (NIKON Co., Tokyo, Japan). The areas of the nucleus and cytoplasm in individual cells were measured and quantified using Image J software (https://imagej.nih.gov/ij/). The data were statistically analyzed and presented as scatterplots using Prism software (version 10; GraphPad Software Inc., La Jolla, CA).

### 2.4. Cell viability assay

Cell viability was determined by Cell Count Reagent SF, a dye reduction assay with water-soluble tetrazolium salt, WST-8 (Nacalai Tesque, Kyoto, Japan). A total of 5000 cells/well were plated in 96-well plates and indicated different (25, 50, 75, 100 nM) concentrations of ATRA and 10 μM of 6AF and further incubated for 72 h. Thereafter, 10 μl

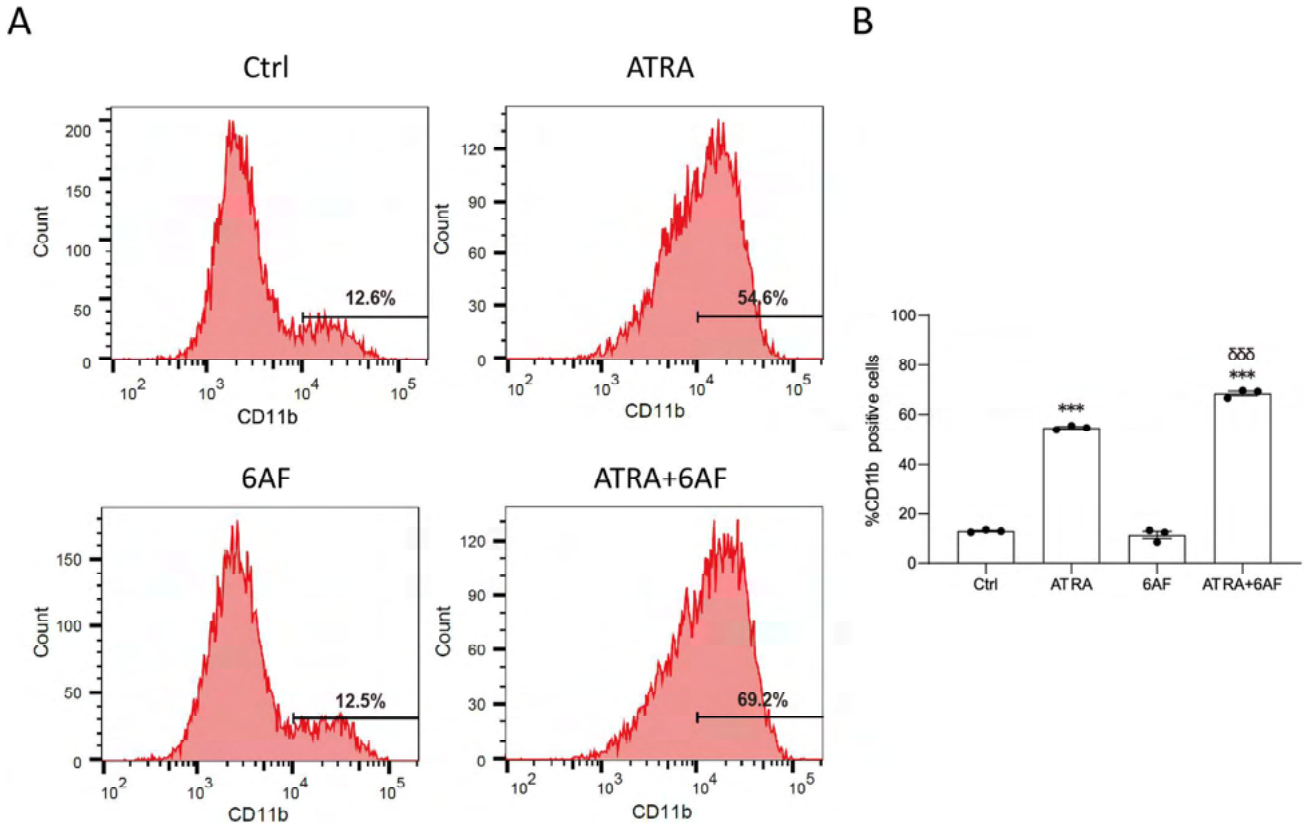


**Fig. 1.** Effects of ATRA and/or 6AF on CD11b expression in HL-60 (A, B) and NB4 (C, D) cells analyzed by FCM. (A, C) Histograms representing the FCM analyses for CD11b in cells with and without ATRA (100 nM) and/or 6AF (10 μM) treatment. (B, D) Data are shown as mean ± SEM for each FCM analysis (n = 3). Two-way ANOVA followed by Tukey's multiple comparisons test was employed for statistical analyses. **p < 0.01, ***p < 0.001 vs. Ctrl; δδδp<0.001 vs. ATRA.

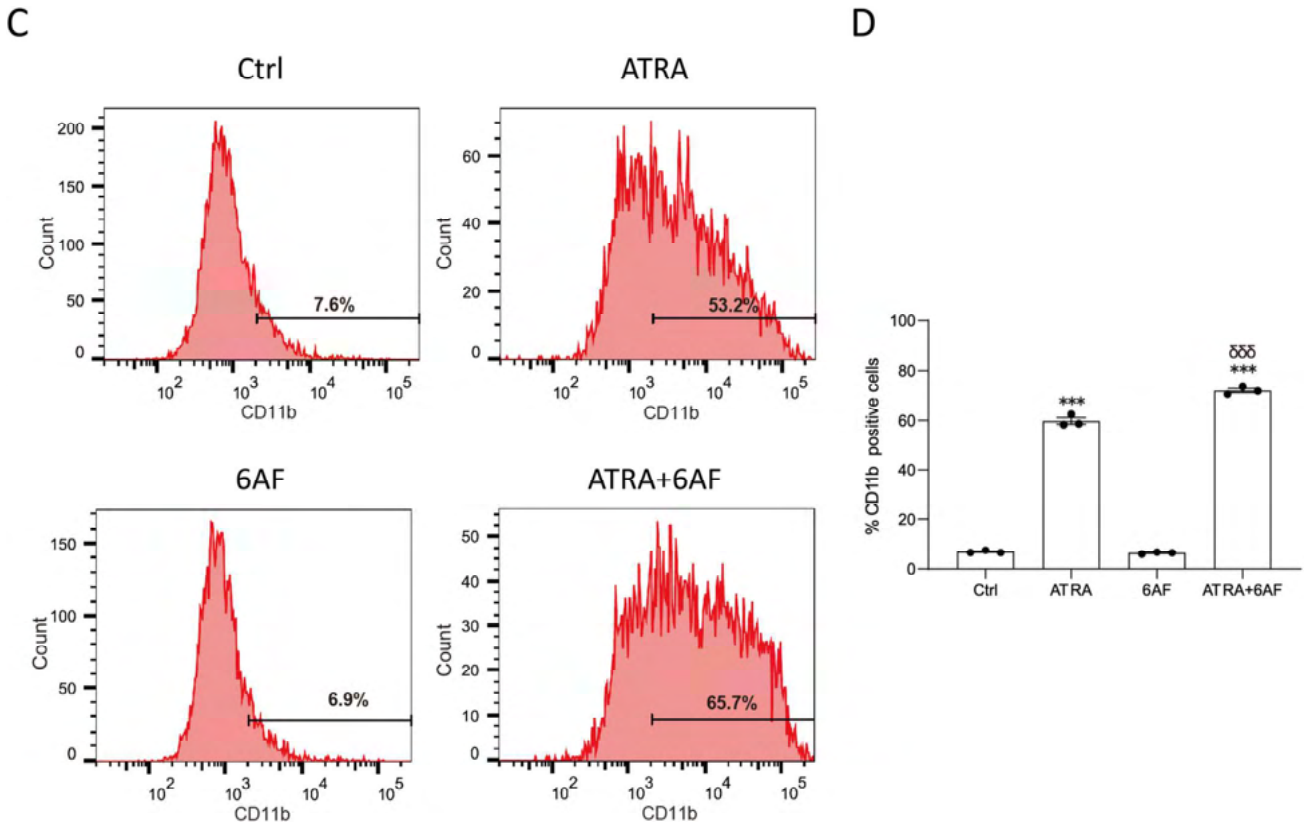


**Fig. 1.** (*continued*).

of WST-8 solution were added to each well, and the plates were incubated for 2h at 37 °C. The absorbance of each well was measured at 450 nm using a microplate reader.

### 2.5. Lectin blotting

Cells were washed three times with chilled phosphate-buffered saline and lysed with cold lysis buffer (20 mM Tris-HCl pH 7.4, 150 mM NaCl, 1 % Triton X-100) containing a protease and phosphatase inhibitor cocktail (Nacalai Tesque). The obtained cell lysates were placed on a rotor shaker for 40 min at 4 °C. Next, the cell lysates were centrifuged at 15,000 rpm for 15 min at 4 °C, and the supernatants were transferred to fresh marked tubes. The protein concentrations were measured using a Pierce™ BCA Protein Assay Kit (Thermo Fisher Scientific, Munich, Germany). Equal amounts of the protein lysates were subjected to reducing SDS-PAGE, and the separated proteins were transferred to PVDF membranes (Millipore, Billerica, MA). The membranes were incubated with appropriate primary and secondary antibodies or with biotinylated lectins. Biotinylated aleuria aurantia lectin (AAL) was obtained from the Seikagaku Corp (Tokyo, Japan). Biotinylated Phaseolus vulgaris erythroagglutinin (E4-PHA; B-1385) and Datura stramonium agglutinin (DSA; B-1185) were acquired from Vector Laboratories (Vector Laboratories, Burlingame, CA). Rabbit mAb against glyceraldehyde-3-phosphate dehydrogenase (GAPDH) (sc-25778) was obtained from Santa Cruz Biotechnology. Immunoreactive bands were detected using an Immobilon Western Chemiluminescent HRP Substrate (Millipore) or a Vectastain ABC Kit (Vector Laboratories) in accordance with each manufacturer's instructions.

### 2.6. Microarray and mRNA expression analyses

NB4 cells were seeded at 2 × 105 cells/mL, treated with 100 nM ATRA and/or 10 μM 6AF, or left untreated as control cells. For microarray analyses, the cells were collected after 72 h, and total cellular RNA was extracted using an RNA Mini Purification Kit (Qiagen, Miami, FL) in accordance with the manufacturer's protocol. The microarray analyses were conducted using the Filgen Clariom™ D Assay (Filgen, Nagoya, Japan). Data were analyzed using Transcriptome Analysis Console software (Thermo Fisher Scientific). KEGG pathway analysis was performed using Database for Annotation, Visualization and Integrated Discovery (DAVID) software (https://david.ncifcrf.gov). The gene expression datasets were deposited in the NCBI Gene Expression Omnibus (http://www.ncbi.nlm.nih.gov/geo/) under the GEO series accession number GSE234103. For real-time PCR analyses, the cells were harvested after 72 h or at specified times. For mRNA expression analyses, cDNAs were prepared from the cells using a ReverTra Ace® qPCR RT Kit (Toyobo, Tokyo, Japan). Quantitative PCR was performed using THUNDERBIRD SYBR qPCR Mix (Toyobo), an Opticon Mini Real-time PCR Instrument (Bio-Rad, Hercules, CA), and a CFX Connect Real-Time PCR Detection System (Bio-Rad) as previously described [18]. The sequences of the primers are listed in Table 1. The thermal cycling conditions used for all of the examined genes were: 95 °C for 15 s; 35

cycles of 95 °C for 10 s, 60 °C for 45 s, and 72 °C for 3 min. The copy number of each sample was calculated as described elsewhere.

### 2.7. Statistical analysis

GraphPad Prism® 10.0 software (GraphPad Software Inc.) was used for all statistical analyses. Two-way ANOVA followed by Tukey's multiple comparisons test was employed to determine the statistical significance of differences in data. Statistical significance was accepted for values of $p < 0.05$.

## 3. Results

### 3.1. The combination of 6AF and ATRA induces expression of the myeloid differentiation marker CD11b

Because N-glycans containing α-1,6-fucose catalyzed by Fut8 were decreased during differentiation and Fut8 activity was reduced during ATRA- and PMA-induced differentiation [10], we first examined the effect of 6AF on ATRA-induced differentiation. We employed the HL-60 and NB4 cell lines, because the addition of ATRA was reported to induce CD11b without changing the surface expression of other markers, such as CD14, CD15, CD33, CD68, and HLA-DR [19]. The FCM analysis revealed that combined treatment with 6AF and ATRA led to synergistic induction of CD11b-positive cells in both HL-60 (Fig. 1A and B) and NB4 (Fig. 1C and D) cells. Consistent with these findings, real-time PCR analyses showed that the combination of 6AF and ATRA significantly increased the myeloid *CD11b* and *CD11c* expression levels in HL-60 and NB4 cells (Fig. 2A–C). *Myeloperoxidase* (*MPO*), which was reported to decrease during ATRA-induced differentiation [19,20], was further reduced by the addition of 6AF in NB4 cells, but not in HL-60 cells (Fig. 2D). No significant effect was observed for the monocytic lineage marker gene *CD14* (Fig. 2E). We further examined whether this combination has any effect on cell viability. As a result, we revealed that, among dose tested (25, 50, 75, 100 nM), ATRA slightly decreased the cell viability, whereas addition of 10 μM of 6AF had almost no effect (Fig. 2F).

### 3.2. Analysis of glycosylation status in cells treated with 6AF and/or ATRA

To examine whether 6AF can directly regulate the fucosylation status in HL-60 and NB4 cells, the levels of fucosylation were confirmed by blotting analyses with AAL lectin, which preferentially recognizes fucosylated N-glycans [21,22]. The results showed that the expression of fucosylated N-glycans was slightly decreased by the addition of ATRA, and markedly decreased by the addition of 6AF (Fig. 3). Interestingly, the combination of ATRA and 6AF further diminished the expression of fucosylated N-glycans. These results clearly indicate that the combination of 6AF and ATRA potently decreases the expression of core fucosylation in HL-60 and NB4 cells. On the other hand, we also compared the reactive abilities with E4-PHA, which recognizes bisecting GlcNAc,

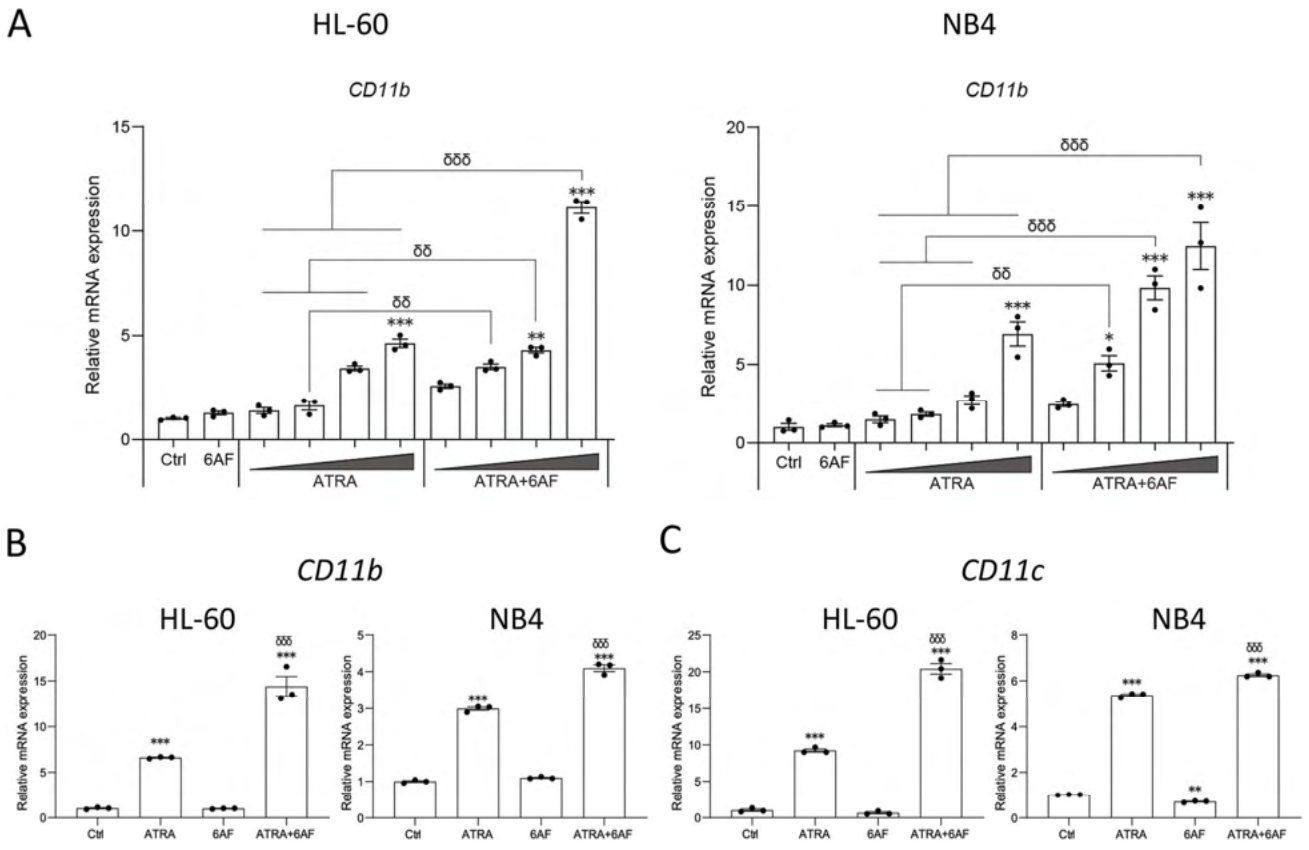


**Fig. 2.** Effects of treatment with ATRA and/or 6AF on differentiation markers and cell viability in HL-60 and NB4 cells. The effects of differentiation markers by ATRA and/or 6AF treatment on HL-60 and NB4 cells were examined by real-time PCR analyses of (A, B) *CD11b*, (C) *CD11c*, (D) *MPO*, and (E) *CD14*. Data are shown as mean ± SEM for three independent PCR amplifications. (F) Cell viability was shown in the mean percentage compared with the value of mock-treated cells (Ctrl). Two-way ANOVA followed by Tukey's multiple comparisons test was employed for statistical analyses. *$p < 0.05$, **$p < 0.01$, ***$p < 0.001$ vs. Ctrl; δδp<0.01, δδδp<0.001 vs. ATRA, NS: not significant.

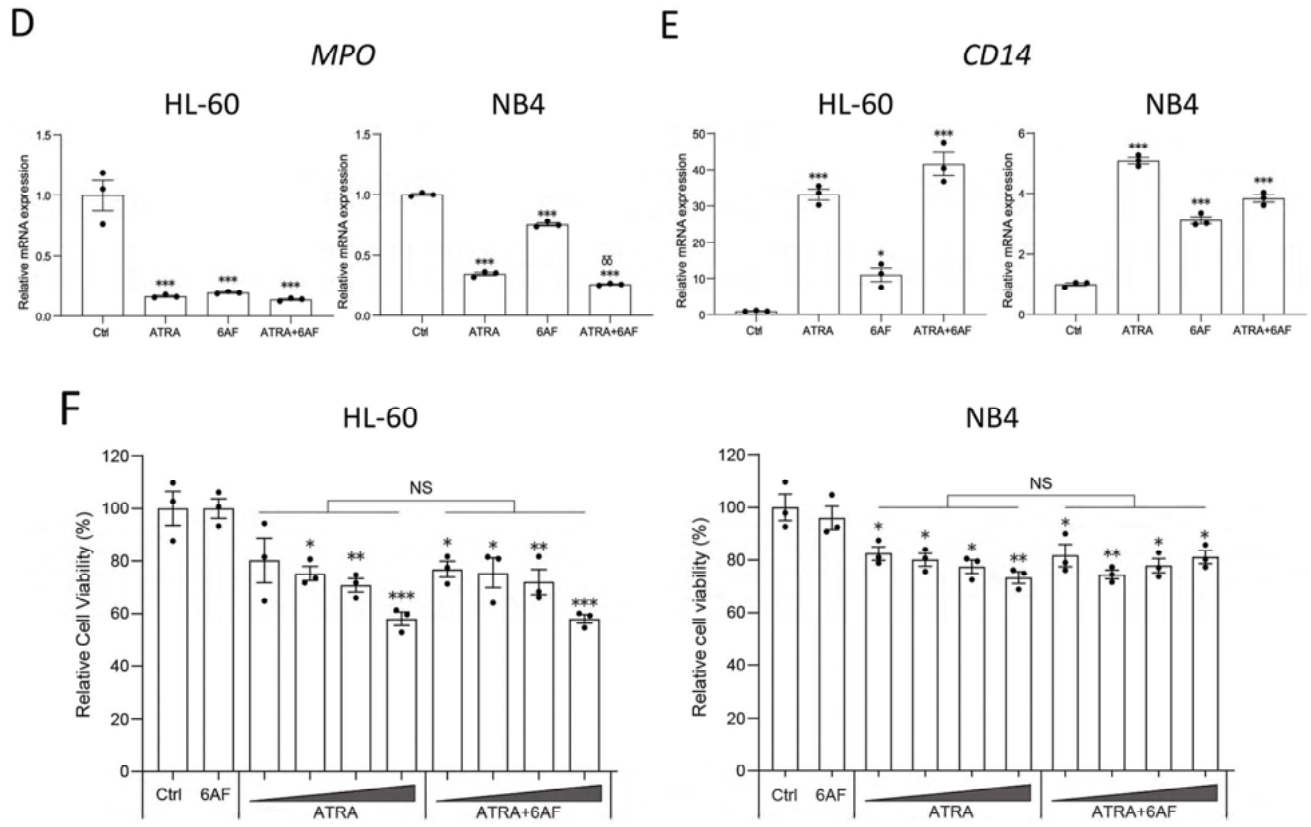


**Fig. 2.** (*continued*).

or DSA, which recognizes beta 1,4 GlcNAc branching-containing total glycans similar among ATRA and/or 6AF treated cells, as these branched N-glycans play crucial biological roles [23,24]. Curiously, decreased E4-PHA staining levels in ATRA or ATRA+6AF-treated NB4 cells and modestly increased E4-PHA staining levels in 6AF-treated NB4 cells were observed (Fig. 3). A similar tendency was also observed in HL-60 cells. In addition, concomitant with decreased E4-PHA staining, an increased DSA staining was observed in ATRA or ATRA+6AF-treated NB4 cells, suggesting the notion that GnT-III suppresses GlcNAc branching formation catalyzed by GnT-IV or GnT-V [25]. The functions of GnT-III and/or GnT-IV in cell differentiation require further study.

### 3.3. *The combination of 6AF and ATRA reduces the nuclear/cytoplasmic (N/C) ratio in HL-60 and NB4 cells*

Next, we examined the morphologies of HL-60 and NB4 cells with or without 6AF and/or ATRA treatment. As shown in Fig. 4A, in the presence of 100 nM ATRA, a significant increase in differentiated cells was noted compared with control cells, together with a decrease in the (N/C) ratio, and indentation and bending of the nuclei, characteristic of granulocytic differentiation in metamyelocytes and the band stage. Treatment with 6AF alone did not induce any noticeable differences compared with control cells. However, the N/C ratio was significantly decreased when 6AF was added to ATRA-treated HL-60 and NB4 cells (Fig. 4B and C). These findings suggest that 6AF significantly enhances ATRA-induced differentiation.

### 3.4. *Gene expression profiling for the effect of 6AF on ATRA-induced differentiation*

To determine the molecular mechanisms for the 6AF effect on ATRA-induced differentiation, we performed microarray analyses using NB4 cells. When upregulation was defined as a ≥2-fold change in expression, treatment with ATRA alone upregulated 1395 genes (Fig. S1), while treatment with 6AF alone upregulated 170 genes (Fig. S2). In the comparison between ATRA+6AF-treated cells and control cells (Fig. 5A, upper panel), 1445 genes were upregulated (≥2-fold change; red dots), and 1634 genes were downregulated (≤1/2-fold change; blue dots). Next, we compared ATRA+6AF-treated cells and ATRA-treated cells using the same definitions, but found only 295 upregulated genes (red dots) and 225 downregulated genes (blue dots). We subjected these genes to pathway analysis using DAVID software, and found that in ATRA treated cells, 44 pathways were enriched with less than ten to the power of minus two, at negative of the log base 10 P-value (Table S1). At the same definition, 69 pathways were enriched in ATRA+6AF treated cells. Among these pathways, 42 pathways are commonly enriched in both ATRA and ATRA+6AF treated cells. However, 27 pathways including "Necroptosis", and "Apoptosis" pathways were enriched only in the ATRA+6AF treated cells, may suggest that the characteristics of the combination of these agents. We next relaxed the definition to ≥1.5-fold change (orange dots) and ≤2/3-fold change (green dots), to see the difference between ATRA+6AF and ATRA treated cells, and found that 1644 genes were upregulated, while 1509 genes were downregulated

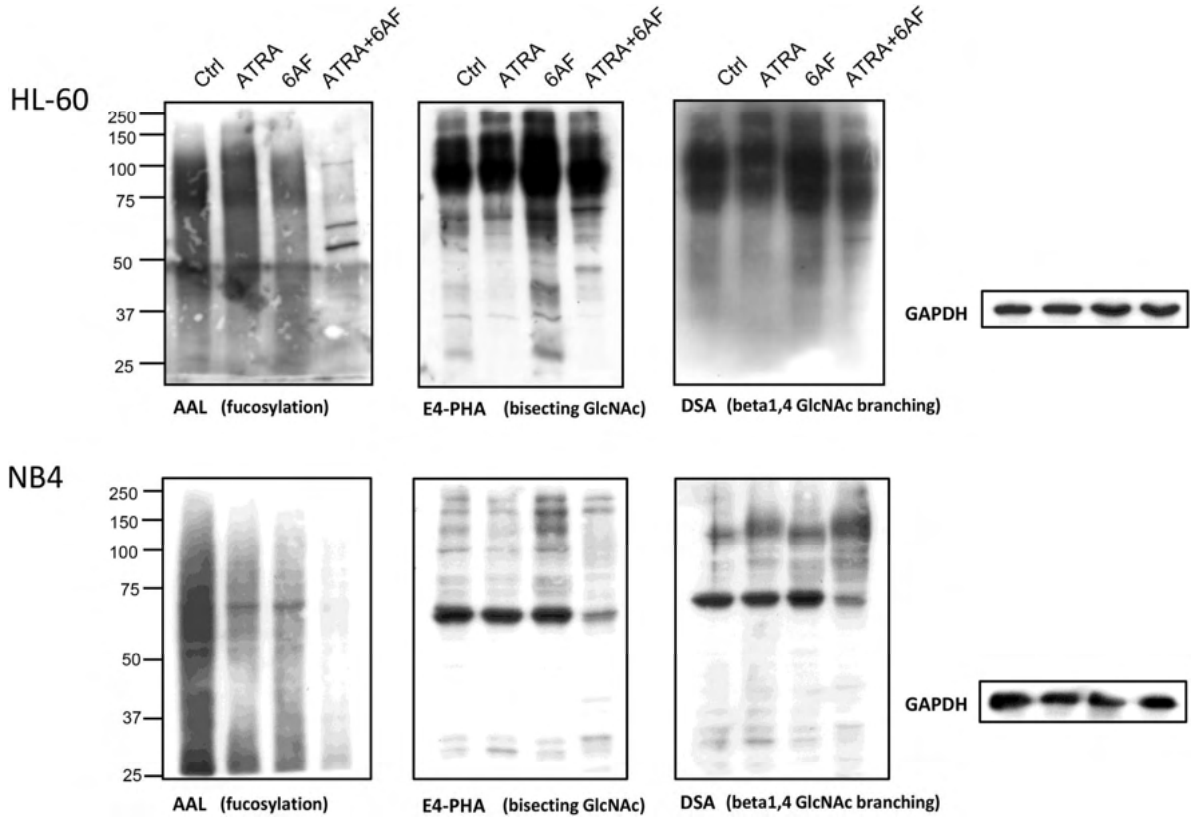


**Fig. 3.** Effects of treatment with ATRA and/or 6AF on fucosylation. The effects of ATRA and/or 6AF treatment on fucosylation in HL-60 and NB4 cells were examined by AAL, E4-PHA, and DSA lectin blotting analyses. Equal amounts of cell lysates were separated by 7.5 % SDS-PAGE and transferred to membranes. The membranes were probed with AAL, E4-PHA, and DSA lectins, and were then re-probed with an anti-GAPDH antibody and used as loading controls.

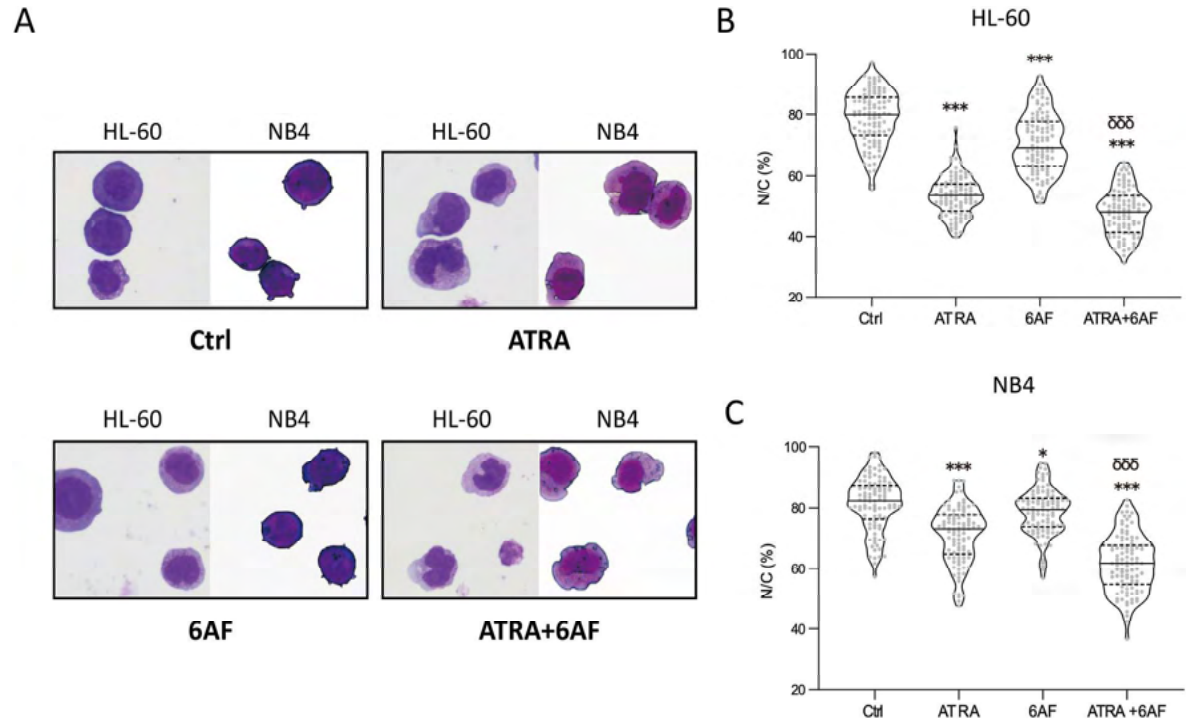


**Fig. 4.** Morphological analyses of HL-60 and NB4 cells treated with ATRA and/or 6AF. (A) HL-60 and NB4 cells were collected and processed for Wright–Giemsa staining. The magnification in the panels is × 400. (B) One hundred cells in each sample were evaluated. The nucleus and cytoplasm areas were measured using Image J software and are shown as a violin plot. *p < 0.05, ***p < 0.001 vs. Ctrl; δδδp<0.001 vs. ATRA.

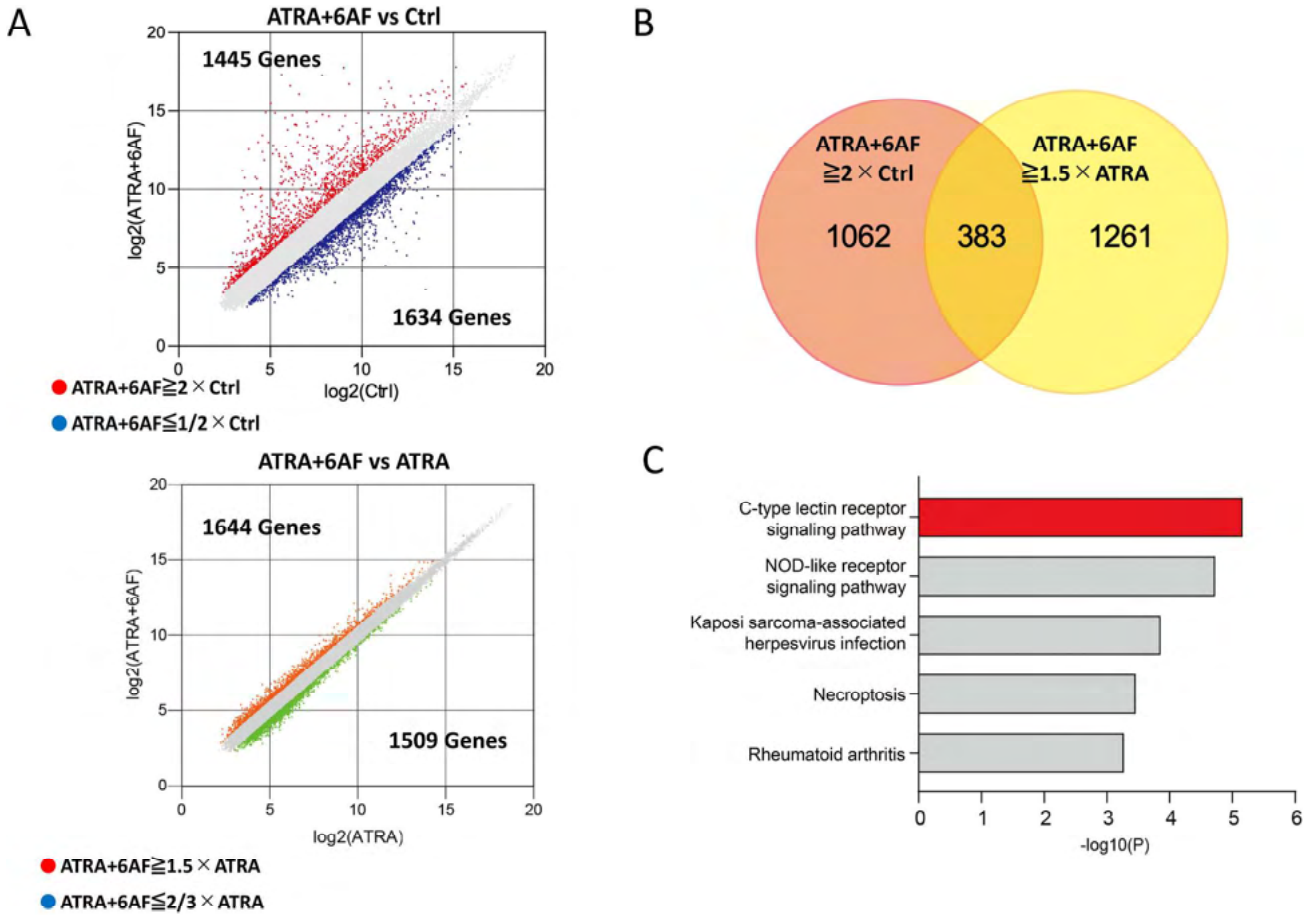


**Fig. 5.** Results of the microarray analyses. (A) Gene expression profiles in NB4 cells comparing ATRA+6AF-treated cells versus control cells (upper panel) and ATRA+6AF-treated cells versus ATRA-treated cells (lower panel). (B) The numbers of upregulated genes in the groups were presented as a Venn diagram. There were 383 commonly affected genes in the two groups. (C) Pathway analysis results using DAVID software (https://david.ncifcrf.gov/home.jsp) for the 383 genes. The X-axis shows the number of the negative log10 p-values. As the number increases, the significance increases.

(Fig. 5A, lower panel). Among the 1445 genes upregulated in ATRA-+6AF-treated cells versus control cells and 1664 genes upregulated in ATRA+6AF-treated cells versus ATRA-treated cells, there were 383 commonly induced genes (Fig. 5B). We subjected these 383 genes to pathway analysis using DAVID software, and found that the C-type lectin receptor (CLR) signaling pathway was enriched with high significance (Fig. 5C). Therefore, we focused on this pathway. Fig. S3 shows the CLR signaling pathway analysis results using the KEGG pathway database evaluated by DAVID software. The red stars indicate genes whose expression levels were upregulated by ≥ 2-fold in ATRA+6AF-treated cells compared with control cells. A list of the genes in the CLR signaling pathway based on the above analysis is shown in Table S2. Similarly, Figs. S4 and S5 show the pathway analysis results for the Fcγ receptor-mediated phagocytosis pathway and FcεRI signaling pathway, respectively. The lists of the genes in these pathways are shown in Tables S3 and S4, respectively. Among the genes in these pathways, we selected 17 genes (Tables S2–S4, bold) and verified them by real-time PCR. In NB4 cells (Fig. 6), *Interferon regulatory factor (IRF)1*, *Caspase (CASP)1*, *IL-1β*, *Early growth response protein (EGR)3*, *C-type lectin domain-containing (CLEC)6A*, *CLEC7A*, *Lymphocyte-specific protein (LSP)-1*, *FcεRIγ*, *vav guanine nucleotide exchange factor (VAV)1*, *CD45*, and *AKT3* were significantly upregulated by 6AF in ATRA-induced differentiation than ATRA alone. We further confirmed these results using HL-60 cells (Fig. 7), and found that *CASP1*, *IL-1β*, *EGR2*, *EGR3*, *CLEC6A*, *CLEC7A*, *FcεRIγ*, *CD45*, and *AKT3* were significantly induced by 6AF in ATRA-induced differentiation than ATRA alone. Collectively, *CASP1*, *IL-1β*, *EGR3*, *CLEC6A*, *CLEC7A*, *FcεRIγ*, *CD45*, and *AKT3* are commonly induced genes by 6AF. These findings suggest that the CLR signaling pathway is involved in the 6AF effect on ATRA-induced differentiation.

## 4. Discussion

Several fucosylation inhibitors have been demonstrated to exhibit therapeutic benefits for different diseases. For example, 2-F-fucose was found to deplete the cellular GDP-fucose pool in a similar manner to 6-Alk-fucose [26]. Advantages of 2-F-fucose were shown for malignant diseases, such as cancers [27], melanoma metastasis [28], and hepatoma invasion [16]. Benefits of 2-F-fucose were also confirmed for *in vivo* mouse models of cancers and sickle cell diseases [27,29]. Furthermore, oral administration of 2-F-fucose in mice showed promising results for inhibition of fucosylation on neutrophil adhesion glycans, tumor xenograft membranes, and endogenously produced antibodies [27]. In the same study, oral 2-F-fucose treatment led to complete protection against tumor engraftment and inhibition of neutrophil extravasation, while 2-F-fucose treatment in immune-deficient mice delayed the outgrowth of tumor xenografts. These findings suggest that fucosylation inhibitors are promising agents not only for basic research but also in clinical settings. Many types of cancers, including lung, breast, ovarian, liver, and prostate cancers, express abnormally high levels of fucosylated glycans [30], and upregulated levels of fucosylation were shown to be required for metastasis and cancer growth [31,32].

In the present study, we found that the CLR signaling pathway was

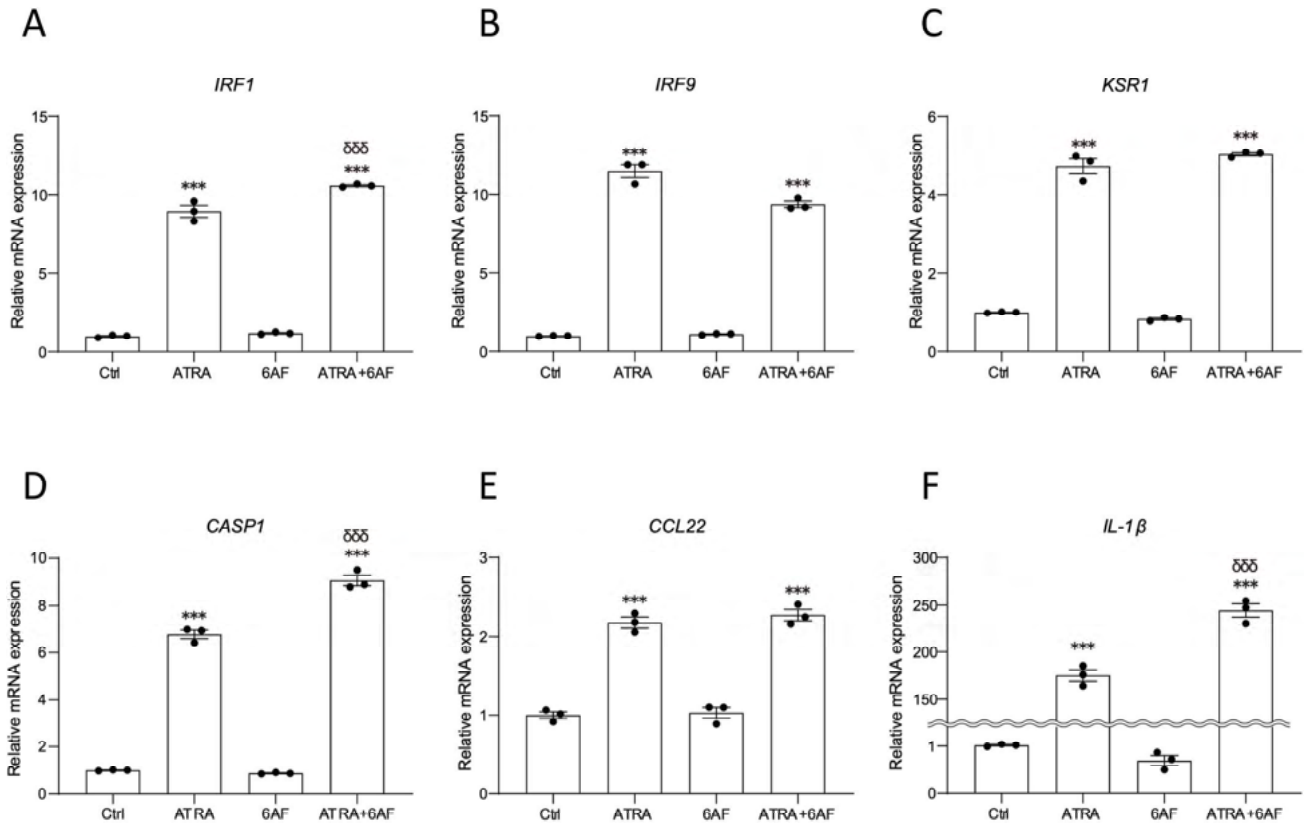


**Fig. 6.** Validation of the microarray results for the selected genes in NB4 cells. Total RNAs from NB4 cells cultured with or without ATRA and/or 6AF for 72 h were analyzed by real-time PCR. (A) *IRF1*, (B) *IRF9*, (C) *KSR1*, (D) *CASP1*, (E) *CCL22*, (F) *IL-1β*, (G) *EGR2*, (H) *EGR3*, (I) *CLEC6A*, (J) *CLEC7A*, (K) *LSP1*, (L) *FcεRIγ*, (M) *VAV1*, (N) *PIK3CD*, (O) *CD45*, (P) *AKT3*, (Q) *RAC2*. The data shown were obtained from three independent PCR amplifications. The reproducibility was confirmed using different cDNA batches. Two-way ANOVA followed by Tukey's multiple comparisons test was employed for statistical analyses. **p < 0.01, ***p < 0.001 vs. Ctrl; δp<0.05, δδp<0.01, δδδp<0.001 vs. ATRA.

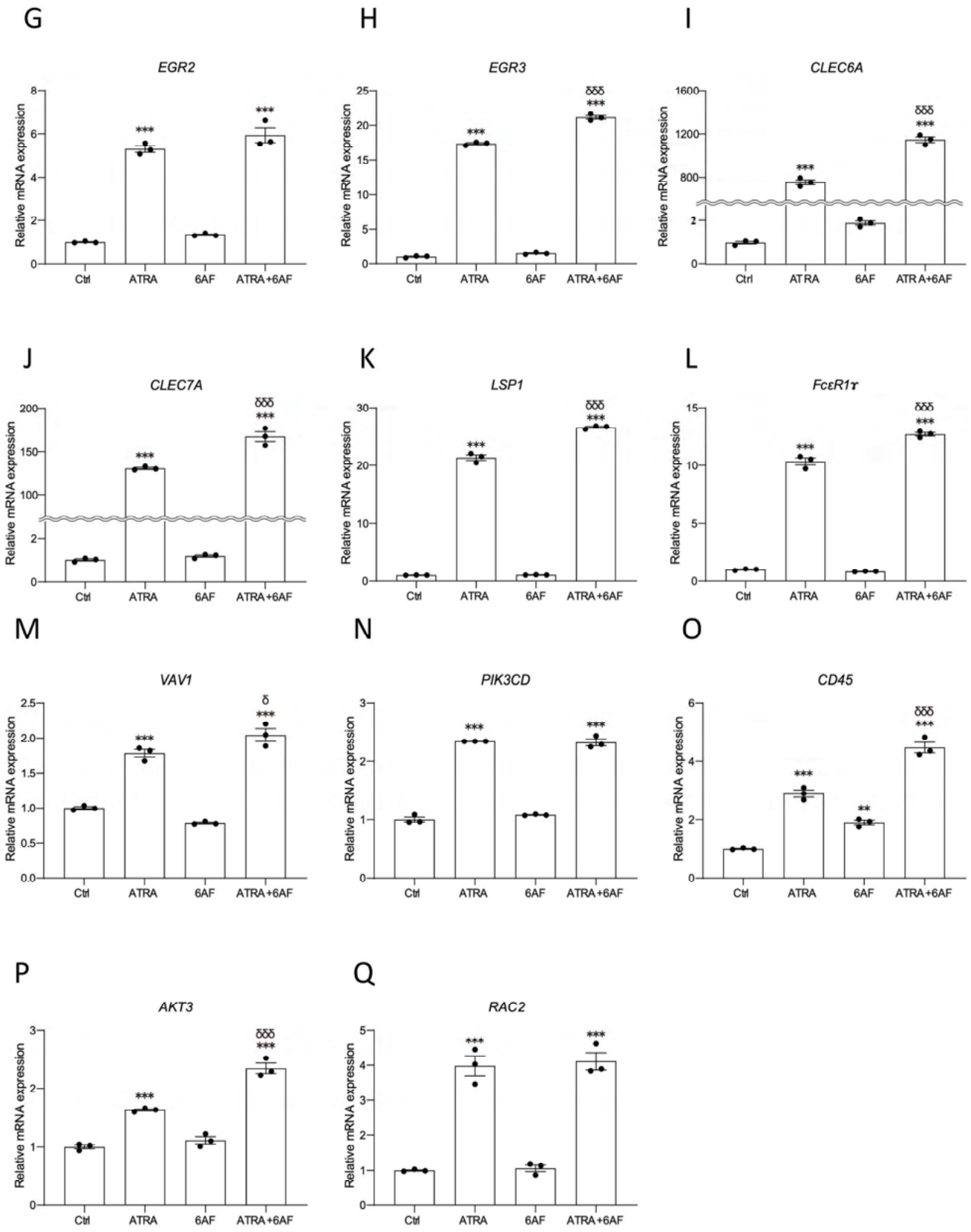


**Fig. 6.** (*continued*).

affected by 6AF and ATRA-induced differentiation. It was reported that a lack of fucose on IgG1 or IgE resulted in potent enhancement of the binding to FcγRIIIA [33–35] or FcεRI [36], respectively. Meanwhile, afucosylated antibodies exhibit increased antibody dependent cellular cytotoxicity activity through an increase in their affinity for FcγRIIIA [33]. Therefore, the addition of 6AF can enhance the binding of immunoglobulins to their Fc receptors, which may lead to activation of Fc receptor downstream signaling pathways.

CASP1 was the first identified human homolog of the *Caenorhabditis elegans* death gene, *Ced-3*, and is also known as IL-1β-converting enzyme (ICE) [37]. The expression levels of *CASP1* and *IL-1β* were increased during ATRA-induced differentiation [38]. Inflammatory cytokines such as IL-1β, adhesion molecules, L-selectin, intercellular adhesion molecule-1, and tumor necrosis factor (TNF)-α are known to be upregulated during APL cell differentiation [39,40]. In the present study, we revealed that the expression levels of *CASP1* and especially *IL-1β* were potently increased by 6AF during ATRA-induced differentiation of HL-60 and NB4 cells. Therefore, we consider that IL-1β may play an important role in the enhancing effect of 6AF on ATRA-induced differentiation.

Marshall et al. [38] reported that a tetrapeptide CASP1 inhibitor, YVAD-CMK, could block the expression of mature IL-1 and CASP1 activity. Specifically, they showed that YVAD-CMK could specifically block ATRA-induced differentiation but did not affect Lipopolysaccharide-induced inhibition of apoptosis. These findings suggest that CASP1 exerts an apoptotic effect on ATRA-induced differentiation. Consistent with this notion, Gianni et al. [41] revealed that caspase activation was essential for ATRA-induced apoptosis, given the inhibition by the caspase inhibitor z-VAD. Furthermore, overexpression of CASP1 was shown to trigger APL cell pyroptosis and differentiation [42]. Collectively, these observations indicate that caspase activation is essential for ATRA-induced apoptosis.

Billottet et al. [43] demonstrated that AKT was activated during ATRA-induced differentiation of NB4 cells, consistent with our microarray results. They reported that class I phosphoinositide 3-kinase (PI3K) inhibition blocked the activation of PI3K/AKT/mammalian target of rapamycin signaling, reduced proliferation, and induced apoptosis. Recently, sequential treatment with ATRA plus PI3K/AKT inhibitors was reported to be an efficient strategy for AML therapy [44].

Fig. 8 shows a schematic representation of the proposed mechanisms for the effect of 6AF-mediated inhibition of fucosylation on enhancement of ATRA-induced differentiation. From the microarray results, activation of the CLR pathway and its downstream CASP1, IL-1β, EGR, and other pathways including CD45 and AKT are induced by 6AF under ATRA-induced differentiation. A combination of ATRA and 6AF, plus inhibitors of kinases such as AKT, maybe the next step for future therapies for AML.

## Data availability statement

The data that support the findings of this study are openly available in the NCBI Gene Expression Omnibus (http://www.ncbi.nlm.nih.gov/geo/) under the GEO series accession number GSE234103, and are provided in the supplementary material of this article.

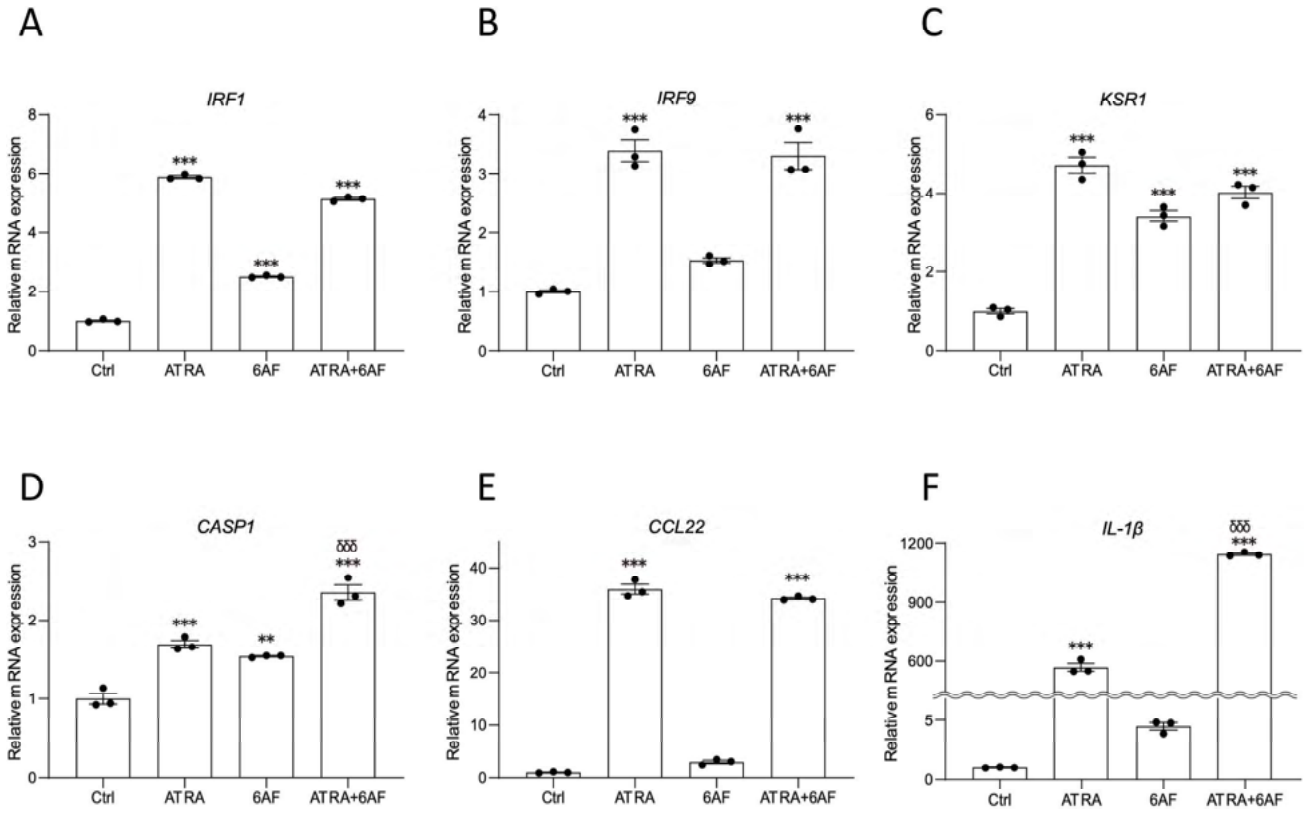


**Fig. 7.** Validation of the microarray data for the selected genes in HL-60 cells. Similar to Fig. 6. Total RNAs from HL-60 cells cultured with or without ATRA and/or 6AF for 72 h were analyzed by real-time PCR. (A) *IRF1*, (B) *IRF9*, (C) *KSR1*, (D) *CASP1*, (E) *CCL22*, (F) *IL-1β*, (G) *EGR2*, (H) *EGR3*, (I) *CLEC6A*, (J) *CLEC7A*, (K) *LSP1*, (L) *FcεRIγ*, (M) *VAV1*, (N) *PIK3CD*, (O) *CD45*, (P) *AKT3*, (Q) *RAC2*. The data shown were obtained from three independent PCR amplifications. The reproducibility was confirmed using different cDNA batches. Two-way ANOVA followed by Tukey's multiple comparisons test was employed for statistical analyses. **p < 0.01, ***p < 0.001 vs. Ctrl; δδp<0.01, δδδp<0.001 vs. ATRA.

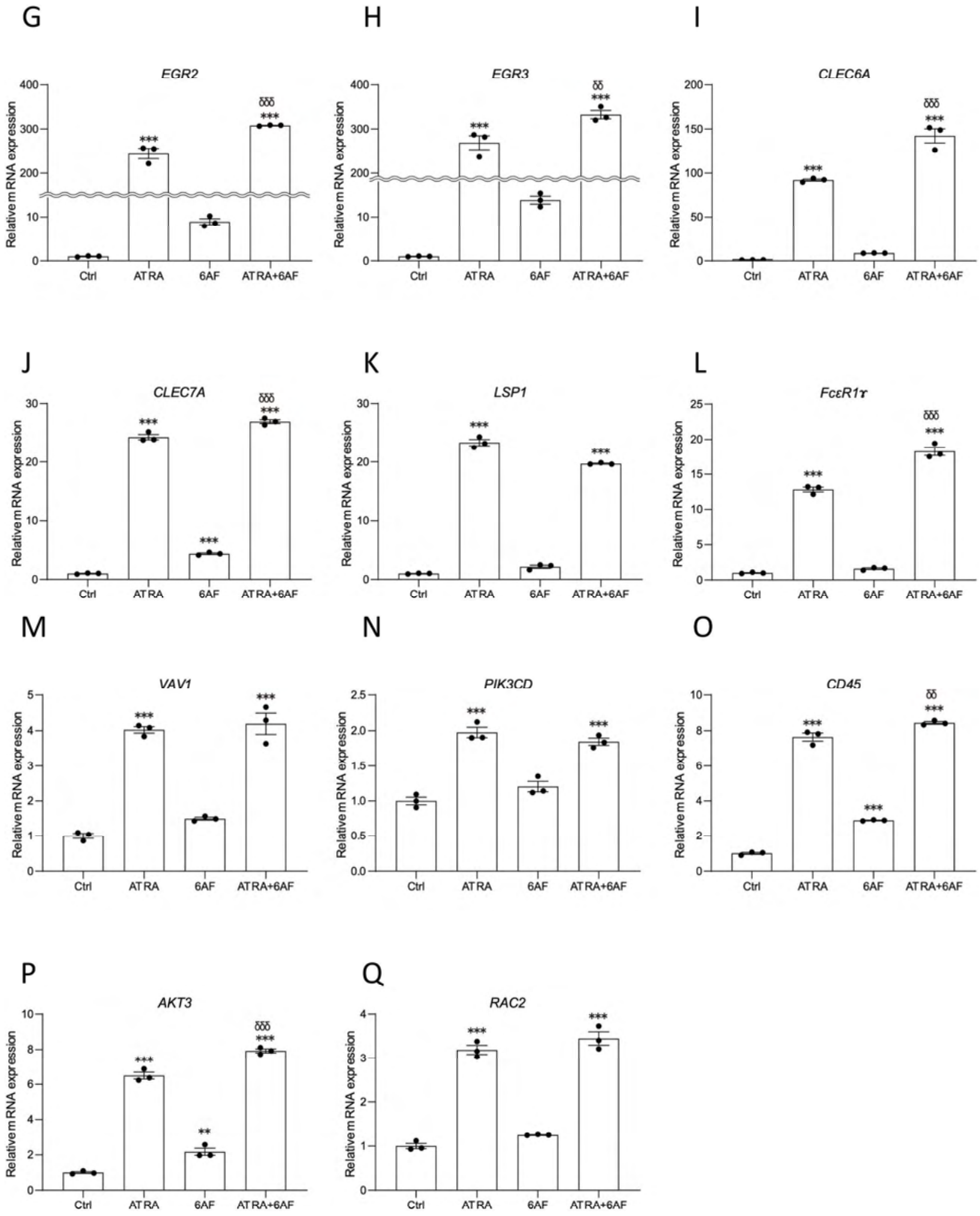


**Fig. 7.** (*continued*).

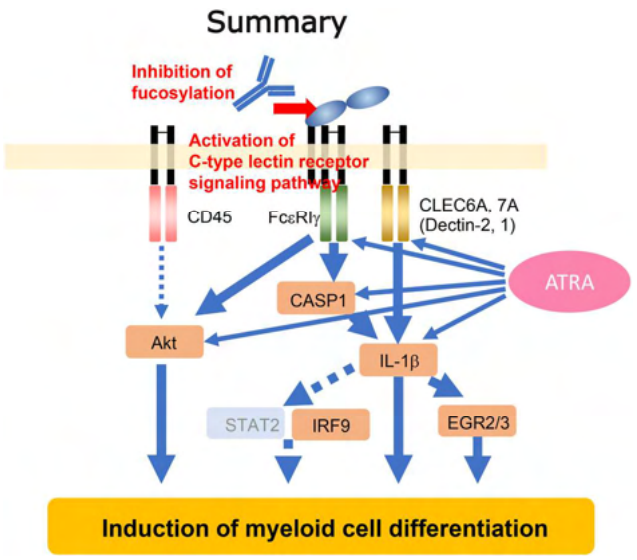


**Fig. 8.** Summary of the molecular mechanisms for the effect of 6AF on the ATRA-induced differentiation of myeloid leukemia cells. Inhibition of fucosylation leads to activation of the CLR signaling pathway, CD45, FcεRIγ, CLEC6A, and CLEC7A, resulting in activation of downstream signaling pathways such as CASP1, IL-1β, EGR2/3, and AKT. Confirmed molecules are shown in brown, while unconfirmed molecules are shown in light blue. The pathways enhanced by ATRA and 6AF are shown as thick lines. (For interpretation of the references to colour in this figure legend, the reader is referred to the Web version of this article.)

## Funding

This work was supported in part by Grants-in-Aid for Scientific Research (21K07346 to S.T., 23H02440 to J.G., 22K06615 to T.I., and 21K06547 to T.F.) from the Ministry of Education, Science and Culture, Japan, Kyowa-Kirin Research Support (Kyowa-Kirin Co. Ltd.) to S.T., and Daiichi-Sankyo Research Support (Daiichi-Sankyo Inc.) to S.T.

## CRediT authorship contribution statement

**Susumu Suzuki:** Investigation, Data curation. **Jianwei Liu:** Investigation. **Yuri Sato:** Investigation. **Rikuto Miyake:** Investigation. **Souma Suzuki:** Investigation. **Yoko Okitsu:** Investigation. **Tomohiko Fukuda:** Writing – review & editing, Investigation, Funding acquisition. **Tomoya Isaji:** Writing – review & editing, Investigation, Funding acquisition. **Jianguo Gu:** Writing – review & editing, Writing – original draft, Funding acquisition. **Shinichiro Takahashi:** Writing – review & editing, Writing – original draft, Resources, Project administration, Funding acquisition, Formal analysis, Data curation, Conceptualization.

## Declaration of competing interest

The authors declare that they have no known competing financial interests or personal relationships that could have appeared to influence the work reported in this paper.

## Acknowledgments

The authors thank Alison Sherwin, PhD, from Edanz (https://jp.edanz.com/ac) for editing a draft of this manuscript.

## Appendix A. Supplementary data

Supplementary data to this article can be found online at https://doi.org/10.1016/j.bbrc.2024.149541.

## References

[1] H. Dohner, D.J. Weisdorf, C.D. Bloomfield, Acute myeloid leukemia, N. Engl. J. Med. 373 (2015) 1136–1152, https://doi.org/10.1056/NEJMra1406184.
[2] F. Lo-Coco, E. Ammatuna, The Biology of Acute Promyelocytic Leukemia and its Impact on Diagnosis and Treatment, Hematology Am Soc Hematol Educ Program, 2006, pp. 156–161, https://doi.org/10.1182/asheducation-2006.1.156, 514.
[3] P.P. Pandolfi, In vivo analysis of the molecular genetics of acute promyelocytic leukemia, Oncogene 20 (2001) 5726–5735, https://doi.org/10.1038/sj.onc.1204600.
[4] L. Di Croce, V.A. Raker, M. Corsaro, F. Fazi, M. Fanelli, M. Faretta, F. Fuks, F. Lo Coco, T. Kouzarides, C. Nervi, S. Minucci, P.G. Pelicci, Methyltransferase recruitment and DNA hypermethylation of target promoters by an oncogenic transcription factor, Science 295 (2002) 1079–1082, https://doi.org/10.1126/science.1065173.
[5] F.J. Dilworth, P. Chambon, Nuclear receptors coordinate the activities of chromatin remodeling complexes and coactivators to facilitate initiation of transcription, Oncogene 20 (2001) 3047–3054, https://doi.org/10.1038/sj.onc.1204329.
[6] M. Grunstein, Histone acetylation in chromatin structure and transcription, Nature 389 (1997) 349–352, https://doi.org/10.1038/38664.
[7] M.A. Smith, D.R. Parkinson, B.D. Cheson, M.A. Friedman, Retinoids in cancer therapy, J. Clin. Oncol. 10 (1992) 839–864, https://doi.org/10.1200/JCO.1992.10.5.839.
[8] J.M. Watts, A. Perez, L. Pereira, Y.S. Fan, G. Brown, F. Vega, K. Petrie, R.T. Swords, A. Zelent, A case of AML characterized by a novel t(4;15)(q31;q22) translocation that confers a growth-stimulatory response to retinoid-based therapy, Int. J. Mol. Sci. 18 (2017), https://doi.org/10.3390/ijms18071492.
[9] H.L. Chen, S.C. Dong, T.Z. Ju, X.P. Yang, Effect of retinoic acid on the structure of N-glycans on the surface of human hepatocarcinoma cells and its enzymatic mechanism, J. Cancer Res. Clin. Oncol. 121 (1995) 397–401, https://doi.org/10.1007/BF01212945.
[10] Z. Li, A.H. Liu, F. Liu, H.L. Chen, Modification of pentasaccharide core of surface N-glycans during differentiation of HL-60 cells, Leuk. Res. 22 (1998) 727–734, https://doi.org/10.1016/s0145-2126(98)00068-x.
[11] A. Mizoguchi, S. Takasaki, S. Maeda, A. Kobata, Changes in asparagine-linked sugar chains of human promyelocytic leukemic cells (HL-60) during monocytoid differentiation and myeloid differentiation. Decrease of high-molecular-weight oligosaccharides in acidic fraction, J. Biol. Chem. 259 (1984) 11949–11957.
[12] A. Mizoguchi, S. Takasaki, S. Maeda, A. Kobata, Changes in asparagine-linked sugar chains of human promyelocytic leukemic cells (HL-60) during monocytoid differentiation and myeloid differentiation. Appearance of high mannose-type oligosaccharides in neutral fraction, J. Biol. Chem. 259 (1984) 11943–11948.
[13] A.H. Liu, F. Liu, Z. Li, J.X. Gu, H.L. Chen, Alterations in glycosyltransferases during myeloid and monocytoid differentiation of HL-60 cells, Cell Biol. Int. 22 (1998) 545–550, https://doi.org/10.1006/cbir.1998.0293.
[14] H. Qiu, S.L. Wu, X.H. Guo, H.J. Shen, H.P. Zhang, H.L. Chen, Expression of beta1,3-N-acetylglucosaminyltransferases during differentiation of human acute myeloid leukemia cells, Mol. Cell. Biochem. 358 (2011) 131–139, https://doi.org/10.1007/s11010-011-0928-9.
[15] M. Lanotte, V. Martin-Thouvenin, S. Najman, P. Balerini, F. Valensi, R. Berger, NB4, a maturation inducible cell line with t(15;17) marker isolated from a human acute promyelocytic leukemia (M3), Blood 77 (1991) 1080–1086.
[16] Y. Kizuka, M. Nakano, Y. Yamaguchi, K. Nakajima, R. Oka, K. Sato, C.T. Ren, T. L. Hsu, C.H. Wong, N. Taniguchi, An alkynyl-fucose halts hepatoma cell migration and invasion by inhibiting GDP-fucose-synthesizing enzyme FX, TSTA3, Cell Chem. Biol. 24 (2017) 1467–1478, https://doi.org/10.1016/j.chembiol.2017.08.023, e1465.
[17] W.T. Dalton Jr., M.J. Ahearn, K.B. McCredie, E.J. Freireich, S.A. Stass, J. M. Trujillo, HL-60 cell line was derived from a patient with FAB-M2 and not FAB-M3, Blood 71 (1988) 242–247.
[18] A. Imoto, M. Okada, T. Okazaki, H. Kitasato, H. Harigae, S. Takahashi, Metallothionein-1 isoforms and vimentin are direct PU.1 downstream target genes in leukemia cells, J. Biol. Chem. 285 (2010) 10300–10309.
[19] Z.B. Hu, W. Ma, C.C. Uphoff, M. Lanotte, H.G. Drexler, Modulation of gene expression in the acute promyelocytic leukemia cell line NB4, Leukemia 7 (1993) 1817–1823.
[20] N. Hirako, H. Nakano, S. Takahashi, A PU.1 suppressive target gene, metallothionein 1G, inhibits retinoic acid-induced NB4 cell differentiation, PLoS One 9 (2014) e103282, https://doi.org/10.1371/journal.pone.0103282.
[21] X. Lu, D. Zhang, H. Shoji, C. Duan, G. Zhang, T. Isaji, Y. Wang, T. Fukuda, J. Gu, Deficiency of alpha1,6-fucosyltransferase promotes neuroinflammation by increasing the sensitivity of glial cells to inflammatory mediators, Biochim. Biophys. Acta Gen. Subj. 1863 (2019) 598–608, https://doi.org/10.1016/j.bbagen.2018.12.008.
[22] W. Gu, T. Fukuda, T. Isaji, H. Hashimoto, Y. Wang, J. Gu, alpha1,6-Fucosylation regulates neurite formation via the activin/phospho-Smad2 pathway in PC12 cells: the implicated dual effects of Fut8 for TGF-beta/activin-mediated signaling, Faseb. J. 27 (2013) 3947–3958, https://doi.org/10.1096/fj.12-225805.
[23] M. Takahashi, Y. Kizuka, K. Ohtsubo, J. Gu, N. Taniguchi, Disease-associated glycans on cell surface proteins, Mol. Aspect. Med. 51 (2016) 56–70, https://doi.org/10.1016/j.mam.2016.04.008.
[24] N. Taniguchi, Y. Kizuka, Glycans and cancer: role of N-glycans in cancer biomarker, progression and metastasis, and therapeutics, Adv. Cancer Res. 126 (2015) 11–51, https://doi.org/10.1016/bs.acr.2014.11.001.

[25] T. Isaji, Y. Kariya, Q. Xu, T. Fukuda, N. Taniguchi, J. Gu, Functional roles of the bisecting GlcNAc in integrin-mediated cell adhesion, Methods Enzymol. 480 (2010) 445–459, https://doi.org/10.1016/S0076-6879(10)80019-9.
[26] C.D. Rillahan, A. Antonopoulos, C.T. Lefort, R. Sonon, P. Azadi, K. Ley, A. Dell, S. M. Haslam, J.C. Paulson, Global metabolic inhibitors of sialyl- and fucosyltransferases remodel the glycome, Nat. Chem. Biol. 8 (2012) 661–668, https://doi.org/10.1038/nchembio.999.
[27] N.M. Okeley, S.C. Alley, M.E. Anderson, T.E. Boursalian, P.J. Burke, K. M. Emmerton, S.C. Jeffrey, K. Klussman, C.L. Law, D. Sussman, B.E. Toki, L. Westendorf, W. Zeng, X. Zhang, D.R. Benjamin, P.D. Senter, Development of orally active inhibitors of protein and cellular fucosylation, Proc. Natl. Acad. Sci. U. S.A. 110 (2013) 5404–5409, https://doi.org/10.1073/pnas.1222263110.
[28] P. Agrawal, B. Fontanals-Cirera, E. Sokolova, S. Jacob, C.A. Vaiana, D. Argibay, V. Davalos, M. McDermott, S. Nayak, F. Darvishian, M. Castillo, B. Ueberheide, I. Osman, D. Fenyo, L.K. Mahal, E. Hernando, A systems biology approach identifies FUT8 as a driver of melanoma metastasis, Cancer Cell 31 (2017) 804–819, https://doi.org/10.1016/j.ccell.2017.05.007, e807.
[29] J.D. Belcher, C. Chen, J. Nguyen, F. Abdulla, P. Nguyen, M. Nguyen, N.M. Okeley, D.R. Benjamin, P.D. Senter, G.M. Vercellotti, The fucosylation inhibitor, 2-fluoro-fucose, inhibits vaso-occlusion, leukocyte-endothelium interactions and NF-kB activation in transgenic sickle mice, PLoS One 10 (2015) e0117772, https://doi.org/10.1371/journal.pone.0117772.
[30] Y. Kizuka, N. Taniguchi, Enzymes for N-glycan branching and their genetic and nongenetic regulation in cancer, Biomolecules 6 (2016), https://doi.org/10.3390/biom6020025.
[31] C.Y. Chen, Y.H. Jan, Y.H. Juan, C.J. Yang, M.S. Huang, C.J. Yu, P.C. Yang, M. Hsiao, T.L. Hsu, C.H. Wong, Fucosyltransferase 8 as a functional regulator of nonsmall cell lung cancer, Proc. Natl. Acad. Sci. U.S.A. 110 (2013) 630–635, https://doi.org/10.1073/pnas.1220425110.
[32] Y. Wang, T. Fukuda, T. Isaji, J. Lu, S. Im, Q. Hang, W. Gu, S. Hou, K. Ohtsubo, J. Gu, Loss of alpha1,6-fucosyltransferase inhibits chemical-induced hepatocellular carcinoma and tumorigenesis by down-regulating several cell signaling pathways, Faseb. J. 29 (2015) 3217–3227, https://doi.org/10.1096/fj.15-270710.
[33] R.L. Shields, J. Lai, R. Keck, L.Y. O'Connell, K. Hong, Y.G. Meng, S.H. Weikert, L. G. Presta, Lack of fucose on human IgG1 N-linked oligosaccharide improves binding to human Fcgamma RIII and antibody-dependent cellular toxicity, J. Biol. Chem. 277 (2002) 26733–26740, https://doi.org/10.1074/jbc.M202069200.
[34] Y. Sun, S. Izadi, M. Callahan, G. Deperalta, A.T. Wecksler, Antibody-receptor interactions mediate antibody-dependent cellular cytotoxicity, J. Biol. Chem. 297 (2021) 100826, https://doi.org/10.1016/j.jbc.2021.100826.
[35] T.T. Wang, J.V. Ravetch, Functional diversification of IgGs through Fc glycosylation, J. Clin. Invest. 129 (2019) 3492–3498, https://doi.org/10.1172/JCI130029.
[36] A.C. Nyborg, A. Zacco, R. Ettinger, M. Jack Borrok, J. Zhu, T. Martin, R. Woods, C. Kiefer, M.A. Bowen, E. Suzanne Cohen, R. Herbst, H. Wu, S. Coats, Development of an antibody that neutralizes soluble IgE and eliminates IgE expressing B cells, Cell. Mol. Immunol. 13 (2016) 391–400, https://doi.org/10.1038/cmi.2015.19.
[37] J. Yuan, S. Shaham, S. Ledoux, H.M. Ellis, H.R. Horvitz, The C. elegans cell death gene ced-3 encodes a protein similar to mammalian interleukin-1 beta-converting enzyme, Cell 75 (1993) 641–652, https://doi.org/10.1016/0092-8674(93)90485-9.
[38] J.C. Marshall, S.H. Jia, J. Parodo, R.W. Watson, Interleukin-1beta mediates LPS-induced inhibition of apoptosis in retinoic acid-differentiated HL-60 cells, Biochem. Biophys. Res. Commun. 369 (2008) 532–538, https://doi.org/10.1016/j.bbrc.2008.02.044.
[39] S. Matikainen, H. Tapiovaara, A. Vaheri, M. Hurme, Activation of interleukin-1 beta gene expression during retinoic acid-induced granulocytic differentiation of promyeloid leukemia cells, Cell Growth Differ. 5 (1994) 975–982.
[40] H.C. Hsu, W.H. Tsai, P.G. Chen, M.L. Hsu, C.K. Ho, S.Y. Wang, In vitro effect of granulocyte-colony stimulating factor and all-trans retinoic acid on the expression of inflammatory cytokines and adhesion molecules in acute promyelocytic leukemic cells, Eur. J. Haematol. 63 (1999) 11–18, https://doi.org/10.1111/j.1600-0609.1999.tb01844.x.
[41] M. Gianni, I. Ponzanelli, L. Mologni, U. Reichert, A. Rambaldi, M. Terao, E. Garattini, Retinoid-dependent growth inhibition, differentiation and apoptosis in acute promyelocytic leukemia cells. Expression and activation of caspases, Cell Death Differ. 7 (2000) 447–460, https://doi.org/10.1038/sj.cdd.4400673.
[42] X. Yu, X. Liu, X. Liu, S. Jin, M. Zhong, D. Nie, X. Zeng, X. Wang, J. Tan, Y. Li, C. Zeng, Overexpression of CASP1 triggers acute promyelocytic leukemia cell pyroptosis and differentiation, Eur. J. Pharmacol. 945 (2023) 175614, https://doi.org/10.1016/j.ejphar.2023.175614.
[43] C. Billottet, L. Banerjee, B. Vanhaesebroeck, A. Khwaja, Inhibition of class I phosphoinositide 3-kinase activity impairs proliferation and triggers apoptosis in acute promyelocytic leukemia without affecting atra-induced differentiation, Cancer Res. 69 (2009) 1027–1036, https://doi.org/10.1158/0008-5472.CAN-08-2608.
[44] K. Wang, Z. Ou, G. Deng, S. Li, J. Su, Y. Xu, R. Zhou, W. Hu, F. Chen, The translational landscape revealed the sequential treatment containing ATRA plus PI3K/AKT inhibitors as an efficient strategy for AML therapy, Pharmaceutics 14 (2022), https://doi.org/10.3390/pharmaceutics14112329.

＜神経科学＞
教授　松坂義哉
准教授　坂本一寛
助教　西村嘉晃

## 機械学習による大規模ニューロンデータの解析

ヒトを含む高等動物は状況の変化に対応して様々な知的行動を学習し、随時使い分けていくことができる。しかし、個体が一生のうちに直面する知的課題はほぼ無限大の可能性があり、その内容をあらかじめ予想することは困難である。一方で、我々の神経回路を構成するニューロンの数は有限であり、しかも海馬歯状回や脳室周囲など一部の神経組織を例外として、生後にニューロンが新生することはない。よって脳は限られた数のニューロンであらゆる事態に対処しなくてはならないことから、一つ一つのニューロンが多面的な機能を持って様々な知的行動を可能にしていると予想できる。

そこで我々はマルチタスクを遂行しているときのニホンザルの神経活動データを機械学習によってクラスター分析し、タスク間でニューロンの特性がどう変化するかを調べた。タスク遂行に関わる要素とそれに対応するニューロンの特性には膨大な組み合わせができ、更にそのようなタスクを複数行う条件下では、タスクの数だけ要素の数が増加する。機械学習によるパターン認識は多数の特性値を持つデータの中から関連する集団を検出する有力な手段である。データ解析の結果、大多数のニューロンはタスクに応じてその特性を変化させることが判明した。このことから、神経系はニューロンの機能を柔軟に切換えることによってマルチタスクの実行を可能にしていることが示唆された。また、個別タスクの遂行に関わるニューロン集団とは独立して、今どのタスクを遂行しているかというタスク情報自体をコードするニューロンの集団が同定された。

行動神経科学研究では、神経回路の活動から生物の知的行動が生じる仕組みの理解を目的とする。しかし、高度な知的行動の仕組みを研究することに伴う実験デザインの複雑化、および実験技術の進歩は解析対象とするデータの複雑化・多次元化と量的な増大という問題をもたらした。動物の行動は単一ニューロンではなく、関連する性質を持つ複数のニューロン集団(クラスター)が関わっていると考えられるが、従来の方法では膨大なデータの中からクラスターを見つけ出すのは限界があった。我々は機械学習によるデータマイニングを行動神経科学研究の他の分野にも応用し、知的行動の生成にかかわる神経機構の解明を目指している。

＜学会発表と講演＞

経路探索課題における背側運動前野と外側前頭前野の機能分化

坂本 一寛, 鈴木 萌々華, 斎藤 尚宏, 吉田 隼, 虫明 元

第 47 回日本神経科学退会, 福岡, 2024 年 7 月, 3P126

形操作課題遂行中のサル背側運動前野の局所場電位の解析

Analysis of local field potentials in the dorsal premotor cortex of the monkey during a shape-manipulation task

○廣中 高太郎 1、坂本 一寛 2,3、川口 典彦 3、虫明 元 3、池田 和司 1

第 102 回日本生理学学会大会, 2025 年 3 月, 千葉, 3P069

経路探索課題遂行中のサル背側運動前野の神経細胞は行動を多重に準備する

Neurons in the monkey dorsal premotor cortex prepare actions in different ways during a pathway planning task

○坂本 一寛 1,2、斎藤 尚宏 2、鈴木 萌々華 1、虫明 元 2

第 102 回日本生理学学会大会, 2025 年 3 月, 千葉, 3P070